Los Alamos
NATIONAL LABORATORY

Theoretical Division
Special Feature 2004

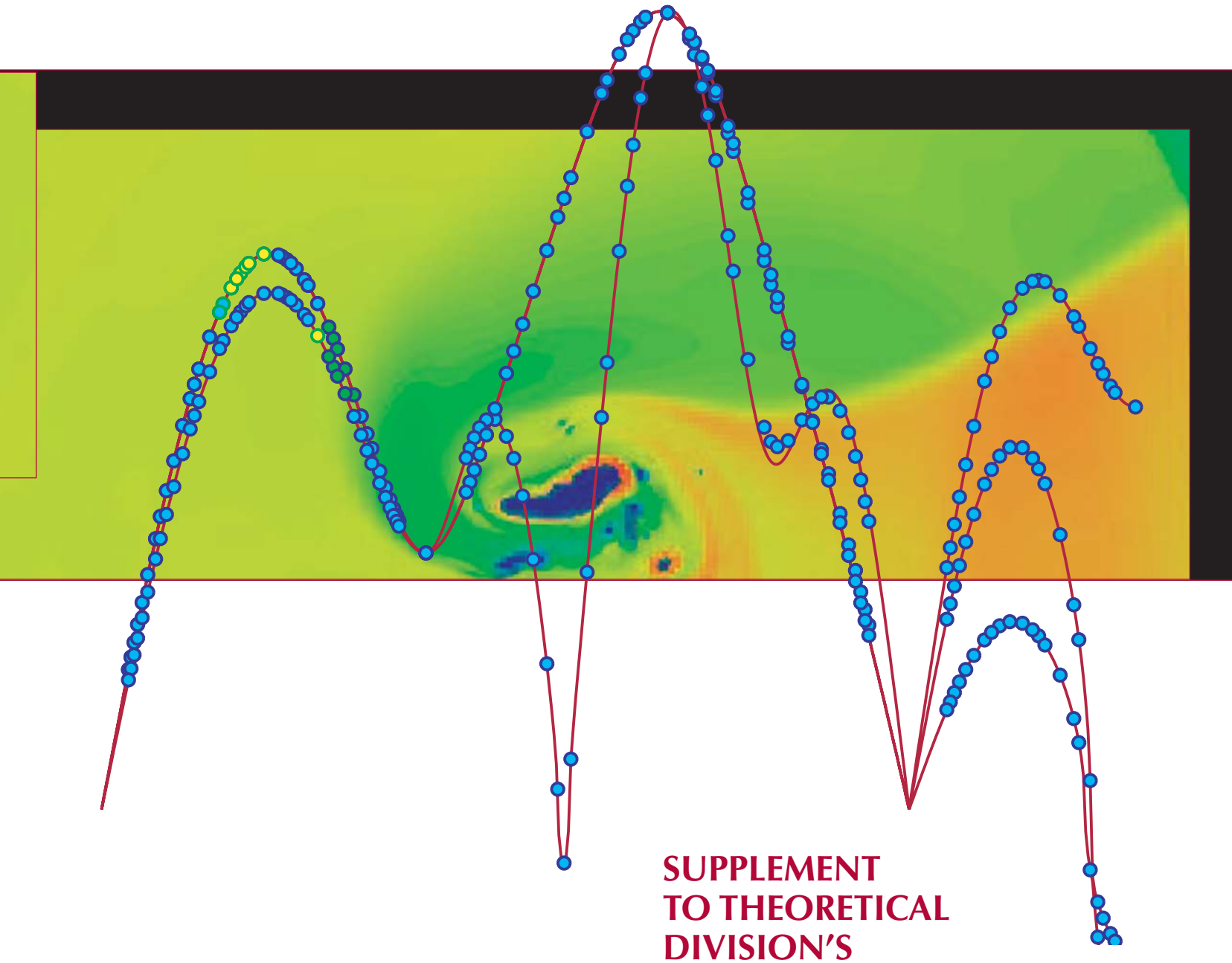

SUPPLEMENT TO THEORETICAL DIVISION'S SELF-ASSESSMENT

LA-UR-04-2143

Published by Los Alamos National Laboratory, Theoretical Division

Publication Design: Shirley Veenis
Proof Editor: Jody Shepard

LA-UR-04-02143

A U.S. Department of Energy Laboratory

Theoretical Division Special Feature 2004

Supplement to Theoretical Division's Self-Assessment

Theoretical Division Leader
Alan R. Bishop

Theoretical Division Deputy Division Leader
Paul J. Dotson

Los Alamos NATIONAL LABORATORY

A U.S. Department of Energy Laboratory. This paper is a portion of LA-UR-04-2143, April 2004.

Theoretical Division Featured Groups

T-3 Fluid Dynamics

W. Brian VanderHeyden, Group Leader
Mark W. Schraad, Deputy Group Leader

T-7 Mathematical Modeling and Analysis

J. Mac Hyman, Group Leader
Joel E. Dendy, Deputy Group Leader

T-10 Theoretical Biology and Biophysics

Angel E. García, Group Leader
Chang-Shung Tung, Deputy Group Leader

T-13 Complex Systems

David H. Sharp, Group Leader
Gennady P. Berman, Deputy Group Leader

T-15 Plasma Theory

Alan H. Glasser, Group Leader

Contents

T-3 Fluid Dynamics

Modeling Phase Transformations in Solids, 4
Francis L. Addessio, T-3; and Dennis B. Hayes, DX-2

Climate, Ocean, and Sea-Ice Modeling, 6
John R. Baumgardner, John K. Dukowicz, Elizabeth C. Hunke, Philip W. Jones, William H. Lipscomb, Mathew E. Maltrud, and Richard D. Smith, T-3

Shear Localization in Tantalum Top Hat Samples, 8
Curt A. Bronkhorst and Paul J. Maudlin, T-3; and Ellen K. Cerreta and George T. Gray III, MST-8

Sea Ice and Climate, 10
Elizabeth C. Hunke and William H. Lipscomb, T-3

Transition Theory for Fragmentation of Solid Bodies, 12
Bryan A. Kashiwa and Rick M. Rauenzahn, T-3

Nonequilibrium Thermodynamics for Granular System and Its Application to Grain-Binder Composites, 14
Xia Ma and Duan Z. Zhang, T-3

Ocean Biogeochemistry, 16
Mathew E. Maltrud, T-3

Eddy-Resolving Ocean Modeling, 18
Mathew E. Maltrud and Justin R. Smith, T-3

Extension of the KIVA Particle/Spray Model to Flows with Compressible Particles, 20
Peter J. O'Rourke and David J. Torres, T-3

Simulation of Multiphase Flow in Centrifugal Contactors for Process Intensification at TA-55, 22
Nely Padial-Collins and W. Brian VanderHeyden, T-3

Modeling the Dynamic Response of Disordered Cellular Materials, 24
Mark W. Schraad and Francis H. Harlow, T-3

Mathematical Models of Turbulence, 26
Michael J. Steinkamp, X-3; Francis H. Harlow, T-3; and Bernhard H. Wilde, X-2

High-Explosive Safety Study, Update II, 28
Qisu Zou, Duan Z. Zhang, W. Brian VanderHeyden, and Nely Padial-Collins, T-3

Predicting Strain Localization in Anisotropic Materials, 30
Q. Ken Zuo, Justin R. Smith, Paul J. Maudlin, and Francis L. Addessio, T-3

T-7 Mathematical Modeling and Analysis

Multilevel Accelerated Optimization for Problems in Grid Generation, 34
Markus Berndt and Mikhail J. Shashkov, T-7

Classification Modulo Invariance: Tangent Approximations and Improved Face Recognition, 36
Andy Fraser, Portland State Univ.; Nick W. Hengartner, D-1; and Kevin R. Vixie and Brendt E. Wohlberg, T-7

Curvature Estimation for Unstructured Triangulations of Surfaces, 38
Rao V. Garimella and Blair K. Swartz, T-7

Aggregate Formation in Myxobacteria, 40
Yi Jiang, T-7

Computer Arithmetic for Probability Distribution Variables, 44
Weiye Li and J. Mac Hyman, T-7

Mimetic Finite Difference Methods for Diffusion Equations on Non-Orthogonal AMR Meshes, 48
Konstantin Lipnikov and Mikhail J. Shashkov, T-7; and Jim E. Morel, CCS-2

ALE INC. New 2-D ALE Code on General Polygonal Meshes, 50
Raphaël Loubère and Mikhail J. Shashkov, T-7

Parallel, Scalable, and Robust Multigrid for Diffusion Problems on Structured Grids, 52
John D. Moulton, Travis M. Austin, Markus Berndt, Benjamin K. Bergen, and Joel E. Dendy, T-7

Mimetic Methods for Partial Differential Equations Discrete Models of Maxwell's Equations in 3-D, 54
Mikhail J. Shashkov and J. Mac Hyman, T-7; and Neil N. Carlson, Independent Consultant

Numerical Methods for Simulation of the Heating through Electromagnetic Induction, 56
Mikhail J. Shashkov, T-7; and Neil N. Carlson, Independent Consultant

A Software Component for a Sign-Preserving and Linearity–Preserving ALE Remapping Method, 58
Martin F. Staley and Mikhail J. Shashkov, T-7

Stochastic Partial Differential Equations: Predictive Modeling–Coping with Uncertainty, 62
Daniel M. Tartakovsky, T-7; and A. Guadagnini, Politecnico di Milano

Noise Sensitivity of Sparse Signal Representations, 64
Brendt E. Wohlberg, T-7

T-10 Theoretical Biology and Biophysics

Fluctuations are Crucial for Protein Function: Slaved and Semislaved Motions Control Protein Dynamics, 68
Paul W. Fenimore, Hans Frauenfelder, and Benjamin H. McMahon, T-10; and Robert D. Young, Northern Arizona Univ.

An Atomic Description of the Folding/Unfolding of Protein A, 70
Angel E. García, T-10; and Jose N. Onuchic, UC-San Diego

Nature of Structural Inhomogeneities on Folding a Helix and Their Influence on Spectral Measurements, 72
S. Gnanakaran, Robin M. Hochstrasser, and Angel E. García, T-10

Modeling Biological Signaling in T-10, 76
Byron Goldstein, James R. Faeder, and William S. Hlavacek, T-10

Design Principles of Genetic Regulatory Networks, 80
William S. Hlavacek, T-10; and Michael E. Wall, CCS-3

Investigation of Novel HIV-1 Recombinant Forms Using the Branching Index, 82
Thomas K. Leitner, T-10

Ribosome, Kinase, and Packaging RNA Modeling, 84
Chang-Shung Tung, T-10

T-13 Complex Systems

Survival of Quantum Effects for Observables after Decoherence, 88
Gennady P. Berman, T-13; Alan R. Bishop, T-DO; F. Borgonovi, Univ. Brescia, Italy; and Diego A. Dalvit, T-15

Analytic Solutions for Quantum Logic Gates and Modeling Pulse Errors in a Quantum Computer with a Heisenberg Interaction, 90
Gennady P. Berman and Dmitry I. Kamenev, T-13; and V. I. Tsifrinovich, Polytech. U., NY

Minimization of Nonresonant Effects in a Scalable Ising Spin Quantum Computer, 92
Gennady P. Berman and Dmitry I. Kamenev, T-13; and V. I. Tsifrinovich, Polytech. U., NY

Strong Effect of Doping on Laser Plasma Interaction, 94
Pavel Lushnikov and Harvey A. Rose, T-13

T-15 Plasma Theory

A System-Scale Theory for Fast Magnetic Reconnection in Plasmas, 98
Luís Chacón, T-15; and Dana A. Knoll, T-3

Shielding of a Thermionically Emitting Dust Grain, 100
Gian L. Delzanno, EES-IGPP/V; and Giovanni M. Lapenta, T-15

Random Attractor Confined by Noise, 102
John M. Finn, T-15; and E. R. Tracy, S. Richardson, and W. Cooke, College of William and Mary

The DCON Fast Fusion Stability Code, 104
Alan H. Glasser, T-15

The SEL Plasma Simulation Code, 106
Alan H. Glasser, T-15

Are Jets Emitted from Accretion Disks around Black Holes Solitons?, 108
Giovanni M. Lapenta, T-15

Plasmon Pole Approximation for Warm Dense Matter Calculations: Application to Temperature Relaxation in Nonequilibrium Systems, 110
Michael S. Murillo, T-15; and George Csanak, T-4

Exact Treatment of Ion Collective Modes in the Fermi Golden Rule Description of Temperature Relaxation, 112
George Csanak, T-4; Michael S. Murillo, T-15; and William S. Daughton, X-1

An Electrostatic Confinement Experiment to Explore the Feasibility of the Periodically Oscillating Plasma Sphere as a Plasma Confinement Device, 116
Richard A. Nebel, T-15; and J. Y. Park, S. Stange, and J. M. Taccetti, P-24

And Then it Turned out it Really was the Butler, 118
Paolo Ricci and Giovanni M. Lapenta, T-15; Jeremiah U. Brackbill, T-3; and William S. Daughton, X-1

Laboratory and Astrophysical Magnetic Helicity Injection: What do Radio Jets/Lobes have in Common with Spheromaks and Spherical Tori for Controlled Fusion?, 120
Xianzhu Tang, T-15; A. H. Boozer, Columbia Univ.; S. C. Hsu, P-24; Hui Li, X-1; and R. Raman, Washington/PPPL

Linking Kinetic and Fluid Scales: First Principle 3-D Particle Simulations of Magnetic Reconnection and Magnetic Turbulence, 122
Xianzhu Tang, T-15; and Hui Li and Kevin Bowers, X-1

Chandrasekhar Equilibria of Compact Toroids with Alfvénic Flows, 124
Xianzhu Tang, T-15; and Zhehui Wang, P-24

Other Theoretical Division Groups

T-1 Equation of State and Mechanics of Materials

John M. Wills, Group Leader

T-4 Atomic and Optical Theory

James S. Cohen, Group Leader
John J. Keady, Deputy Group Leader

T-6 Theoretical Astrophysics

Francis X. Timmes, Group Leader

T-8 Elementary Particles and Field Theory

Rajan Gupta, Group Leader

T-11 Condensed Matter and Statistical Physics

Robert C. Albers, Group Leader
Avadh Saxena, Acting Deputy Group Leader

T-12 Theoretical Chemistry and Molecular Physics

Antonio Redondo, Group Leader
Joel D. Kress, Deputy Group Leader

T-14 Explosives and Organic Materials

Edward M. Kober, Group Leader

T-16 Nuclear Physics

Mark B. Chadwick, Group Leader
Eric J. Pitcher, Deputy Group Leader

CNLS Center for Nonlinear Studies

Robert E. Ecke, Acting Center Director

T-1 Equation of State and Mechanics of Materials

Unified Model of the Gruneisen Parameter, Melting Temperature, and Shear Modulus, 128
Leonid Burakovsky, T-1; and Dean L. Preston, X-7

Equation of State Developments in T-1, 130
Eric D. Chisolm, Scott D. Crockett, Giulia De Lorenzi-Venneri, Denise C. George, J. D. Johnson, Duane C. Wallace, and John M. Wills, T-1

Estimating the Accuracy of the TFD Cold Curve, 132
Eric D. Chisolm, Scott D. Crockett, Duane C. Wallace, and John M. Wills, T-1

Extending the CCW EOS: Extending the Cold and Nuclear Contributions to High Compression, 134
Eric D. Chisolm, Scott D. Crockett, and Duane C. Wallace, T-1

Liquid Dynamics Estimates of the Viscosity Coefficient of Liquid Metals, 136
Eric D. Chisolm and Duane C. Wallace, T-1

Variation of Thermal and Cold Curve Contributions to Thermodynamic Functions along the Hugoniot, 138
Eric D. Chisolm, Scott D. Crockett, and Duane C. Wallace, T-1

Developments toward a Continuum-Level Non-Spherical Void Growth Model Using a Micro-Mechanics Basis, 140
Brad E. Clements and Eric M. Mas, T-1; and Paul J. Maudlin, T-3

Improved Continuum Models for Polymers and Associated Experiments, 142
Brad E. Clements and Eric M. Mas, T-1; Dana M. Dattelbaum, Edward B. Orler, and Eric Brown, MST-7; Philip Rae and George T. Gray III, MST-8; Stephen Sheffield and David L. Robbins, DX-2; Neil J. Henson, T-12; Eric N. Harstad, T-3; Luca A. Maciucescu and Matthew W. Lewis, ESA-WR; Holmann V. Brand, Kerri Jean Kress, and Jessica M. Ryan, X-7

A Comparison of Theory and Experiment of the Bulk Sound Velocity in Aluminum Using a Two-Phase EOS, 144
Scott D. Crockett, Eric D. Chisolm, and Duane C. Wallace, T-1

The Promise of Liquid Dynamics Theory, 146
Giulia De Lorenzi-Venneri and Duane C. Wallace, T-1

Effect of Anisotropic Interfacial Energy on Grain Boundary Distributions during Grain Growth, 148
Denise C. George and Andrew P. Kuprat, T-1; and Gregory S. Rohrer, Anthony D. Rollett, and Jason Gruber, Carnegie Mellon Univ.

Two-Mesh Computation for the Telluride Casting Project, 150
Andrew P. Kuprat, T-1

Direct Numerical Simulations of PBX 9501, 152
Eric M. Mas, Brad E. Clements, and Denise C. George, T-1

Quantum Perturbation Theory in O(N), 154
Anders M. N. Niklasson, T-1; Valery Weber, T-12;
and Matt Challacombe, T-12

Quantum-Size Induced Interface Stability in Thin Film Nanomaterials, 156
Anders M. N. Niklasson and John M. Wills, T-1; Erik Holmström, Uppsla, Sweden

Anisotropy of Magnetic Interlayer Coupling, 158
Sven P. Rudin, Anders M. N. Niklasson, and John M. Wills, T-1

First Principles Calculations for the Simulation of Nuclear Fuels, 160
Sven P. Rudin and John M. Wills, T-1

Lattice Effects in Gallium-Doped Plutonium, 162
Sven P. Rudin and John M. Wills, T-1

Stable and Unstable Phonon Modes in and around bcc Plutonium, 164
Sven P. Rudin, T-1

HMX Crystal Diameter Distributions from Image Analysis, 166
Bernd R. Schlei, T-1

Hyper-Surface Extraction in Four Dimensions, 168
Bernd R. Schlei, T-1

Magnetic Anisotropy in Strained-Layer Nanomaterials, 170
John M. Wills, Anders M. N. Niklasson, and Sven P. Rudin, T-1

T-4 Atomic and Optical Theory

ATOMIC Benchmark Opacity Calculation, 174
Joseph Abdallah, Jr., Peter Hakel, David P. Kilcrease, Norman H. Magee, Stephane F. Mazevet, and Manolo E. Sherrill, T-4; and Christopher J. Fontes
and Honglin Zhang, X-5

Time Dependent Boltzmann-Kinetic Model of the X-Rays Produced by the Ultrashort Pulse Laser Irradiation of Argon Clusters, 176
Joseph Abdallah, Jr. and George Csanak, T-4; Y. Fukuda, Y. Akahane, M. Aoyama, N. Inoue, H. Ueda, and K. Yamakawa, Advanced Photon Research Center; A. Ya. Faenov, A. I. Magunov, T. A. Pikuz, and I. Yu. Skobelev, Multicharged Ions Spectra Data Center

Benchmarking Aluminum Opacity Libraries Using Quantum Molecular Dynamics, 178
Stephane F. Mazevet, Lee A. Collins, and Norman H. Magee, T-4; Joel D. Kress, T-12; Eric D. Chisolm and Scott D. Crockett, T-1; and M. Desjourlais, Sandia National Laboratory

Quantum Molecular Dynamics Simulations of Shocked Nitrogen Oxide, 182
Stephane F. Mazevet and Lee A. Collins, T-4; Joel D. Kress, T-12; and P. Blottiau, DPTA

Generating a Portable Version of CATS, 186
Manolo E. Sherrill, T-4

T-6 Theoretical Astrophysics

Dynamo Experiment Status Report, 190
Stirling A. Colgate, T-6

The Physics of Yttrium Equivalence for Radiochemical Detectors, 192
Anna C. Hayes and Gerard Jungman, T-6

Code Verification for Thermonuclear Supernovae, 194
Peter A. Milne, T-6; Aimee L. Hungerford, CCS-4; and Christopher L. Fryer, T-6

The Distribution of Dark Matter in the Universe on Scales of 10^{10} to 10^{15} Solar Masses, 196
Michael S. Warren, T-6; and Luís F. Teodoro, T-8

T-8 Elementary Particles and Field Theory

Constraining Neutrino Masses from Cosmology, 200
Kev Abazajian and Salman Habib, T-8; Katrin Heitmann, ISR-1; Scott Dodelson, FNAL; and Eric Switzer, Princeton

Active Cooling of Atoms in Cavity QED: New Results, 202
Tanmoy Bhattacharya, Salman Habib, and Daniel Steck, T-8; Kurt Jacobs, Griffith; and Hideo Mabuchi, Caltech

A Flexible Mesh-Based Cosmology Code, 204
Salman Habib, T-8; Katrin Heitmann, ISR-1; Adam Lidz, Columbia, Univ.; Robert Ryne, LBL; and Luis F. Teodoro, T-8

A New Method for Characterizing the Lyman Alpha Forest, 206
Salman Habib, T-8; Katrin Heitmann, ISR-1; Lam Hui, FNAL; Adam Lidz, Columbia, Univ.; Michael Rauch, Carnegie Observatories; and Wallace Sargent, Caltech

Comparing State-of-the-Art Cosmology Codes, 208
Salman Habib, T-8; Katrin Heitmann, ISR-1; Paul Ricker, Illinois; and Michael S. Warren, T-6

Constraining and Testing Cosmology with Relative Pairwise Velocities of Galaxies, 210
Salman Habib and Luís F. Teodoro, T-8; Hume Feldman, Kansas, Univ.; and the SDSS Collaboration

Hunting for the Intergalactic Magnetic Field, 212
Salman Habib, T-8; Philipp Kronberg, IGPP; Yongzhong Xu, T-8; and the SDSS Collaboration

Measuring Dark Energy with Weak Gravitational Lensing, 214
Salman Habib, T-8; Derek Donley, Univ. of Pennsylvania; Katrin Heitmann, ISR-1; and Bhuvnesh Jain, Univ. of Pennsylvania

Measuring the Primordial Power Spectrum with the Lyman Alpha Forest, 216
Salman Habib, T-8; Katrin Heitmann, SR-1; Lam Hui, FNAL; Adam Lidz, Columbia, Univ.; and the SDSS Collaboration

Nonlinear and Nonequilibrium Dynamics in Geomaterials, 218
Salman Habib, T-8; Katrin Heitmann, ISR-1; David Higdon, D-1; Paul Johnson, EES-11; Donatella Pasqualini, EES-11; and James A. TenCate, EES-11

Precision Characterization of the Power Spectrum: Measuring the Baryonic Wiggles, 218
Salman Habib, T-8; Katrin Heitmann, ISR-1; Alex Szalay, Johns Hopkins; and the SDSS Collaboration

The Quantum Emergence of Chaos, 222
Salman Habib, T-8; Kurt Jacobs, Griffith; and Kosuke Shizume, Tsukuba

The Semiclassical Regime of the Chaotic Quantum-Classical Transition, 224
Salman Habib, T-8; Ben Greenbaum, Columbia, Univ.; Kosuke Shizume, Tsukuba; and Bala Sundaram, CUNY

Counts in Cells Statistics in the SDSS, 226
István Szapudi, Univ. of Hawaii; Luís F. Teodoro, T-8; Michael S. Warren, T-6; and the SDSS collaboration

Measurements of Cosmological Parameters Using Long Duration Gamma-Ray Bursts, 228
Yongzhong Xu and Salman Habib, T-8

Extracting Information from the Cosmic Microwave Background and the Galaxy Distribution: Frequency Dependence of the WMAP-SDSS Cross-Correlation, 230
Yongzhong Xu and Salman Habib, T-8; and the SDSS Collaboration

T-11 Condensed Matter and Statistical Physics

Atomistic Understanding of Ti Phase Transformations, 234
Robert C. Albers, T-11; Sven P. Rudin, T-1; S. G. Srivilliputhur, MST-8; in collaboration with M. D. Jones, SUNY-Buffalo; R. G. Hennig, D. R. Trinkle, and J. W. Wilkins, Ohio State, Univ.; and D. M. Hatch and H. T. Stokes, BY Univ.

New Pseudostructure for α-Pu, 236
M. Johan Bouchet and Robert C. Albers, T-11

Nondemolition Measurements of a Single Quantum Spin, 238
Lev Bulaevskii and Marina M. Hruska, T-11; A. Shnirman, Institüt für Theoretische Festkörperphysik Universität Karlsruhe, Germany; Darryl L. G. Smith, T-11; and Yu. Makhlin, Institüt für Theoretische Festkörperphysik Universität Karlsruhe, Germany and Landau Institute for Theoretical Physics, Russia

Atomistic Description of Rayleigh-Taylor Instabilities, 240
Kai Kadau and Peter S. Lomdahl, T-11; Timothy C. Germann, X-7; Brad Lee Holian, T-12; Guy Dimonte, X-4; Nicolas G. Hadjiconstantinou, Massachusetts Institute of Technology; and Berni Alder, Lawrence Livermore National Laboratory

Molecular-Dynamics Study of Mechanical Deformation in Nano-Crystalline Metals, 242
Kai Kadau, T-11; Timothy C. Germann, X-7; Peter S. Lomdahl, T-11; and Brad Lee Holian, T-12

Structural Phase Transitions in Ga: Massive Parallel Implementation and Application of the Modified Embedded-Atom Method, 244
Kai Kadau, T-11; Timothy C. Germann, X-7; Peter S. Lomdahl, T-11; and Brad Lee Holian, T-12

Understanding and Predicting the Initiation of DNA Transcription, 246
Kim Ø. Rasmussen, T-11; Georgios Kalosakas, T-11/CNLS; Alan R. Bishop, T-DO; and C. H. Choi and A. Usheva, Division of Endocrinology, Harvard Medical School

Elastic Moduli of Multiblock Copolymers, 248
Russell B. Thompson, Kim Ø. Rasmussen, and Turab Lookman, T-11; and Edward M. Kober, T-14

T-12 Theoretical Chemistry and Molecular Physics

Quantum Chemical and Classical Studies of The High-Pressure Phase of Teflon, 252
Holmann V. Brand, X-7; Dana M. Dattelbaum, MST-7; Jessica M. Ryan and Kerri Jean Kress, X-7; and Neil J. Henson, T-12

All-Electron Density Functional Studies of Hydrostatic Compression of Pentaerythritol Tetranitrate (PETN), 254
Chee Kwan Gan, T-12; Thomas D. Sewell, T-14; and Matt Challacombe, T-12

EPnet, an Explicit Polymer and Node Network Model to Compute Micromechanical Properties of Crosslinked and Filled Polymer Systems, 256
David E. Hanson, T-12

Theoretical Studies of Surface Chemistry and Bulk Electronic Structure of Actinide Materials, 258
P. Jeffrey Hay, Joel D. Kress, and Henry S. Ashbaugh, T-12

Conformational Dependence of a Protein Kinase Phosphate Transfer Reaction, 260
Graeme Henkelman, Matt Challacombe, and Karoly Nemeth, T-12; and Montiago LaBute, Chang-Shung Tung, Paul W. Fenimore, and Benjamin H. McMahon, T-10

How Do Hotspots Happen?, 262
Brad Lee Holian, T-12; and Timothy C. Germann, X-7

Theory and Simulation of Polymer Aging: Degradation via Free-Radical Oxidation, 264
Joel D. Kress, T-12; Mike Salazar, Union Univ.; and Russell T Pack, T-12

Fibrillar Templates and Soft Phases in Systems with Short-Range Dipolar and Long-Range Interactions, 266
Cynthia J. Reichhardt, T-12; Charles Reichhardt, T-13; and Alan R. Bishop,T-DO

Mesoscale Modeling of Nanocrystalline Metals, 268
Cynthia J. Reichhardt, Brad Lee Holian, Joel D. Kress, and Antonio Redondo, T-12

Accelerated Dynamics Study of Vacancies in Pu, 270
Blas P. Uberuaga and Arthur F. Voter, T-12; and Steven M. Valone and Michael Baskes, MST-8

Radiation-Damage Annealing in MgO, 274
Blas Pedro Uberuaga, T-12; Roger Smith, MST-8; Antony R. Cleave, Imperial College, UK; Graeme Henkelman MST-8/UK; T-12; F. Montalenti, Universitá degli Studi di Milano-Bicocca, Italy; R. W. Grimes, Imperial College, UK; Kurt E. Sickafus, MST-8; and Arthur F. Voter, T-1

T-14 Explosives and Organic Materials

Numerical Simulation of Full Densification of Foams, 280
Scott G. Bardenhagen, T-14

Numerical Simulation of Stress Wave Propagation in PBXs, 282
Scott G. Bardenhagen, T-14

The Nexus between Reactive MD Simulations of RDX and the Reactive Euler Equations, 284
Shirish M. Chitanvis, T-14

On Validating SCRAM, 286
John K. Dienes, T-14; John Middleditch, CCS-3; and Q. Ken Zuo, T-3

Fundamental Detonation Behavior from Molecular Dynamics Simulations, 288
Andrew J. Heim, T-14/UC-Davis; Timothy C. Germann, X-7; Brad Lee Holian and Edward M. Kober, T-14; and Niels G. Jensen, UC-Davis

β-HMX Isotherms at Multiple Temperatures and Liquid HMX Equation of State, 290
Eugenio Jaramillo and Thomas D. Sewell, T-14

Constitutive Model Development for Filled Polymer Systems, 292
Edward M. Kober, T-14; and James S. Smith and Grant D. Smith, Univ. Utah

Models for the Aging of Fogbank, 294
Edward M. Kober, T-14

Pore Collapse and Hot Spots, 296
Ralph Menikoff, T-14

Multiscale Mapping Techniques for Polymers, 298
Thomas D. Sewell, T-14; Kim Ø. Rasmussen and Russell B. Thompson, T-11; and Dmitry Bedrov and Grant D. Smith, Univ. of Utah

Detonation Products Equation of State, 300
M. Sam Shaw, T-14

Polymer and Foam Products Equation of State, 302
M. Sam Shaw, T-14

Energy Exchange between Mesoparticles and Their Internal Degrees of Freedom, 306
Alejandro Strachan, T-14; and Brad Lee Holian, T-12

Molecular Dynamics Studies of Reactive Processes in RDX I: Thermal Loading, 308
Alejandro H. Strachan, T-14

Molecular Dynamics Studies of Reactive Processes in RDX II: Shock Loading, 312
Alejandro H. Strachan, T-14

The Physics of SemiFlexible Polymers, 316
Paul M. Welch and Shirish Chitanvis, T-14

T-16 Nuclear Physics

The Energy Surface at a Critical Point, 320
Joseph N. Ginocchio, T-16

Data for Charged-Particle Capture Reactions, 322
Gerald M. Hale, T-16

Leptoquark Contributions to Atomic Electric Dipole Moments, 324
Peter Herczeg, T-16

Correlated Neutron Emission in Fission: Initial Results, 326
Sebastien Lemaire, Patrick Talou, Toshihiko Kawano, David. G. Madland, and Mark B. Chadwick, T-16

Fission Barriers at the End of the r-Process, 328
Peter Möller and Arnold J. Sierk, T-16; and Ragnar Bengtsson and Peter Olivius, Lund, Sweden

Potential-Energy Sufaces for Heavy-Ion Collisions, 330
Peter Möller and Arnold J. Sierk, T-16; Akira Iwamoto, Tokai, JAERI; and Takatoshi Ichikawa, Tokai, JAERI

Studies of Fission-Product Yields with Improved Data Bases for β-Decay Half-Lives and β-Delayed Neutron-Emission Probabilities (II), 334
Peter Möller and William B. Wilson, T-16

The ^{8}Be Nuclear Data Evaluation, 338
Philip R. Page and Gerald M. Hale, T-16

Iridium Nuclear Cross Sections for Radchem, 340
Patrick Talou, Mark B. Chadwick, and Robert MacFarlane, T-16; Ronald O. Nelson, LANSCE-3; Holly R. Trellue, D-5; Morgan C. White and Stephanie C. Frankle, X-5; and Nikolaos Fotiadis, LANSCE-3

New Suite of Evaluated Nuclear Reaction Cross Sections on Uranium Isotopes, 342
Phillip G. Young, Patrick Talou, Robert MacFarlane, Mark B. Chadwick, Toshihiko Kawano, David G. Madland, Peter Möller, and William B. Wilson, T-1

Theoretical Division Special Feature 2004

Supplement to Theoretical Division's Self-Assessment

Introduction

The Theoretical Division is an intellectual resource to Los Alamos National Laboratory and the nation, providing creative scientific and technological solutions to challenges in national security and related problems of national and global importance. LANL's national security mission has an enduring need for science and technology beyond today's frontiers. T-Division responds to this need by striving to provide the best science and scientists to LANL missions, pursue frontier science to ensure excellence in science capabilities, create new scientific directions, and attract scientific leaders to LANL.

Working with teams across the Laboratory, T-Division is central to the Laboratory Strategic Goals and especially the great multidisciplinary challenge of integrating theory, modeling, simulation, and visualization with experimental and other data — in a strategy to provide cutting-edge, validated tools to interpret and guide experiments and expand predictive capability and uncertainty quantification to truly complex phenomena. The core Nuclear Weapons Program, the centerpiece of the DOE Weapons Complex, depends critically on the viability of this approach. However, virtually every major initiative at LANL also relies heavily on this integrated capability — threat reduction and homeland security, manufacturing science, biology, nanoscience, energy, infrastructure, and so on.

Each year, T-Division staff self-select a collection of brief topical reports on their progress, as part of our Self-Assessment process. This collection is not intended to be complete. Rather it aims to demonstrate, through examples, the energy and progress across (and between) many disciplines in the Division in pursuit of the grand challenge of serving the Laboratory and nation by furthering our fundamental understanding of, and predictive capabilities for, complex phenomena.

Theoretical Division Leader
Alan R. Bishop

Theoretical Division Deputy Division Leader
Paul J. Dotson

T-3 Fluid Dynamics

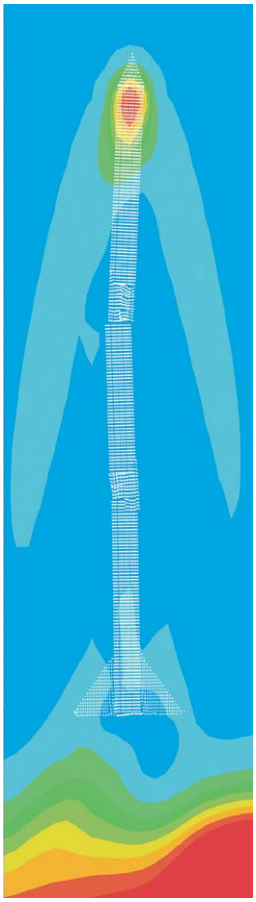

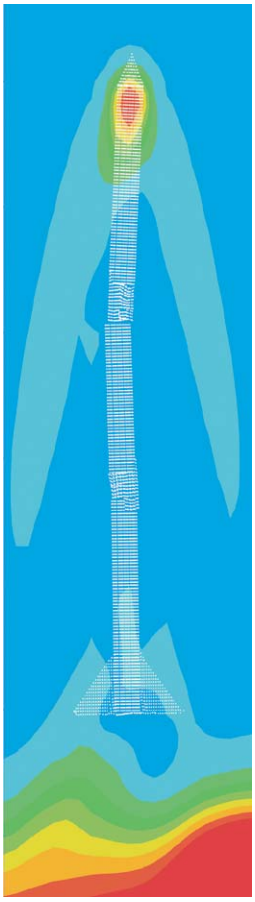

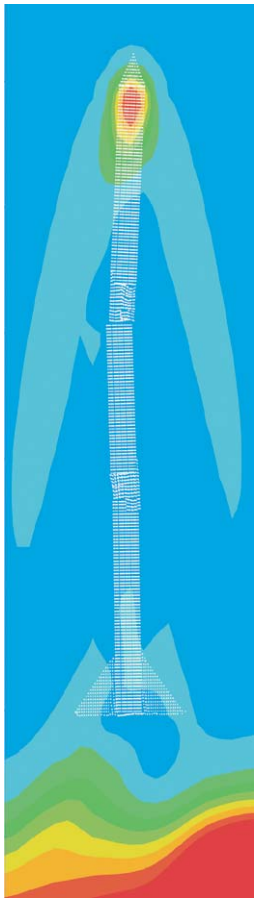

Modeling Phase Transformations in Solids

Francis L. Addessio, T-3 and Dennis B. Hayes, DX-2; in collaboration with Frank J. Cherne, DX-2; Eric D. Chisolm, T-1; Brad E. Clements, T-1; Carl W. Greeff, X-7; Eric N. Harstad, T-3; James N. Johnson, Eric M. Mas, Sven P. Rudin, and Duane C. Wallace, T-1; Todd O. Williams, T-3; John M. Wills, T-1; and Q. Ken Zuo, T-3; addessio@lanl.gov

A material model that includes phase transformations in solids is being developed. Consideration has been provided to deriving a model that is compatible with weapons engineering design computer analyses. The model is derived from thermodynamic considerations for a multi-component, multi-phase mixture. The model includes both pressure driven phase transformations [1,2] as well as shear-dominated transformations [3] that are characteristic of displacive or martensitic transitions. Consider the Helmholtz free energy

$$\psi = \sum_k \xi_k \psi_k + \psi^{mix} \qquad (1)$$

where the sum is over the material phases and ψ^{mix} accounts for the mixing of the different components and inhomogeneities in the material eigenstrains that result from phase transformations. In (1), ξ_K is the mass fraction of the k^{th} phase. The free energy for each phase is written

$$\psi_k\left(\bar{\varepsilon}_k^e, T, \varepsilon_k^p, \bar{\alpha}_k^p\right) = \psi_k^{EOS}\left(\varepsilon_k^e, T\right) + 2\nu_k\mu_k\bar{e}_k^e\bar{e}_k^e + \psi_k^p\left(\varepsilon_k^p, \bar{\alpha}_k^p\right). \qquad (2)$$

In (2), $\bar{\varepsilon}_k^e$, T, ε_k^p, $\bar{\alpha}_k^p$ are the elastic strain, temperature, effective plastic strain, and back stress, respectively. Also, μ_K and ν_K are the shear modulus and specific volume ($\nu_K=1/\rho_K$). Barred quantities are second order tensors. The first term in (2) is the component of the free energy that is used to provide the pressure versus specific volume (equation of state) response of the material. Functional forms for this term may be obtained from lattice dynamics calculations [4,5]. The second and third terms account for the deviatoric component of the deformation (shear) and inelasticity (plasticity), respectively. Included in the plastic model are strain hardening (ε^p) and a back stress ($\bar{\alpha}^p$). A back stress has been included to allow the modeling of materials that exhibit different strengths in compression and tension.

Knowing the free energy, either from a functional or tabular form, the material response may be obtained

$$\bar{\sigma} = \bar{s} - P\bar{\delta} = \rho\frac{\partial\psi}{\partial\bar{\varepsilon}^e} \qquad (3)$$

where $\bar{s}$ is the stress deviator, P is the pressure, and $\bar{\delta}$ is the Kronecker delta. The kinetics of the phase transformation is required for closure. An empirical form that will drive the system to thermodynamic equilibrium has been selected:

$$\frac{d\xi_i}{dt} = -\sum_{k\neq i}\frac{g_i - g_k}{\tau_{ik}}. \qquad (4)$$

In (4), g is the Gibbs free energy, which may be obtained from the Helmholtz free energy ($g = \psi + \nu\bar{\sigma}\bar{\varepsilon}$) and τ_{ik} is a material parameter that provides the transformation rate from phase i to phase k. A simulation, which models the response of a single computational cell in compression, is provided for bismuth in Figure 1 for different values of τ_{ik}.

In principle, this approach requires few modifications to the models that are currently being used in engineering design codes. If a free energy is not available, a formulation based on an equation of state and a strength model may be used in place of (3). A phase diagram may be used to obtain reference energies and entropies

$$de = \sum_k \xi_k \left[\frac{\partial e_k}{\partial \nu_k} d\nu_k + \frac{\partial e_k}{\partial T} dT + \frac{\partial e_k}{\partial \bar{e}^e_k} d\bar{e}^e_k + \frac{\partial e_k}{\partial \varepsilon^p_k} d\varepsilon^p_k + \frac{\partial e_k}{\partial \bar{\alpha}^p_k} d\bar{\alpha}^p_k \right] + \sum_k e_k d\xi_k + de^{mix}. \quad (5)$$

for the pure phase. However, additional terms now appear in expressions of the internal energy (e), for example: The relative magnitude of the terms that appear in (5) are under investigation, Figure 2. Currently, it appears that although the additional dissipation terms are small with respect to the terms containing the specific volume (ν_k) and the temperature, they are not negligible. Consideration is being given to implementing the model into a three-dimensional, Lagrangian, finite-element analysis.

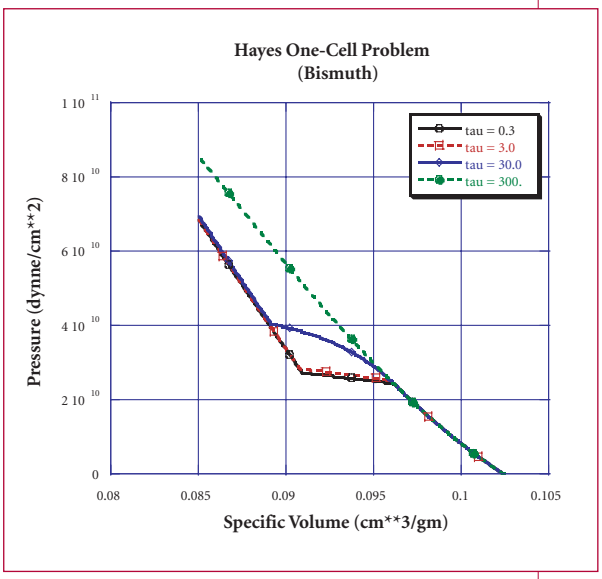

Figure 1—Simulation of a single computational cell in compression for the phase transformation of bismuth for different values of t.

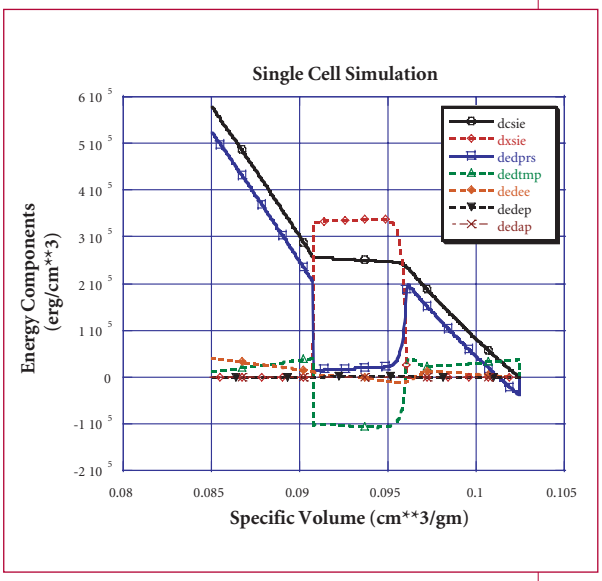

Figure 2—Investigation of the relative magnitude of terms appearing in the internal energy.

[1] D. J. Andrews, "Equation of state of the alpha and epsilon phases of iron", *J. Phys. Chem. Solids* **34**, 825 (1973).

[2] D. B. Hayes, "Wave propagation in a condensed medium with N transforming phases: Application to solid I –solid II-liquid bismuth", *J. App. Phys.* **46**, 8, 3438 (1975).

[3] F. L. Addessio, Q. H. Zuo, T. A. Mason, and L. C. Brinson, "Model for high-strain-rate deformation of uranium-niobium alloys", *J. Appl. Phys.* **93**, 12, 9644, (2003).

[4] C. W. Greeff, D. R. Trinkle, and R. C. Albers, "Shock-Induced α–ω transition in titanium", *J. Appl. Phys.* **90**, 5, 2221 (2001).

[5] J. C. Boettger and D.C. Wallace, "Metastability and dynamics of the shock-induced phase transition in iron", *Phys. Rev. B* **55**, 5, 2840, (1997).

Climate, Ocean, and Sea-Ice Modeling

John R. Baumgardner, John K. Dukowicz, Elizabeth C. Hunke, Philip W. Jones, William H. Lipscomb, Mathew E. Maltrud, and Richard D. Smith, T-3; johnrb@lanl.gov

A growing body of evidence is pointing to the likelihood that human actions may be altering the Earth's climate. While observations and historical records are suggesting the reality of climate change, computer modeling represents our most viable strategy for actually predicting future climate, and for distinguishing human-caused climate change from the climate system's own natural variability. Numerical climate models, built by coupling together individual models of the atmosphere, ocean, land, and sea ice, are becoming more consistent in their predictions and more complete in their representations of physical processes. Over the last ten years, Los Alamos has built a strong program in computer modeling of the Earth's oceans, sea ice, and climate. In particular, our development of the Parallel Ocean Program (POP), and the CICE sea-ice model as well as the application of these models in fully-coupled climate model simulations have made Los Alamos nationally recognized for ocean, sea-ice, and climate-related research.

The Los Alamos POP code is a numerical ocean circulation model designed specifically for parallel and high-performance computers. Simulations of ocean circulation with POP have successfully reproduced many aspects of the wind-driven ocean circulation, including the Gulf Stream separation from the coast at Cape Hatteras, the North Atlantic current whose path is in good agreement with float data, and an Azores current that loosely matches observations. New features in POP are correctly being introduced to improve the fidelity of deep ocean currents and long term variability associated with the thermohaline circulation—the century-scale overturning of the ocean produced by density differences due to heat (thermo) and salt (haline) content. POP also includes an ocean biogeochemistry model for studying of the uptake and redistribution of carbon dioxide and other trace gases associated with ocean plant and animal life.

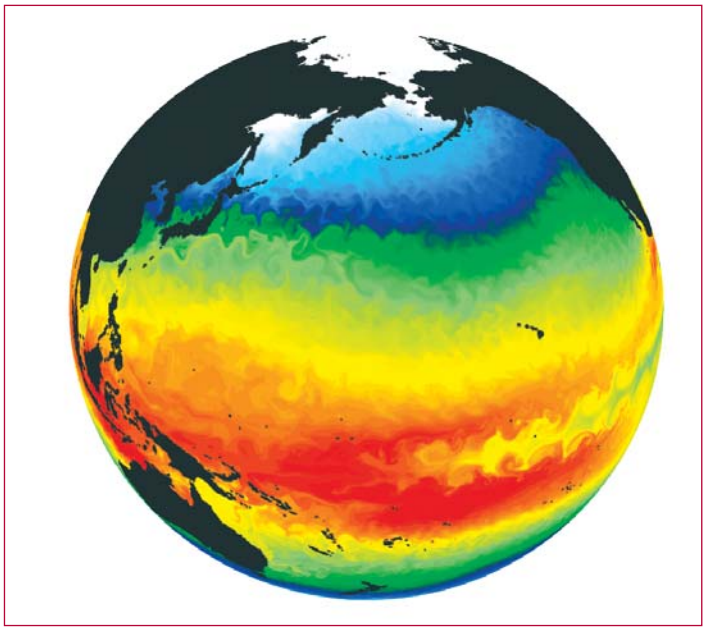

***Figure 1—** Sea surface temperature from a global 0.1-degree POP simulation.*

The Los Alamos CICE model began as an effort to improve the numerical efficiency of the calculation of internal ice stress and ice velocity. The resulting changes not only improved the computational efficiency of the model, but also improved its correspondence to physical reality. In particular, the model is more responsive to rapid changes in wind forcing. Further developments have resulted in better estimates of ice strength, growth and melt rates, surface energy, and water fluxes. An improved thermodynamics model better resolves temperature and salinity profiles and more accurately treats the energy budget within the ice. Finally, a new formulation of ice transport significantly improves the large-scale transport of ice from region to region.

The success of both POP and CICE has resulted in widespread adoption of these models throughout the climate community and has greatly expanded the user base of both models. For example, POP and CICE are used as the ocean and sea-ice components of the National Center for Atmospheric Research Community Climate System Model (CCSM), a fully coupled climate model that combines atmosphere, ocean, land, and ice components to create a simulation of the Earth's climate system. CCSM is used widely by climate researchers throughout the country and is one of the models being applied to current national and international climate assessments.

Figure 1— Sea surface temperature from a global 0.1-degree POP simulation.

Figure 2— Tripole grid and bottom topography used in coarse resolution POP simulations.

Shear Localization in Tantalum Top Hat Samples

Curt A. Bronkhorst and Paul J. Maudlin, T-3; Ellen K. Cerreta and George T. Gray III, MST-8; *cabronk@lanl.gov*

The ductile failure process for polycrystalline metals is a sophisticated sequence of physical events occurring at different length scales. One element of that process is believed to be shear localization and subsequent shear band formation. In general, the shear localization process involves initiation and growth where initiation is expected to be a stochastic process in material space where anisotropy in the elastic-plastic behavior of single crystals and inter-crystalline interactions serve to form natural perturbations to the material's local stability. A common sample geometry used by MST-8 to study shear localization growth is the "top hat." As the name implies, it is an axi-symmetric sample with an upper "hat" portion and a lower "brim" portion with the gage section between the hat and brim. Figure 1(a) shows one-half of the cross-sectional geometry (line of symmetry along Z axis) for a typical sample. The gage section length is generally on the order of 0.9 mm. The samples were deformed in a Split-Hopkinson Pressure Bar system at maximum top-to-bottom velocity in the range of 10-25 m/s We have attempted to model these experiments through both continuum and polycrystal plasticity finite element models.

Experimental and continuum model results for an initial sample temperature of -100 °C can be found in Figures 1 and 2. Figure 1 shows contour plots of equivalent plastic strain at 50 μs after the wave hits the hat. Figure 2 shows the mean top surface traction applied to the sample during loading. For the continuum model, the finite element code EPIC was used with a Mie-Gruneisen equation of state and the rate and temperature sensitive MTS flow stress model. Adiabatic conditions were assumed. The numerical results suggest a maximum strain rate on the order of 10^5 s^{-1} in the gage section. The model also suggests that a temperature in the neighborhood of 700 °C is reached within the gage section due to the substantial plastic

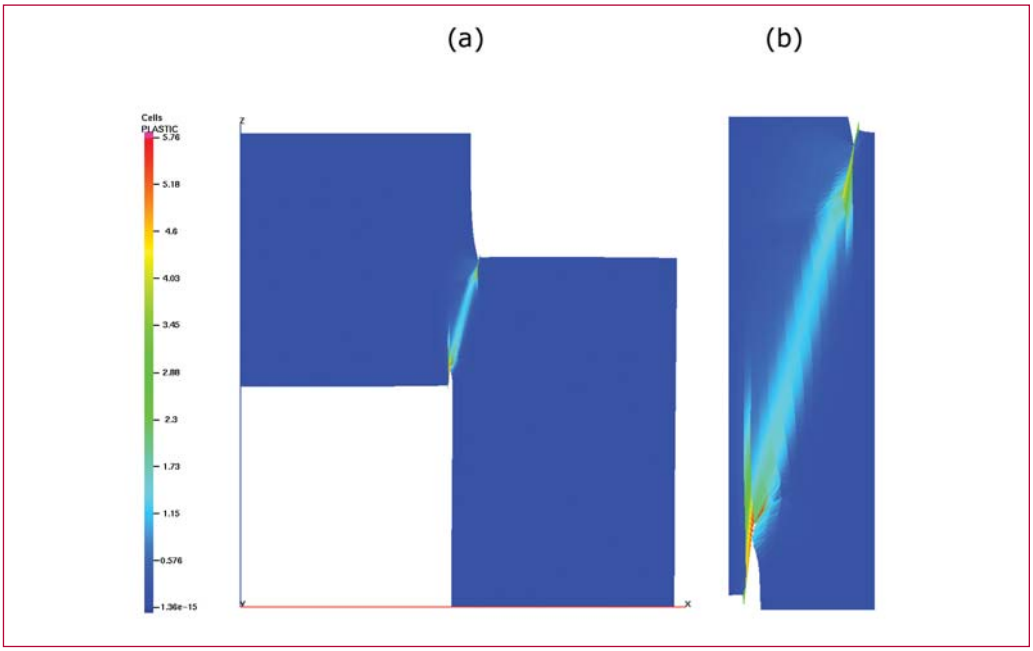

Figure 1— Total equivalent plastic strain at a time of 50 μsec for an initial temperature of -100 °C; (a) axi-symmetric continuum model; (b) gage section only.

deformation (up to 500%) that takes place over a small period of time.

Using a polycrystal plasticity approach we have attempted to link the localization behavior of these samples to the crystallographic characteristics of Tantalum. Figure 3 shows shear stress results of simulations where groups of elements were used to represent a single crystal, each group with a different initial crystallographic orientation. A total of 127 crystals spanned the gage section region. The finite element code ABAQUS along with a rate-dependent crystal plasticity model was used. The crystal plasticity model allowed for slip to occur on the twelve $\{110\}\cdot\langle 111\rangle$ and twelve $\{112\}\cdot\langle 111\rangle$ slip systems. The model determined active slip systems based upon loading conditions and crystallographic orientation. Figure 3 shows the high level of heterogeneity that one might expect in the sample gage section for a polycrystalline material. The shear stress contour results suggest a factor of three difference between high and low values.

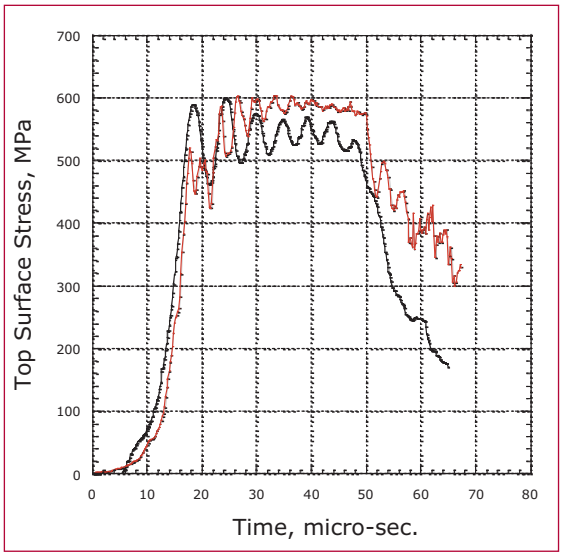

Figure 2—Experimental (black) versus continuum simulation (red) top-surface stress response for an initial sample temperature of -100 °C.

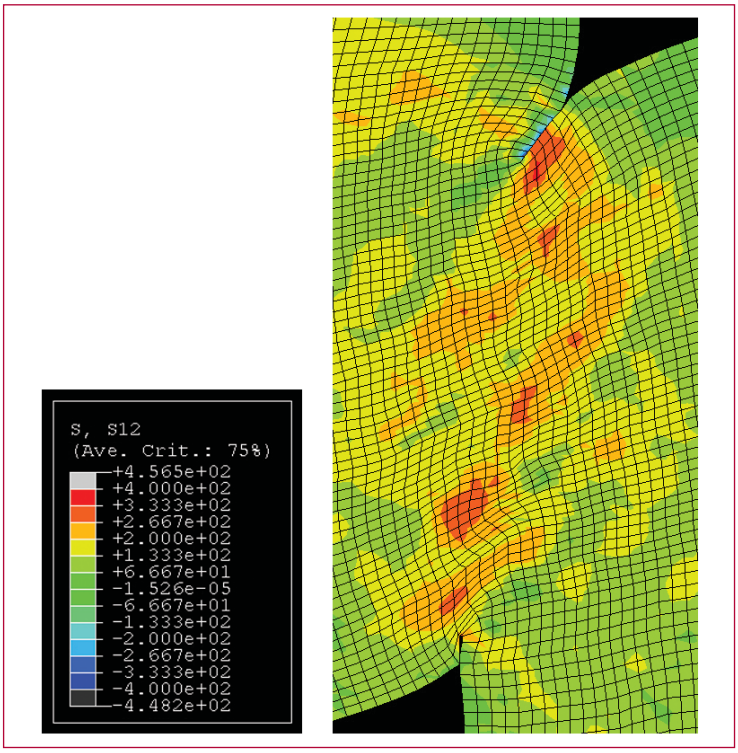

Figure 3—Shear stress within the gage section of a polycrystal plasticity simulation.

Sea Ice and Climate

Elizabeth C. Hunke and William H. Lipscomb, T-3; eclare@lanl.gov

Sea ice has long been recognized as important for climate because of its high-albedo, strong insulating effect, and potential sensitivity to greenhouse warming. Many global models predict that reductions in sea-ice thickness and extent will amplify climate change at high latitudes. Sea ice reflects most incoming solar radiation and prevents this radiation from heating the ocean surface while simultaneously insulating the surface ocean from very cold arctic air in the winter, thus maintaining warmer ocean temperatures and cooler atmospheric temperatures. Sea ice creates competing dynamic effects in high-latitude oceans: new ice formation contributes to higher surface ocean density through the rejection of salt during the freezing process, thereby helping to drive the global overturning (thermohaline) circulation, but the insulating effect of the ice cover protects the ocean from cooling and further densification, thereby weakening the thermohaline circulation. In spring, leads (polynyas) opened up by diverging ice flows expose the surface ocean to solar radiation, heating the surface ocean and accelerating the melting of ice. Such ice feedbacks are important in the response of the climate system to global climate change.

For many years sea ice was represented fairly crudely in large-scale models. More sophisticated approaches were available, but were considered too complex and expensive for global climate simulations. Recently, however, sea-ice models have become more realistic as computing power has increased. CICE is a numerical model developed at Los Alamos to examine sea-ice physics using high-performance computers. It contains state-of-the-art methods for simulating ice dynamics, thermodynamics, and transport. As the sea-ice component of the Community Climate System Model (CCSM), CICE is coupled to atmosphere, ocean, and land surface models for a fully integrated simulation of the Earth's climate system. The CCSM is currently being used to run a series of simulations for national and international climate assessments, including simulations of present climate and future climate warming scenarios. The data from these simulations will be used to examine the role of sea ice in either accelerating or mitigating climate change. Such simulations will also be used to determine causes of the observed thinning of Arctic sea ice in recent decades. The CICE model is also used in ice-only simulations, driven with observed atmosphere and ocean conditions. This mode is effective for validating the model against observed data and has been used to simulate the formation of polynyas off the coast of Antarctica. Recently, simulations using CICE coupled to the Los Alamos Parallel Ocean Program (POP) are being used in the Arctic Ocean Model Intercomparison Project and in studies of the effects of sea ice and ice sheets on ocean thermohaline circulation. A simulation coupled with POP at eddy-resolving resolutions (2.5 km in the polar regions) is being prepared and will be used as an intermediate step before a fully coupled very high-resolution climate simulation. Together, these simulations performed with the CICE models will lead to improved understanding of seaice and its effects on the climate system.

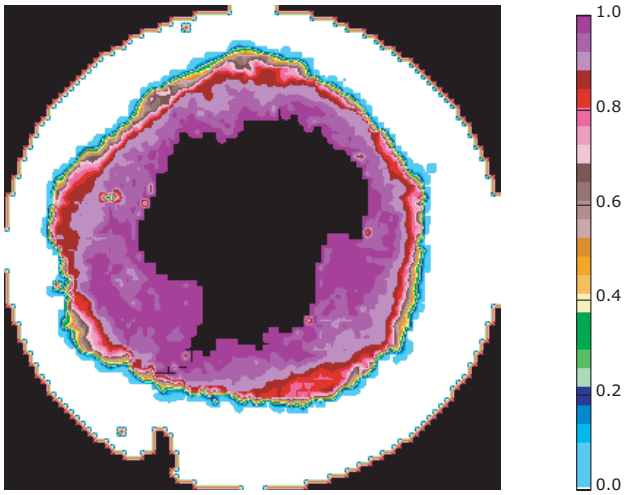

iceh_mavg.0025—09.nc aice

Surface heat flux (including SW)- (Yr 30)

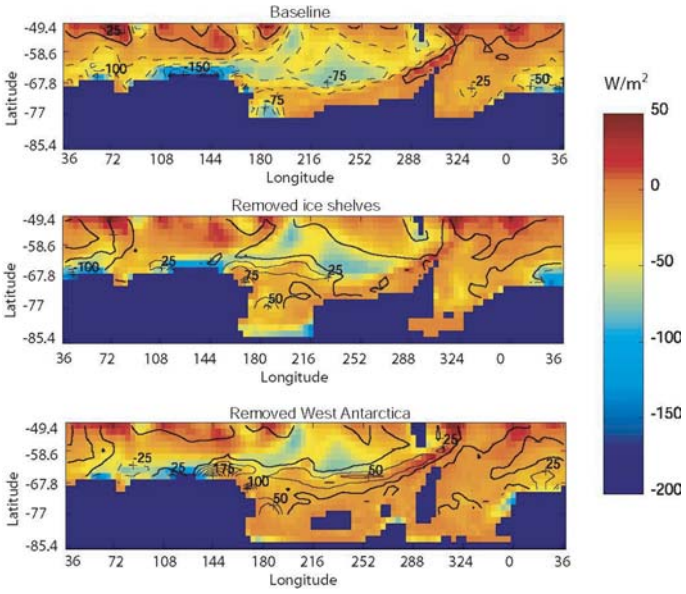

Transition Theory for Fragmentation of Solid Bodies

Bryan A. Kashiwa and Rick M. Rauenzahn, T-3; bak@lanl.gov

A physical modeling formalism for solid bodies undergoing fragmentation is being developed. The purpose is to provide a rigorous framework for posing physical models that can be used for the computer simulation of certain problems of current importance in both defense and in industry. The nature of the problem, and the formal approach to it, can be understood most easily by way of example.

Consider a rigid rod of steel, called a rod penetrator, launched from a tank cannon aimed at a target. A system near the target senses the launch and immediately fires a counter munition that meets the rod penetrator at about midflight. The counter munition explodes near the nose of the rod penetrator causing a blast wave that imparts a pressure impulse to the rod. There are two questions: 1) "Is the impulse sufficient to deflect, bend, or break the rod?"; and 2) "What, if anything, hits the target?"

The following frames of a three-dimensional computer simulation suggest answers to both questions. Here the steel rod is shown as a collection of white dots (elements of mass) on a background of color contours of pressure; red indicates high pressure. The frames are moving with the initial velocity of the rod, so the burst from the counter munition appears to move from right to left. In the first frame the speeding steel rod has experienced the full effect of the pressure impulse, which is just exiting the left side of the view. Already the rod has experienced sufficient bending to break in tension on the top side. The first break causes a whipping action that results in a second tension break on the bottom side, leaving the rod in three large pieces to tumble through the air and completely miss the target.

The forgoing is an example of a so-called Fluid-Structure-Interaction problem. The fluid impulse on the structure is large enough to affect the dynamics of the structure, which in turn causes a significant thrust on the fluid. The FSI problem described here encompasses the fragmentation of an initially solid body. Other examples include the compaction of initially separate solid catalyst grains into a solid body, which can (undesirably) occur at the bottom of a fluidized bed reactor in a chemical plant.

Fragmentation of a solid can be characterized as a continuum-to-kinetic transition; compaction of separate grains into a solid is a kinetic-to-continuum transition.

The formalism being developed assigns a special identity to every element of mass in the domain; as the character of the mass element changes with time, so may the identity. In the FSI problem described here, the initial identity is that of "continuum" for each element of steel making up the rod penetrator. When the yield condition is approached on any given mass element of the rod, its identity begins to change from continuum to "noncontinuum." The noncontinuum behavior is described by the collisionless Boltzmann equation for the velocity distribution. The continuum behavior is simply that of the original material. The transition is determined, in this example, by the speed at which a fracture can run its way across the diameter of the rod.

The formalism provides a consistent framework within which a wide range of similar phenomena can be studied.

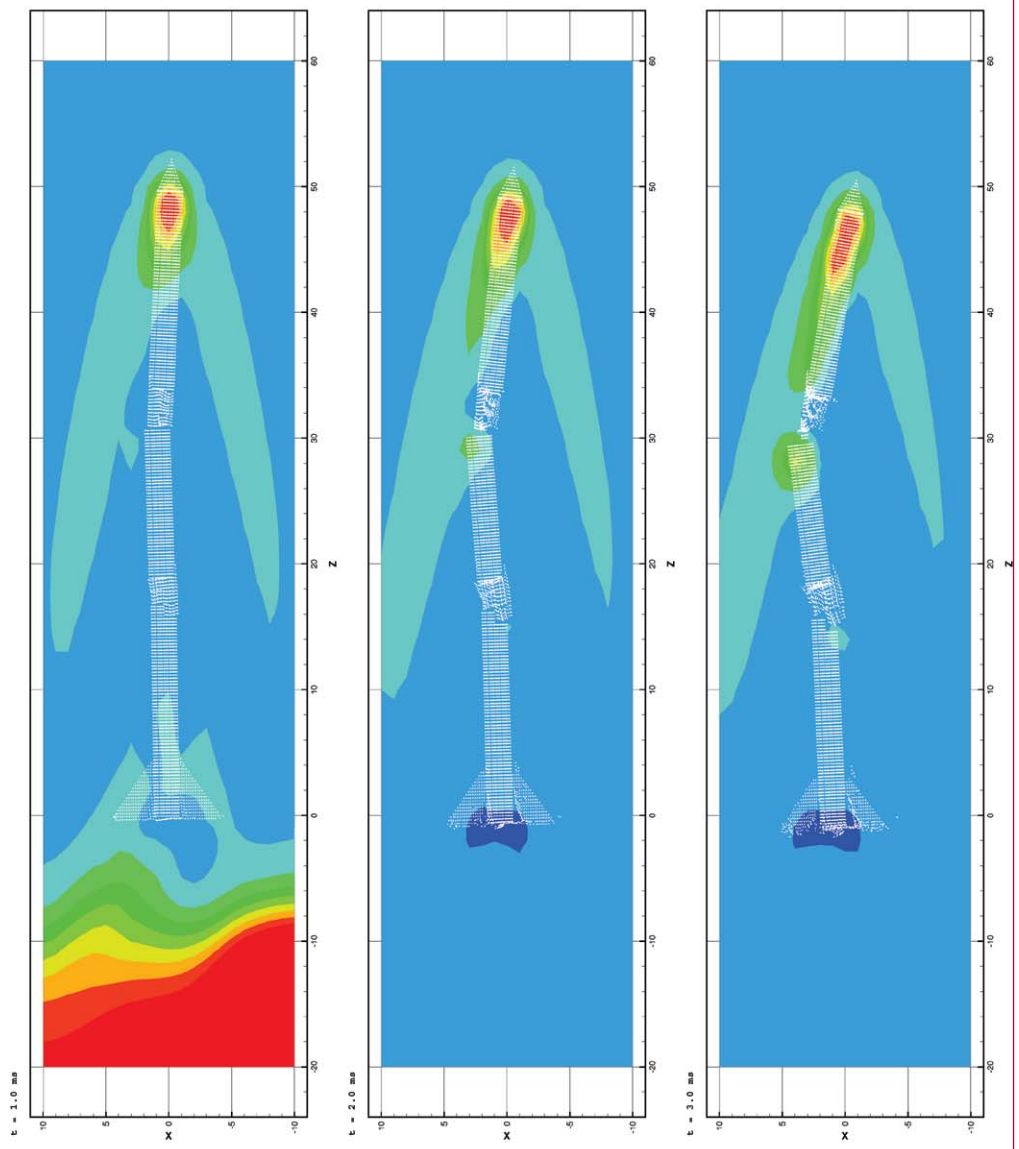

Figure— Brittle steel rod penetrator subjected to a blast impulse during flight. a) 1.0 ms after blast; b) 2.0 ms after blast; c) 3.0 ms after blast.

Nonequilibrium Thermodynamics for Granular System and Its Application to Grain-Binder Composites

Xia Ma and Duan Z. Zhang, T-3; xia@lanl.gov

Although granular flows (such as flow of salt and sugar grains) are encountered daily in our lives, the understanding of the material behavior is still primitive even in this electronic age. The dynamics of an individual grain is well understood, while the behavior of a granular system cannot be easily predicted by any existing theory, with the exception of simple flows with low-grain volume fractions. Many natural and particularly important granular phenomena happen in a dense flow regime. Examples of these phenomena include a snow avalanche and land sliding in the nature. The major difficulty associated with the understanding of the material is the lack of a suitable mathematical description about the system. The positions and size of the grains are random; therefore the use of statistical method is inevitable. Many statistical methods developed for physical systems are based on the assumptions that the system is a small perturbation away from the thermodynamic equilibrium and that the system is nondissipative. The granular system is a dissipative system. Most granular systems, especially dense granular systems, are too far away for the thermodynamic equilibrium. A new method has to be introduced to study them. Similar to many nonequilibrium thermodynamic theories, we based ours on the Liouville equation to build theories for the granular system. Many new concepts have been introduced. Our study of time correlations in the granular system has received considerable attention in the related communities.

Recently, we find that our theory has interesting applications in our programmatic efforts related to safety and surety of high-explosive materials. Failure pattern and constitutive relations of PBX 9501, a grain-binder composite, possess many characters of dense granular flows. Currently we are studying the relation between inter-particle interaction force model and the macroscopic constitutive relation. Numerical simulations of Taylor impact are performed. Shock propagation, dissipation, and dispersion in the material are studied. It is observed that the damage pattern of the composite after the impact varies significantly for different force models. As shown in Figure 1, if a noncohesion force model is used between particles, the column spreads out like sands when it impacts on the plate. When the cohesion is added in the force model, the patterns of failure after an impact change considerably as shown in Figure 2. The column does not spread out as much as the one shown in Figure 1. We have also observed other material failure patterns, depending on the different force models used. Some of these patterns are very similar to observations from the experiments performed in MST-8. This indicates the significant effects of binder-grain interactions on the macroscopic behavior of the material. Understanding these effects could provide guidance to process the material and enhance the safety and surety of the material under various environments.

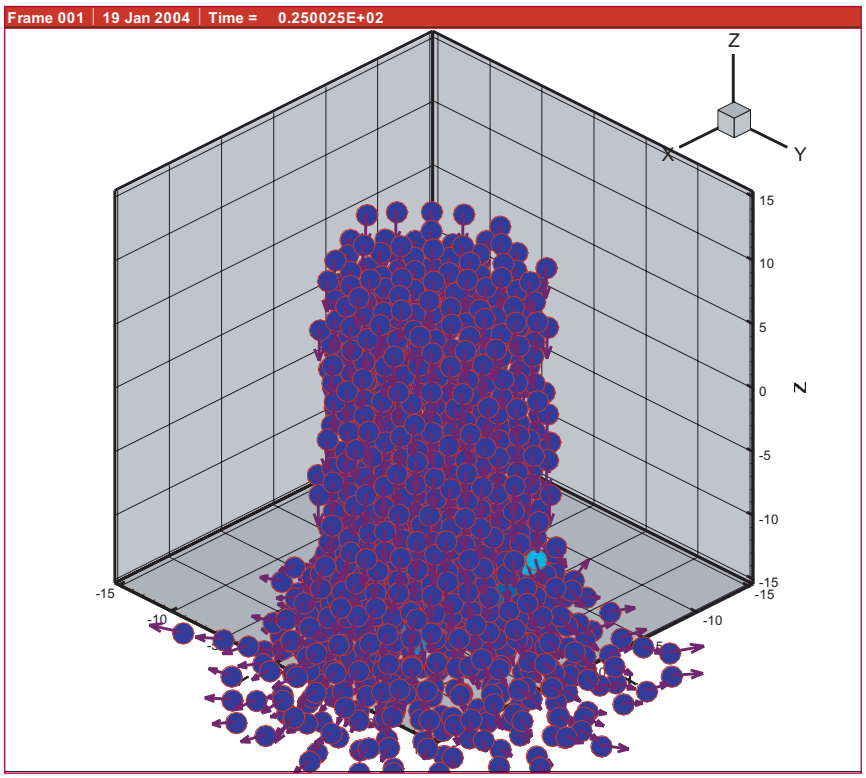
Frame 001 | 19 Jan 2004 | Time = 0.250025E+02
Z
X
Y
15
10
5
0
-5
-10
-15
Z
-15
-10
-10
-15

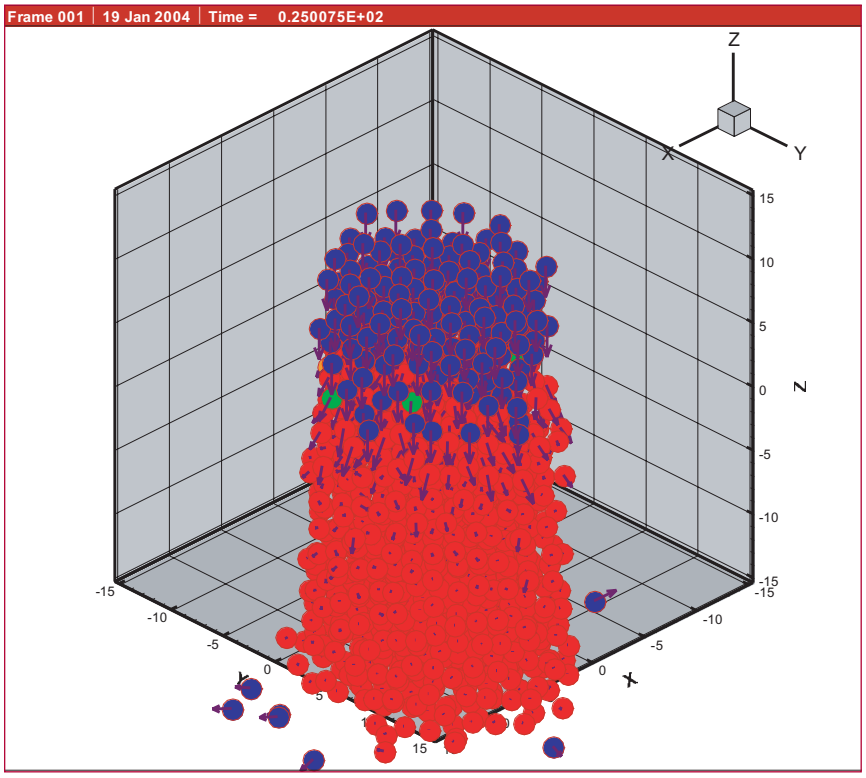
Frame 001 | 19 Jan 2004 | Time = 0.250075E+02
Z
X
Y
15
10
5
0
-5
-10
-15
Z
-15
-10
-5
0
Y
-15
-10
-5
0
X
15

Ocean Biogeochemistry

Mathew E. Maltrud, T-3; maltrud@lanl.gov

Computer models of the Earth's climate system have, until recently, primarily simulated the distribution of heat and water throughout the atmosphere, ocean, land, and sea ice. In order to more accurately simulate responses to carbon dioxide and other emissions from human activities, climate models are now including capabilities for simulating the distribution and interaction of the many chemical species that have a significant influence on climate. Atmospheric aerosols also play an important role in cloud formation and in reflecting or scattering incoming solar radiation and the addition of these effects to climate models is very important.

As part of our ocean modeling efforts with the Parallel Ocean Program (POP), ocean ecosystem and biogeochemistry modules are being added and tested. These models simulate the distributions of important marine ecosystem species like phytoplankton, zooplankton, and bacteria, as well as nutrients like nitrate, ammonium, iron, and silicate that plant and animal species need to flourish. These components interact to process a variety of important chemical species like carbon dioxide, nitrogen, silicon, sulfur, and trace gases like dimethyl sulfide, carbonyl sulfide, methyl halides, and nonmethane hydrocarbons. Combining all these effects permits ocean biogeochemical models to predict how much carbon dioxide the oceans can remove from the atmosphere due to both ecosystem dynamics and gas transfer, and how oceans produce chemical species important for the formation of atmospheric aerosols.

The addition of biogeochemical capabilities to our ocean modeling efforts have enabled us to contribute to simulations of the full carbon cycle in the Earth's climate system and examine how human-produced carbon dioxide can be taken up by the oceans. Also, several simulations using POP and its imbedded biogeochemical model have been used to simulate the use of iron fertilization to increase the activity of biological organisms and enable them to ingest and sequester more carbon dioxide from the atmosphere. The biogeochemistry model will continue to improve and will be used for simulations of climate with fully interactive carbon and sulfur cycles. Ocean carbon sequestration strategies like surface fertilization and deep injection will also be examined using ocean biogeochemistry simulations.

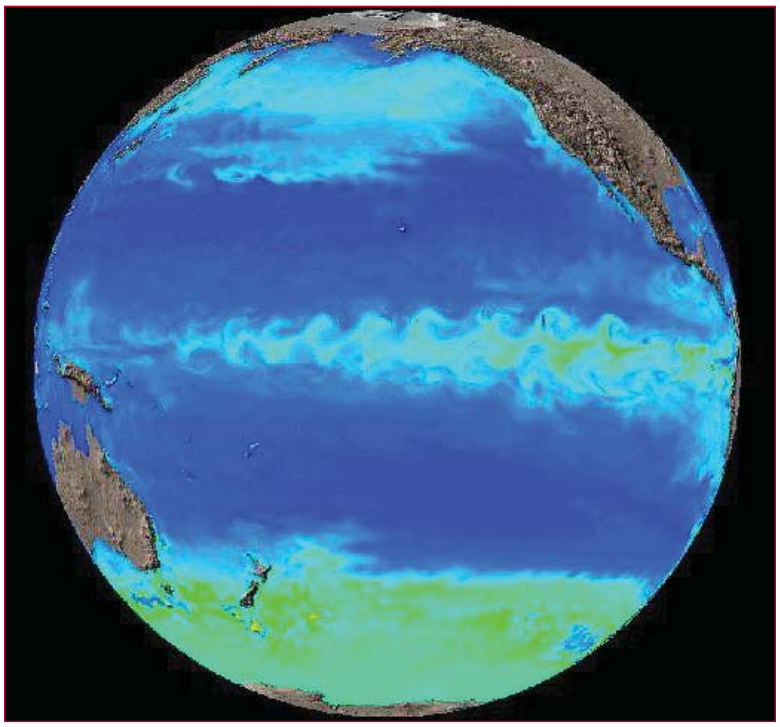

Figure 1— Phytoplankton concentration from a POP biogeochemistry simulation.

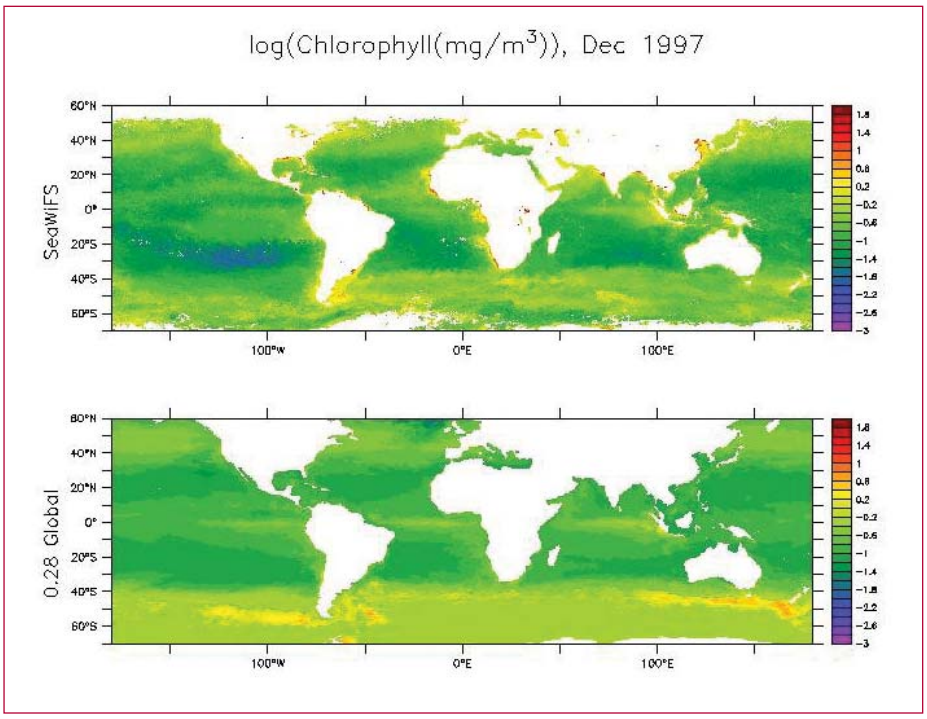

Figure 2— Chlorophyll concentration from satellite ocean color observations (top) and a POP ocean biogeochemistry simulation at 0.28-degree resolution (bottom).

Eddy-Resolving Ocean Modeling

Mathew E. Maltrud and Richard D. Smith, T-3; maltrud@lanl.gov

Ocean circulation is responsible for almost half of the transport of heat from the Earth's equator to its poles, substantially affecting the climate. Much of this circulation occurs in very narrow boundary currents (such as the Gulf Stream) and is influenced by ocean bottom topography and energetic eddies with horizontal sizes less than 50 km. Using numerical models as a means of understanding transport processes in the ocean therefore requires high-horizontal grid resolution to accurately simulate these flows. Los Alamos has over a decade of experience in setting the worldwide standard for such high-resolution ocean circulation simulations.

The Parallel Ocean Program (POP) is a numerical ocean circulation model designed to take advantage of the computational capabilities of Los Alamos to enable successful high-resolution simulations of global ocean circulation. Early simulations using POP at 0.28-degree (30 km) equatorial resolution demonstrated the value of high-resolution modeling, but suggested the need for even higher resolution to capture the full spectrum of mesoscale eddy variability and to improve the simulation of the wind-driven circulation. This simulation was followed by a higher resolution 0.1-degree (10 km) simulation of the North Atlantic basin. Results from this simulation agree well with sea-surface height variability from satellite altimetry measurements. The magnitude and geographical distribution of eddy kinetic energy and other measures of eddy variability also agree well with observations. The simulated mean wind-driven circulation shows significant improvements, including a better Gulf Stream with separation from the coast at Cape Hatteras, good agreement with free-drifting float data following the path of the North Atlantic current and an Azores current consistent with observations. Identical simulations at 0.2- and 0.4-degree resolutions showed that the excellent results at 0.1-degree resolution were rapidly lost at coarser resolutions and indicate that a resolution of 0.1-degrees is an important threshold for realistic ocean simulations. The success of the 0.1-degree North Atlantic simulation encouraged us to extend the domain to the full global ocean and begin a 0.1-degree global ocean simulation. The results of this simulation also demonstrated improved simulation of various boundary current systems like the Kuroshio off the coast of Japan. While many aspects of the global 0.1-degree simulation were greatly improved over previous global simulations, the results for the Gulf Stream and North Atlantic current were not as realistic as the results from the North Atlantic simulations. Further experimentation showed that appropriate choices of viscosity formulation, ocean bottom topography, and proper simulation of deep ocean water properties are also necessary for the realistic simulation of the Gulf Stream.

Performing very high-resolution simulations is computationally intensive, so we can only simulate 10–20 years of ocean circulation using currently available high-performance computers. This precludes the possibility of conducting century-long climate simulations or ensembles of shorter runs at this resolution. On the other hand, current generation climate models typically feature an ocean component that cannot resolve the small spatial scales necessary for an accurate representation of narrow currents and eddies. Thus, an important use of the high-resolution simulation data is

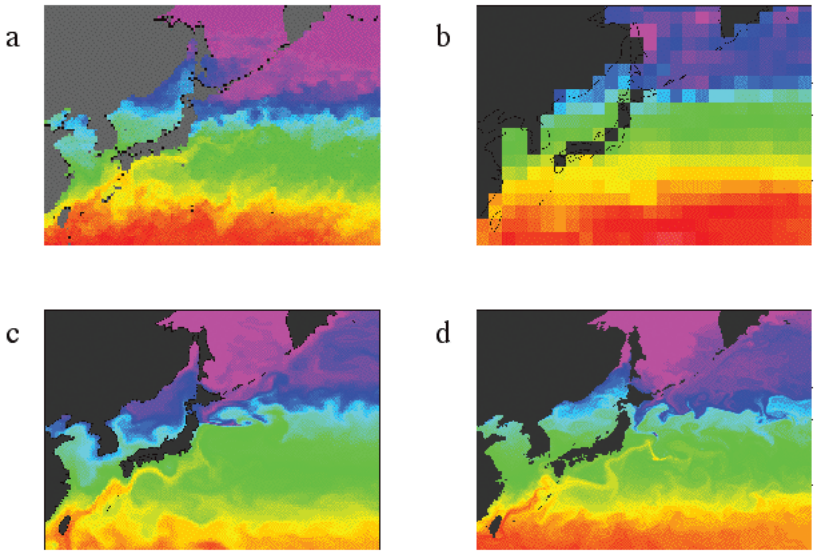

Figure 1— Sea surface temperature in the warm Kuroshio current region from a) satellite observations and POP simulations at b) coarse 2-degree resolution, c) eddy-permitting 0.28-degree resoultion and, d) eddy-resolving 0.1-degree resolution. Although the eddy-permitting case shows substantial improvement, only the eddy-resolving simulation can capture the detail and full extension of the Kuroshio current.

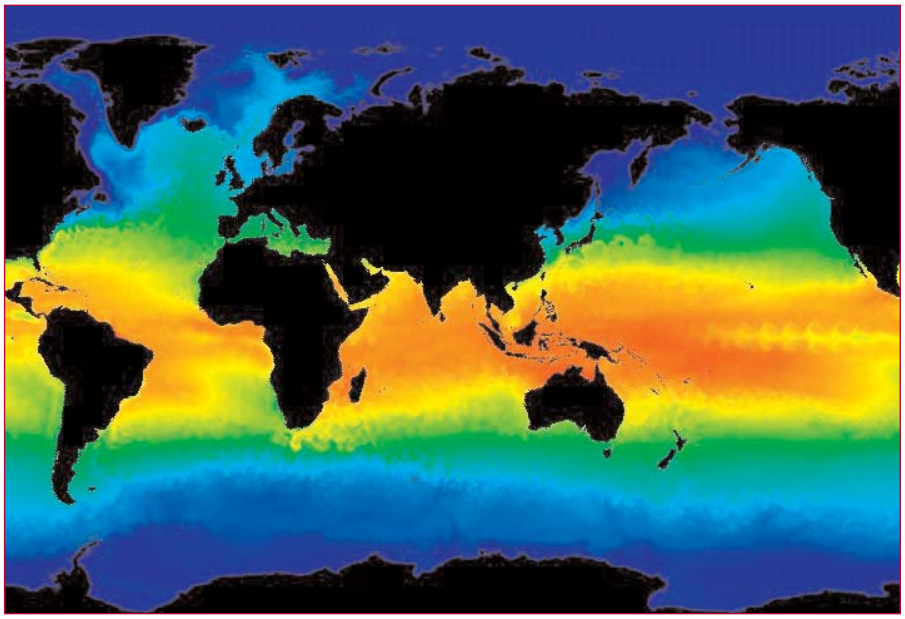

Figure 2— Temperature at 15-m depth from a global 0.1-degree eddy-resolving POP simulation.

to study eddy properties and eddy-mean flow interactions and attempt to represent these processes at coarser resolutions to improve simulations of the climate at timescales of centuries and beyond. Another important application of high-resolution simulations is the short-term prediction of the ocean state, much like that which is done for weather prediction.

Extension of the KIVA Particle/Spray Model to Flows with Compressible Particles

Peter J. O'Rourke and David J. Torres, T-3; pjor@lanl.gov

In work supported by ASCI's Turbulence Mix Project, we are extending the highly successful KIVA [1] particle/spray model to flows with compressible particles. The KIVA model uses a Monte Carlo particle method to solve the equations for a two-phase, gas-particle flow in which the particles have a distribution of sizes. In the KIVA code, it is assumed that the particle material is incompressible. This assumption is not valid in flows in which the particles experience large changes in pressure and temperature, such as occur when shocks pass over the particles. This work is motivated by the need to relax the assumption of incompressibility.

Our extended equations incorporate the following additional physical effects into the KIVA model [2]. First, the density of the particle material, and hence particle sizes, can vary according to an arbitrary equation of state. Second, there can be both reversible compressive and viscous heating of particle material. Third, the particles can experience accelerations due to large gradients in the pressure field of the two-phase mixture. All physical effects included in the KIVA model have been retained—including particle aerodynamic drag, gas/particle heat transfer and particle vaporization, and particle dispersion due to interaction with gas-phase turbulence.

The finite difference approximations [3] of this extended model are formulated for both co-located variables hydrodynamics codes, such as the CHAD code [4] being developed by Group T-3, and for staggered-mesh codes, such as KIVA. For either type of code, two particle-model subroutines, which are called from the main hydrodynamics solver, provide the computational interface to the coupled gas/particle equations. The new finite-difference approximations improve upon those of KIVA in many ways, two of which we mention here. First, the energy of the combined gas-particle system is numerically conserved. (The KIVA finite-difference approximations conserve mass and momentum, but not energy.) Second, in the staggered-mesh case, we propose an improved method for calculating momentum exchange that reduces spurious numerical velocity fluctuations in calculations with vaporizing particles.

Implementation of the approximations in CHAD is well underway because portions of the KIVA particle/spray model had already been incorporated in a CHAD module a number of years ago for another project [5]. This old implementation, which assumes incompressible particles moving in an ideal gas, was largely undocumented and untested. In recent progress, we have updated the computational interface for this old particle module so that it is compatible with the latest version of CHAD.

We have also begun testing of the particle module in comparisons with known analytic solutions. One of these tests is of the deceleration of a uniform slug of particles moving relative to a gas, and the resulting acceleration of a gas in which this slug is embedded. This problem tests the implementation of the particle drag terms, as well as conservation of momentum and energy in the combined gas-particle mixture. The slug of

particles is uniformly distributed across the cross-section of a rectangular channel, as shown in Figure 1, and moves in the direction of the long dimension of the channel. Periodic boundary conditions are imposed on the top and bottom boundaries of the channel. The plot in Figure 2 shows the relative error between the computed and analytic solutions for the particle velocities. This error is always less than 0.18%.

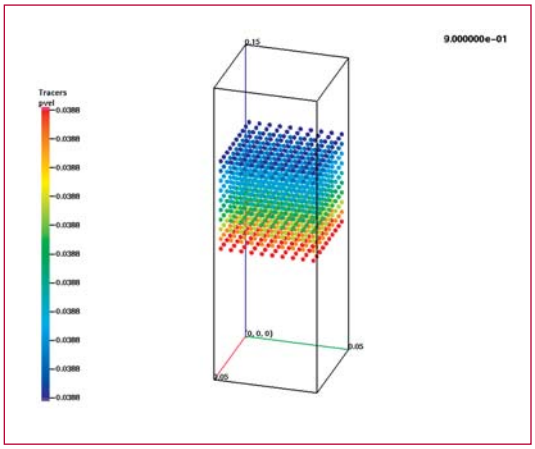

Figure 1— Particle positions at end of particle-slug calculation. The particles are colored according to their velocity, which are all equal to 0.0388 to three significant figures. The particle velocities are spatially constant in the analytic solution.

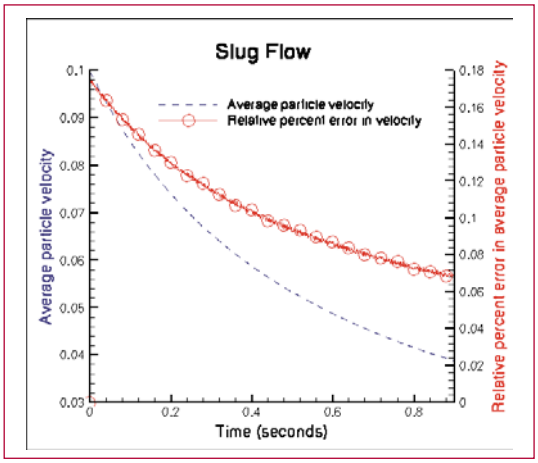

Figure 2— Particle velocities and relative error between analytic and computed particle velocities, versus time.

[1] A. A. Amsden, P. J. O'Rourke, and T. D. Butler, "KIVA-II: A Computer Program for Chemically Reactive Flows with Sprays," Los Alamos National Laboratory Report LA-11560-MS (May 1989).

[2] P. J. O'Rourke and D. J. Torres, "Extension of the KIVA Particle/Spray Model to Flows with Compressible Particles and Large Pressure Gradients," Los Alamos Report LA-UR-03-2918 (April 2003).

[3] P. J. O'Rourke and D. J. Torres, "Finite Difference Approximation of the Equations of the Extended KIVA Particle/Spray Model," Los Alamos Report LA-UR-03-2917 (April 2003).

[4] P. J. O'Rourke and M. S. Sahota, "NO-UTOPIA: The Flow Solver for the CHAD Computer Program," Los Alamos National Laboratory Report (in preparation).

[5] M. S. Hubbard and P. J. O'Rourke, unpublished work.

Simulation of Multiphase Flow in Centrifugal Contactors for Process Intensification at TA-55

Nely Padial-Collins and Brian VanderHeyden, T-3, nelylanl@lanl.gov

The T-3 Group began work on the simulation of mixing and separation of two-phase flow in the TA-55 centrifugal contactor in the last half of FY03. The contactors are used to recover actinides from acid solutions through contact with paraffinic hydrocarbons, [1]. Centrifugal contactors are attractive for this service for many reasons including criticality issues. The ultimate goal of the project is to use simulation to help increase the capacity of the contactors, [1]. With increased capacity, valuable floor space at TA-55 would be made available for other purposes. In the following, the basics of the contactor are discussed along with a summary of results from FY03 and plans for FY04.

Background

A cutaway schematic diagram and photograph of the contactor is shown in Figure 1.

The inner cylindrical element of the contactor is rotated at around 3600 rpm with a motor. The aqueous (acid) and organic (paraffin) are pumped into the annular chamber where there is mixing from Taylor-Couette flow and multiphase turbulence. The mixed two-phase flow proceeds through stationary vanes at the bottom of the annular chamber and then enters the inner rotating chamber. In the inner chamber, separation occurs due to centrifugation. The aqueous and organic phases exit the chamber at the top through a set of weirs placed at different radii.

FY03 Work Package Objectives

- Demonstrate multiphase flow simulation in contactor geometry –June 2003.

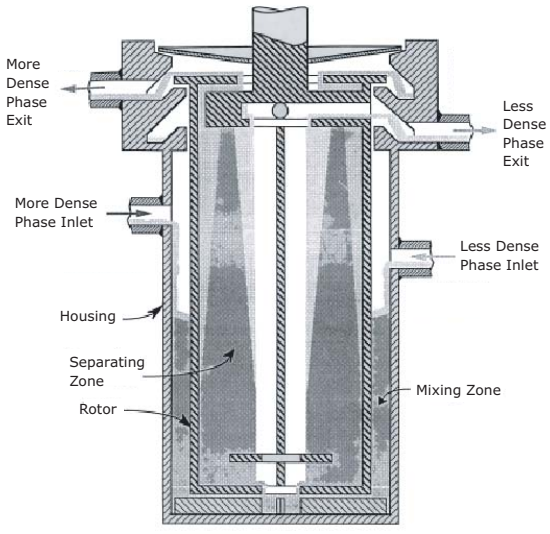

Cutaway Schematic

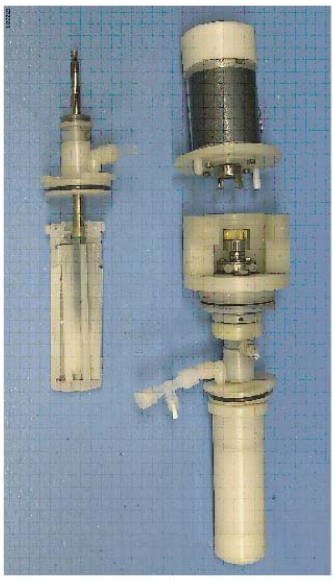

Cutaway of contactor

Figure 1— Cutaway Schematic and Photo.

- Demonstrate multiphase flow with mass transfer on a base case.
  Both objectives were met.

FY03 Accomplishments

The FY03 work included the implementation and testing of a rotating frame effect (centrifugal and Coriolis forces), development and installation of an impeller force model, a species and phase mass transfer model, the generation of several detailed 3D meshes based on the contactor, and the calibration of a droplet drag model as well as several 3D simulations. In addition, a data link to the RAVE facility was established and prototype 3D visualization movies of the data from the base case simulation were developed and demonstrated. Finally, an extensive literature survey was performed that yielded an interesting data set for code validation [2]. The data set provides experimental information on the maximum throughput of the contactor as a function of the ratio of the flow rates of the organic and aqueous phases. It is anticipated that this information will be used in FY04 for model validation and as a basis for potential process intensification studies of the contactor.

Below are illustrations showing the contactor meshes and flow field results from the 3D demonstration calculation.

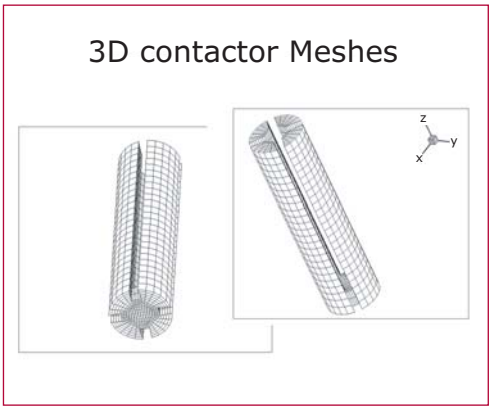

Figure 2—
3D meshes for contactors.

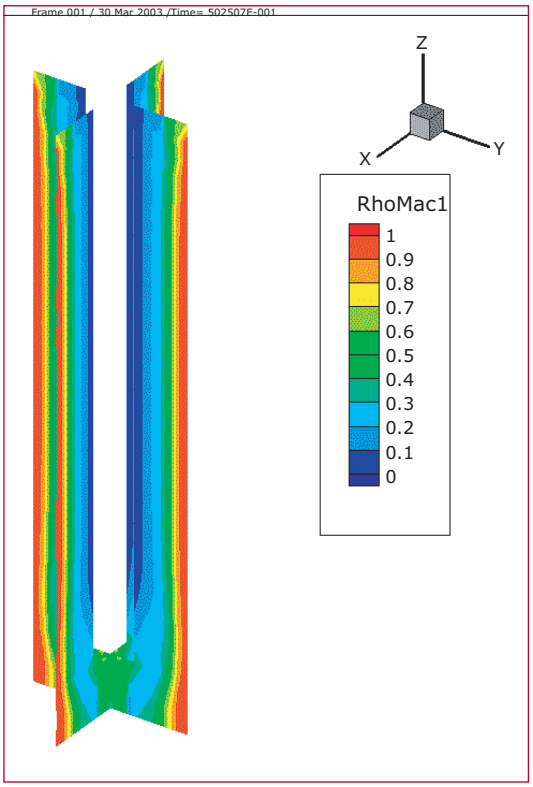

Figure 3—
Phase distribution in z-y and z-x plane.

[1] Stephen L. Yarbro and Stephen B. Schreiber, "*Using Process* Intensification in the Actinide Processing Industry," Journal of Chemical Technology and Biotechnology, **78** (2–3), pp. 254–259 (2003).

[2] R. A. Leonard, G. J. Bernstein, A. A. Ziegler, and R. H. Pelto, "Annular Centrifugal Contactors for Solvent Extraction," Separation Science and Technology, **15**, pp. 925–943 (1980).

Modeling the Dynamic Response of Disordered Cellular Materials

Mark W. Schraad and Francis H. Harlow, T-3; schraad@lanl.gov

The purpose of this project is to develop a constitutive law and a general modeling approach for describing the mechanical response of cellular materials to highly dynamic, large-strain, and high-rate loading conditions. The programmatic relevance of this project derives from the implementation and use of this modeling approach within large-scale codes for simulating the behavior of cushioning materials.

Cellular materials consist of two separate but interacting material fields—the cellular solid and the permeating fluid (e.g., usually air)—each with its own distinct velocity field. The modeling effort, therefore, begins with the derivation of a governing set of macro-scale conservation equations in two-field form. For example, the linear momentum equations for both the cellular solid and the fluid describe the response to stress gradients within the cellular solid, as well as to pressure gradients arising in the fluid and to the drag impedance arising from the relative flow between the two materials.

This form of the governing equations is chosen to allow for consideration of evolving closed-cell fluid pressure and open-cell fluid flow in the overall description of the cellular material response. Solutions to the linear momentum equations and the corresponding conservation of mass equations provide the velocities, densities, and volume fractions for each material. Models for the fluid pressure and the momentum-exchange rate, which couples the behavior of the fluid and the cellular solid, are used to close this set of equations, along with an appropriate constitutive law for the evolving stress state in the cellular solid.

A general, three-dimensional, finite-deformation constitutive law has been developed to describe the mechanical response of a single foam cell. A probability distribution function, which describes the initial cell-size distribution and the corresponding cellular-scale structural evolution, has been formulated and is coupled with the single-cell model to form the macro-scale constitutive law. This constitutive law relates the macro-scale stress in the cellular solid to the continuum-level strain, strain rate, and stress rate. Most importantly, as the cellular structure evolves, so too does the probability distribution function, thereby bridging the cellular and macroscopic length scales by representing the cellular-scale structural evolution within the macro-scale constitutive response.

The macro-scale constitutive law has been implemented in a small-scale test code and a large-scale performance code. The material model parameters have been calibrated against both single-cell numerical simulations and macro-scale experimental data, and small-scale tests have been performed for parameter refinement. The model also has been verified and validated against experimental data for low-rate but large-deformation compressive, tensile, shear, and combined loading of a low-density, open-cell, polyurethane foam and the high-density, S-5370 silicone foam. In the near future, attention will be focused on the rate-dependent behavior of cellular materials and the effects of the permeating fluid on the cellular solid response under dynamic loading conditions.

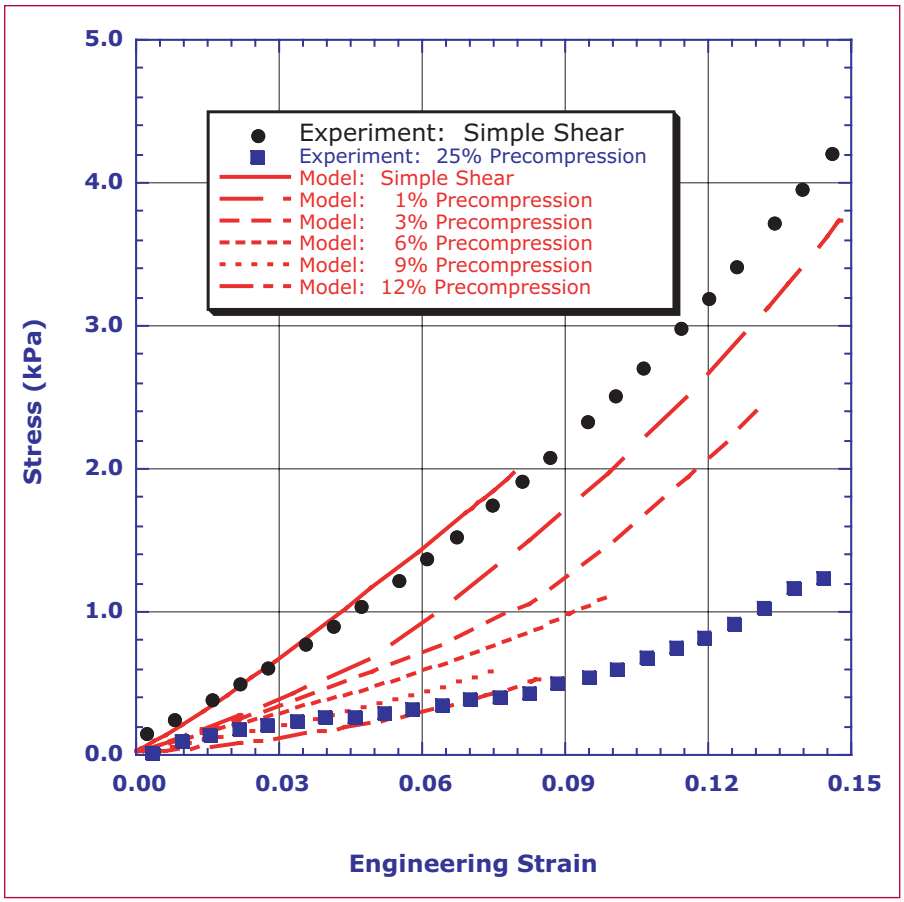

Figure— Shear stress versus shear strain for a low-density polyurethane foam, showing the softening effects of various levels of pre-compression.

Mathematical Models of Turbulence

Michael J. Steinkamp, X-3; Francis H. Harlow, T-3; and Bernhard H. Wilde, X-2; steinmj@lanl.gov

The high-speed dynamics of fluids or gases are almost invariably unstable to perturbations, resulting in the creation of turbulence. The consequences of turbulence include the very rapid mixing of materials and the greatly enhanced transport of momentum and energy. To analyze experimental observations and to develop methods by which to utilize or mitigate the effects of turbulence almost always requires the use of large computer codes. The goal is to describe both the mean flow and the appropriately averaged consequences of the relatively fine-scale fluctuations. Because even the largest and fastest of modern computers are not able to resolve all the fine details of the motion, we derive and use mathematical models to describe the essence of what is going on.

These models have been used to study turbulence at all scales, from laboratory sizes to those of wind gusts during the propagation of wildfires, and to the scale of many light years in the explosion of a supernova. Our current activity is to compare the results of turbulence-model calculations with those of carefully controlled experiments. Of prime concern is the validation of the techniques over as wide-range of circumstances as possible. For this purpose we interact with three different experimental groups at our Laboratory, who use shock tubes, laser-induced jets, and laser-driven collapse of irregular material shapes for their investigations. The results of these studies are revealing some remarkable properties of the models and of turbulence itself, especially regarding circumstances of structural universality and the effects of geometrical constraints on the growth of the mean scale of fluctuations.

These and many other experimental comparisons are crucial to the development of credible confidence for the turbulence transport models. Although much remains to be done, we are nevertheless demonstrating success for a remarkably wide scope of circumstances for which the effects of the fine-scale fluctuations are essential to describe.

High-Explosive Safety Study, Update II

Qisu Zou, Duan Z. Zhang, W. Brian VanderHeyden, Nely Padial-Collins, T-3; qisu@lanl.gov

We investigate nonshock initiation of High Explosive (HE) material. The current research is focused on the Dyer and Taylor (D&T) experiment as sketched in Figure 1. For certain combinations of the applied pressure and velocity (V) and the friction surface of the plate, the experiment may produce explosion. In the case that the plate is a smooth glass plate, if there is no sand grit on it, it will not produce explosion, while if there is sand grit on it, it may produce explosion. Besides, the number of sand grit particles initially on the glass plate plays an important role in ignition. The more the initial number of grit particles is, the easier the explosion is. The explanation from Dyer and Taylor is that a particle of sand grit causes a high friction between the grit and the plate and creates a hot spot around it; if there are more particles, there are more hot spots. Although the thermal interaction from heat conduction between the hot spots or contact of sand grit particles are not important because the initial sand grit particles are placed far apart, the high pressure in a hot spot located near the center will not be able to escape due to other hot spots present with high pressure, hence the case of multiple grit particles will more easily develop into a full ignition. From our simulation on this problem, we suggest that gas motion can also increase the explosion tendency with multiple grit particles. When the plate is sliding under the HE, friction heat melts a layer of HE, and chemical reaction can generate some product gas near the hot spots. The liquid HE together with the gas are carried downstream by the sliding plate and heat up the HE downstream. Thus, the hot spot downstream will have a higher temperature, enhancing the tendency of explosion.

Figure 2 shows the result of a simulation using a general multipurpose Computation Fluid Dynamics (CFD) code CartaBlanca. A Particle-in-cell (PIC) method is used to model the solid HE with mechanical strength. Chemical reactions, gas generation, and mechanical and thermal interactions between the solid HE and gas are considered by solving appropriate equations numerically. Two phases (materials) are used in the simulation. One is the solid phase (the HE), the other is the gas phase (product gas from chemical reaction). A simplified one-step chemical reaction is used. The data in the chemical reaction are from a study of different experiments. The plot on the left is the gas temperature at time of 0.005 second with one initial hot cell, while the plot on the right is the gas temperature at the same time with two initial hot cells. At this

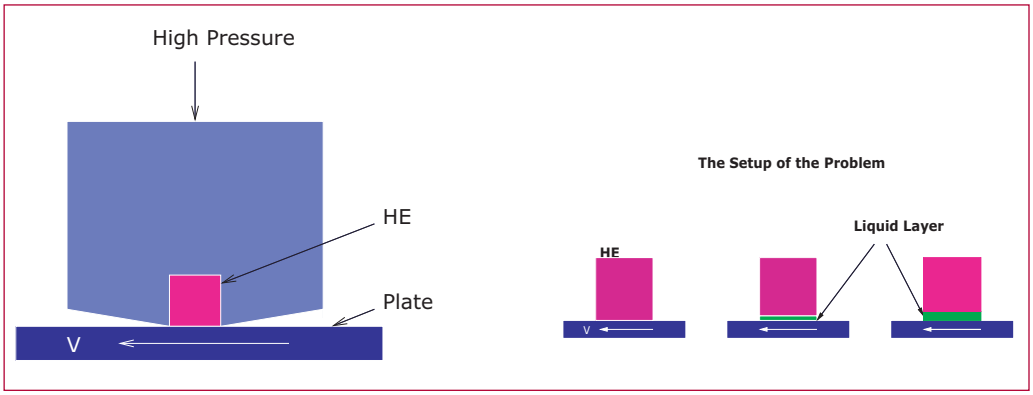

Figure 1—The Dyer and Taylor experiment and the setup of the problem.

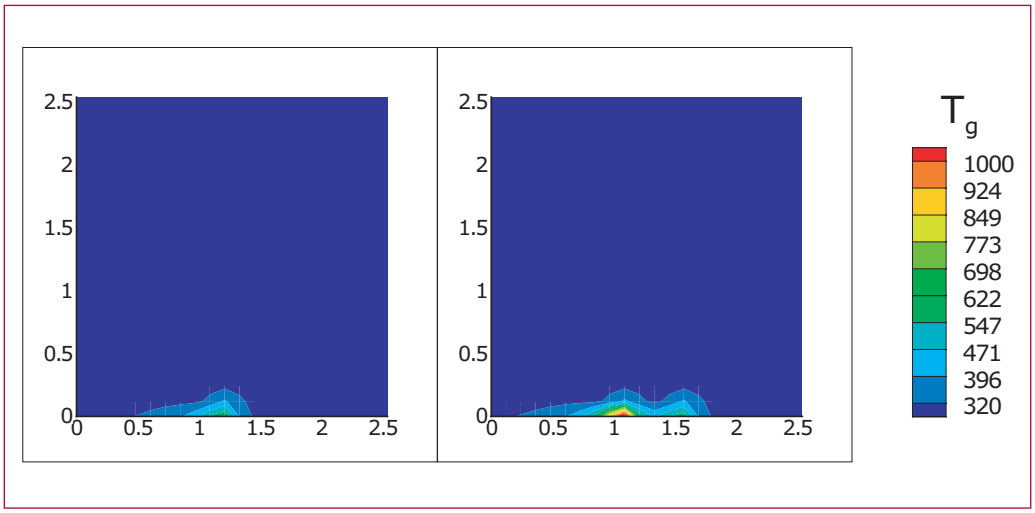

Figure 2—Comparison of the gas temperature at time of 0.005 S. Left plot: one initial hot cell, right plot: two initial hot cells.

time, the maximum gas temperature of the one hot cell is 347 °C, which does not lead to an explosion, while the maximum gas temperature of the two-hot cell case is 852 °C, which eventually leads to an explosion.

Predicting Strain Localization in Anisotropic Materials

Q. Ken Zuo, Justin R. Smith, Paul J. Maudlin, and Francis L. Addessio, T-3; zuo@lanl.gov

We have developed a framework for predicting the onset and orientation of shear bands in metals under large plastic deformation. Shear banding refers to the formation of a highly localized deformation in the form of thin planar bands (of the order of 10 μm) caused by material softening. Material anisotropies in both the elastic and plastic responses are included in the framework. The criterion for localization is the loss-of-ellipticity condition proposed by Rudnicki and Rice, which is associated with a change of the characteristics of the governing equations. Loss-of-ellipticity occurs when the acoustic tensor becomes singular. The acoustic tensor is the inner product of the tangent stiffness tensor with a normal vector defining the localization plane. A computer program (using Mat-Lab) has been written to calculate the onset and orientation of the band for materials with general anisotropy (both in the elastic stiffness and the shape of the yield surface) subjected to an arbitrary, three-dimensional stress state. The program searches through all orientations to find that orientation for which the acoustic tensor becomes singular (having a zero eigenvalue) at the minimum value of the equivalent plastic strain. We have studied strain localization in several application materials (Cu, Zr, Ta) under different processing conditions (i.e., rolled, wire drawn, forged). The material anisotropy resulting from processing-induced texture can have significant effects on strain localization.

Consider the plastic deformation of a thin tantalum plate under uniaxial tension (Figure 1). During the early stage of deformation, the material is stable and the deformation is uniform with the stress state in the plate being uniaxial. As deformation proceeds, the material reaches a critical state where two thin bands (i.e., a doublet) of highly localized deformation emerges from the weakest

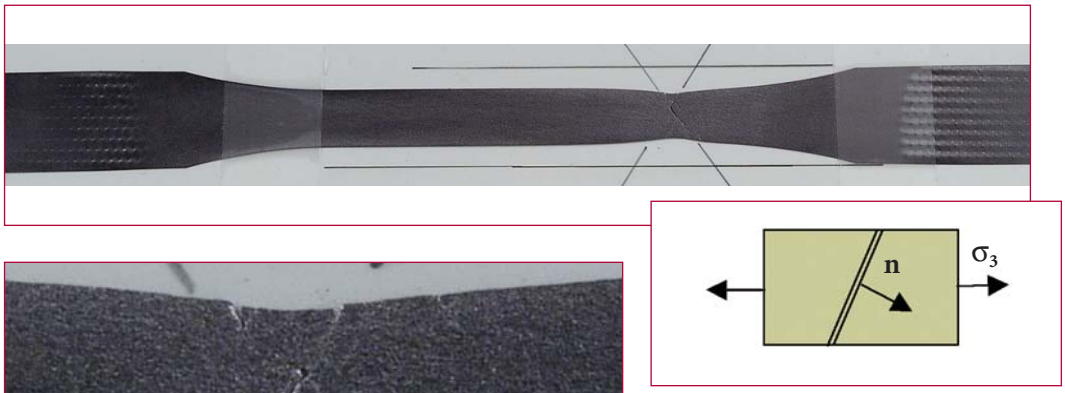

Figure 1—
A thin Tantalum plate under uniaxial tension showing the doublets of localized deformation.

Figure 2—
The details of the Tantalum plate showing the doublets (shear bands) and the final failure.

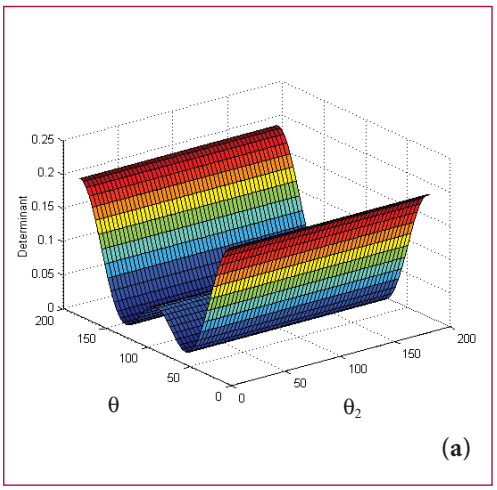

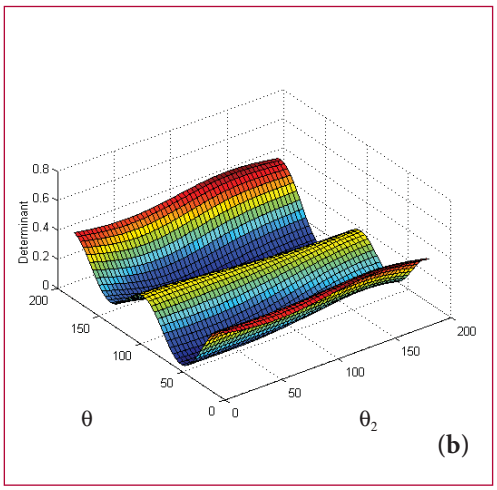

Figure 3— The determinant of the acoustic tensor depends on the orientation of the localization plane for copper with different textures, (a) isotropic, (b) anisotropic.

locations in the plate (e.g., for a uniform plate with no defects inside, the bands initiate from the free sides and propagate towards the middle of the plate). Under further deformation, one of the bands becomes dominating while the other diminishes and the material failure occurs across the dominating band (Figure 2). Since the material often fails (either by shearing or a combination of shear and normal modes) along the localization plane, it is important to predict the orientations of the localization planes. The loss-of-ellipticity condition states that localization initiates when the acoustic tensor first becomes singular. The orientation for which the acoustic tensor first becomes singular corresponds to the orientation of localization plane. Figure 3 shows the prediction of the dependence of the determinant of the acoustic tensor (normalized to the value for the elastic deformation) on the orientation the localization planes (in terms of Euler angles for the normal) for copper with two different processing conditions. The value of the determinant measures the material's resistance to strain localization. The determinant (normalized) starts with some positive value (unit for materials with isotropic elasticity), and gradually reduces the value as the plastic deformation accumulates. Figure 3a is for a copper plate with random initial distribution of grain orientations (hence an isotropic texture). It is seen that the determinant depends very strongly on the orientation of the band, and that localization will initiate along the planes 54° from the loading axis, a result confirmed by experiments. It also shows that the determinant of the acoustic tensor is invariant with respect to θ_2, the angle with the thickness direction, due to the isotropic nature of the texture. Figure 3b is for a rolled copper plate with the <111> directions of the grains aligned along the plate thickness direction. The determinant now depends also on the angle θ_2, due to strong texture effects. Another major effect of anisotropy (texture) is that the two localization planes are no longer symmetrically oriented with the loading axis, as in the isotropic cases.

T

T-7 Mathematical Modeling and Analysis

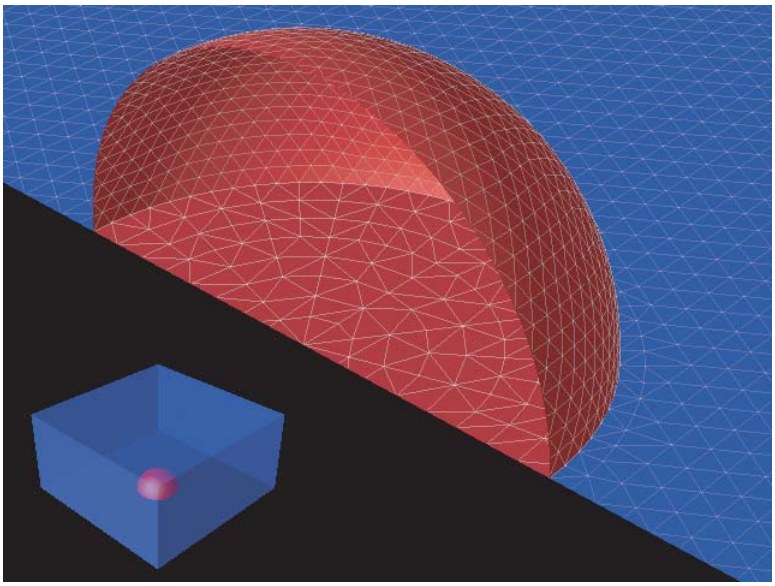

Multilevel Accelerated Optimization for Problems in Grid Generation

Markus Berndt and Mikhail J. Shashkov, T-7; berndt@lanl.gov

The quality of numerical simulations of processes that are modeled by partial differential equations strongly depends on the quality of the mesh that is used for their discretization. This quality is affected, for example, by mesh smoothness or discretization error. To improve the mesh, a functional that is in general nonlinear must be minimized. This minimization is constrained by the validity of the mesh, since no mesh folding is allowed. Classical optimization techniques, such as nonlinear CG or Gauss-Seidel steepest descent, perform very poorly on this class of minimization problems. We introduce a new minimization technique that utilizes the underlying geometry of the problem. By coarsening the mesh successively in a multilevel-like fashion, minimizing appropriate coarse grid quality measures, and interpolating finer meshes from coarser ones, a more rapid movement of fine mesh points results, and the overall convergence of the minimization procedure is accelerated [1].

We first describe the coarsening strategy. In an initial step in Delaunay coarsening [2], the list of vertices is reordered in such a way that all boundary vertices come first. In a loop over this list of vertices, the current vertex is added to the list of coarse vertices and its neighbors are deleted from the list of vertices. Hence, initially the boundary is coarsened, and then the interior is coarsened. As a slight modification of this algorithm, we first consider such boundary vertices that are necessary to properly resolve the shape of the domain. An example for such vertices are the four corner vertices of a square. The resulting list of coarse vertices is then triangulated using a Delaunay algorithm, e.g. [3].

Interpolating a grid from a coarser one is achieved by injection in the case of coarse vertices that are also fine vertices. All other fine vertices are interpolated using their barycentric coordinates with respect to their underlying coarse triangle as interpolation weights. In this procedure, the resulting grid might be tangled in some places. We handle this situation by using the untangling procedure described in [4].

For an approximate minimization procedure, we will call it relaxation, we use a few iterations standard gradient-

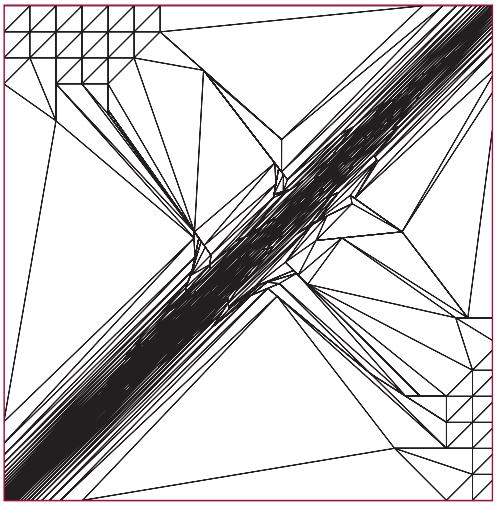

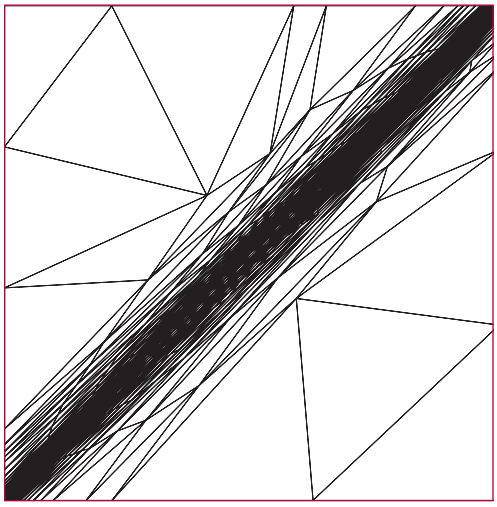

based optimizer, such as Gauss-Seidel steepest descent.

The three components restriction, interpolation, and relaxation are combined to yield a multigrid-style V-cycle iteration [5] In the figure, we show the final grid after 500 iterations of Gauss-Seidel steepest descent (left), and the final grid after three iterations of our new V-cycle optimization procedure (right). The objective was to minimize the approximation error of a given function with a steep gradient by moving the underlying grid. In both cases the initial grid was a regular triangular grid. The V-cycle procedure was completed in 25.9 seconds, while 500 iterations of the fine level Gauss-Seidel steepest descent procedure took more than 1000 seconds.

For this approach it is essential that a coarse grid representation of the objective function that is to be minimized can be derived. In other words, the change in the initial grid that is required to obtain the optimal grid must be expressible as small changes of vertex positions relative to the positions of neighbor vertices, plus larger changes of positions of groups of vertices. This is possible for applications where the objective is to find a grid that is optimal for the approximation of a function. We plan to extend this work to include the case where an error estimate, and not the actual error, is to me minimized.

[1] Markus Berndt and Mikhail Shashkov, "Multilevel Accelerated Optimization for Problems in Grid Generation," Proceedings of the 12th International Meshing Roundtable, 2003, Santa Fe, NM, USA.

[2] H. Guillard, "Coarsening Unstructured Meshes by Edge Contraction," INRIA Report No. 1898, 1993.

[3] S. J. Fortune, "A Sweepline Algorithm for Voronoi Diagrams," *Algorithmica*, 1987, pp. 153–174.

[4] P. Vachal, R. V. Garimella, and M. J. Shashkov, "Untangling of 2-D Meshes in ALE Simulations," under review in *J. Comput. Phys.*

[5] U. Trottenberg, C. W. Osterlee, and A. Schueller, "Multigrid," *Academic Press*, 2001.

Classification Modulo Invariance: Tangent Approximations and Improved Face Recognition

Andy Fraser, Portland State Univ.; Nick W. Hengartner, D-1; Kevin R. Vixie and Brendt E. Wohlberg, T-7; brendt@t7.lanl.gov

As a first step in building a principled, geometrically informed, high-dimensional data analysis capability, we have designed a classification scheme that can approximately factor out arbitrary invariances. The scheme uses first and second derivatives of functions that describe manifolds to which classification should be invariant. We have tested the scheme on a face recognition task using free software from CSU [1] that lets us make statistically meaningful performance comparisons with existing techniques.

The *geometrical view* (Figure 1) illustrates the intuition behind our modified within-class variance C_k, which combines the data-derived C_w and the effective variance term C_τ. We derive C_τ in a principled way from tangent approximations to the orbits (known *a priori*) by balancing the conflicting goals of de-emphasizing variations in invariant directions while remaining within the region of validity of the tangent approximation (estimated in terms of second derivatives). The results are quite good: we have the best three algorithms in comparison with the thirteen implemented in the CSU archive.

The *rank 1 comparisons* (Figure 2) was constructed using the following Monte Carlo experiment. An image I_0 was chosen, followed by 160 other images, exactly one of which (I') was a different image of the individual pictured in I_0. A distance vector was computed and the distances were used to rank the 160 images. The trial was a success if I' was the closest (rank 1) image. The fraction of successes was recorded over 160 such trials, and a histogram was constructed by repeating this entire procedure 10,000 times. Figure 1 represents Gaussian distributions fitted to these histograms.

Further details are available in a short conference proceedings article [3] and a detailed article [4] that has recently been published in a special issue of *The Journal of Computational and Graphical Statistics* consisting of presentations made to the National Academy of Sciences.

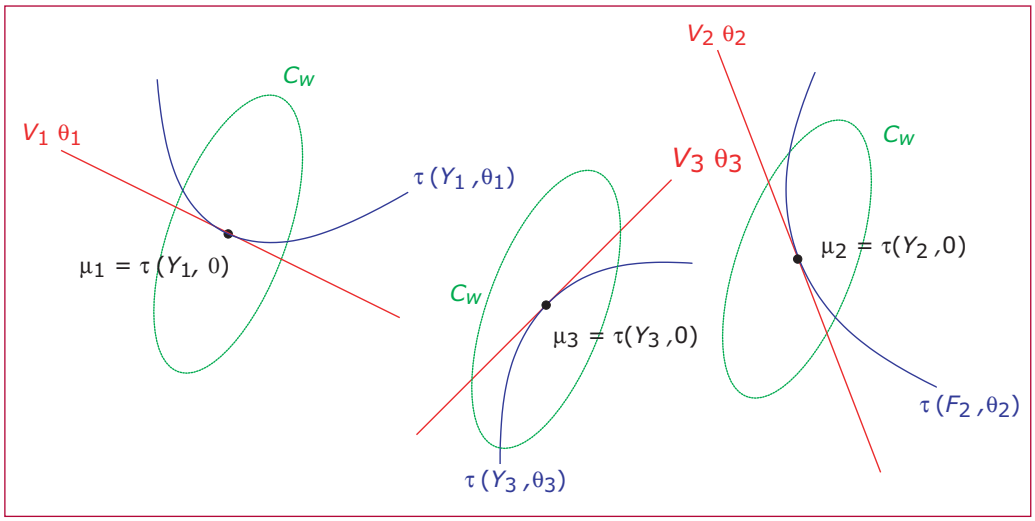

***Figure 1—** A geometrical view of our approach that improves on tangent distance methods [2] for translation, scaling, and rotation invariance. Each μ_k represents the mean of a class, the surrounding ellipses represent the pooled within-class variance C_w, that is estimated from training data. The curves, τ, parameterized by θ_k, represent the orbits of the known transforms to which the classification should be invariant. The $V_k\theta_k$ represent tangent approximations to those orbits.*

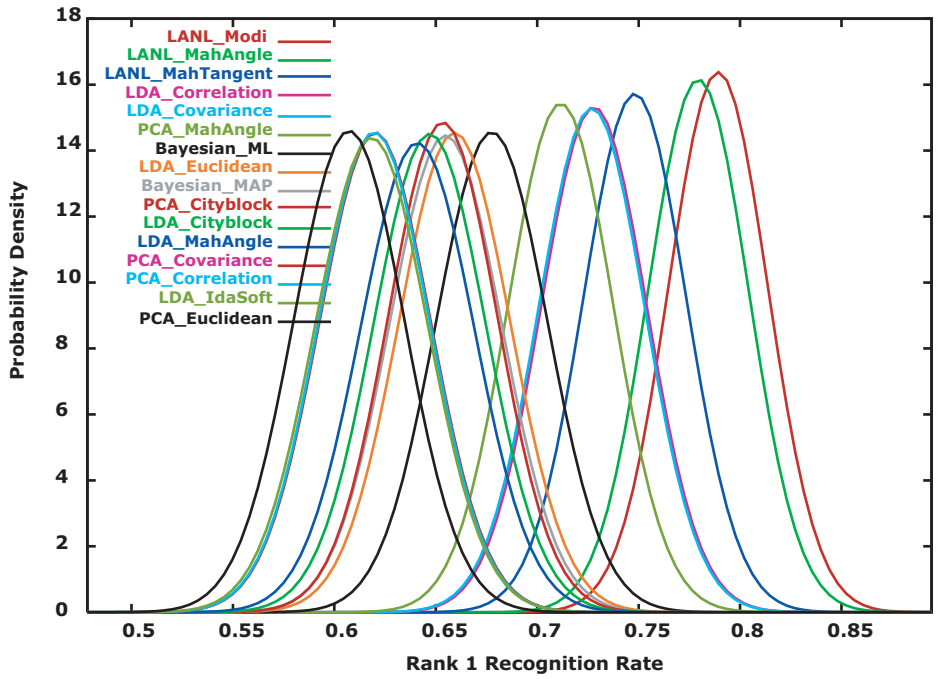

Figure 2— Plots of Gaussian approximations to the distributions of rank 1 recognition rates for each algorithm: note that the three best performing algorithms are variants of our approach.

[1] J. R. Beveridge, K. She, B. Draper, and G. H. Givens, http://www.cs.colostate.edu/evalfacerec/index.html "A nonparametric statistical comparison of principal component and linear discriminant subspaces for face recognition," *Proceedings of the IEEE Conference on Computer Vision and Pattern Recognition* (2001).

[2] P. Y. Simard, Y. A. L. Cun, J. S. Denker, and B. Victorri, "Transformation invariance in pattern recognition: Tangent distance and propagation," *International Journal of Imaging Systems and Technology*, **11(3)**, 181–197 (2000).

[3] A. Fraser, N. Hengartner, K. Vixie, and B. Wohlberg, http://math.lanl.gov/~brendt/Publications/fraser-2003-classification.shtml "Incorporating invariants in mahalanobis distance based classifiers: Application to face recognition," *Proceedings of International Joint Conference on Neural Networks (IJCNN) 2003* (Portland, OR, USA, July 2003).

[4] A. Fraser, N. Hengartner, K. Vixie, and B. Wohlberg, *http://math.lanl.gov/~brendt/Publications/fraser-2003-classification.shtml* "Classification modulo invariance, with application to face recognition," *Computational and Graphical Statistics*, **12 (4)**, 829–852 (December 2003).

Curvature Estimation for Unstructured Triangulations of Surfaces

Rao V. Garimella and Blair K. Swartz, T-7; rao@lanl.gov

Knowledge of the curvature of surfaces is important in a number of applications such as flow simulations, computer graphics and animations, and pattern matching. It is of particular importance to applications dealing with evolving surface geometry. Such applications usually do not have smooth analytical forms for the surfaces forming the model geometry. Instead, they have to deal with discrete data consisting of points on the surface connected to form an unstructured triangulation. Hence, it is important to be able to reliably estimate local curvatures at points on discrete surfaces.

In this study, a comparative analysis and convergence study were done of several curvature estimation methods suggested in the literature and a new, improved method was proposed as an extension of one of those methods [1]. The new method robustly estimates normals, principal curvatures, mean curvatures, and Gaussian curvatures at vertices of general unstructured triangulations. The method has been tested on complex meshes and has provided very good results shown in the examples.

It was found that the most reliable methods are those that fit a smooth surface to a set of nodes in the local neighborhood of each node and use its curvature as the estimate of the curvature for the discrete surface [2]. Since surface curvatures are based on second order derivatives, it is common to use quadratic polynomials as a local approximation to the surface. In each of these methods, a quadric of the form

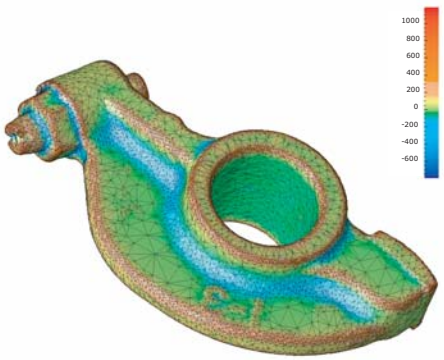

$Z' = f(X', Y')$ is fitted to the nodes in a local coordinate system (X', Y', Z') whose origin is at the node under consideration and the Z' axis is along an estimated surface normal at the node.

The simplest of the surface fitting methods performs a least squares fit of the quadric $Z' = aX'^2 + bX'Y' + cY'^2$ to the 1-level or edge-connected neighbors of the node mapped to a local coordinate system. The Z-coordinate of the local coordinate system is along a normal that is estimated by averaging the normals of the triangles connected to the node.

A more robust version of the quadric fitting method includes linear terms in the quadric, i.e., $Z' = aX'^2 + bX'Y' + cY'^2 + dX' + eY'$. This results in an improved estimate for the tangent plane and normal at the node. The improved

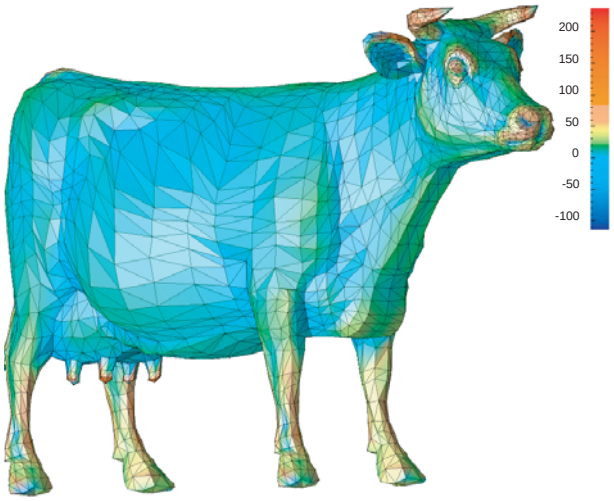

normal is then used to calculate a new local coordinate frame in which to fit a new quadric. This iterative process is carried out until the local coordinate frame does not change much. The extended quadric fitting works well but requires more points than the simple quadric without which the system of equations becomes under-determined and does not have a unique solution. It is also possible to use a full quadric in which the addition of the constant term allows the surface to not pass through the node under consideration.

The method devised by Garimella and Swartz fits an extended quadric to the one-level neighborhood of the node whenever possible and includes the two-level neighbors of the node (neighbors of the node neighbors) when the system is under-determined. The method also includes a technique for estimating curvature at vertices on surface boundaries where a full cycle of faces may not exist around the vertex. At such boundary nodes, existing neighbors are reflected to form ghost nodes that can then be used for fitting the surface.

In the study, convergence tests were performed by estimating the curvature at the central node of a shrinking hexagonal patch of triangles superimposed on a cylinder. The hexagonal patch was shrunk in a nearly self-similar way so that the quality of and relative sizes of the triangles did not change significantly. It was found that the simple quadric fitting had higher errors and converged to the wrong answer while the extended quadric technique showed very good accuracy and convergence to the right solution. In other tests involving the triangulation of a sphere, similar results were obtained with the addition that the extended quadric, extended patch

method of Garimella and Swartz, was needed to get an estimate at points in the mesh that did not have enough one-level neighbors. Surprisingly, the full quadric method gave very high errors for this test case.

The modified curvature estimation method was tried on complex meshes and has shown to give very good results. The accompanying illustrations show mean curvature estimates for unstructured meshes of complex geometric models.

[1] S. Petitjean. "A Survey of Methods for Recovering Quadrics in Triangle Meshes," *ACM Computing Surveys* **34**, pp. 211–262, June 2002.

[2] A. M. McIvor and R. J. Valkenburg, "A Comparison of Local Surface Geometry Estimation Methods", *Machine Vision and Application* **10**, pp. 17–26, 1997.

T

Aggregate Formation in Myxobacteria

Yi Jiang, T-7; jiang@lanl.gov

Fruiting body formation in bacteria occurs in response to adverse conditions and is critical for species survival. Complex morphogenesis must be robust despite internal and external noise. Myxobacteria, a social swarming bacteria, are one such example. When starved, myxobacteria undergo a process of alignment, rippling, streaming, and aggregation that culminates in the three-dimensional fruiting body (Figure 1).

Canonically, models for bacteria (e.g., *E. Coli* and *B. subtilis*) and amoebae (e.g., *Dictyostelium discoideum*) aggregation have been based on attractive chemotaxis, a long-range cell interaction that shares many features of chemical reaction-diffusion dynamics. Initialization of chemotactic signals plays an important role in the initial position of aggregates. Cells following the maximal chemical gradient navigate toward aggregates that are large and near. In myxobacteria, however, aggregates form without the aid of chemotactic cues. Yet myxobacteria travel large distances to enter an aggregate. How do the myxobacteria cells know where to go to form aggregates of optimal size? Understanding the aggregate formation in myxobacteria will shed new light into collective bacterial motion.

During aggregation, myxobacteria cells are elongated with a 7:1 length to width ratio. They move on surfaces by gliding along their long axis. Fruiting body development are controlled by the C-signal morphogen, which is exchanged at cell poles by cell-cell contact (hence the name C-signaling). Different levels of C-signal, encoded by the csgA gene, induce the different stages of fruiting body formation. The expression of csgA is regulated by two feedback loops in the signal transduction pathway. Each time a cell receives the C-signal it increases expression of csgA.

Based on these observations, we designed a lattice cell model [1], in which cell interactions are contact-mediated. The local rules demand that cells turn preferentially in directions that increase their level of C-signal. Cells move on a hexagonal lattice with unit velocities *(or channels)* in each of the six directions. We model identical rod-shaped cells as 3 x 21 rectangles, corresponding to a cell size of 1 x 7 μm. Each cell is represented as: 1) a single lattice node as the cell's center in the *xy* plane, 2) an occupied channel designating cell's velocity, and 3) a local neighborhood defining the physical size and shape of

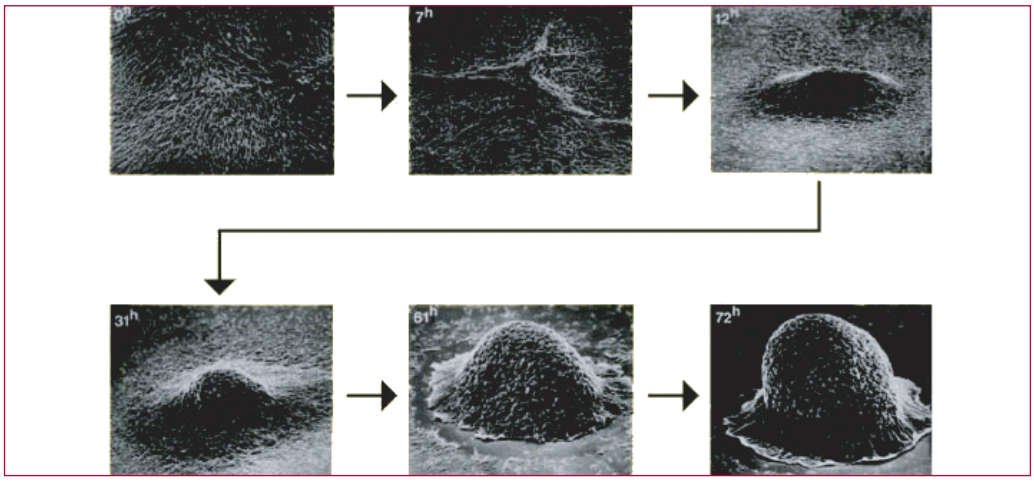

Figure 1—Snapshots of the life-cycle of Myxococcus xanthus.

the cell. This cell representation is computationally efficient, yet approximates aggregates more closely than point-like cells. Cells may turn stochastically 60 degrees clock-wise or counter-clockwise, or stay in its current direction, but favors directions that maximize the overlap of the C-signal exchange neighborhood at the poles of a cell with that of its neighboring cells. All cells then move synchronously one node in the direction of their velocity by updating the positions of their centers.

Our simulations show that cells aggregate in two distinctive stages. First, initially randomly distributed cells condense into small stationary aggregates (Figure 2a). These aggregate centers grow by absorbing immediately surrounding cells. Next, some adjacent stationary aggregates merge and form long, thin streams that extend and shrink dynamically on their own or in response to interactions with other aggregates (Figure 2b). These streams are transient and eventually disappear, leaving behind a new set of larger, denser stationary aggregates that are stable over time (Figure 2c). These results agree with experimental observations and explain how some aggregates can "mysteriously" disappear while their neighbors grow (when the streams are below the resolution of the observation). The simulated aggregates also reproduce the unique structures of several fruiting bodies.

We measured the areas and densities of every stationary aggregate that appeared over the course of two large simulations. They all fall within a narrow range in the area-density phase diagram, indicating that for an aggregate of a given cell number, it has a fixed structure and its area and density is prescribed within a narrow region, which we call an

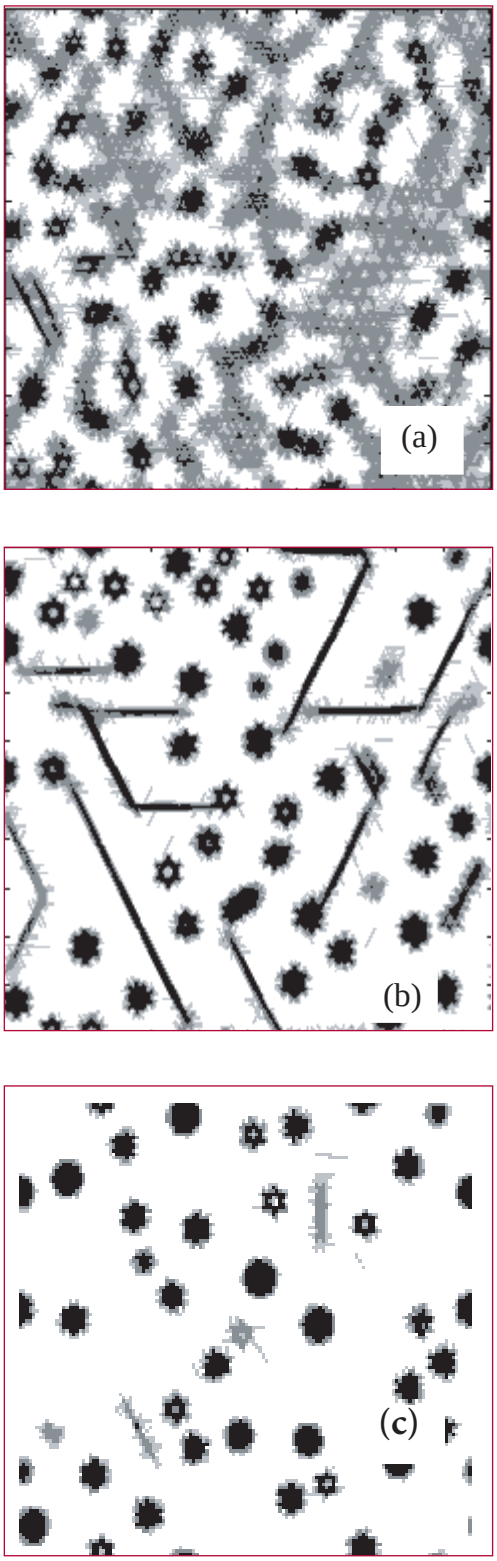

Figure 2— Aggregation stages on a 500 x 500 lattice, corresponding to an area of 2.8 cm^2. Local cell density at (a) 200, (b) 900, and (c) 25,000 timesteps. The darker shade of gray corresponds to higher cell density. Small aggregates form first at random positions; some of them interact and form long streams, which disappear and leave behind larger, denser, and more stable aggregates.

attractor region. As this attractor region covers continuous space rather than disconnected, the different aggregate structures can continuously transform from one to another.

We perform several tests to analyze the stability of this attractor region. Different initial random cell distributions result in statistically the same aggregates. When we slowly add cells to an aggregate, it "walks" in the phase space within the attractor region to a larger area and density. When we put two aggregates together, making an artificial aggregate with double area but the same density, the aggregate settles back into the attractor region rather quickly. These tests show that this attractor region is stable with respect to the external noise (initial condition and our perturbation).

We have also devised a deterministic version of the model, describing the cell-turning probability by a function that is equivalent to averaging over a large number of stochastic cell-turning events (similar to converting a lattice gas model to a lattice Boltzmann model). Both models evolve very similarly, indicating that the aggregation dynamics are not sensitive to internal noise that originates from the stochastic nature of the cell's turning process. There are, however, a few important differences between these two models. One difference is that streams in the deterministic model are fewer and smaller. Another difference is that streams are shorter-lived, and the deterministic simulation reaches a steady state much faster. These differences have a critical effect on the way aggregates reorganize—with the internal noise, aggregates can reach much larger sizes. This is not surprising because noise slows the process of stream contraction so that streams persist longer and span a greater area, which enables more aggregates to interact and form larger, more stable aggregates. In other words, the presence of some internal noise is required to efficient streaming. It is as if the cells must make short-term mistakes for the formation of unstable transients that ultimately results in more efficient aggregation.

To summarize, our lattice cell model is based on a very simple local rule in which cells align by turning preferentially to make end to end contact, mimicking C-signaling in myxobacteria that drives myxobacteria aggregation. The model reveals a novel two-stage process of aggregation mediated by transient streams. Noise in individual cell behavior increase the effects of streams and result in larger, more stable aggregates.

This work is in collaboration with Prof. M. Alber and M. Kiskowski at the University of Notre Dame.

[1] M. Alber, M. Kiskowski, and Y. Jiang, "Two-Stage Aggregation Formation via Streams in Myxobacteria," preprint LA-UR-03-8696, to appear in *Phys. Rev. Lett.* (2004).

Computer Arithmetic for Probability Distribution Variables

Weiye Li and J. Mac Hyman, T-7; liw@lanl.gov

Computational uncertainties are unavoidable in numerical calculations. The generation and propagation of uncertainties in the initial conditions, data, and the constants in mathematical models can have serious implications in the reliability of the simulation and the decisions being made based on the simulation. These uncertainties can be quantified by probability distributions and the correlations or dependency relationships between the variables.

Monte Carlo is a classical approach in handling probabilistic uncertainty and it is still widely used. However, it becomes less powerful when encountering the uncertainties that have unknown dependency relationships or distributions that are not fully specified. Various non-Monte Carlo methods have been developed to deal with unknown dependency relationships and imprecise probabilities since 1960s. Interval arithmetic is one of the main approaches, in which intervals are considered independent in order to bound all the possible solutions. The bounds obtained by this are usually pessimistic when dependency relationships exist.

It is important to know the dependency relationships between variables in computation in order to obtain tight bounds for the possible results. Various researchers have been working on approaches concerning dependency, and progresses have been made in gaining tight bounds. However, no approach that calculates the sharp bounds had been found until our recent discovery of *Probability Distribution Variable Arithmetic,* or *PDV Arithmetic*, which extends the interval arithmetic approach with the exclusive feature of complete dependency tracking throughout computation. A PDV is a random variable and is characterized by its generalized probabilistic discretization, which is a set of pairs of bins and probabilities. Using generalized probabilistic discretization is required because computers can only store discrete quantities. It is also an effective way to represent uncertainty, especially when the probability distributions are not fully specified from lack of sufficient information. In view of the fact that different random variables may have the same generalized probabilistic discretization, a PDV may be considered as a family of random variables that have the same generalized probabilistic discretization. In this point of view, every random variable in the family is a representative of the PDV.

In a computation, all variables involved are put into two category: input variables and derived variables. The latter is derived from the former via deterministic function expression. Thus, the dependency relationship between two derived variables can be well-defined by the relationship between the two pre-image sets, which are the sets of the input variables that define the derived variables. The extent of dependency can be represented by how much the two pre-image sets overlap.

Every binary operation between two PDVs is turned into the same operation between the corresponding bins. Dependency tracking requires that not every arbitrary pair of bins can be grouped to be operated on. We know that a bin of a derived PDV is fully determined by some bins of the input

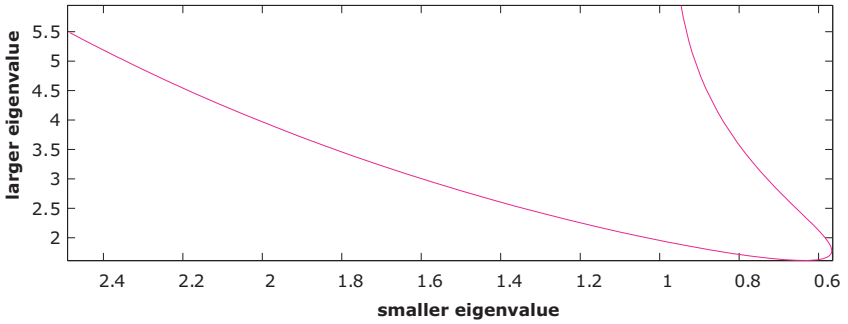

Figure 1— Illustration of dependency between the two eigenvalues of matrix $((a, c)^T,(b,d)^T)$ ***where*** $a = 3d^2 + 1$, $c = 2a - 1$, $b = 0.5c/a + 0.5$, $d \in [-1, 1]$ ***and d is uniformly distributed.***

PDVs. To see whether two bins from the two PDVs can be paired, one needs to compare their corresponding bins from the input PDVs and justify whether they are compatible. Only the bins with compatible bins from the input PDVs can be grouped and then operated on using interval arithmetic. Under the assumption that all input PDVs are probabilistically independent, the associated probabilities of the bins can be computed.

PDV Arithmetic is formulated based on the above ideas. It can be proved that the bounds calculated by using PDV Arithmetic include all the possible solutions and these bounds converge to the sharp bounds as the widths of the refinements of the input PDVs tends to 0. Sensitivity analysis shows that these bounds are stable in the sense that small perturbations of the input bins do not affect the bounds significantly provided that no singularity occurs in the computation.

As an application, we implement PDV Arithmetic in Fortran 77 by including PDV as a basic data type. A software package PDVFOR77 that includes a preprocessor written in Perl and a subroutine library in Fortran 77 enables the user to write PDV in a program as simple as writing real and integer. Every statement in the program involving a PDV data type is parsed into a sequence of subroutine calls that implement PDV Arithmetic.

An example about the eigenvalues of a 2 x 2 random matrix are demonstrated in the following two figures. The first figure illustrates the dependency relationship between the two eigenvalues, and the second figure compare PDV Arithmetic with Monte Carlo simulation.

Another example is given in the last figure to illustrate the probability distribution bounds (p-box, in red) calculated by PDV Arithmetic for the output of system $y = (a + b)^a$, where a belongs to three independent intervals [0.8, 1.0], [0.5, 0.7], [0.1, 0.4], and $\ln b$ follows $N(\mu, \sigma)$ where μ belongs to three independent intervals [0.6, 0.8], [0.1, 0.4], [0.0, 1.0], and σ belongs to three independent intervals [0.4, 0.5], [0.25, 0.35], [0.1, 0.2]. In contrast, the trend of a special probability distribution (refined p-box, in blue) is calculated with an additional assumption that a, μ, and σ are uniformly distributed on each of the above intervals.

The details about PDV Arithmetic can be found in [1]. The PDVFOR77 package and the above paper can also be found at *http://math.lanl.gov/~liw/*.

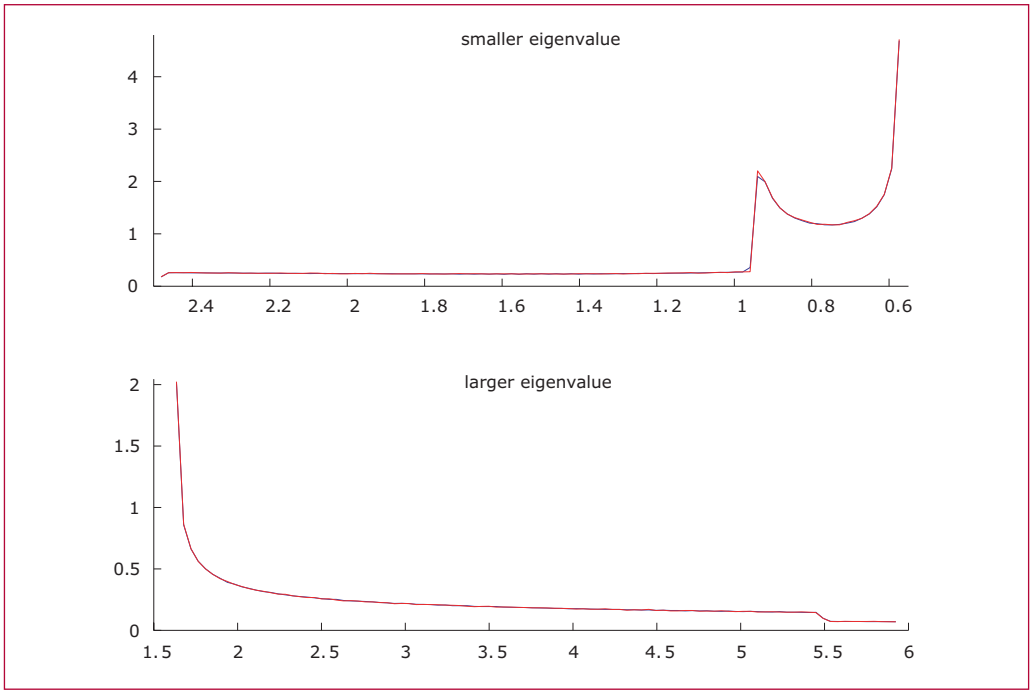

Figure 2—Comparisons between PDV Arithmetic (red line) and Monte Carlo simulation (blue line) for the probability density functions of the eigenvalues of the matrix in Figure 1.

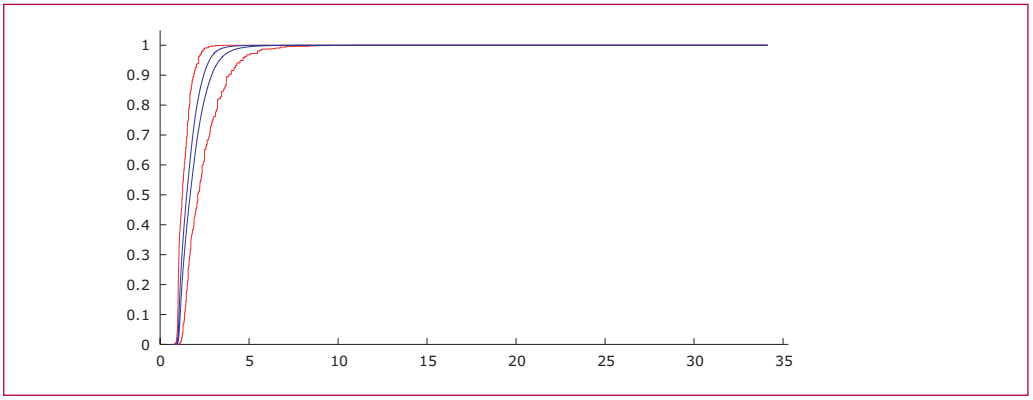

Figure 3—Probability distribution bounds for the output of $y = (a + b)^a$.

[1] W. Li and J. M. Hyman, "Computer Arithmetic for Probability Distribution Variables," *Reliability Engineering and System Safety*, in print, 2004.

Mimetic Finite Difference Methods for Diffusion Equations on Non-Orthogonal AMR Meshes

Konstantin Lipnikov and Mikhail J. Shashkov, T-7; Jim E. Morel, CCS-2; lipnikov@lanl.gov

The predictions and the insights gained from simulations are no better than the physics models or the numerical methods used to solve them. The discrete approximations used to predict diffusion of heat or matter on a mesh covering the domain is often the determining factor for the reliability, accuracy, and efficiency of the simulations. One of the most effective approaches to derive these discrete approximations is to preserve and to mimic the underlying mathematical properties of the physical system. This task is made more difficult when the mesh is distorted and/or locally refined so that it can conform and adapt to the physical domain and problem solution.

In our research [1] we have extended a class of mimetic finite difference approximations for modeling the diffusion equations on distorted locally refined meshes of a particular type of importance to the ASCI projects. Our new method is both accurate (second-order accurate on nonsmooth nonconformal meshes with or without material discontinuities) and it produces a linear system with symmetric positive-definite matrix, which is relatively easy to solve. The new method is a major advance over the capabilities of the existing discrete approximations and will lead to more accurate and robust predictions. It is slated for immediate use in the ASCI projects.

We use the local support-operators, SO, method to generate mimetic discretizations on nonorthogonal quadrilateral meshes having hanging nodes. Hanging-node meshes are generally used in adaptive mesh refinement algorithms. Note that a hanging node occurs when two cells share a face with one cell, see the figure below. We do not allow any cell to share a face with more than two cells, or equivalently, there is never more than one hanging node associated with an interface. This is a restriction motivated by considerations of both simplicity and accuracy that is usually seen in quadtree-based adaptive-mesh algorithms. While the vast majority of existing adaptive mesh refinement (AMR) schemes use orthogonal meshes, it is clear that nonorthogonal mesh schemes are more versatile. Nonorthogonal hanging-node meshes have been used in adaptive Arbitrary Lagrangian-Eulerian, ALE, hydrodynamics algorithms [2]. Our scheme would be suitable for coupled radiation diffusion/hydrodynamics calculations on such meshes.

The local SO method is particularly amenable to hanging-node meshes, because the discretization process occurs in two steps. The first step is to consider each cell in the mesh as an independent domain and generate an independent discretization for each cell. The second step is to obtain a global discretization by imposing continuity of the intensity and continuity of the normal component of the flux across cell interfaces. Since each cell in a hanging-node mesh is a quadrilateral, the first step in applying the SO method is identical to that for standard quadrilateral meshes. However, imposing continuity of the intensity and continuity of the normal component of the flux is not straightforward on hanging-node meshes because the intensity and flux unknowns do not coincide as they do on standard meshes. Thus, one of our new results determines

how to impose continuity of the intensity and the normal component of the flux at three-cell hanging-node interfaces. The most accurate results were obtained when we imposed strong continuity of fluxes (the flux on the coarse-grid interface coincides with the fluxes on the fine-grid interface) and weak continuity of intensities.

The new discretization has been tested on a number of cases. It has been shown that the discretization preserves the uniform flow. A textbook example is shown in the top figure. The solution of the diffusion equation has a sharp peak in the middle of the domain and close to zero near the domain boundary. The calculation were performed on locally refined and quasi-uniform grids. As shown in the figure, the adaptive grid has three levels of refinements. The solution obtained with this grid is very close to the solution computed on a quasi-uniform grid with approximately four times more mesh cells.

[1] Konstantin Lipnikov, Jim Morel, and Mikhail Shashkov. "Mimetic Finite Difference Methods for Diffusion Equations on Non-Orthogonal, AMR Non-conformal Meshes," LAUR-03-1765, submitted to *J. Comput. Phys.* http://cnls.lanl.gov/~shashkov.

[2] R. Anderson, R. Pember, and N. Elliott. "An Arbitrary Lagrangian-Eulerian Method with Local Structured Adaptive Mesh Refinement for Modeling Shock Hydrodynamics," presented at the 40'th AIAA Aerospace Sciences Meeting and Exhibit, January 14–17, 2002, Reno Nevada, AIAA paper 2002-0738, published by the *American Institute of Aeronautics and Astronautics*,1801 Dr. Alexander Bell, Suite 500, Reston, VA 20191-4344.

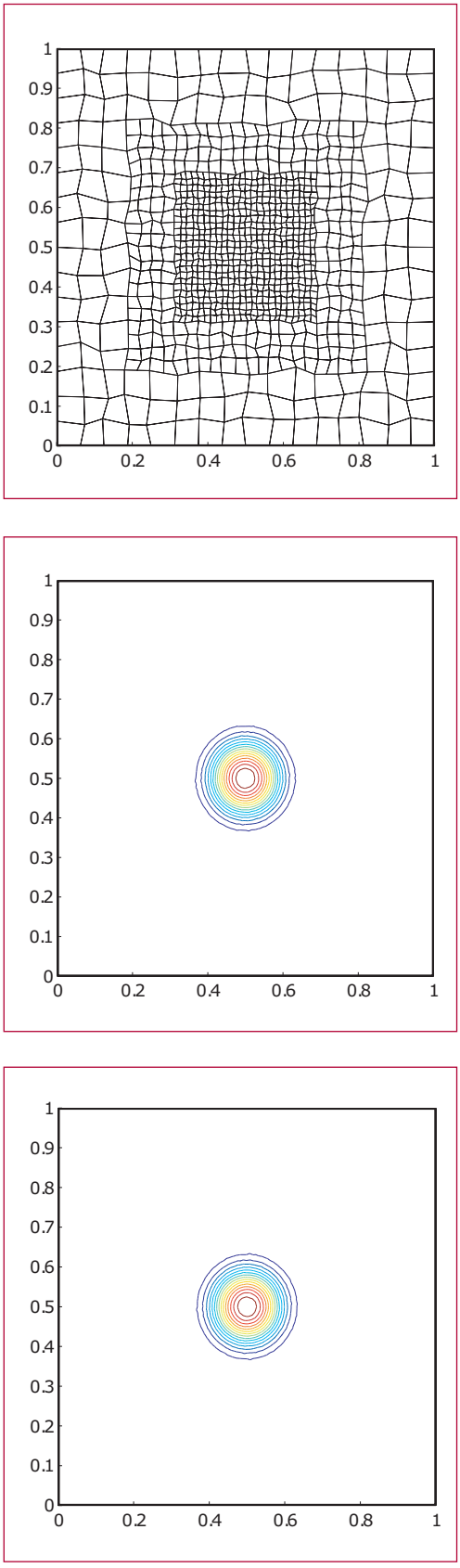

***Figures—** The textbook example showing the locally refined mesh (top picture) and isolines of discrete solutions computed on locally refined mesh (middle picture) and quasi-uniform mesh with approximately four times more elements (bottom picture).*

ALE INC. New 2-D ALE Code on General Polygonal Meshes

Raphaël Loubère and Mikhail Shashkov, T-7; loubere@lanl.gov

In this work we have developed a 2-D unstructured Arbitrary-Lagrangian-Eulerian code. This code is devoted to solve CFD problems for general poygonal meshes with fixed connectivity. Main components of the method are

I– A Lagrangian Scheme. Each polygon is split into subcells. The compatible Lagrangian hydrodynamics equations are solved during one time step and the mesh is moved according to the fluid velocity [7], [8], [5], [6].

II– An Untangling process which ensures the validity of the mesh, if the mesh was tangled as a result of the Lagrangian step. The method finds an untangled mesh which is as close as possible to the previous Lagrangian grid [4], [3], [9].

III– A Reference Rezone Jacobian Strategy, which improves the quality of the untangled mesh and, at the same time, requires the new mesh to be close to the original untangled grid (from step II) and preserve interfaces between materials [2].

IV- a Remapping method, which gives the linear and bound preserving remapped hydrodynamics variables on the new mesh [1], [11].

These four steps have been adapted to the subcell description of the scheme and the polygonal meshes. The untangling and the reference rezone Jacobian processes deal now with general polygonal meshes and preserve the interfaces between materials. The remapping step is performed from a subcell point of view.

Code can be used as a purelly Lagrangian one (only step I is used), an ALE one (*x* Lagrangian steps are performed then steps II, III, IV are activated) or as an Eulerian one (steps I and IV are used and the remapping is done on the same initial grid).

Some examples of simulations using ALE INC. code are presented on methods on the unstructured 3-D grids.

Figure 1 shows the triple point problem, this simulates the interaction between a planar shock wave and a heavy corner shape obstacle, the mesh is presented. The Dukowicz problem is solved with an unstructured mesh, the results are shown in Figure 2.

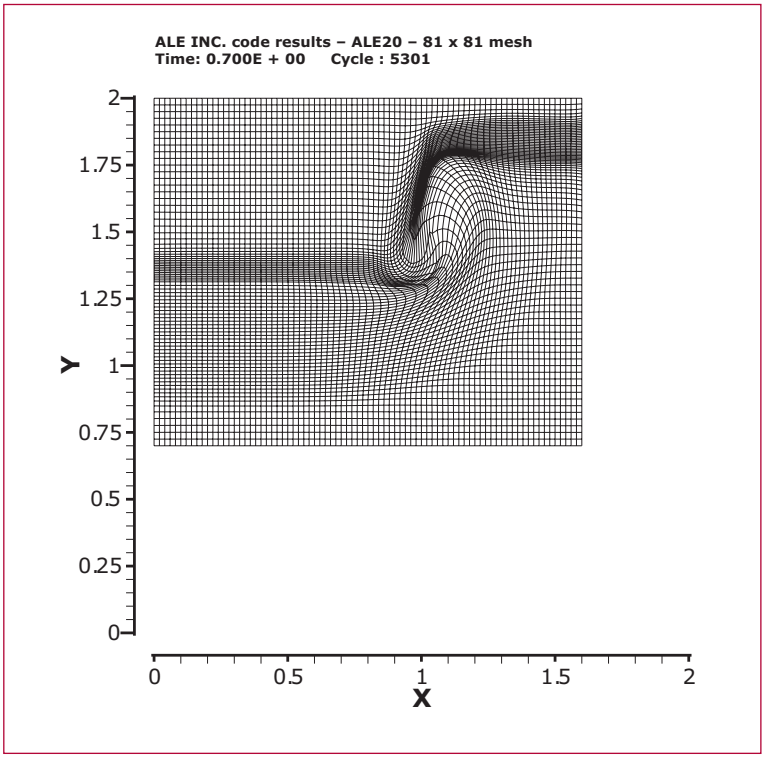

Figure 1— Triple point problem– Uniform logical rectangular grids, 81 x 81.

[1] L. G. Margolin and M. J. Shashkov, "Second-order Sign-preserving Conservative Interpolation (remapping) on General Grid," *Journal of Computational Physics* **184,** 266–298 (2003) .
[2] P. Knupp, L. G. Margolin, and M. J. Shashkov, "Reference Jacobian Optimization-based Rezone Strategies for Arbitrary Lagrangian Eulerian Methods," *Journal of Computational Physics,* **176,** 93–12 (2002).
[3] P. Knupp, "Hexaedral and Tetrahedral Mesh Untangling," *Engineering with Computers* **17,** 261–268 (2001).
[4] P. Vachal, M. Shashkov and R. Garimella, "Untangling of 2D Meshes in ALE Simulations," *Journal of Computational Physics.*
[5] J. Campbell and M. Shashkov, "A Compatible Lagrangian Hydrodynamics Algorithm for Unstructured Grids," LA-UR-00-3231.
[6] J. Campbell and M. Shashkov, "A Tensor Artificial Viscosity using a Mimetic Finite Difference Algorithm," *Journal of Computational Physics* **172,** 739–765 (2001).
[7] E. J. Caramana and M. Shashkov, "Elimination of Artificial Grid Distortion and Hourglass-Type Motions by Means of Lagarangian Subzonal Masses and Pressures," *Journal of Computational Physics* **142**, 521–561, (1998).
[8] E. J. Caramana, D. E. Burton, M. J. Shashkov, and P. P. Whalen, "The Construction of Compatible Hydrodynamics Algorithms Utilizing Conservation of Total Energy," *Journal of Computational Physics*, **146**, 227–262, (1998).
[9] P. Vachal, R. Garimella, M. J. Shashkov, and R. Loubere, "Untangling of meshes in ALE simulations," *7th U. S. Nat. Congress on Computational Mechanics*, "Albuquerque, July 2003.
[10] M. Kucharik, M. J. Shashkov, and B. Wendroff, "Efficient Local Bound-preserving Conservative Interpolation," *7th U, S. Nat. Congress on Computational Mechanics*, Albuquerque, July 2003.
[11] M. Kucharik, M. J. Shashkov, and B. Wendroff, "An Efficient Linearity and Bound-preserving Remapping Method," *Journal of Computational Physics.*

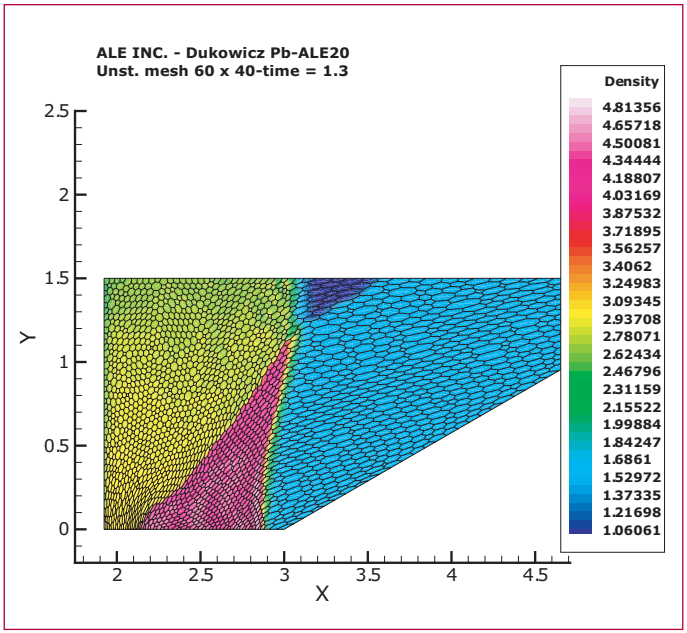

Figure 2—Dukowicz problem, unstructured polygonal mesh, density and mesh at t = 1.3.

Parallel, Scalable, and Robust Multigrid for Diffusion Problems on Structured Grids

John D. Moulton, Travis M. Austin, Markus Berndt, Benjamin K. Bergen, Joel E. Dendy, T-7; moulton@lanl.gov

Introduction:

Robust and efficient multilevel iterative solvers are vital for the predictive simulation of complex multiscale and multicomponent nonlinear applications. Specifically, diffusive phenomena play a significant role in applications of interest to ASC, including radiation transport, flow in porous media, and composite materials. In fact, the solution of the diffusive component (elliptic component) of these systems frequently dominates the simulation cost because it is characterized by a discontinuous diffusion coefficient with fine-scale spatial structure. Thus, efficient multilevel iterative methods are crucial because their solution cost scales linearly with the number of unknowns (i.e., optimal algorithmic scaling). In particular, this optimal scaling facilitates the efficient three-dimensional multiscale simulations of linear problems. It also expands the applicability and enhances the effectiveness of large three-dimensional multicomponent nonlinear simulations that advance implicitly in time (e.g., matrix-free Newton-Krylov methods) through efficient and robust preconditioning of the Krylov iteration.

Robust Multigrid Algorithms:

Multigrid methods gained recognition in the late 1970s as an efficient algorithm for the solution of the discrete linear systems that arise from models of diffusive phenomena (e.g., heat conduction, neutron diffusion, single-phase saturated flow). These methods achieve their efficiency through the recursive use of successively coarser discrete problems (i.e., a sequence of coarse-grid discrete operators) in conjunction with smoothing on each level (e.g., a single Gauss-Seidel iteration on each level) to damp the highly oscillatory errors associated with each grid. Unfortunately, early multigrid algorithms were fragile, with their efficiency strongly dependent on the variability of the model's coefficients. Considerable research in the early 1980s, much of it in T-7, led to the first multigrid algorithms that could be used reliably for a large class of practical problems. The key to the success of these robust *Black Box* methods, was the use of the fine-scale discrete model to construct, through a variational principle, the successively coarser coarse-grid operators. More recently, this class of practical problems has been expanded further by using multigrid methods as preconditioners for various Krylov methods.

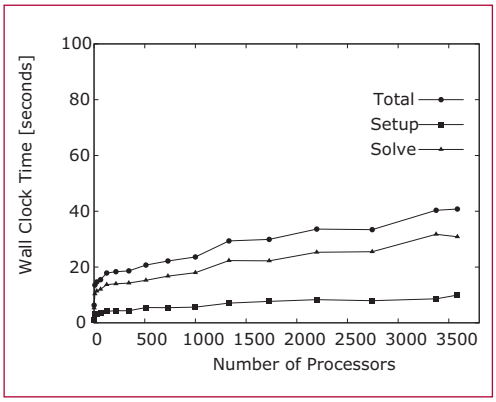

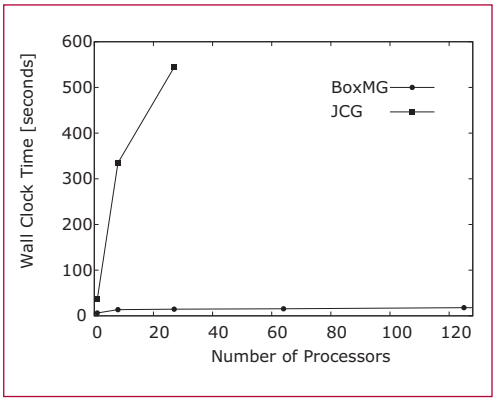

Figure—
A scalability study of the three-dimensional BoxMG code on QB for a standard discretization of a Poisson problem on the unit cube is shown in the left plot. The local problem size of 100 x 100 x 100 is kept fixed while the global problem size grows with the increasing number of processors. In the right plot zxv b b the scalability of BoxMG is contrasted with the poor scaling of Jacobi preconditioned conjugate gradient iterations.

A Parallel Scalable Implementation of BoxMG:

We implemented an MPI-based parallel version of the Dendy's Black Box Multigrid Code for structured grids [1] in both two and three dimensions that scales well over one sector of Q. In particular, we developed a customized version of the Message Passing for Structured Grid Toolkit (MSG) from netlib, created the necessary data structures, and established the necessary communication patterns to facilitate the reuse of the core computational kernels from the serial BoxMG code. At present, these codes have been tested on QSC, Q, and Theta, as well as T-7's Linux-based Beowulf clusters. As part of the SC&S Q milestone we demonstrated the scalability of these codes for a standard finite difference discretization of the Poisson equation. Specifically, for the three-dimensional case, shown in the figure, we considered a fixed local problem size of 100 x 100 x 100, growing the global problem size by increasing the number of processors. A common measure of parallel efficiency for this type of scalability study is the ratio of the time to solution on one processor to the time on *N* processors. For perfect scaling the ratio is one; very poor scaling is near zero. When solving a problem with over three billion unknowns to a relative residual in the 2-norm of 10^{-12} in 40 seconds, the three-dimensional BoxMG code achieved a parallel efficiency of 15.5%. A similar study in two dimensions acheived a parallel efficiency of 25.8%.

We anticipate that the BoxMG solvers will have a positive impact on ASC-related code projects. Thus far, we have integrated the two-dimensional parallel BoxMG code into the ZATHRAS gray thermal radiation transport equation solver. Although ZATHRAS is designed primarily for simulation on unstructured grids, it is also used for computations on structured grids. For this case we created the necessary interface routines to map the unstructured storage to the structured data structures of BoxMG. The initial timing results on small problems are very promising, and likely to improve with larger problems on more processors. Based on this success we plan to continue this collaboration and integrate the three-dimensional parallel BoxMG code into ZATHRAS in an analogous fashion.

[1] J. E. Dendy, Jr., "Black Box Multigrid," *Journal of Computational Physics* **48**, 366–386 (1982).

Mimetic Methods for Partial Differential Equations: Discrete Models for Maxwell's Equations in 3-D

Mikhail J. Shashkov and J. Mac Hyman, T-7; and Neil Carlson, Independent Consultant; shashkov@lanl.gov

We have developed high-quality algorithms for numerical modeling of electromagnetic problems. The new discrete models mimic many fundamental properties of the underlying physical problem, including the conservation laws, and the non-divergence of electric and magnetic fields. This new class of numerical methods will enable scientists to gain greater insights into electromagnetic systems, and solve new problems of interest to theDOE mission, and effectively use the inherent power of the current and future generations of scalable parallel supercomputers.

Electromagnetism must be accurately modeled in predicting the behavior of electromagnetic devises, such as motors, actuators and transformers, accelerators, astrophysical phenomena, and many biological systems. Computer simulations of electromagnetic problems with complex 3-D geometry rely on solving partial differential equations on unstructured meshes.

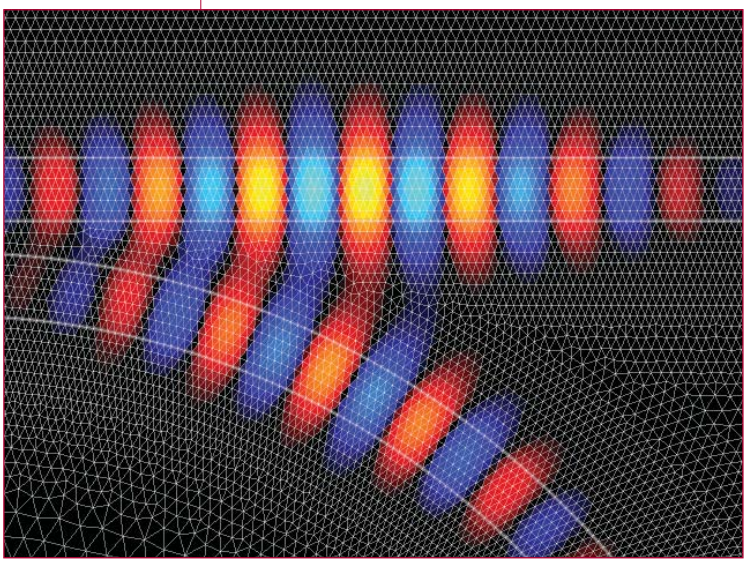

Figure 1—Magnetic field of the evanescent coupling of a light pulse from one semiconductor wave guide into another. A close-up showing a fragment of the mesh and field in the middle of the calculation.

The accuracy of these simulations depends on the quality of the numerical methods and is a challenging problem for electromagnetic problems on 3-D unstructured meshes. We have devised reliable unstructured mesh discretizations for the numerical solution of Maxwell's equations, which are the main element of any electromagnetic modeling. The improvements in the reliability, accuracy, and efficiency of these methods for solving systems of these equations will lead to significant advances in computer models based on these equations.

The new discrete analogs of differential operators mimic important properties of underlying mathematical and physical models. These methods automatically preserve conservation laws and other physically important quantities that can be derived for the continuum equations, but are often lost in the discretized approximations.

This advance is part of a larger effort to derive discrete analogs of first-order differential operators, including the divergence, gradient, and curl on general grids. These operators satisfy discrete analogs of the main theorems of vector and tensor analysis. That is, the finite difference methods satisfy discrete analogs of identities, symmetries and duality properties of the corresponding differential operators.

Because the finite difference discretizations satisfy these theorems, they do not have spurious modes in the solution, and the divergence-free conditions for electrical and magnetic fields are automatically satisfied. The tangential components of the electric field and the

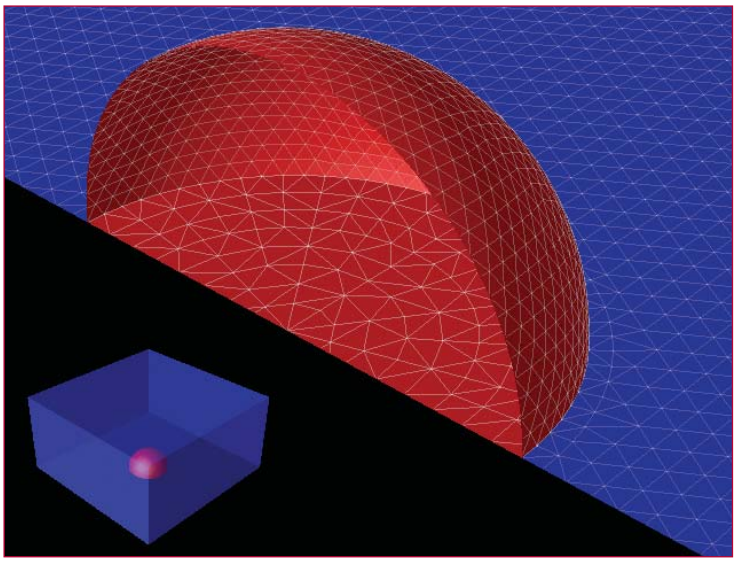

Figure 2— Mesh used for predicting the scattering of a y-polarized electric plane wave off of a low-index spherical inclusion. The grid on the interface between the two materials and on the z = 0 symmetry plane; the small inset is a transparent view of the entire computational domain.

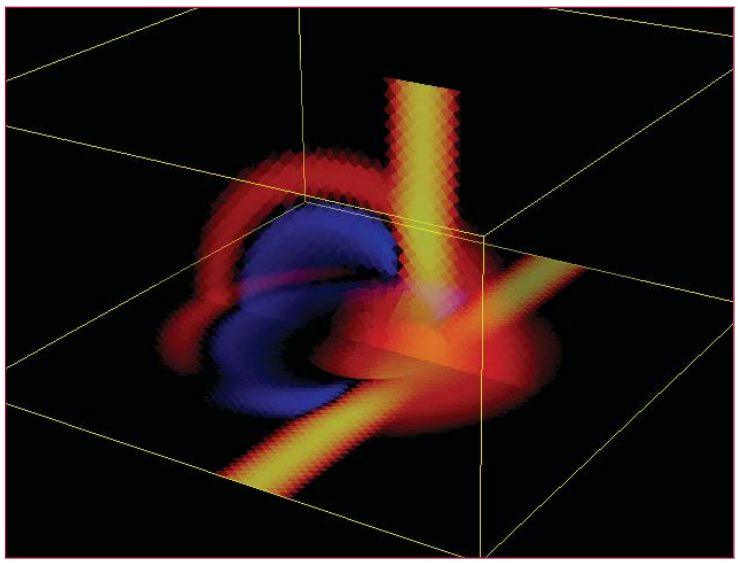

Figure 3— A close-up view of the y-component of electric field over three cut-planes through the domain.

normal components of magnetic flux used in the finite difference method are continuous even across material discontinuities. We choose these components as a description of the electromagnetic field in discrete case, which guarantees that the problems with strong discontinuous coefficients are treated correctly.

Figure 1 illustrates the effectiveness of our mimetic methods in simulating evanescent coupling of a light pulse from one semiconductor wave guide into another guide. The unstructured triangular mesh, carefully follows guides geometry. Figures 2 and 3 show an example of 3-D scattering. The methods used in these simulations are the foundation for the next generation of mimetic discrete models for electromagnetic simulations on general polyhedron.

Numerical Methods for Simulation of the Heating through Electromagnetic Induction

Mikhail J. Shashkov, T-7
and Neil Carlson, Independent consultant; shashkov@lanl.gov

The Telluride Code Project is tasked to develop and apply a new simulation tool designed to model and optimize the gravity-pour casting processes that are currently ongoing at LANL foundries in support of the U. S. Department of Energy (DOE) alloy manufacturing needs. The Telluride simulation tool must accurately model the entire alloy casting process in one integrated simulation. This process begins with molten alloy-free surface flow characteristic of the pouring and filling of a mold cavity. Cooling and solidification of the alloy follows shortly thereafter, followed by a more gradual cooling of the solid alloy to room temperature, which completes the casting process. Further homogenization heat treatment and machining prepare the alloy part for integration into the engineering system for which it is designed .

This work comes out of the development of an electromagnetic modeling capability for the Telluride project's materials processing/metal casting simulation tool Truchas. Of particular importance is the simulation of the heating of heavy metals and graphite mold and filling structures through electromagnetic induction. We have constructed reliable discretizations for the solutions to Maxwell's equations on general 3-D unstructured meshes for media with strongly discontinuous properties. These discretizations are based on discrete analogs of differential operators that satisfy the identities and theorems of vector and tensor calculus in discrete form. Our new methods mimic many fundamental properties of the underlying physical problem, including the conservation laws, the symmetries in the solution, and the nondivergence of particular vector fields. These methods do not allow spurious modes.

Here we present numerical results for the modeling of the following problem: a finite-length graphite cylinder exposed to an external, alternating magnetic field directed along its axis. The sinusoidally varying field induces an azimuthal current near the surface of the cylinder, which, because of the finite conductivity, dissipates energy in the form of a Joule heat in the graphite. Symmetry is exploited by modeling only a 60-degree wedge of the top half of the cylinder.

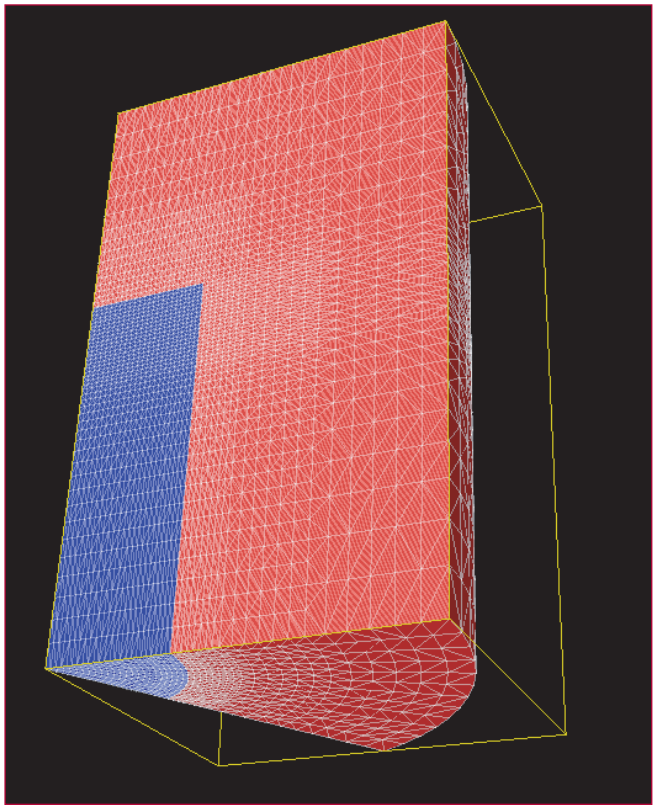

***Figure 1—** Shows the computational domain and grid (200-K tets). The blue region is the graphite cylinder, and the red region is free space.*

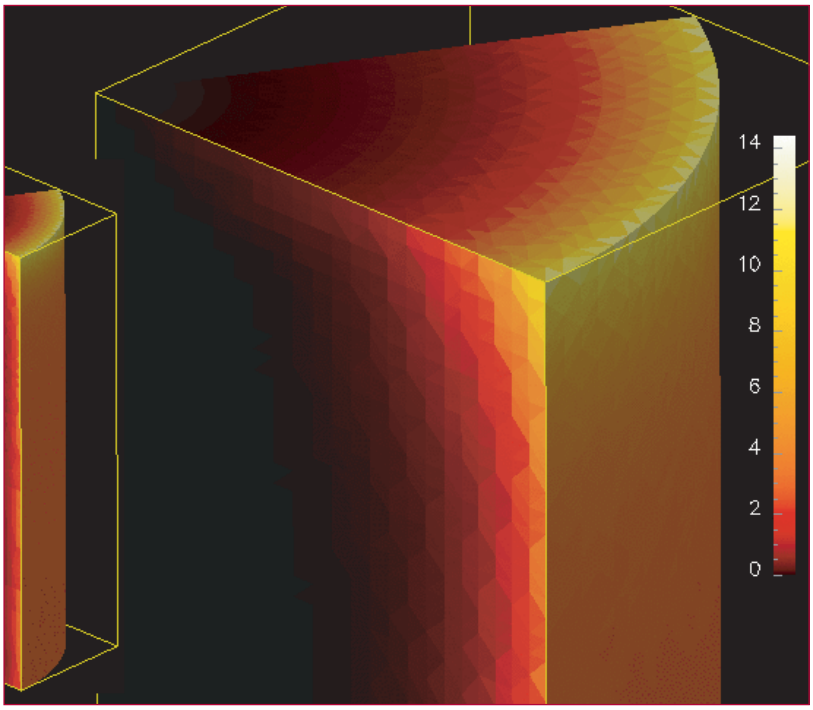

Figure 2— Shows the average of the Joule heat in the graphite cylinder over a cycle of the external field. This is the effective heat source that is used to model the heat conduction.

[1] James M. Hyman and Mikhail J. Shashkov, "Mimetic Discretizations for Maxwell's Equations," *Journal of Computational Physics*, **151**, 881–909 (1999).

[2] James M. Hyman and Mikhail J. Shashkov, "The Orthogonal Decomposition Theorems for Mimetic Finite Difference Methods," *SIAM Journal on Numerical Analysis* **36**, No. 3, 788–811 (1999).

[3] James M. Hyman and Mikhail J. Shashkov, "Mimetic Discretizations for Maxwell's Equations and the Equations of Magnetic Diffusion," *Progress in Electromagnetic Research, PIER* **32**, 89–121 (2001).

A Software Component for a Sign-Preserving and Linearity-Preserving ALE Remapping Method

Martin F. Staley and Mikhail J. Shashkov, T-7; mstaley@lanl.gov

Background

We have developed a software component implementation of the remapping algorithm described in [1].

Consider that we have a two-dimensional grid consisting of nonoverlapping cells that cover some region. Call this the old grid. Next, consider that we have another grid, with the same number of cells and the same connectivity, and that covers the same region. Call this the new grid. We assume that the new grid is a small perturbation of the old grid.

This situation arises in the context of arbitrary Langrangian-Eulerian (ALE) methods, in which the old grid is the result of the Lagrangian step, and the new grid is the result of a rezoning step in which the quality of the Lagrangian grid is improved in some way. This remapping algorithm is effective as long as the new grid is a small perturbation of the old grid. It is not required that the grids arise in an ALE context.

Algorithm

The remapping problem we will address here can be stated as follows: given mean densities of cells on the old grid, compute mean densities of cells on the new grid. The algorithm achieves this by performing three stages: density reconstruction, mass exchange, and mass repair. We will henceforth consider *density* to mean *mean density.*

For the *density reconstruction* stage, consider that the cell densities obey some underlying, theoretical density function ρ. We don't know what ρ is, but if we assume it is piecewise linear—one piece per cell—then we can use our discrete densities to reconstruct a reasonable candidate for ρ. For each cell, we consider a linear density function that achieves the cell's density at the cell's center of volume. Then, we use values of density in nearby cells to compute a reasonable gradient for the function. With a point and a gradient, we have our linear density function.

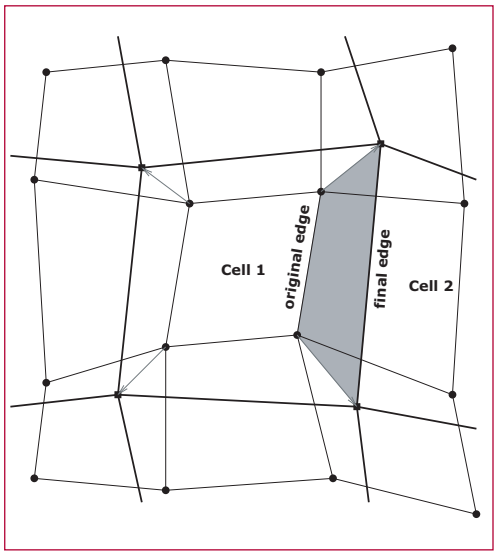

Figure 1— Swept region of an edge. When the original edge moves to its final position, the shaded region is swept.

For the *mass exchange* stage, consider that each edge of the grid has two adjacent cells. For each edge, we identify which cell the edge "moves into" more when we go from the old grid to the new grid. We then compute the integral of that cell's reconstructed density over the region swept by the edge as it moves. The resulting mass is removed from that cell, and added to the other cell.

For the *mass repair* stage, we first recognize that the mass exchange stage involved inexact integration of the overall density function ρ, in the sense that the mass exchange term was obtained by computing the integral over the swept region of the reconstructed density function on one particular cell, even though the swept region may have intersected

other cells. This made the algorithm efficient, because we did not need to compute exact intersections of new cells with old cells. However, as a result of inexact integration, new densities in individual cells can conceivably violate local bounds. The repair stage fixes out-of-bounds masses and densities while still conserving total mass.

Figure 1 shows the swept region of an edge. If we imagine moving the illustrated edge from the old grid (thin lines) to its position on the new grid (thick lines), then the shaded region is swept by the edge as it changes position. In the case illustrated, the edge moves into Cell 2 more so than into Cell 1, and therefore, the algorithm integrates the reconstructed density function for Cell 2 over the entire swept region. In the mass exchange stage, the resulting mass is subtracted from Cell 2 and added to Cell 1. In the mass repair stage, we recognize that the integration was inexact because the swept region intersected with the cells above and below Cell 2, not just with Cell 2 itself, and that there may therefore be out-of-bounds physical quantities in need of repair.

Software Component

The remap library is written entirely in ANSI standard C++, and is designed to be a true software component. It provides a structure into which you place a minimal set of geometry information, consisting of node coordinates on the old and new grids, and vertices (in counterclockwise order) of each cell. From this information, the library computes all other geometry information it needs. To make the remap library work with your grid, then, you must only provide an interface to put your grid into the remap library's simple form.

All relevant constructs in the library are written generically, with C++ templates, so that you can tell the remapper to use any suitably equipped array or array-element type.

The entire library consists of C++ header files, not C++ source files, and therefore requires no compilation—that is, no complicated configuration scripts or makefiles. To use the library with your C++ source file, you include a single C++ header file called `remap` at the top of your code, and then compile your code in whatever way you usually do.

Users may provide plug-ins to redefine stages within the remap process, including computation of cell volumes, cell centers-of-volume, minimum and maximum density bounds, density gradients for the piecewise-linear reconstruction, cell masses, mass exchange terms, minimum and maximum mass bounds, and finally mass repair and recomputation of densities given repaired masses.

Remaps may be performed on general unstructured two-dimensional Cartesian *(x,y)* and cylindrical *(r,z)* grids. The library does not require, say, that your cells are triangles or quadrilaterals. Cells may have any number of vertices greater than or equal to three. The library does assume, as the underlying remap algorithm does, that the cells are convex and that the grid's boundary is stationary.

Parallel Remapping

You may use the remap library on a serial machine or a SIMD (single instruction, multiple data) parallel machine. No special actions are required on a serial machine. On a parallel machine, you must provide either one (for a simple global mass repair) or two (for an iterative local mass repair)

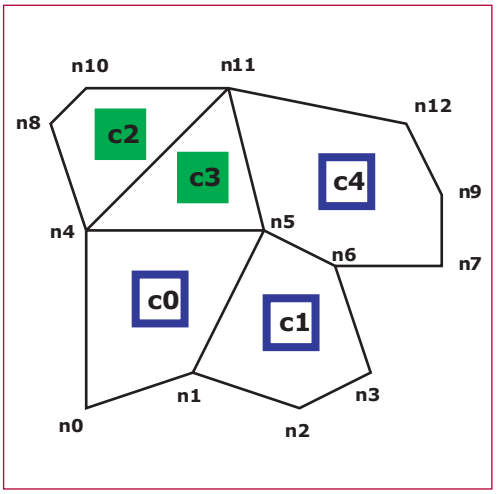

Figure 2—Geometry for the first processor. Cells shown in green are on-processor cells. Cells shown in blue are off-processor cells that touch on-processor cells.

plug-ins to perform parallel communication steps. The remap library itself makes no assumptions about your parallel communication library.

Consider a six-cell grid on a two-processor machine, with two cells on the first processor and four cells on the second processor. Figure 2 shows the portion of the grid on the first processor. There are 13 nodes, labeled `n0` through `n12`, and five cells, labeled `c0` through `c4`. Cells `c2` and `c3` are on this processor. Cells `c0`, `c1`, and `c4` are not, but they must be known to this processor because they touch one or more of its cells. Figure 3 shows the portion of the grid on the second processor. There are 14 nodes, labeled `n0` through `n13`, and six cells, labeled `c0` through `c5`. Cells `c0`, `c1`, and `c5` are on this processor. Cells `c3` and `c4` are not, but they must be known to this processor because they touch one of more or its cells.

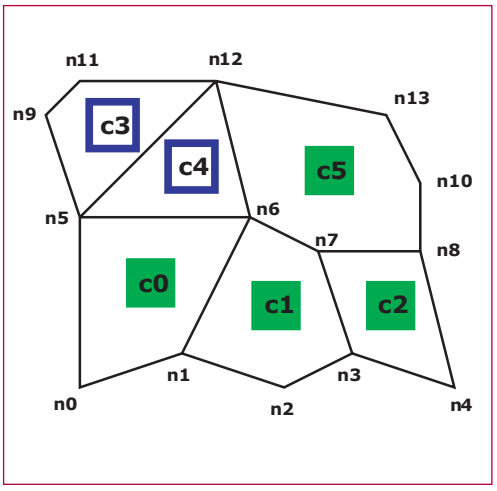

Figure 3—Geometry for the second processor. Cells shown in green are on-processor cells. Cells shown in blue are off-processor cells that touch on-processor cells.

In general, each processor must know about its own cells (numbering, say, $O(n^2)$), plus the small number (typically $O(n)$) of touching off-processor cells.

For each processor, you supply the old and new node coordinates, a list of each cell's vertices in counterclockwise order, and a flag telling whether the cell is on- or off-processor. Then, for each cell, you provide an input physical quantity, for example density, and tell the library to perform the remap.

Acknowledgements:
This work was funded under the Component Definition and Architecture R&D sub-subcomponent of ASCI. Project Leaders: R. Lowrie and T. Urbatsch.

[1] M. Kucharik, M. Shashkov, and B. Wendroff, "An efficient linearity-and-bound-preserving remapping method," *J. Comput. Phys.* **188**, 462–471 (2003).

Stochastic Partial Differential Equations: Predictive Modeling–Coping with Uncertainty

Daniel M. Tartakovsky, T-7;
and A. Guadagnini, Politecnico di Milano;
dmt@lanl.gov

Our ability to make accurate predictions of the behavior of most physical and social systems is often hampered by the lack of sufficient data. Recent advances in the theory and application of stochastic partial differential equations provide a powerful tool for coping with the uncertainty that arise from our limited knowledge of such systems.

Although it has long been recognized that simulations of most physical systems are fundamentally stochastic, this fact remains overlooked in most practical applications. Even essentially deterministic systems must be treated stochastically when their parameters are under-specified by data. Parameter uncertainty limits our ability to accurately simulate and predict the manufacturing of composite materials, scaling in condensed and soft matter, earthquakes and seismic monitoring, reservoir exploitation, environmental remediation, and other complex systems important to the core mission of the Department of Energy.

To improve our ability to predict the dynamics of systems with limited data, we have assembled an interdisciplinary team of researches from applied mathematics, statistics and scientific computing. Our research has led to new approaches that improve the accuracy of the predictions and give tighter bounds on uncertainty arising from stochastic simulations of physical system states and parameters.

We have developed a method of random domain decomposition (RDD) that provides a novel doubly stochastic model to quantify the impact of the type of spatially heterogeneous random processes that typically appear in realistic simulations of physical systems. The problem domain is decomposed according to stochastic geometries into disjoint random fields. The stochastic decomposition is determined by variations in the parameter space based on additional (uncertain) geometric information that can be derived from new characterization techniques and also from expert knowledge.

Previous work has tended to concentrate on spatially homogeneous parameterizations, or at most on heterogeneous parameter fields whose geometry is assumed known with certainty. This is almost never the case in natural systems. RDD allows scientists to predict the behavior of multiscale systems with heterogeneous parameterizations that depend on realistic geometric uncertainty.

RDD has also led to new approaches for reconstructing images from sparse and noisy data. In addition to providing a best estimate of an image, RDD yields its probabilistic description.

One application, where RDD has already made a significant impact, is contaminant transport in subsurface environments. Such environments are notoriously heterogeneous and their characterizations are highly costly and often inaccurate. Since contaminants tend to move through highly conductive regions, it is paramount to identify them from available data. Since such data are scarce, it is important to quantify uncertainties in our predictions in terms of the uncertainty of the data, and to evaluate the corresponding risks.

Figure 1 shows an example of a boundary between two heterogeneous materials computed from available data with various degrees of certainty. The turquoise regions serve as contaminant conduits in the otherwise impermeable rock that is shown in red. Note, that as our predictions become more conservative (i.e., have higher probability of low-conductivity occurrence), the size of the highly conductive regions diminishes.

Combined with the probabilistic image reconstruction, RDD has allowed us to make predictions of physical processes, such as fluid flow, occurring in this composite medium with accuracy not attainable by other approaches.

Our future research efforts in predictability of physical systems in complex heterogeneous environments will involve developing (i) state-of-the-art statistical techniques for parameter estimation and probabilistic image reconstruction, (ii) new methods of analysis of stochastic partial differential equations, and (iii) efficient methods for their numerical implementation.

For further information on this subject contact: Dr. Charles H. Romine, Program Manager Applied Mathematical Sciences Division Office of Advanced Scientific Computing Research Phone: 301-903-5152, romine@er.doe.gov

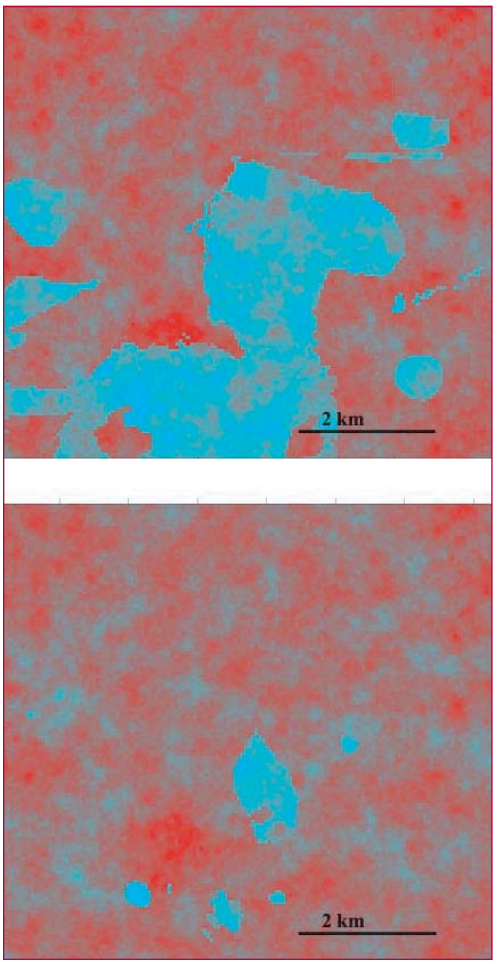

Figure 1— Porous media composed of two heterogeneous materials, one of high (turquoise) and the other of low (red) conductivity. The material distributions are reconstructed from a sparse geophysical data set. The top figure shows the boundary configuration corresponding to 74% probability of low-conductivity occurrence. The bottom figure provides a more conservative estimate of the boundary configuration (87% probability of low-probability occurrence).

Noise Sensitivity of Sparse Signal Representations

Brendt E. Wohlberg, T-7; brendt@t7.lanl.gov

Fourier and wavelet transforms, ubiquitous in signal processing and data analysis, represent a signal as a linear combination of vectors from a basis set that is *complete*, meaning that the number of basis vectors is such that there is no redundancy, with exactly one possible representation for every signal to be decomposed. An alternative approach, which has recently been the subject of considerable research, is to decompose a signal onto an *overcomplete* set, usually referred to as the *dictionary*, in which the number of basis vectors (or *atoms*) is such that there are many different possible representations for a specific signal. To make the decomposition well-defined, it is necessary to define some criterion for selecting one particular solution. The simplest of these is the minimum l^2 norm solution, which corresponds to the pseudo-inverse of the matrix with the atoms of the dictionary as its columns. Minimum sparsity, the number of nonzero coefficients in the solution, offers significant advantages as an optimality criterion. Such sparse representations have found a number of applications [1], including EEG (electroencephalography) and MEG (magn toencephalography) estimation [2], time-frequency analysis [3], and spectrum estimation [4].

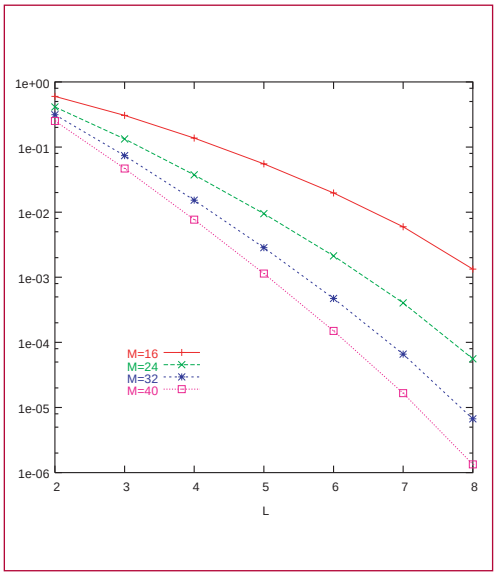

***Figure 1—** Graph illustrating the increase in noise sensitivity with decreasing sparsity for DFT dictionaries with M atoms, each of which is a vector of eight coefficients. The sparse representation error magnitude may be as large as ζ_L^{-1} times the signal error magnitude.*

Sparse representations are of particular interest when one has reason, based on physics or other prior knowledge, to expect the signals in question to consist of a superposition of only a few fundamental functions, the coefficients of which are significant. In this case, it is useful to know when the sparse decomposition of the signal may be expected to correspond to the original generating coefficients. A number of recent unique results [2,5,6,7,8] provide conditions under which a unique sparse decomposition exists, so that exact reconstruction of the original generating coefficients is possible in the absence of any noise.

These results, however, are of little assistance when the signal is known to include a noise component. Under these more realistic conditions, one would like to bound the reconstruction error in terms of the signal noise magnitude (that is, given a bound on the size of the noise in the signal, provide a bound on the maximum distance between any two appropriate sparse reprentations of that signal). The construction of such bounds is described in detail in a recent publication [9]. Of these bounds, the simplest to describe is constructed in terms of ζ_L, a measure of the stability of the linear independence of L-sized subsets of atoms of a dictionary; given signal $\mathbf{s}$ with sparse representation $\boldsymbol{\alpha}$ and signal $\mathbf{s}'$ with sparse representation $\boldsymbol{\beta}$, one has the bound

$$\| \Delta \boldsymbol{\alpha} \| \leq \zeta_L^{-1} \| \Delta \mathbf{s} \|$$

on the difference $\Delta\boldsymbol{\alpha}$ between the two solutions in terms of the difference $\Delta\mathbf{s}$

between the two signals, where L is the sum of the number of nonzero coefficients in solutions α and β.

The figures compare ζ_L values for two example overcomplete dictionaries; one based on the Discrete Fourier Transform (DFT) and the other on the Discrete Cosine Transform (DCT). Except at very low-noise levels, very high degrees of sparsity, or small overcompleteness factors, these results indicate very high-noise sensitivities for the common DFT and DCT dictionaries. Reconstructions with respect to the overcomplete DCT dictionary are vastly more noise sensitive than those with respect to the overcomplete DFT dictionary. In superresolution applications using overcomplete sinusoidal dictionaries [4], for example, these results allow an explicit quantification of the tradeoff between spectral resolution (depending on the degree of overcompleteness of the dictionary) and noise sensitivity of the result, and also suggest that the DFT dictionary is a better choice for superresolution than the DCT dictionary due to the significantly lower noise sensitivity of the former dictionary.

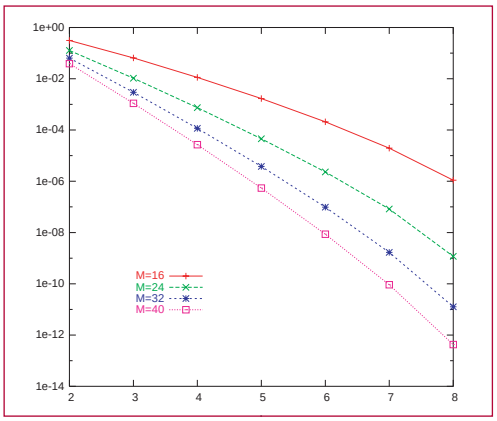

Figure 2— Graph illustrating the increase in noise sensitivity with decreasing sparsity for DCT dictionaries with M atoms, each of which is a vector of eight coefficients. The sparse representation error magnitude may be as large as ζ_L^{-1} times the signal error magnitude.

[1] B. D. Rao, "Signal processing with the sparseness constraint," In "Proceedings ICASSP-98" (IEEE International Conference on Acoustics, Speech and Signal Processing) **3**, 1861–1864, Seattle, WA, USA, (May 1998).

[2] I. F. Gorodnitsky and B. D. Rao, "Sparse signal reconstruction from limited data using FOCUSS: a re-weighted minimum norm algorithm," *EEE Transactions on Signal Processing* **45** (3), 600–616, (March 1997).

[3] S. G. Mallat and Z. Zhang, "Matching pursuits with time-frequency dictionaries, *IEEE Transactions on Signal processing* **41**(12), 3397–3415 (December1993).

[4] S. Chen and D. Donoho, "Application of basis pursuit in spectrum estimation, in "Proceedings ICASSP-98 (IEEE International Conference on Acoustics, Speech and Signal Processing) **3**, 1865–1868 Seattle, WA, USA, (May 1998).

[5] D. Donoho and X. Huo, "Uncertainty principles and ideal atomic decomposition," *IEEE Transactions on Information Theory* **47** (7), 2845–2862 (November 2001).

[6] M. Elad and A. M. Bruckstein, "A generalized uncertainty principle and sparse representation in pairs of bases," *IEEE Transactions on Information Theory* **48** (9), 2558–2567 (September 2002).

[7] R. Gribonval and M. Nielsen, "Approximation with highly redundant dictionaries," in "Proceedings of SPIE: Wavelets: Applications in Signal and Image Processing," **5207**, San Diego, CA, USA (August 2003).

[8] R. Gribonval and M. Nielsen, "Sparse representations in unions of bases," *IEEE Transactions on Information Theory* (December 2003) To appear.

[9] B. Wohlberg, http://math.lanl.gov/~brendt/Publications/wohlberg-2003-sensitivity.shtml "Noise sensitivity of sparse signal representations: Reconstruction error bounds for the inverse problem," *IEEE Transactions on Signal Processing* **51** (12) 3053–3060 (December 2003) LA-UR-02-1827.

T-10 Theoretical Biology and Biophysics

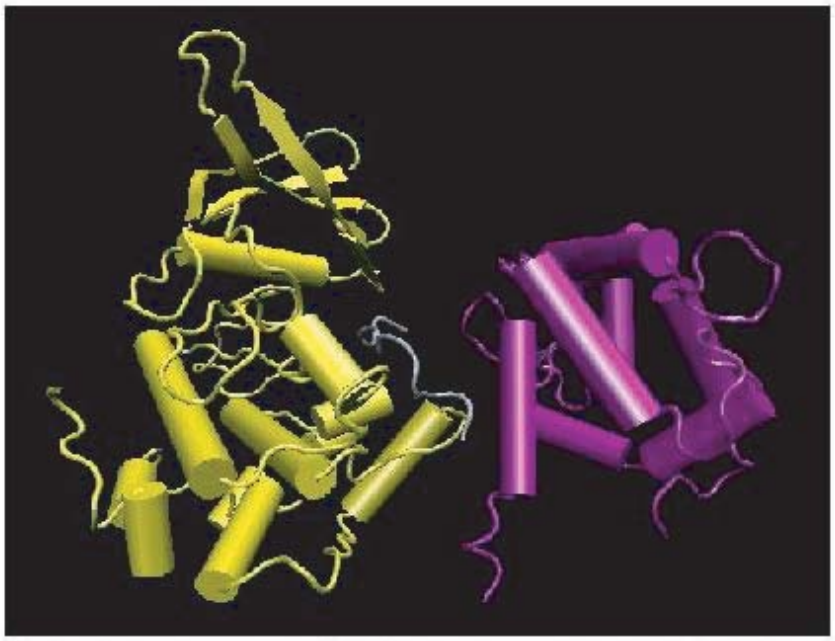

Fluctuations are Crucial for Protein Function: Slaved and Semislaved Motions Control Protein Dynamics

Paul W. Fenimore, Hans Frauenfelder, and Benjamin H. McMahon, T-10; and Robert D. Young, Northern Arizona Univ.; paulf@lanl.gov

Proteins are the dynamic workhorses of biology; they wiggle and move to perform their functions. Analyzing a range of experiments, particularly neutron scattering and Mössbauer effect, we show that the protein motions fall into three classes, slaved, semislaved, and nonslaved. Slaved motions follow the dielectric fluctuations in the bulk solvent, are absent in a solid environment, and their rate coefficients can be approximated by a Vogel-Tammann-Fulcher relation. They involve large-scale conformational changes and allow, for instance, the entrance and exit of ligands such as dioxygen in myoglobin. Semislaved motions follow fast fluctuations in the protein's hydration shell, occur even if the protein is embedded in a solid, but are absent in dehydrated proteins; their rate coefficient can be approximated by a Ferry relation. They involve side-chains and the hydrogen-bond network and may permit processes such as the passage of ligands inside myoglobin. Nonslaved motions are independent of the external fluctuations and are, for instance, involved in covalent binding of ligands to the heme iron inside myoglobin. The fluctuations responsible for slaving are similar to the α relaxation in glasses. The fluctuations responsible for semislaving are similar to the β relaxations in glasses. The recognition that the slaved and the semislaved protein fluctuations are different processes changes the energy landscape of myoglobin. Tier 1, containing the statistical substates (CS1) involves two "subtiers," CS1α and CS1β. Slaved motions are fluctuation among the substates in CS1α, semislaved motions are fluctuations among the substates in the newly identified CS1β. Dynamics lessons learned from proteins may be useful for other fields such as glasses, nonaqeous chemistry, and food sciences.

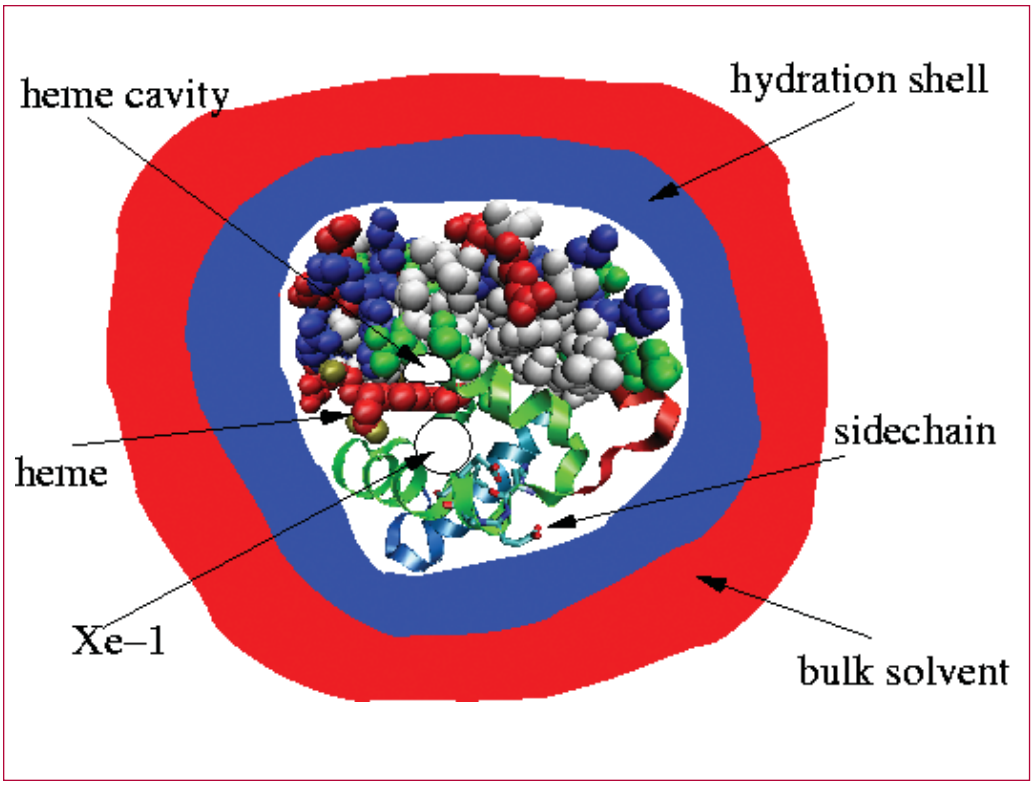

Figure — A look into myoglobin. The lower half of the structure shows three alpha helices, part of the protein backbone, with one side chain as an example. The upper half provides a space-filling view. Between the two halves is a heme group, in red. Two cavities, the heme cavity and the Xe1 cavity, are also depicted. The hydration shell (blue) and the bulk solvent (red) envelop the protein.

An Atomic Description of the Folding/Unfolding of Protein A

Angel E. García, T-10;
and Jose N. Onuchic, UC-San Diego;
axg@lanl.gov

We studied the folding mechanism of a three-helix bundle protein at atomic resolution, including effects of explicit solvation, and over a broad range of temperatures spanning the folded and unfolded states. Using the replica exchange molecular dynamics (REMD) we performed sufficient sampling to obtain free energy, entropy, and enthalpy surfaces as a function of structural reaction coordinates. This is the first all atom simulation to observe protein folding/unfolding transitions, done with explicit solvent and without any constraints. For the first time, multiple transitions from the unfolded ensemble to the native minimum have been observed in a computer simulation with a fully atomistic description. The highly parallel REMD algorithm allowed us to make numerical investigations that were practically unfeasible about one year ago. This new picture also adds new features to our previous understanding of folding.

Simulations were done in an explicit solvent, under periodic boundary conditions. The 46 amino acid system was contained in a cubic box containing 5107 water molecules, and over 16-k atoms. We simulated 82 replicas of the water-protein system, with temperature ranging from 277 to 548 K. All replica calculations are done at constant volume and temperature. The temperatures of the replicas were chosen to maintain an exchange rate among replicas of 8–20%. Exchanges are attempted every 250 integration steps (0.375 ps). To generate a set of initial conditions that broadly covers the configuration space of the protein, we performed independent simulations, extending from 0.5 to 2 ns, at temperatures T = 275 to 1000 K. We choose configurations at random from this sampling and kept structures that were partially collapsed as initial structures for the replicas. The REMD simulation was carried out for 13.085 ns/replica (1.07 μs total simulation time). The calculation took a total of 22 weeks CPU time on 82,750-MHz PIII processors.

Free-energy surfaces, $\Delta G(\rho,d)$, were calculated from histograms of the occurrence of selected order parameters (the fraction of native contacts, ρ, and the distance from the folded structure, d) in the configurational ensembles generated for each temperature. Any of the two order parameters used, d or ρ, was sufficient to distinguish the folded and unfolded states, suggesting that a collective folding transition is occurring with concurrent secondary and tertiary structure formation and side chain packing, as expected from a funnel-like landscape. Also, the unfolded basin shows sufficient resemblance to the native state indicating that this ensemble is not fully disordered. We decompose the free-energy landscape into its enthalpic and entropic components by fitting all free-energy surfaces at all sampled temperatures. We also explore the interplay between folding and water dewetting (Figure 2). This work was published in December, 2003: A. E. Garcia and J. N. Onuchic, "Folding a protein in a computer; an atomic description of the folding/unfolding of protein A," *Proc. Natl. Acad. Sci.* **100** 13898–13903 (2003).

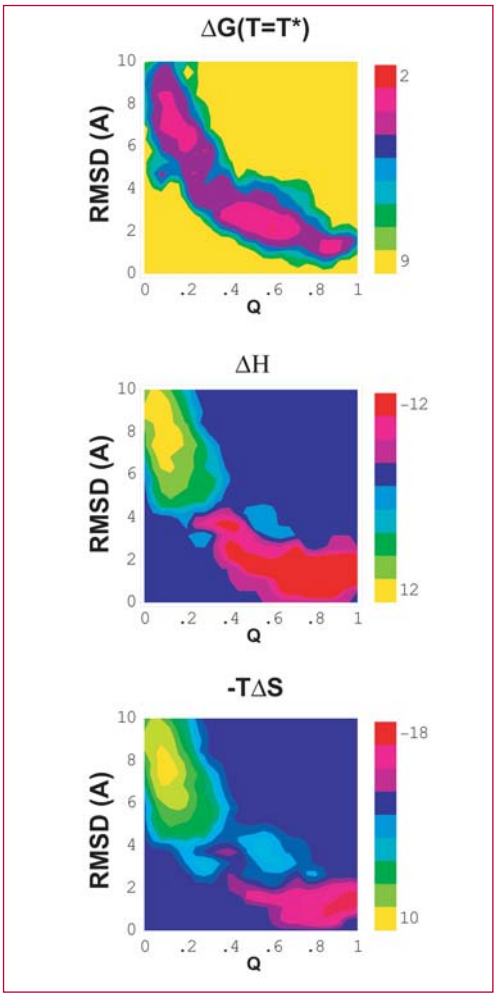

Figure 1—
Contour maps of the (a) free energy at the transition temperature, ΔG(T=T=421 K) as a function of the root mean square distance from the experimental folded structure, d, and the fraction of native contacts, ρ. Native contacts are defined as pairs or amino acids that have atoms within 6.5 A of each other in the folded structure. Protein A has 52 native contacts. At T=T* there are two large free-energy basins that are equally populated. The folded state is defined by d < 4 A and ρ > 0.3, and the unfolded state is defined by d > 4.0 A and ρ < 0.3. (b) Enthalpy, ΔH and, (c) entropy, TΔS. The folded basin is dominated by low enthalpy and low entropy. The unfolded basin is dominated by high entropy and high enthalpy. The deep minimum in ΔH covers the whole folded state basin (d< 4 A, ρ > 0,3). The entropy has a deep minimum in the region corresponding to the desolvated folded state (ρ > 0.7, d< 2 A).*

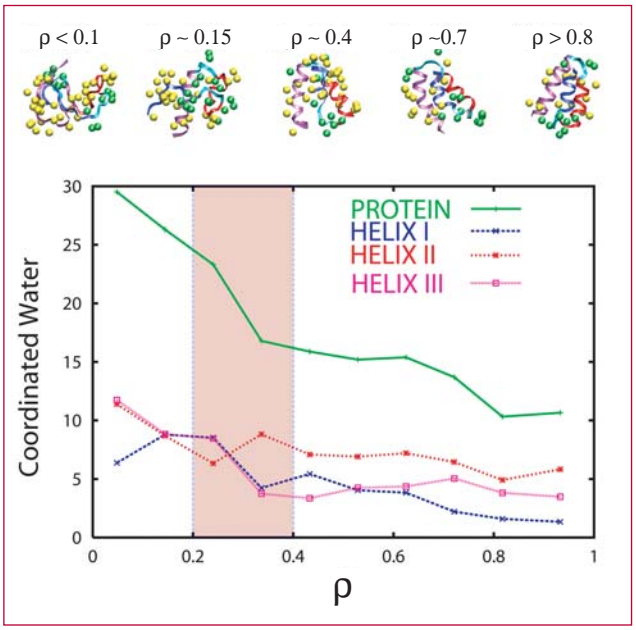

Figure 2—
Water coordination of the backbone carbonyl oxygen atoms in helices I, II, III, and turns, as a function of the fraction of native contacts formed, ρ. The top figures show selected configurations of the protein and the water molecules as the folding progresses along the reaction coordinate ρ. These plots show how structure formation and desolvation are coupled along the folding reaction.

Nature of Structural Inhomogeneities on Folding a Helix and Their Influence on Spectral Measurements

S. Gnanakaran, Robin M. Hochstrasser, and Angel E. García, T-10; gnana@lanl.gov

The knowledge of unfolded state distributions and how they represent the ensemble of pathways to folded states is a key element in understanding the folding of proteins. Our goal is to interface thermal denaturation experiments with theoretical simulations in a manner that will enable the capture of the structural origin and the detailed characterization of these distributions. Short alanine based peptides that form stable helices in aqueous solution have been the focal point of several experiments aimed at probing the thermodynamics and kinetics of helix formation by means of the temperature (T) dependence of their infrared (IR) spectra. These peptides are highly α-helical at low T and undergo thermal denaturation. The amide-I band of peptides is highly sensitive to secondary structure and shows a characteristic behavior upon thermal denaturation for helical peptides. At lower T, it is narrower with higher peak intensity. During unfolding it shifts to higher frequency and broadens. The loss of peak intensity is generally associated with the loss of helical content. Until now, attempts to realistically model the changes in their spectra upon unfolding have been hampered by a lack of detail regarding the structural heterogeneity that evolves during thermal denaturation. If the structure distributions could be visualized and modeled more sharply the temperature dependent changes of the spectra could be used more effectively to provide invaluable information concerning local helix structures and unfolded state distributions.

The theoretical challenge is to capture the relevant structural ensembles of the peptide that arise on thermal denaturation. It requires an efficient conformational sampling technique that can gather the appropriate canonical population from the free-energy landscape of the peptide. The replica-exchange molecular dynamics (REMD) methodology, which has emerged as an efficient technique to sample the conformational space of short peptides in explicit solvent, appears to offer a much improved approach to determining the unfolded state distributions relevant to experimental spectra. The model system considered is a 20-residue alanine-based helical peptide with three lysines (K), the AK peptide, in explicit aqueous solution. It has been the focus of linear IR, nonlinear IR, and vibrational circular dichroism experiments. The local information within this peptide has also been characterized utilizing isotope labeling. REMD simulations of the capped helical peptide, $AA(AAKAA)_3AAY$, is carried out over a range of T where the system populates the folded and unfolded states. The ensembles from REMD provide insight into how the underlying inhomogeneities due to hydrogen bonding (H-bond) and conformational variability of a folding/unfolding solvated helix are manifested in an IR spectrum. This sampling also enables one to define a set of ensemble that characterizes the conformational variability for configurations identified by their fraction of helical content. The definition of h-ensembles permits the evaluation of vibrational frequencies and inter-mode coupling in terms of states characterized by their helical content.

The backbone carbonyl H-bonding along the helix reveals that the nature

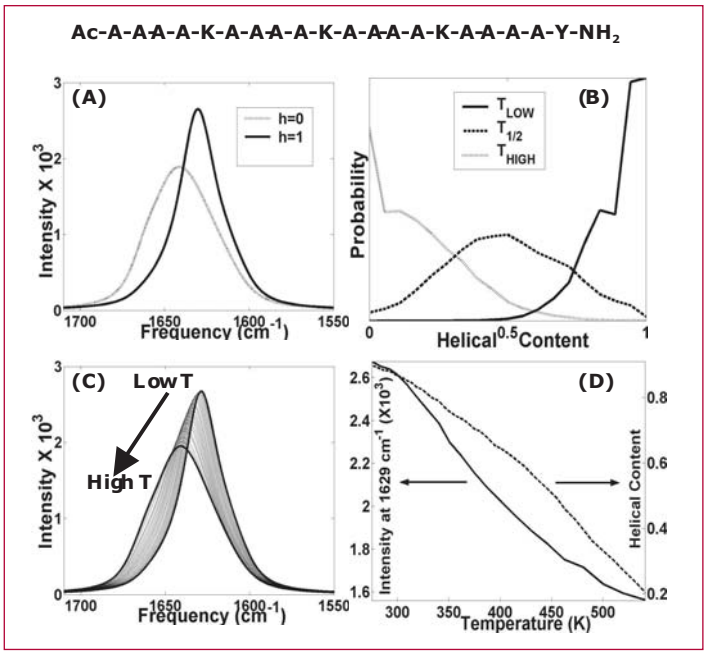

Figure 1— The behavior and nature of amide-I band upon thermal denaturation of AK peptide (sequence shown on top). The amide-I band calculated from completely helical (h=1) and nonhelical (h=0) ensemble is shown in Plot A. The distribution of helical ensembles (marked with fractional helical content) is shown in plot B at 3 different T. Plot C shows the IR spectra at 21 different T. In Plot D, the loss in intensity at 1629 cm^{-1} (max. peak at low T) and the helical content are plotted as function of T.

and behavior of solvent H-bonding is different depending on the position, temperature, and helicity of the AK peptide. The geometrical nature of the internal H-bond for the folded and unfolded peptides calculated from the simulations generally follows the experimental parameters often used in the definition of H-bonds in peptides and proteins. When the peptide is fully helical, the inter-mode coupling is uniform across the helix and has narrow distributions. In the completely nonhelical ensemble the translational symmetry of the coupling along the helical backbone is not found. These properties are incorporated into a simple exciton model to simulate and capture the trends associated with amide-I band upon solvation and thermal denaturation.

The solvent H-bonding to backbone carbonyl, which is present at all T, shifts the solvated amide-I band towards lower frequency compared to the de-solvated/buried AK peptide. Significant specific shielding from solvent due to Lys side chains is also evident indicating nonuniform exposure to solvent.

We evaluate how accurate is the association of amide-I band to existence of helical and random configurations from measurements at low and high T, respectively. Figure 1A shows the calculated amide-I band from helical (h=1) and random coil (h=0) h-ensemble configurations. The helical ensemble gives rise to a narrower band at lower frequency compared to the random coil ensemble. Figure 1B provides the distributions of h-ensembles at low T, $T_{1/2}$, and high T. The canonical ensemble subjected to the IR measurements will be the sum of these pure h-ensembles with different fraction of helical content weighted by the Boltzmann factor. The calculated IR spectra are plotted in Figure 1C for 21 different temperatures, ranging from 273 K to 551 K with intervals of 10–15 degrees. The T-dependent changes are consistent with the measured amide-I spectra of AK peptide. Upon thermal denaturation of the peptide, the amide-I

band shifts to higher frequency because the increase in solvent H-bonding is not adequate to compensate the loss in internal (helical) H-bond. The broadening of the amide-I band is mainly caused by the increase in nonuniformity of the amide-I mode coupling along the helix at higher T. The fractional helical content, which was calculated independently from the same trajectories, is plotted in Figure 1D as a function of T alongside the loss in intensity at 1629 cm^{-1} (the peak maximum at the lowest T). The Lifson-Roig helical content profile describes a helix-coil transition that is not strongly cooperative with a transition temperature ($T_{1/2}$) of ~ 450 K. Interestingly, the helix-coil transition from the amide-I band intensities calculated from the same set of trajectories describes a more cooperative transition, and the half-height of the peak intensity occurs at much lower T (~ 380 K).

The underlying conformational distribution of AK peptide can be exposed by isotope labeling of AAAA segments. Both linear and nonlinear IR experiments on the isotopomers of AK peptide have shown promise for generating such structural information at a local level. The AAAA segmental inhomogeneities are calculated and compared to isotope-edited infrared measurements. The ^{13}C and ^{12}C amide-I peak intensities from the calculated spectra correlate well with the measurements and the helical content of the labeled and unlabeled segments obtained independently from the trajectories. The C-terminus AAAA segment has the lowest helical content and showed the least amplitude for the ^{13}C band. Our calculations demonstrate that the observations from isotope IR aimed at the characterization of the unfolded state along the chain can be interpreted with a solid structural basis.

Modeling Biological Signaling in T-10

Byron Goldstein, James R. Faeder, and William S. Hlavacek, T-10; bxg@lanl.gov

A group of scientists in T-10 are working in collaboration with other modelers and experimental investigators to develop detailed, quantitative models of signal transduction in biology with an emphasis on the immune system and human disease. The group is comprised currently of three T-10 staff members—Byron Goldstein, James Faeder, and William Hlavacek—and two postdocs, Michael Blinov and Jin Yang. See below for additional information on collaborations and funding.

Background

Cells are exquisite detectors, constantly monitoring their environment through the use of cell-surface receptors. Despite the massive accumulation of information about the molecules and molecular interactions involved, a coherent understanding of signal transduction remains elusive, and presents a grand challenge for cell biology and predictive science. Understanding how cells detect disease-causing agents and generate the intracellular signaling cascades that turn on the body's responses to fight infection is also critical for our defense against naturally occurring or engineered pathogens. Predictive models of cell signaling are an emerging component of systems biology and will become a vital tool in the development of new drugs to treat human disease and the development of new strategies to defend against biothreats. The goal of this modeling is to understand how the components in a signaling cascade work together as a system to direct cellular responses to changes in the extracellular environment.

Signaling is typically initiated when a molecule outside the cell (the ligand) binds to a receptor on the surface of the cell, triggering a complex cascade of biochemical reactions. The transfer of information about the ligand-receptor binding event often begins when multiple receptors bind to the same ligand, forming an aggregate on the cell surface, which leads to large molecular complexes forming around the cytoplasmic tails of the receptors. A key characteristic of these signaling complexes that emerges from our modeling is that they are transient—even in the presence of a constant stimulus, complexes are continually building up and breaking down.

The major focus of our work has been to develop techniques for generating, simulating, and analyzing the large biochemical networks that arise when the details of complex formation in signal transduction are considered.

FcεRI

The high-affinity receptor for IgE, FcεRI, plays a central role in allergic responses and is a major target for drug intervention against allergy-related diseases. We have developed a model of early events in FcεRI signaling that lead to the activation of the protein tyrosine kinase Syk within a receptor complex. The model vividly illustrates a general feature of biological signaling—the combinatorial explosion in the number of molecular complexes and modification states of those complexes that can form from a small number of proteins. Although the model considers just four protein components, it contains 354 distinct chemical species that arise from the multiple ways the components can combine and be modified through phosphorylation. The biochemical reaction network formed by these species contains 3680 unidirectional reaction channels. The model we have developed groups these reactions into a relatively small number

of classes, which reduces the number of required rate parameters to a manageable size (21 for the current model). A computer program is used to generate the network, and numerical integration is used to solve the model's 354 ordinary differential equations. In combination with experiments this model has provided a number of insights that could not be gleaned from experimental data alone: that a single Lyn kinase associated with an FcεRI in an aggregate is sufficient to induce receptor phosphorylation; that the amount of Lyn available to the receptor is limiting and that the amount of Syk kinase is not; and that the rate of dephosphorylation of receptors is much faster than observations suggest. Further analysis of the model for a wide range of parameters shows that only a relatively small subset of the 354 species plays a significant role during activation. The identity of the species, however, can change dramatically depending on the rate parameters and the initial concentrations of the protein components. These results show that reaction dynamics alone can lead to highly specific formation of complexes even in the absence of cooperative interactions.

T-Cell Receptor

There is a fundamental difference in complexity between signaling initiated by ligands on the surface of one cell binding to receptors, such as T-cell receptors (TCR), on the surface of another cell and ligands in solution binding to these receptors. For cell signaling through the TCR to proceed, a T-cell and an antigen presenting cell must come into proximity and form a number of intercellular bonds of different types, all within the restricted geometry of the intercellular contact region. This leads to complex spatio- temporal dynamics of surface receptors not seen when the ligand is soluble. In collaboration with experimental colleagues we have shown that once TCRs become activated they remain marked for degradation (a way to turn off a signal) even after they dissociate from their ligand.

EGFR

The epidermal growth factor receptor (EGFR) regulates cell proliferation and survival through binding with a number of ligands, including epidermal growth factor (EGF). This receptor is the most widely studied and best understood receptor found in higher organisms, and is one of the few in which signaling pathways have been extensively modeled. Previous models, however, all are based on assumptions that restrict the number of potential signaling complexes to a small fraction of those that are implied by the interactions included in the models a pathway-like rather than a network description of signaling complexes. To investigate which complexes are important for signaling and to test the assumptions of previous models, we have developed a network model of early events in EGFR signaling that accounts for the full spectrum of molecular species (356) and transitions among these species (3749) implied by specified interactions and activities of EGF, EGFR, the adapter proteins Grb2 and Shc, and the guanine nucleotide exchange factor Sos. We find that during transient signaling a fairly broad range of these signaling complexes is active, which leads to significant differences between the network and pathway-like models. These differences become much smaller at steady state, where the distribution of complexes becomes much narrower and coincides closely with the complexes considered in a pathway-like model. In addition to a more accurate

description of protein-protein interactions, the network model makes a broader range of predictions that can be tested experimentally.

BioNetPack

We have developed a general-purpose software package that implements our approach to modeling signaling networks. We have used this software to model signaling through FcεRI, EGFR, erythropoietin receptor, interleukin-1 receptor, the yeast α-factor pheromone receptor, and MAP kinase cascades. Unlike typical models of receptor signaling, a network generated by this software is complete for the scope of specified inputs. We have analyzed these models to identify the molecular species, reactions and pathways that are prevalent during signaling and to investigate different assumptions about signaling mechanisms.

Recent Publications

1. B. Goldstein, J. R. Faeder, W. S. Hlavacek, M. L. Blinov, A. Redondo, and C. Wofsy, "Modeling the early signaling events mediated by FceRI," *Mol. Immunol.* **38**, 1213–1219 (2002).
2. D. Coombs, A. M. Kalergis, S. G. Nathenson, C. Wofsy, and B. Goldstein, "Activated TCR remain marked for internalization after dissociation from peptide-MHC," *Nature Immunol.* **3**, 926–931 (2002), [Commentary pp. 895–896].
3. J. R. Faeder, W. S. Hlavacek, I. Reischl, M. L. Blinov, H. Metzger, A. Redondo, C. Wofsy, and B. Goldstein, "Investigation of early events in FcεRI-mediated signaling using a detailed mathematical model," *J. Immunol.* **170**, 3769–3781 (2003).
4. W. S. Hlavacek, J. R. Faeder, M. L. Blinov, A. S. Perelson, and B. Goldstein, "The complexity of complexes in signal transduction," *Biotechnol. Bioeng.* **84**, 783–794 (2003).
5. M. L. Blinov, J. R. Faeder, and W. S. Hlavacek, "Software and procedures for creating mathematical/computational models of cellular signaling," US Patent Application **S–100**, 635 (2003).
6. D. Coombs, M. Dembo, C. Wofsy, and B. Goldstein, "Equilibrium thermodynamics of cell-cell adhesion mediated by multiple ligand-receptor pairs," *Biophys. J.* **86**, 1408–1423 (2004).
7. B. Goldstein, J. R. Faeder, and W. S. Hlavacek, "Mathematical models of immune receptor signaling," *Nat. Rev. Immunol.* (2004) (in press).
8. D. Coombs, and B. Goldstein, "T-cell activation: Kinetic proofreading, serial engagement and cell adhesion," *J. Comp. And Applied Math.* (submitted)

Collaborators

Modeling: Dan Coombs, University of British Columbia; Antonio Redondo, T-12; Alan Perelson, T-10; Chang Shung Tung, T-10; Shuling Chou, T-13; and John Pearson, X-8.
Experiments: Chikako Torigoe, University of New Mexico School of Medicine (UNM-SOM); Janet Oliver, UNM-SOM; Steve Dower, University of Sheffield); John Cambier, University of Colorado Health Sciences Center; Juan Rivera, NIH-NIAMS; and Marc Daeron, Inserm U255, Paris.

Funding

Funding is provided through an NIH grant to model signaling in the adaptive immune system (R37 GM35556-18, B. Goldstein), an NIH grant to model interleukin-1 signaling (NIH/NCRR: RR-1P20RR18754, W. S. Hlavacek), and an LDRD DR grant to model pathogen recognition within the innate immune system (20040087DR, B. Goldstein).

Design Principles of Genetic Regulatory Networks

William S. Hlavacek, T-10; and Michael E. Wall, CCS-3; wish@lanl.gov

The identification of predictive design principles is recognized as one of the grand challenges of systems biology. We are studying design principles of genetic regulatory circuits in bacteria, i.e., trying to understand how the structure of a system for regulating gene expression affects the system's function. An understanding of gene regulation is important because the cellular circuitry that controls gene expression is largely responsible for the ability of a cell to cope with changes in its environment. Genes must be expressed when needed and, for efficiency, turned off when not in demand. Gene regulation has been the subject of countless studies since the pioneering work of Jacob and Monod. Today, diverse systems, mostly in bacteria, have been characterized, and are beginning to be examined together to identify patterns and rules. Recently, Alon and coworkers examined approximately 150 transcription factors (TFs) and their DNA binding sites to identify patterns of transcriptional interactions common in the genetic regulatory network of Escherichia coli. Their results, and others, suggest that the vast majority of genes in E. coli are regulated by either one or two TFs, indicating that unary and binary circuits represent major classes of bacterial circuit design.

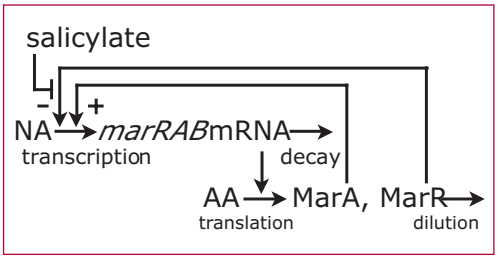

Figure 1— A binary circuit. The transcription factors MarR and MarA in E. coli jointly regulate expression of genes involved in resistance to multiple antibiotics. Salicylate and other phenolic derivatives induce transcription of the marRAB operon by inactivating MarR, the repressor of transcription. Elevated expression of MarA then leads to upregulated expression of a number of genes under the control of MarA, an activator of transcription.

A binary circuit, in which two TFs jointly control the expression of genes, is illustrated in Figure 1.

The elucidation of biological design principles, particularly of genetic regulatory circuits, has received much attention lately for several reasons. 1) Our biological knowledge base is extensive after decades of experimental investigations of gene regulation, and this knowledge is now being collected and organized in electronic databases, such as EcoTFs (http://ecotfs.lanl.gov/) [1]. 2) Methods of genetic engineering allow synthetic circuits to be readily built, and researchers are beginning to consider practical applications of such circuits. 3) Recent technological advances, such as the development of cDNA microarrays, allow gene expression to be monitored coarsely on a genome-wide scale or on a smaller but still multiple-gene scale with high accuracy and fine time resolution. This ability to comprehensively and quantitatively monitor dynamic changes in gene expression opens the door for model-based studies of the type that are more common in physics and chemistry than in biology.

Theoretical studies of gene regulation were initiated by Szilard and Goodwin, contemporaneously with the seminal experimental studies of Jacob and Monod. Not long after, model-based comparisons of different types of unary, or elementary, gene circuits began. Our current theoretical understanding of these circuits, in which a single TF is involved in the response to a signal, is advanced and has been largely confirmed by experimental observations [1], as discussed briefly below. The challenge we now face is to obtain this level of understanding for the other major class of bacterial gene circuit, the more complex binary circuits.

One aspect of elementary gene circuits that has been examined carefully is the response of the regulator gene in such circuits to signals [2, 3]. The question asked in these studies was the following. Are there rules that govern regulator gene expression? We found that it is possible to predict whether expression of the regulator in a circuit (i.e., the TF) is inducible (elevated in response to a signal that affects effector gene expression), constitutive (unresponsive to a signal that affects effector gene expression), or repressible (downregulated in response to a signal that affects effector gene expression) based on various properties of the gene circuit (Figure 2). In these studies, we also found that negative autoregulation of the regulator gene, meaning that the regulator acts as a repressor at its own promoter, is important for performance of a gene circuit as judged by robustness (insensitivity to parameter perturbations), dynamic stability, and temporal responsiveness to signals. We, thus, predicted that negative autoregulation of regulator gene expression should be common and would enhance stability, robustness, and responsiveness. Our predictions for elementary circuits have been confirmed by exhaustive surveys of well-studied systems [1–3] and/or through direct experimental tests [4–6]. It is this type of theoretical insight, and supporting experimental observations, that we are now pursuing for binary circuits.

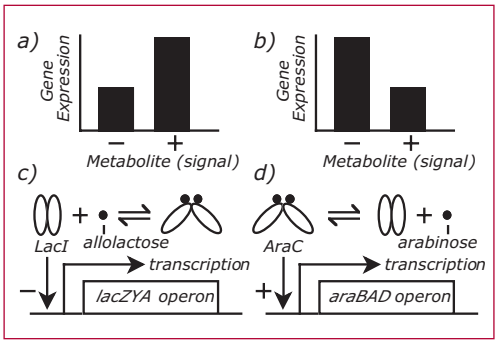

Figure 2— The response of regulator gene expression to a signal depends on whether effector gene expression is a) inducible or b) repressible and whether the regulator is a c) repressor or d) activator of effector gene expression.

We collaborate with Uri Alon (Senior Scientist, Department of Molecular Cell Biology and Department of Physics of Complex Systems, Weizmann Institute of Science); Vlastimil Krivan (Head, Department of Theoretical Biology, Institute of Entomology, Academy of Sciences of the Czech Republic); and Michael A. Savageau (Distinguished Professor, Department of Biomedical Engineering, University of California, Davis). Our work is supported by the ER component of the LDRD program. Funding began October 1, 2003.

[1] M. E. Wall, W. S. Hlavacek, and M. A. Savageau, "Design of gene circuits: lessons from bacteria," *Nat. Rev. Genet.* **5**, 34–42, (2004).

[2] M. E. Wall, W. S. Hlavacek, and M. A. Savageau, "Design principles for regulator gene expression in a repressible gene circuit," *J. Mol. Biol.* **332**, 861–876, (2003).

[3] W. S. Hlavacek and M. A. Savageau, "Rules for coupled expression of regulator and effector genes in inducible circuits," *J. Mol. Biol.* **255**, 121–139, (1996).

[4] J. W. Little, D. P. Shepley, and D. W. Wert, "Robustness of a gene regulatory circuit," *EMBO J.* **18**, 4299–4307, (1999).

[5] A. Becskei and L. Serrano (2000) "Engineering stability in gene networks by autoregulation," *Nature* **405**, 590–593 (2000).

[6] N. Rosenfeld, M. B. Elowitz, and U. Alon, "Negative autoregulation speeds the response times of transcription networks," *J. Mol. Biol.* **323**, 785–793, (2002).

Investigation of Novel HIV-1 Recombinant Forms using the Branching Index

Thomas K. Leitner, T-10; tkl@lanl.gov

In this work we have developed a method for determining if parental DNA sequence representatives are available or are not for recombination analysis.

HIV-1 displays one of the most genetically plastic genomes known to man. Since its introduction to man and during its spread over the world, HIV-1 has formed several levels of rather well defined clusters of genetically related variants. On the highest level, HIV-1 is divided into groups M, N, and O, which are probably reflecting separate introductions of HIV-1 to man. Groups N and O are very rare, while group M (which stands for Main) is responsible for the worldwide epidemic. Group M is further divided into several subtypes (A, B, C, D, F, G, H, J, K). Furthermore, some of the subtypes have been divided into sub-subtypes. To give a perspective of the extraordinary genetic variation of HIV-1, note that the different genetic variants a single HIV-1 infected individual carries has as much genetic diversity as influenza (another very genetically diverse organism) has in the whole world during a typical flu season.

In addition to all the genetic diversity that HIV-1 accumulates through substitutional errors, HIV-1 also frequently recombines, further expanding the diversity. Recombining different subtypes, which may happen when a person gets multiple infections, makes it possible for the virus to rapidly explore new genetic space.

For many reasons, including future vaccine design and monitoring the epidemic, it is important to accurately describe and classify the forms of HIV-1 that are spreading in different geographic regions and among different risk groups.

The subtypes are defined based on the clustering in phylogenetic trees, and are clear in any part of the genome. To discover recombinants and their structure is more difficult and several methods have been developed for this purpose. For instance, a breakpoint analysis is done by χ^2 analysis of informative sites and clustering is assessed by bootstrap analysis. To accurately describe how a recombinant genome is composed, however, requires sequence information from parental representatives. Bootstrap, χ^2 analysis, and other statistical measures will be misleading if the parental information is missing.

In order to facilitate the classification of potentially recombinant genomes we developed a simple metric, the branching index (Figure 1A), for characterization of "problematic" sequence fragments that associate to a subtype cluster with a high-bootstrap value but are only distantly related to the reference sequences. The branching index is able to signal when parental representatives may be missing and a subtype classification thus is not meaningful. When a sequence fragment shows a branching index below a certain cut-off value there are no available parental representatives among the reference sequences analyzed (Figure 1B). Conversely, values above the cut-off value will give meaningful classifications.

This work has been published in:
K. Wilbe, M. O. Salminen, T. Laukkanen, F. Cutchan, S. C. Ray, J. Albert, and T. Leitner, "Investigation of novel HIV-1 recombinant forms using the branching index," *Virology* **316**, 116–125 (2003).

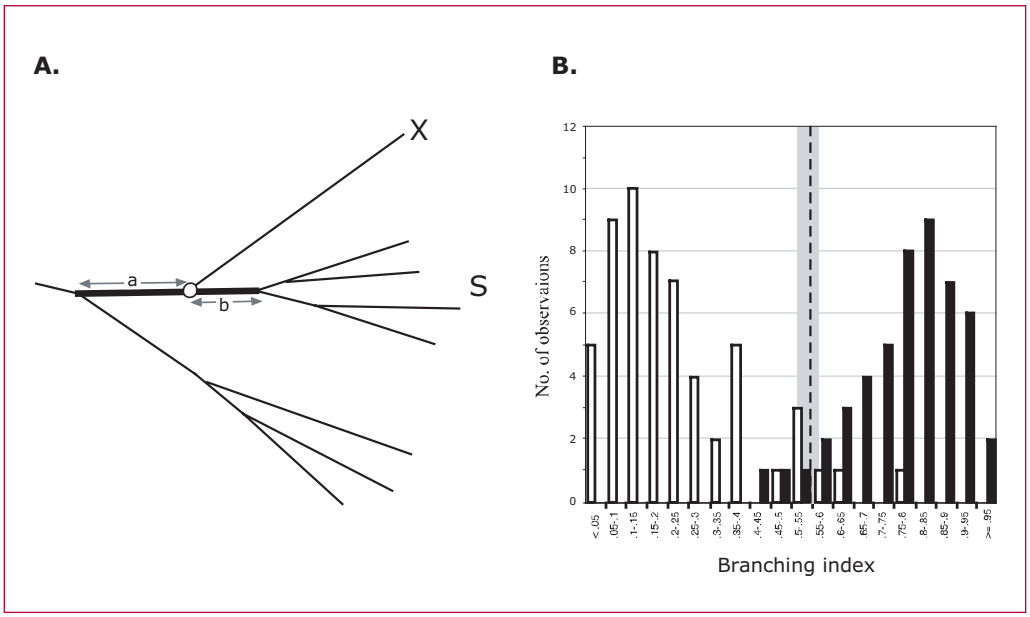

Figure 1A—
Schematic picture of the branching index. Here the association of sequence X to the subtype cluster S is investigated. Letters a and b are genetic distances that depend on the position of the node of sequence X (white circle) at the bold branch. The branching index is defined as a/(a+b) and can take values between 0 and 1. (B) Comparison of branching indexes (BIs) from situations when parental representatives are present or not. White bars shows the situation with subtype partners absent, and black bars shows the situation with subtype partners present. The BI categories are shown on the x-axis and the number of observations on the y-axis. The vertical dotted line indicates the suggested cut-off value 0.55 for subtype verification, and the gray zone is a zone of uncertainty (<95% correct classifications).

Ribosome, Kinase, and Packaging RNA Modeling

Chang-Shung Tung, T-10; ct@lanl.gov

Ribosome modeling:
After modeled the atomic structure of the *E. coli* small ribosomal subunit (Tung et al., 2002, *Nature Structural Biology*), we took the challenge of modeling the structure of the whole ribosome (3 rRNAs and > 50 proteins with ~200,000 heavy atoms). Using the low-resolution structure (contains phosphorus and Ca atoms) derived from x-ray crystallography and knowledge-based modeling method developed in our group, we have modeled the atomic structure of the *T. thermophilus* 70S ribosome (Tung and Sanbomatsu, 2004, submitted to *Biophys J*). Currently, collaborating with Prof. Rajendra Agrawal (Univ. at Albany), we are modeling the structures of *Bovine* mitochondrial tRNAs based on cryo-EM data. Collaborating with both Prof. Rajendra Agrawal and Prof. Stephen Harvey (Georgia Tech), we are developing The atomic model for *Bovine* mitochondrial ribosome.

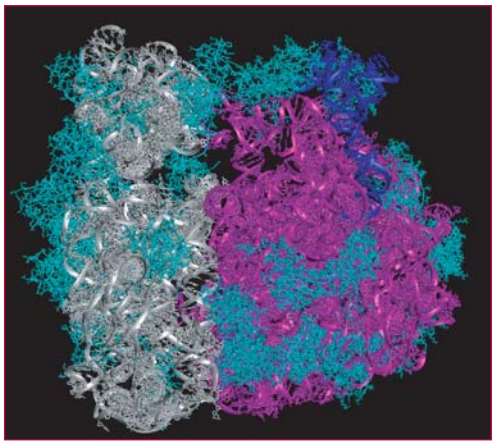

Figure 1—Structural model of the T. thermophilus 70 S ribosome.

Kinase modeling:
Using information derived from neutron contrast and mutation studies, we have developed an atomic model for the regulatory/catalytic complex of the c-AMP-dependent protein kinase (Tung et al., 2001, *JBC*). Currently, collaborating with Jill Trewhella (LANL) and others, we are developing models for MLCK/Calmodulin and c-GMP dependent protein kinase. The main goal of these studies is to understand regulation (activation/inhibition) of the enzyme based on these structural models.

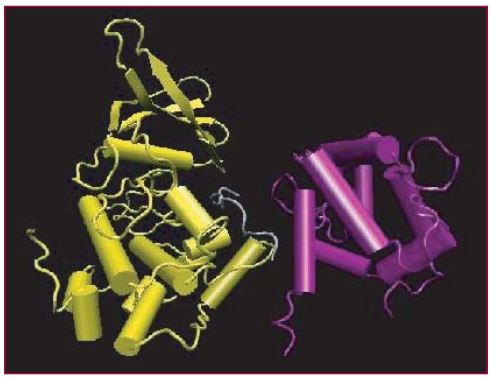

Figure 2—Modeled structure of the MLCK catalytic core (in yellow), inhibitory prptide (in gray) and calmodulin (in purple).

Packaging RNA modeling:
The packaging RNA (pRNA) functions as a key component in the strongest biomachinery known up-to-date. The system is complex and large that consists of both protein and RNA molecules. The multimeric nature of the molecular complexes makes the problem even more difficult. One of the crucial components in the complex is the packaging RNA (pRNA) with its detailed and reliable structure not known. The proposed work combines the low-resolution structural data and *in silico* modeling method to develop atomic structure(s) of the target molecular assembly for probing its dynamics and functional roles. At the completion of the project, we will gain a detailed and reliable model and have an understanding of the structures and dynamics of pRNA in the viral

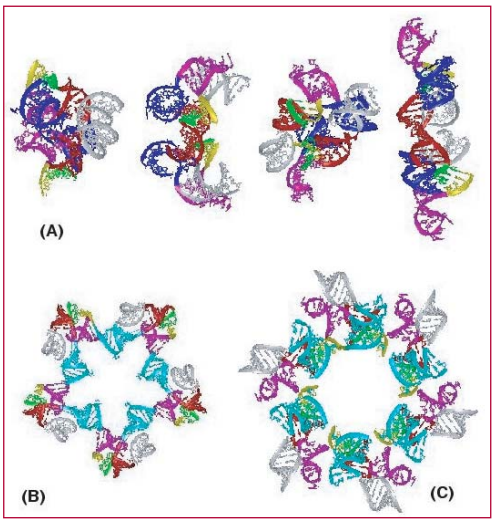

Figure 3— (A) A sample of four of the dimer structures derived from our modeling approach. (B) One of the modeled pentamer structure. (C) One of the modeled hexamer structure. In this figure, all structures are color coded according to different secondary structural segments.

DNA packaging machinery. It has demonstrated that the method combining low-resolution experiments and *in silico* approaches is a viable alternative to the traditional for high-resolution structural determining methods (i.e., X-ray crystallography, NMR) for deriving structures of large bio-molecular complexes as well as understanding the mechanisms involved in molecular nano-machines. This type of approach is extremely important to the expediting of the understanding of the human genomic functions. In a broad sense, the application can contribute to many aspects of improving human health as well as homeland defense.

T-13 Complex Systems

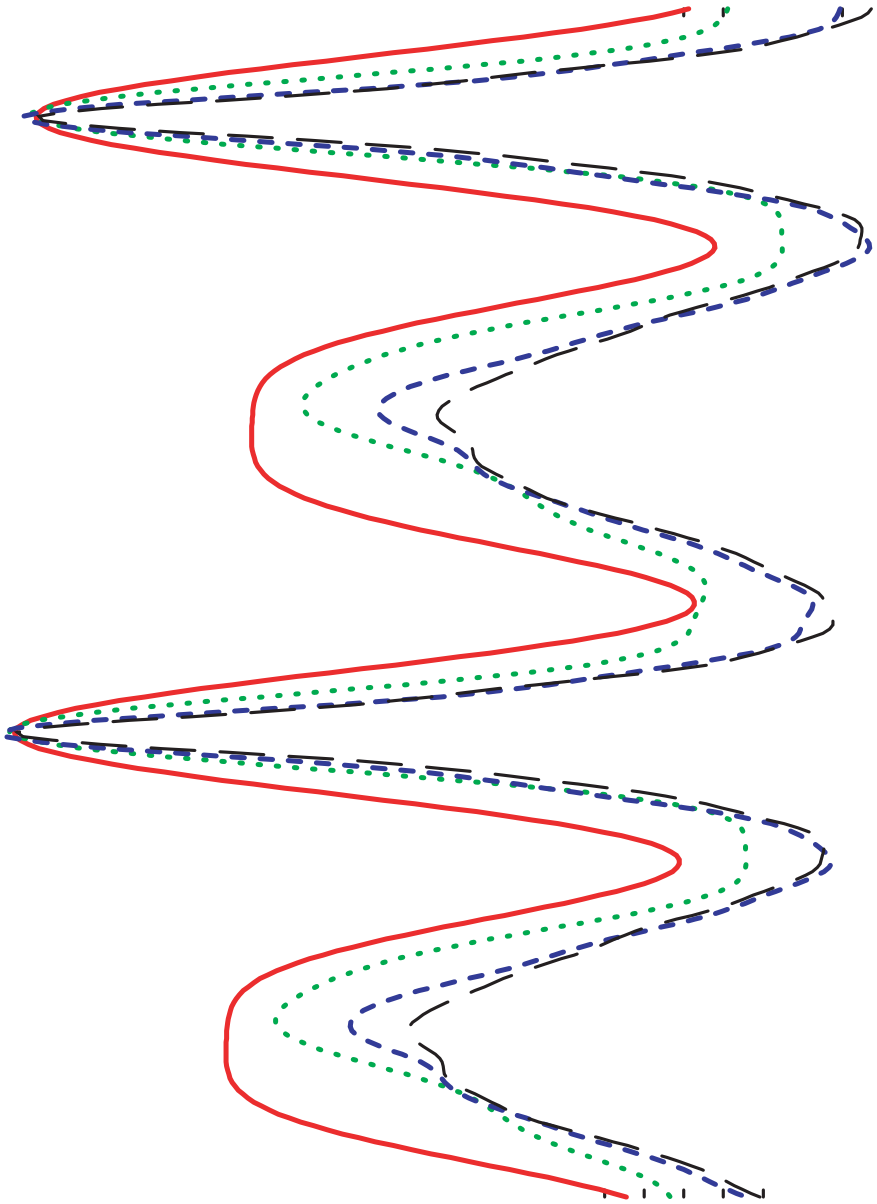

Survival of Quantum Effects for Observables after Decoherence

Gennady P. Berman, T-13; Alan R. Bishop, T-DO; F. Borgonovi, Univ. Brescia, Italy; and Diego A. R. Dalvit, T-DO/QC; gpb@lanl.gov

When a quantum nonlinear system is linearly coupled to an infinite bath of harmonic oscillators, quantum coherence of the system is lost on a decoherence time-scale. Nevertheless, quantum effects for observables may still survive environment-induced decoherence, and be observed for times much larger than the decoherence time-scale. In particular, we show that the Ehrenfest time, which characterizes a departure of quantum dynamics for observables from the corresponding classical dynamics, can be observed for a quasi-classical nonlinear oscillator for times much larger than the decoherence time-scale. We discuss this observation in relation to recent experiments on quantum nonlinear systems such as Bose-Einstein condensates and nano-mechanical cantilevers in the quasi-classical region of parameters.

[1] quant-ph/0401038 (submitted to *Physical Review A*)

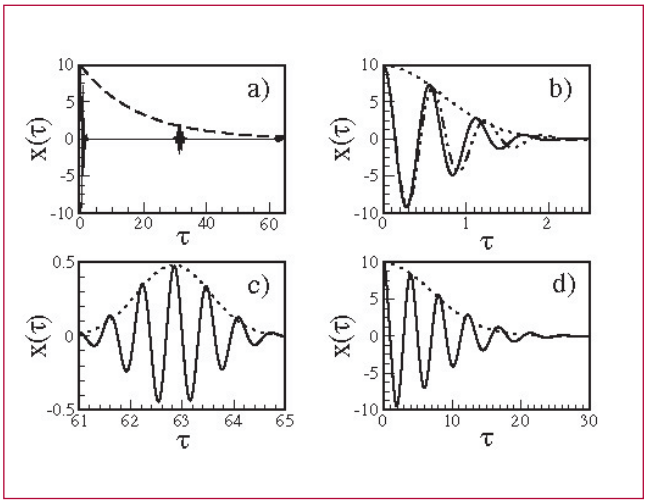

Figure 1—Mean position of the nonlinear oscillator as a function of time. The quantum revivals are damped out due to the environment on a decoherence time-scale. For parameters such that decoherence time is much smaller than the Ehrenfest time, time (insert d), the temporal behavior within each revival bump still shows quantum effects.

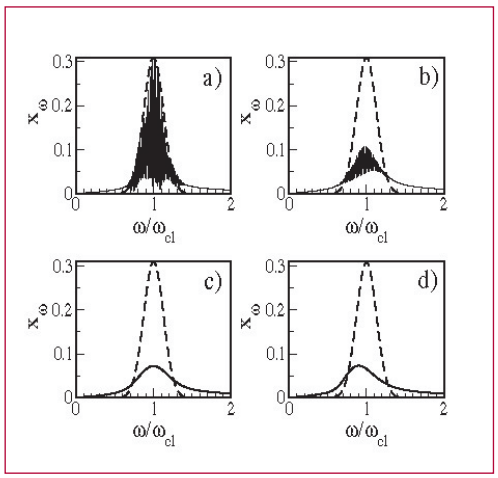

Figure 2—Fourier spectrum of the mean position. The width of the spectrum is determined by the Ehrenfest time-scale, even in situations where the decoherence time-scale is much shorter than the Ehrenfest time, showing survival of quantum effects after decoherence.

Analytic Solutions for Quantum Logic Gates and Modeling Pulse Errors in a Quantum Computer with a Heisenberg Interaction

Gennady P. Berman and Dmitry I. Kamenev, T-13; and V. I. Tsifrinovich, Polytech. U., NY; kamenev@cnls.lanl.gov

It is possible to control a quantum computer (QC) dynamics by controlling only interaction between quantum bits (qubits) without affecting the qubits themselves. This type of QC is convenient for implementation in solid-state scalable (in the number of qubits) models since the inter-qubit interaction can be controlled by applying local voltages without application of electromagnetic pulses. This allows one to eliminate decoherence associated with the electromagnetic pulses and to simplify the QC design.

We analytically calculated [1] optimal parameters for one-qubit gates and swap gate in the QC with the controlled exchange interaction. We also numerically calculated probability and phase errors (see figure) caused by random deviations of pulse parameters from their ideal values that always are present in an experimental situation. The probability error in the figure is equal to $3 \times 10^4 \varepsilon$ and the phase error is equal to 10ε, where ε is the average deviation from the ideal pulse parameters.

[1] G. P. Berman, D. I. Kamenev, and V. I. Tsifrinovich, "Analytic solutions for quantum logic gates and modeling pulse errors in a quantum computer with a Heisenberg interaction," (2003).

[2] quant-ph/0311152 (2003), accepted for publication in *International Journal of Quantum Information (IJQI)*.

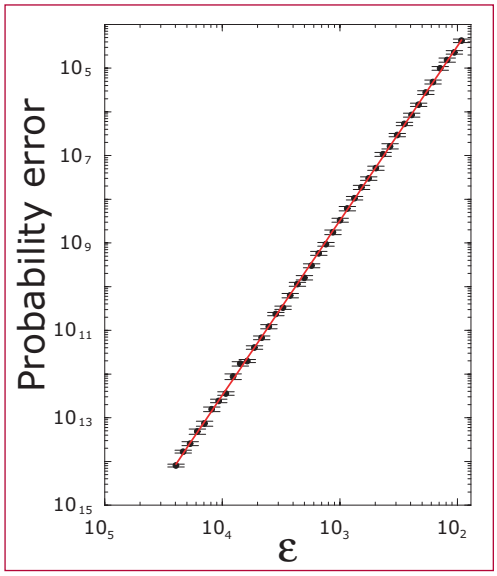

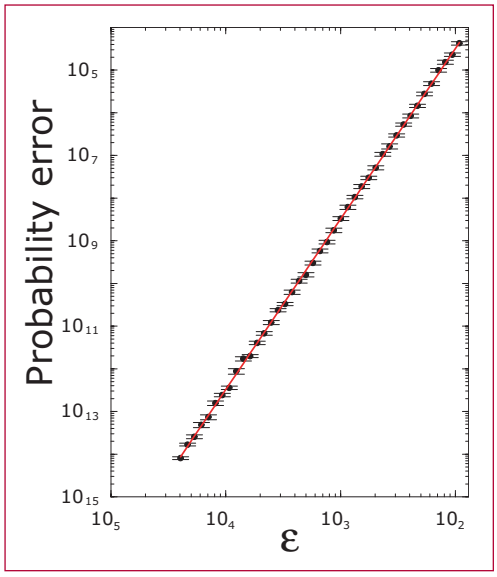

Minimization of Nonresonant Effects in a Scalable Ising Spin Quantum Computer

Gennady P. Berman and Dmitry I. Kamenev, T-13; V. I. Tsifrinovich, Polytech. U., NY; kamenev@cnls.lanl.gov

If a quantum computer (QC) is operated by radio-frequency pulses, the errors in implementation of quantum logic gate can accumulate due to nonlocal action of these pulses on all quantum bits (qubits) of the quantum register.

The selective excitations of definite qubits in our model are provided by the gradient of permanent magnetic field. Due to the magnetic field gradient each qubit has its unique transition frequency. If the frequency of the pulse is close to the transition frequency of a particular qubit, the state of this qubit is strongly affected by this pulse. Otherwise, if the transition frequency of a qubit is different from the external pulse frequency, the probability of flip of this qubit is very small. The latter transitions, called nonresonant transitions, are unwanted and create errors in a QC.

Analytically and numerically we calculated the errors associated with the nonresonant transitions as a function of magnetic field gradient (figure) for different states and different numbers of qubits [1]. In the figure, $\delta\omega$ is the difference of the permanent magnetic field amplitude in locations of neighboring qubits, Ω is the amplitude of the radio-frequency field, k is the number of the spin with the resonant frequency, and L is the number of qubits in the quantum register. We found that by choosing the optimal value of the magnetic field gradient the error can be decreased by 80%.

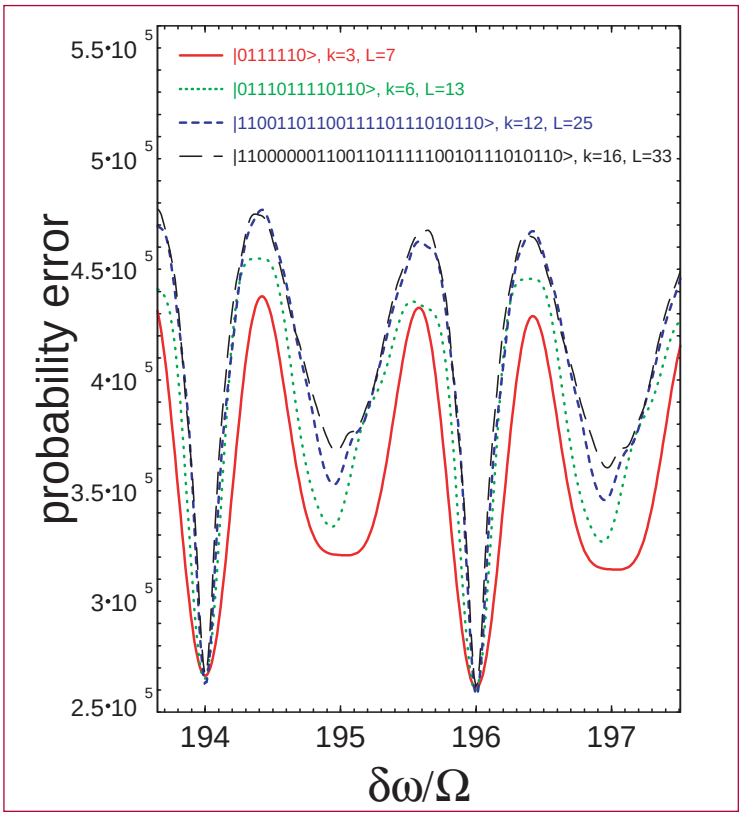

[1] G. P. Berman, D. I. Kamenev, and V. I. Tsifrinovich, "Minimization of nonresonant effects in a scalable Ising spin quantum computer" (2003).

[2] quant-ph/0310049 (2003), accepted for publication in *International Journal of Quantum Information (IJQI)*.

Strong Effect of Doping on Laser Plasma Interaction

Pavel Lushnikov and Harvey A. Rose, T-13; har@lanl.gov

Understanding the propagation of high-intensity laser beams in plasma has been an outstanding research objective for more than two decades. As a laser beam traverses plasma, it couples to backscattered light and either an ion acoustic wave (stimulated Brillouin scattering [SBS]) or a high-frequency Langmuir wave (stimulated Raman scattering (SRS)). Typical intensities exceed threshold for a broad spectrum of waves, leading to plasma turbulence (see Figure 2).

SBS is of particular concern for ultraviolet laser beams since a relatively small amount of backscattered light may cause significant optical damage. Recent experiments [1] at the Atomic Weapon Establishment in the UK have demonstrated reduction of both SBS and stimulated Raman scattering by the addition of high-ionization state dopants (hereafter referred to simply as dopants) to a low ionization state plasma, e.g., a 1% dopant reduced backscatter by more than a factor 10! Control of transport of laser beam by dopants can be compared with the corresponding leverage gained on electrical transport in semiconductors by dopants that led to modern transistor technology. At this time there is no theory of these striking plasma experiments, which have exited strong interest of the scientific community and were subjects of recent invited talks at APS plasma meeting [1].

Initial hopes that the induced plasma turbulence could be successfully modeled by following the example of fully developed fluid turbulence theory,

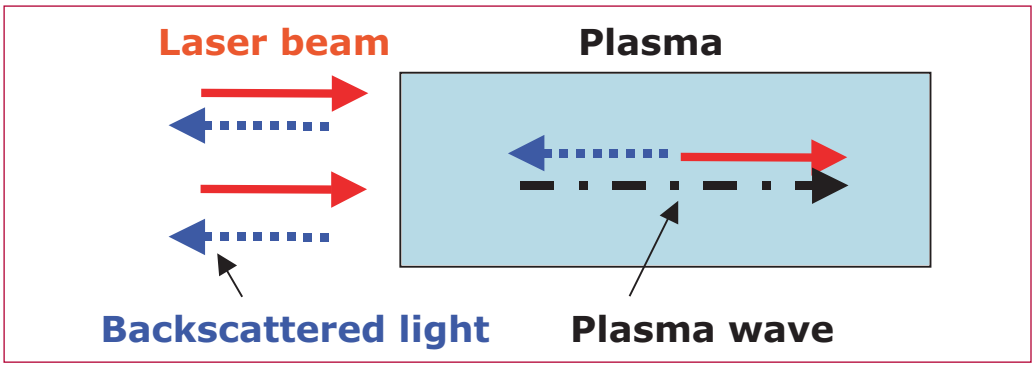

Figure 1—Schematic representation of stimulated scatter.

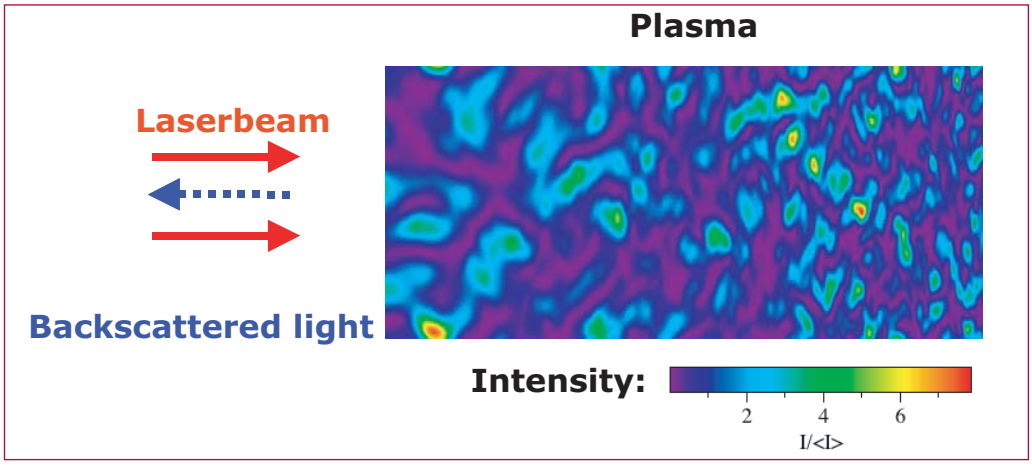

Figure 2—Turbulent intensity fluctuations in plasma obtained from numerical simulations.

have foundered in face of the many kinds of unstable waves, and the general absence of an extended inertial range, where damping and pumping are negligible. Pioneering work by Zakharov [2] on a kinetic theory of weakly interacting light waves (weak turbulence theory), developed in analogy to Kolmogorov's fluid theory, is limited by the phenomenon of self-focusing, where a wave packet digs a cavity in which the wave packet is trapped, leading to a deeper cavity, and so on. Self-focusing results in strong turbulence (characterized by intermittent/non-Gaussian fluctuations) in contrast with almost Gaussian fluctuations in weak turbulence regime. However, an intermediate regime was recently discovered [3], characterized by strong density-intensity correlations, as in self-focusing, but without significant departure of electric field fluctuations from Gaussian. In contrast to the weak turbulence regime, laser beams angularly diffuses much more rapidly than suggested by weak turbulence theory, leading to a dramatic reduction of correlation length with beam propagation. And, in contrast to strong turbulence regime, the laser beam does not disintegrate into many small beams (beam spray). As light intensity increases, first there is a transition from the weak turbulence, to intermediate regime, and then to strong turbulence.

Dopants are effective at reducing thermal transport in plasma because their contribution to electron-ion collisions is a quadratic function of their ionization state [4]. Reduced thermal transport in plasma results in larger temperature fluctuations and hence a larger thermal contribution to self-focusing that is otherwise small for low-ionization state plasma at high temperature (as in the UK experiments). Our estimates suggest that small amounts of dopant alters self-focusing to induce a transition into the intermediate turbulence region at fixed laser intensity. Thus dopants control SBS by altering the laser beam's statistical properties. There is evidence (numerical [5], experimental [6], one dimensional theory [7]) that SBS is controlled by laser beam correlation length. If successful, our research will have an essential technological impact on future designs of thermonuclear fusion experiments by providing a guide how to choose plasma parameters, including concentration of dopants to avoid dangerous laser backscatter that can damage expensive high power laser used for such experiments.

[1] Invited talks by L. Suter, *Bull. Amer. Phys. Soc.* **48**, 124 (10/2003); and M. Stevenson, *Bull. Amer. Phys. Soc.* **48**, 125 (10/2003).
[2] V. E. Zakharov, V. S. Lvov, and G. Falkovich, "Kolmogorov Spectra of Turbulence I: Wave turbulence." (Springer-Verlag, New York, 1992).
[3] P. M. Lushnikov and H. A. Rose, "Instability versus equilibrium propagation of laser beam in plasma," submitted to *Phys. Rev. Lett.,* Nov. 2003 (LA-UR-03-8705) [e-print xxx.lanl.gov/physics/0312055].
[4] E. M. Epperlein, *Phys. Rev. Lett.* **65**, 2145 (1990).
[5] Harvey A. Rose and D. F. DuBois, *Phys. Rev. Lett.* **72,** 2883 (1994).
[6] Juan. C. Fernandez, J. A. Cobble, B. H. Failor, W. W. Hsing, H. A. Rose, B. H. Wilde, K. S. Bradley, P. L. Gobby, R. Kirkwood, H. N. Kornblum, D. S. Montgomery, and M. D. Wilke, *Phys. Rev.* **E53**, 2747 (1996).
[7] Ph. Mounaix, *Phys. Plasmas* **2,** 1804 (1995).

T-15 Plasma Theory

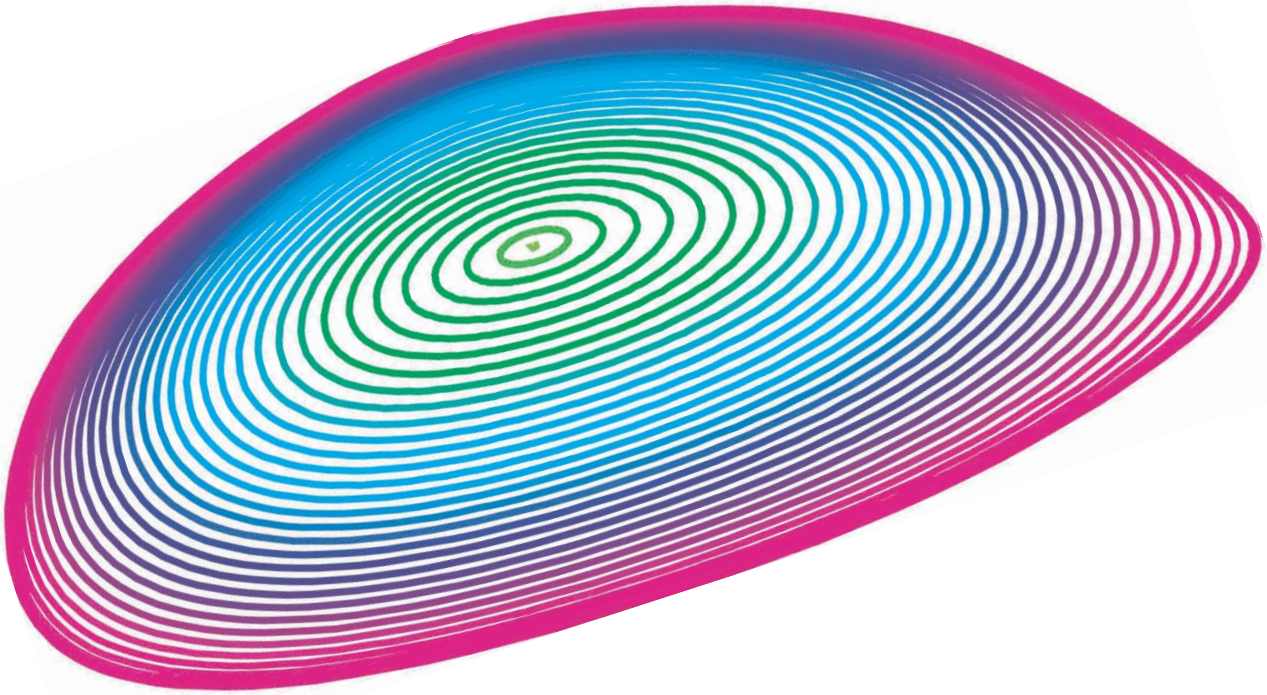

A System-Scale Theory for Fast Magnetic Reconnection in Plasmas

Luís Chacón, T-15; and Dana A. Knoll, T-3; chacon@lanl.gov

The plasma state is pervasive in our universe and in many interesting laboratory environments. Virtually all these plasmas have embedded magnetic fields, either externally imposed or self-generated. In magnetized plasmas, mass, momentum, and energy preferentially flow along magnetic field lines. In addition, significant magnetic energy can be stored when magnetic fields are sheared. Magnetic reconnection is a fundamental process whereby the sheared magnetic field topology is altered via some dissipation mechanism, resulting in a rapid conversion of magnetic field energy into plasma energy and significant plasma transport. Thus, magnetic reconnection dominates the energetics and dynamics of most of these plasmas, and is at the root of explosive phenomena such as solar flares, coronal mass ejections, plasmoid ejection from the earth's magnetotail, and major disruptions in magnetic fusion energy (MFE) experiments.

Magnetic reconnection requires some dissipation mechanism to occur, such as resistive diffusion. However, plasmas in all the above-mentioned cases are known to have a negligible electrical resistivity η. This negligible resistivity cannot explain the reconnection timescales observed in nature, and this issue has drawn significant attention over the last 50 years.

Much study has been devoted to this problem, mostly within the context of the resistive magnetohydrodynamics (MHD) model. A fundamental breakthrough for fast reconnection came when the resistive MHD model was extended with electron Hall physics. Hall electron physics has been shown [1] to suffice to produce fast magnetic reconnection. Hall physics effectively decouples ions and electrons within a thin layer, the so-called ion inertial layer. Within that layer, ions slow down due to inertia, while (effectively) massless electrons are able to continue. At this point, the magnetic field is transported much more efficiently by electrons, thus resulting in increased reconnection rates.

However, in many systems of interest, the current layer thickness is much larger than the relevant Hall scale (ion inertial length, d_i), and hence fast reconnection cannot be explained *a priori*. To date, there is not a unifying system-level theory that explains the observed fast reconnection rate in such situations, since a general current layer "*thinning*" mechanism is not presently accepted.

We consider here the Kelvin-Helmholtz flow shear instability (KHI) as such current layer thinning mechanism. There are several observed phenomena where fast reconnection is occurring in the presence of known, or suspected, KHI activity. We briefly mention three. 1) Fast reconnection is known to occur on the dayside of earth's magnetosphere, where a region of magnetic field shear co-exists with a KHI-active region of flow shear [2]. 2) The process of current sheet thinning down to the scale of d_i has been well documented in earth's magnetotail, along with the connection to the onset of fast reconnection [3]. 3) Flow shear is known to exist on the solar surface as well as in the interface between the fast solar wind and the slow flows inside a helmet streamer [4], which could very well drive fast magnetic reconnection.

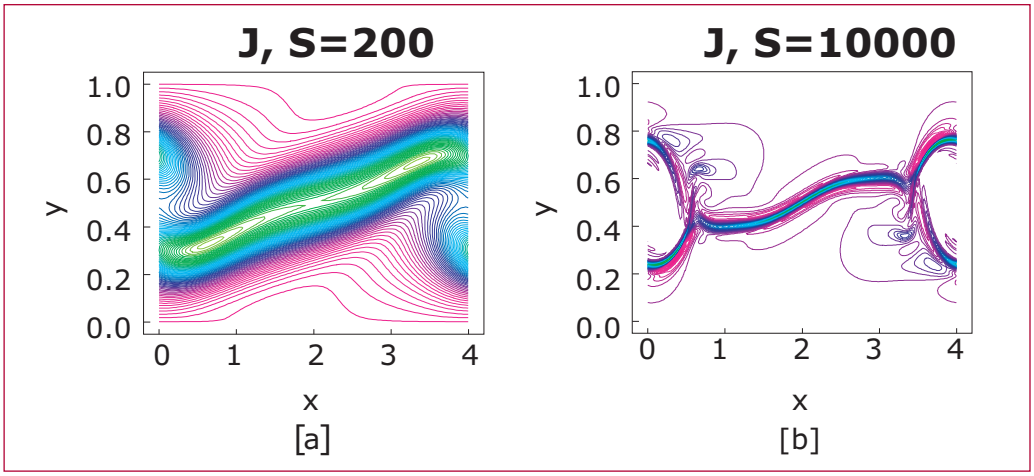

Figure — Current layer thinning via KHI for decreasing resistivities [5].

On the theoretical side, the fact that the KHI can produce fast current sheet thinning at the system scale in the absence of magnetic pressure buildup is now established [5]. The reconnection rate was computationally studied in the framework of a current-vortex sheet in resistive MHD [6]. These studies found η-independent (fast) reconnection rates in a range of resistivities even within the resistive MHD model. Figures 1a and 1b depict the current density J at the time of peak reconnection rate for inverse resistivities (Lundquist numbers), $S = \eta^{-1}$, equal to *200* and *10000*, showing the thinning effect of KHI with decreasing η. Three-dimensional computational studies [2] have also found KHI to be a valid current layer thinning mechanism in more general KH configurations.

These computational results are consistent with published analytical results on *transient* reconnection [8], which have found η-independent reconnection rates for idealized, flow-driven plasma configurations. We point out that the familiar Sweet-Parker *steady-state* reconnection theory (which predicts much longer reconnection time scales [7]) is not relevant for the case of interest, since the KHI is a fundamentally transient phenomenon.

It is thus plausible that the KHI, for sufficiently small plasma resistivity, can force the current thinning process until Hall MHD physics are relevant. At that point, ions become irrelevant from the magnetic field standpoint, and electrons take over the reconnection process, allowing the reconnection to proceed at a fast time scale [1]. However, a fundamental question remains unanswered, namely, the effect of magnetic pressure buildup, which inevitably accompanies the thinning of the current layer, on the thinning process itself. Investigation of this effect is underway that will validate —or reject—KHI as a plausible explanation for fast reconnection in nature.

[1] J. Birn *et al., J. Geophys. Res.* **106**, 3715 (2001).
[2] D. A. Knoll and J. U. Brackbill, *Phys. Plasmas* **9**, 3775 (2002).
[3] G. Lapenta and J. U. Brackbill, *J. Geophys. Res.* **102**, 27099 (1997).
[4] G. Lapenta and D. A. Knoll, *Solar Physics* **214**, 107 (2003).
[5] D. A. Knoll and L. Chacón, *Phys. Rev. Lett.* **88**, (2002), art. no. 215003.
[6] L. Chacón, D. A. Knoll, and J. M. Finn, *J. Comput. Phys.* **178**, 15 (2002).
[7] D. Biskamp, "Magnetic Reconnection in Plasmas" (Cambridge University Press, Cambridge, UK, 2000).
[8] A. Clark, *Phys. Fluids* **7**, 1299 (1964).

Shielding of a Thermionically Emitting Dust Grain

Gian L. Delzanno, EES-IGPP/V; and Giovanni M. Lapenta, T-15; lapenta@lanl.gov

The charging process of an object immersed in a plasma is a classic problem of plasma physics with many applications ranging from space physics and astrophysics to dusty plasmas to probe theory for plasma diagnostic. In absence of any other process (primary charging), it is well known that the higher mobility of the electrons tends to charge the object negatively; the resulting electric field on the object repels the electrons and attracts the ions until a dynamical steady state is reached. However, often other processes need to be included. For instance, it has been shown recently that the heating of a meteoroid during its fall in the Earth's atmosphere can produce a considerable amount of thermionic electrons and affects the charging process by reducing, or even reversing, the object polarity. Similar considerations apply to photo emission and secondary emission.

The present contribution deals with how thermionic emission affects the charging process of an object in a plasma, considering self-consistently charge collection by the object and the screening by the surrounding plasma. In order to complete this task, we have developed a highly accurate Particle-In-Cell (PIC) code in spherical geometry. Simulations have been performed by choosing the physical parameters of the system according to common experimental and natural situations. We start from a Maxwellian plasma and let the system relax self-consistently until the charge on the grain and the shielding potential around it reach a steady state.

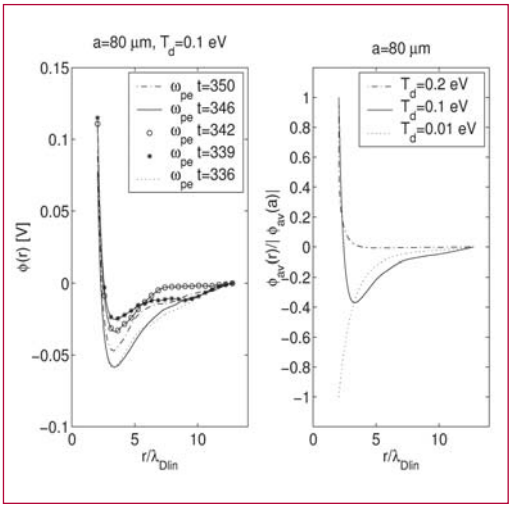

Figure 1—Potential well around an emitting dust particle.

Here we focus on the most important result we have obtained: the appearence of a potential well in the shielding potential when thermionic emission is included, in contrast with the typical monotonic behaviour by the Debye-Huckel theory. The appearance of a potential well is of great practical interest since it can lead to attractive forces on another dust particle, even if it has the same sign of charge. Further details can be found in [1]. Figure 1 shows the behaviour of the shielding potential for a simulation with dust temperature Td = 0.1 eV. On the left panel, one can see the shielding potential at different times, showing an oscillatory trend. On the right panel, the time averaged shielding potential is shown and the well is clearly present. For comparison, we have also shown the time averaged shielding potential for two simulations with Td = 0.01 eV (which practically corresponds to the primary charging case; dotted line) and with Td = 0.2 eV (dash-dotted line).

How can a potential well form? Since the dust grain is positively charged, the resulting electric field attracts electrons and repels ions. As a consequence, the thermionically emitted electrons are slowed down in a region close to the grain. The more energetic electrons can

escape the field attraction and contribute to the thermionic current, but the rest of the electrons create a cloud around the grain. The electron cloud determines a local excess of negative charge which is responsible for the well. With this picture in mind, it is easy to understand why the well disappears as the temperature grows beyond a certain threshold: at high-dust temperatures more electrons have enough kinetic energy to escape the dust attraction, thus reducing the local excess of negative charge until the shielding potential becomes a monotonic function of radius.

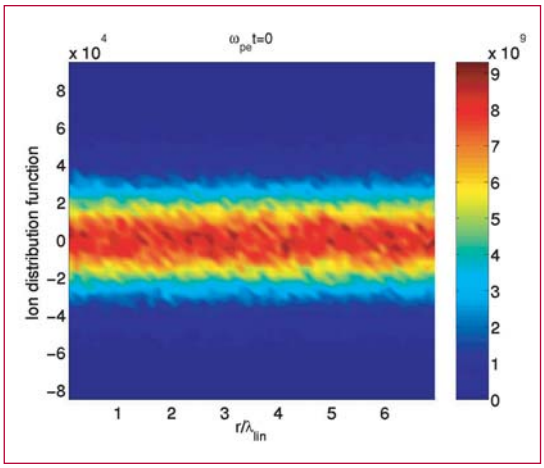

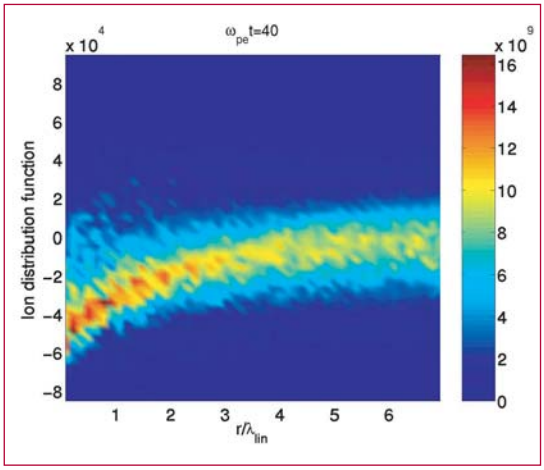

Further investigations with our PIC code are devoted to study the time-evolution of the phase space during the charging process. This issue is of great relevance in the community since many theories rely on the assumption of Maxwellian distribution functions while there is evidence that this might not be the case. Figure 2 and 3 show the ion phase space for a simulation where thermionic emission is not included: the initial distribution function is Maxwellian (Figure 2) while the subsequent evolution corresponds to a Maxwellian shifted towards higher velocities until nonlinearities repopulate the low-velocity region of the phase space (Figure 3).

[1] G. L. Delzanno, G. Lapenta, M. Rosenberg, *Phys. Rev. Lett.* **92** (3), 035002 (2004).

Random Attractor Confined by Noise

John M. Finn, T-15; E. R. Tracy, S. Richardson, and W. Cooke, College of William and Mary; finn@lanl.gov

In 1963, E. Lorenz derived a low-order model for thermal convection showing deterministic chaos. Since that time there has been much effort in modeling complex physical processes in terms of low-dimensional systems, and in developing time series methods to determine whether observed phenomena (in experiments or simulations) are due to low-dimensional dynamics that might be modeled by a low-order ordinary differential equation (ODE). The effects of noise in such deterministic chaotic systems—systems in which there is a chaotic attractor for zero noise—have been studied. The effect of adding noise to such systems is typically to smear out the fractal nature of the attractor, but leave the qualitative behavior pretty much unchanged.

We have developed a low-order model for edge-localized-modes (ELMs) in tokamaks, in which noise plays a more central role. This model takes the form of a nonlinear second order stochastic ODE with additive uncorrelated gaussian dynamical noise. The system has an instability, called a ballooning mode, which is related to the Rayleigh-Taylor instability, but is driven by the pressure gradient rather than the mass density gradient and is electromagnetic, i.e., it involves the evolution of the magnetic field. The dynamical noise represents fluctuations in the tokamak that have a much shorter correlation time than the ELM dynamics being studied. The zero noise version of this system is of the predator-prey variety, and for certain parameters is the Lotka-Volterra (L-V) system. However, the L-V system is Hamiltonian (in noncanonical variables) and therefore has no dissipative nature: any orbit is on a neutrally stable cycle whose amplitude is completely determined by its initial conditions.

Our system for non-LV parameters with zero noise has an unstable fixed point and invariant manifolds along the x- and y-axes. (That is, orbits starting along these axes stay on the axes.) In a large range of parameters, called Range II, typical orbits with $x > 0$, $y > 0$ spiral away from the fixed point in increasing bursts, as shown in Figure 1.

Each successive burst is larger, and the time interval between the bursts increases, with the bursts eventually going off to infinity. Because of symmetry in x, orbits with $x < 0$ have identical bursty behavior with x remaining to the left of $x = 0$. For other parameters, called Range III, orbits go directly to infinity in finite time without oscillations about the fixed point.

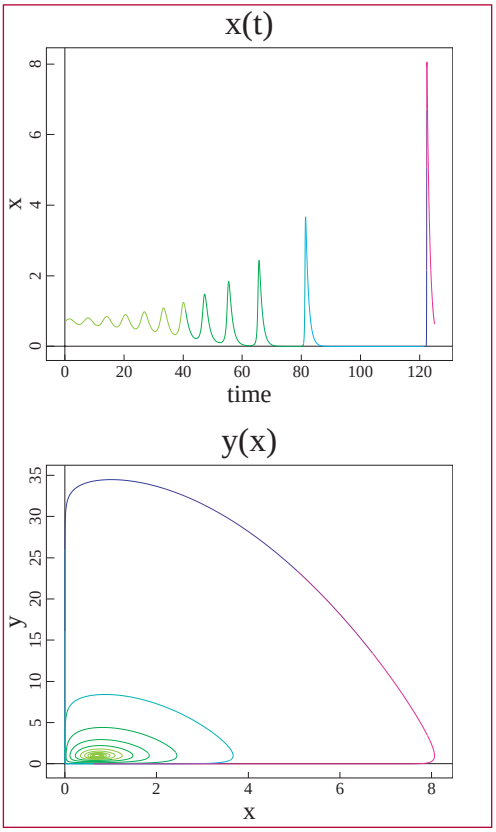

Figure 1—Successive bursts in x(t) and in the phase plane (x,y) for zero noise. Each successive burst is larger in magnitude and the time interval between them is increasing. The bursts correspond to spirals about the fixed point at x = 0.7, y = 1.

With even very small noise the behavior is completely different, as shown in Figure 2 for parameters in Range II.

The successive bursts appear random in height and the number of bursts with $x < 0$ is equal to those with $x > 0$ as time approaches infinity. The noise is effective even for very small magnetic field levels, x, and has the effect of preventing the field from decaying much below the noise level, even when it is stable. A simple Fokker-Planck equation governs the behavior for small magnetic field and leads to a distribution function of peak burst values, which has a power-law tail. Denoting x_n as the successive maxima of the magnetic field and T_n as the time interval between x_n and x_n, we find that x_n and T_{n+1} are highly correlated (nonlinearly), but that T_n and x_n are uncorrelated, consistent with the fact that the noise is important only for a small magnetic field. Further, the Lyapunov exponent is positive for these "random attractors," and varies weakly with the noise variance, σ^2. We are working on methods of time series analysis to distinguish this behavior from deterministic chaos, based on these results.

We have reproduced these results experimentally in a nonlinear circuit with externally generated white noise, obtaining good agreement. The experiments have also shown that colored noise (noise with a power spectrum other than flat in frequency) leads to locking behavior apparently associated with the characteristic frequency scales of the noise. This preliminary result may be quite significant, because, as we have mentioned, the "noise" in a model actually represents other physical phenomena not modeled deterministically, and the assumption of white noise is usually not well justified. This is particularly true because of the ability of the circuit to lock onto insignificant-looking features in the power spectrum. Further studies of this are underway.

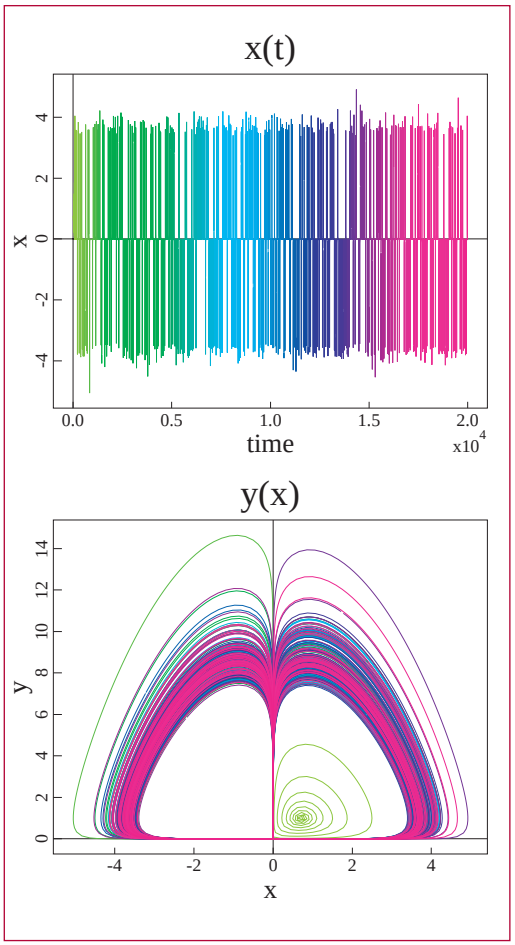

Figure 2— Random bursts for small noise level σ =0.01 over a much longer interval of time, again x(t) and the phase plane (x,y). The orbits initially spiral out from the fixed point at x = 0.7, y = 1, and then have random bursts with symmetric statistics on both sides of x = 0.

The DCON Fast Fusion Stability Code

Alan H. Glasser, T-15; ahg@lanl.gov

Controlled thermonuclear fusion, the quest to tame the energy of the sun, the stars, and the hydrogen bomb, holds the promise of clean, safe, and abundant energy from rocks and ocean water. The main fuel for this reaction consists of deuterium and tritium, the heavy isotopes of hydrogen. A gallon of water contains enough energy in its 1 part in 6000 of naturally occurring deuterium to equal the energy from burning 300 gallons of gasoline. Comparable energy is available from breeding the lithium in rocks into tritium. Most of the earth is covered with water to a depth of several miles. And don't forget all those rocks!

To obtain this energy, the fuel must be heated to thermonuclear temperatures, on the order of 100 million degrees C. On its way there, all matter passes through its successive phases of solid, liquid, gas, and plasma, or ionized gas. Contact with any solid container would either cool and contaminate the plasma fuel, preventing the reaction, or destroy the container. So the real trick is to confine the hot plasma without contact with anything material. If this can be done at a high enough plasma density and for a long enough time, then more energy is released from fusion reactions than is required to produce, confine, and heat the fuel, a condition called break-even. This is the holy grail of fusion research.

Among the most promising confinement methods is a toroidal, or donut-shaped, magnetic field. The high-magnetic field energy on the outside is used to hold a high-pressure plasma on the inside. Experiments of this type include the Alcator C-MOD Tokamak at MIT, the DIII-D Tokamak at General Atomics in San Diego, the National Spherical Torus Experiment (NSTX) at the Princeton Plasma Physics Laboratory (PPPL), and many others in the US, Europe, Russia, and Japan. There are tentative plans to build a much bigger one called ITER, the International Tokamak Experimental Reactor, to be sited in either France or Japan, designed to achieve break-even.

Such magnetically-confined plasmas are subject to a large variety of magnetohydrodynamic (MHD) instabilities. If the electric current flowing through the plasma—or the ratio of plasma pressure to magnetic field energy—exceed certain thresholds, the plasma can experience either large disruptions, terminating the discharge, or small-scale turbulence, which reduces the efficiency of confinement. These thresholds depend in a complicated way on the detailed structure of the plasma and magnetic field. The ability to understand and control these instabilities may determine the practicality of obtaining net energy from any particular configuration. This is the subject of extensive experimental and theoretical effort at all magnetic fusion labs.

DCON is a fast, accurate computer code, developed in T-15, for determining the stability of a given plasma equilibrium. Specification of the plasma equilibrium is provided by other computer codes, making use of extensive experimental data on the configuration of the magnetic field and the plasma density and temperature. A typical discharge (experimental run) lasts several seconds. During and after the discharge, hundreds of equilibrium reconstructions, or time slices, may be performed. DCON can determine the stability of each of these time slices on a fast workstation in about 10 seconds, allowing many such analyses in the 15 minutes or so between discharges. This provides experimentalists with an understanding of the

conditions leading to disruptions, which can be used to help decide on conditions for the next discharge. This kind of shot-to-shot analysis, made possible for the first time by the speed and accuracy of DCON, provides a new level of understanding. It is being used at the three experiments mentioned above, as well as in design studies for future experiments. Three lines of development have been emphasized over the past year.

First, a collaboration has been pursued with researchers at PPPL/NSTX to systematically analyze large numbers of reconstructed equilibriums and use the results to understand overall features of the behavior. This device is especially challenging for any MHD stability code because of its low-aspect ratio, low-magnetic field strength, high-vertical elongation, high-plasma pressure, and magnetic separatrix. The flux surfaces that confine the plasma are illustrated in the figure.

Second, in collaborations with Columbia University, Princeton University, and General Atomics, DCON is being used to provide the detailed plasma response as input to a several feedback stabilization efforts.

Third, DCON is being extended to treat instabilities with more realistic dynamics than ideal MHD, including resistivity and kinetic and nonlinear effects. These more subtle instabilities are believed to be responsible for a large range of tokamak behavior. Because of their greater subtlety, accurate computation is much more difficult. Resistive DCON is expected to be the only code capable of analyzing this important class of instabilities.

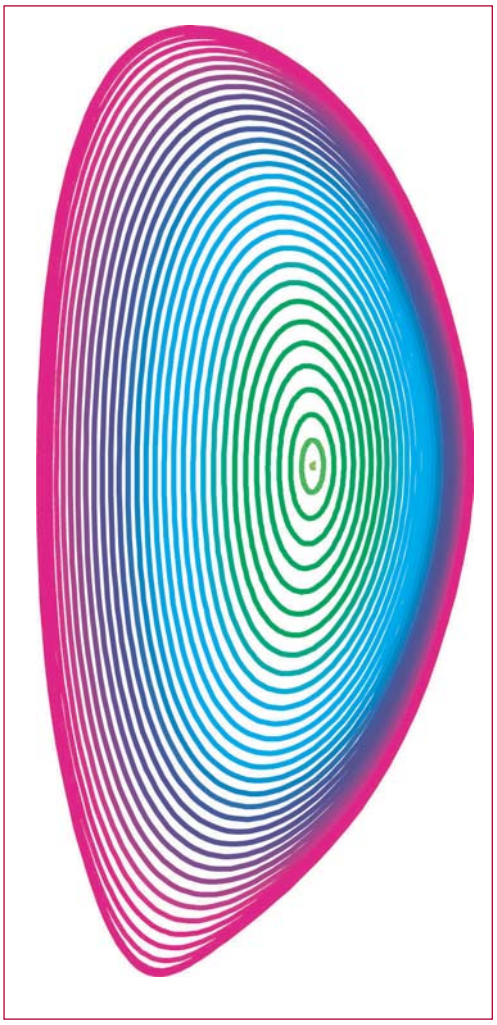

Figure– Flux surfaces for NSTX equilibrium. These are the magnetic surfaces that confine the plasma pressure. The detailed shape of the magnetic surfaces plays a major role in determining stability.

The SEL Plasma Simulation Code

Alan H. Glasser, T-15; ahg@lanl.gov

One of the major activities of T-15 Group is theoretical and computational studies of magnetically confined plasmas for fusion energy. (For a discussion of this research, see the discussion in this volume of the DCON Fast MHD Stability Code.) Numerical simulation of such plasmas presents one of the most difficult challenges in all of computational physics. In response to this challenge, T-15 is developing the SEL code [1], using some of the most advanced numerical methods in existence.

A principal source of difficulty is multiple time scales. There are time scales in this problem ranging from the gyration period of an electron about the magnetic field, of order 10^{-12} s, to the time it takes the plasma to diffuse across the magnetic field, of order 1 s, and many others in between. The simplest and most common method, the explicit approach, limits the time step to the fastest motions in the problem, which would require a prohibitively large number of steps to treat the long times of interest. To avoid this, SEL uses implicit time steps, requiring the solution of large systems of equations on each time step. This allows the user to choose time steps governed by the physical process of interest, not the faster, uninteresting time scales.

Similarly, there are multiple length scales in the problem, ranging from the electron gyration radius, of order 0.1 mm, to the mean free path between collisions, of order 10 km, and many others in between. Many phenomena of interest are characterized by small regions of sharp gradients interspersed with much larger regions of small gradients. To deal with this problem, we are developing new approaches to the problem of adaptive gridding, automatically concentrating the computational grid in regions of sharp gradients while leaving it coarse and therefore economical in regions of small gradients.

A unique feature of magnetically confined plasmas is a very high degree of anisotropy, or directionality. The nature of magnetic confinement is that particles and fluids are very effectively restrained from moving across magnetic field lines but are free to move along them. This in highly different behavior along and across field lines. For example, the ratio of parallel to transverse thermal conductivity can be as large as 10^{10}. If a small amount of the large parallel conduction "leaks" into the transverse direction because of numerical error, the accuracy of the description can be hopelessly compromised. The most effective way to avoid this is the use of a flux coordinate grid aligned with the magnetic field. If the magnetic field varies in time, the grid must occasionally be updated to maintain this property. We are developing new methods to accomplish this.

Another key issue is the method of spatial discretization. Many methods have been developed by computational physicists to express continuous variables like density and temperature in terms of discrete numbers that can be handled on the computer. The oldest and most common is finite differences, in which gradients are expressed as ratios of differences between quantities on a fine grid. A similar approach is linear finite elements, in which variables are represented as piecewise linear on a grid. A third method is spectral, in which the variables are represented as Fourier series of trigonometric functions. Each of these methods have advantages and disadvantages. SEL uses a very recent and powerful method called spectral elements, which combines the best features of several of these methods.

It is essential to make efficient use of massively parallel computers in order to benefit from these most powerful computational resources. SEL makes extensive use of the MPI and PETSc libraries to achieve a high degree of parallel efficiency.

As a preliminary example of the SEL code, Figures 1 and 2 show the results of modeling 2-D incompressible magnetic reconnection. There are four dependent variables in the problem: a) magnetic flux function, c) current density b) velocity stream function, and d) vorticity. The initial configuration has both a sheared magnetic field, directed right above the midplane and left below and a sheared velocity, directed right above the midplane and left below. The magnetic shear drives a tearing instability while the velocity shear drives a Kelvin-Helmholtz instability. The plasma has very small resistivity and viscosity, 10^{-4} in scaled units, leading to the formation of thin layers about a magnetic separatrix that are difficult to resolve numerically. Figure 1 shows the amplitudes of the four functions, initially growing

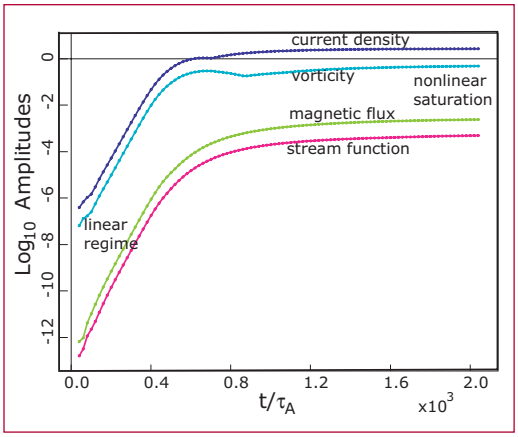

Figure 1—

exponentially during a linear phase, then saturating in the nonlinear phase. Figure 2 shows the configuration of the four functions at nonlinear saturation, illustrating the development of a thin layer of sharp gradients about the magnetic separatrix.

[1] A. H. Glasser and X. Z. Tang, "The SEL Macroscopic Modeling Code," accepted for publication in *Computer Physics Communications*.

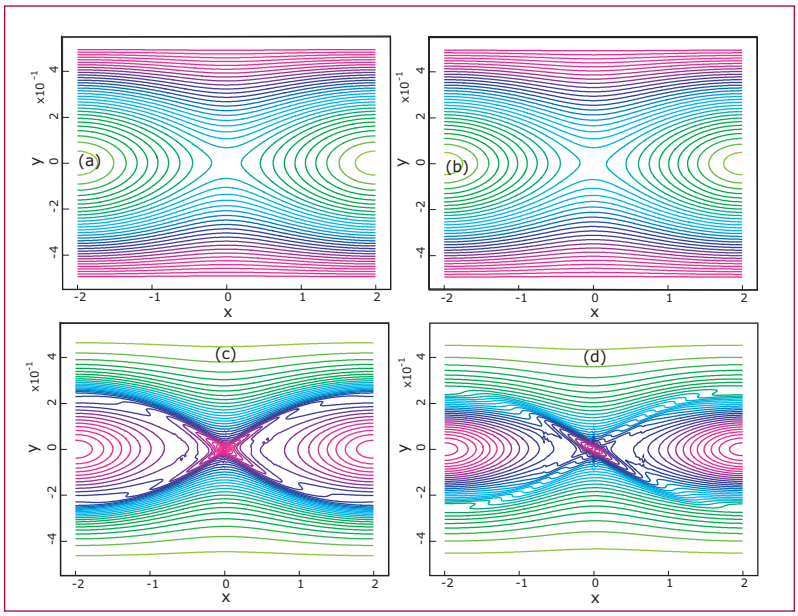

Figure 2—

Are Jets Emitted from Accretion Disks around Black Holes Solitons?

Giovanni M. Lapenta, T-15; lapenta@lanl.gov

A long standing mystery in astrophysics is the mechanism that allows jets emitted from accretion disks around black holes to remain collimated for distances of the order of the kiloparsec (several thousands of light years).

We have conducted a theoretical study of jet collimation that suggests that a possible explanation for the mystery might be found in a seemingly unrelated area of physics: the physics of solitons. We have based our description of the astrophysics jets on a mathematical analogy between the model for jets and the description of the propagation of solitons in non linear optical waveguides.

The resulting solution of the governing equations is a soliton-like state that represents astrophysics jets. A well-known property of solitons is the ability to keep their confinement while travelling for very long distances in spite of dissipations that would spread linear waves enormously over the same distances. Similarly, we propose that solitonic states can explain how the collimation of astrophysics jets is kept for thousands of light years.

To probe this idea further, we have conducted a simulation study of the evolution of a system initially in a state characterized by the soliton solutions. We used a MHD code developed by Jerry Brackbill (T-3) in collaboration with staff members in T-15: FLIP3D-MHD. Using the specific example of the jets observed from the active galactic nucleus (AGN) in the radio galaxy 3C303 and M87, we investigate the ability of the proposed model to explain the observational evidence. Typical conclusions derived from the simulations are shown in Figures 1 and 2 where one can observe the phase where the jet remains collimated and the eventual loss of coherence and the creation of the giant radio lobes seen also in the real radio galaxies.

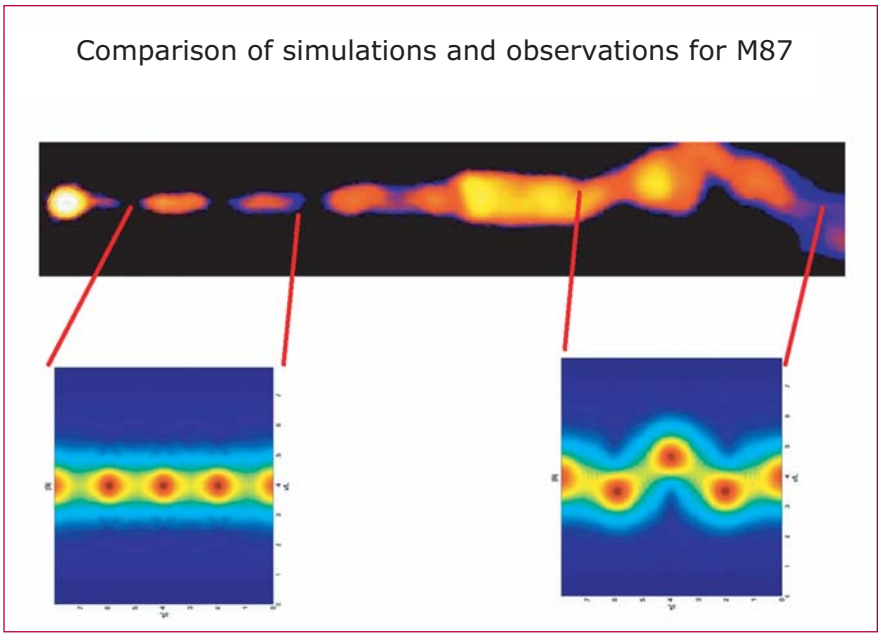

Figure 1—

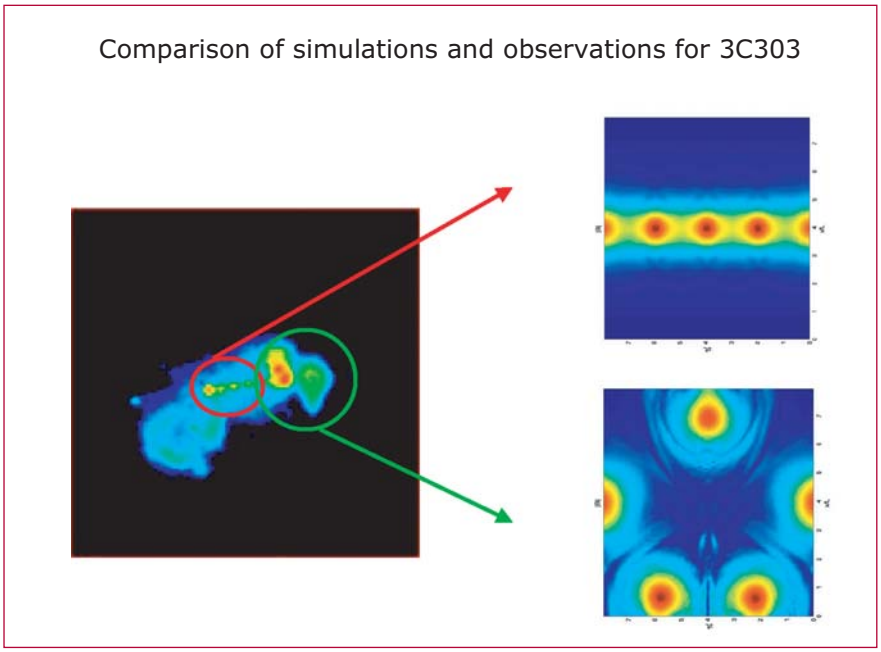

Figure 2—

Plasmon Pole Approximation for Warm Dense Matter Calculations: Application to Temperature Relaxation in Nonequilibrium Systems

Michael S. Murillo, T-15 and George Csanak, T-4, murillo@lanl.gov

Warm dense matter is defined as matter that is partially degenerate, moderately to strongly coupled, and has important atomic physics. It is believed that collective modes can play an important role in determining a wide variety of microscopic properties, such as stopping power, opacities, and temperature relaxation. Our goal is to develop reduced models for these processes that capture most of the important physics while being useful within hydrodynamic modeling codes. Our strategy is to evaluate highly accurate expressions for validation of the reduced models. The highly accurate forms, however, include the collective behavior through a linear response function that has very narrow peaks at the resonance frequency.

We have developed several approximate numerical techniques that allow us to perform integrations over the narrow peaks, which yield very accurate results that can validate the simpler models. As an example, consider how a fast particle (e.g., a fission fragment) slows down due to energy transfer to a dense electron gas. Part of the energy loss is due to plasmon excitation that appears as a very narrow peak within an integral. Since the plasmon is well defined at long wavelengths, the peak is too narrow to directly integrate numerically. This problem is usually solved by resorting to a sum rule that becomes exact in some limit; however, the limit may not apply to all cases. For stopping power calculations a useful limit is that of a very fast particle, which is obviously violated as the particle slows and thermalizes.

We have generalized the sum rule approach for use in calculations for which a sum rule does not exist, or is difficult to calculate. The basic idea is to factorize the integrand $I(x)$ into a product of two functions $I(x)=J(x)D(x)$ where one of the functions $D(x)$ is a so-called delta function distribution. We then break the integral into two regions: one that is easy to integrate numerically and one for which the limit to the delta function $D(x) \rightarrow \delta(x)$ is approximately valid. The use of a delta function $\delta(x)$ for $D(x)$ is the "plasmon pole approximation" and can be integrated analytically. A priori it is not clear that such an approach will work, since there may be a region for which the brute force integration fails *and* the delta function limit is too inaccurate.

We have tested our simple model for the problem of temperature relaxation [1]. Physically we consider two-temperature warm dense matter and calculate the relaxation time to equilibrium; such a quantity is important since warm dense matter is often created through a nonequilibrium process, such as laser radiation or charged particle deposition into the electron subsystem. We employ fully quantal linear response functions for the electrons and a semi-classical version for the ions. Strong coupling is accounted for via local field corrections. Physically the process of interest is energy exchange between the species through

collective modes, as opposed to simple binary collisions. We have computed the relaxation rate using both the plasmon pole approximation just described, brute force integration, and using a sum rule approach [2] as a check. The results are shown in the figure for ion temperature of T_i=3.75, 10.01, 100.14 eV and three electron temperatures T_e=0.35, 10.0, 100.0 eV, respectively. In the figure we vary the point at which we break the integration between brute force integration and the plasmon pole approximation. Larger values correspond to breaks at longer wavelengths where the collective behavior is strongest (the width is smallest). We see that the method works very well for higher temperatures, but the warm dense matter region is particularly difficult to compute.

In the future we will apply these results to more sophisticated relaxation models for which the sum rule approach cannot be used as a test. Such calculations, which describe the coupling between various modes of the multi-species system, are underway.

[1] See following article in this volume for a detailed description of the relaxation model.

[2] H. H. Brouwer, W. D. Kraeft, M. Luft, T. Meyer, P. P. I. M. Schram, B. Strege, *Contrib. Plasma Phys.* **30**, 263 (1990).

Acknowledgement: We thank Dirk Gericke, T-15, for drawing our attention to reference [2].

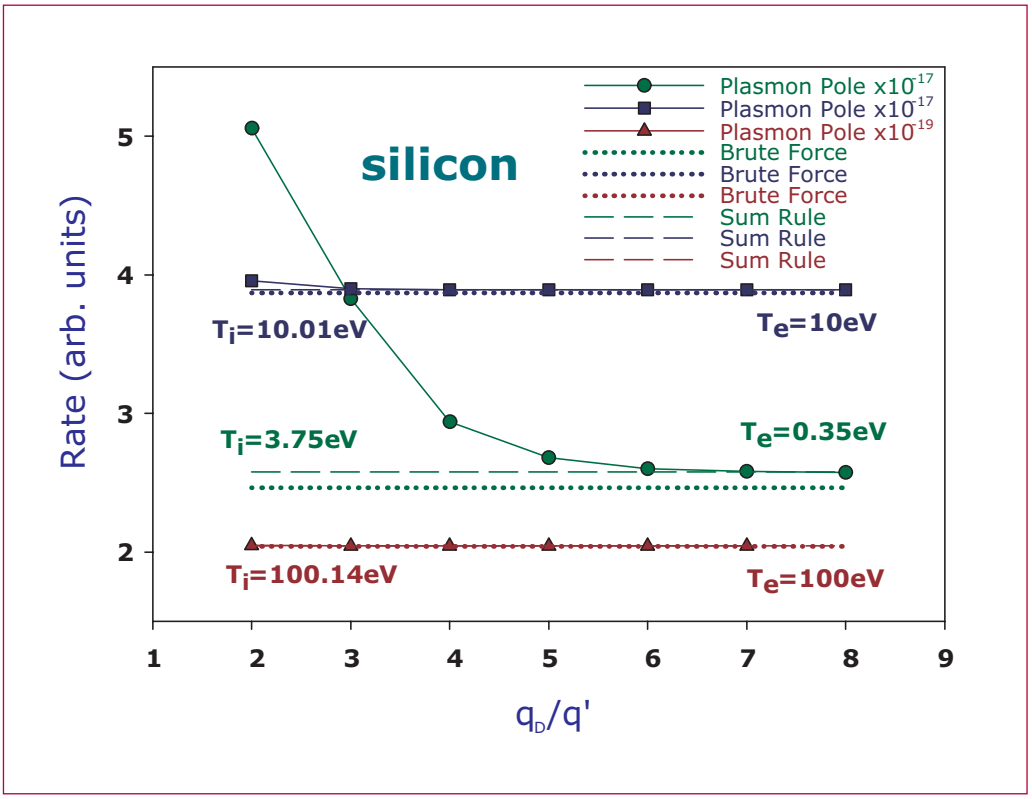

Figure—
The energy relaxation rate version inverse wavevector of the break between the plasmon pole approximation and a brute force integration that employs an adaptive procedure. Results for three temperatures are shown; the results have been scaled by the numbers given in the legend. Calculations have been performed using the plasmon pole approximation (solid), brute force integration (dotted), and with a sum rule approach (dashed). The larger the number q_D/q', the longer wavelength of the transition. It is clear that all methods yield essentially the same result at high temperatures with much larger discrepancies in the warm dense matter regime.

Exact Treatment of Ion Collective Modes in the Fermi Golden Rule FGR Description of Temperature Relaxation

George Csanak, T-4; Michael S. Murillo, T-15; William S. Daughton, X-1; georgec@lanl.gov

Introduction

The purpose of the present work is to present results from a calculation using the Kogan formula that explicitly incorporates the plasmon poles into the calculation. This calculation uses the method of Brouwer *et al.* [1] for this purpose. The essence of the method of Brouwer *et al.* is that a small region from the integral around the plasmon pole is excluded from the numerical integration, and the contribution from the small region to the integral is obtained by the explicit use of the f-sum rule. The results obtained by this method agree well with the MKF (modified Kogan formula) results.

The Kogan formula and the Modified Kogan Formula

We begin with the formula for the energy relaxation rate in the FGR approximation (the Kogan formula), which describes the relaxation rate in terms of the imaginary parts of the dynamic electron and ion response functions

$$\frac{dE_i}{dt} = \int_0^\infty \frac{d\omega}{2\pi}\,\omega \int \frac{d^3q}{(2\pi)^3}\left|U_{ei}(q)\right|^2 \times A^e(q,\omega,T_e)\,A^i(q,\omega,T_i)\,N_{ei}(\omega,T_e,T_i), \tag{1}$$

where $N_{ei}(\omega)$ is the difference of the Bose factors. The electron-ion coupling constant g is then defined by

$$\frac{dE_i}{dt} = (T_e - T_i)\,g.$$

There are two essential approximations that lead from the FGR or Kogan formula (1) to the MKF. The approximations are: linearization of the Bose function and the low-frequency approximation (linearization) for the electron response function. We can use the exact f-sum rule and obtain the MKF in the form,

$$g = 4\int \frac{d^3q}{(2\pi)^3}\left|U_{ei}(q)\right|^2 \frac{\chi''_{ee}(q,\omega)}{\omega}\bigg|_{\omega=0}. \tag{2}$$

The Explicit Incorporation of the Plasmon Pole Contribution into the Numerical Evaluation of the Kogan Formula

In the calculation of the energy relaxation rate according to the Kogan formula, as given by (1), first the ω integral can be calculated:

$$I(q) = \int_0^\infty \frac{d\omega}{2\pi}\,\omega A^e(q,\omega,T_e) \times A^i(q,\omega,T_i)\,N_{ei}(\omega,T_e,T_i). \tag{3}$$

As discussed earlier, for small q values the $A^i(q, \omega, T_i)$ function displays sharp peaks (plasmon poles) that are not easily incorporated into numerical integration schemes. A special technique is needed to ensure that the contribution from those peaks are taken into account in the calculation of the above integral.

This technique, introduced by Brouwer *et al.* [1], is based on the f-sum rule for the ion spectral function, $A^i(q, \omega, T_i)$. The essence of the technique is that if we denote the location of the plasmon pole by ω_{pl}, then the

integration range in calculating $I(q)$, as given by (3), is divided into three segments: $(0, \omega_{pl} - \delta)$, $(\omega_{pl} - \delta, \omega_{pl} + \delta)$, and $(\omega_{pl} + \delta, \infty)$ where δ is a small frequency range compared to ω_{pl}. The crucial step now is to calculate the contribution from the middle range accurately. With the help of the f-sum rule this integral can be written in the following way:

$$\int_{\omega_{pl}-\delta}^{\omega_{pl}+\delta} d\omega\omega A^i(q,\omega,T_e) = \pi \frac{n_i}{m_i} q^2 - \int_0^{\omega_{pl}-\delta} d\omega\omega A^i(q,\omega,T_i) - \int_{\omega_{pl}+\delta}^{\infty} d\omega\omega A^i(q,\omega,T_i). \quad (4)$$

The last thing we need to discuss is the choice of ω_{pl}. A simple formula for the location of such plasmon-like peaks was provided by Kraeft *et al.* [2] in the form,

$$\omega_{pl} = \omega_{ip} + \Delta \quad (5)$$

where ω_{ip} is the ion plasma frequency, and Δ is a correction term.

Numerical Results

We have used the above scheme in the numerical implementation of the Kogan formula. We have explicitly included the plasmon pole contribution to $I(q)$ for $q < q_D$ where q_D is the Debye wave-vector. The numerical results are summerized in the table, where they are compared with FGR (Kogan formula) results and with MKF results. Clearly, the original Kogan calculation results disagree with the MKF results at low temperatures, which can be attributed to the inability of the numerical integration technique to integrate through the very narrow plasmon poles. Since this direct integration technique often misses the very narrow plasmon poles, it underestimates the value of the electron-ion coupling constant. Furthermore our numerical results demonstrate that the approximations that led to the MKF introduce only extremely small errors (or none at all) for the cases considered. Therefore, based on just this one study, it appears promising that the numerically much easier MKF can be applied for the calculation of the electron-ion coupling constant. Other cases need to be investigated.

		$g\ (W/Km^3)$		
T_e (eV)	T_i (eV)	Kogan (numerical)	Kogan (plasmon)	MKF
0.10	3.75	2.47×10^{17}	2.57×10^{17}	2.58×10^{17}
0.25	3.75	2.46×10^{17}	2.57×10^{17}	2.58×10^{17}
0.35	3.75	2.45×10^{17}	2.56×10^{17}	2.57×10^{17}
0.50	3.75	2.44×10^{17}	2.55×10^{17}	2.55×10^{17}
0.75	3.75	2.44×10^{17}	2.55×10^{17}	2.55×10^{17}
0.95	3.75	2.43×10^{17}	2.54×10^{17}	2.54×10^{17}
1.65	3.75	2.42×10^{17}	2.53×10^{17}	2.54×10^{17}
3.74	3.75	2.30×10^{17}	2.41×10^{17}	2.42×10^{17}
10.0	10.01	3.87×10^{17}	3.89×10^{17}	3.89×10^{17}
30.0	30.01	3.13×10^{18}	3.13×10^{18}	3.13×10^{18}
100.0	100.14	2.04×10^{19}	2.04×10^{19}	2.04×10^{19}
300.0	300.14	4.39×10^{18}	4.39×10^{18}	4.39×10^{18}
1000.0	1001.4	2.09×10^{18}	2.09×10^{18}	2.09×10^{18}

***Table 1—** Kogan and MKF results for the coupling constant of solid density shocked silicon. Here "Kogan (numerical)" refers to our results obtained via double numerical integration. "Kogan (plasmon)" refers to our results that includes the plasmon pole contributions explicitly. MKF refers to our MKF results.*

[1] H. H. Brouwer, W. D. Kraeft, M. Luft, T. Meyer, P. P. I. M. Schram, and B. Strege, "Stopping Power of Charged Particles I," *Contrib. Plasma Phys.* **30**, 263 (1990).

[2] W. Kraeft, D. Kremp, W. Ebeling, and G. Ropke, *Quantum Statistics of Charged Particle Systems* (Plenum Press, New York, 1986) pp. 98–99.

See previous article in this document by Michael Murillo and George Csanak, "Plasmon Pole Approximation for Warm Dense Matter Calculations: Application to Temperature Relaxation in Nonequilibrium Systems."

An Electrostatic Confinement Experiment to Explore the Feasibility of the Periodically Oscillating Plasma Sphere as a Plasma Confinement Device

Richard A. Nebel, T-15; J. Y. Park, S. Stange, and J. M. Taccetti, P-24; rnebel@lanl.gov

Theoretical work [1,2] has suggested that a tiny oscillating ion cloud (Periodically Oscillating Plasma Sphere or POPS) may undergo a self-similar collapse that can result in the periodic and simultaneous attainment ultra-high densities and temperatures. Theoretical projections [1] indicate that such a system may have net fusion gain even for an advanced fuel such as Deuterium-Deuterium. Schemes have also been suggested where a massively modular system consisting of tens of thousands of these spheres (see Figure 1) can lead to a very high-mass-power-density device (similar to a fission light water reactor)[1] while still having conventional wall loads (~ 1 MW/m2).

POPS also has the feature that the total fusion power scales inversely with the device radius [1]. This favorable surface to volume scaling leads to high-mass-power density and thus a device that will be competitive with fission, coal, gas, and renewable energy sources. The lightweight, modular design is also an excellent fit for the space propulsion systems that will be required for interplanetary space travel.

The fusion energy development path for the POPS system is also very different from conventional fusion systems. Conventional systems tend to get larger and more expensive with each generation. (For instance, the next generation

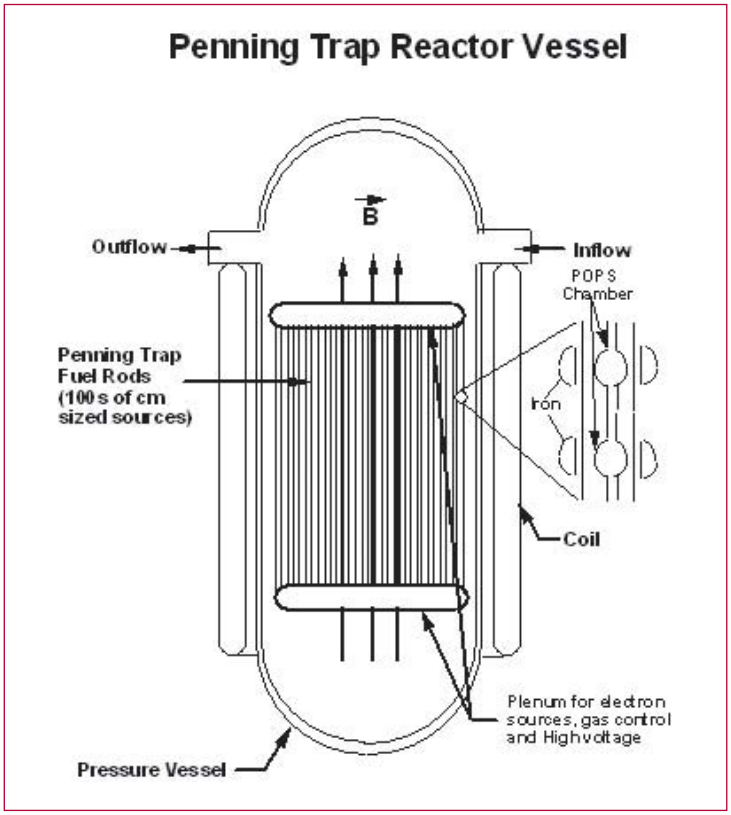

Figure 1— The massively modular penning trap reactor.

magnetic confinement device (ITER) is projected to cost twelve billion dollars.) For POPS, we will demonstrate the physics on a single cell so each generation device should be smaller than the previous generation. The costs of any successive device should be similar to our present device that was less than $100 K.

Thus, this device combines the following three attributes: a high-mass-power-density device with favorable economics, a low-cost development path where no device costs more than $100 K, and a system that can operate with advanced fuels. However, a number of issues need to be addressed to determine the efficacy of the POPS scheme. Some of these issues are phase locking and control of the ion oscillations, space charge neutralization during the ion collapse phase, electron cloud uniformity and control, stability of the electron cloud, and maintenance of the virtual cathode. These issues are being addressed both theoretically and experimentally. A picture of our present experiment is shown in Figure 2.

[1] R. A. Nebel and D. C. Barnes, *Fusion Technology* **38**, 28 (1998).

[2] D. C. Barnes and R. A. Nebel, *Physics of Plasmas* **5**, 2498 (1998).

Figure 2—The POPS experiment.

And Then it Turned out it Really was the Butler!

Paolo Ricci and Giovanni M. Lapenta, T-15; Jeremiah U. Brackbill, T-3; and W. S. Daughton, X-1; lapenta@lanl.gov

Reconnection is observed in a great variety of systems—from laboratory experiments especially designed for it, to fusion devices, to space and astrophysics plasmas. The attention of our studies has been focused on magnetospheric plasmas where reconnection develops primarily at the magnetopause, where the solar wind meets the Earth's magnetic field, and in the Earth magnetotail.

Magnetic reconnection is one of the most important energetically active processes in plasmas. Through reconnection, magnetic field lines break and reconnect into a lower energy state. Magnetic energy is thus released to plasma particles in the form of plasma heating and plasma jetting.

But a great mystery has puzzled the researchers involved in reconnection studies. Based on our best understanding, based even on the most advanced models, reconnection should not happen. From fluid theories, one expects reconnection to develop on scales so long that processes that we observe to happen in a second take the age of the solar system to develop. From more advanced kinetic theories, reconnection might start at a reasonable pace, but would stop at levels so tiny as to be of no practical consequence. And yet it moves! Observations in the laboratory, in space, and in astrophysical plasmas have documented reconnection to be ubiquitous and fast.

In the sixties, the suggestion was made that turbulence and plasma microinstabilities could solve the puzzle. For example, if the Earth's environment (magnetosphere) is considered, the most likely candidate was suggested to be the Lower-Hybrid-Drift Instability (LHDI). It was proposed that the LHDI waves would scatter and exchange momentum with the plasma particles and effectively act as a friction force. This friction would result in an anomalous resistivity and allow fast reconnection. Forty years of research along those lines yielded nothing. LHDI was indeed observed in satellite data but in the wrong locations, not where reconnection develops. Theories and simulations proved that LHDI remains localized outside the current sheets where reconnection develops and its saturation level is far too small to cause enough anomalous resistivity.

When the goings got tough, the tough got going. In order to address the physics of magnetic reconnection, we have used three codes that represent the state of the art in the kinetic study of plasmas: a kinetic linear code and two Particle-In-Cell (PIC) codes, one explicit and one implicit. The linear code is used to address the linear evolution of the system, by evaluating both the growth rate and the eigenmode of the plasma instabilities. It is a massively parallel code, able to solve the linear kinetic theory exactly. The PIC codes address the nonlinear behavior of the system. The explicit plasma simulation code, NPIC, is a massively parallel PIC code, based on a well-known explicit electromagnetic algorithm. The explicit simulations are run on the second fastest computer in the world, the Los Alamos Q-machine. CELESTE3D, an implicit PIC code, solves the full set of Maxwell-Vlasov equations using the implicit moment method, by discretizing implicitly in time. It can run on a standard Pentium processor machine, but, thanks to the

implicit method, can reach system sizes and parameter ranges inaccessible to the explicit code (albeit at a coarser level).

Our results show that the LHDI has a new, previously unimagined role in promoting reconnection, the new role has nothing to do with anomalous resistivity.

First, we discover that the nonlinear evolution of the LHDI introduces not only an electron heating (an effect documented in many previous works) but causes an anisotropic heating that heats the electrons preferably in the perpendicular direction to the magnetic field. Previous works had suggested that systems with an electron (or an ion) anisotropy are more unstable to reconnection when the anisotropy is such that the perpendicular temperature exceeds the parallel temperature.

Second, we show that the plasma current of a typical reconnecting configuration is made thinner and more peaked by the LHDI. The effect can be explained by considering the nonlinear effects of the LHDI on the electron distribution function. The thinning has the direct effect of promoting the growth of reconnection.

The linear code and the PIC codes show that electron anisotropy and current peaking have an important effect on the saturation level and growth rate of reconnection. Together, they allow the reconnection onset and enhance the reconnection growth rate, thus explaining observations of magnetic reconnection in natural and man-made plasmas.

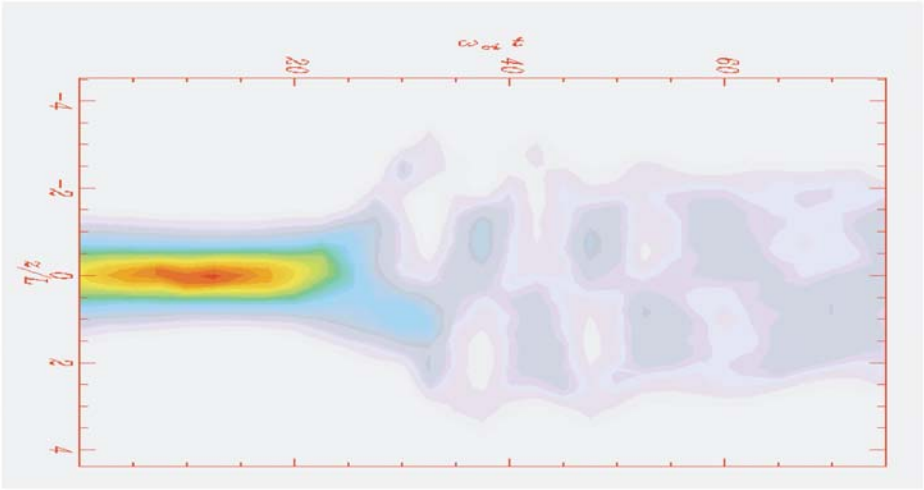

Figure— Effects of the LHDI: current peaking and subsequent disruption by secondary instabilities caused by the LHDI.

Laboratory and Astrophysical Magnetic Helicity Injection: What do Radio Jets/Lobes have in Common with Spheromaks and Spherical Tori for Controlled Fusion?

Xianzhu Tang, T-15; A. H. Boozer, Columbia Univ.; S. C. Hsu, P-24; H. Li, X-1; and R. Raman, Washington/PPPL; xtang@lanl.gov

The connection between two spectacular astronomical observations inspires a number of basic plasma physics problems that have laboratory relevance. The first is the ubiquity of 10^{8-9} solar-mass super-massive black holes at the center of galaxies [1] and on the order of 10^{62} ergs of gravitational energy released via accretion. The second is the existence of an almost equally large amount of magnetic energy ($\sim 10^{61}$ ergs) in galactic jet radio lobes [2]. The physical process by which the accretion disk drives the jet/lobe is thought to be magnetic helicity injection, in which the differential Keplerian disk rotation twists up a magnetic arcade above the disk, directly converting mechanical energy into magnetic energy. In the laboratory, a radial electric field imposed by coaxial electrodes faithfully simulates the same process by drawing current from a power supply to run through a plasma threaded by an externally imposed poloidal magnetic field (see figure right). The toroidal magnetic flux is then injected by the current into the discharge chamber, driving a magnetic bubble expansion.

Laboratory electrostatic helicity injection has found wide usage from spheromak formation [3] to noninductive current drive in spherical tori [4,5]. Spherical torus (ST) is a Tokamak in the limit of the aspect ratio approaching unity. In other words, the donut is so fat that the center hole becomes tiny. STs are known for their outstanding MHD stability that leads to higher confinement efficiency. Coupled with the compactness of the device (it is a sphere after all!), ST is a compelling candidate for economic fusion reactors. World-wide ST experimental programs have seen substantial advances in the past decade and their findings on stability and confinement are overwhelmingly encouraging in support of the promises of a low-aspect ratio device.

The Achilles heel of the ST concept for a practical fusion reactor has long been recognized as the limited real estate at the center stack (donut hole) due to small aspect ratio. A working ST reactor, by necessity, will be solenoid-free. A critical component of the world-wide ST research programs is developing efficient noninductive startup and sustainment schemes. On the U.S. National Spherical Torus Experimental (NSTX) device [6], the primary noninductive startup method under investigation has been coaxial helicity injection (CHI).

Our recent theoretical and computational work [5] has developed a comprehensive picture on how noninductive current drive is realized by helicity injection. In an axisymmetric CHI equilibrium, it is the ExB flow induced by the electrostatic bias that drives toroidal plasma current, even though the electric field identically vanishes in the toroidal direction. When the Tang-Boozer normalized voltage limit is surpassed, the CHI plasma becomes unstable to line-tied kink. Closed flux in the toroidally averaged mean field is generated and sustained by a cascade of open-to-closed field line instabilities.

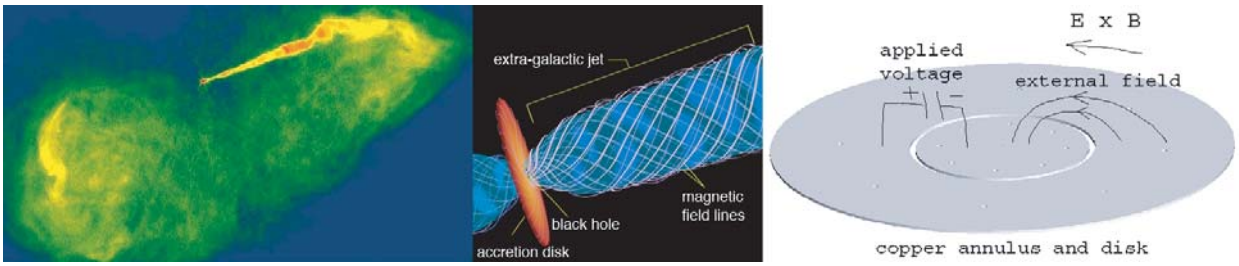

The helicity injection physics that underlies the collimated extra-galactic radio jet/lobes share many similar challenges with those of laboratory fusion applications, but with a number of new twists. The fundamental plasma physics questions that we are interested in, are 1) why jets form, the collimation mechanism for an under- and over-pressured jet; 2) jet stability limit; 3) jet magnetic energy and helicity content; and 4) jet PdV work, cosmic shoveling, and angular momentum transfer from the accretion disk by electromagnetic torque. Our theoretical/computational efforts have identified that the primary collimation mechanism for an under-pressured jet is external ambient pressure, while for over-pressured jet, the dimensionless helicity injection rate (super-Alfvénic: disk rotation speed is greater than disk corona Alfvén speed) has a prominent role. The jet stability is constrained by a normalized rotation speed limit similar to the Tang-Boozer normalized voltage in CHI experiments, except for the complication that the new stability scalings suggest good stability when either toroidal field is small compared with poloidal field or vice versa. This points to a paradoxical picture that significant magnetic energy and helicity can be pumped into the jet/lobe by the accretion disk only if a way is found to overcome the curse of the spheromak, i.e., the worst stability condition at comparable toroidal and poloidal magnetic fields. Motivated by these findings, we are pursuing a dedicated laboratory astrophysical experimental program on the LAPD-U device at UCLA [7]. The integrated experimental/modeling approach is a rarity in astrophysical research in that coordinated theory/numerical modeling guides the initial experimental campaign, which in turn provides much needed code/model validation.

This work was supported by DOE Office of Fusion Energy Sciences and LANL LDRD program on plasma astrophysics.

[1] D. Richstone et al., *Nature* **395**, A14 (1998).
[2] T. E. Clarke et al., *Astrophys. J.* **547**, L111 (2001); P. P. Kronberg, Q. Dufton, H. Li, S. Colgate, *ibid* **560**, 178 (2001).
[3] S. C. Hsu and P. M. Bellan, *Phys. Rev. Lett.* **90**, 215002 (2003); J. M. Finn, C. R. Sovinec, D. del-Castillo-Negrete, *ibid* **85**, 4538–41 (2000).
[4] R. Raman et al., *Phys. Rev. Lett.* **90**, 075005 1–4 (2003).
[5] X. Z. Tang and A. H. Boozer, *Phys. Plasmas* **10**, 3661 (2003); i*bid* **11**, 171 (2004); to appear in *special issue* (2004).
[6] Y. K.M. Peng, *Phys. Plasmas* **7**, 1681 (2000).
[7] S. C. Hsu and X. Z. Tang, "A research white paper for LAPD-U: underlying plasma physics of astrophysical jet collimation," LANL report LA-UR-04-0764 (2004).

Figure—
Left: Galaxy M87 jet and radio lobes, extending over 4,000 light years, observed in radio wavelengths. Center: accretion disk at center of galaxy and jet collimation region. Right: basis for laboratory study of jet collimation. Jet figures courtesy of NRAO/NASA.

Linking Kinetic and Fluid Scales: First Principle 3-D Particle Simulations of Magnetic Reconnection and Magnetic Turbulence

Xianzhu Tang, T-15; Hui Li and Kevin Bowers, X-1; xtang @lanl.gov

Magnetic reconnection enables a magnetized plasma system to convert magnetic energy into particle energy. It has broad importance in nearly all plasma systems, ranging from laboratory experiments to Earth's magnetosphere, the solar corona and the astrophysical environment—rendering it one of the premier scientific topics in plasma physics.

Studies on magnetic reconnection have a long history since the basic ideas were laid out by Sweet and Parker in the 1950s. Reconnection necessarily requires the breaking of the ideal MHD frozen-in-flux condition. Classical dissipation processes such as resistivity often underestimate the rate of magnetic energy release by many orders of magnitude. Furthermore, in collisionless plasmas, breaking the frozen-in condition occurs at small spatial scales in a narrow boundary layer known as the "dissipation region."

A major theoretical discovery has been the identification of the critical role of dispersive waves in driving fast reconnection [1]. Satellite measurements taken in Earth's magnetosphere [2] have confirmed key predictions of the theory. In dedicated laboratory experiments the 2-D structure of the current sheet that defines the "dissipation region" has been measured and an enhancement of the effective resistivity over its classical value has been observed in low-collisionality cases [3]. The explosive growth in our understanding of fast reconnection in the past decade has particularly benefited from the advances in numerical simulations. Computers are for the first time sufficiently powerful to resolve the complete 3-D kinetic dynamics from first-principles, opening up a new era in the exploration of magnetic reconnection and its implications. Our particle-in-cell simulation code (V4PIC) has been meticulously optimized for modern microprocessors and demonstrated to run at near theoretical peak performance on massively parallel computers [4].

Harnessing the available computing resources and efficiency of our PIC code, we are carrying out a study of a long-standing question in reconnection, which has not been addressed adequately before, namely how magnetic energy dissipation on a global fluid scale is linked to the topological magnetic field changes at small scales (i.e., particle kinetics). We are particularly interested in the physical processes responsible for self-organized global magnetic structures, and the bulk plasma energization in terms of the generation and sustainment of significant nonthermal plasma population.

Our recent 3-D first-principles PIC simulations of reconnection [5] have demonstrated the self-consistent development of high-frequency turbulence with intense localized electric fields that scatter electrons, producing anomalous resistivity and energetic particles (see Figure 1a). The evolution of the ***k***-space power spectrum of magnetic energy and helicity showed a cascade from the inertial range to the dissipation range where it is destroyed (see Figure 1b). The dissipation region is found to be intense current filaments between the ion skin depth and electron skin depth: Figure 2.

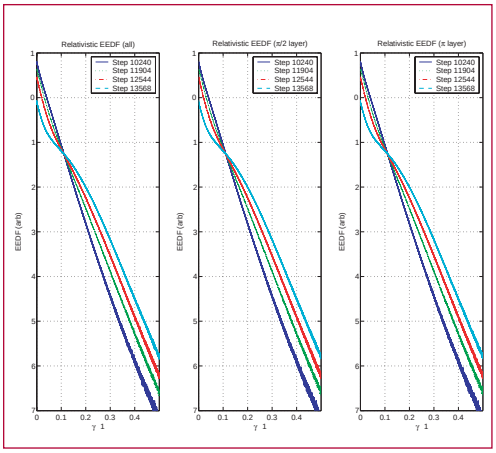

Our future plans include 512–2048 processor runs that resolve the full particle kinetics via first-principles over hundreds of ion skin depths size systems. These should capture the essential physics of volumetric reconnection driven magnetic turbulence, plasma energization, and global magnetic self-organization. Dedicated physics analysis of these first-principles simulation data, in close comparison with analytic theory and experimental data, will provide key insights into how the physics on fluid-scale is coupled to microscopic particle kinetics.

[1] J. Birn et al., "GEM Magnetic Reconnection Challenge," *J. Geophys. Res.* 1**06**, 3715 (2001).

[2] M. Oieroset et al., "In situ detection of collisionless reconnection in the Earth's magnetotail," *Nature* **412**, 417 (2001).

[3] H. Ji et al., "Experimental test of the Sweet-Parker model of magnetic reconnection," *Phys. Rev. Lett.*, **80**, 3256 (1998).

[4] K. J. Bowers, "Speed Optimal Implementation of a Fully Relativistic Particle Push with Charge Conserving Current Accumulation on Modern Processors," ICNSP, Cape Cod, MA (2003); *J. Comput. Phys.* **173**, 393 (2001).

[5] H. Li, K. J. Bowers, and X. Z. Tang, "Magnetic dissipation in force-free astrophysical plasmas," *Phys. Rev. Lett.*, to be submitted (2004); Invited talk at APS/DPP meeting (Oct, 2003).

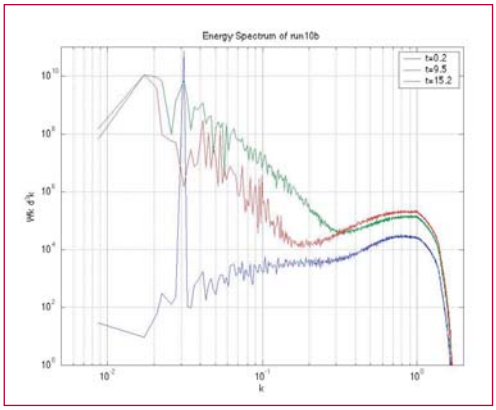

Figure 1— a) Particle distribution functions showing energization by volumetric reconnection. b) Time evolution of the turbulent magnetic spectral energy density in k-space. Magnetic energy initially stored at a large scale is transferred to small scales for dissipation.

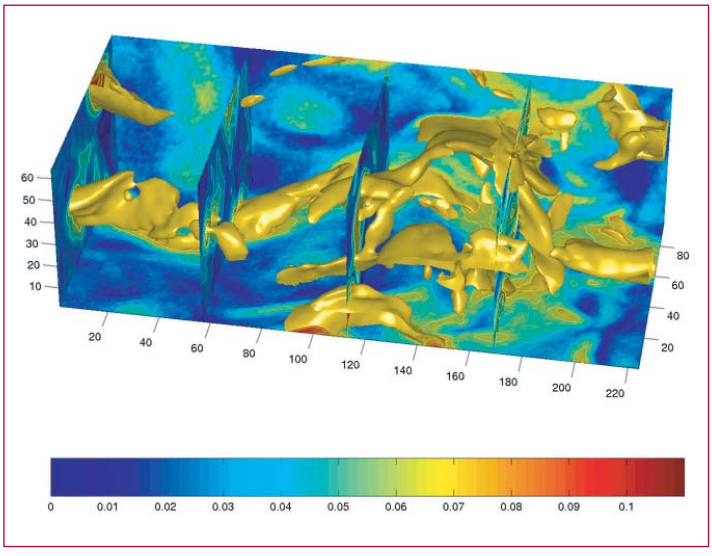

Figure 2— 3-D current filaments in multiple layer reconnection. The magnetic energy and helicity dissipation rates are higher at these filaments.

Chandrasekhar Equilibria of Compact Toroids with Alfvénic Flows

Xianzhu Tang, T-15; and Zhehui Wang, P-24; xtang@lanl.gov

Tracing a magnetic field line in a three-dimensional toroidal geometry is like following the phase space trajectory of a one degree of freedom nonlinear pendulum with the toroidal angle simulating the time coordinate. In the most general case, this is a one-and-a-half degree of freedom Hamiltonian mechanics problem. It can be integrable where phase space trajectories wrap on the constant-action tori, or chaotic in which case a single trajectory seems volume-filling. Similarly the magnetic field can have closed magnetic flux surfaces or stochastic regions.

Magnetic field configurations with closed flux surfaces are generally thought to be necessary for magnetic confinement of high-temperature plasmas in the laboratory due to draft orbit concerns. In a three-dimensional space, a closed flux surface has to take the topology of a torus. The tokamak and stellerator are two examples that have a hole in the center of a doubly connected torus. The hole in the center provides room for external field coils. An alternative is compact toroids (or plasmoids) that are singly connected. Examples of compact toroids (CT) are spheromak [1] and field-reversed configuration (FRC) [2]. Magnetic field configuration of a CT is usually generated by an internal plasma current and external coils that are topologically disconnected from the plasmoid. This reduces the engineering complexity for coil design and maintenance against radiation damage in a fusion reactor. Compact toroids are favorable objects in the studies of plasma self-organization. Naturally occurring plasmoids, such as those ejected by an accretion disk, are likely compact toroids due to the rotational symmetry of the disk and absence of external circuitry.

Compact toroids are known to be susceptible to global ideal magneto-hydrodynamic (MHD) instabilities in the laboratory. In the case of an FRC, the tilt mode is so robust that an MHD equilibrium is expected to be lost on the Alfvénic time scale. Plasma flow, finite Larmor radius effects, and energetic ions can have stabilizing effects [3]. But neither simulations nor experiments have seen complete stabilization. If one interprets knots in radio telescope images of an accretion-disk-powered jet [4] as detached plasmoids, the spatial regularity of the knots would suggest stability on a long time scale compared with the Alfvénic time in order to maintain adequate confinement of high-energy electrons.

The Chandrasekhar equilibria are a class of stationary ideal magnetohydrodynamic equilibria stabilized by magnetic-field-aligned Alfvénic flows against fixed-boundary ideal MHD modes with a solenoid-free perturbation in the displacement vector [5]. The basic idea of the Chandrasekhar equilibrium is to have the inertia of a field-aligned Alfvénic plasma flow balance the magnetic curvature force plus the parallel gradient of magnetic pressure,

$$\rho \mathbf{U} \cdot \nabla \mathbf{U} = 1/\mu_0 \mathbf{B} \cdot \nabla \mathbf{B}. \qquad (1)$$

The overall force balance is then reduced to

$$\Pi \equiv p + B^2 / 2\mu_0 = constant, \quad (2)$$

for a steady state plasma. The stabilization effect of a field-line-aligned Alfvénic flow is not limited to ideal modes. For example, in the Chandrasekhar

equilibrium of a Harris sheet, the Alfvénic flow is found to stabilize the resistive tearing modes [6]. Unlike the Grad-Shafranov equilibrium of a static plasma where two free functions of magnetic flux, usually pressure and plasma current, are required to specify an equilibrium, the specification of a Chandrasekhar equilibrium admits total freedom in magnetic field design. For any specified **B**, the plasma flow is solved from equation (1) and the corresponding plasma pressure is found from equation(2). Analytic Chandrasekhar equilibrium of FRC and spheromak can be elegantly solved [7] with Chandrasekhar-Kendall modes [8] from a field constraint of the form

$$\sum_n c_n(\nabla \times)^n(\mu_0 J) = \lambda \mathbf{B}$$

where c_ns (n = 0, 1, 2, • • •) are constant coefficients and

$$(\nabla \times)^n \equiv \overbrace{\nabla \times \nabla \times \cdots \nabla \times}^{n}.$$

The figure plots a pressure-confining, ideal MHD-stable, analytic Chandrasekhar FRC equilibrium with a vertical guide field (Figure 2 from [7]). Favorable confinement property of nested closed flux surfaces and the unusual ideal magneto-hydrodynamic stability of such compact toroids are of interest for both magnetic trapping of high-energy electrons in astrophysics and confinement of high-temperature plasmas in the laboratory. We have also clarified [7] the similarity and important distinctions between Chandrasekhar compact toroid equilibria and those predicted by relaxation theories [9]. This work was supported by DOE OFES.

[1] P. M. Bellan, *Spheromaks*, (Imperial College Press, London, 2000).
[2] M. Tuszewski, *Nuclear Fusion* **11**, 2033 (1988).
[3] E. V. Belova, R. C. Davidson, H. Ji, and M. Yamada, *Phys. Plasmas* **10**, 2361 (2003).
[4] A. H. Bridle, D. H. Hough, C. J. Lonsdale, J. O. Burns, and R. A. Laing, *Astron. J.* **108**, 766 (1994); S. K. Chakrabarti, P. Goldoni, P. J. Wiita, A. Nandi, and S. Das, *Ap. J.* **576**, L45 (2002).
[5] S. Chandrasekhar, *Hydrodynamic and Hydromagnetic Stability*, (Dover, New York, 1981).
[6] L. Chacon, D. A. Knoll, and J. M. Finn, *Physics Letters A*, **308**, 187 (2003).
[7] Z. Wang and X. Z. Tang, accepted for publication in *Phys. Plasmas* (2004).
[8] S. Chandrasekhar and P. C. Kendall, *Astrophys. J.* **126**, 457 (1957).
[9] L. C. Steinhauer and A. Ishida, *Phys. Rev. Lett.* **79**, 3423 (1997); S. M. Mahajan, and Z. Yoshida, *ibid* **81**, 4863 (1998); B. Dasgupta, P. Dasgupta, M. S. Janaki, T. Watanabe, and T. Sato, *ibid* **81**, 3144 (1998).

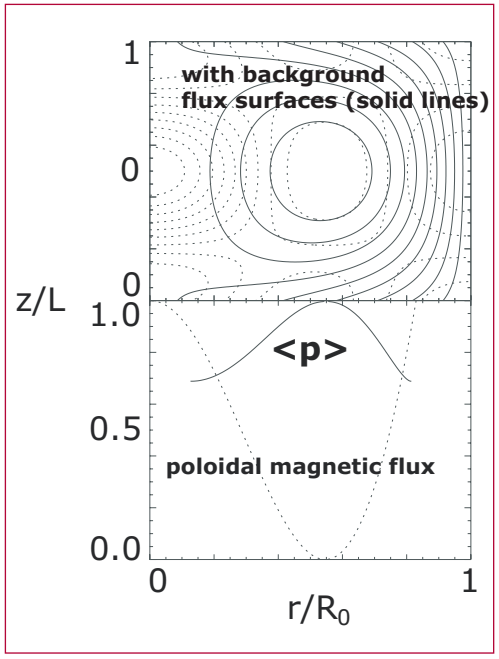

Figure—
A Chandrasekhar FRC equilibrium with vertical background field. Top: dashed line are pressure contours. Down: flux-surface-averaged pressure and poloidal flux are normalized to their peak value, respectively.

T-1 Equation of State and Mechanics of Materials

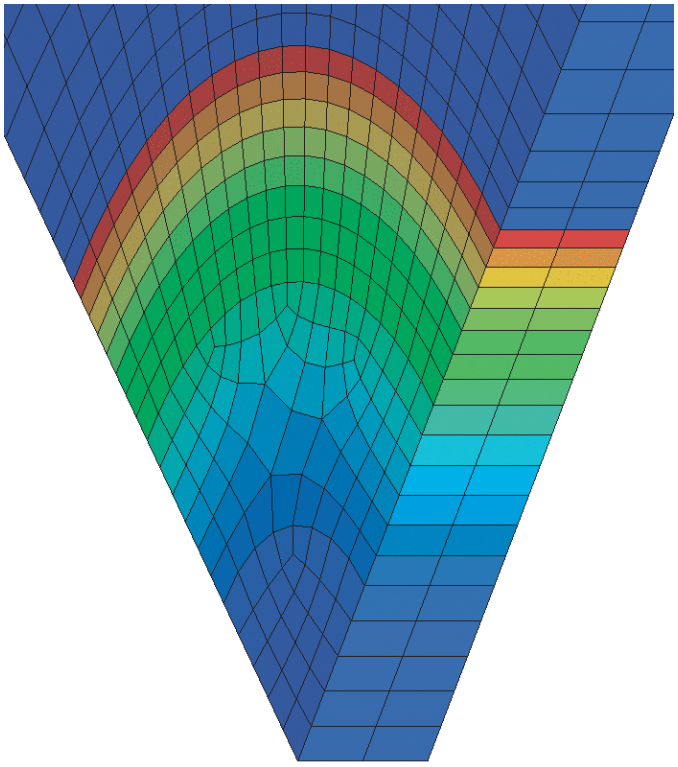

Unified Model of the Gruneisen Parameter, Melting Temperature, and Shear Modulus

L. Burakovsky, T-1 and D. L. Preston, X-7, burakov@lanl.gov

A reliable model of the adiabatic (isentropic) shear modulus of a polycrystalline solid at temperatures up to the melting temperature, and up to megabar pressures is needed for many applications. It is generally assumed that the ratio of the plastic flow stress (shear stress necessary to induce plastic deformation at a given strain rate) to the shear modulus is approximately independent of pressure. In other words, the predominant pressure dependence of the plastic flow stress is contained in the shear modulus. An accurate, simple analytic (for fast evaluation) model of the shear modulus is therefore essential for numerical simulations of material deformation over extremes of pressure and temperature.

We have developed a new unified analytic model of the Gruneisen parameter, melting temperature and shear modulus. It is based on three essential components. First is a relation between the melting temperature and the shear modulus at melt obtained from our dislocation-mediated melting model. The second ingredient is a relation between the Gruneisen parameter and the density derivative of the zero-temperature shear modulus, and the third is a linear approximation for the temperature dependence of the shear modulus at a given density. The model allows one to construct all three, the Gruneisen parameter, melting curve, and shear modulus, in terms of a common set of input parameters, thus providing independent tests for its validity, by comparing each of the three to the corresponding data.

The reliability of the model has been proven by means of good to excellent agreement of the predicted melting curves and shear moduli to available experimental data and theoretical calculations on over a quarter of the elements in the periodic table.

The model has been used for the construction of the new SESAME melting curve and shear modulus tables. In Figures 1 and 2, new SESAME shear modulus tables (solid curves) are compared to experimental data and theoretical calculations (points of different sizes) for iron and gold, respectively, to compressions of two.

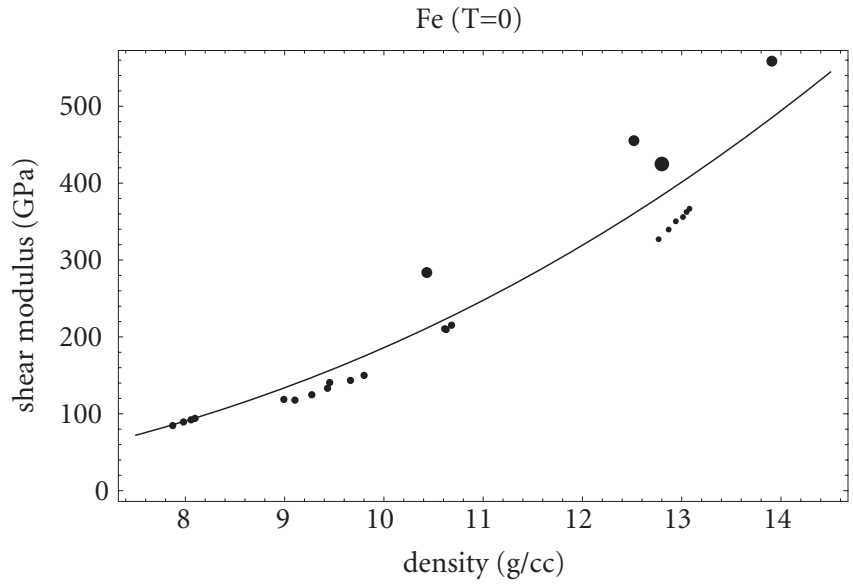

Figure 1—Shear Modulus (GPa).

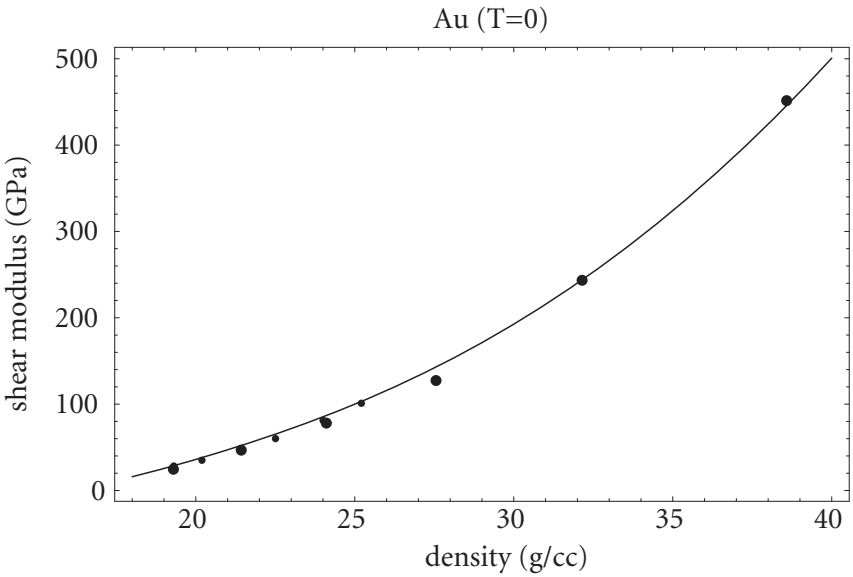

Figure 2—Shear Modulus (GPa).

Equation of State Developments in T-1

Equation of State, Eric D. Chisolm, Scott D. Crockett, Giulia De Lorenzi-Venneri, Denise C. George, J. D. Johnson, Duane C. Wallace, and John M. Wills, T-1. echisolm@lanl.gov

We released an updated version of the unclassified and classified SESAME databases on January 31, 2003. We released the unclassified database with eleven modified and three new materials (see memo t1-2003-02-07-sdc).

A new SESAME Aluminum equation of state (EOS) has been produced. A manuscript with the details is currently being written. Also, several classified EOS have been modified. Three new classified materials have also been created.

A new cold curve for elemental Pu has been calculated, using a first-principles electronic structure method, in the range of compression $V_0/V = 0.5$ to 100. Several candidate structures were evaluated, including two experimentally suggested high-pressure structures and a theoretical simple monoclinic phase found to have a low energy over a certain pressure range. The result is being evaluated in the context of the SESAME Pu EOS to assess the impact of the difference. A document, "A calculated cold curve for elemental Pu," is in preparation.

We have served the user community by delivering a modified test plutonium EOS with some physics improvements. Also, six versions of modified plutonium EOSs were provided for sensitivity studies. J. D. Johnson's paper with Carl Greeff (X-7) on plutonium was published in *Defense Research Review*. A long memo on other issues about lutonium (coauthor Carl Greeff) was distributed.

We have merged the opacity comment tables into the opacity library as a service to T-4.

We have performed work on a new technique for constructing elemental solid and liquid EOS, using results from lattice dynamics, liquid dynamics, and density functional theory.
(a) We have published a full description of the technique (E. D. Chisolm, S. D. Crockett, and D. C. Wallace, *Phys. Rev.* **B68**, 104103 (2003)), and we are continuing our efforts to extend this technique over the entire range required for a SESAME EOS. Our results on the extension problem thus far are described in LA-UR-03-7344 and the report on **p#**. of this volume.
(b) We have constructed an EOS for Al using these techniques, and we have used it to study the relative contributions of each part of the EOS (cold, nuclear, electronic) to the thermodynamic functions along the Hugoniot, attempting to understand when each part dominates. Our results are described in LA-UR-03-4928 and the report on **p#** of this volume.
(c) We have also compared the bulk sound speeds predicted by this EOS with experimental data, finding good agreement, and we tested a conjecture concerning the shear modulus by comparing with longitudinal sound speed data, again finding good agreement. Our results are described in LA-UR-03-5088 and the report on **p#** of this volume.

We have continued development of liquid dynamics theory, which has now

reached the stage where it can provide accurate equations of state for liquid metals at all compressions (as shown in the previous point). We have also recently developed two applications:
(a) We have created a semi-empirical method for computing the viscosity coefficient of a liquid metal at melt over a range of densities, using either liquid entropy data or density functional theory. The method is described in more detail in LA-UR-03-6847 and the report on **p#** of this volume.
(b) We have also applied the theory to inelastic neutron scattering, as described in the report on **p#** of this volume.

We have surveyed theoretical and computational results to better understand at what compression the cold curve of a material is correctly described by the Thomas-Fermi-Dirac (TFD) model. Our results are described in LA-UR-03-7346 and the report on **p#** of this volume.

We have kept abreast of the controversy over the laser shock data on deuterium. This included service on a panel discussion at the International Conference on Strongly Coupled Coulomb Systems in 2002 and attending a workshop in January of 2003. After the workshop J. D. Johnson felt that it was time to declare victory on the side of the Sandia data. He then wrote a summary memo and distributed such to some managers. We have also completed modifying the total table of our existing deuterium EOS, taking into account the Sandia data, diamond anvil data, gas gun data, and molecular dynamics/Monte Carlo modeling. We have corrected two mistakes. Work is now underway to modify the subtables, including correcting a mistake in the electronic table.

We were represented in varying capacities for four committees/meeting series on planning the future of materials work. These are the X- Division Science Council, the Shivano MATWOG, Paul Dotson's study group, and the headquarters workshop at Livermore.

We have rewritten Opensesame in FORTRAN 90.
(a) It takes advantage of modern programming features of the language: pointers, dynamic memory, derived types, and modular structure.
(b) Input to Opensesame is now specified in namelist format.
(c) The Opensesame GUI has been modified to provide namelist input to correspond to item (b).
(d) Documentation may be found at *http://t12www.lanl.gov/home/opensesame.*

We have begun an analysis of the numerical vulnerabilities in Grizzly and Opensesame that lead to different results on different platforms.

Estimating the Accuracy of the TFD Cold Curve

Eric D. Chisolm, Scott D. Crockett, Duane C. Wallace, and John M. Wills, T-1; echisolm@lanl.gov

A component in the standard decomposition of equations of state (EOS) at Los Alamos is the cold curve, the electronic contribution to the T=0 isotherm. It is known that the cold curve predicted by the Thomas-Fermi-Dirac (TFD) model converges to the true quantum mechanical cold curve as compression increases without bound; however, it is not known how rapidly this convergence occurs. Early efforts to determine this [1] suggested the two had converged by a pressure of 10 Mbar; however, later calculations showed that convergence had not occured by 100 Mbar for some materials [2]. Since the SESAME tables require the cold curve for a material up to compressions around 10^4, well beyond any practical electronic structure calculation at the moment, and since TFD yields results much more easily than density functional theory, it is of great interest to establish the compression, if any, at which TFD correctly predicts the cold curve pressure to a given accuracy, say 10%.

To try to determine this, we reviewed some basic theoretical properties of TFD, which allowed us to conclude only that convergence will require compressions above 10^4 for all but the smallest values of Z; beyond this, however, we could conclude nothing about the magnitude, sign, or density dependence of the discrepancy. We then turned to numerical comparisons of TFD with electronic structure calculations of the cold curve for two elements, Al and Li.

The Al results are a compilation of three separate electronic structure calculations; only one calculation was available for Li. In both cases we see the general feature that the TFD pressure is too high near normal density; this is because TFD has much weaker binding, hence much larger zero-pressure volume, than electronic structure theory. In Al, the error oscillates from positive to negative twice, then remains positive and decreases monotonically, down to 5% at $\eta = 60$ (P = 9000 Mbar) and 1% at $\eta = 300$ (P =10^5 Mbar). It is reasonable that the error continues to approach zero as compression increases. The less extensive Li results show no such trend; the error fluctuates around -5% at compressions up to 60, showing no evidence of a steady decrease. Thus these two test cases give us little guidance for understanding how rapidly TFD approaches the true quantum mechanical cold curve as a function of compression.

Given these uncertain results, we make two recommendations regarding the construction of cold curves for EOS: (1) experimental data and density functional theory results should be used in combination to construct the cold curve whenever possible, and (2) when this is not possible, the TFD cold curve should be tacked on where the density functional theory result terminates. In the first case, we can have great confidence in the accuracy of the cold curve; we have less confidence in the second case, particularly at the lowest compressions where TFD is used.

This work is described in more detail in LA-UR-03-7346.

[1] H. Jensen, *Z. Physik* **111**, 373 (1938).

[2] W. G. Zittel, J. Meyer-ter-Vehn, J. C. Boettger, and S. B. Trickey, *J. Phys. F: Met. Phys.* **15**, L247 (1985).

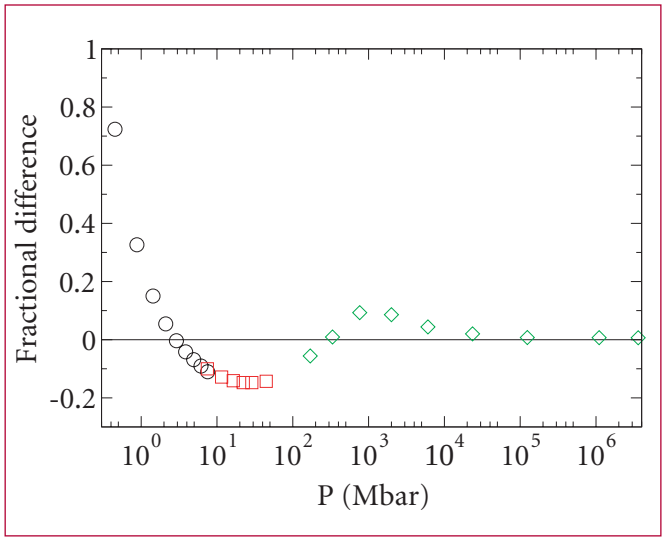

***Figure 1—** The fractional deviation of the T=0, Z=13 TFD pressure from the electronic pressure predicted at T=0 for Al by electronic structure calculations, as a function of pressure.*

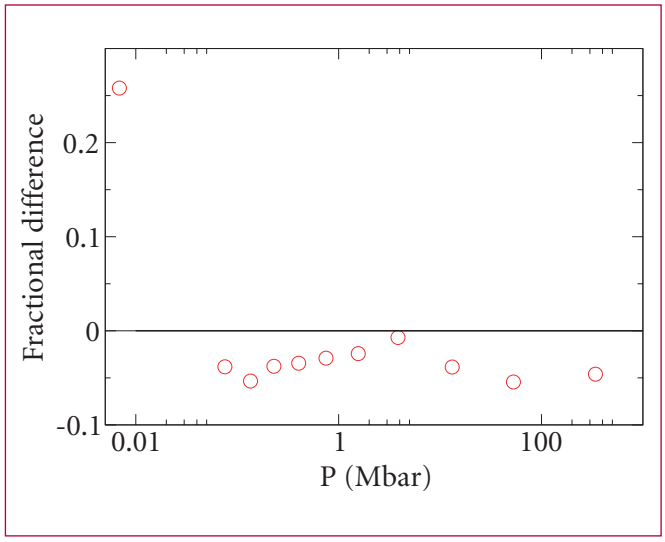

***Figure 2—** The deviation of the T=0, Z=3 TFD pressure from the electronic pressure predicted at T=0 for Li.*

Extending the CCW EOS: Extending the Cold and Nuclear Contributions to High Compression

Eric D. Chisolm, Scott D. Crockett, and Duane C. Wallace, T-1; echisolm@lanl.gov

Recent work in T-1 has been undertaken to apply the results summarized in [1] to make new equations of state (EOS) for real materials in the "condensed matter regime" ($\rho \geq \rho_{ref}$), and to extend the procedures as necessary to generate new SESAME tables, intended to be the most accurate such tables it is possible to produce. We refer to EOS developed in this program by the initials CCW, standing for the authors of the first paper to make such an EOS [2].
The range of this first EOS is limited to compressions between 1.0 and 2.2 and temperatures below 3 eV by (*a*) the availability of density functional theory (DFT) and experimental results required as inputs and (*b*) the requirement that the temperature is not so high that the nuclear motion becomes gaslike, rendering the liquid theory inapplicable (for a review of the liquid theory, see [3]). This range is still considerable, but a typical SESAME EOS [4] covers compressions from 10^4 to 10^4 and temperatures up to 10^5 eV; thus to construct SESAME EOS using this theory we must consider how to extend its range of validity substantially.
This requires meeting two challenges:

1. We must develop a means to extend the EOS to higher densities, where DFT and experimental results are not available but the theory is still sound.
2. We must extend the theory itself to high temperatures, where the nuclear motion becomes gaslike, and to densities below ρ_{ref}.

Here we report our progress on the first challenge; later work will address the issues that remain.

Our strategy is to rely on basic conclusions from condensed matter theory and observed trends in low-compression material behavior to form a picture of a generic material at extreme compressions; we then develop both the thermal properties of this high-compression state and interpolations between this state and our original EOS. Specifically, since nonmetals become metals under high compression while metals remain metallic, we assume all elements at high compressions to be a generic metal in both phases, with thermodynamic properties that depend only on density and temperature (no crystal structure dependence, no distinct solid phases). Since both crystal and liquid are metallic, melting is "normal" (no significant change in electronic structure at melt; see [3]), at high compressions. This picture of a structureless metal crystal that melts normally to a metal liquid is what we will investigate at high compressions, together with the required inteprolations.

A CCW EOS requires several inputs for each phase: the cold curve Φ_0; the quantities θ_0 and θ_2, calculated from moments of the phonon spectrum and used in the nuclear contribution to the EOS; and the electronic density of states $n(\varepsilon)$. The melt curve $T_m(P)$, which follows from the crystal and liquid EOS jointly, is also useful. Here we will describe extensions of the cold curve, nuclear parts, and T_m, leaving the electronic part to a later report. For the crystal cold curve, we draw on the Thomas-Fermi-Dirac (TFD) one-atom

statistical model, which carries no dependence on the particular crystal structure. It is known that T = 0 TFD converges to the true cold curve in the limit of infinite compression, but it is not known how the error term behaves [5]. In the absence of such knowledge, we simply interpolate between the CCW EOS cold curve and the TFD cold curve such that the interpolation is twice differentiable at the point where our knowledge of the CCW cold curve ends.

The quantity needed to extend θ_0 and θ_2 to high densities is the Gruneisen parameter γ_0, which can be integrated to yield θ_0, from which θ_2 can be approximated to a high degree of precision. The rule $\rho\gamma$ = constant, often used in shock studies, not helpful here because γ is the total Gruneisen parameter, which is close to γ_0 at compressions of two to three at most along the Hugoniot (beyond this point the electrons, not the nuclei, dominate). However, results from the one-component plasma at high densities [6] suggest $\gamma_0 \rightarrow 1/2$ as a possible limit. Once the limit is determined, γ_0 from the CCW EOS can be interpolated to it, allowing computation of θ_0, θ_2, and the nuclear contributions in both phases.

We find the melt curve and liquid cold curve by using the melt rule on page 236 of [1] to calculate $T_m(\rho_{lm})$, where ρ_{lm} is the density of the liquid at melt, at high compressions. We then smoothly join this curve to the low-compression melt curve from the CCW EOS, and finally we determine $T_{m(P)}$ and $\phi_0{}^l$ iteratively; we guess $\Phi_0{}^l$, calculate the difference in Gibbs free energies between liquid and crystal along the melt curve, and use the result to correct $\Phi_0{}^l$, continuing until the difference becomes negligible.

At this point, the remaining tasks are:
1. to extend the electronic excitation contribution to higher compressions and
2. extend the theory itself down in density and up in temperature. Work in these areas is underway and will be described in later reports.

Details of this work can be found in LA-UR-03-7344.

[1] D. C. Wallace, *Statistical Physics of Crystals and Liquids* (World Scientific, Singapore, 2002).
[2] E. D. Chisolm, S. D. Crockett, and D. C. Wallace, *Phys. Rev. B* **68**, 104103 (2003).
[3] E. D. Chisolm and D. C. Wallace, J. Phys.: Condens. Matter **13**, R739 (2001).
[4] S. P. Lyon and J. D. Johnson, "*T-1 Handbook of the Sesame Equation of State Library*," Los Alamos Report LA-CP-98-100.
[5] E. D. Chisolm, S. D. Crockett, D. C. Wallace, and J. M. Wills, "*Estimating the Accuracy of the TFD Cold Curve*," Los Alamos Report (see p. 4 of this volume).
[6] D. A. Young, *Phase Diagrams of the Elements* (Univ. of California Press, Berkeley, 19910.

Liquid Dynamics Estimates of the Viscosity Coefficient of Liquid Metals

Eric D. Chisolm and Duane C. Wallace, T-1; echisolm@lanl.gov

Values of the viscosity coefficient η for liquid metals, over a wide range of densities and for all temperatures above melting, are needed for computer simulations related to the function of primary nuclear explosive systems. Viscosity measurements have been conducted only at a pressure of 1 bar, so this need can be met only by developing means for predicting η when data are unavailable. With this in mind, we have created a simple semiempirical method for calculating η which uses a liquid dynamics model developed by Wallace [1] to compute the self-diffusion coefficient D, and then determines η from the Stokes-Einstein relation. We tested the accuracy of this technique by computing D and η for 21 liquid metals at melt at a pressure of 1 bar; we then compared the D results to experiment for 14 of these metals (no data are available for the others), and we compared with η results for all 21 metals; we found

$$D_{theory} / D_{expt} = 1.03 \pm 0.18$$
$$\eta_{theory} / \eta_{expt} = 1.00 \pm 0.18,$$

as also shown in Figure 1. This is a noticeable improvement over other empirical models; for example, one of the best such models, the Da Andrade formula, was used to compute η for 20 liquid metals at melt at 1 bar (Table III of [2]), with the result

$$\eta_{theory} / \eta_{expt} = 1.15 \pm 0.34.$$

In fact, this technique is not much less accurate than first principles molecular dynamics calculations [3], while being considerably less computationally intensive.

This method provides an easy means of computing η, and it can easily be extended to arbitrary densities purely theoretically by means of electronic structure calculations of θ_0 as a function of density. Since θ_0 is also used in the newer means of generating equations of state currently under development [4], this method also provides a connection between equilibrium and transport properties. In order to use these results at higher temperatures, though, the model in [1] must be extended to include temperature dependence. This work could be completed in the foreseeable future, providing a means for computing η for primary calculations over the full range of ρ and T they require.

This work is described in further detail in LA-UR-03-6847.

[1] D. C. Wallace, *Phys. Rev. E* **58**, 538 (1998).
[2] J. A. Alonso and N. H. March, *Phys. Rev. E* **60**, 4125 (1999).
[3] D. Alfe and M. J. Gillan, *Phys. Rev. Lett.* **81**, 5161 (1998).
[4] E. D. Chisolm, S. D. Crockett, and D. C. Wallace, *Phys. Rev. B* **68**, 104103 (2003).

Variation of Thermal and Cold Curve Contributions to Thermodynamic Functions along the Hugoniot

Eric D. Chisolm, Scott D. Crockett, and Duane C. Wallace, T-1; echisolm@lanl.gov

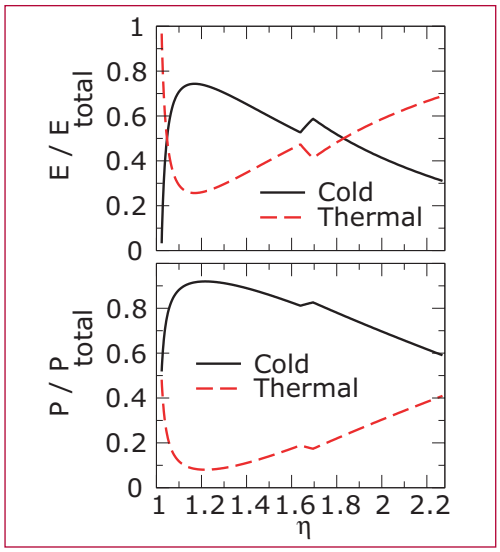

Figure 1—Cold curve and thermal energy and pressure as fractions of total energy and pressure along the Hugoniot.

Equations of state (EOS) constructed in the program in T-1 consist of three parts: the cold curve (T=0 isotherm), the thermal contribution from the nuclei, and the thermal contribution from the electrons. A material's EOS, together with the Rankine-Hugoniot relations, determine the material's principal Hugoniot, the set of all equilibrium states accessible by a single shock from room temperature and pressure. The importance of each part of the EOS in determining the Hugoniot varies with pressure; standard shock physics lore asserts that (1) the cold curve dominates the Hugoniot at low pressures and (2) at high pressures, the thermal components dominate over the cold curve, with the electronic thermal part dominating over the rest at very high P. It is not clear, however, where the low pressure regime ends, where the high pressure regime begins, and exactly what happens in between. To try to make these assertions more quantitative we have used the EOS for Al we developed in [1] to compute each contribution to the energy, entropy, and pressure along the Hugoniot, allowing us to study how they vary relative to one another as pressure increases.

The range of validity of our EOS allowed us to calculate the Hugoniot to a compression $\eta = \rho/\rho_{ref} = 2.28$. Over this range, Figure 1 shows the cold curve and total thermal (nuclear plus electronic) contributions to the energy and pressure, respectively, as fractions of the total energy and pressure. By η=1.83 (P = 225 GPa) the energy is dominated by the thermal contribution, and the pressure is on track to suffer a similar fate by η= 2.5 or so. Thus we see that by moderate compressions the thermal contribution to the EOS is non-negligible along the Hugoniot.

To see how the two thermal contributions compare, Figure 2 shows the nuclear and electronic contributions separately as fractions of the thermal energy, entropy, and pressure. (We did not discuss entropy in the previous paragraph because it is purely thermal.) The nuclear part clearly dominates through the entire range, dominating most in entropy and least in energy. Thus in this compression range, unsurprisingly, it is the nuclear thermal contribution, not the electronic contribution, which is most important.

Finally, in [1] we saw that the P-ρ Hugoniot predicted by this EOS agrees with available data to an accuracy of 1% or so, which suggests the following

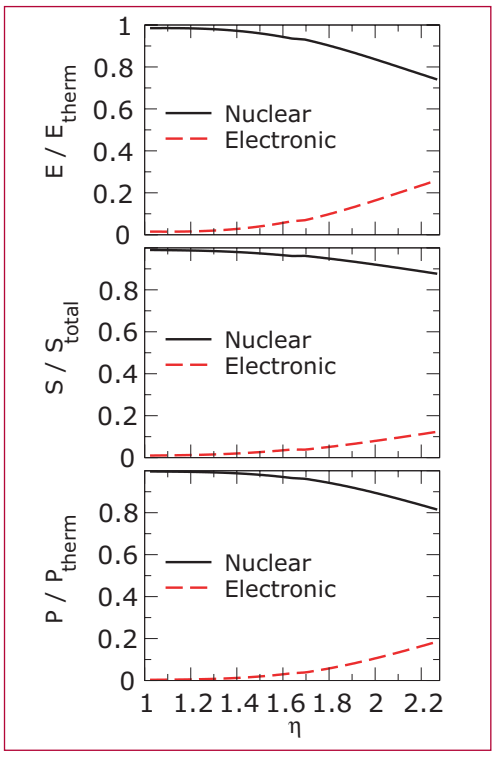

question: How much could one change any one contribution to the pressure along the Hugoniot without spoiling the agreement with experiment? The answer is found in Figure 3, which shows as a function of compression the fractional change in each part of the pressure along the Hugoniot required to shift the total pressure by 1%. Clearly the Hugoniot is sensitive to very small changes in the cold curve pressure, on the order of 1 to 2% at all compressions, but for $\eta \geq 1.8$ it is sensitive also to the nuclear contribution at the 5% level. Even the electronic contribution is significant at the higher pressures; at compressions above 2.1, a 20% change in the electronic part is sufficient to shift the total pressure out of agreement with experiment. Thus it is clear that while the cold curve contribution dominates, the nuclear thermal contribution still contributes significantly throughout the domain of validity of this EOS, and at the high end

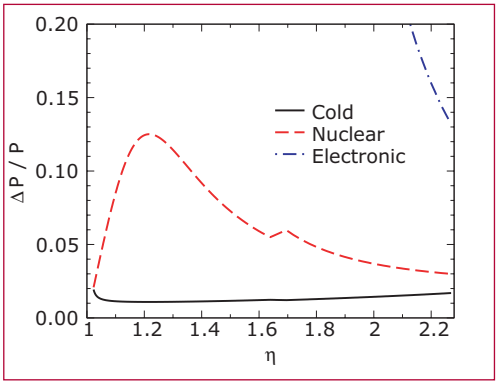

even the electronic part should be determined accurately to achieve acceptable agreement with available data.

Although these results were found specifically for Aluminum, we expect all metals across the periodic table to follow similar trends as functions of compression, differing primarily by a scale factor of around two for the heavier metals. Hence we argue that both the thermal nuclear and thermal electronic contributions to the EOS need to be understood to some accuracy to properly account for Hugoniot data at compressions of two and higher.

[1] E. D. Chisolm, S. D. Crockett, and D. C. Wallace, Phys. Rev. *B* **68**, 104103 (2003).

Figure 2— Nuclear and electronic energy, entropy, and pressure as fractions of thermal contribution along the Hugoniot.

Figure 3— Fractional change in cold curve, nuclear thermal, or electronic thermal pressure required to shift total pressure along the Hugoniot by 1%.

Developments towards a Continuumum-Level Non-Spherical Void Growth Model Using a Micro-Mechanics Basis

Brad E. Clements and Eric M. Mas, T-1; and Paul J. Maudlin, T-3; bclements@lanl.gov

Metallographic fractography shows that low concentrations of manganese sulfide (MnS) impurities have a significant role in the fracture of 1080 and HY-100 steels [1]. Examination of spalled 1080 and HY-100 samples reveal that the MnS impurities act as microvoid initiation sites necessary for ductile fracture to occur. The MnS form into high-aspect ratio aligned inclusions. The alignment results in the orientation dependence observed in fracture. Consequently, to model the fracture occurring in these steels it is important to include the non-spherical shape and orientation of the MnS impurities.

While the scientific literature contains many articles on spherical void growth, substantially fewer attempts have been made to model ductile failure in materials characterized by nonspherical void growth. It is of considerable interest to inquire if a purely continuum model can be constructed that has the advantage over micro-mechanics-based models for being of greater numerical efficiency. There are several candidate theories in the scientific literature but in this work we have focused on the Continuum Damage Mechanics (CDM) that appears to have been originated by Kachanov [2] and Rabotnov [3]. Since the work of these authors, CDM has burgeoned—background literature can be found in Lemaitre and Chaboche [4], for example. In spite of successes demonstrated by CDM very little literature is available that directly tests the conjectures of the theory. Given that the conjectures are not transparent, in the present work we have undertaken the task of applying a rigorous method, namely Green's Functions (GF), to test the reliability of CDM theory.

Kachanov [2] and Rabotnov [3] were among the first to conjecture the existence of an effective stress $\tilde{\sigma}$ defined such that the complete continuum mechanics of a damaged material can be described by invoking a corresponding set of constitutive equations, given for an undamaged material, but with the simple replacement, $\sigma \rightarrow \tilde{\sigma}$. As discussed below, this replacement includes, for example, the stresses appearing in inelastic constitutive equations. Sidoroff and Cordebois [5] conjectured that $\tilde{\sigma}$ could be uniquely determined by making an assumption of elastic energy equivalence. Chow and coworkers [6] have extended this idea and assume, in the presence of inelastic work (for example, plasticity), one should determine $\tilde{\sigma}$ and an effective strain $\tilde{\varepsilon}$ by equating the total stored energies. Letting D denote a measure of the damage state, called the damage field, the conjecture states that

$$W(\sigma,D)=W(\tilde{\sigma},D=0),$$

where the left (right) side of the equality is the energy stored in the damaged (undamaged, with $\sigma \rightarrow \tilde{\sigma}$, $\varepsilon \rightarrow \tilde{\varepsilon}$).

Kachanov and Rabotnov gave a physical interpretation for $\tilde{\sigma}$ by proposing that for systems with isotropic damage, $\tilde{\sigma}$, the Cauchy stress σ, and D should obey the simple relationship:
where D is interpreted as the fraction of damaged to the total cross-sectional areas. These concepts have been extended to anisotropic damage, for example, a system containing aligned nonspherical

voids. For that case D becomes a tensor quantity. The damage tensor $M(D)$ connects the true stress to $\tilde{\sigma}$. A large body of work has followed from these initial ideas. We refer to the book by Lemaitre and Chaboche [4] for further discussions. Interestingly, we find little theoretical work has been done to justify these conjectures.

The elastic-plastic stress and strains surrounding a void in an isotropic matrix can be calculated by Green's function techniques [7]. This requires the numerical solution of an integro-differential equation that we solve by an iterative procedure. Examples of the Green's function solutions are shown for uniaxial loading both aligned (longitudinal to the long-axis of an ellipsoidal void) and transverse to it (Figure 1). Next, we calculate, using CDM, the matrix $M(D)$ and substitute this into a standard set of equations for a homogeneous elastic perfectly plastic material with the simple substitutions $\sigma \rightarrow \tilde{\sigma}$ and $\varepsilon \rightarrow \tilde{\varepsilon}$ and where we take $\tilde{\varepsilon} = M^{-1}(D)\,\varepsilon$.

By comparing to the GF solution we found that the conjectures of CDM worked remarkably well for general loads (Figure 2). However, seldom could we use the exact area ratios given by the GF solution to achieve agreement. For example, the agreement in Figure 2 came about by using CDM area ratios about half the GF values, indicating that effective area ratios must be used in the CDM theory.

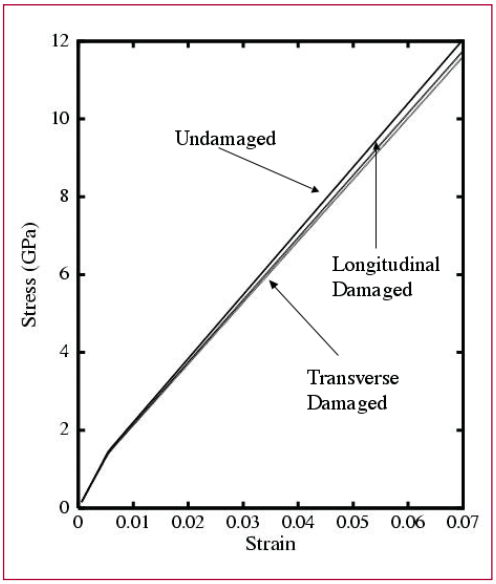

Figure 1—Stress-strain GF solutions.

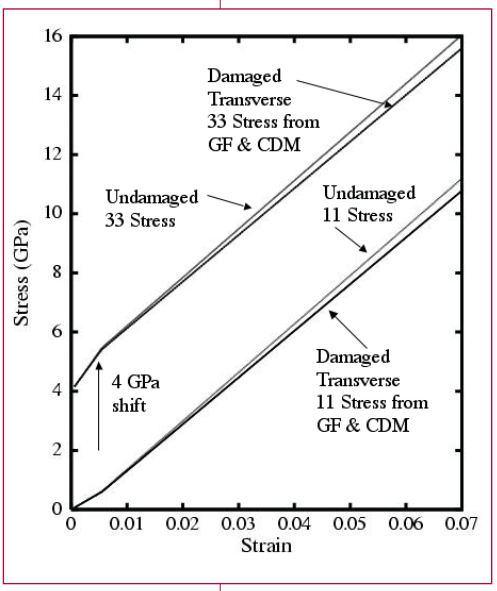

Figure 2—Comparison of CDM and GF solutions.

[1] V. Jablokov, D. Goto, D. Koss, and J. McKirgan, *Mat. Sci. Eng. A* **302**, 197–205 (2001); B. E. Clements, E. M. Mas, and G. T. Gray, III, "Shock Compression in Condensed Matter –2001," ed. M. D. Furnish, N. N. Thadhani, and Y. Horie, AIP Conference Proceedings 620, New York, (2002), pp. 535–538.

[2] L. M. Kachanov, Izv. Akad. Nauk *USSR Otd. Tekh.* **8**, 26–31 (1958).

[3] Y. N. Rabotnov, *Creep Problems in Structural Members,* North Holland, Amsterdam (1969).

[4] J. Lemaitre and J. L. Chaboche, *Mechanics of Solid Materials*, University Press, Cambridge (1990).

[5] J. P. Cordebois and F. Sidoroff, *Euromech*, 115 ed. Villard de lans (1979).

[6] T. J. Lu and C. L. Chow, *Theoretical and Appl. Fract. Mech.* **14**, 187–218 (1990) and references therein.

[7] T. Mura, *Micromechanics of Defects in Solids*, 2nd ed., Martinus Nijhoff, Dordrecht, (1987).

Improved Continuum Models for Polymers and Associated Experiments

Brad E. Clements and Eric M. Mas, T-1; Dana M. Dattelbaum, Edward B. Orler, and Eric Brown, MST-7; Philip Rae and George T. Gray III, MST-8; Stephen Sheffield and David L. Robbins, DX-2; Neil J. Henson, T-12; Eric N. Harstad, T-3; Luca A. Maciucescu and Matthew W. Lewis, ESA-WR; Holmann V. Brand, Kerri Jean Kress, and Jessica M. Ryan, X-7; bclements@lanl.gov

A new project titled "*Polymer Behavior under Dynamic Loading*," with Project Leader Brad Clements, under the Joint DoD/DOE Munitions Technology Development Program has the goal of producing improved physics-based polymer models. This project will have an impact on any DOE and DoD system where the use of polymeric materials is crucial to the functioning of the system. The project will strive to

- improve our understanding of system survivability,
- reduce uncertainties in performance assessments,
- improve our understanding of conditions for chemical reaction (reactive material and high-explosive safety),
- achieve a predictive capability of polymer impact and penetration, and
- advance material models for improved composite and energetic material design.

The technical goal of this project is to generate high-quality experimental data for polymers of interest to the DOE and DoD, develop physics-based continuum models for these polymers, and validate the models by implementing them into finite element codes and comparing their predictions to further experiments. Experiments include

- compressive stress-strain measurements over many temperatures and rates.
- tensile stress-strain measure ments.
- Split Hopkinson Pressure Bar (SHPB).
- Taylor impact tests, see Figure 1.
- plate impact data (for Hugoniot, sound speed, and damage), see Figure 2.
- differential scanning calorime try (DSC) measurements, see Figure 3.
- Torsional and Youngs dynamic mechanical analysis (DMA) (for viscoelasticity).
- high-pressure diamond anvil cell (DAC) and Raman analysis (for EOS), see Figure 4.
- Neutron scattering data.

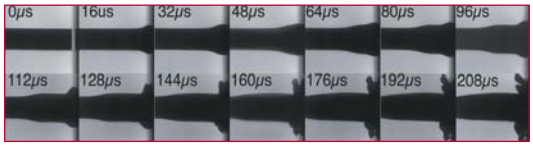

Figure 1—Taylor impact studies on PTFE.

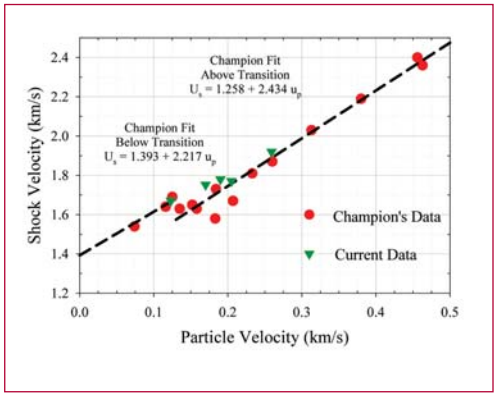

Figure 2—Hugoniot measurements on PTFE.

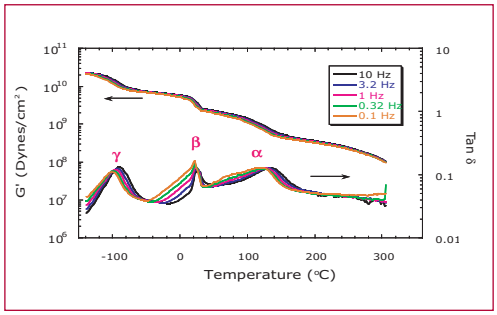

Figure 3—DMA measurements on PTFE.

In FY03 the polymers Kel-F and PTFE (Teflon) were investigated. Our theoretical model being developed is based on finite deformation analysis enabling us to simulate large deformation processes important to the DoD and DOE. Teflon and Kel-F are semicrystalline, which implies that they are heterogeneous at the crystalline domain-size scale. Our model uses the generalized method of cells (GMC) to handle this heterogeneity.

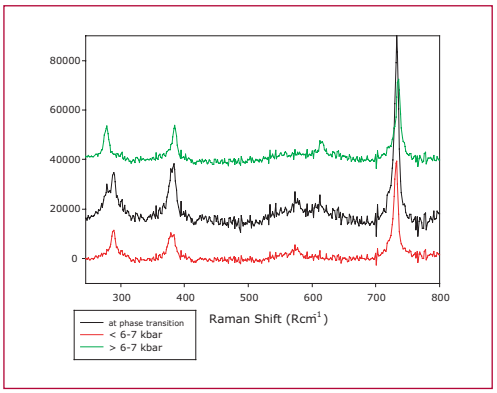

Figure 4—Raman measurements on PTFE.

Small crystalline domains of Teflon (Kel-F) are embedded in the amorphous Teflon (Kel-F) matrix. The GMC analysis is sufficiently general to allow the treatment of loaded Teflon in future studies. The amorphous background is treated as nonlinear hyperelastic-viscoelastic, with viscoelastic properties determined by (DMA) over a large range of frequencies and temperatures. The elastic properties of the various crystal structures relevant to the crystalline domains are calculated using ab initio first principal electronic structure theory (Figure 5).

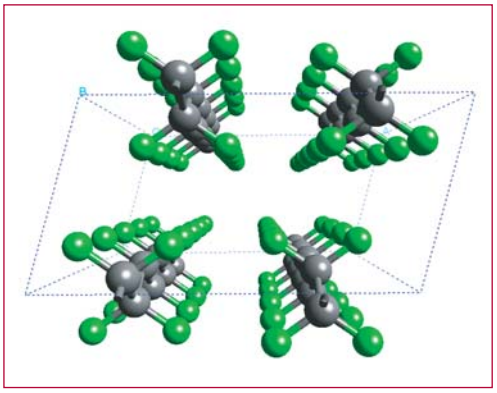

Figure 5—Crystal structure of the high-pressure phase of PTFE.

Presently, slip planes and yield processes important to the crystalline phases are treated using classical Bodner-Partom plasticity theory. The parameters in the model are fit to a host of experiments: MTS, SHPB, and plate impact, all of which are discussed. Equation of state input from the model comes from (DAC) and plate impact studies. All constitutive models, and the GMC analysis are written in a finite deformation framework. The associated computer algorithm has been implemented in the finite element code EPIC. Figure 7 shows a simulation of a Taylor impact test.

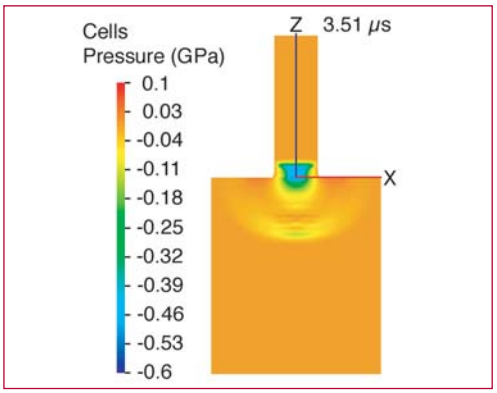

Figure 6—Finite element simulation of PTFE impacting steel.

A Comparison of Theory and Experiment of the Bulk Sound Velocity in Aluminum Using a Two-Phase EOS

Scott D. Crockett, Eric D. Chisolm, and Duane C. Wallace, T-1, echisolm@lanl.gov

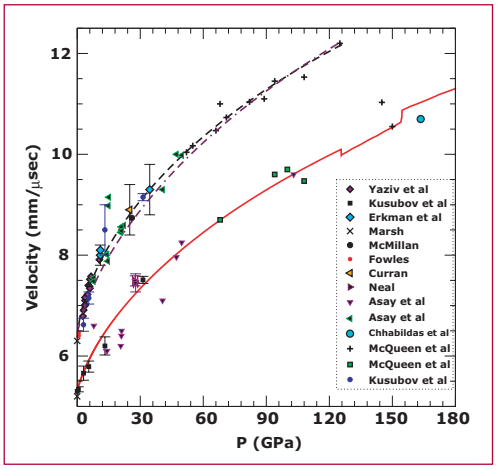

Figure 1— ***c_l and c_b vs P on the Hugoniot. The solid line is the calculated cb from our EOS. The dashed line is a numerical fit to c_b Eq. (1), and the dot-dashed line results from setting G_S / B_S equal to a constant. The data at P = 0 from Marsh are from ultrasonic measurements.***

The following is a summary of work that has been published and presented at the 13th SCCM symposium [4] (LAUR-03-5088).

An aluminum equation of state was created recently using results from lattice dynamics, liquid dynamics, and electronic structure theory [1]. With this EOS, we calculated the adiabatic bulk modulus and bulk sound velocity. We then compared the results of these calculations to experimental bulk sound speed measurements along the Hugoniot. The comparison of theory and experiment is an additional guide to testing the validity of an EOS. The data covers the part of the Hugoniot that crosses the solid-liquid coexistence region, allowing us to test the EOS in the two phase region. Using longitudinal sound speed data and the bulk modulus from the EOS, a reasonable estimate of the shear modulus is computed, and this estimate can be used to test approximations for the shear modulus.

The longitudinal sound velocity c_l and the bulk sound velocity c_b are commonly measured in shock experiments. For the solid phase, the leading edge of the rarefaction wave is presumed to travel at the velocity c_l. This leading edge is observed as an initial drop in the wave profile. The velocity c_b is identified by a second drop in the wave profile where the material response changes from elastic to plastic. It is important to note that for the liquid phase, longitudinal waves do not propagate and the leading edge of the rarefaction wave travels at the bulk sound velocity. The theoretical c_b for pure aluminum along the Hugoniot is compared with experiment in Figure 1. Notice that the theory shows a slight decrease in c_b through the solid-liquid two phase region. This reflects the fact that the P– ρ adiabats cross the solid-liquid two-phase region at a slightly smaller slope than in the separate solid and liquid phases. The figure illustrates that our theory is in excellent agreement with experiment for c_b, or equivalently for B_S.

Using the longitudinal sound velocity data we can learn something about the shear modulus. The shear modulus is an important material property and is needed to calculate plastic flow processes in hydrodynamic codes. In explosively driven processes, the shear modulus is needed over a wide range of the equation of state surface, and not just in the vicinity of the Hugoniot. An estimate of G_S for the solid phase at all temperatures up to melt and to pressures of a megabar or so, reliable to an accuracy of 25%, would be most useful for practical hydrodynamical calculations.
Using a previously developed an approximation for G_S based on setting G_S / B_S = *constant*, where the constant is to be determined separately for each metal [2], allows us to calculate G_S from an equation of state at any pressure and

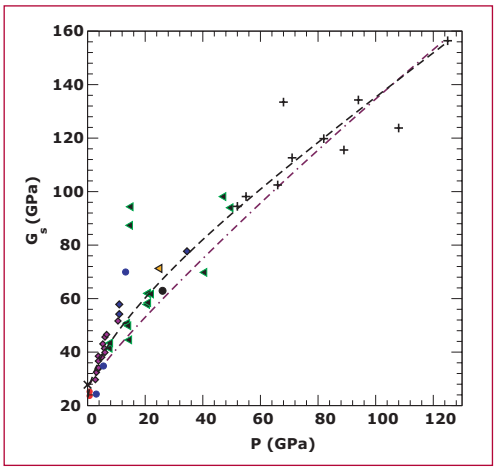

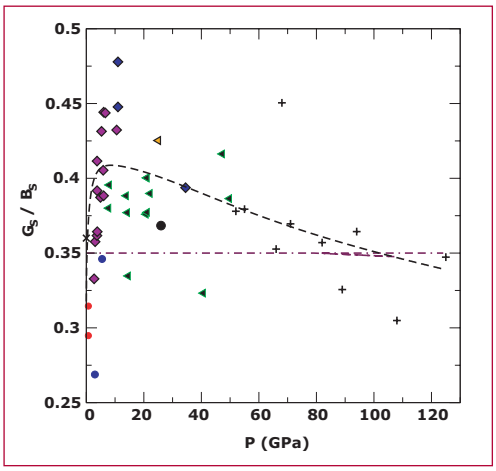

Figure 2— GS vs P on the Hugoniot.

Figure 3— G_S / B_S vs P on the Hugoniot. The dashed line is a result of using the numerical fit for c_l, and the equation of state for B_S and Eq. (1) to calculate G_S.

density, since B_S can be calculated from the equation of state. The approximation was developed from a study of ultrasonic data, and it was used in making qualitative estimates of strength and dissipative effects in overdriven shocks in metals. With the data we have collected for aluminum we can now test this approximation up to 125 GPa along the Hugoniot, the point where aluminum starts to melt.

From the theory for an isotropic material, we have

$$\rho c_l^2 = B_s + 4/3\, G_s.$$

We used this equation, together with the experimental data for c_l from Figure 1 and with ρ and B_S determined from our EOS, to accurately calculate G_S along the Hugoniot. The results are shown by the points in Figure 2. The ratio G_S / B_S from the G_S points of Figure 2, and again with B_S from our EOS, is shown by the points in Figure 3.

To approximate G_S / B_S by a constant, we might choose any one of three values: 0.37, the mean value of the points in Figure 3, 0.36, the ultrasonic value for 2024 aluminum at $P = 0$ and 295 K, or 0.35, the ultrasonic value for pure aluminum at $P = 0$ and 295 K. At the level of accuracy we are concerned with, all these constants are equally acceptable. Further, to an accuracy of 10% in G_S, any of these constants for G_S / B_S is as good as the fitted curve in Figure 3. The result for $G_S / B_S = 0.35$ is shown by Figure 3.

We compare theory and experiment for sound velocities in aluminum, and reach the following conclusions. The bulk sound velocity c_b , or equivalently the bulk modulus B_S from our aluminum EOS is in excellent agreement with experiment on the Hugoniot, throughout the solid and two-phase regions. The approximation G_S/B_S = constant agrees with experiment within error bars, on the Hugoniot through the solid phase. We expect this approximation to hold equally well away from the Hugoniot, throughout the entire solid phase region.

[1] E. D. Chisolm, S. D. Crockett, and D. C. Wallace, *Phys. Rev B* **68**, 104103 (2003).
[2] Wallace, D. C., *Phys. Rev. B* **24**, 5607 (1981).
[3] Wallace, D. C., *Statistical Physics of Crystals and Liquids,* (World Scientific, 2002).
[4] "A comparison of theory and experiment of the bulk sound velocity in aluminum using a two-phase EOS," S. Crockett, E. Chisolm, D. Wallace, appearing in SCCM 2003 proceedings.

The Promise of Liquid Dynamics Theory

Giulia De Lorenzi-Venneri and Duane C. Wallace, T-1, gvenneri@lanl.gov

An accurate description of the atomic motional dynamics is of paramount importance in the theoretical physics of matter. This description was given to us by Boltzmann for gases, starting around 1872, and by Born and colleagues for crystals in 1912. Based on these early works, the physics community has achieved quantitative understanding of a vast range of equilibrium and nonequilibrium properties of gases and crystals, and this understanding has spawned many practical applications. As one small example, it is now possible to carry out an apriori calculation of the equation of state of a monatomic crystal at normal density, or compressed by a factor of 10, or 1000, and know that we will get the right answer.

An accurate description of the atomic dynamics of a liquid has been given only in the last few years [1], and that for the simplest case of a monatomic liquid. In this system, each atom is in continuous interaction with a dozen or so neighbors, like a crystal but not like a gas, while the atoms undergo massive diffusive motion, like a gas but not like a crystal. The corresponding atomic motion consists of two parts, nearly harmonic vibrations in one of many identical many-body potential energy valleys, and nearly instantaneous transits of small groups of atoms that carry the system from one such valley to another. The liquid dynamics Hamiltonian is tractable in leading order, and exhibits small details that present theoretical challenges. As these challenges are solved, just as with gases and crystals, we shall achieve quantitative understanding of a wide range of liquid equilibrium and nonequilibrium properties, from equation of state to viscosity.

An example of how Liquid Dynamics Theory can explain a result otherwise unexpected, is the case of the intermediate scattering function F(q,t), the Fourier transform of the inelastic neutron scattering cross section S(q,w). Molecular dynamics calculations are shown in the figure for two cases: (a) at three temperatures below the glass transition, where the system is trapped within a single random valley, and (b) in the liquid at T just above melting. The curves are characterized by oscillations at short time, which are the source of the Brillouin peak in S(q,w), and by long time decay to a constant value. The oscillations have approximately the same frequency in the glass and in the liquid, showing that the Brillouin peak is at the same frequency in the glass and the liquid. This confirms a prediction of liquid dynamics theory. Another prediction of liquid dynamics theory is that the long time value of F(q,t) for the glass is a positive constant. This is something of a surprise, and apparently has not previously been noticed, especially since the long time constant is zero for both the liquid and crystal state. When the long time constant is calculated from liquid dynamics in the harmonic approximation, the results are close to the MD calculations, and when anharmonicity is included, the theoretical results are in excellent agreement with MD, as one can see from the Figure.

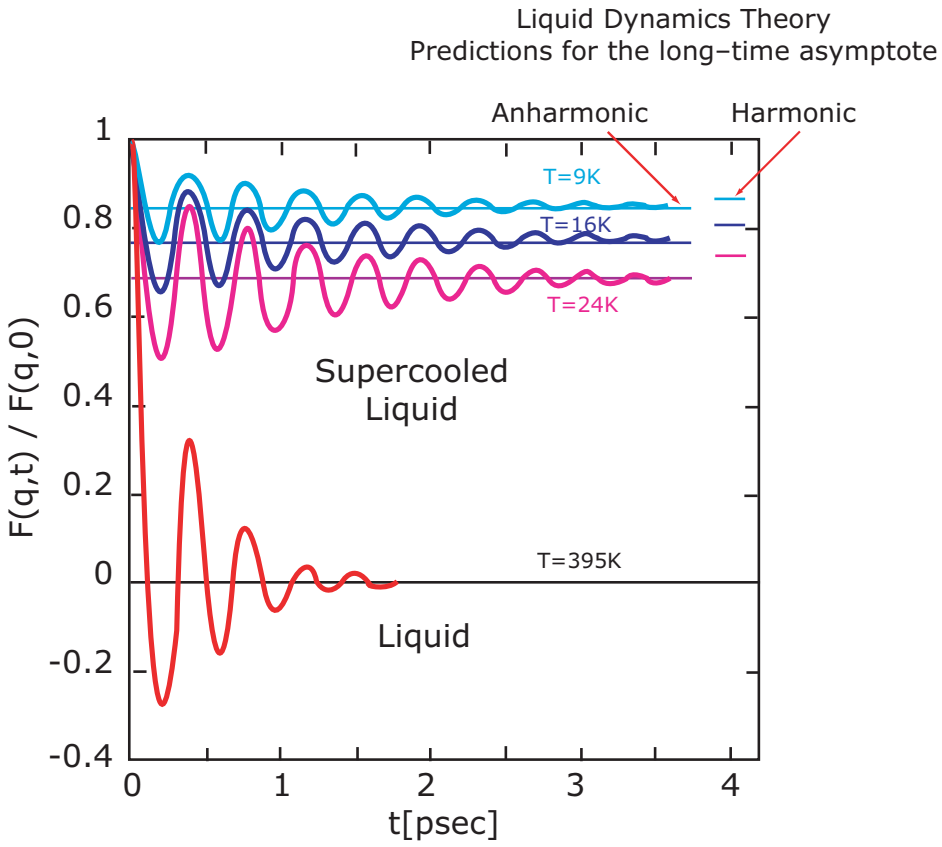

Figure— Intermediate Scattering Function F(q,t) for q=0.29711 a_o^{-1}, on a system of 500 particles of Na. The functions evaluated from Molecular Dynamics at four different temperatures are shown, together with the predictions for the long–time asymptotes from Liquid Dynamics Theory.

This is accomplished by doing the LD calculation in the average configuration, instead of the random configuration: one effect of anharmonicity is in fact to shift the average positions away from the bottom of the valley.

[1] Duane Wallace, *Physical Review* E **56**, 4179 (1997)

Effect of Anisotropic Interfacial Energy on Grain Boundary Distributions during Grain Growth

Denise C. George and Andrew P. Kuprat, T-1; Gregory S. Rohrer, Anthony D. Rollett, and Jason Gruber, Carnegie Mellon Univ.; dcg@lanl.gov

The relative populations of various interface types in polycrystalline materials are known to affect a wide range of materials properties. Examples include electrical resistivity, susceptibility to intergranular corrosion, susceptibility to intergranular fracture, and resistance to high-temperature creep, among others. Understanding how interface populations develop is a major goal of microstructure research, but the complexity of the systems studied has led to relatively little progress with direct experimental measurements. In fact, perhaps the simplest population characterization, the grain boundary distribution of a single-phase polycrystal, has been measured only a few times [1, 2] with coarse resolution. With simulations we can quickly produce relevant data without the great effort and error inherent in these measurements.

Specifically, we have begun a study of the effect of anisotropic energy, anisotropic mobility and crystallographic texture on the relative populations of grain boundary planes in single-phase microstructures during the grain growth process through simulations with GRAIN3-D. The GRAIN3-D code can be easily modified to run with any user-defined energy and/or mobility function and predetermined texture. We have completed a series of simulations with an anisotropic energy function that resembles that hypothesized for magnesia, isotropic mobility, and random initial grain orientations. The grain boundary populations produced by the GRAIN3-D simulations are in excellent agreement with those obtained from measurement [2], see Figure 1–4.

Several important results are suggested by these initial simulations. First, the grain growth process appears to have no effect on crystallographic texture or the distribution of boundary misorientations under the conditions used. For any fixed misorientation, the grain boundary plane population quickly reaches a quasi-steady state. The distribution of boundary plane types reflects an inverse relation with energy. More exactly, local minima (maxima) in the boundary plane distribution correspond to local maxima (minima) in the energy function. The population of boundary planes for a fixed misorientation also appears to be independent of the crystallographic texture or the distribution of boundary misorientations, as close agreement with the experimental measurements of a highly textured sample [2] suggests. Further work will concentrate on testing the above results with different energy functions and initial crystallographic texture.

[1] D. M. Saylor, B. S. El-Dasher, T. Sano, and G. S. Rohrer, "Distribution of Grain boundaries in SrTiO3 as a Function of Five Macroscopic Parameters," *J. Amer. Ceram. Soc.*, in press.

[2] D. M. Saylor, A. Morawiec, and G. S. Rohrer, "Distribution of Grain boundaries in Magnesia as a Function of Five Macroscopic Parameters," *Acta Mater.*, **51** 3663–3674 (2003).

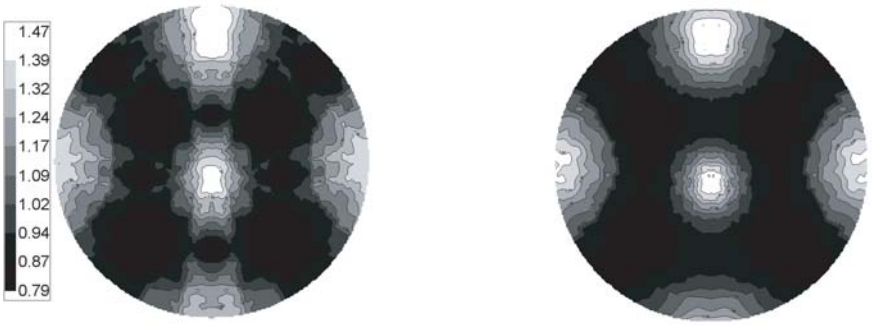

Figure 1— Grain boundary plane distribution for fixed misori-entaion of 15° rotation about [100], simulated (left), experimen-tal (right).

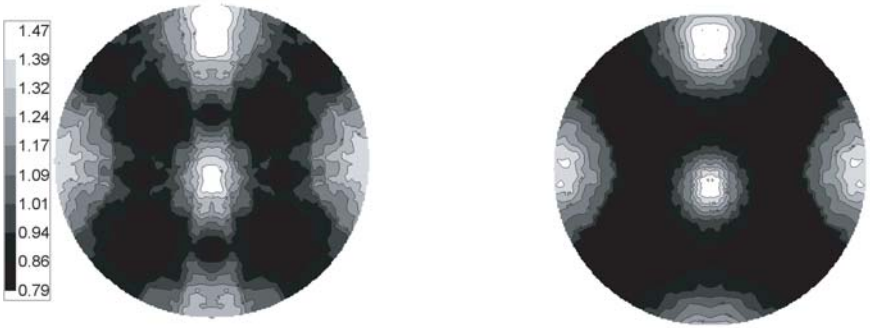

Figure 2— Grain boundary plane distribution for fixed misori-entaion of 25° rotation about [100], simulated (left), experimen-tal (right).

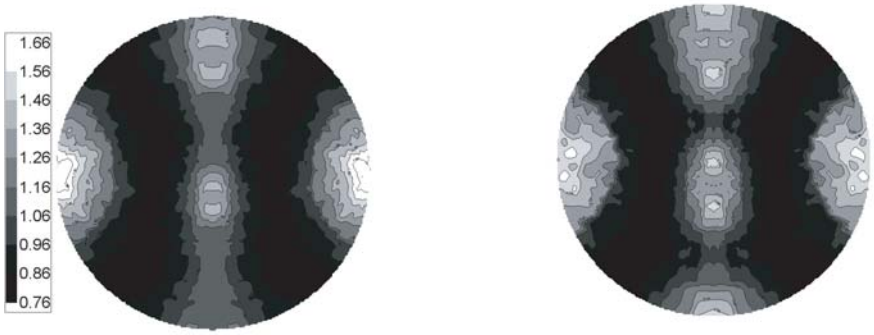

Figure 3— Grain boundary plane distribution for fixed misori-entaion of 35° rotation about [100], simulated (left), experimen-tal (right).

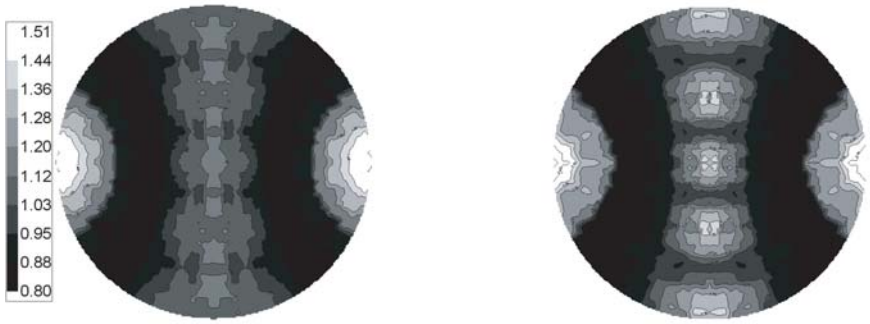

Figure 4— Grain boundary plane distribution for fixed misori-entaion of 45° rotation about [100], simulated (left), experimen-tal (right).

Two-Mesh Computation for the Telluride Casting Project

Andrew P. Kuprat, T-1; kuprat@lanl.gov

This past year, T-1 devised and implemented a two-mesh capability for the ASCI funded Telluride project (a collaboration involving MST, CCS, T, and other divisions), which is now available in the 3-D Truchas casting simulation code. Truchas simulates the entire casting process: flow of molten alloy, heat transfer, solidification of alloy, induced stresses, etc.

The two-mesh capability that we implemented allows Truchas to compute electromagnetic fields and the resulting inductive heating source terms on a tetrahedral mesh (using a finite element method that requires tetrahedra for computation) and transfer the heat source terms onto the regular hexahedral mesh used for heat flow and phase change computation.

More generally, the two-mesh capability allows the transfer of any cell-based field computed on a tetrahedral mesh to a cell-based field on an unstructured hexahedral mesh. Conservation is obeyed; i.e., the integral of the field over the tetrahedral mesh is equal to the integral of the mapped field over the hexahedral mesh, to within round-off error.

With the new two-mesh capability, different kinds of physics requiring different kinds of meshes can now be coupled. Truchas requires this capability for coupling electromagnetism and heat-flow, but other physical combinations are of course possible.

Figures 1 and 2 represent a demonstration of this capability. In Figure 1, we have the heat source field as computed on the tetrahedral mesh. In Figure 2, we see the heat source field as mapped conservatively onto the hexahedral mesh.

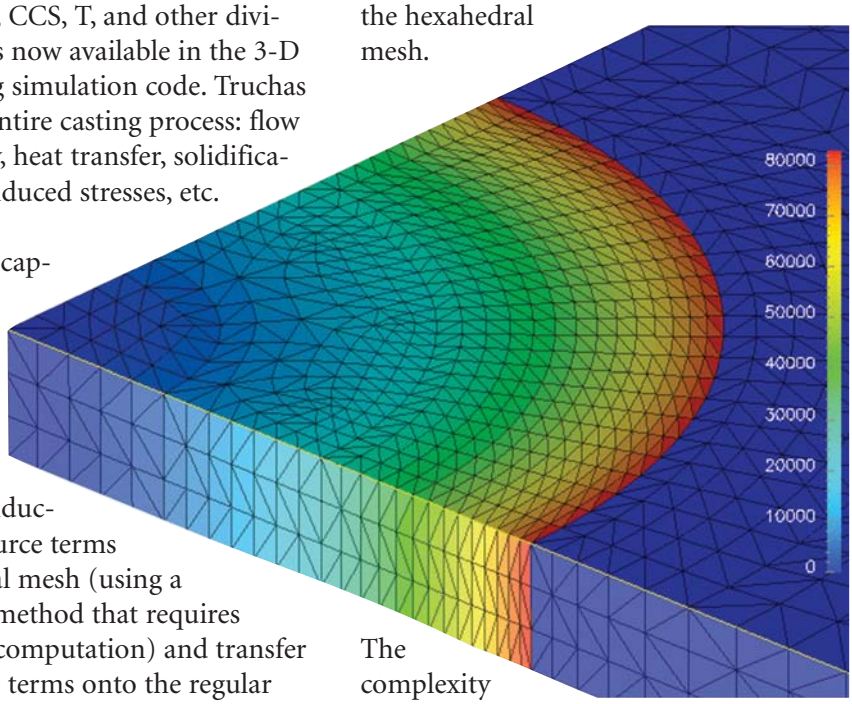

Figure 1—Truchas tetrahedral mesh for electromagnetic inductive heating computation. The dark blue outer region represents vacuum where inductive heating does not take place. The inner "quarter cylinder region represents graphite, which experiences inductive heating. The heat source is strongest near the curved s urface of the graphite (red color) where the electromagnetic fields do not have to penetrate very far. Units are in Joules per cubic meter.

The complexity of the mesh mapping is of order N log N, where N is a bound on the number of elements in the two meshes. This low complexity implies that mesh mapping is feasible between very large meshes. In fact, computation of the mesh mapping for a typical electromagnetics/heat transfer simulation takes up a small fraction of the overall run time.

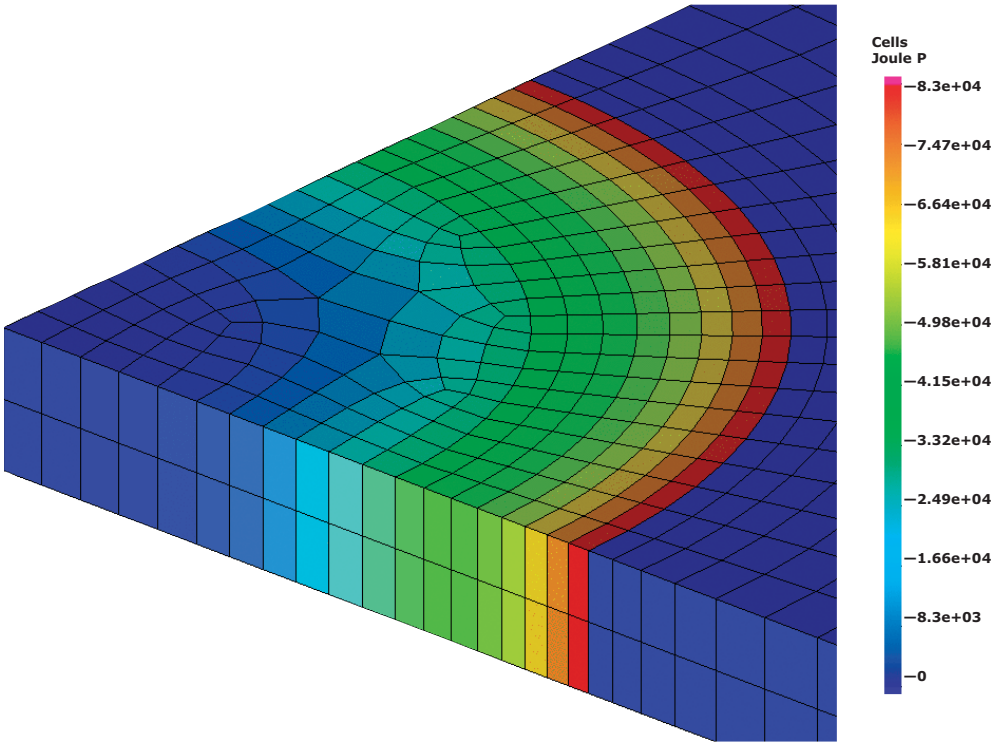

Figure 2— Truchas hexahedral mesh for heat flow computation. The heat source field of Figure 1 has been conservatively mapped onto this hexahedral mesh. The mapping is conservative over both the vacuum and graphite regions. Thus, there is no spurious mapping of heat onto the vacuum region of the hexahedral mesh.

Direct Numerical Simulations of PBX 9501

Eric M. Mas, Brad E. Clements, and Denise C. George, T-1; mas@lanl.gov

We have conducted direct numerical simulations (DNSs) on the high-explosive composite PBX 9501 using finite element analysis (FEA). As much of the microstructure is explicitly gridded as is numerically tractable, this resolution allows us to observe some of the localization effects. PBX 9501 has a very complicated microstructure, consisting of high-melting explosive (HMX) grains (95 wt %) embedded in a plasticized estane polymer matrix (5 wt %). The HMX grains range in size from several hundred micrometers to sub-micrometer diameters.

To conduct DNSs on PBX 9501, two key factors must be addressed: first, a finite element grid must be created that captures as much of the microstructure as possible without being too complex to simulate in a reasonable amount of time, and second, the constitutive models must capture the necessary physics while also being numerically efficient.

In 1997, a study in DX-Division by Skidmore, Phillips, Son, and Asay reported a study of HMX grain sizes in PBX 9501. They removed the plasticized estane binder with a solvent and measured the particle size distribution by laser diffraction. That study provides us with an experimentally derived grain size distribution. In our DNSs we approximate their continuous distribution with seven discrete grain diameters (450, 350, 250, 200, 150, 100, and 50 μm), effectively accounting for grains down to a 25-μm diameter. Assuming one 450-μm grain, we used the distribution to calculate the approximate number of other grains, leading us to a total of approximately 1600 grains.

The finite-element grid was generated using LaGriT, the Los Alamos Grid Toolbox, on a regular tetrahedral mesh of approximately one million elements. A picture of the grid after the last 200-μm-diameter grain has been positioned is shown in Figure 1. A picture of the final microstructure model is provided in Figure 2. The front surface represents a slice that is approximately 20% of the way through the sample. Individual grains can be observed, as can percolating paths of dirty binder. This appears to

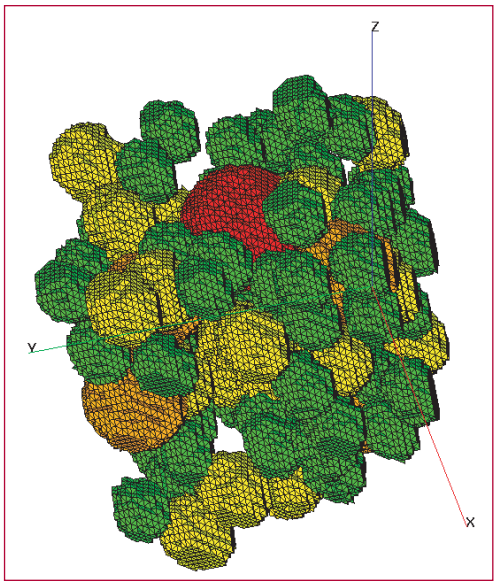

Figure 1— A picture of the finite-element grid after grains of 450, 350, 250, and 200 μm in diameter have been allocated (80 total grains).

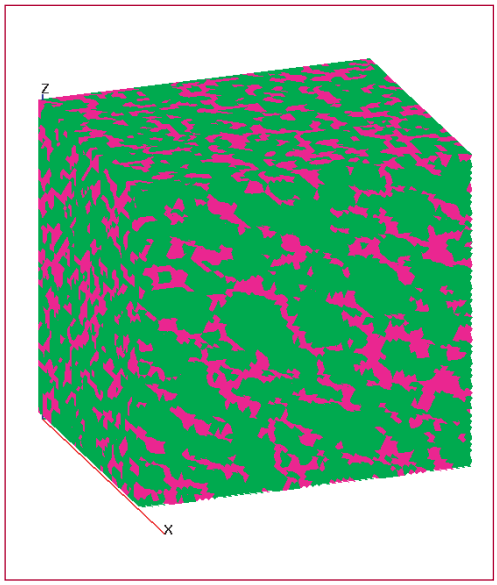

Figure 2— A direct numerical simulation picture of the microstructure of the high-explosive PBX 9501. Green denotes HMX and pink is the "dirty binder."

be a much better representation of PBX 9501 than has previously been seen in the modeling literature.

Parameters for our model come from three sources; values calculated directly from experiments (elastic moduli, densities, etc.), values fit to experiments on constituents (relaxation spectra of the viscoelastic binder, etc.), and those fit to experiments on the composite (parameters in our HMX micro-crack growth model and plastic yield stress). The latter were determined by our method of cells (MOC)-dirty binder hybrid model fit to experiments. The resulting stress-strain fit is shown in Figure 3.

The DNSs, using the above constitutive theories and finite element grid, were carried out using the FEA code EPIC. We modeled a load similar to a split Hopkinson pressure bar experiment, specifically uniaxial stress with an applied strain rate of 2000 s^{-1}, by applying velocity boundary conditions on the top and bottom nodes of the sample box. A simulation to a strain of 8% took about 4 days on a single-processor alpha workstation. In the future, and with the arrival of a parallel version of EPIC, we plan to simulate larger, more representative samples of PBX 9501 under more complicated loading conditions.

The purpose of the results is twofold: to show agreement with experiment to validate the above-described procedure and to analyze the DNS data for information elucidating qualitative or quantitative information about the deformation processes occurring in the composite as it is loaded. This information can then be used as a tool for general understanding of explosives and as a guide for other meso- and macro-models that might be missing important properties of the composite.

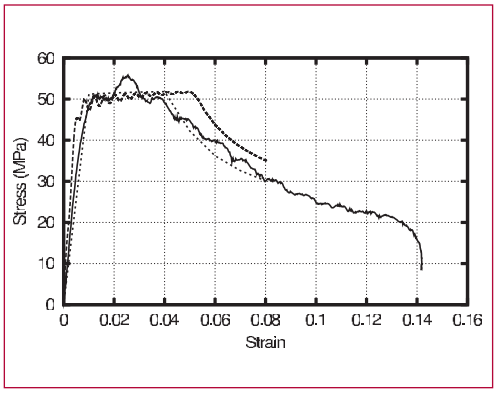

Figure 3—A comparison of model stress-strain curves to experiment. Experimental data are represented by the solid line, the direct numerical simulation is the dashed line, and the method of cells simulation is the dots.

The DNSs agree satisfactorily with the experimental stress-strain curve, as shown in Figure 3. The agreement is also close to the MOC simulation described above that produced the parameters used in the simulation.

Other information gleaned from these simulations is more interesting. In the course of a simulation, we observed stress bridging between HMX crystals, as one might expect. We also observed that the distribution of most quantities,

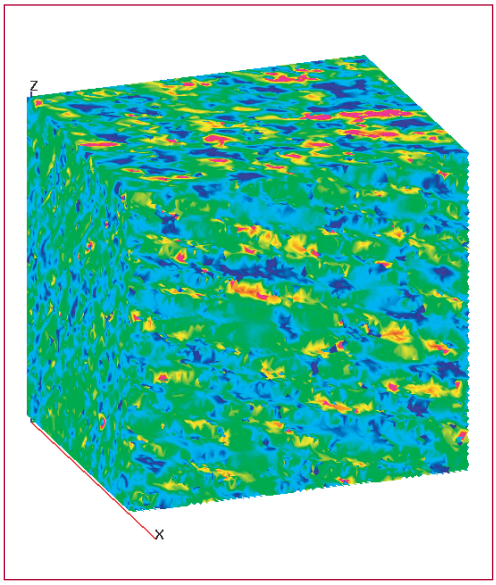

Figure 4—Pressure distribution at the same surface as shown in the Figure 2 simulation at 17 μs, or a 4% volume-averaged strain. Blue, light blue, green, yellow, and red denote 0, 10, 25, 35, and 45 MPa, respectively.

Quantum Perturbation Theory in O(N)

Anders M. N. Niklasson, T-1; Valery Weber, T-12; and Matt Challacombe, T-12; amn@lanl.gov

We have proposed a new orbital-free quantum perturbation theory for linear scaling electronic structure calculations. The method is based on the zero-temperature density matrix and its response upon variation of the Hamiltonian. The approach is surprisingly simple and efficient. It allows treatment of both embedded quantum subsystems and response functions. Traditional textbook perturbation theory based of wave functions can be replaced by a quadratically convergent explicit recursion that gives the expansion terms of expectation values to any order.

Move a comb through your hair and place it next to the thin stream of water falling from the tap into your sink. What happens? The water moves! The static electric field from the comb polarizes the water and a force acts on the string of falling water molecules. The question we are interested in is how we can calculate, from the first principles of quantum mechanics, various response properties of complex systems, like the falling water droplets with their millions of molecules.

Recently we proposed a new computational approach for the calculation of adiabatic response properties of complex systems [1]. It is a first very promising step in a scientific field that may have a large future impact on computational materials science, bridging the gap between nanoscience, chemistry, and biology.

During the last 10 years a significant effort has been devoted to the development of electronic structure methods that are sufficiently efficient to study very large systems consisting of thousands of nonequivalent atoms [2]. The success has been based on the linear scaling paradigm, where no single part of a calculation is allowed to scale in computational complexity more than linearly as a function of the number of atoms N. Until recently most attention was focused on linear scaling $\boldsymbol{O(N)}$ methods for computing the ground state electronic energy. However, an important problem that was given little attention is the $\boldsymbol{O(N)}$ calculation of materials response properties, such as vibrational frequencies, the polarizability, nuclear magnetic resonance, and Raman intensities. Also of great interest is extending $\boldsymbol{O(N)}$ electronic structure theory to quantum embedding where the computational complexity scales linearly with the size of a locally perturbed region $O(N_{\text{pert.}})$ and therefore as $O(1)$ with the total system size. This would allow efficient studies of quantum subsystems, for example surface chemistries or the catalytic

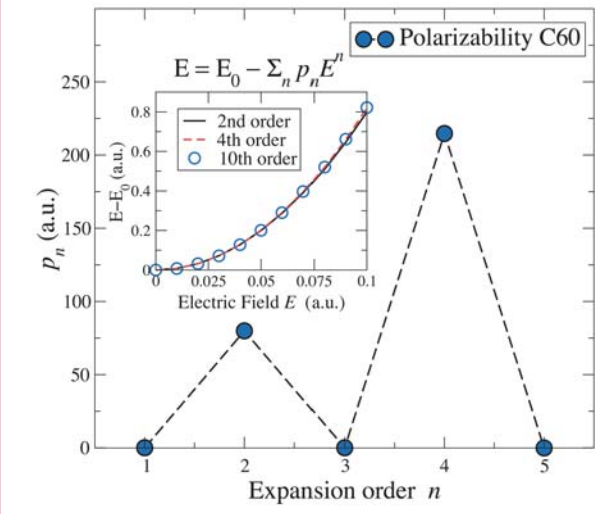

***Figure 1—** The static uncoupled polarizability (up to 10th order) for a C60 molecule (RHF/6-31G) with the field aligned along the z-axis. Odd orders vanish due to symmetry.*

domains of proteins, without recalculation of the entire system.

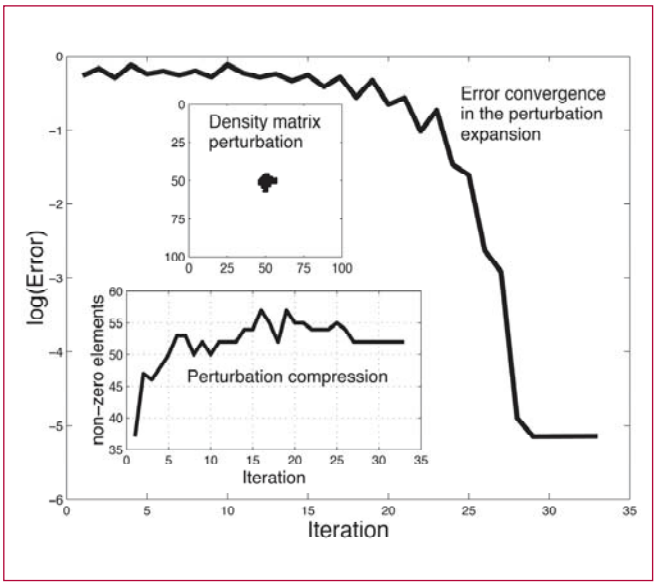

Figure 2— The convergence error for a local perturbation as a function of iterations n. The lower inset shows the number of nonzero matrix elements above a numerical threshold (10^{-6}). Only about 50 out of 10^4 matrix elements are necessary to inlcude in the expansion. The upper inset shows the density matrix perturbation.

We have introduced a new and surprisingly simple $O(N_{pert.})$ approach to quantum perturbation theory [1]. The method makes it possible to study embedded quantum subsystems and response functions to any order, within linear scaling effort. The approach is based on recently developed spectral projection schemes for purification of the time-independent zero-temperature density matrix, replacing the conventional eigenvalue problem in tight-binding or self-consistent Hartree-Fock and Kohn-Sham theory.

The eigenvalue and orbital-free perturbation theory is based on the density matrix and avoids using the more elaborate wave function or Green's function formalism. The main problem in constructing a density matrix perturbation theory is the nonanalytic relation between the zero temperature density matrix and the Hamiltonian, given by the discontinuous Heaviside step function θ, with the step formed at the chemical potential μ,

$$P = \theta(\mu I - H). \qquad (1)$$

This discontinuity makes an expansion of the density matrix P about the Hamiltonian H difficult. Explicit density matrix derivatives for a perturbed Hamiltonian are therefore hard to calculate.

Our new perturbation theory avoids the discontinuity problem by dividing the perturbation expansion in sequential steps of projections, where perturbations are performed exactly, or to any order, at each projection level. Our perturbed projection method yields an explicit and quadratically convergent recursive construction of the density matrix response.

In linear scaling purification schemes the density matrix is constructed by recursion;

$$X_0 = L(H),$$

$$X_{n+1} = F_n(X_n), \quad n = 0,1,2,\ldots \qquad (2)$$

$$P = \lim_{n\to\infty} X_n.$$

Here, $L(H)$ is a linear normalization function mapping all eigenvalues of H in reverse order to the interval of convergence [0,1] and $F_n(X_n)$ is a set of functions projecting the eigenvalues of X_n toward 1 (for occupied states) or 0 (for unoccupied states). Purification projection schemes are quadratically convergent, numerically stable, and can even solve problems with degenerate eigenstates, finite temperatures, and fractional occupancy [3,4,5]. Thanks to an exponential decay of the density matrix elements as a function of the interatomic distance for insulators, all operators have sparse matrix representations and the number of nonzero matrix elements

Quantum-Size Induced Interface Stability in Thin Film Nanomaterials

Anders M. N. Niklasson and John M. Wills, T-1; Erik Holmström, Uppsala, Sweden; amn@lanl.gov

Magnetic thin film nanomaterials have several interesting properties of both scientific and technological importance. In collaboration with MST-Division and Uppsala University, we have performed theoretical studies of layered thin film materials and their novel magnetic behavior. Quantum-size effects, due to interference between the interfaces, determine many properties specific to magnetic thin film nanomaterials. The ability to understand and control interface roughness is therefore very important. In this brief report we discuss recent findings indicating that quantum-size effects can be used to modify the interface stability and thereby enhance or reduce quantum interference in magnetic thin film systems.

During the last 10 years, the field of magnetism in nanostructures has gained a lot of attention, in particular in connection with technological applications for memory storage, magnetic sensors, and spintronic devices. Thanks to the reduced dimensionality of nanomaterials, surface and interface effects, together with quantum-size effects from interference between interfaces and surfaces, contribute to the materials properties. By careful design these effects can be exploited to create tailor-made materials with new unique properties previously out of reach of conventional materials science.

Of particular interest to this study are the quantum-size effects due to interference between the interfaces in a layered nanostructure. The quantum-size effects strongly depend on the quality of the interfaces. If the interfaces of a layered structure are even slightly intermixed, the quantum-size effects are strongly reduced. Since many important technological properties that are specific to nanosystems are determined by the finite-size effects it is important to understand the underlying mechanism determining the interface quality. The roughness of an interface is usually controlled by the deposition process used to construct the thin film systems, where deposition rate and temperature are two crucial parameters. This process is very hard to model from *ab initio* theory. To get an understanding of interface quality we have instead looked at the interface mixing energy [1], a measure of the relative change in energy, when an alloy is formed in the interface region between two materials A/B. Generally this stability can be estimated from the bulk heat of formation of the two materials on each side of the interface. By scaling the formation energy by a coordination number depending on interface crystal orientation and thickness of the intermixed region, an approximate estimate is given

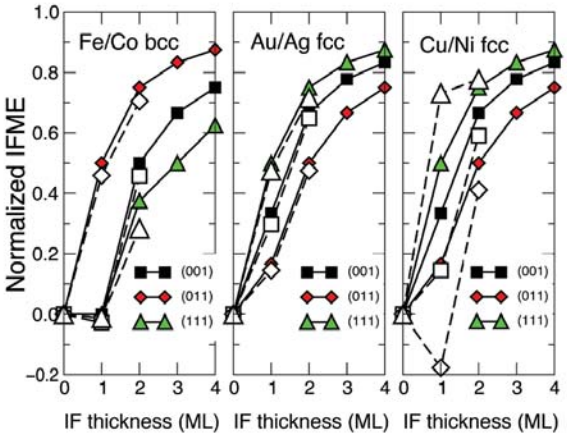

***Figure 1—** The normalized interface mixing energy (IFME) in units of the bulk mixing energy is a measure of the relative interface stability. The open symbols shows the IFME calculated from density functional theory and the local spin density approximation, where the interface alloy has been described by the coherent potential approximation. The filled symbols show the prediction from the rule of thumb based on coordination scaling of the formation energy of the bulk alloy [1].*

for the relative interface stability [1]. Figure 1 shows the normalized interface mixing energy in comparison with the estimated mixing energy derived from the bulk formation energy. From this analysis we find that some open interfaces, such as bcc(001), are thermodynamical unstable to alloying in a single monolayer, regardless of the formation energy of the bulk alloy. This could be a serious problem creating stable sharp interfaces for layered nanomaterials. An important question is therefore if it is possible to modify this interface stability, for example, by exploring quantum-size effects occurring in layered structures such as an $A/B_N/A$ sandwich. The idea behind a quantum-size induced interface stability in thin film nanomaterials is based on the fact that B bulk Bloch states are "quantized" due to interference between the A/B and the B/A interface. Only states with the right interface boundary conditions can exist. The energy of the discrete states oscillates as a function of the B spacer thickness *N*. For a certain number of B spacer layers the energy may be reduced by the quantization. For these particular thicknesses the A/B and B/A interfaces may gain in stability, since in the case of intermixing, the reduction in energy due to quantum interference is lost. In general, the energy fluctuations due to quantum-size effects can be expected to be very low compared to the interface mixing energy. However, for particular interfaces, such as the bcc(001) it may possibly be large enough to influence the stability. To investigate this hypothesis we performed total energy calculations based on density functional theory for $Fe/V_N/Fe$ bcc(001) multilayers, with and without intermixed interfaces. The result is displayed in Figure 2, which shows the interface mixing energy of both ferro- and anti-ferromagnetically aligned Fe interfaces. What we find is that for thin V films the mixing energy is positive, and for thicker films it converges to a constant negative energy. This means that the $Fe/V_N/Fe$ films are stable for thin V spacers, but unstable for thicker films. Even if one could expect that the size dependent interface stability is due to interface interference, either due to a quantization of states, as discussed above, or due to interacting interface states, present only in the case of sharp interfaces (lowering the energy by forming a bounding and an antibounding state), we have so far been unable to identify any particular mechanism behind the novel ordering behavior. Another additional complication is that the interface mixing energy represents a stability of an interface, but not necessarily the sharpness of an actual interface, which is more strongly determined by the specific growth process. Thus, the idea of a quantum-size induced interface stability has not yet a solid support, but we hope that future experimental studies may give further insights.

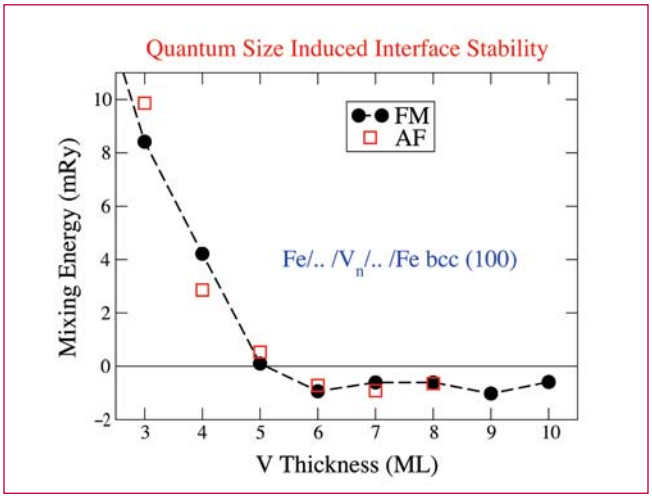

Figure 2— The interface mixing energy as a function of V spacer thickness N for a Fe/VN/Fe bcc(001) trilayer structure. Around five monolayers of V the interface stability changes sign, indicating a strong-size dependent interface stability, where the interface roughness can be expected to be reduced for thin films.

[1] A. M. N. Niklasson, I. A. Abrikosov, and B. Johansson, *Phys. Rev. B* **58**, 3613 (1998).

Anisotropy of Magnetic Interlayer Coupling

Sven P. Rudin, Anders M. N. Niklasson, and John M. Wills, T-1; srudin@lanl.gov

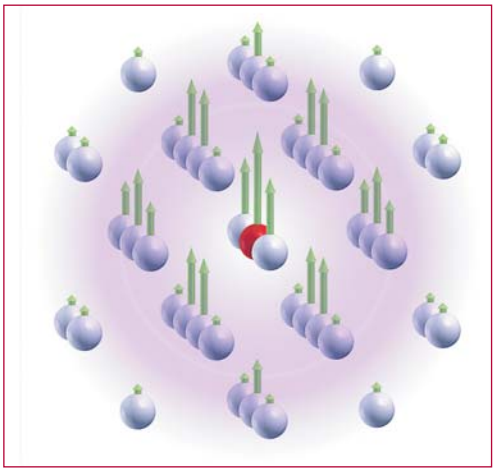

Figure 1— An iron impurity (red) embedded in a lattice of palladium induces spin moments on the palladium atoms situated near the impurity.

Palladium is a paramagnetic material with a high-spin susceptibility. This means that it does not spontaneously show spin polarization, but it will develop such a magnetic moment if coaxed by a magnetic field. For example, a (naturally spin polarized) iron impurity embedded in palladium induces a polarization of the Pd atoms in the vicinity of the impurity: the Fe impurity carries a moment of about $3\mu_B$, and the total moment induced in the nearby Pd atoms (within a sphere of approximately 10 Å radius) is roughly three times that.

Recent research has focused on making the iron impurity not just a single atom but an entire layer of iron atoms. The effect is similar: the palladium atoms near the iron layer take on a moment parallel to that of the iron atoms. One could say that the palladium extends the spatial extent of the iron's magnetic properties. This has led to research into how the palladium affects two separate Fe layers, and indeed one finds strong magnetic interlayer coupling that varies with separation of the layers. Some controversy remains as to when the layers couple antiferromagnetically.

How the magnetic interlayer coupling is affected by the relative directions of the moments in the layers remains an interesting topic. We are looking into a related question: how is the magnetic interlayer coupling affected by the direction of the moments relative to the crystal structure? Depending on the separation between the layers, is a magnetization more favorable in the direction perpendicular or parallel to the layers? The results of our work will further the understanding of this effect and perhaps lead to novel storage devices.

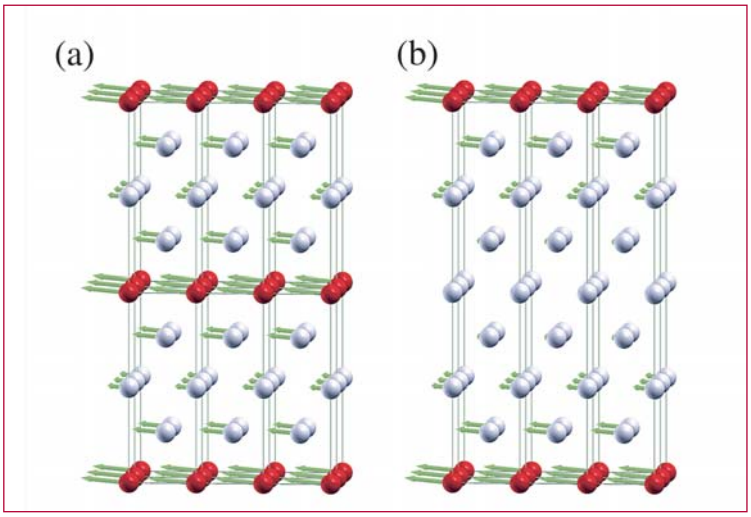

Figure 2— Iron atoms embedded as layers in a palladium crystal will induce a spin polarization in the Pd atoms in the vicinity of the Fe layer. This effect on the palladium in turn mediates a magnetic interaction between two iron atom layers, an interaction that varies with separation between the Fe layers.

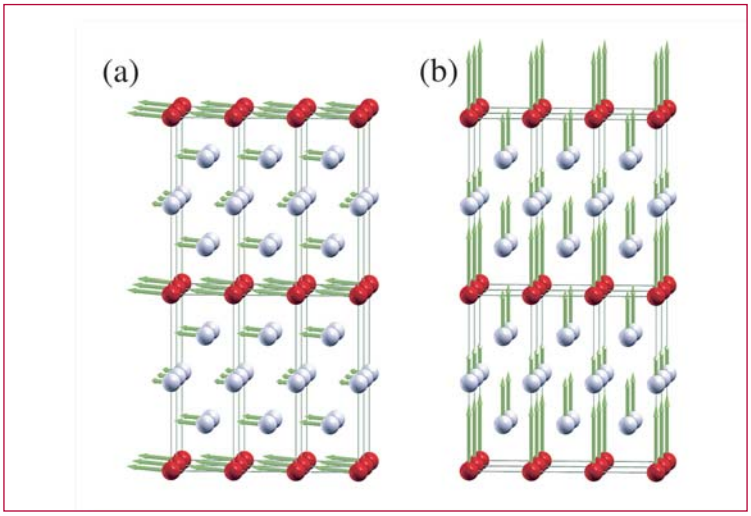

Figure 3— The magnetic interlayer coupling is not only a function of the separation between the layers but also depends on the orientation of the moments with respect to the lattice. We are studying this magnetic interlayer coupling anisotropy by comparing the energies for moments that are oriented (a) parallel and (b) perpendicular to the layers.

The magnetic anisotropy is a very delicate effect: the energy differences are on the order of μRy, i.e., many orders of magnitude smaller than energy differences electronic structure calculations deal with in calculating structural energy differences. In addition to the need for highly precise calculations, relativistic effects must be included as these determine the coupling of the spin moments to the lattice. We use first principles methods based on the local spin density approximation that have been shown to be accurate enough to capture the magnetic anisotropy in elemental solids, which involves energy scales that are at least an order of magnitude smaller than those considered here.

Preliminary results for a three-monolayer spacing show that the perpendicular orientation of the moments is preferred by about two μRy. Relaxation of the lattice around the iron layer increases this difference by roughly a factor of ten, indicating the strong influence strain can have on the magnetic interlayer coupling anisotropy—another effect we are studying.

First Principles Calculations for the Simulation of Nuclear Fuels

Sven P. Rudin and John M. Wills, T-1; srudin@lanl.gov

Nuclear energy will be produced differently in the future. Based on past experience, future production will be pushed heavily towards three improvements:

- Produce less nuclear waste per amount of energy delivered to customers.
- Reduce reactor waste destined for disposal and eliminate the need for a second repository.
- Reduce the proliferation threat despite an increase in global nuclear energy use.

Can new fuels be developed that show these improvements? The Advanced Fuel Cycle Initiative (AFCI) aims to answer technical questions surrounding such new fuels that will either make better use of existing reactors (series one) or require new reactors (series two).

Among the candidates for new fuels are actinide-based ceramic fuels (oxides, nitrides, and carbides). In addition to the experimental work being done to study their behavior a theoretical effort is underway aimed at improving the modeling of such nuclear fuels. The theoretical effort involves researchers at LANL (MST, NMT, and T Divisions) as well as domestic and foreign universities and research labs.

The theoretical research involves many length scales, from the microscopic to the macroscopic. The research done at a particular length scale is coupled to that done at other length scales: what we learn at the atomic scale feeds into the work done on grains, results of which in turn improve the models used to simulate the behavior of nuclear fuel rods, etc.

We are involved in improving the understanding of actinide-based ceramics at the microscopic length scale, using first principles calculations for two parallel approaches:

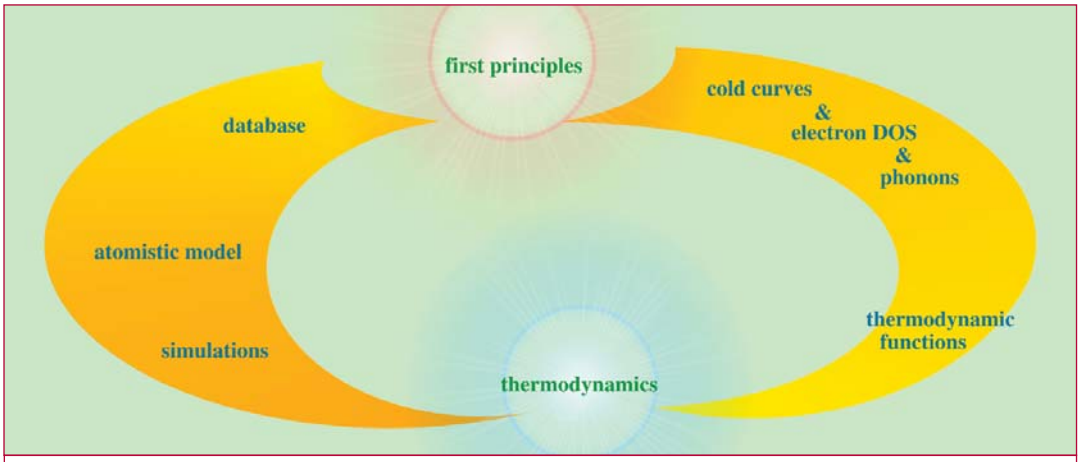

Figure 1—**(1) Construction of databases used in the fitting of atomistic models, e.g., the modified embedded atom model (MEAM). The models are then used to simulate the materials and their thermodynamic properties. (2) Calculation of cold curves, electron density of states (DOS), and phonons. From these we calculate thermodynamic functions that let us describe the thermodynamics of the material.**

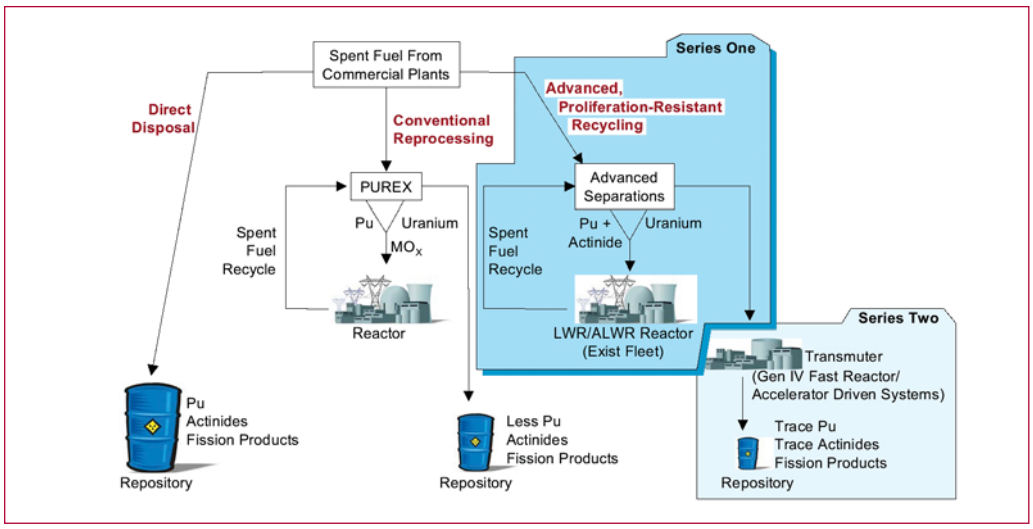

Figure 2—

A typical database for MEAM fitting purposes consists of cold curves for select structures, the elastic constants for a reference structure, and vacancy energies. For example, we have calculated for AmN the cold curves for the B1, B2, $L1_2$, B3, and C1 structures as well as the elastic constants in the B1 structure. The model for AmN is based on individual models for both Am and N, for these we have also provided results from calculations of cold curves and vacancy energies. M. I. Baskes and S. G. Srinivasan (MST-8) are using our results to fit a MEAM with which they will study the behavior of AmN under various conditions.

The calculations needed for a direct construction of thermodynamic functions start with the cold curves, i.e., the internal energy. This is by far the largest component of the energy but contains no information on how temperature affects the materials. To address this the contributions to the free energy from the electrons and the phonons must be included. The electronic contribution is often the smaller of the two and easy to calculate: part of the output of first principles calculations is the electronic DOS, which determines their contribution. Similarly, the phonon DOS determines their contribution, but calculating even a few phonon frequencies quickly becomes very time consuming. Nonetheless, this contribution cannot be neglected, and so we calculate as many frequencies as needed to get reliable estimates of the phonon DOS and with it the phonon contribution to the free energy.

Lattice Effects in Gallium-Doped Plutonium

Sven P. Rudin and John M. Wills, T-1, srudin@lanl.gov

The δ phase of plutonium has many advantages over the other phases when it comes to machining, but in its pure form plutonium can be found in the δ phase only at temperatures well above those practical for machining. However, by doping with a few percent of gallium, the δ phase can be made stable at room temperatures. Though this gallium-stabilized δ phase appears mostly in the face-centered cubic (fcc) crystal structure, experiments reveal in the vicinity of the Ga atom a significant departure from the fcc crystal structure.

The lattice distortion in the δ phase due to the gallium doping has been studied experimentally and theoretically. But what happens in the other crystal phases when doped with gallium, and what can we learn from studying them to help us understand the gallium-stabilized δ phase? We report here work in progress on the α and ε phases of gallium doped plutonium. Figure 1 shows the somewhat complicated crystal structure of the α phase; the ε phase is simpler with a body-centered cubic (bcc) crystal structure.

The sixteen atoms in the unit cell of α-Pu see eight different environments. Some of these are more favorable for Ga substitution as shown in Figure 2, where a correlation between the energies (calculated with first principles methods) and the radial density of neighbor atom positions is evident: when the nearest neighbors are further away the site becomes more favorable.

For the bcc crystal structure we are investigating the effect of a gallium atom on the surrounding lattice structure. Figure 3 illustrates our preliminary results, which indicate a roughly 2% elongation of the bonds between the gallium and its neighboring plutonium atoms. This result is somewhat surprising: the gallium atom is in some sense smaller than the plutonium atom, hence one would expect the bonds to neighboring plutonium atoms to get smaller, not larger. This is in contrast to the fcc lattice where the same computational scheme shows the plutonium atoms relaxing inward [1].

These results are preliminary: a larger

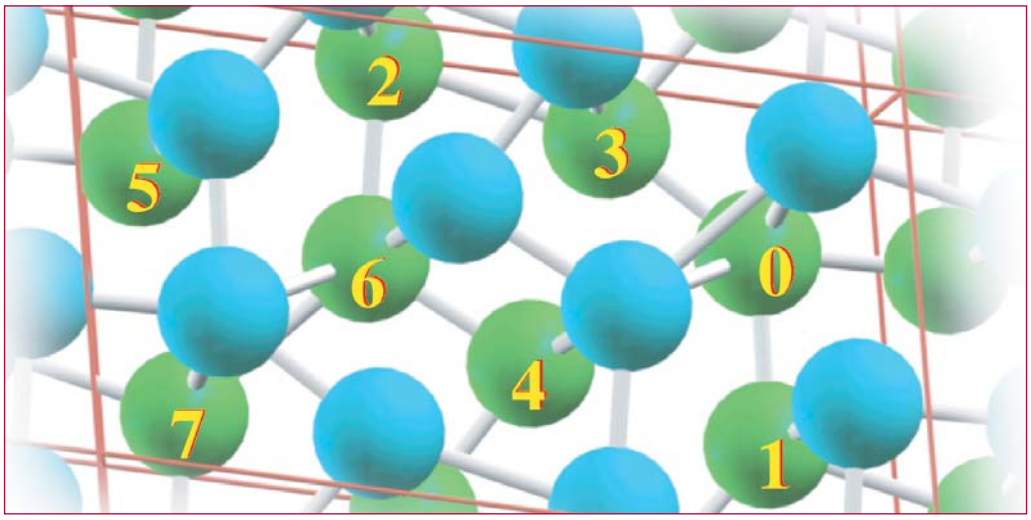

Figure 1— Sixteen atoms make up the unit cell (outlined in red) of alpha-Pu. The atoms are arranged in pairs that span two layers (shown in cyan and green). The two atoms in each pair see the same environment.

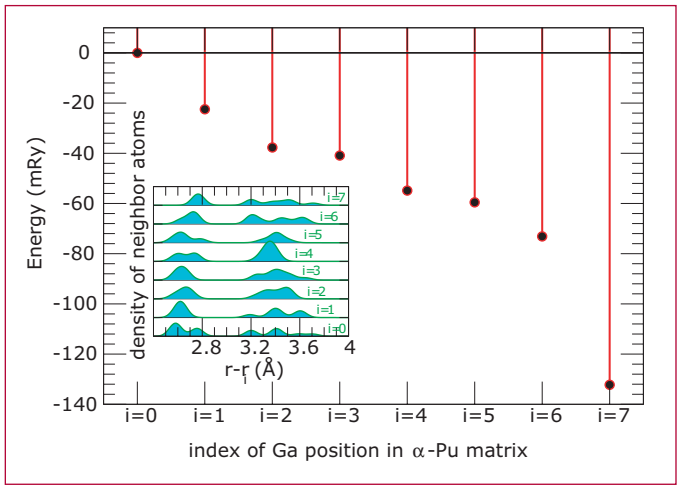

Figure 2— First principles energy for substitutional doping with gallium in the α-Pu matrix. The calculated energy is shown for the eight distinct possible sites, relative to the energy of the first case.

Inset: radial density of neighbor atom positions as seen from each of the eight sites. For visualization purposes the density has been plotted with a 0.05 Å Gaussian broadening.

simulation cell for the bcc crystal structure will reveal whether the Ga atom indeed pushes on its plutonium neighbors; a refined view of the Ga atom's preference among the eight possible substitutional sites in the α-Pu can be expected from relaxing the lattice. These results, if confirmed with additional calculations, have significant implications on the modeling of crystal phases of alloyed plutonium.

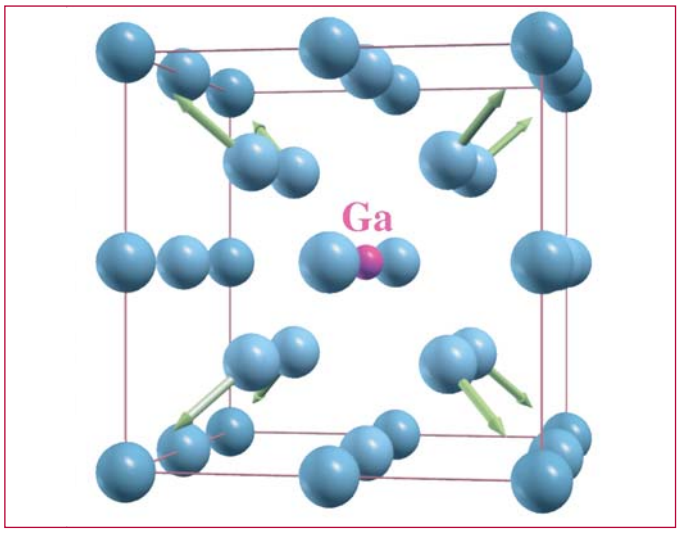

Figure 3— Substitutional doping with gallium in the body-centered cubic (bcc) plutonium matrix. The gallium atom takes the place of a very different plutonium atom, resulting in forces on its neighbors. In the case illustrated here, the Ga atom's position in a sixteen-atom cell constrains the symmetry such that the eight nearest neighbors can move toward it — or away from it. Preliminary calculations show the Ga atom pushes its neighboring plutonium atoms away.

[1] J. D. Becker, J. M. Wills, L. Cox, and B. R. Cooper, *Phys. Rev.* B **58**, 5143 (1998).

Stable and Unstable Phonon Modes in and around bcc Plutonium

Sven P. Rudin, T-1; srudin@lanl.gov

Theoretical studies of the stability of a material's crystal structures often involve calculations of phonon frequencies, for two reasons:
1. the frequencies determine the vibrational contribution to the free energy, which can determine the energetically favored crystal structure among competing candidates;
2. any frequency calculated to be imaginary signifies an unstable phonon mode, indicating that the current crystal structure is mechanically unstable. The wave vector and polarization of the unstable phonon mode directly describe the distortion the crystal would follow to lower its energy. Reported here are distortions of the bcc phase of plutonium calculated in the modified embedded atom model (MEAM) [1], aimed at generating a better understanding of the stability of this high temperature phase. A popular method of calculating phonon frequencies is the frozen phonon method, most often used with first principles codes. The method is straightforward: the atoms in a simulation cell are distorted according to a phonon mode's wave vector and polarization, and the energy is calculated for several magnitudes of the amplitude, allowing direct determination of the frequency. The method requires that the simulation cell be commensurate with the wave vector and that the polarization is known, hence the method has only been used for wave vectors corresponding to high-symmetry points in the Brillouin zone.

Preliminary results from a *generalized* frozen phonon method are reported here. The method does *not* require knowledge of the polarization. Figure 1 shows the frequencies of phonon modes along high-symmetry directions of the

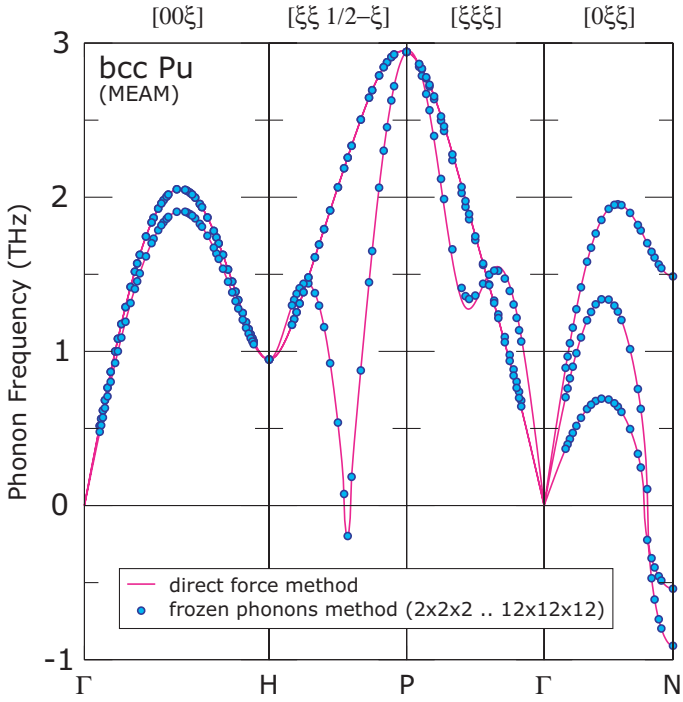

***Figure 1—** Phonon dispersion curves along high- symmetry directions of the bcc crystal for the MEAM of plutonium. The solid line is calculated using the direct force method; the circles are the values from frozen phonon calculations on regular meshes from 2^3 to 12^3 grid points. Imaginary frequencies are plotted as negative.*

bcc crystal for the MEAM of plutonium. The results calculated with the generalized frozen phonon method agree with those obtained by the direct force method. The frequencies were calculated throughout the Brillouin zone on points sitting on 2 x 2 x 2, 3 x 3 x 3, and through 12 x 12 x 12 meshes. Compared to what was previously possible, such mesh sizes are enormous.

In addition to not requiring knowledge of the polarization, the method easily allows an unstable phonon mode to be followed to the distorted crystal structure predicted to be lower in energy by the unstable mode. By proceeding stepwise from small to larger mesh sizes the possible distortions are systematically explored. Figure 2 shows that the magnitude of the imaginary frequency does *not* correlate with the resulting distorted structure's gain in energy over the original crystal.

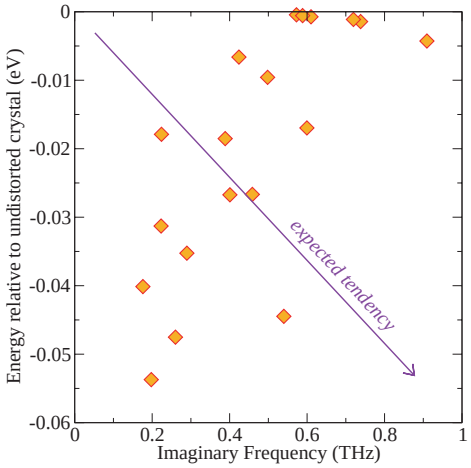

Figure 2— Energy of the distorted structures (relative to the bcc structure) plotted versus the value of the imaginary frequency. There is no systematic relationship between the two entities, i.e., the magnitude of the imaginary frequency does **not** *determine the stability of the resulting structure.*

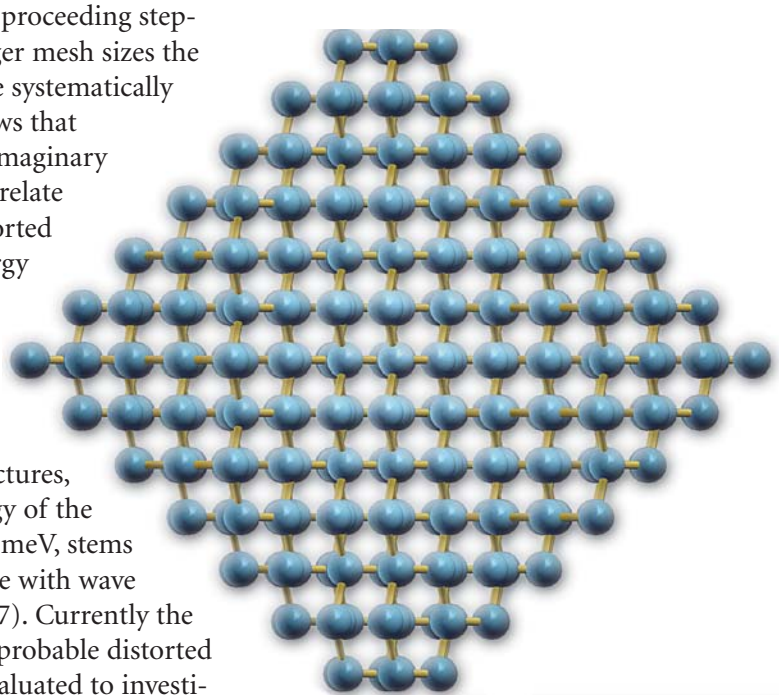

Figure 3— The most favorable of the possible distorted structures. This distortion appears on the 7 x7 x 7 mesh, i.e., in a simulation cell with 343 atoms.

Figure 3 shows the most favorable of the possible distorted structures, which lowers the energy of the crystal structure by 54 meV, stems from a transverse mode with wave vector q = (2/7, 2/7, 5/7). Currently the phonons for the most probable distorted structures are being evaluated to investigate their stability.

[1] M. I. Baskes, *Physical Revue B* **62**, 15532 (2000).

HMX Crystal Diameter Distributions from Image Analysis

Bernd R. Schlei, T-1, schlei@lanl.gov

I perform image analysis of micro graphs of high explosives such as PBX 9501 [1]. The micro-structural features of these materials are of great importance to the weapon materials community.

Digital image processing as it is outlined in [1] can provide a number of different two-dimensional (2D) distribution functions for areas, aspect ratios, separations, etc., of HMX crystals (major component of the high-explosive PBX 9501). In particular, one can compute a distribution function of crystal counts, *1/N dN/dD*, as a function of the diameter *D*, where $D = 2r$ (cf. Figure 4, black curve). Here, *r* denotes the geometric mean between the length and the width of a minimum-enclosing rectangle around a single HMX crystal and it is corrected for the totally covered single crystal area.

Naturally, the question arises, how such a 2D number distribution function, *1/N dN/dD*, relates to measured three-dimensional (3D) volumetric distribution functions, *1/V dV/dD*, of HMX crystals in pressed PBX 9501. Figure 1 shows a measured volume distribution function of HMX crystals [2]. However, the authors [2] forgot to divide each bin of their histogram by the exponentially growing bin width.

The properly corrected distribution function, *1/V dV/dD*, is shown in Figure 2, and it shows three maxima (i.e., a three-modal distribution function). Assuming that $V = D^3$, one can easily-

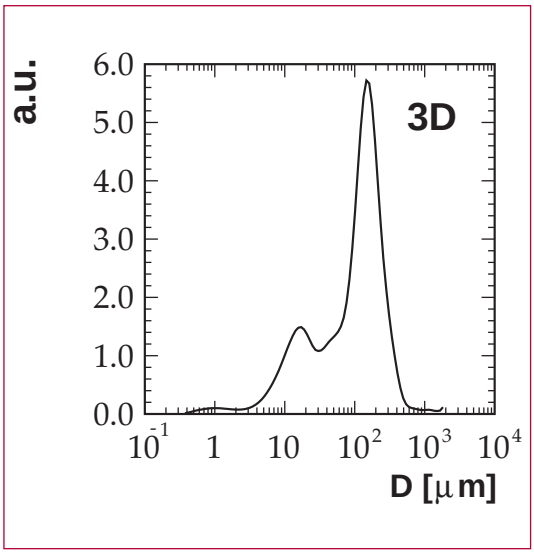

Figure 1—Particle volume distribution of HMX after processing into PBX 9501 [2].

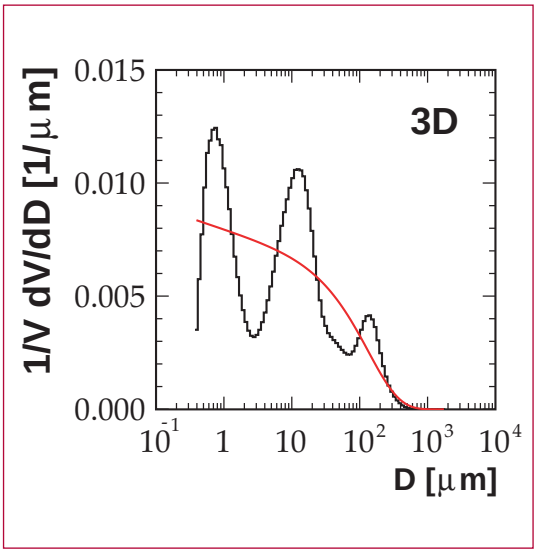

Figure 2—Corrected volume distribution function of Figure 1 (black) and volume distribution function (red) derived from the parameterization function in Figure 3.

transform the 3D volumetric distribution function, *1/V dV/dD*, into a 3D number distribution function, *1/N dN/dD*. The result is shown in Figure 3, and has been parameterized with the analytical expression

$$F(r) = 1/N\ dN/dD = 0.3\ D^{-3.05}\ e^{-D/150} \qquad (1)$$

The function, $F(r) = F(D)$, is shown in Figure 3 compared to the measured number distribution function. Note that the parameterization (1) does not reflect

the three modes of the originally measured distribution function *1/V dV/dD* (cf. also Figure 2).

The distribution function (1) represents a power law with an exponential suppression factor as a function of the crystal diameter *D*. F(r) is a 3D number distribution function. It can be transformed into a 2D number distribution function, $\varphi(x) = \varphi(D)$, where $x = 0.5D$, by following the work of S. D. Wicksell [3]. $\varphi(x)$ is given through the integral

$$\varphi(x) = x/r_o \int_x^R F(r) / \sqrt{r^2 - x^2}\, dr \qquad (2)$$

In Figure 4, $\varphi(D) = 1/N\ dN/dD$ is compared to the 2D distribution function of crystal counts, *1/N dN/dD*, which has been obtained from digital image processing.

The agreement between the two curves in Figure 4 is quite remarkable, since it means that digital image processing can provide useful information about the microstructure of high explosives such as PBX 9501, because the results relate to the 3D experimental measurements so well. Further details, such the effects of the three modes in the experimental distribution functions, are currently being investigated.

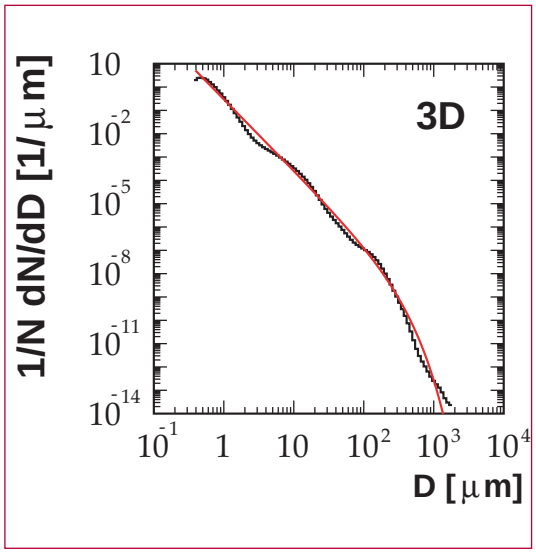

Figure 3— Three-dimensional number distribution function derived from the volume distribution function in Figure 2 (black) and its parameterization (red).

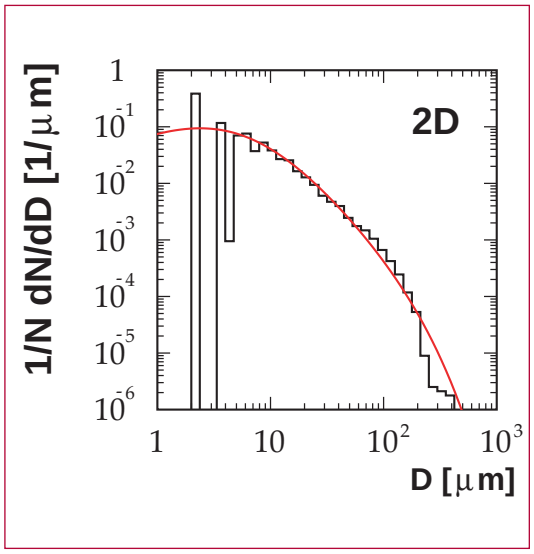

Figure 4— Two-dimensional number distribution function extracted with digital image processing techniques [1] (black) and result of the integrated three-dimensional number distribution function (red).

[1] B. R. Schlei, L. Prasad, A. N. Skourikhine, "*Geometric morphology of granular materials,*" in Vision Geometry IX, Proceedings of SPIE's 45th Annual Meeting, San Diego, CA, Vol. **4117** (2000), pp. 196–201.

[2] C. B. Skidmore, D. S. Phillips, S. F. Son, and B. W. Asay, "*Characterization of HMX Particles in PBX 9501,*" in *Shock Compression of Condensed Matter – 1997*, American Institute of Physics (AIP) Conference Proceedings Vol. **429** (1997), pp. 579–582.

[3] S. D. Wicksell, "*The Corpuscle Problem,*" Biometrika, Vol. **17** (1925), pp. 84–99.

Hyper-Surface Extraction in Four Dimensions

Bernd R. Schlei, T-1; schlei@lanl.gov

The four-dimensional (4-D) analogon to a three-dimensional (3-D) surface is called a hyper-surface. In particular, such a hyper-surface is a volume, which is embedded in a 4-D space. A 4-D space may be given through a 3-D space plus 1-D (one-dimensional) time as the fourth dimension, or by a 3-D space plus a spectral range of gray-levels (e.g., as in 3-D digital image data) as the fourth dimension, etc.

In such 4-D spaces, hyper-surface extraction may be important. For example, in 3+1-D (i.e., 3-D space and 1-D time) hydrodynamic simulations of relativistic heavy-ion collisions, the extraction of a freeze-out hyper-surface (FOHS) allows one to calculate various probability distribution functions for subatomic multiparticle production, which may be compared to experimental observables.

Another important application of hyper-surface extraction lies, e.g., in the field of proton-radiography (pRad). In this field of research, 3-D digital image data are acquired as a function of time. The resulting data sets are therefore (at least!) 4-D. In pRad applications, where the dynamic behaviour of high-explosives (HE) is studied, hyper-surface extraction allows the researcher to better understand the properties of the HE material through quantification. A hyper-surface represents in such an application the continuous temporal evolution of 3-D surfaces. Each 3-D surface may represent—at any given time—a particular shape feature of the material (e.g., a 3-D burn-front).

The STEVE (Space-Time-Enclosing Volume Extraction) [1] algorithm and software is a novel invention, which allows for the extraction of hyper-surfaces from 4-D digital data sets. In particular, the STEVE algorithm is not based on—rather slow—template matching. Because 2^{16} = 65,536 local site neighborhood configurations exist, a much faster linear construction technique is used for the hyper-surface extraction instead.

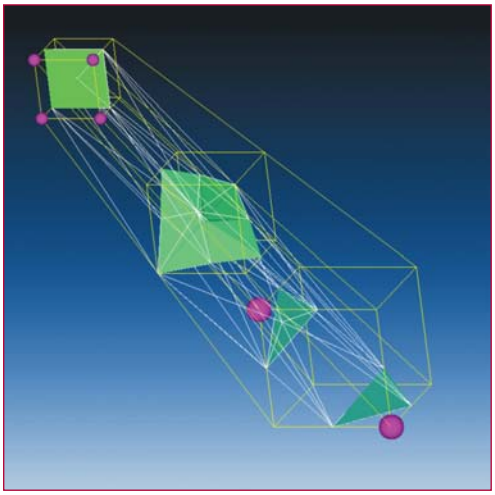

Figure 1—A hyper-surface section in space-time, which is intersected at three constant times (see text)[2].

In Figure 1, a 2 x 2 x 2 x 2 site neighborhood in 3+1-D space-time is shown. Six (purple) sites (four in the past and two in the future, respectively) are separated from the other ten sites by a hyper-surface section, which consists of tetrahedrons (white lines) in this 4-D space.

The hyper-surface section is intersected at three constant times (initial, half, and final time), which results in three different 3-D surface tilings. Please note, that the hyper-surface section can be intersected at any desired time. Therefore, the initial 3-D surface tiling can be transformed continuously and smoothly into the final 3-D surface tiling.

In Figure 2, an example of hyper-surface extraction is shown for 3+1-D hydrodynamic simulation data. The spheres in Figure 2(a) and Figure 2(h) represent

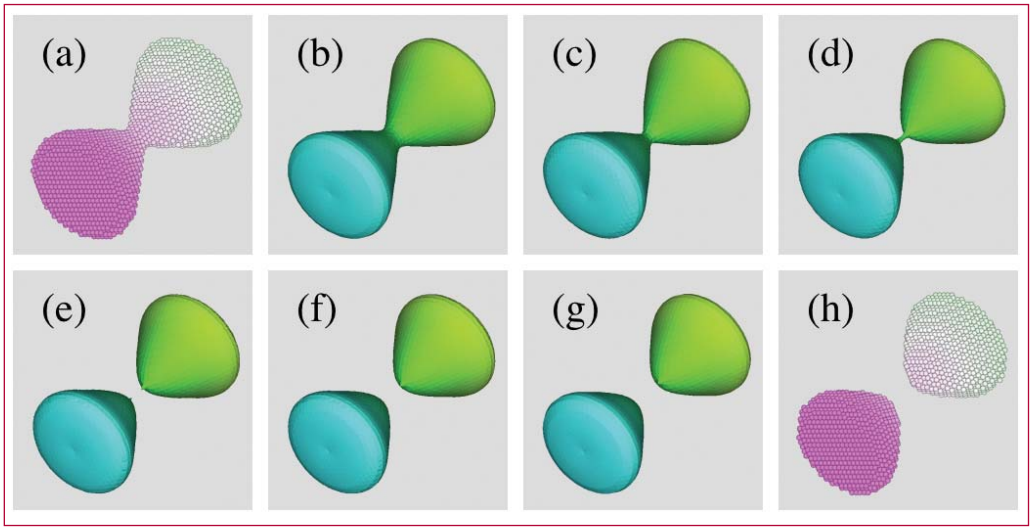

Figure 2— (a) and (h) Selection of sites (spheres) in an initial and a final 3-D data set; (b) and (g) 3-D surfaces, which enclose the sites in (a) and (h); (c)–(f) further 3-D surfaces, which have been extracted by intersecting the hyper-surface of the 4-D union of the sites in (a) and (h).

grid points of the discretized 3-D temperature fields at two subsequent time steps in the numerical simulation, which are enclosed with a FOHS (of fixed temperature) by applying the STEVE algorithm. Various time projections of the FOHS are shown in Figures 2(b)–2(g).

Please note, that it is sufficient to digitally store the data as shown in Figures 2(a) and 2(h), in order to extract an infinite number of temporarily evolving 3-D surfaces. Therefore, the STEVE algorithm will enable also a memory efficient storage technology for temporarily evolving digital 3-D surfaces, because of its 4-D reconstruction capability.

[1] B. R. Schlei, "STEVE–Space-Time-Enclosing Surface Extraction," in preparation.

[2] B. R. Schlei, "Isosurfacing in Four Dimensions," in Theoretical Division Quarterly, Spring 2004, LA-UR-04-tbd.

[3] B. R. Schlei, "Hyper-Surface Extraction in Four Dimensions," 2004, in LA-UR-04-1546.
http://t1web.lanl.gov/schlei/

Magnetic Anisotropy in Strained-Layer Nanomaterials

John M. Wills, Anders M. Niklasson, and Sven P. Rudin, T-1; jxw@lanl.gov

A key challenge in nanotechnology, an institutional research goal at LANL, is to understand how the tailoring of materials on the nanoscale can lead to novel and enhanced functionalities. A collaboration between MST, T, and LANSCE, led by Michael Nastassi (MST-8), is probing the structural, transport, and magnetic properties of nanolayered materials through an iterative process of experiment and theoretical calculations.

Properties of nanoscale materials, which affect material properties, include quantum size effects, interfacial chemistry, interference, and induced strain. We are studying the effects of induced strain on magnetic anisotropy in metallic nanolayers. A magnetic material, cobolt, is sandwiched between layers of gold (nonmagnetic) deposited on copper, and the crystal structure and magnetic moment direction of the Co layer are measured as a function of substrate Au thickness.

Figure 1 shows a TEM image of the experimental system. Successive layers of Cu, Au, Co, and Au are deposited in a 111 Si substrate. Cu and Au are (111) fcc. When the Au substrate is six monolayers, the Co layers have a hexagonal-close-packed crystal structure, and the magnetic moment is out-of-plane (normal to the crystalline planes). In contrast, on two monolayers of Au, Co grows in a tetragonally distorted face-centered cubic crystal structure, with a magnetic moment lying in-plane at room temperatures, and out of plane at low temperatures.

We are using first-principles electronic structure calculations to study this behavior. An LMTO-Greens function method is being employed for semi-infinite layered nanostructures, where density functional theory and the local spin density approximation are used to calculate total energies and the spin density. For structural properties and magnetic anisotropy, we use a full potential LMTO method.

The full system is beyond the scope of first-principles calculation; we are studing the material by calculating properties of isolated (and idealized) subsystems. Figure 2 shows a

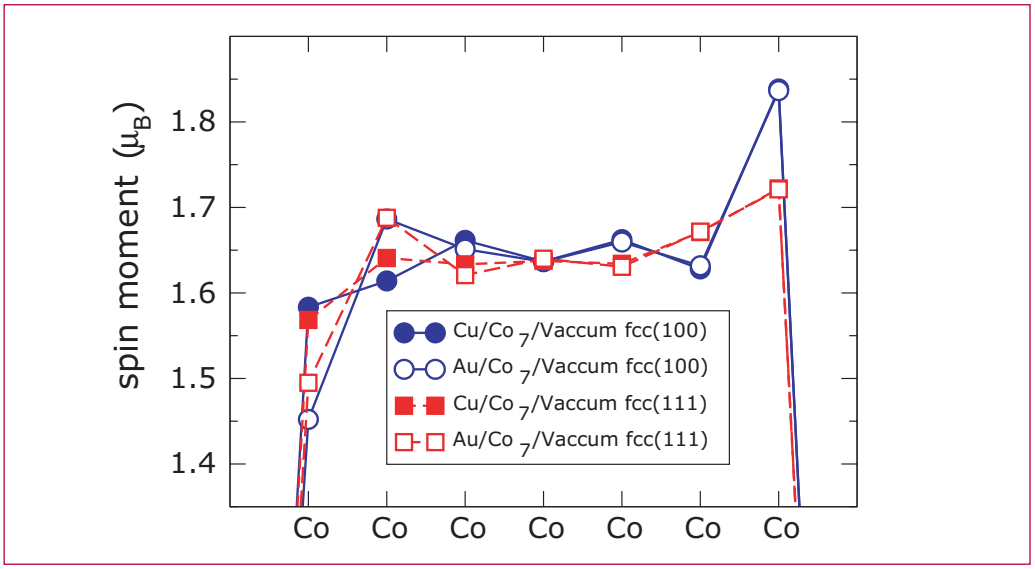

Figure 1—

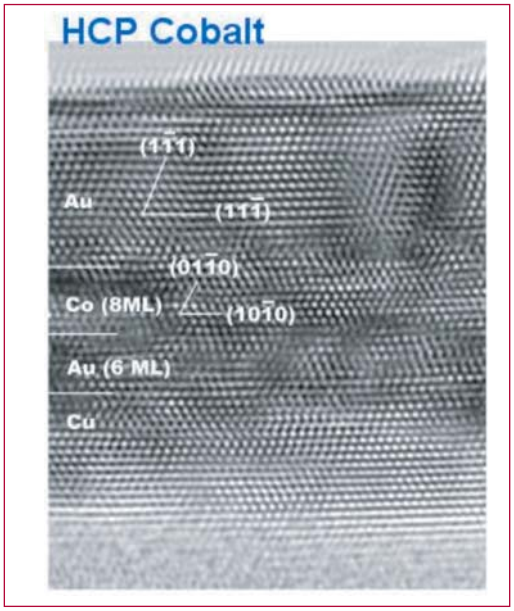

Figure 2—

calculation of the magnetic moment of a Co surface on two Cu and Au substrates. In this calculation, Co has its natural volume, controlling the lattice spacing of the Cu or Au substrates.

With this calculation, we study an effect of interfacial chemistry on magnetic behavior. We see in Figure 2 that the Co moment in the interfacial layer is reduced by approximately 10% by the proximity of Au, as compared with Cu. The difference may be understood as an increase in hybridization between Au and Co electronic states compared to the Cu/Co interface.

Another influence on magnetic properties is the strain induced in the Co layers by the substrate. We expect that two monolayers of Au would have a lattice constant close to that of the Cu substrate (see Figure 1), while six monolayers of Au would have a lattice constant closer to that of bulk Au, accumulated strain being relieved by a dislocation mechanism.

We therefore are studying the behavior of bulk Co as a function of "in-plane" strain. Calculations are being performed for both hcp Co (with strains perpendicular to (001)) and fcc Co (with strains perpendicular to (111)). Figure 3 shows the difference in energy, in units of temperature (dE/kb), between strained hcp and fcc Co as a function of in-plane lattice constant. The trend disagrees with the experimental structural observation. Near the gold lattice constant, corresponding to the six monolayer configuration, structural effects are small and most likely dominated by other effects. Calculations of the corresponding anisotropy are in progress.

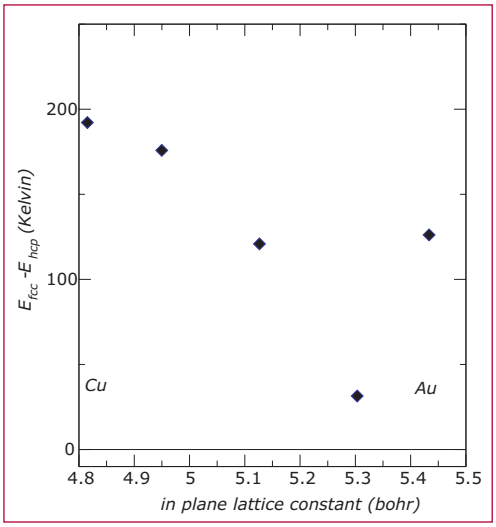

Figure 3—

The ability to modify the magnetic anisotropy by strain, interfacial chemistry, and quantum size effects will be investigated systematically for a variety of layered nanosystems. In particular, we look for interface stabilizing mechanisms, material properties that can enhance quantum size effects, as well as materials where strain effects can be modified reversibly. The systematic knowledge of separate effects will help us predict a new generation of nanomaterials previously out of reach of traditional materials science.

T-4 Atomic and Optical Theory

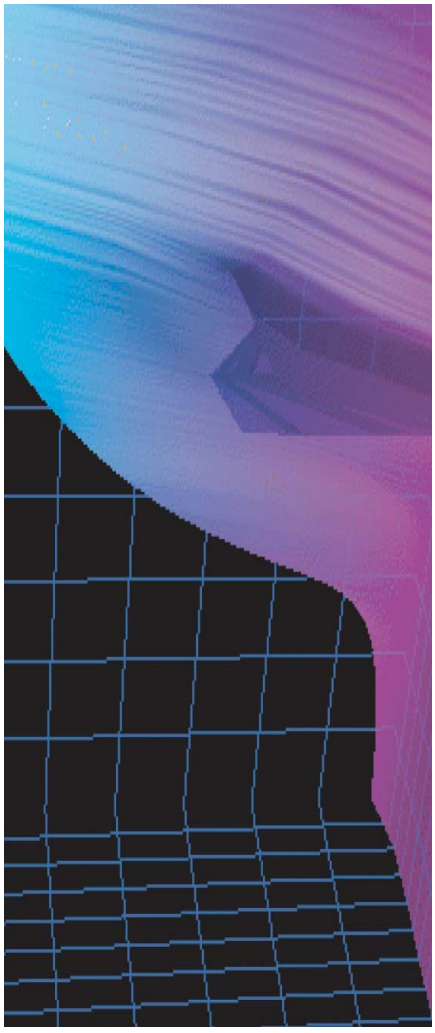

ATOMIC Benchmark Opacity Calculation

Joseph Abdallah, Jr., Peter Hakel, David P. Kilcrease, Norman H. Magee, Stephane F. Mazevet, and Manolo E. Sherrill, T-4; Christopher J. Fontes and Honglin Zhang, X-5; abd@lanl.gov

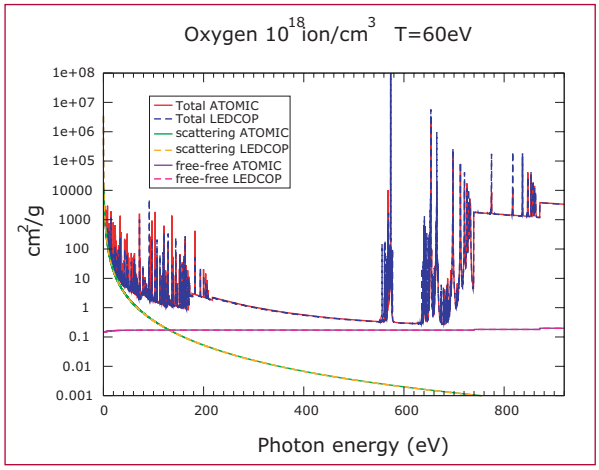

Figure 1—Comparison of the frequency dependent opacities calculated by ATOMIC and LEDCOP.

We report on meeting the first milestone for the development of ATOMIC, a code designed to compute opacities under both LTE (local thermodynamic equilibrium) and non-LTE conditions for a large range of elements. ATOMIC will become the successor of the T-4 opacity code LEDCOP, and our first milestone calculation centers on a direct benchmark comparison of opacities computed by each code. This benchmark calculation aims at demonstrating that all the major physics capabilities of LEDCOP have been successfully transfered to ATOMIC.

The basis of ATOMIC is the FORTRAN 90 reconstruction of the FINE nonequilibrium spectral modeling code, to which physics packages extracted from the T-4 opacity code LEDCOP have been added. ATOMIC provides improved atomic physics data, a user-friendly interface, modularity to facilitate code improvements, platform independence, and less manipulation of the atomic physics databases than is currently necessary for LEDCOP. The development of ATOMIC in FORTRAN 90 also provides a platform for parallelization of both LTE and non-LTE calculations in the future. The bound-bound and bound-free treatments from FINE remain mostly intact in ATOMIC. The LEDCOP physics packages necessary to compute opacities, the free-free, Thomson and Compton scattering, Stark and collisional broadening as well as conductive opacity were converted to FORTRAN 90 and implemented in ATOMIC.

ATOMIC makes use of a new scheme to include plasma and density effects. A preliminary package has been developed, implemented in ATOMIC and tested against the LEDCOP results. It is hoped that this package will also overcome some of the limitations of the equation of state (EOS) used in LEDCOP. A method involving histograms for binning the line strength as a function of photon energy was also developed and implemented in ATOMIC to process the enormous amount of spectral line information that is required. This method greatly reduces the amount of computer time necessary over traditional methods where a shape is computed separately for each spectral line. Parallel implementation of the calculation of the bound-bound contribution has also been explored. The initial scaling obtained, which corresponds to number of processors divided by two for up to eight processors, is encouraging and the will method be further developed and implemented in ATOMIC in the coming year. In the FORTRAN 90 conversion of FINE every effort was made to preserve

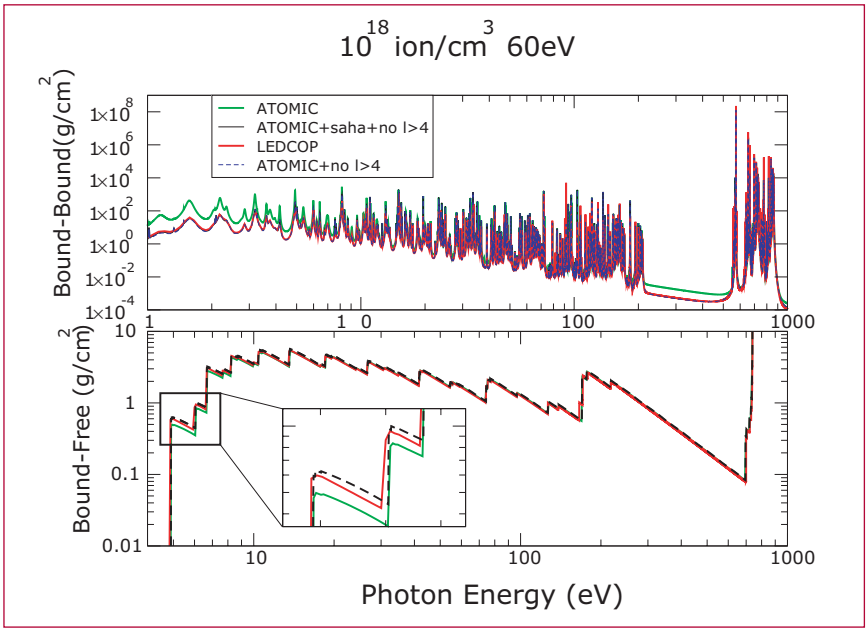

Figure 2— Comparison of the bound-bound and bound-free contributions between ATOMIC and LEDCOP.

(cm^2/g)	κ_R^{AT}	κ_R^{LED}	κ_P^{AT}	κ_P^{LED}
$\rho = 1.10^{18}$ ion / cm^2 T=30eV	1.06×10^{1}	1.02×10^{1}	1.03×10^{2}	1.16×10^{2}
$\rho = 1.10^{18}$ ion / cm^2 T=60eV	9.48×10^{-1}	9.32×10^{-1}	7.97×10^{3}	4.64×10^{3}
$\rho = 2.5\times10^{19}$ ion / cm^2 T=30eV	3.39×10^{2}	3.46×10^{2}	1.94×10^{3}	1.72×10^{3}

Table— Comparison between the ATOMIC and LEDCOP opacity calculations for oxygen. AT: ATOMIC, LED: LEDCOP, R: Rosseland, P: Planck.

the non-LTE capabilities. Most of the important non-LTE options in ATOMIC have been debugged, tested, and give identical results to the F77 FINE code. ATOMIC has been used to calculate test cases for the upcoming NLTE3 workshop being held in December 2003 at NIST in Gaithersburg. A suite of regression tests for ATOMIC was developed for quality control. This project also makes use of the RAZOR database management software for version control.

Figures 1 and 2 and the table show a sample of the initial comparison between ATOMIC and LEDCOP. This initial comparison shows that ATOMIC has been successfully converted into an opacity code and contains the main components required for an opacity calculation.This effort will continue in the coming year by extending the temperature-density range of the new EOS model, by improving the physics models used in the transfered LEDCOP packages, and by developing an edge broadening model to account more accurately than in LEDCOP for the density effects on the bound and continuum states. The parallel calculation of different density-temperature points and the bound-bound contribution will also be implemented in ATOMIC.

Time Dependent Boltzmann-Kinetic Model of the X-rays Produced by the Ultrashort Pulse Laser Irradiation of Argon Clusters

Joseph Abdallah, Jr. and George Csanak, T-4; Y. Fukuda, Y. Akahane, M. Aoyama, N. Inoue, H. Ueda, and K. Yamakawa, Advanced Photon Research Center; A. Ya. Faenov, A. I. Magunov, T. A. Pikuz, and I. Yu. Skobelev, Multicharged Ions Spectra Data Center; abd@lanl.gov

The Boltzmann equation and a detailed collisional radiative model are solved simultaneously as a function of time to model the time integrated X-ray spectra of the transient plasma produced by a high, intensity ultra-fast laser source. Level populations are calculated by solving the rate equations as a function of time using rate coefficients corresponding to a time varying electron energy distribution function (EEDF) determined by the solution to the Boltzmann equation including inelastic and elastic collision processes. The elastic electron-electron interactions are included through the solution of the Fokker-Planck equation. To our knowledge, this is the most detailed calculation of the spectroscopic properties of a plasma using nonequilibrium electron energy distribution functions. The calculations solve for the distribution of 100 electron energy bins simultaneously with the populations of over 3000 levels for Ne-like to H-like argon. The calculations took 215 hours of CPU time on a single processor of an SGI Origin 200 computer.

It is assumed that all the ions are initially in the Ne-like ground state as a result of irradiation by the laser prepulse with an electron density of 6×10^{20}. Initially all the free electrons are assumed to have a mono-energetic distribution of 5 KeV as a result of the fast laser deposition from the main pulse. The results are compared to highly resolved F-like to He-like K-shell emission spectra recorded recently during ultra-short laser experiments with argon cluster targets in Japan. The laser had a 30fs duration and an intensity of 1.3×10^{19} W/cm^3.

Figure 1 shows the calculated EEDF for various times between 0 and 3 picoseconds. Note that the 0 ps EEDF is spiked at 5 KeV and corresponds to the initial conditions discussed above. At first, the EEDF broadens very quickly around 5 KeV and starts building up a small low-energy component. As time increases the low-energy component gets larger and the beam-like component around 5 KeV gets smaller. By 3 ps the tail is gone and the EEDF is completely Maxwellian with a temperature near 1500 eV. The calculated timescale for emission is consistent with estimates of cluster decay times for these conditions.

Figure 2 shows a comparison of the calculated time integrated spectra to 3 ps compared to the experimental measurement. The agreement with experiment for the He-like to Be-like emission is quite good. Note that the experimental spectral line occurring near 4 angstroms is spurious and corresponds to He radiation from a different order of crystal reflection. Also note that for Li-like to B-like that the fine details of the calculated spectra within an ion stage, including relative line positions and intensities are in remarkable agreement with experiment. However, the calculated relative intensities of the lower charged ions, C-like to F-like are somewhat low. The calculations also show the typical Li-like and Be-like satellite structure, sometimes attributed to a hot electron component in the EEDF, can also be due to transient effects in a high-temperature ionizing plasma.

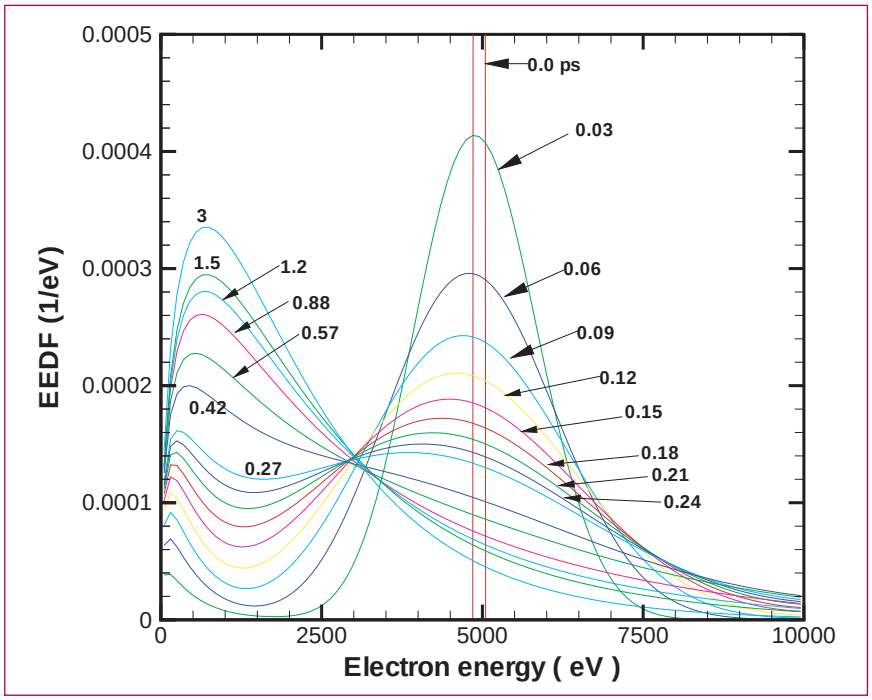

Figure 1— The calculated EEDF at various times between 0 and 3 ps.

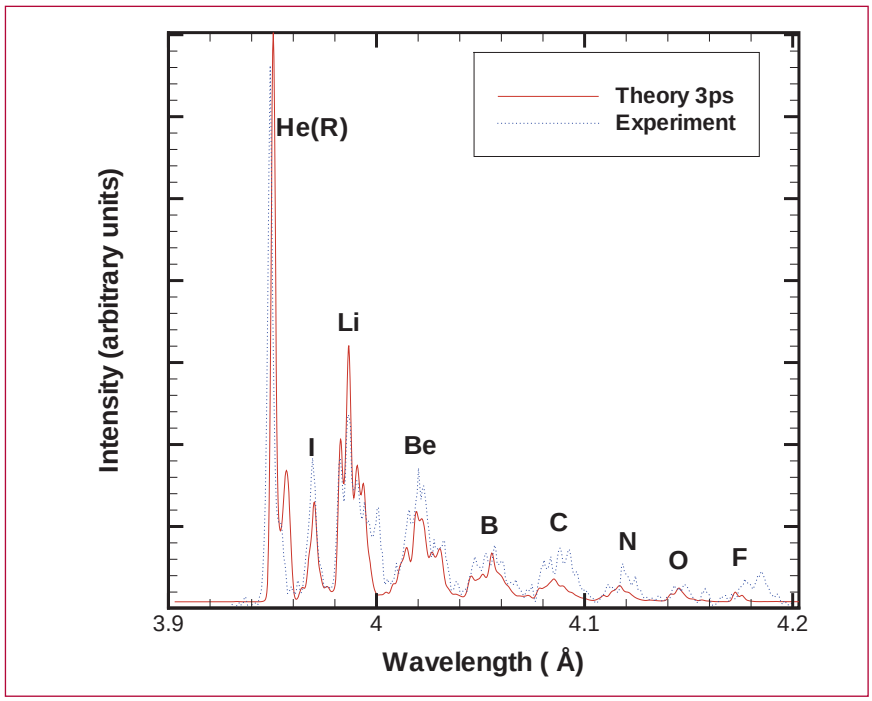

Figure 2— Comparison of spectra calculated at 3 ps and experiment.

Benchmarking Aluminum Opacity Libraries Using Quantum Molecular Dynamics

Stephane F. Mazevet, Lee A. Collins, and Norman H. Magee, T-4; Joel D. Kress, T-12; Eric D. Chisolm and Scott Crockett; T-1, and M. Desjourlais, Sandia National Laboratory; smazevet@lanl.gov

Many opacity libraries commonly in use for standard macroscopic modeling programs such as in hydrodynamic codes use absorption cross sections derived for isolated atoms or ions while many-body and plasma effects are modeled as perturbations to the population distribution over these atomic states, reintroduced as adjustments to the final results, or both. In the mean time, developments in a wide variety of fields, including dense plasma, inertial confinement fusion, and astrophysics, require an extension of the opacity libraries into new and complex regimes where such a simple approach to the many-body effects quickly becomes questionable.

The relatively low-temperature, high-density regime (a few eV and few g/cm^3), often labeled as "warm dense matter," is an example of such a situation where the intricate nature of the medium, partially dissociated and ionized, intermediate coupling, $\Gamma \sim 1$, and partially degenerate $\eta \sim 1$, requires a careful validation of the physical models that produce the opacity data either from experiments or more sophisticated theoretical methods. In this regime, usually reached experimentally by shock compression in the Mbar range, the accurate knowledge of opacities drives the modeling of diverse systems from white dwarf atmospheres, which play a key role in latest attempts to date various astrophysical objects, to strongly coupled plasmas produced by exploding aluminum wires.

Quantum Molecular Dynamics (QMD) simulations provide an effective venue to calculate and benchmark Rosseland mean opacities in this regime [1,2]. This *ab-initio* approach produces a consistent set of material, electrical, and optical properties from the same simulation and can be applied without restriction to various mixtures of atomic, ionic, or molecular species [3,4]. This contrasts

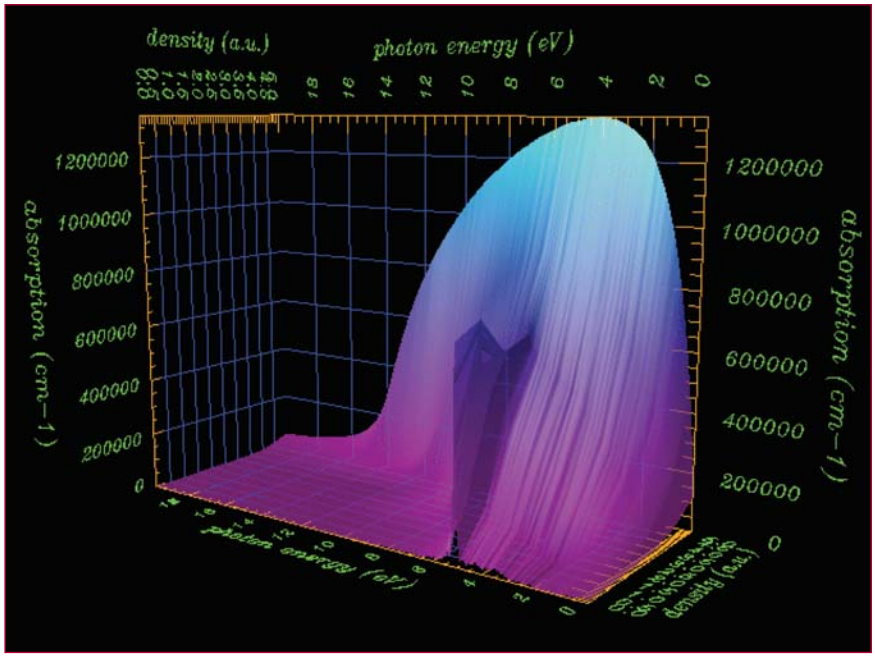

***Figure 1—** Variation of the QMD aluminum absorption coefficient as a function of density and for a temperature of 10000 K.*

with the opacity libraries, which consist of an integrated collection of approximate models leading sometimes to inconsistencies on the overall nature of the medium. This situation is illustrated here, for the case of aluminum, where we use QMD to benchmark the opacities calculated using the Los Alamos Light Element Opacity code, LEDCOP, for densities and temperatures ranging from gas (~ 0.01 g/cm^3 and T = 10,000 K) to liquid density (~ 2 g/cm^3 and T = 10,000 K). We choose aluminum in this particular density-temperature range as it exacerbates the limitation of the model used in the LEDCOP opacity code and illustrates the difficulty in extending current opacity libraries into the warm dense matter regime.

For a density varying from 0.01g /cm^3 to 2 g/cm^3 and temperatures ranging from 10,000 K to 30,000K, aluminum, which starts as an atomic gas, gradually becomes a liquid metal at the highest density. This situation is illustrated in Figure 1, where we show the absorption coefficient calculated using the QMD method at a fixed temperature of 10,000 K and for the density range given above. At the lowest density, ρ = 0.01 g/cm^3, the QMD absorption coefficient exhibits a maximum centered around 5.1eV. This maximum corresponds to the atomic 3s-3p transition, which value is in good agreement with the averaged configuration energy value of 5.18 eV. As the density slowly increases, the maximum at 5.1 eV gradually decreases with a rise of the absorption coefficient at zero photon energy corresponding to an increase in conductivity. This clearly indicates that as the density increases, aluminum gradually ionizes and forms a metal. At the highest density shown, ρ = 2 g/cm^3, and a temperature of 10,000 K, aluminum is known to be a metal and the absorption coefficient shows a broad maximum around 15 eV, characteristic of the optical response for a plasma [1]. For this photon energy region, the corresponding index of refraction shows a broad minimum with a value less than unity centered at a photon frequency corresponding to the plasma frequency of the system. In this regime, the low-frequency part of the QMD absorption coefficient, AC conductivity, and index of refraction, all related by the Kramer relations, can be easily fitted by a Drude form.

In Figure 2, we show a direct comparison of the QMD and LEDCOP absorption coefficients at this same density-temperature point. The two maxima around 100 and 1000 eV for the LEDCOP absorption coefficient correspond to the ionization of the 2s, 2p, and 1s inner shells of atomic aluminum. While formally an all-electron potential can be used in the QMD, these electronic shells are not included in the current calculations. For the density-temperature case considered here, this has little effect on the calculation of the Rosseland opacity

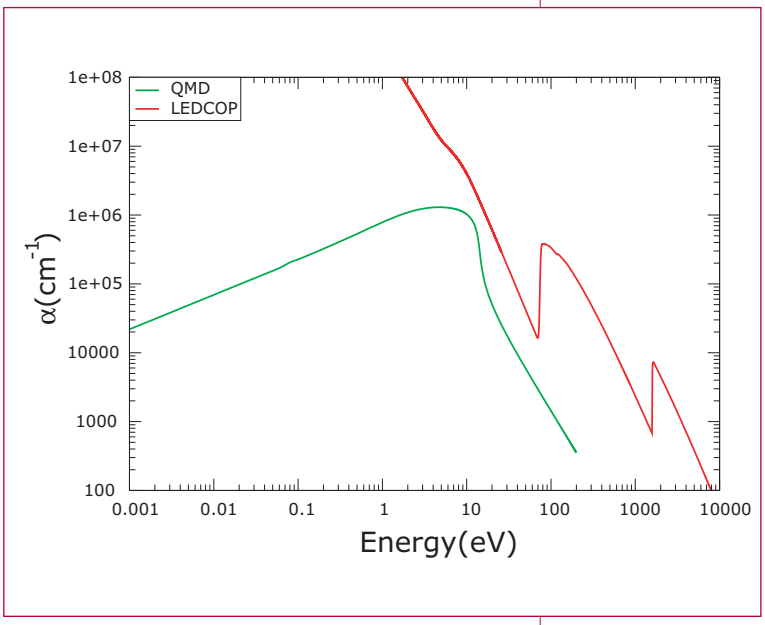

Figure 2—Comparison between the QMD and LEDCOP absorption coefficient for a density of 2 g/cm^3 and a temperature of T = 10,000 K.

as the derivative of the Planck function, and hence the Rosseland mean, samples the absorption coefficient at photon energy around 4 eV. For photon energies less than 10 eV, we see in Figure 2 a significant deviation between the two calculations. This can be traced back to the inadequacy of the free-free approximation used in the LEDCOP calculation. This limitation was already pointed out for the case of hydrogen [1,2], and a free-free approximation accounting for the metallic behavior of the sample at these conditions needs to be developed to enable the extension of the opacity library into this regime.

We now turn to the second major limitation for extending the current LEDCOP opacity library to the warm dense matter regime. We show in Figure 3 the calculation of the 10,000 K and 30,000 K isotherms for densities corresponding to the range shown in Figure 1. First, for the whole density range and for both isotherms, we find a remarkable agreement between the QMD and the predictions of the best current SESAME EOS for aluminum [6], and another aluminum EOS developed for high densities using lattice dynamics, Wallace's liquid dynamics, and density functional theory [7]. This confirms that QMD captures the physical processes in action as the media evolves from an atomic system to a metallic fluid. For densities below 0.1 g/cm^3, we also find a good agreement between the QMD and the LEDCOP isotherms. As the density increases and density effects become more important, the LEDCOP isotherms drastically deviate from the other calculations for densities between 0.2 g/cm^3 and 2 g/cm^3. For this density range, the LEDCOP inaccurate isotherms are due to limitations in the EOS model. In this regime, the effect of the environment on the atomic system can no longer be treated as a perturbation and the competing ionization and recombination processes need to be accounted for accuratly. The current LEDCOP EOS model, while appropriate for low-density calculations, is pushed here outside of its range of validity.

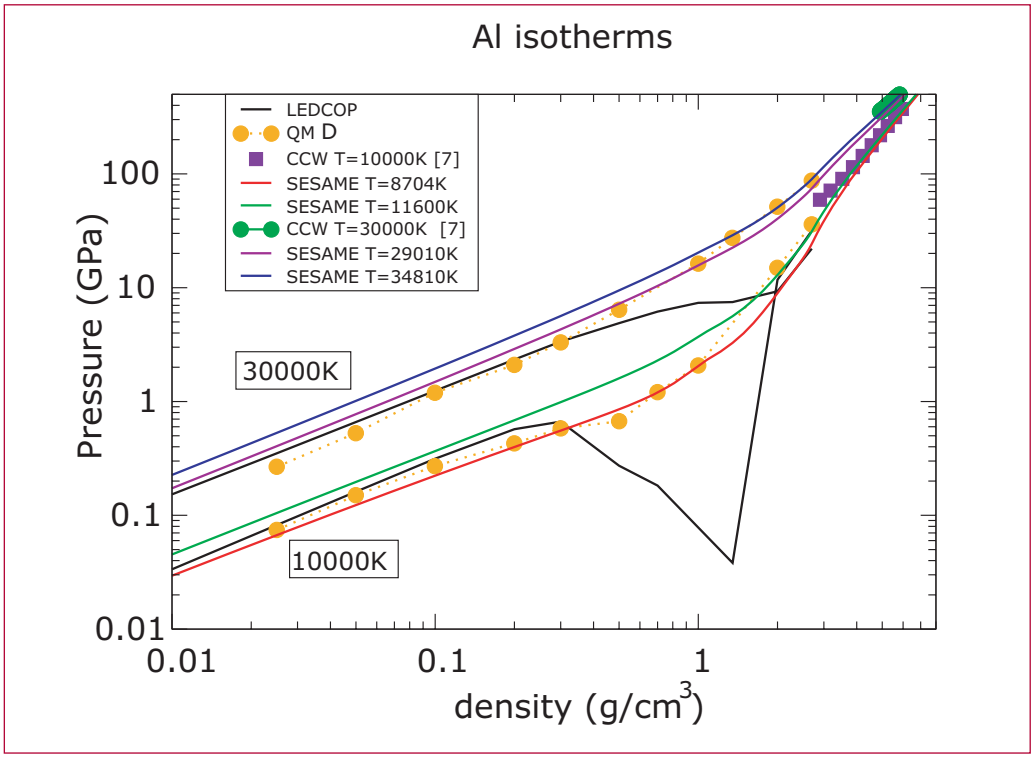

Figure 3—Comparison of the QMD aluminum isotherms with SESAME and LEDCOP isotherms.

In conclusion, we benchmarked the aluminum opacity calculations performed by the LEDCOP opacity code using QMD. We find that to extend the library into the warm dense matter regime, a new model of the free-free contribution, accounting for the metallic behavior of the media, is required. A new EOS model is also needed to successfully describe the smooth transition from an atomic system to a metallic fluid. This requires us to account more accurately for density effects and how the atomic bound states are gradually depopulated due to the increasing density. This issue is at the heart of the new EOS model developed for the new T-4 opacity code named ATOMIC.

[1] S. Mazevet et al., LANL report, LA-UR-02-1342 (2002).
[2] S. Mazevet et al., *Astronomy & Astrophysics* **405**, L5 (2003)
[3] S. Mazevet et al., *Phys. Rev. B* **67**, 054201 (2003).
[4] L. A. Collins et al., *PRB* **63**, 184110 (2001).
[5] C. Neuforge-Verheecke et al., *APJ* **561**, 450 (2001).
[6] SESAME EOS 3717, found in S. P. Lyon and J. D. Johnson, "T-1 Handbook of the SESAME Equation of State Library," LANL report, LA-CP-98-100.
[7] E. Chisolm, S. Crockett, and D. Wallace, *Phys. Rev. B* **68**, 104103 (2003).

Quantum Molecular Dynamics Simulations of Shocked Nitrogen Oxide

Stephane F. Mazevet and Lee A. Collins, T-4; Joel D. Kress, T-12; and P. Blottiau, DPTA; smazevet@lanl.gov

The study of materials under extreme conditions of temperature and pressure has made significant progress in the past few years due to noticeable advances in both the experimental and theoretical techniques. On the experimental side, Z-pinch and laser-driven experimental setups have pushed Hugoniot measurements up to the Mbar range. On the theoretical side, simulation methods, such as Quantum Molecular Dynamics and Path Integral Monte Carlo, now allow the study of materials under such conditions from a mostly "ab-initio" standpoint. Up to now, however, applications of these methods primarily focused on pure systems such [1] as hydrogen, nitrogen [2], and oxygen, and lately on complementing the study of the equation of state (EOS) with the determination of the associated optical and electrical properties [2–5].

We report here on the study of the EOS and dissociation of NO along the principal and second shock Hugoniots using Quantum Molecular Dynamics (QMD). While NO presents a natural extension to study the EOS of multicomponents systems, it also serves as a prototype for the study of explosive compounds and their associated reactive chemistry. Furthermore, the determination of reactive potentials, necessary for the study of technologically relevant and more complex systems such as H-C-N-O, also requires first a calibration to the NO system. Up to now, this calibration has been solely supported by the experimental measurements of the first- and second-shock Hugoniots. To complement the latter, we calculate the first- and second-shock Hugoniots as well as the corresponding temperature up to pressures of, respectively, 80 GPa and 65 GPa. We further pay particular attention to the constituency of the fluid along each Hugoniots since the chemistry induced by such an increase of pressure and temperature remains among the most challenging aspects in the modeling of such systems. Quantum molecular dynamics methods, where the electrons receive a fully quantum mechanical treatment, are particularly suited for the study of such chemical processes as ionization, recombination, dissociation, and association of the various atomic species present in the media are treated on an equal footing within the framework of the Density Functional Theory (DFT).

In Figure 1 we compare the results of initial QMD calculations, using 54 atoms in the simulation cell, with the available experimental measurements for the principal (first) and highest second-shock Hugoniots. Principal Hugoniot points are the density-pressure (and internal energy) points reached when the shock wave crosses the media while the second-shock Hugoniots occur experimentally when the shock wave bounces back across the sample a second time. For the first shock, we plot the individual measurements instead of the averaged ones as the highest density points represent the initial conditions for the second shock points that will be discussed below. For the highest density reached experimentally along the first shock, $\rho = 2.38$ g/cm^3, we find good agreement between the calculations and the measurements. The QMD pressure at this density is P = 26.87 GPa and compares well with the experimental one P = 28.47 GPa. This agreement carries over to the particle and shock velocities where we obtain $u_p = 3.16$ kms^{-1} and $u_s = 6.73$ kms^{-1} compared to the

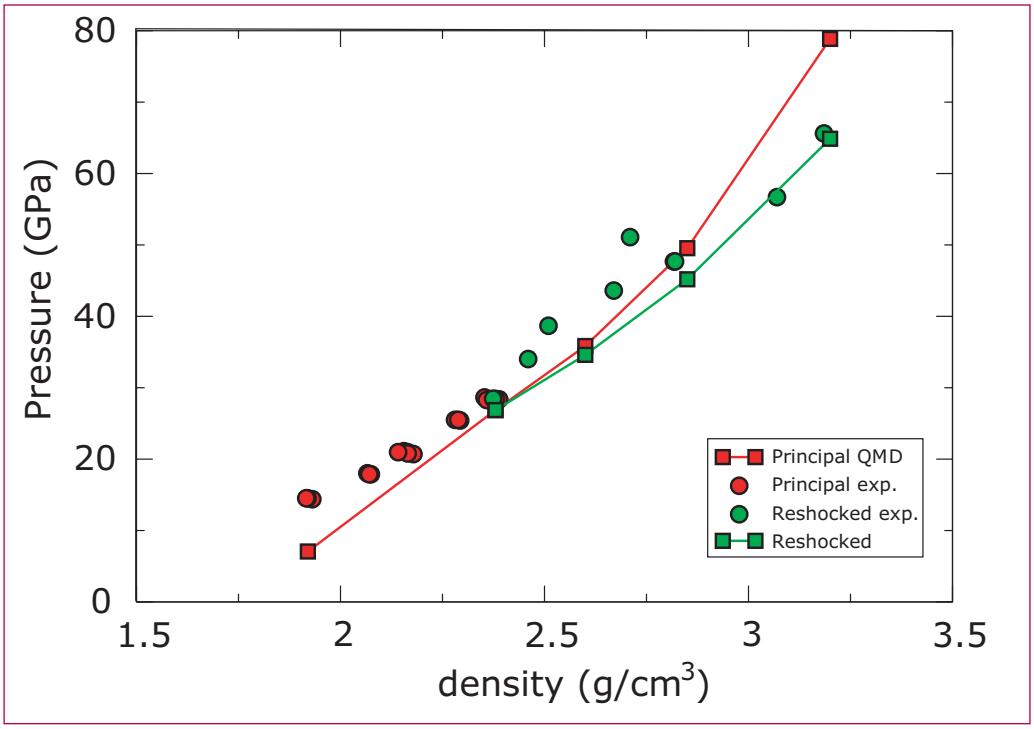

Figure 1—Principal and reshocked NO Hugoniots.

experimental results of, respectively, 3.245 and 6.94 kms^{-1}. The agreement along the first-shock Hugoniot deteriorates as the density is lowered, with a factor of two lower for the QMD pressure at the lowest density measured. This disagreement could be due to the limited number of particles used in the simulation and is currently under investigation using a larger sample in the simulation cell.

For the second-shock Hugoniot, we plotted as experimental results the pressure points obtained for the highest first-shock densities, between 2.28 and 2.38 g/cm^3. The theoretical second-shock Hugoniot is calculated using the calculations performed at ρ = 2.38 g/cm^3 only. Such a small variation in the initial conditions does not substantially affect the final second-shock pressures. This variation does not, for example, explain the consistently higher experimental pressures measured for the second shock at densities between 2.5 and 2.75 g/cm^3. However, a closer inspection of Figure 1 reveals that, first, this disagreement mostly disappears as the density increases and, second that a significant scatter exists in the experimental data for densities above 2.75 g/cm^3. These two points combined with the good description of the first-shock Hugoniot in the region around 2.38 g/cm^3 suggests that QMD provides a satisfactory description of the state of the fluid as the simultaneous increase in pressure and temperature breaks the molecular bonds.

To quantify the state of the fluid as the density increases, we calculate the pair correlation functions representative of each possible diatomic species, NO, O_2, and N_2. Figure 2 shows such a result along the first Hugoniot and extendbeyond the density range explored experimentally. At the lowest density, ρ = 1.92 g/cm^3, the NO correlation function $g_{N-O}(r)$ peaks at around $2a_B$, the internuclear distance of the NO

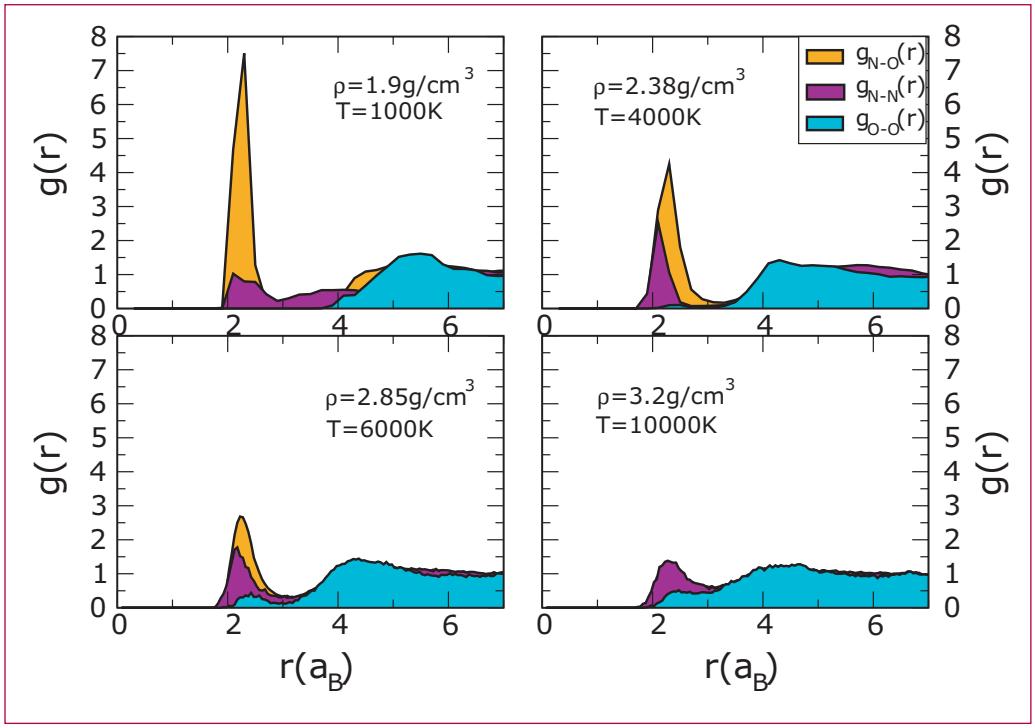

Figure 2—
Pair correlatiion functions along the Principal NO Hugoniot

molecule. The lack of structure in the pair correlation functions of the other two species indicates that the fluid mostly consists of NO molecules at this condition. As the density increases to $\rho = 2.38$ g/cm^3, the sizable reduction and broadening of the maximum of $g_{N–O}(r)$ around $2a_B$ indicates that the fluid has partially dissociated. At this density, a similar structure is now also present for the nitrogen pair correlation function $g_{N–O}(r)$. As the equilibrium internuclear radius of N_2 and NO are similar, $r_{N–O} = 2.17a_B$ and $r_{N\text{-}O} = 2.06a_B$, the pair correlation functions at 2.38 g/cm^3 indicate that the NO fluid has partially dissociated and is constituted of a mixture of NO and N_2 molecules, as well as atomic oxygen. We also notice that at this density, the lack of structure in the oxygen correlation function $g_{O–O}(r)$ indicates that, in contrast to nitrogen, oxygen does not recombine upon dissociation of NO at this density. Figure 2 shows that the constituency of the fluid preserves the same characteristics up to a density of 3.2 g/cm^3. While NO and N_2 continue to dissociate as the density increases, molecular nitrogen represents a significant fraction of the molecules in the sample while oxygen stays mostly in an atomic state.

Despite the limited number of atoms used in the simulations, the variation of the molecular fraction of each species along the Hugoniot can be understood by an inspection of their respective dissociation energies. Nitrogen has the highest dissociation energy of the molecular species considered here and, as such, is expected to be the last molecular species present in the sample as both the density and temperature increase. Furthermore, that oxygen has a lower dissociation energy than nitrogen oxide also suggests that oxygen is less likely to associate for density-temperature conditions where NO is dissociated. While this argument, based on the dissociation energy of the isolated molecular species, explains the simulation results, the sensitivity of the QMD results to the number of particles used requires further exploration and validation by performing larger scale simulations.

In summary, we studied the dissociation of nitrogen-oxide along the first-and second-shock Hugoniots. We find that QMD provides a good description of the experimental data for both Hugoniots. Initial simulations with a restricted number of particles (54 atoms) show that molecular nitrogen is forming in the media along both Hugoniots when NO dissociates. As the constituency of the fluid is highly sensitive to the number of particle used in the simulation, this result is currently being verified by performing larger scale simulations.

This work was performed under the auspices of an agreement between CEA/DAM and NNSA/DP on cooperation in fundamental science.

[1] T. J. Lenosky et al., *Phys. Rev. B* **61**, 1 (2000).
[2] S. Mazevet et al., *Phys. Rev. B* **65**, 014204 (2001).
[3] S. Mazevet et al., *Phys. Rev. B* **67**, 054201 (2003).
[4] S. Mazevet et al., *Astronomy & Astrophysics* **405**, L5 (2003).
[5] L. A. Collins, *Phys, Rev. B* **63**, 184110 (2001).

Generating a Portable Version of CATS

Manolo E. Sherrill, T-4. manolo@lanl.gov

To calculate opacities, the energy level structure and oscillator strengths of the element of interest are required. For low-Z elements, these two quantities are typically obtained from the CATS [1] program. Due to the state of the Fortran 77 (F77) version of CATS, with its computer architecture specific features needed for memory management [2] and the expectation of future CATS execution on different computer platforms, a more portable version of CATS was needed. Since much of the basic syntax would remain the same, reducing the probability of introducing errors into the code during the conversion, along with the ability to include all the memory management requirements under one portable standard. CATS was ported by T-4 opacity group to Fortran 90.

Accomplishments

The porting of CATS to Fortran 90 (F90) began in the second week of April, 2003; by July 9th of the same year, after passing a small number of preliminary tests, the first Beta version of the new code was announced. Extensive testing and fine tuning through the month of July lead to the August 6th reproduction and replacement of the 56-gigabyte Oxygen database used in the development of the new opacity model by T-4. Comparisons against the binary output files generated by the old Fortran 77 version with the new Fortran 90 version of CATS showed that all 56-gigabytes were bit wise equivalent. As a further consistency check, ATOMIC was ran using the new CATS generated data through its seven standard test cases, and the final results were identical to the results obtained earlier. In addition, even with the inclusion of extensive error checking code, the F90 version of CATS produces nominally identical execution times as its F77 predecessor.

Motivated by discussions with members of X-5 about the growing desire by the Laboratory to increase the number of codes maintained under formal version control with regression tests (version control is currently not required for CATS), a series of tests with the original F77 version of CATS was preemptively created to examine all CATS's options used in generating atomic databases. With this regression test, the new version of CATS has been shown option-by-option to produce the same results as its predecessor.

[1] Los Alamos Report LA-11436-M Theoretical Atomic Physics Code Development I CATS: Cowan Atomic Structure Code.

[2] Dynamic memory allocation is not a Fortran 77 feature. It was introduced into CATS through the use of in-house C programs and the use of the platform dependent CRAY pointers.

T-6 Theoretical Astrophysics

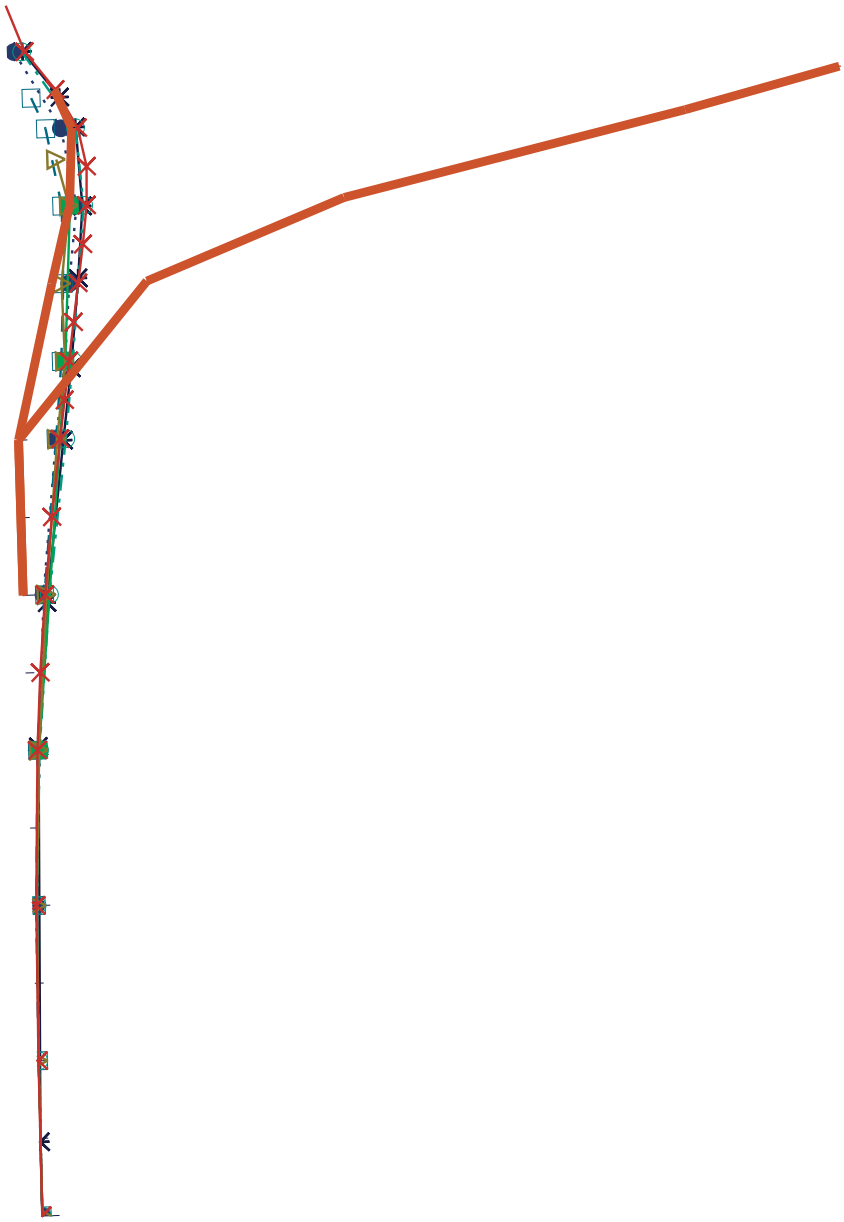

Dynamo Experiment Status Report

Stirling A. Colgate, T-6; colgate@lanl.gov

The dynamo experiment has demonstrated the stable Couette flow at 70 Hz in water, R(1) inner cylinder, Re = 10^7.

The liquid sodium alpha-omega dynamo experiment depends upon 1) establishing a high rate of rotational shear in cylindrical geometry and Couette flow (the analog of a Keplerian accretion disk) and 2) producing large scale helicity by driven jets or plumes (the analog of star-disk collisions). The limiting stable Couette flow is uniform angular momentum, omega proportional to $1/R^2$. Suggestions in the literature—Jean-Paul Zahn—are that such flows are unstable despite theory, e.g., "Taylor columns" and therefore accretion disks require no additional source of turbulence. If true, this conjecture would also negate the possibility of creating high-velocity stable Couette flow in the laboratory because of the immense fluid drag and hence power required as well as the confusion in observing the MRI or dynamo in the presence of large turbulence. The experiment was designed on the basis that this instability conjecture is false, and the small level of turbulence observed in prior experiments at lower Reynolds number, ~ 10^5, was due to the torque of the Ekman flow at the end walls.

On Saturday, February 7, we completed a series of measurements of torque and the radial pressure distribution in five locations (in the rotating frame) between the inner cylinder, R_1 = 15 cm and R_2 = 30 cm. The analysis of the data is very preliminary, but 1) the torque is consistent with stable Couette flow and the associated Ekman flow at the ends and therefore <~1% of what fully developed turbulence would give and 2) the pressure distribution is consistent with differential stable Couette flow where for $R_1/R_2 = 1/2$ and $\omega_1/\omega_2 = 4$. This is the limiting stable Couette flow ratio for which the experiment is designed. The rotation velocity is 1/2 of that to be used at EMRTC, the field safety test site. Five rotation ratios, (R_1/R_2), at four different (lower) rotation rates were investigated.

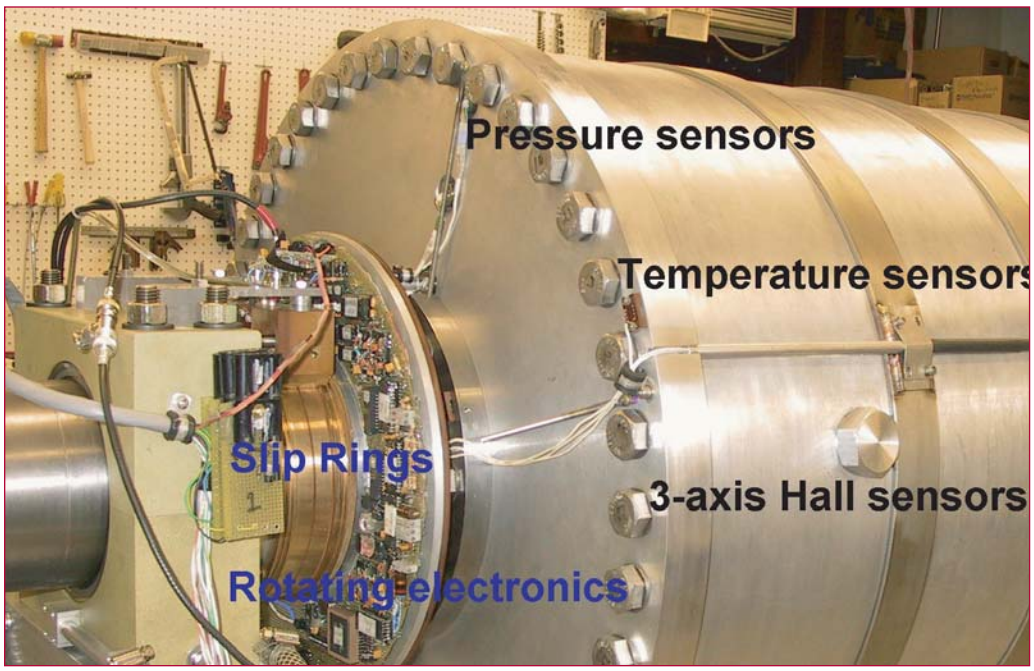

The problem with fluid contact with the inner, R_1, surface was solved by pumping water into the flow during rotation. The 100 Mbytes of data will be analyzed in due course. The electronics, mechanics, and physics all worked.

The Physics of Yttrium Equivalence for Radiochemical Detectors

Anna C. Hayes and Gerard Jungman, T-6; anna_hayes@lanl.gov

Radiochemical detector systems provide the fundamental method for measurement of neutron properties in the thermonuclear environment. These measurements are important in the determination of fission and fusion yields, and therefore provide a basis for interpretation of Nevada Test Site (NTS) data.

The key diagnostic for fusion yields is the ratio $^{87}Y/^{88}Y$ in the Yttrium system, which is determined by neutron fluence in the high-energy region, above about 8 MeV. Other radiochemical isotope systems provide additional information. The information from these other systems is typically converted into "Yttrium equivalences." For a short introduction to Yttrium equivalences, see[1].

The basic point about equivalences is that, since systems utilizing different isotope networks are sensitive to different parts of the neutron spectrum, equivalence measurements yield differential information about the neutron spectrum. By comparing NTS data on equivalences to theoretical calculations, we test our understanding of the physical processes which affect the neutron spectrum. Our collaborators in C-INC provide data on equivalences. With collaborators in X-2, we are able to perform sophisticated calculations using weapons codes. We also perform simplified analytic and semi-analytic calculations which expose the fundamental physics of the processes determining Yttrium equivalences. Some results from this study were presented at an X-2 seminar by Jungman in July 2003. For a general overview of our recent work on radiochemical system, see reference [2].

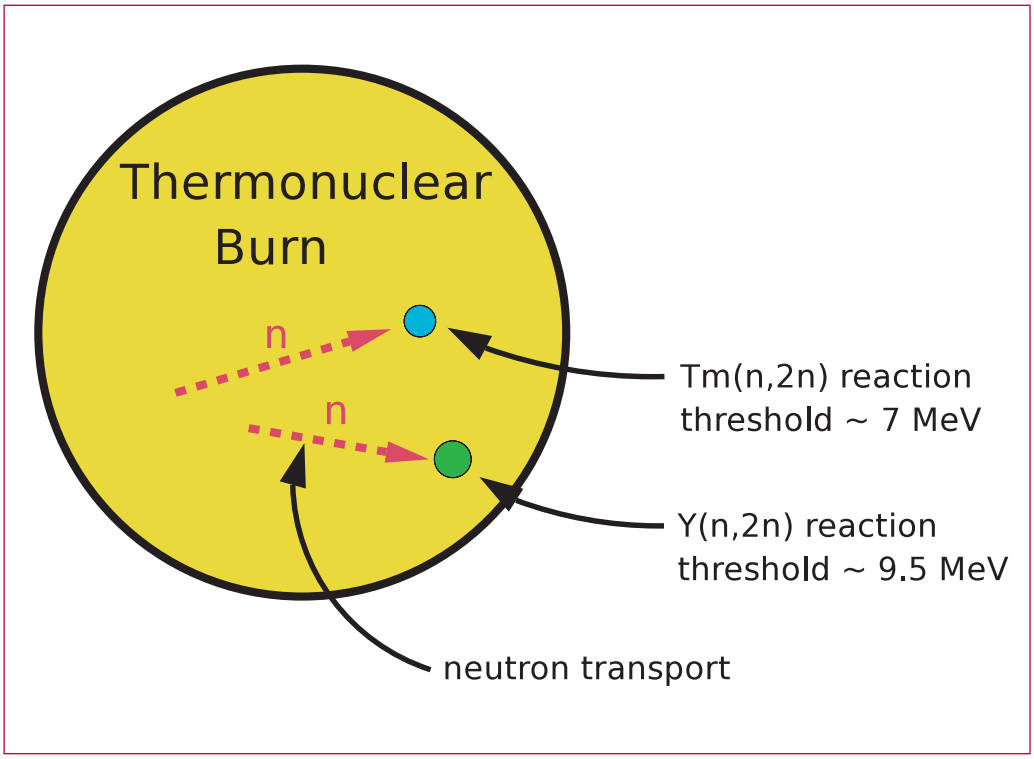

[1] Anna C. Hayes and Gerard Jungman, "Yttrium Equivalences in Weapons Radiochemistry and Fusion Yields," in *T-Division Activities in Support of the Nuclear Weapons Program: 2002/2003,* LA-UR-03-0001 (2003).

[2] Anna C. Hayes and Gerard Jungman, "Weapons Sensitivity Studies for Nuclear Physics (U)," LA-CP requested (2003).

Code Verification for Thermonuclear Supernovae

Peter A. Milne, T-6; Aimee L. Hungerford, CCS-4; and Christopher L. Fryer, T-6; pmilne@lanl.gov

Thermonuclear supernovae are among the largest explosions in the universe, releasing 10^{51} ergs (>10^{28} megatons) of energy in a fusion bomb of epic proportions. Most of this fusion energy is converted to kinetic energy and is difficult for astronomers to detect. However, these cosmic explosions produce a considerable amount of radioactive nickel (^{56}Ni) which, when it decays, releases energetic gamma-ray photons. These photons are reprocessed into optical light and are subsequently observed by astronomers. Unfortunately, using these observations to learn about the actual explosion can be problematic due to the many layers of theory that lie between models of the thermonuclear explosion and the observed optical emission.

A more direct measurement of the explosion comes from observing the gamma-rays themselves. The opacities at these high energies are simpler (mostly continuum instead of line opacities) and don't depend strongly upon the ionization state of the material. However, until recently, the different codes calculating the gamma-ray emission for thermonuclear supernovae disagreed by nearly an order of magnitude on the gamma-ray line flux. Our project concentrated on doing detailed code comparisons of the existing gamma-ray line transport codes to apply programmatic techniques in code verification to this astronomy problem.

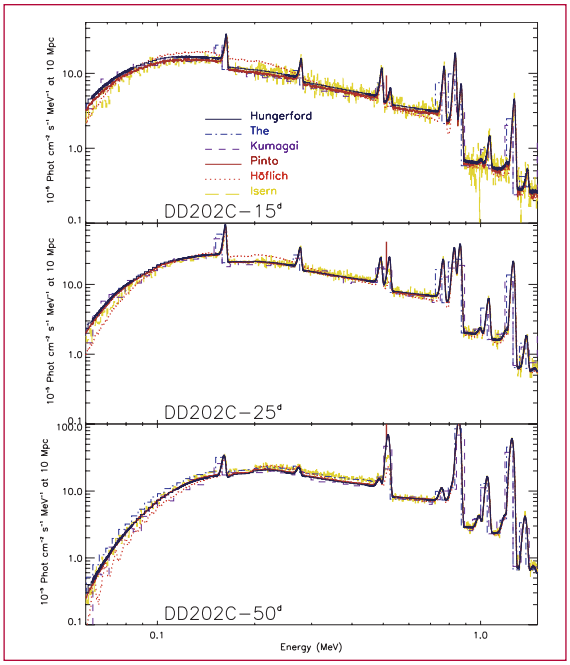

Figure 1—A sequence of spectra for the thermonuclear model, DD202C. The spectra, at 15d, 25d and 50d, show the level of agreement between simulations for both the line and continuum emission. Comparisons between the two algorithms that do not treat line broadening/shifting (The Kumagai) and the others that do, show the early effects of blue-shifting. The HWK98 spectra clearly transitions from being brighter than the other spectra, to being fainter.

All in all, we compared seven different gamma-ray line codes devloped across the world from simple escape techniques (Boggs: Coburn & Boggs 2003) to one-dimensional Monte-Carlo algorithms (FASTGAM: Woosley, Hartmann & Pinto 1989; The: Bussard, Burrows & The 1989, Höflich: Müller, Höflich, & Khokhlov 1991; Kumagai: Shigeyama *et al.* 1991) to three-dimensional codes (Isern: Isern, Gomez-Gomar & Bravo 1996; Maverick: Hungerford, Fryer & Warren 2003). Although these codes mostly used Monte-Carlo transport, their drivers were different and used different physics implementations. Some included additional physical effects that others did not. Using a variety of initial conditions we were able to track down many of the errors in the existing codes to get agreement in the spectra at nearly all wavelengths for these codes. Figure 1 shows the gamma-ray spectra for a specific thermonuclear supernova progenitor at a series of times in the explosion. Except at low energies for the Höflich simulation, all codes agree. Figure 2 shows the 812-keV line fluxes for our models in comparison to past work (HWK98: Höflich, Wheeler, & Khokhlov 1998; Kum 97: Kumagai & Nomoto 1997). The large discrepancies of the past, which were previously explained as differences in physics implementations,

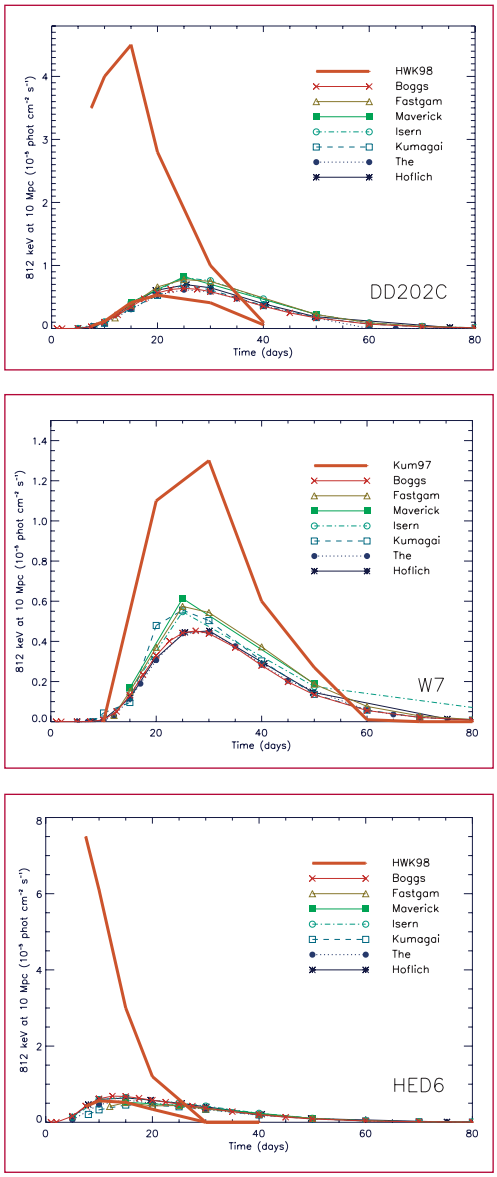

were merely errors in codes that we have now corrected. With the fixes, we not only can better interpret our observations, but we have gained a better understanding of the relative importance of the various physical effects included in the simulations.

With these more reliable calculations, astronomers can now more effectively interpret their gamma-ray line observations. But this project had a much more programmatic aspect. This project allowed us to test the newly developed 3-D Direct Monte-Carlo code ``Maverick" (CCS-4) on a new astrophysics problem. Using codes on as many different environments as possible can be a much more powerful test of a code than the standard test problems. The excellent performance of this new LANL-based 3-D code bolsters our confidence in its design and ultimately drives home the computational excellence at the Laboratory to the academic community.

[1] R. W. Bussard, A. Burrows, and The L. S., *ApJ* **341**, 401 (1989).
[2] W. Coburn and S. E. Boggs, 2003, *Nature* **423**, 415, *ApJ* **341**, 401 (1989).
[3] P. Höflich, J. C. Wheeler, and A. Khokhlov, *ApJ* **492**, 228 (1998).
[4] A. L. Hungerford, C. L. Fryer, and M. S. Warren, M. S. *ApJ* **594**, 390 (2003).
[5] J. Isern, J. Gómez-Gomar, and E. Bravo, 1996, *Memorie della Societa Astronomia Italiana* **67**, 101.
[6] S. Kumagai and K. Nomoto, 1997, "X-Ray Imaging and Spectroscopy of Cosmic Hot Plasmas", Proceedings of an International Symposium on X-ray Astronomy ASCA Third Anniversary, 11–14 March, 1996, Waseda University, Tokyo. Edited by F. Makino and K. Mitsuda (1997), p. 387.
[7] E. Müller, P. Höflich, and A. Khokhlov, *A&A* **249**, L1 (1991).
[8] T. Shigeyama, S. Kumagai, H. Yamaoka, K. Nomoto, and F. K. Thielemann, *A&AS* **97**, 223 (1993).
[9] S. E Woosley, D. Hartmann, and P. A. Pinto, *ApJ* **346**, 395 1989.

Figure 2—Line fluxes of the 812-keV line for the supernova models, DD202C (upper panel), W7 (middle panel) and HED6 (lower panel). As with the 812-keV line emission, the spectral extraction and tagging light curves agree, and are fainter than the HWK98 and Kum97 light curves.

The Distribution of Dark Matter in the Universe on Scales of 10^{10} to 10^{15} $M_\odot$

Michael S. Warren, T-6; and Luís F. Teodoro, T-8; mswarren@lanl.gov

The art of using simulations has become an essential tool not only in the interpretation of observational data, but also in making predictions from cosmological models that are physically well-motivated. Cosmological *N*-body simulations with a few million particles are limited in their ability to resolve the necessarily wide range of scales, from linear to nonlinear, with sufficient statistical accuracy.

The increasing sophistication in software and the use of large parallel computers have allowed us to perform a suite of *N*-body simulations using on the order of a billion particles. This allows us to study deeply nonlinear gravitational clustering, a regime, which has not been well-studied, with other cosmological *N*-body simulations. Statistically, rather than basing results on just one or two large simulations, now one can investigate the role of the different numerical and physical effects on the statistics used to characterize the mass distribution of the universe.

Preliminary convergence tests of the halo mass function, *N*-point correlation functions, power spectrum, and pairwise velocity show good agreement with analytical work present in the literature as well as some new information that can lead to a better understanding of large scale structure formation theories.

Figure 1 shows an early stage (redshift 5) of an *N*-body simulation using about 140-million particles, which represent the dark matter in the universe. The cosmological parameters correspond to the currently favored "concordance model," with $\Omega = 0.3$, $\Lambda = 0.7$ and $H_0 = 70$

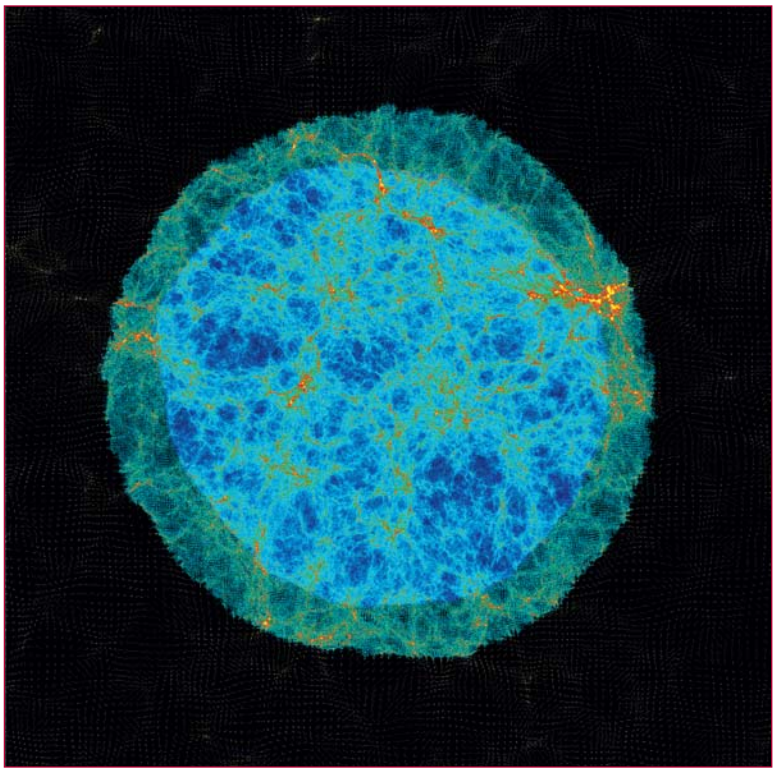

Figure 1—

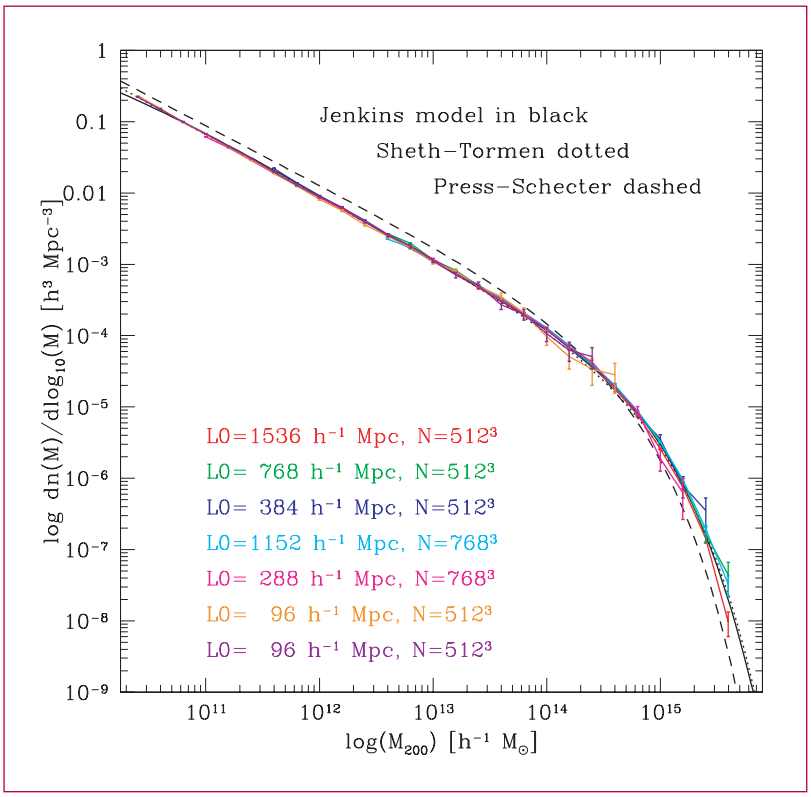

Figure 2—

km/s/Mpc. This simulation uses small particles in the center, surrounded by a shell of medium mass particles, and then finally the heaviest particles. This allows us to probe the behavior of halos with small masses, while maintaining appropriate boundary conditions with the larger particles.

Figure 2 shows the mass function of dark matter halos from a series of seven simulations with varying mass resolution. The mass function is remarkably consistent among the simulations, showing little deviation from the theoretical model over five orders of magnitude in mass.

T-8 Elementary Particles and Field Theory

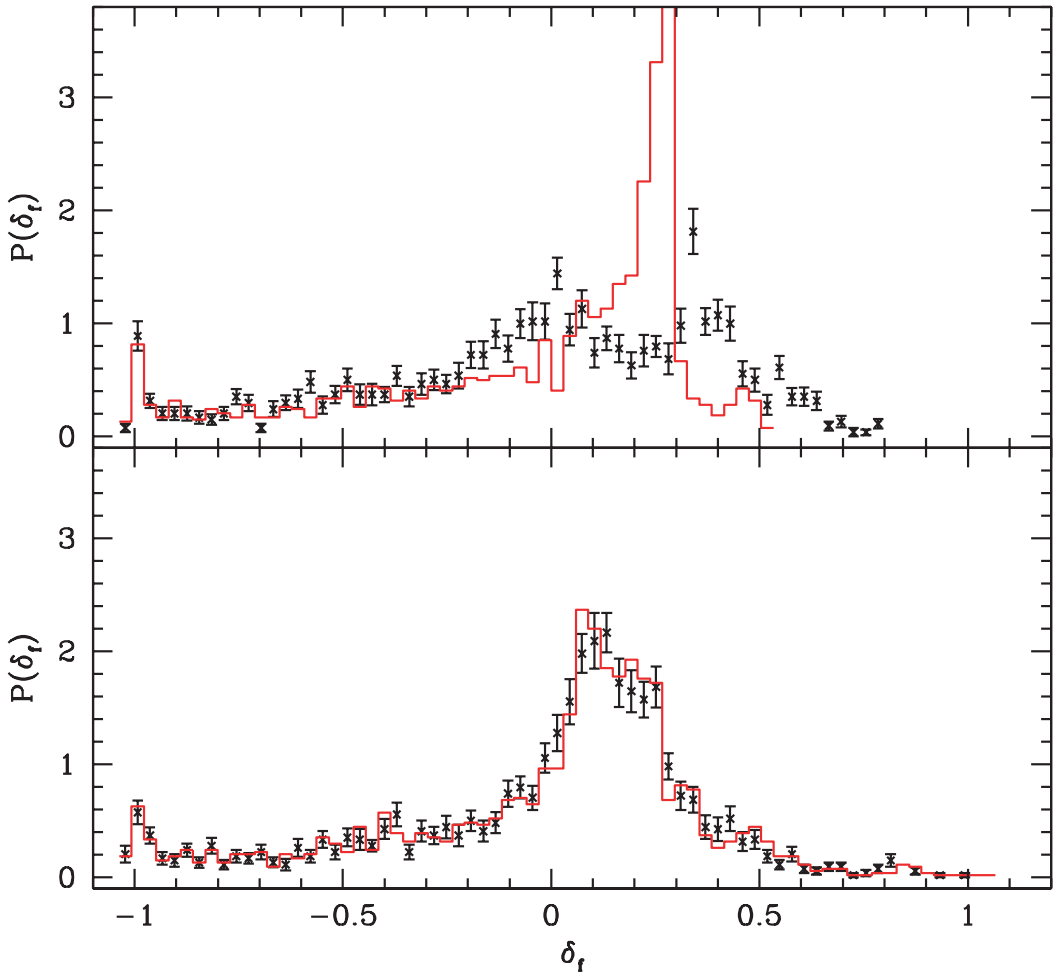

Constraining Neutrino Masses from Cosmology

Kev Abazajian and Salman Habib, T-8;
Katrin Heitmann, ISR-1;
Scott Dodelson, FNAL; and Eric Switzer, Princeton; kaba@lanl.gov

Traditional methods based on direct detection in conjunction with cosmological arguments have led to tight constraints on neutrino mass eigenvalues. Neutrino flavor oscillations have been confirmed by solar, atmospheric, and reactor neutrino experiments. However, where these experiments constrain neutrino mass differences, cosmological observations lead to competitive constraints on the total mass. As cosmological observations improve, these constraints will become much better.

The original cosmological constraint on the mass of neutrinos was derived by Gershtein and Zeldovich by arguing that neutrinos cannot overclose the universe. The more recent approach is based on understanding the effect that massive neutrinos have on the large scale structure of the universe. Arguments based on the linear regime of the gravitational instability that leads to structure formation, and therefore matter correlation on large scales, have constrained the sum of neutrino mass eigenvalues. Estimates of the upper mass limit range from 0.7 to 1.8 eV, for the sum, depending on assumptions and the observational data sets employed. These results are based on the effect of neutrino free-streaming in the early horizon-crossing epoch, and do not take into account what has happened on smaller scales at more recent epochs.

The idea behind the present work is to use nonlinear scales in setting limits on neutrino masses. These scales will soon be probed by weak lensing observations that measure mass directly and thus bypass the complex problem of understanding galaxy bias in order to extract the mass distribution at those scales. To this end, we employ both semi-analytic and numerical approaches.

Detailed studies of the nonlinear power spectrum have been attempted in the framework of the halo model of structure formation. We extend these analyses to include massive neutrinos, in particular accounting for the late-time accretion of massive neutrinos onto cold dark matter (CDM) halos (Figure 1). The effect of the neutrinos in the late structure epoch is to cluster into the CDM halos and thereby influence their evolution. This nonlinear interaction of

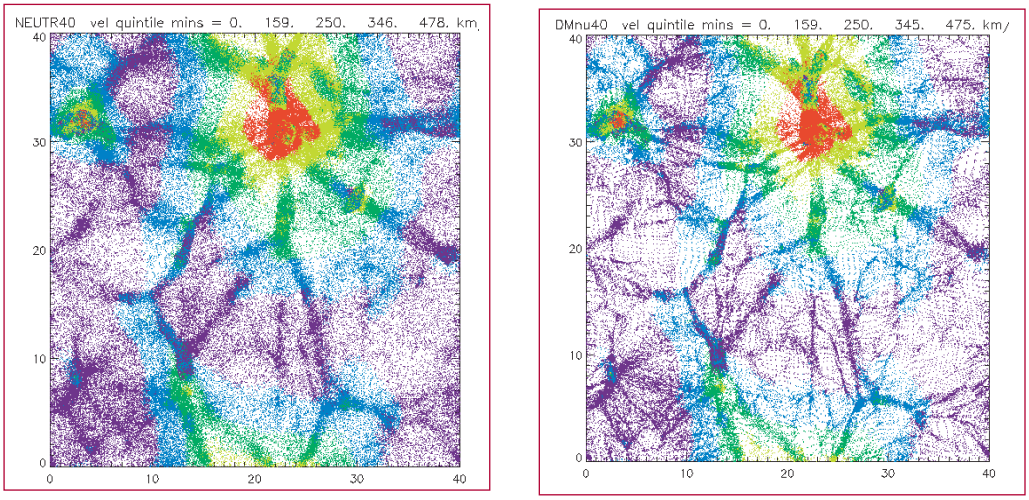

***Figure 1—** An example of a CDM run with massive neutrinos in a LCDM cosmology. The distribution of neutrinos (left panel) is seen to track the high-density CDM distribution (right panel) but it is much more diffuse than the underlying dark matter. The simulation was carried out in a three-dimensional box of size 40 Mpc.*

the halo with itself further suppresses the power of perturbations on small scales. The advantage of the halo model is that it is computationally much easier than running a N-body simulation with neutrinos and yields analytic results in certain asymptotic limits.

The advantage of running high-quality N-body simulations with neutrinos is clear: this is the only way at present to obtain accurate quantitative results without having to optimize any approximation parameters. One could imagine tuning a halo model against a limited number of N-body runs and then efficiently exploring parameter space using the halo model (which requires much less computation). We have recently included massive neutrinos into our cosmological structure formation code, MC^2 (Mesh-based Cosmology Code). Massive neutrinos are essentially another form of dark matter (a "hot" component), so no new interactions have to be introduced into the code. However, the initial conditions for the neutrino velocities are quite different from CDM initial conditions.

Since neutrinos are "hot," their velocities at early times are not dominated by the gravitational flow velocities, as is true for CDM, but by their thermal velocities as sampled from a Fermi-Dirac distribution (the actual situation is a little more complicated, but this is sufficient for our purposes). In order to make sure that numerical effects from a large number of very fast-moving particles are suppressed, the initial condition for neutrinos is imposed in a momentum-conserving way on particles taken in pairs, so that, while it is nonzero for each particle, the thermal velocity cancels out in its contribution to the overall mass flow velocity. In addition, the linear growth

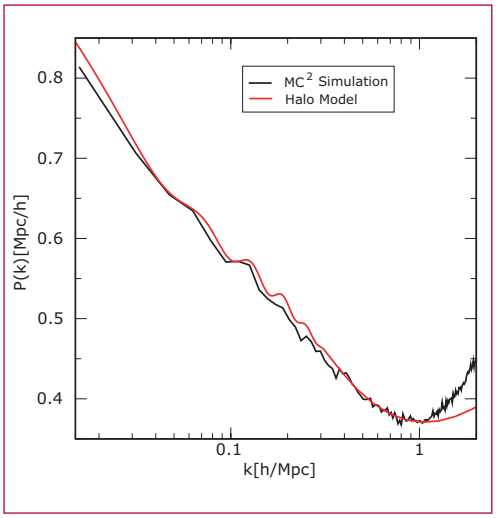

Figure 2—Ratio of CDM and CDM + neutrino power spectra at z = 0 with Ω_m held fixed. The black line is the result from simulations using MC^2 whereas the red line is the result from a simple halo model. The agreement between the two is good and both predict a suppression of nonlinear power at k = 1 Mpc^{-1}.

factor for neutrinos is scale-dependent, unlike the case of CDM, and this must also be taken into account.

In Figure 2 we show the ratio of the CDM power spectrum at z = 0 and CDM with three neutrino species (m_ν = 0.6 eV) also at z = 0 calculated both by N-body techniques and by using a simple halo model. (A subtle point to keep in mind is that in these two cases we kept the total matter density the same in the two simulations.) The agreement between the two methods is already very good, and both agree on a dip near k = 1 Mpc^{-1} that reflects the suppression of nonlinear power due to the neutrinos.

The ultimate goal here is to use theoretical nonlinear neutrino and dark matter clustering to either limit the presence of massive neutrinos, or, more interestingly, potentially detect the presence of massive cosmological neutrino clustering and a measure of the absolute neutrino mass level. This may be done by future precision measurements of dark matter structure statistics via galaxy clustering or cosmological weak lensing.

Active Cooling of Atoms in Cavity QED: New Results

Tanmoy Bhattacharya, Salman Habib, and Daniel Steck, T-8; Kurt Jacobs, Griffith; and Hideo Mabuchi, Caltech; tanmoy@lanl.gov

The control of quantum systems is a problem that lies at the heart of several fields, including atom optics and nanomechanics. Many of the techniques developed thus far for controlling quantum systems in an initially unknown state involve the use of dissipative processes to achieve a well-defined final state, as in the laser cooling methods in atom optics. A different paradigm for cooling involves modifying the system Hamiltonian based on information provided by measurements (i.e., quantum feedback control). Such a strategy for control is generally applicable to quantum as well as classical systems. As quantum-limited measurement techniques become more available, quantum feedback control is likely to soon be an essential element in atom-optical and nanomechanical toolkits.

One of the most promising avenues for the study of quantum feedback control centers on experiments in cavity quantum electrodynamics (CQED), where a single quantum system may be monitored continuously in real time, as has been demonstrated in a series of pioneering experiments over the last few years. Furthermore, the optical potential due to the cavity light provides an easily adjustable means for applying forces on the atom (Figure 1). Feedback has been shown to increase the storage time for atoms in such an experimental system. Despite these efforts, however, CQED feedback cooling has not yet been conclusively demonstrated, highlighting the need for a deeper theoretical understanding of this system as well as more sophisticated, higher performance cooling algorithms. Our goal in this work is to develop approximate estimation and control algorithms for cooling the atomic motion in such a CQED system—an "active cooling" approach that is distinct from passive cavity cooling methods. This problem is of particular significance due to its nonlinear nature, both in the potential and the form of the measurement operator: an important issue that we address here is whether the (Gaussian) estimation methods developed for linear systems are effective in nonlinear cases.

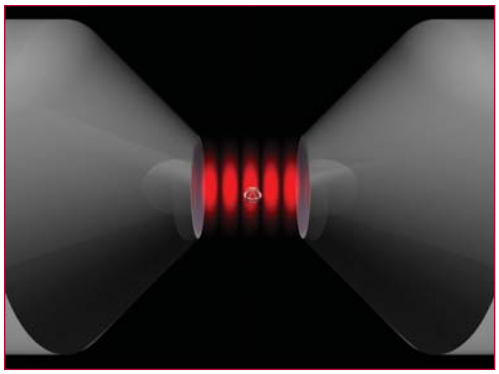

Figure 1—This figure depicts an atom trapped by electromagnetic fields in a high-finesse optical cavity.

The setup we are considering is an atom in a microcavity in the strong-coupling regime, as in the aforementioned CQED experiments, but where the output light is monitored via homodyne detection, which gives information about the atomic position in the cavity. We consider the case where the light is resonant with the cavity, but the detuning from atomic resonance is much larger than the natural atomic linewidth. We thus analyze the coupled atom-cavity system after adiabatic elimination of the cavity and internal atomic dynamics.
While integration of the associated stochastic master equation (SME) in order to obtain a state estimate is sensible in principle, in practice it is much too difficult to integrate the SME in real time. To solve this problem we must simplify the

estimator. We make a Gaussian ansatz for the atomic Wigner function (which, equivalently, prescribes how the Weyl-ordered moments of the atomic state factorize). In doing so, we reduce the effort of integrating a partial differential equation to the much more manageable effort of integrating a set of five coupled ordinary differential equations. The tracking behavior of the Gaussian estimator is illustrated in Figure 2; this compares the evolution of an atom evolving according to the SME with a Gaussian estimator evolution beginning with a different initial condition. The estimator rapidly locks on to the true solution. The ability of the estimator to track both quantities well is crucial to the success of our control algorithm.

Intuitively, an algorithm that responds to the wave-packet centroid, raising the optical potential while the atom is climbing one side of a well, should cool the atom. However, such a strategy eventually breaks down due to uncontrolled pumping of energy into the wave-packet variances. The key to obtaining an effective control algorithm is to consider the energy evolution due to the Hamiltonian part of the SME. From this expression, it becomes clear that a "bang-bang" strategy is optimal for cooling if we consider only cyclic modulations of the potential amplitude within a limited range. The potential should be switched to the extreme low value when the quantity $-\langle\cos^2(kx)\rangle$ is maximized and to the extreme high value when this quantity is minimized. Such a control strategy is sensitive to energy in both the centroids and variances of the atom. Of course, it is not possible to tell whether $-\langle\cos^2(kx)\rangle$ is at an extremum based only on information at the current time. Thus, to complete the feedback algorithm, we fit a quadratic curve to the history of this quantity at each time step and trigger on the slope of this curve at the current time.

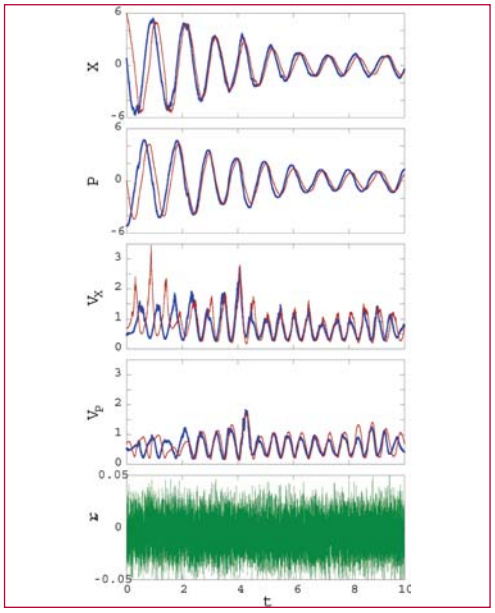

Figure 2—Locking behavior of the Gaussian estimator for centroids and variances for a sample trajectory. The expectation values for the true wave packet (heavy lines) are shown with the corresponding Gaussian estimator quantities (narrow lines). The cooling algorithm was activated at t = 2. The bottom graph shows the corresponding photodetector signal increments plotted for the time increments used by the estimator.

The cooling algorithm turns out to be very effective, allowing cooling to the ground state. We have found that the algorithm is quite robust to variations in the feedback strength, feedback delay, and to the efficiency of the measurement (Figure 3). These are crucial aspects for the application of this technique to experiments in the near future.

D. A. Steck, K. Jacobs, H. Mabuchi, T. Bhattacharya, and S. Habib, *Phys. Rev. Lett.* (to appear), LAUR-03-6826.

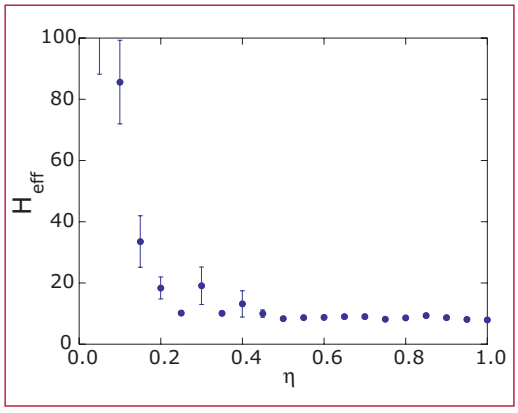

Figure 3—Final energies as a function of the detection efficiency η. Error bars reflect standard errors over 128 trajectories. Note the essentially flat behavior from η = 0.5 to η = 1.

A Flexible Mesh-Based Cosmology Code

Salman Habib, T-8; Katrin Heitmann, ISR-1; Adam Lidz, Columbia; Robert Ryne, LBNL; and Luis Teodoro, T-8; habib@lanl.gov

There are several different computational approaches to model structure formation in cosmology in the dominant dark matter component. These include tree-based N-body, particle-mesh (PM), and hybrid methods. Each of these methods attempts to solve the Vlasov-Poisson equations for a collisionless gas of gravitating particles. In addition, the structure of galaxy clusters and galactic halos depends on baryon hydrodynamics, as does the analysis of Lyman-alpha clouds. Therefore, hydro-solvers are also needed for cosmological simulations.

PM codes model the self-gravitating fluid by tracer particles, integrating the equations of motion for particles interacting self-consistently via Newtonian forces. The particles interact with each other via the potential field created by all of them, computed on a three-dimensional spatial grid. Particles are deposited on the grid by interpolation methods to create a density field [we use both linear (Cloud-In-Cell, CIC) and quadratic interpolation (Triangle-Shaped-Cloud, TSC)]; the Poisson equation is then solved by any of the available fast methods (FFT, multi-grid). This method drastically reduces the computational complexity of a direct particle-particle calculation. The number of grid cells per dimension, N_g, determines the code's spatial resolution. PM codes are the fastest of all N-body codes and have been extensively tested in a variety of applications. In addition, being grid codes, they are relatively easy to couple to grid-based hydro and plasma codes. However, since the resolution of the code is tied to the grid size, they do not have the spatial resolution offered by tree codes.

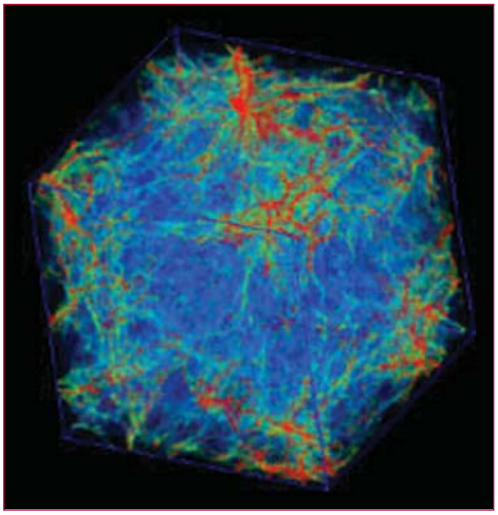

Figure 1—The baryonic distribution in a 30 Mpc box at redshift z = 2.5 (134-million particles on a 512^3 grid). Colors track the density. The visualization is by Pat McCormick of CCS-1.

MC^2 is a parallel PM dark matter code based on Vlasov-Poisson solvers developed at Los Alamos (the IMPACT code) and at UCLA (Viktor Decyk's UPIC framework). MC^2 also incorporates a simplified treatment of baryons via the Hydro-Particle-Mesh (HPM) method; a neutrino module has been recently added, and a more complete hydrodynamic module is under development. MC^2 is designed to provide excellent performance for maximum values of $N_g^3 = 2048^3$; this number will increase as available computational resources continue to improve in size and performance. Because of the ubiquity of periodic boundary conditions in cosmology problems, MC^2 uses a FFT-based solver for the Poisson equation; time-stepping is handled via a symplectic method. MC^2 has undergone a rigorous program of testing and verification against other cosmology codes such as HOT, GADGET, HYDRA, and the Princeton Tree PM code.

MC^2 is a Fortran code and exists in two versions, one based on High Performance Fortran (HPF), the other on a Fortran95/MPI-based framework

implementation (UPIC). These latest variants of Fortran provide a powerful high-level language designed for mathematical modeling, safety, and performance. MC^2 has a classic, modular program structure consisting of a main program, initialization routines, a processing driver, and analysis and reporting routines. The code is easy to modify and enhance; the HPF version can be easily understood, used, and modified by someone with only minimal parallel programming experience. This makes this version invaluable for use by students, post-docs, and researchers who are primarily scientists and not programmers. The simplicity of the code structure also helps with defensive programming (error checks, debugging). The UPIC version uses trusted legacy Fortran77 routines in the lowest layer; these routines have been very carefully programmed to provide the highest performance possible. The middle layer is written in Fortran95 and encapsulates legacy code with simple interfaces and provides additional safety checks. The UPIC version is one of the world's fastest portable parallel PM codes.

The HPM version of MC^2 adds a second particle species (baryons); these particles, aside from the usual gravitational interaction, also feel pressure gradient forces. These forces are modeled by assuming an ideal gas equation of state and a temperature-density relation for the gas. The specific enthalpy now plays a role identical to that of the gravitational potential, in that the gradient of this quantity provides the pressure-gradient force on each particle. Thus at each time-step the sum of the potential and the enthalpy lead to a generalized potential whose gradient provides the total force on the baryonic particles (the dark matter particles only interact gravitationally).

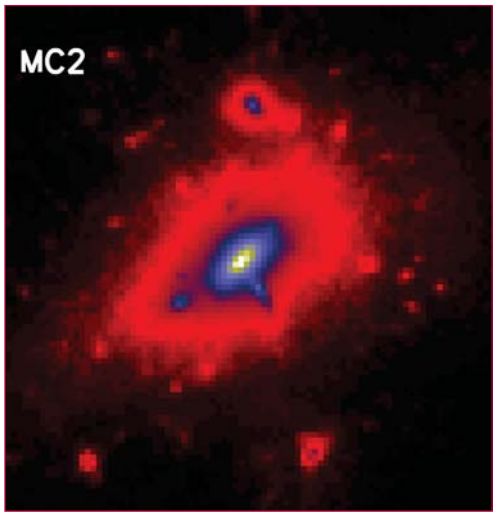

Figure 2— The density profile of the Santa Barbara cluster from a MC^2 simulation on a 1024^3 grid, projected down to a 1024^2 grid. The box size is 64 Mpc, only the inner 8 Mpc is shown.

We now turn to two application examples: simulations of the baryon distribution in the Lyman alpha forest and of the "Santa Barbara cluster." MC^2 simulations of Lyman-alpha absorption are being used to analyze data from approximately 3000 Sloan Digital Sky Survey QSO lines of sight. Measurements of the Lyman-alpha forest probe the primordial power spectrum at very small scales which can never be achieved by CMB measurements. This presents unique opportunities for constraining cosmological parameters, in particular the running of the spectral index. The simulations are carried out using both the HPM and pure dark matter versions. As large numbers of particles are needed in order to reduce shot noise in the numerically obtained density field, production simulations are carried out with 134-million particles. Figure 1 shows a simulation cube from one of our runs. The Santa Barbara cluster simulation is a standard test problem used to check code accuracy and resolution. MC^2 has been successfully used to run this problem, as shown in Figure 2.

A New Method for Characterizing the Lyman Alpha Forest

Salman Habib, T-8; Katrin Heitmann, ISR-1; Lam Hui, FNAL; Adam Lidz, Columbia; Michael Rauch, Carnegie Observatories; and Wallace Sargent, Caltech; habib@lanl.gov

Over the last decade, the Lyman alpha forest has become one of the premier tools for cosmology. This has been primarily due to the combination of high-resolution spectra from the HIRES spectrograph on the Keck telescope and an enhanced understanding of the diffuse intergalactic gas responsible for the Lyman alpha forest. Many more quasar spectra are now available from the Sloan Digital Sky Survey (SDSS), and as our theoretical reach also improves, the Lyman alpha forest promises to become a precision tool for research on the matter power spectrum, reioinization, the geometry of the Universe, and other issues.

The Lyman alpha forest is a series of absorption lines in the spectrum of a quasar blueward of the quasar Lyman alpha emission. Consider a neutral hydrogen cloud between an observer and a quasar—any light from the quasar that is redshifted down to Lyman alpha will be absorbed by the cloud, and will be visible to the observer as a sharp dip in the observed quasar spectrum. Given a distribution of clouds strung along the line of sight, one gets a distribution of closely spaced absorption dips with differing amplitudes depending on the local density: this is the "forest."

It turns out that at the high redshifts characteristic of the Lyman alpha clouds, neutral hydrogen is a good tracer of the dark matter distribution. Thus data from the forest can be used to constrain the distribution of dark matter. However, it is important to note that in order to get any cosmological constraints from the forest one must know the amplitude of any ionizing background as a function of the redshift, as this will change the neutral hydrogen density. In previous work on constraining the matter power spectrum, the amplitude of the ionizing background was fixed by calibrating simulations to match the observed mean transmitted flux in the Lyman alpha forest. This procedure is undesirable as it requires the estimation of the unabsorbed quasar continuum level (i.e., a knowledge of the quasar spectrum in the absence of absorption from the cloud), a difficult undertaking subject to various sources of systematic error and bias.

There have been two main approaches to estimating the unabsorbed continuum level. One approach is to extrapolate the continuum from the redward side of the Lyman alpha forest, where there is (obviously) no Lyman alpha absorption. The other method is to locate regions in the forest where there is apparently no absorption, fit these with a high-order polynomial, and call this the continuum level. Each approach has systematic difficulties. The first may cause an underestimate of the mean transmitted flux: this is because there may be a break in the slope of the quasar continuum near the Lyman alpha emission line; the continuum becoming less steep as one moves across the line from red to blue, as seen in low-redshift quasar spectra. The fitting together of "unabsorbed" regions in the second method adds an undesirable subjective element to the data analysis, and inevitably breaks down at sufficiently high redshift where there are no unabsorbed regions in the Lyman alpha forest. This approach tends to overestimate the mean transmitted flux in the forest.

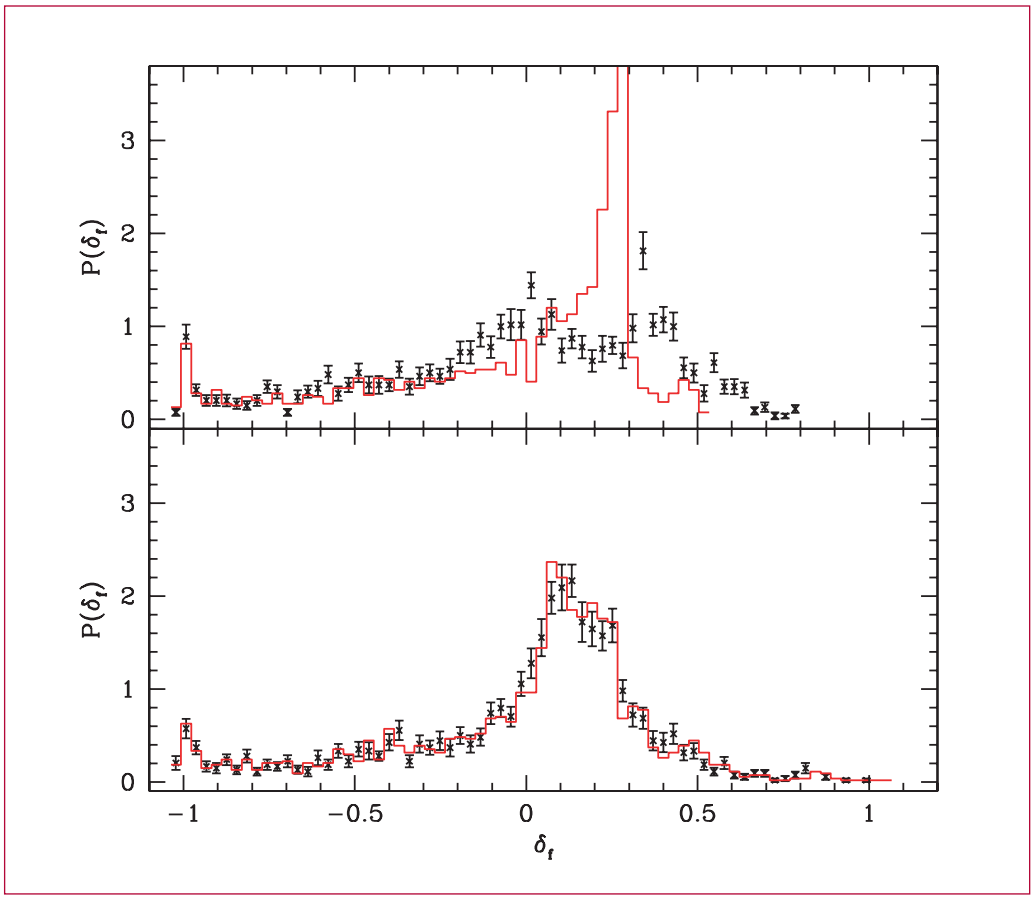

Figure—
The flux PDF from continuum fitted data (red histogram) and from the raw data (black points with error bars). The flux PDFs in the top panel were formed assuming a flat mean to estimate δ_f, while the PDFs in the bottom panel used a large-scale smoothing of R = 500 km/s to form δ_f. The error bars on the PDF measured from the continuum fitted data are comparable to those from the raw data and are not shown for clarity. The close agreement between the PDF of the flux field measured from the raw data and that measured from the continuum-fitted data, when both are smoothed on the scale R, illustrates that our procedure is robust to the continuum.

We have suggested an alternative approach based on measuring the one-point probability distribution (PDF) of the fluctuations in the the flux about the mean, relative to the mean, i.e., the PDF of $\delta_f = (f - \langle f \rangle)/\langle f \rangle$. This statistic, while sensitive to the amplitude of the ionizing background, has the virtue that its measurement does not require an estimate of the unabsorbed continuum level (Figure 1). We thereby sidestep one of the biggest loopholes in parameter estimation from the Lyman alpha forest—by going straight from quasar spectra to parameter constraints.

We have presented a measurement of the PDF of δ_f from Keck HIRES data and shown that our measurement is robust to the treatment of the quasar continuum and illustrated how this measurement helps to tighten constraints on the slope and amplitude of the mass power spectrum. Simulations were used to obtain constraints on the mean transmission in the Lyman alpha forest, as well as the amplitude and slope of the mass power spectrum at a redshift of z = 2.72. This technique is now being used to measure the linear mass power spectrum from SDSS quasars where some 3000 lines of sight provide data with excellent statistics (though not with as high a resolution as HIRES).

A. Lidz, L. Hui, K. Heitmann, S. Habib, M. Rauch, and W. L. W Sargent, *Ap. J.* (to be submitted) LA-UR-04-0072.

Comparing State-of-the-Art Cosmology Codes

Salman Habib, T-8; Katrin Heitmann, ISR-1; Paul Ricker, Illinois; and Michael S. Warren, T-6; habib@lanl.gov

There is strong evidence that structure formation in the Universe is largely driven by gravitational instability. In the cosmological "standard model," the evolution and structure of the mass distribution is supposed to be dominated by "dark matter," an as yet undetected type of matter that interacts only gravitationally. In order to study spatial and temporal aspects of the mass distribution today, it is convenient to consider three length scales: very large length scales where a linear treatment of the instability suffices, an intermediate length scale where nonlinearities cannot be neglected yet the dynamics of baryons are not of significant importance, and a high-resolution regime where gas dynamics, star formation, etc., need to be taken into account. While an analytic treatment is adequate at the largest scales, because of the nonlinearity, both the intermediate and small-scale regimes require a numerical approach.

In cold dark matter dominated cosmologies, the transition from the linear regime to the nonlinear regime today (redshift z = 0) occurs at length scales of order several Mpc (or wave number k ~ 0.1 Mpc^{-1}). Length scales larger than this can be satisfactorily treated by linear theory, augmented by perturbative corrections, if needed. Galaxies exist within dark matter halos, and typical halo size scales are ~ 0.1–1 Mpc. Thus, in order to resolve the dynamics of halos, a spatial resolution ~ 10 kpc appears to be necessary.

We have carried out a convergence and comparison study of cosmological simulations focusing mainly on the dynamics of the cold dark matter component. Given the importance of the dark matter component and expected precision observations from large scale structure and lensing oservations, this study is timely and important. We have focused on medium resolution simulations, i.e., where the spatial resolution is ~ 100 kpc. These simulations are adequate for matter power spectrum computations, for weak lensing, and for gathering cluster statistics.

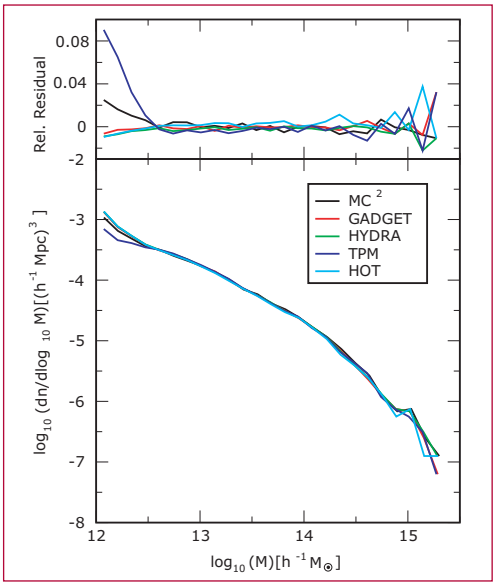

Figure 1— The mass function for halos from different codes for a 360 Mpc box with 17 million simulation particles. The halos were found using a standard "friends of friends" algorithm. The smallest halo has 10 simulation particles. Allowing for statistical scatter at both ends, the agreement is very good, at approximately the 1% level.

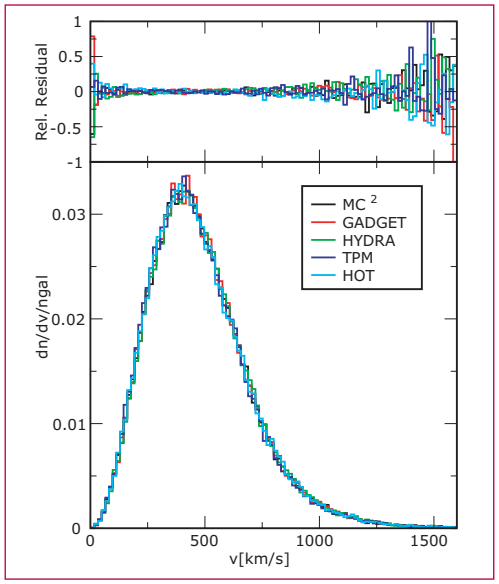

Figure 2— The velocity distribution for all halos with a maximum velocity of 1600 km/s. The distribution has been normalized by dividing out by the number of halos in each simulation. Aside from the tails of the distribution, the agreement is again very good, substantially lower than 2% over most of the physically interesting range.

Next-generation observations of these quantities promise control of systematic and statistical errors at the few percent level, thus it is crucial that confidence in the codes be established to at least the same level of uncertainty, if not better.

Six different codes have been utilized in our work. These represent a broad sampling of the present state-of-the-art: the PM code MC^2 (Mesh-based Cosmology Code); the AMR code FLASH; the tree code HOT (Hashed-Oct Tree); the tree code GADGET (GAlaxies with Dark matter and Gas intEracTions); TPM, a tree particle mesh code, and HYDRA, an adaptive-mesh P^3M-SPH code. (MC^2 and HOT were developed at Los Alamos.) Since all the codes have quite different algorithms and differing error modes, convergence to a single solution is a strong test of the validity of the N-body approach in modeling dissipationless gravitational dynamics at the resolution scales probed by the tests.

A variety of tests and diagnostic tools have been employed. We begin with the Zel'dovich pancake test to investigate issues of convergence and collisionality. These tests are important to arrive at conclusions regarding the appropriate compromise between mass and force resolution in N-body codes. We then focus on two realistic situations, the Santa Barbara cluster and "concordance" LCDM simulations. Several diagnostic tools such as velocity distributions, mass functions, power spectra, etc., were used to compare code results.

On the whole, our conclusions are very positive. Over the range of mass and force resolutions that we deemed to be reasonable for comparison purposes, the codes agreed with each other at roughly the few percent level. Thus, at medium resolutions, theoretical support for next-generation precision cosmology is in good shape.

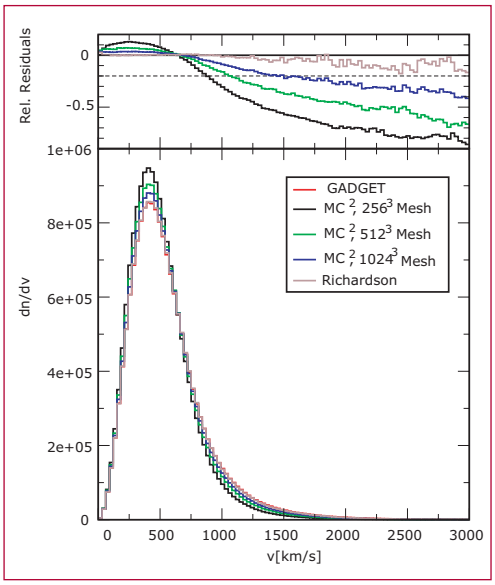

Figure 3—Results from a convergence test for MC^2 using the particle velocity distribution: in all cases 17 million particles were run with identical initial conditions on 256^3, 512^3, and 1024^3 grids. The distribution converges linearly, and this was first checked by extrapolating from the 256^3 and 512^3 meshes to obtain an answer that agreed with the result from the 1024^3 simulation. Finally, an extrapolation to a grid size of zero was performed using the 512^3 and 1024^3 grids. This result is in excellent agreement with a run using the (gridless) tree code GADGET (red curve—hard to see since it is so closely overlaid by the extrapolated result).

We now give two examples of code comparison: the mass distribution of halos and their velocity distribution. Dark matter halos of various sizes are the homes of individual galaxies as well as galaxy groups and clusters and their statistics are one of the prime targets of simulations. As Figures 1 and 2 show, the simulations display very close agreement. One should keep in mind that this agreement holds even though the actual number of halos varies from a minimum of 56,000 to a maximum of 75,000 across the simulations.

Convergence of N-body codes has remained a poorly understood issue. We have addressed this using Richardson extrapolation applied to statistical quantities such as the particle velocity distribution (Figure 3). Using this method, we can verify the convergence properties of the code, and then use convergence acceleration to provide a higher quality result without running a new, much more expensive, simulation.

K. Heitmann, P. M. Ricker, M. S. Warren, and S. Habib, in preparation.

Constraining and Testing Cosmology with Relative Pairwise Velocities of Galaxies

Salman Habib and Luis Teodoro, T-8; Hume Feldman, Kansas; and the SDSS Collaboration; habib@lanl.gov

The statistical analysis of the relative velocity of galaxies taken pairwise, $v_{12}(r)$, turns out to contain very useful cosmological information. Here r is the intergalaxy separation. When galaxies are far apart, the relative velocities are negligible as the uniform Hubble flow dominates. When galaxies are very close together, they are typically in clusters where at very short cosmological distances (less than a few Mpc) the velocities are virialized hence, again, the statistical average of the pairwise velocities vanishes. In an intermediate regime, however, on average, the galaxies do see their mutual gravitational attraction and v_{12} is nonzero and negative. The behavior of $v_{12}(r)$ can be used to constrain cosmological parameters such as the matter density Ω_m and the amplitude of primordial matter fluctuations characterized by σ_8, the rms mass fluctuation in a sphere of radius 8 Mpc.

Combining data from relatively shallow surveys, Feldman et al. have already employed $v_{12}(r)$ to deduce cosmological constraints. But the reach of these surveys was restricted to only a few tens of Mpc. Using the early-type galaxy catalog from the Sloan Digital Sky Survey (SDSS), which now contains some 40,000 galaxies, we aim to go out much further and investigate, among other things, how $v_{12}(r)$ asymptotes to the Hubble flow, vanishing on a scale of 50–100 Mpc.

Because of the lack of three-dimensional velocity information for galaxies, $v_{12}(r)$ cannot be computed directly from redshift surveys. For an individual galaxy, if the redshift and physical distance are known separately, then the line of sight peculiar velocity v_{pec} can be immediately determined. Physical distances to galaxies can be estimated using empirical relations such as the Tully-Fisher relation for spirals or the Fundamental Plane for ellipticals. Ferreira et al. have succeeded in developing an estimator that, given the angular coordinates, distance, and v_{pec} for individual galaxies, can be used to compute $v_{12}(r)$. These authors have also presented an approximate analysis based on nonlinear perturbation theory with Gaussian initial conditions that connects $v_{12}(r)$ at a given separation r to $\Omega_m^{0.6}\,\sigma_8^2$ (this degeneracy can be broken by making independent measurements at different r values). The key assumptions underlying the application of this approach to galaxy surveys are that galaxies can be employed as mass tracers and that $v_{12}(r))$ for galaxies is essentially the same as that for dark matter. Although galaxies are well-known to possess clustering bias this does not seem to affect the method; velocity bias needs to be understood, but, at the level of systematic and statistical errors achieved so far, it has not yet been an issue. The major disadvantage is that, distance estimate errors being substantial (~20%), the method is best applicable to shallow surveys (which SDSS is not).

The SDSS early-type galaxy sample now contains approximately 40,000 galaxies along with their Fundamental Plane (FP) distances and redshifts. The redshift range for these galaxies is very roughly $0.01 < z < 0.3$. In principle, this galaxy catalog can be used for the analysis described above. Even though the scale of the survey is an order of magnitude larger than those previously analyzed

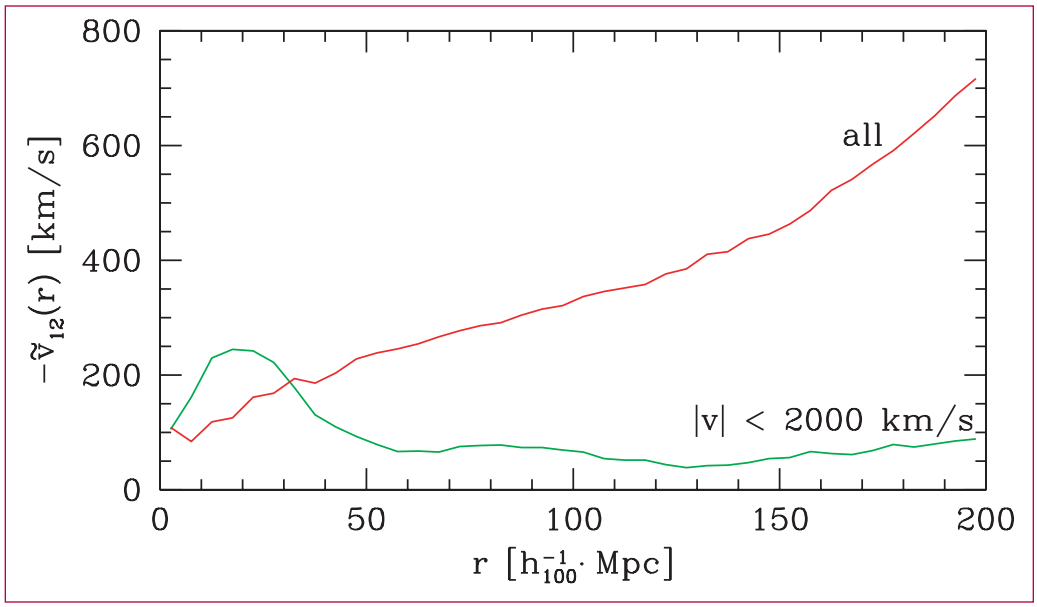

Figure—The figure shows $v_{12}(r)$ computed with all available SDSS early-type galaxies using fundamental plane distance measurements (red line). The unphysical divergence at large values of the separation r is due to the enormous velocity errors that swamp the estimator used for computing $v_{12}(r)$. By removing galaxies with peculiar velocities above 2000 km/s (almost no galaxies have physical peculiar velocities above 1000 km/s) we obtain the result shown in the green curve. Remarkably, these data are roughly consistent with what is expected from cosmological theory, but a more extensive analysis is necessary before any solid conclusion can be reached.

(leading to substantially greater uncertainty in determining individual peculiar velocities), the number of galaxies is already an order of magnitude larger, which should more or less compensate the scatter in determination of peculiar velocities. There is also the advantage that the data are homogeneous and do not arise from a combination of different surveys. Finally, a baseline measurement of $v_{12}(r)$ for the galaxies can be compared to a similar measurement of SDSS clusters as a probe of velocity bias.

Despite the formidable obstacle posed by the depth of the survey, we have carried out a first analysis of $v_{12}(r)$. Because of the very large distance errors, the measurement of peculiar velocities is highly contaminated, and this makes the present estimator unreliable. However, by throwing out manifestly unphysical values of the peculiar velocities (say, above 2000 km/s), the situation is seen to improve dramatically (see figure), suggesting that either a better distance estimate is possible or that a different estimator, robust to distance errors, should exist.

We are now testing the SDSS catalog for quality assurance issues such as completeness and for determining errors in the methodology used for distance estimation (the fundamental plane method). The use of SDSS mock catalogues drawn from very large N-body simulations will play a crucial role in understanding the several physical and statistical biases that the observational procedure is prone to. For instance, to measure $v_{12}(r)$ from observational noisy data will involve a nontrivial correction for homogeneous and inhomogeneous Malmquist biases. There is also the possibility of using very high resolution simulations to directly compare with observations and measure Ω_m and σ_8 without any recourse to perturbation theory.

[1] H. Feldman et al., *Ap. J.* **596**, L131 (2003).

[2] P. G. Ferreira, R. Juszkiewicz, H. A. Feldman, M. Davis, and A. H. Jaffe, *Ap. J.* **515**, L1 (1999).

Hunting for the Intergalactic Magnetic Field

Salman Habib, T-8; Philipp Kronberg, IGPP; Yongzhong Xu, T-8; and the SDSS Collaboration; habib@lanl.gov

Magnetic fields in intergalactic space have a strength typically in the 10^{-6} Gauss range, but they can have enormous scale lengths, of order Megaparsecs (Mpc). Polarimetry has emerged as a powerful tool to study magnetic fields on cosmological scales, however, till recently, there was insufficient observational data to investigate the magnitide and distribution of these fields. In this work our aim is to bring together this technique from radio astronomy with observations of the large scale distribution of galaxies as measured by modern surveys such as the Sloan Digital Sky Survey (SDSS) and 2MASS.

Magnetic fields are measured by studying the Faraday rotation in the radio sources shining through the intergalactic gas. As the waves pass through a magnetic field, the polarization rotates from its original orientation. The angle through which the polarization rotates can be used to deduce the strength of the magnetic field.

The idea is to search for a magnetized diffuse intergalactic plasma associated with large scale structures in the Universe at moderate to low redshifts, most likely the galaxy filaments observed in surveys such as SDSS. Measurements of the Faraday rotation of radio galaxies and quasars away from the galactic plane correlated with the SDSS data can be analyzed statistically for a significant excess. Statistical analyses based on N-body simulations can then be carried out in support of the measurement. A clear result would be the detection of excess Faraday rotation above 2–3 rad/m^2. A clear nondetection at his level would also provide a useful limit on B n_e^2 (n_e is the electron density).

Phil Kronberg's most recent extragalactic radio source Faraday RM list contains approximately 1500 rotation measures for a mix of radio galaxies and quasars out to z ~ 3. Considering the large amount of time needed for polarimetry, this is a unique and fascinating resource for several science studies. The sources cover the northern sky fairly uniformly, except for largely avoiding the galactic plane. In order to cross-correlate this dataset with the much shallower reach of the SDSS and 2MASS surveys, only sources with redshifts less than z = 0.3 are usable. Even with this restriction, and the limited sky coverage of SDSS

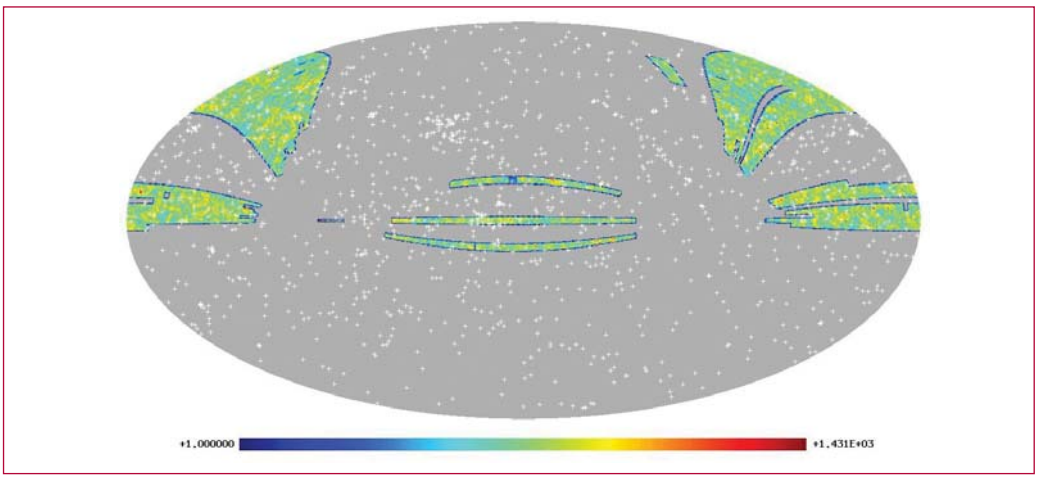

***Figure 1—** This color image shows the distribution of galaxy density in the SDSS in Aitoff projection of equatorial coordinates. White crosses indicate the position of radio sources from Phil Kronberg's rotation measure catalog.*

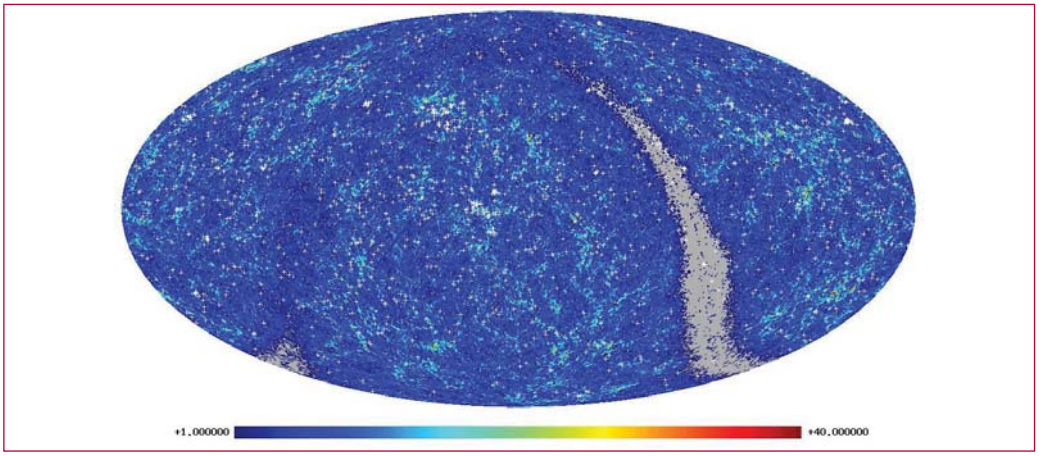

Figure 2— This image shows the distribution of galaxy density in the 2MASS survey in Aitoff projection of equatorial coordinates. White crosses indicate the position of radio sources.

(several thousand degrees), we expect to have approximately 200 radio sources available for statistical analysis (Figure 1).

2MASS is a very shallow all-sky photometric survey, which constains all locally known clusters and filaments (see Figure 2). From Figure 2 it is clear that there are many radio sources passing through or being located inside those structures, thus 2MASS is also a good data set for our purposes.

In order to carry out the cross-correlation analysis, a subset of relatively low-z sources behind nearby filaments of relative galaxy overdensity will be selected. (The most nearby filaments have the advantage that they project the largest solid angle on the sky.) The subset of low-z sources (~ 50–100) would be chosen to be statistically free of other intervenors at the larger redshifts. As a first cut, we will try to correlate the source rotation measure with intervening galaxy density by making two populations of sources: a "low-B" population (sources shining through the least matter density) and a "high-B" population (sources seen through the highest matter density). If the rotation measures in these two populations are statistically distinct then we will have measured the intergalactic magnetic field, otherwise, we can only put limits.

This project is possible only because of the wonderful photometric data from SDSS, which covers a sky area of more than five thousand square degrees. Using this data set, we have made some two-dimensional maps of galaxy density distributions. These 2-D maps show the projected or integrated galaxy density distributions along the lines of sight. These maps also indicate the mass distributions if we apply linear biasing. We can identify those regions with higher mass density, which may imply the positions of filaments and galaxy clusters, even possibly indicate the positions of filaments located along the lines of sight. The photometric redshift of almost all the galaxies is also available, which makes it possible for us to make three-dimensional maps of mass density distributions. Therefore, we can probably identify filaments and clusters. Since we will know the absolute magnitude of each galaxy, it is easy to transfer the galaxy densities into luminosity densities. This provides another means of cross-correlating with the radio source catalog.

Measuring Dark Energy with Weak Gravitational Lensing

Salman Habib, T-8; Derek Donley, Penn; Katrin Heitmann, ISR-1; and Bhuvnesh Jain, Penn; habib@lanl.gov

The recent observation of an accelerating universe, initially via supernovae measurements of the redshift-distance relation, followed by indirect corroboration from the Wilkinson Microwave Anisotropy Probe (WMAP), is the most striking of the remarkable string of cosmological observations in recent years.

It is no exaggeration to say that the existence of dark energy, as implied by this observation, is the most significant unsolved fundamental problem faced by theoretical physics. While we appear to be at an impasse in terms of understanding the nature of dark energy—except in terms of phenomenological models—the prospects of learning more about its equation of state from next-generation observations remain bright.

Because the contribution of dark energy to the evolution of the universe scales more slowly with redshift than that of ordinary matter, it is subdominant till relatively recent reshifts, $z \sim 1$. Thus, in order to disentangle the contribution of the dark energy to the evolution of the universe, one must focus attention on the evolution history of the universe in the redshift range $z = 0.5$–2.

There are two main strategies to obtain information about the dark fluid: the first, as already mentioned, is precision information from the traditional supernova Hubble diagram, while the second is aimed at the distribution of galaxies and clusters: classical tests such as galaxy number counts from surveys such as DEEP2, baryonic oscillations from next-generation surveys ("cosmic ruler" vs. "standard candle"), and the cluster mass function from Sunyaev-Zeldovich observations also promise very tight constraints on the dark energy equation of state. Since systematic errors are a concern in all of these techniques, it is important that multiple methods be employed so as to be confident about the result.

In recent years the power of weak lensing surveys to measure the large scale mass distribution, both statistically and via mapping techniques, has been amply demonstrated. While these methods have been largely targeted towards characterizing the mass distribution, they can also be employed as very useful probes of the dark energy. The clustering of mass depends on linear and nonlinear evolution, both of which are altered by the presence of the dark fluid. While linear effects can be computed analytically, the nonlinear dependence on dark energy requires high-quality numerical simulations which, in large part, remain to be carried out.

Weak gravitational lensing refers to the distortion of the images of background galaxies by the intervening matter. The deformation is characterized by the convergence, K, and the shear. In the weak lensing limit, the convergence is related directly to the mass distribution, moreover, in this limit, K is not difficult to obtain from observations. The convergence power spectrum is then a good probe of the dark energy that influences it both through geometrical factors as well as direct modification of the matter power spectrum. In order to do better than the statistical errors, the systematic errors in individual lensing measurements have to be very small, approximately 1%. Next-generation missions such as SNAP will be able to provide

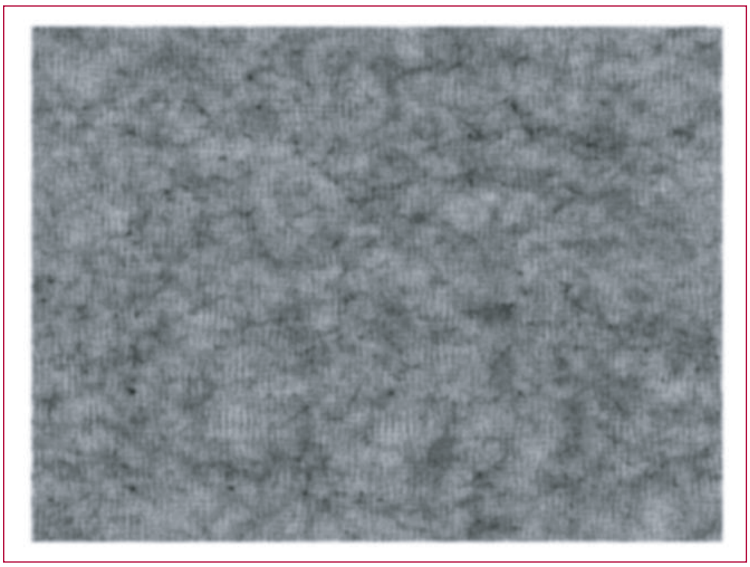

Figure—
A two-dimensional map of the convergence, K, from a test MC² simulation. In weak lensing, the convergence provides direct information regarding the mass distribution. The clustering of mass depends in turn on the dark energy, and hence provides information on the dark energy equation of state.

observations of this quality over a reasonable range of length scales.

To address the nonlinear regime, researchers have used fitting formulae of dubious merit for precision work, with different formulae typically disagreeing with each other at the 15% level and by as much as 50% in some cases. Considering the final accuracy requirement of 1%—in order to match the experimental situation—this is clearly unacceptable. We are carrying out simulations to develop and assess weak lensing as a precision probe for dark energy. The simulations are carried out using MC² (Mesh-based Cosmology Code), each simulation employing 134-million particles. Many simulations are needed to obtain statistics, and presently we are analyzing data from 20 separate runs. We believe that the tight accuracy requirements in the nonlinear regime can be met by these simulations.

The analysis is carried out by joining together a sequence of simulation results at multiple (typically, ~ 10) redshifts, in order to simulate a single very deep line of sight. In this "stacking" technique, the information from each 3-D simulation box is reduced to two-dimensional density planes by projecting down the 3-D density field. A typical simulation consists of 512^3 particles on a 512^3 grid with the density fields projected onto a 1024^2 grid plane. Using open supercomputing resources at LANL (QSC), we have carried out 20 such simulations. This constitutes the largest database of simulations for lensing analysis that currently exists. The database is now being analyzed; a test convergence pattern is shown in the figure.

At present, our code, MC², does not allow for a variable dark energy equation of state. We are in the process of adding this capability. Another future difficulty that needs to be overcome is the sheer number of simulations required to sample parameter space. In principle, one can vary 15 cosmological parameters more or less independently. Statistical analysis in such a high-dimensional space via brute force methods coupled with running large-scale simulations is totally impractical. Thus, along with improving the power of simulation methods, we also have to create a new generation of analysis methods and tools.

Measuring the Primordial Power Spectrum with the Lyman Alpha Forest

Salman Habib, T-8; Katrin Heitmann, SR-1; Lam Hui, FNAL; Adam Lidz, Columbia; and the SDSS Collaboration; habib@lanl.gov

The Lyman alpha forest is a series of absorption lines in the spectrum of a quasar blueward of the quasar Lyman alpha emission. Consider a neutral hydrogen cloud between an observer and a quasar—any light from the quasar that is redshifted down to Lyman alpha will be absorbed by the cloud, and will be visible to the observer as a sharp dip in the observed quasar spectrum. Given a distribution of absorbers strung along the line of sight, one gets a distribution of closely spaced absorption dips with differing amplitudes depending on the local density: this is the "forest." From Sloan Digital Sky Survey observations we now have more than 3000 examples of quasars with associated forests (Figure 1).

It is now generally accepted that the intergalactic medium (IGM), responsible for the Lyman alpha forest, is the main reservoir of baryons up to a relatively recent redshift ($z \sim 2$). Simulations show that the forest arises from a hierarchy of structures with shapes varying from sheets to filaments to clumps of gas as the density increases. Since the physics of the forest is relatively simple, and the gas traces dark matter very closely in an essentially unbiased way (unlike galaxies at the same or later epochs), Lyman alpha forest spectra are a unique source of information for tracking the formation of structure in the universe at redshifts between $z = 2.5$–6. At moderate redshifts ($z \sim 3$), density fluctuations on Lyman alpha forest scales of ~ 100 kpc (comoving) are mildly nonlinear, so that the gas has not yet been subjected to strong dissipative and virialization effects.

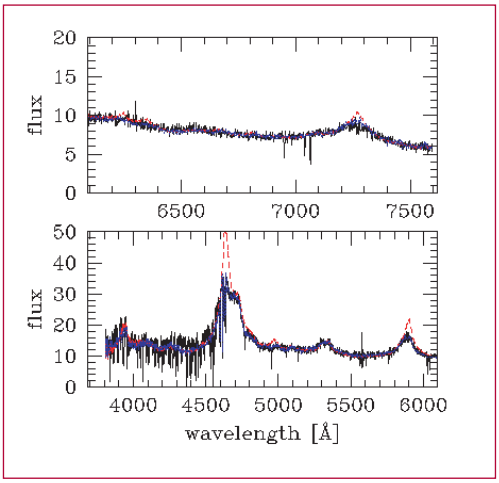

Figure 1—Spectrum of a quasar at emission redshift $z = 2.8$ as viewed by the SDSS, broken into two pieces to aid viewing. The main bump in the lower figure is the Lyman alpha emission from the quasar. The raw observed flux is given by the black line. Blueward of the bump are the jagged features of the Lyman alpha forest, to be contrasted with the smooth behavior of the spectrum on the redward side. The dashed red line is the quasar composite and the blue dotted line is a PCA fit.

The lack of two- and three-dimensional information, however, is a major shortcoming. The basic question is how to extract information about the power spectrum from data available only from individual lines of sight? The first generation of simulations focused on determining the physical properties of the Lyman alpha absorbers. A Lyman alpha spectrum is fixed by the Hubble constant and the gas neutral fraction, peculiar velocity, density, and temperature along the line of sight. This being the case, artificial lines of sight can be run along simulations and connections established between the absorbers and physical properties of the IGM.

In order to use the forest as a cosmological probe, in principle one has to run many copies of a code, which contains all the relevant physics, while varying cosmological parameters. However, this is a very expensive strategy so for many purposes it is sufficient to use semi-analytic methods or simplified simulations. In our work, we have adopted two strategies: (i) work with a dark matter-only simulation but attempt to model the distribution of baryons by

smoothing the dark matter distribution to mimic the effects of gas pressure, or (ii) include a simplified treatment of hydrodynamics assuming a density-temperature relation for the IGM gas and then solving for the local pressure using the ideal-gas law. This second method is called Hydro-Particle-Mesh (HPM) and is known to be accurate to a few percent for the type of analyses we are carrying out. HPM simulations also require a model for the reionization history of the universe, thus even though they are simpler than a full hydro-solver, they too are very computationally intensive for a parameter variation study. (Fortunately, our work has shown that the reioization history has only a minor effect on the extraction of the linear power spectrum from the Lyman-alpha forest.) A comparison of the two methods is shown in Figure 2.

One of the unique aspects of Lyman alpha forest measurements is the ability to probe the primordial power spectrum at small scales—this presents excellent opportunities for constraining cosmological parameters, in particular the running of the spectral index. An example of how the SDSS data can constrain the normalization of the spectrum is shown in Figure 3. Green points with error bars are SDSS measurements of the flux power spectrum at z = 2.85, the curves are MC^2 predictions for the flux power spectrum for a range of amplitudes parametrized by
$\Delta^2 = k_p{}^3P(k_p, z = 2.85)/(2\pi^2)$ at
$k_p = 0.008$ s/km = 0.877 h Mpc^{-1}.
Calculations are now in progress to provide constraints on the running of the spectral index as well as the normalization of the mass power spectrum.

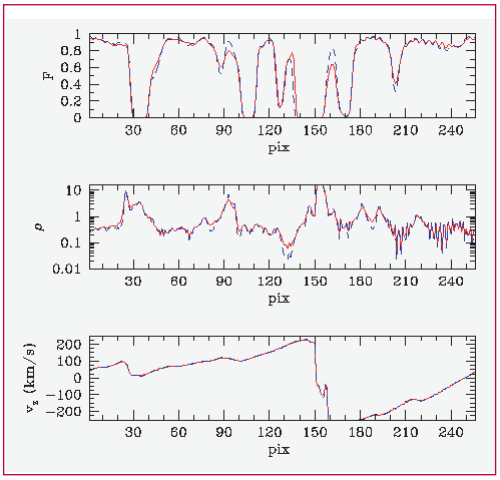

Figure 2— This figure shows a simulated QSO line of sight from a simulation with the HPM version of MC^2. The top panel shows the flux field, the middle the density, and the bottom, the peculiar velocity field. The red curve are measurements from the baryons directly, while the blue curves are extrapolations using only the dark matter distribution. As the data show, the agreement between the two is very good.

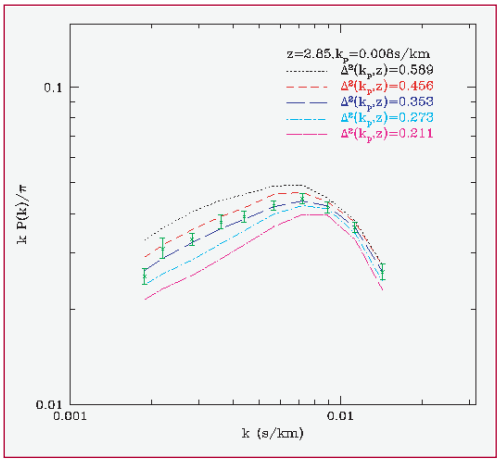

Figure 3— Constraining the amplitude of the power spectrum from SDSS data and HPM simulations from MC^2.

Nonlinear and Nonequilibrium Dynamics in Geomaterials

Salman Habib, T-8; Katrin Heitmann, ISR-1; David Higdon, D-1; Paul Johnson, EES-11; Donatella Pasqualini, EES-11; and James A. TenCate, EES-11; habib@lanl.gov

The transition from linear to nonlinear dynamical elasticity in rocks is of considerable interest in seismic wave propagation as well as in understanding the basic dynamical processes in consolidated granular materials. Rocks possess a variety of remarkable nonlinear elastic properties including hysterisis with end-point memory; variation of attenuation and sound velocity with strain; strong dependence of elastic and loss constants on pressure, humidity, and pore fluids; long-time relaxation phenomena ("slow dynamics"); and nontrivial variation of resonance frequency with strain. Significantly, materials as diverse as sintered ceramics and damaged steels are now known to display similar effects. Thus rocks may be viewed as representative members of a class of fascinating, but poorly understood, nonlinear elastic materials: fundamental questions still to be resolved relate not only to the underlying causes of the nonlinear phenomena but also to the conditions under which they occur.

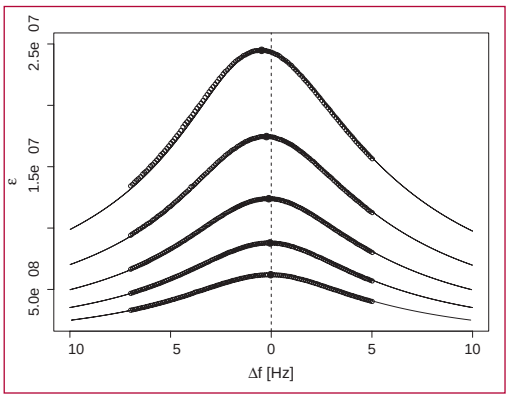

***Figure 1—** The average strain amplitude as a function of drive frequency for Fontainebleau sandstone. The reference center frequency is 1155.98 Hz. The open circles are the experimental data; the filled circles mark the peak positions. The solid lines are our theoretical predictions.*

The elastic behavior of rocks at small strains has been studied extensively for a long time, yet essential questions remain: while it has been previously claimed that at strain levels below parts per million (albeit with some uncertainty), rocks behaved as linear elastic materials—more recent data have been used to support an extension of the nonlinear region to substantially lower strains; doubt has been cast even on the very existence of a threshold for linear behavior. In addition, results from resonant bar experiments have been interpreted to exhibit a "nonclassical" frequency and loss dependence on the drive amplitude, i.e., frequency and the loss factor, Q, softening linearly with drive amplitude rather than quadratically as predicted by Landau theory, even at strains as small as 10^{-8}.

Using Fontainebleau and Berea sandstone samples, we have carried out a new set of well-characterized experiments, over a wide dynamic range, to unambiguously settle these questions The basic quantity measured in these experiments is the resonance frequency, f_0 , of the bar as a function of the strain, defined by the peak of the resonance curve (Figure 1).

Our major conclusions are as follows. Below a threshold strain of $10^{-8} - 10^{-7}$ (lower end for Fontainebleau, upper end for Berea), there was no discernible dependence of the resonance frequency on the strain—the materials behaved linearly to better than 1 part in 10^4. Above this level of strain, the materials displayed a reversible softening of the resonance frequency with strain, in excellent qualitative agreement with the quadratic prediction of classical nonlinear theory up to a point where memory and conditioning effects became apparent. In addition we also showed that, up to the conditioning threshold, the dynamical behavior is

accurately captured by a phenomenological macroscopic model incorporating a (softening) Duffing nonlinearity and linear losses (Figure 2). Beyond the conditioning threshold, the simultaneous presence of nonlinearity and nonequilibrium dynamics complicates the characterization of dynamical behavior; in the absence of a separation of these effects, the data cannot be interpreted to support the existence of nonclassical behavior.

We now turn to the behavior of f_0 beyond the point where conditioning begins to play a role. Here the frequency softening is such that f_0 no longer returns to the starting point when the drive is removed, but to a lower value. It is clear that in this regime the measured softening at a given strain cannot be interpreted as wholly due to an intrinsic nonlinearity. Analyzing a f_0 vs. ε curve without taking this effect into account would introduce an unknown systematic effect exaggerating the actual nonlinearity. To illustrate these issues, Figure 3 shows response curves for Berea sandstone in two different regimes. The left curve represents an experiment where, at each frequency, the sample is allowed to come to a new steady state (10 minutes at each frequency), while the right curve allows for 10 minutes between rapidly taken individual measurements to allow a return to thermal equilibrium between measurements. In both cases, the measurement protocols are designed to reduce relaxation effects as much as possible, in one case by staying at all times in a nonequilibrium steady state, and in the other, by allowing a close-to-equilibrium return between measurements. The key point is that, in this strain regime, the rock transitions to a nonequilibrium state characterized by a different set of macroscopic

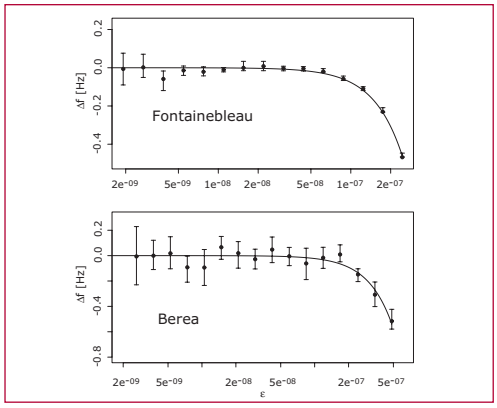

Figure 2— The resonant frequency shift as a function of the effective strain for Fontainebleau and Berea samples. The solid lines represent predictions of the theoretical model.

parameters, as evidenced by the 5-Hz shift between the left and right curves. If measurements could be made rapidly enough so that each point on the right curve corresponds to an equilibrium state, then it is precisely these response curves that are equivalent to data taken at lower strains (e.g., Figure 2). In practice, however, this procedure is very difficult to carry out as it requires stringent long-term environmental stability. Thus, all measurements to date in this higher strain regime are dangerously contaminated by memory and conditioning effects. Because of this competition of material nonlinearity and nonequilibrium effects, present experimental data cannot distinguish classical from nonclassical effects in this regime. Experiments to do so are in progress.

J. A. TenCate, D. Pasqualini, S. Habib, K. Heitmann, D. Higdon, and Paul A. Johnson, *Phys. Rev. Lett.* (submitted) LA-UR-04-1122.

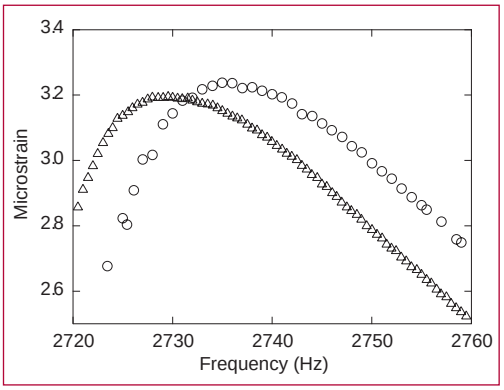

Figure 3— Avoiding relaxation effects: The left curve is for Berea maintained in a nonequilibrium steady state by continuous driving, while the right curve allows for a long relaxation to take place between the individual data points.

Precision Characterization of the Power Spectrum: Measuring the Baryonic Wiggles

Salman Habib, T-8; Katrin Heitmann, ISR-1; Alex Szalay, Johns Hopkins; and the SDSS Collaboration; habib@lanl.gov

The primordial density fluctuations that gave rise to structure in the universe are known to be essentially adiabatic and Gaussian. The power spectrum of these density fluctuations, P(k), is close to power-law but has yet to be characterized over a substantial dynamic range. Theories of the nature of the spectrum all invoke physics of the early universe (inflation and its alternatives). Methods to observe the spectrum include CMB anisotropy (WMAP), large-scale structure (SDSS, 2dF), and the Lyman alpha forest (SDSS, HIRES). Nongaussianity in the spectrum can be probed by CMB and large-scale structure observations. A much hunted for feature of the density fluctuation spectrum are the big bang predictions for the "baryonic oscillations" superimposed on the primordial spectrum as the universe underwent the fireball phase responsible for the CMB relic radiation.

These oscillations are acoustic modes of the coupled baryon-photon plasma in the fireball. Because the oscillations are imprinted on the matter distribution at a very early redshift ($z = z_{dec} \sim 1000$), on a length scale that corresponds to the sonic horizon at that epoch, they constitute a very useful "cosmic ruler" against which later measurements can be compared to measure the evolution history of the universe. The cosmic ruler technique provides an independent measure of the z-dependent Hubble parameter, and leads to an alternative method for characterizing the dark energy. The linear physics underlying the oscillations makes theoretical predictions and interpretations of the observations potentially much simpler than is the case with smaller-scale cosmological probes of dark energy such as galaxy clusters and supernovae.

The baryonic oscillations in the photons have been measured very precisely by recent CMB observations. An even more exquisite measurement will be performed by the Planck satellite towards the end of the present decade. From these CMB observations we have, in turn, very good measurements of cosmological parameters characterizing the large-scale universe, fixed by physics at the redshift of decoupling, z_{dec}. However, these results do not help in constraining dark energy parameters, since dark energy is completely subdominant till a much smaller redshift, $z \sim 1$. Because of this precondition, probing the physics of dark energy via baryon oscillations requires investigating the matter/galaxy distribution via large-scale surveys in the range $z \sim 1$.

But before such surveys are undertaken, it is important to have solid evidence for the oscillations from present large-scale structure surveys such as the Sloan Digital Sky Survey (SDSS). The amplitude of the oscillations is small as the baryon fraction of the Universe is quite low, $\Omega_b = 0.048$, compared to the dark matter contribution, $\Omega_{dm} = 0.27$. In addition, as observations cover only finite parts of the sky with geometrically complex shapes, it is important that one be certain that any oscillations in the power spectrum are not artifacts due to the window function of the survey. Finally, a problem with surveys of the local universe, such as the SDSS, is that nonlinear effects of gravitational cluster-

ing smear out most of the oscillations, so that at best only one or two of the oscillations may be visible (see figure). Hence, these features are best looked for at higher redshifts.

In the figure, results are shown from an N-body simulation with realistic cosmological parameters, consistent with present observations. The linear power spectrum is what the primordial power spectrum would be, if after being processed by plasma processes, it was amplified by the gravitational instability treated only in linear approximation. The nonlinear power spectrum must be computed numerically: at large scales, nonlinear efffects are negligible as the figure demonstrates. However, at smaller scales, mode coupling amplifies the power spectrum and smears out the already faint wiggles in the power spectrum. In the linear power spectrum of the figure, a few wiggles can be discerned, beginning with the one at ~ 0.06 h/Mpc (small features are not wiggles but numerical artifacts). However, in the nonlinear power spectrum, all oscillations at scales smaller than 0.1–0.2 h/Mpc are smoothed over. With a survey like SDSS, it is quite unlikely that one can observe more than one or two wiggles at z = 0. There is an ongoing effort in the SDSS to ferret out the baryonic oscillations from the large scale distribution of galaxies. A purely two-dimensional approach, relying on only the galaxy positions and densities on the sky, does not suffice since projection effects wash out the oscillations. Hence redshift information, either spectroscopic or photometric, is also required. In addition, careful numerical simulations are necessary to interpret the data. These simulations are now being performed using MC^2 (Mesh-based Cosmology Code, recently developed by us). The

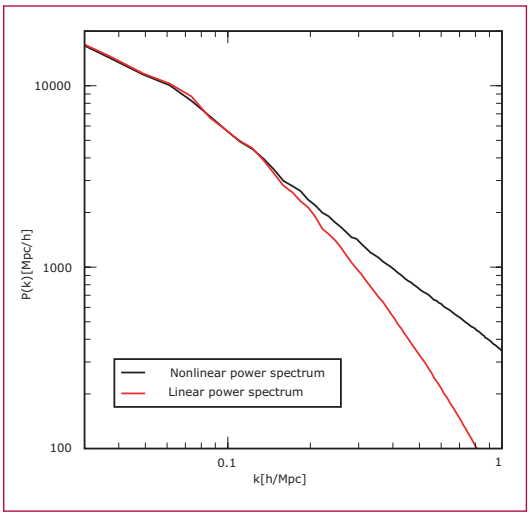

Figure—
The linear and nonlinear power spectrum at the present epoch (z = 0) showing baryonic oscillations. These are the smooth, low-amplitude, wave-like features; smaller glitches are numerical artifacts. For more details, see text. The nonlinear rise between k = 0.1–0.2 h/Mpc is also a target for present observations.

baryonic oscillations lie in the wave number range k ~ 0.03–0.3 Mpc^{-1}, therefore very high resolution is not required for numerical accuracy. Nevertheless, statistical sampling is an issue, so large simulation volumes are needed.

Future large-volume redshift surveys, either earth-based or conducted from space, aim at looking much deeper than the SDSS, out to z ~ 2–3. With these surveys it is possible in principle to measure several of the oscillation peaks, since the nonlinear smearing effect enters at larger k-values. Such measurements promise very good constraints on the dark energy equation of state, of order 10%, quite competitive with other currently-suggested methods. We are also carrying out simulations to assess systematic issues relevant to these surveys, such as galactic bias (with Karl Glazebrook [Johns Hopkins]).

The Quantum Emergence of Chaos

Salman Habib, T-8; Kurt Jacobs, Griffith; and Kosuke Shizume, Tsukuba; habib@lanl.gov

Macroscopic mechanical systems obey classical mechanics to very high accuracy; nevertheless these systems are made up of atoms that ultimately follow a quite different set of dynamical rules, i.e., those given by quantum mechanics. The emergence of classical mechanics from the underlying quantum physics—the quantum to classical transition—has elicited great interest ever since the inception of quantum theory. A central issue in the study of this transition is the very existence of chaos in quantum mechanics.

One of the major, perhaps *the* major problem of quantum chaos relates to the nature of the chaos that we observe in the natural world. Chaos manifestly exists in the nonlinear differential equations of classical dynamics but not in the time-dependent Schrödinger equation. If quantum mechanics is truly the fundamental theory that describes our world, a resolution to this apparent tension must exist.

A key insight into the solution of this puzzle is provided by the fact that all experimentally accessible systems are observed systems. The necessity for taking the observation process into account was pointed out by Chirikov.

We had shown earlier that modern measurement theory resolves the puzzle of how classical chaos is connected with the dynamics of open quantum systems. Recently, we have demonstrated that it also provides tools to address two fundamental questions: can the existence of chaos be addressed in quantum dynamical systems outside of the localized classical regime? And, if so, how can the emergence of chaos out of the deep (nonchaotic) quantum regime be characterized and understood?

Fortunately, with the aid of parallel supercomputers (in this case, LANL Q), quantum trajectories characterizing the evolution of observed systems can be found numerically and analyzed for chaotic behavior far from the classical regime. These trajectories have some special features that need to be considered carefully in order to define and extract Lyapunov exponents. Nevertheless, these difficulties can be overcome, and we have succeeded in defining appropriate exponents, as well as measuring them. We have also found that constructs such as stroboscopic maps are helpful in understanding the nature of chaos as an emergent quantum phenomenon.

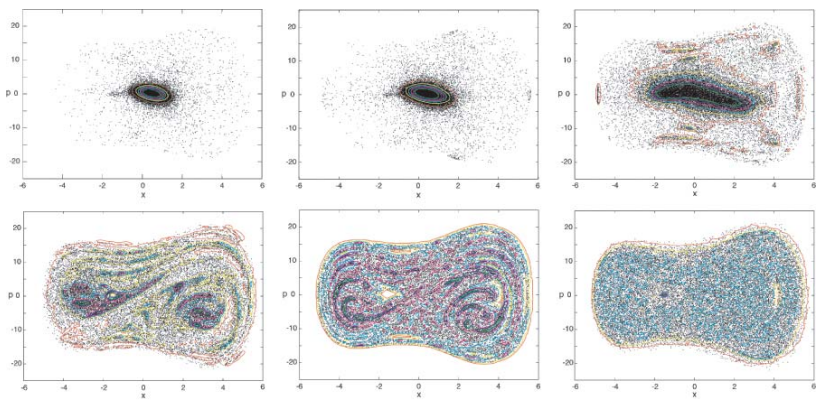

Figure 1—Stroboscopic maps for six different values of k, clockwise: $k = 5 \times 10^{-4}$, 0.001, 0.01, 0.1, 1, 10. Contour lines are superimposed to provide a measure of local point density.

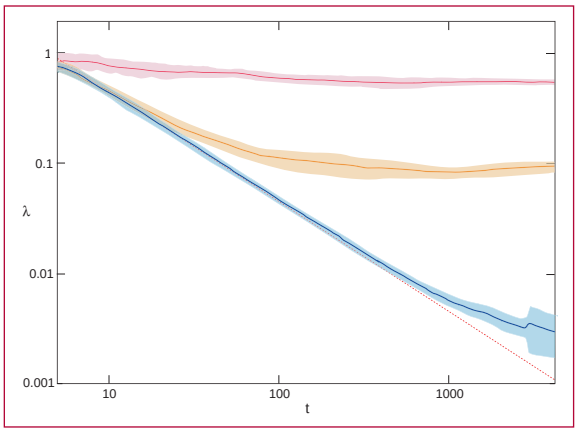

Figure 2—The finite-time Lyapunov exponent for quantum trajectories at different values of the measurement strength. Note the peeling away from the asymptotic 1/t behavior.

An important result follows from our definition of the Lyapunov exponent: In unobserved dynamical systems, it is possible to prove that the exponent vanishes; the finite-time Lyapunov exponent, decaying away as 1/t. This theorem codifies the expectation that, since the quantum evolution is linear, any measure of chaos applied to the evolution of smooth distributions should yield a vanishing Lyapunov exponent. Once measurement is included, however, the resultant nonlinear conditioning makes the quantum evolution nonlinear, and the Lyapunov exponent need no longer vanish.

We studied the emergence of chaos in a paradigmatic example, the driven Duffing oscillator—a particle in a double-well potential driven sinusoidally in time by a linear force.

To systematically explore how the nature of the dynamics changes from the deep quantum regime to the classical regime, we vary the value of the measurement strength, k, over a dynamic range of roughly five orders of magnitude. As a global diagnostic of the dynamics, we first construct stroboscopic maps for six different values of the measurement strength (Figure 1). For very small k, the system is largely confined to a small region in the center of phase space. As k is increased, the confinement is reduced, and the system explores more of the phase space. Somewhat remarkably, at k = 0.01, although the quantum distribution is largely delocalized, nontrivial structure appears in the stroboscopic map, with the system spending considerable time in certain outer regions of the phase space. At k = 0.1 the localized regions have formed into swirling structures, and this continues for k = 1, with the structures becoming narrower and sharper. At k = 10 the swirls disappear, and we retrieve the uniform chaotic sea of the classical map. It is important to note that the maps shown in Figure 1 are the result of long-time integration, hence essentially time-invariant.

The swirls visible in the stroboscopic maps at k = 0.1 and k = 1, in fact correspond to the unstable manifolds of the classical motion. Classically, these are only visible at short times, as the continual and repeated folding of the manifold eventually washes out any structure in the midst of a uniform tangle. In the quantum regime, however, the weakness of the measurement, with its inability to crystallize the fine structure, has allowed the structure of the unstable manifold to survive in the stroboscopic map.

The corresponding behavior of the Lyapunov exponent is shown in Figure 2. Note that the exponent follows the 1/t behavior expected for k = 0, before peeling off to a nonzero asymptotic value. Thus dynamical chaos exists even in the delocalized quantum regime.

Salman Habib, Kurt Jacobs, and Kosuke Shizume, LAUR-04-1245 (to be submitted).

The Semiclassical Regime of the Chaotic Quantum-Classical Transition

Salman Habib, T-8; Ben Greenbaum, Columbia; Kosuke Shizume, Tsukuba; and Bala Sundaram, CUNY; habib@lanl.gov

The process by which a classical dynamical system emerges as a sufficient approximation to a quantum dynamical system has been a topic of investigation since the inception of quantum mechanics. Recent applications of quantum mechanics in computing, communication, nanoscience, and optics have only increased the practical importance of gaining a greater theoretical understanding of this issue. From a purely dynamical perspective, the difficulty arises because nonlinear classical evolution equations violate the unitary symmetry of quantum mechanics, as reflected in the singular nature of the limit of the Planck constant tending to zero. Likewise, the symplectic geometry of a chaotic classical phase space generates infinitely fine structures that the uncertainty principle prevents a quantum dynamical system from tracking at late times. For these reasons, classical behavior cannot emerge as the smooth limit of a closed nonlinear quantum system.

As all observed systems interact with their environment, the modern approach to understanding the quantum-classical transition relies on the open system paradigm. Quantum decoherence and conditioned evolution arising as a consequence of environmental couplings and observation provide a quantitative framework for addressing this issue. As we have shown earlier, effectively classical dynamics at the level of individual trajectories is ensured when inequalities involving the Planck constant, the system action S, and the measurement coupling k are satisfied. However, having a system satisfy these inequalities still leaves open an understanding of the physics underlying the transition and the degree to which a classical system may be a sufficient approximation at the level of expectation values even if these inequalities are not satisfied.

In the present work, we demonstrate that, for a bounded open system with a classically chaotic Hamiltonian, the quantum-classical transition is generated by two parallel processes. First, the semiclassical approximation for quantum dynamics, which eventually breaks down for classically chaotic systems due to overwhelming nonlocal interference effects, is rendered local via the measurement interaction. This leads to a well-defined effectively classical limit, albeit with residual noise. Second, this measurement noise restricts the foliation of the unstable manifold, the set of points, which approach a hyperbolic point in reverse time, allowing the semiclassical wave function to track this modified classical geometry.

We begin by first considering the effect of weak noise on a classical evolution. Our analysis shows that, for a bounded phase space region, the noise leads to a termination in the development of fine-scale phase space structures at some finite time t^*, whose scaling behavior can be determined. One does not see an ergodic phase space region, but rather one in which the large, short-time features that develop prior to t^* are pronounced and the small, long-time features that develop after t^* are smoothed over in the averaging process. Therefore, to approximate noisy classical dynamics, a quantum system need not track all of the fine scale structures of a classically chaotic system, but only the larger

features that develop before the production of small scale structures terminates.

In the case of zero noise, it is known that the semiclassical approximation fails due to the proliferation of momentum branches arising from the infinite number of foldings of a bounded chaotic curve as time increases. Interference fringes stemming from a given branch cannot be distinguished after a certain time from those emanating from the many neighboring branches. However, the presence of noise acts as a dynamical Gaussian filter, dynamically filtering the long "De Broglie" wavelength contributions to the semiclassical integral, the very sort of contributions which generally invalidate such an approximation. If we combine the above result with our understanding of how noise effects classical phase space, we can qualitatively estimate whether or not a semiclassical picture is a valid approximation to the dynamics. As discussed above, t^* is the time when the formation of new classical structures ceases and $l(t^*)$ is an associated length scale over which classical structures are averaged. The key requirement is then that the semiclassical phase filters contributions of roughly this scale, if so, for a given branch, the phases with associated wavelengths long enough to interfere with contributions from neighboring branches will be strongly damped, and the intuitive semiclassical picture of classical phase distributions decorated by local interference fringes will be recovered.

To illustrate these mechanisms we considered a driven Duffing oscillator with unit mass (see figure. The evolution of the Duffing system was solved numerically on the IBM SP-3 at the National Energy Research Scientific Computing Center (NERSC) for both the classical and quantum master equations. For $D = 10^{-5}$, the classical and quantum sections show no similarities, as one would expect for a chaotic Hamiltonian. On increasing the value of D to $D = 10^{-3}$ the magnitude of quantum coherence decreases dramatically and the classical and quantum slices have the same average value, as well as specific agreement on some large scale features. The two disagree, as expected, on the small scale structures. This indicates that, while the quantum and classical distributions functions do not exactly match, the Wigner function has now become sensitive to the larger features of the noise-averaged classical distribution function, indicative of the transition to a semiclassical regime. At $D = 10^{-2}$, there is near perfect agreement between classical and quantum distribution functions, save on the smallest scales.

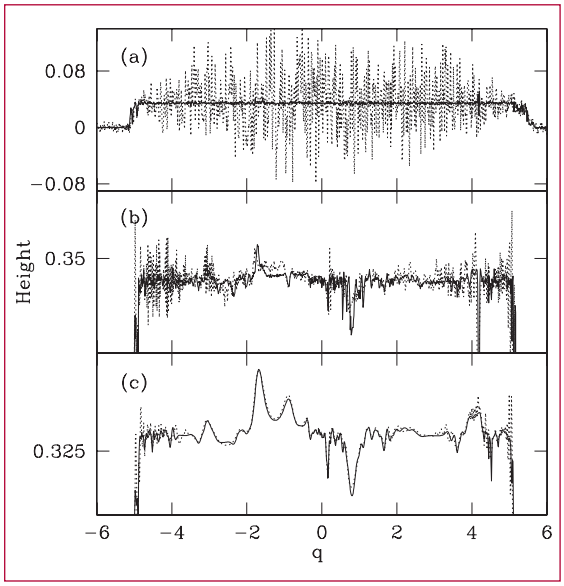

***Figure—** Sectional cuts of Wigner functions taken at p = 0 after 149 periods of evolution for (a) D = 10-5; (b) D = 10-3; (c) D = 10-2. D is the noise diffusion coefficient. In each case, the dashed line shows the full quantum evolution while the solid line results from classical Liouvillian dynamics. The height is specified in scaled units.*

B. D. Greenbaum, S. Habib, K. Shizume, B. Sundaram, *Phys. Rev. Lett.* (submitted) LA-UR-03-9308.

Counts in Cells Statistics in the SDSS

István Szapudi, Univ. of Hawaii; Luís F. Teodoro, T-8; Michael S. Warren, T-6; and the SDSS collaboration; teodoro@lanl.gov

The main aim of statistical analysis of galaxy catalogs is to extract information about the initial mass fluctuations in the early universe, their subsequent gravitational evolution, and the processes relevant for galaxy formation. To decode the available data, the distribution of the underlying dark matter has to be inferred from the galaxy distribution. In principle, one can assume the two distributions are quite different, i.e., galaxies are biased tracers of the underlying density field. For a class of phenomelogical models, galaxy fluctuations, δ_g, are assumed to be a monotonic function of the matter fluctuation field, $f(\delta_m)$ (these include the simplest case of linear bias $\delta_g = b \cdot \delta_m$). Hence, an accurate knowledge of such a function is required to interpret galaxy statistics in light of theories of structure formation and evolution.

A popular methodology is to extract the bias function from measurements of large scale structure and the Cosmological Microwave Background (CMB). For instance, one can use second order statistics from several sources, especially CMB maps together with galaxy catalogs to constrain bias. In the framework of CMB fluctuations having a direct relationship with the density fluctuations in the early universe, the comparison with present day galaxy statistics reveals information on both the gravitational amplification and galaxy formation. The use of these techniques is limited to fairly large scales since the secondary anisotropies of the CMB, as well as growth and bias for galaxies, become more and more complex and cumbersome to handle on small scales. A complementary approach is to use higher order statistics or velocity information from galaxy catalogs to derive the bias function internally. These methods, however, are limited to linear or weakly nonlinear scales, where both gravitational instability and linear bias are well understood.

The latest generation of overwhelmingly large galaxy surveys (for instance, Sloan Digital Sky Survey [SDSS] and 2dF) will enable high-precision determination of the N-point correlation functions. Since the most reliable data are available on smaller scales it is natural to look for methods that constrain bias on such (nonlinear) scales. One of the most successful methods for extracting the amplitude of higher order correlations is based on measuring the distribution of counts in cells (CIC) from galaxy surveys. We are applying the method developed by Colombi & Szapudi (2004) [1] to the SDSS galaxy catalogs. This technique allows us to compute the most accurate estimation of CIC in realistic data sets since it is the first edge corrected CIC estimator, which also uses a fast algorithm for massive oversampling. The resulting information will be used to estimate the bias function via a comparison of the cumulative distributions in simulated dark matter and galaxy catalogs (see Szapudi & Pan [2004] [2] for more details). Preliminary studies based on SDSS mock catalogs drawn from high-resolution dark matter simulations show that we can reconstruct the nonlinear bias function down to highly nonlinear scales with high precision in the mass fluctuations range of $-1 < \delta_m < 5$ (see Figure).

[1] S. Colombi and I. Szapudi, in preparation.
[2[I. Szapudi and *J. Pan, ApJ* **602**, 26 (2004).

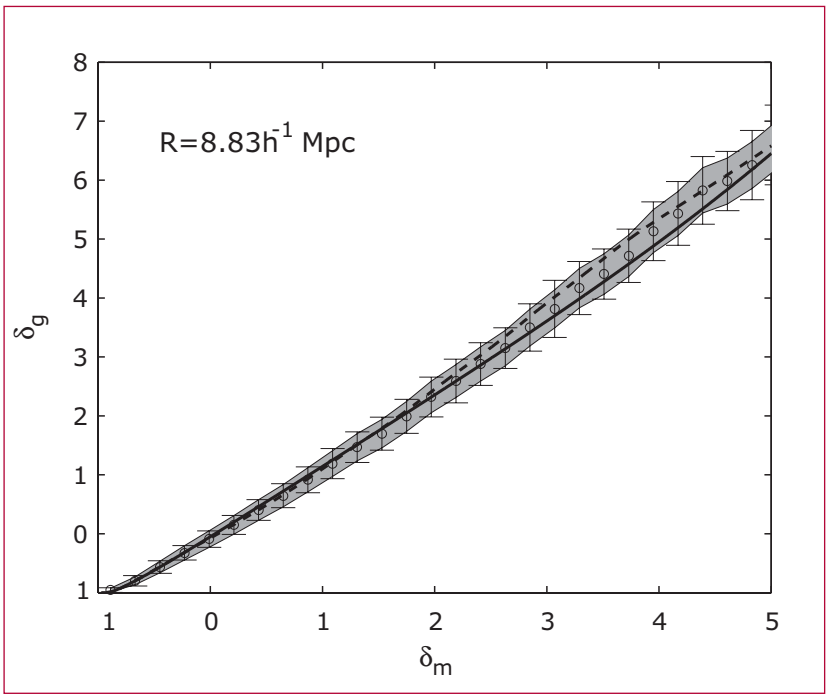

Figure—Bias function $\delta\gamma = f(\delta\mu)$ ***from a Sloan Digital Sky Survey mock catalog. The CIC measurements were obtained using 8.83*** h^{-1} ***Mpc cells. Solid and dashed lines represent two different techniques that are being applied to the Sloan Digital Sky Survey galaxy survey (see Szapudi and Pan [2004] [2] for more details) for computing the bias function. Circles are the*** $\langle\delta\gamma|\delta\mu\rangle$ ***measured directly from a galaxy mock survey and the respective dark matter simulation; error bars show their 1-*** σ ***scatter. The shaded area represents simple Poisson scatter, which appears to be an excellent approximation to the stochasticity of the bias in these mock catalogs.***

Measurements of Cosmological Parameters Using Long Duration Gamma-Ray Bursts

Yongzhong Xu and Salman Habib, T-8; xuyz@lanl.gov

Type Ia supernovae (SNIa) have proved to be a powerful probe for cosmology, in particular, dark energy detection, because they are luminous, hence can be seen for large distances, and also because they are excellent standard candles for distance estimations. The high luminosity makes distant SNIa visible out to a redshift z ~ 2, which allows for covering the interesting range of z = 0.5–1.5 for characterizing dark energy using the Hubble diagram (distance-redshift relation). Besides the measurement of supernova redshifts, the fact that they can be used as high-quality distance indicators is equally important. Strong constraints on cosmological parameters, such as the cosmological constant, matter density, the cosmological equation of state, and the Hubble constant, can all be inferred from the supernova redshift-distance relation. Gamma-ray bursts (GRBs) have some properties similar to supernovae. Since the first optical and radio counterparts of gamma-ray bursts were discovered in 1997, there is no doubt that at least the long-duration GRBs originated at cosmological distances. It is now believed that GRBs are one or two orders more luminous than supernovae. Therefore, one can probe the universe at redshift up to 6 or higher. (The SWIFT GRB satellite mission might see GRBs at much deeper redshifts.) Recently, two research groups have proposed that long-duration GRBs probably have two luminosity or distance indicators. One proposal is that the luminosity of GRBs is related to the spectral lag, the time delays between high- and low-energy X-ray photons. The other proposal is that the burst luminosity is connected to the variability, the number of spikes of the GRB light curve. In short, the long duration GRBs have the potential to possess all three properties that SNIa have: they originated at cosmological distances; they are extremely luminous; and they may be standard candles. Therefore, theoretically, we can already begin to put constraints on cosmological parameters by analysing long-duration GRBs. This method provides another route, independent of supernovae, the cosmic microwave background (CMB), and large-scale structure (i.e., the distribution of galaxies at large scales), for this purpose. The small number of GRBs and yet unknown systematics are problems that will both definitely lessen with time.

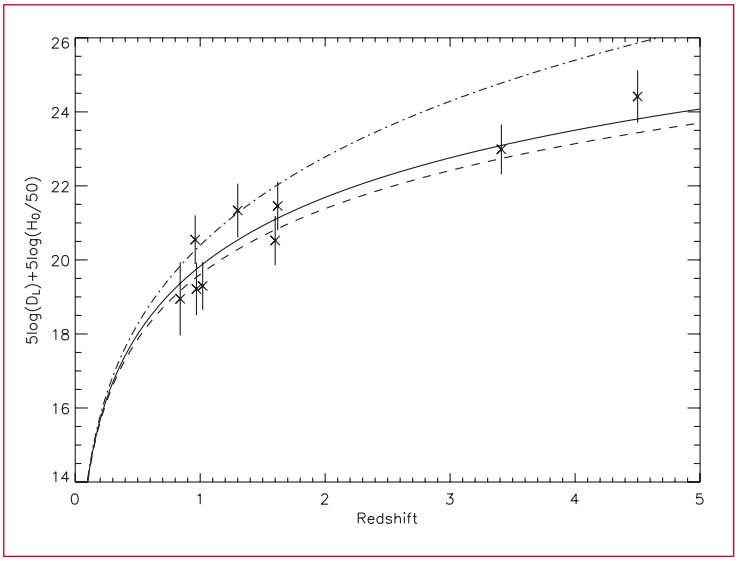

***Figure 1—** The luminosity distance d_L as a function of redshift z. The data points are recalculated from Schaefer (2003). All three theoretical curves are for a flat universe. The solid curve is the d_L–z relation with matter density Ωm = 0.3, the dashed curve is for Ωm = 0.5, and the dashed-dot curve is for Ωm = 1.*

Using the two distance indicators mentioned above, Schaefer has built a GRB Hubble diagram, i.e., the luminosity distance as a function of redshift, from nine well-observed GRBs (Figure 1). Given this GRB Hubble diagram, the rest of the calculation is straightforward: we use the maximum likelihood method to constrain parameters. Specifically, we calculated the theoretical curves for various cosmological models (the relevant parameters are the cosmolgical

constant, the matter density, and the Hubble constant), then used those curves to obtain fits to the GRB Hubble diagram and calculated the χ-squared for each curve. Marginalizing over one parameter, say the Hubble constant, we obtain a contour plot for the other two parameters, the cosmological constant and the matter density (Figure 2). As shown in Figure 2, we find that the matter density parameter $\Omega_m = 0.2 \pm 0.2$ and the cosmological constant $\Lambda = 0.4 \pm 0.6$. If we assume the universe is flat, as follows from CMB observations, most recently the results from the WMAP satellite, then results are much improved. We find, $\Omega_m = 0.25 \pm 0.1$. Figure 3 shows constraints on the Hubble constant assuming a flat universe. The Hubble constant $H_0 = 68$ km/s/Mpc $\pm$ 6 km/s/Mpc if the matter density $\Omega_m = 0.3$, which is the preferred value as found from CMB and large-scale structure observations.

These results are of course preliminary (only nine GRBs have been used!). Nevertheless, they are in good agreement with all other cosmological observations. After SWIFT flies (within the next year), hundreds of well-defined GRBs are expected to be observed. The major improvement in statistics and systematics from this dataset will help make GRBs an exciting cosmological probe, with Hubble diagrams constructed out to redshifts impossible to reach with any other method.

[1] B. E. Schaefer, *Ap. J.* **583**, L67 (2003).
[2] Y. Xu and S. Habib, LAUR-04-0364.

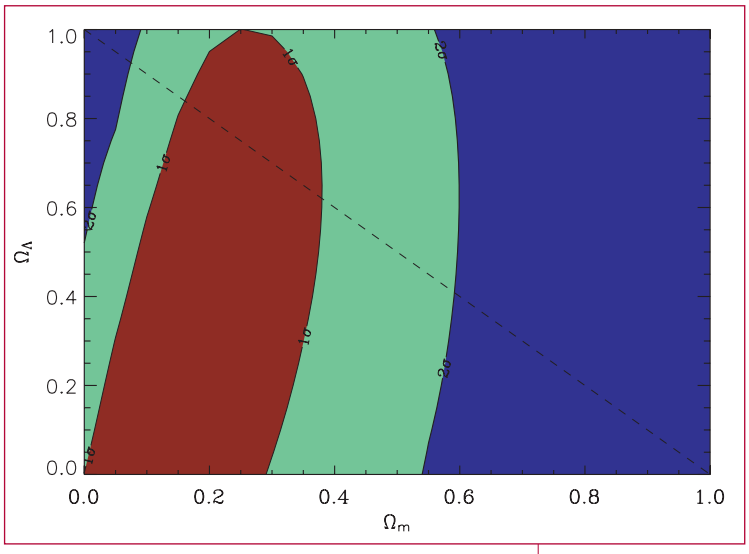

***Figure 2—** The contour plot of the constraint on matter density and cosmological constant with a fixed value of the Hubble constant, $H_0 = 68$ km/s/Mpc. The dashed line is for a flat universe.*

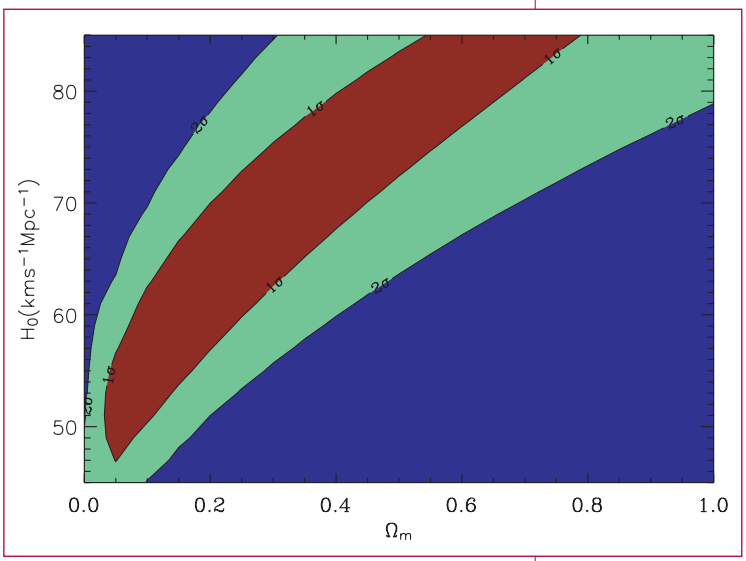

***Figure 3—** Constraint on H_0 with a prior of a flat universe. $H_0 = 68$ km/s/Mpc $\pm$ 6 km/s/Mpc setting $\Omega m = 0.3$.*

Extracting Information from the Cosmic Microwave Background and the Galaxy Distribution: Frequency Dependence of the WMAP-SDSS Cross-Correlation

Yongzhong Xu and Salman Habib, T-8; and the SDSS Collaboration; xuyz@lanl.gov

Recent work on spatial correlation between the cosmic microwave background (CMB) temperature and large-scale structure (LSS) in the galaxy distribution (hence also the mass distribution) has found evidence for the integrated Sachs-Wolfe (ISW) effect, a long-range gravitational effect that does not occur in a purely matter-dominated universe. As such, the measurement of this effect is a significant extra piece of evidence for the existence of dark energy.

This sort of cross-correlation analysis between the CMB and the matter distribution also has other uses, one of which we now describe. The distribution of bound hot gas in the universe is correlated with the local dark matter density.

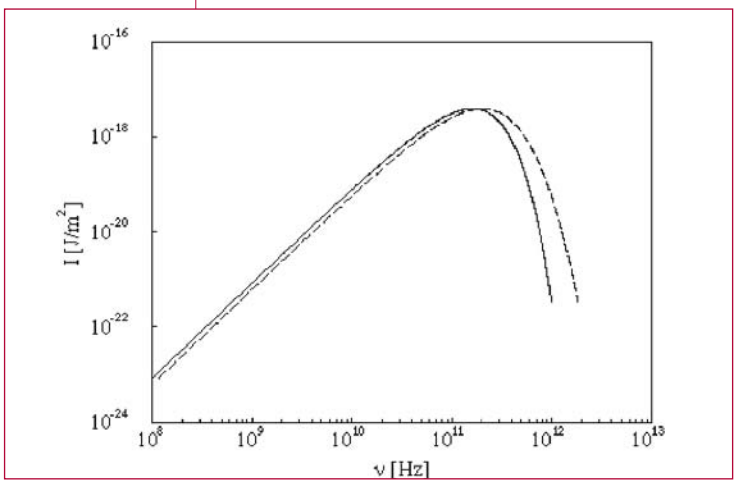

***Figure 1—** An example of the thermal SZ effect: the solid line is the original CMB thermal distribution along the line of sight, the dashed line is the spectrum as distorted after passing through a cluster.*

CMB photons passing through this gas suffer spectral distortions, which, at a given frequency, appear as brightness temperature shifts. While the ISW effect causes a positive correlation between CMB temperature and the large-scale mass distribution, the effect of the hot gas is in the opposite direction.

When CMB photons pass through galaxy clusters, they scatter off hot electrons (with temperatures up to 10^8 K, known from cluster X-ray observations) and gain energy via inverse Compton scattering. Thus, the spectrum of the CMB photons gets distorted from the original black-body spectrum and moves blueward. As a result, at lower frequencies, the flux of CMB photons becomes lower than the black-body power spectrum, and at the higher frequency end, the flux increases (Figure 1). This is known as the thermal Sunyaev-Zeldovich effect (SZ effect). The frequency dependence provides an important observational discriminant for detecting the effect. Our main goal is to find how the CMB temperature-mass density correlation depends on frequency, providing direct evidence for intracluster medium (ICM) hot gas. Since the ICM hot gas is known to exist, this project is essentially a proving ground for an even more ambitious cross-correlation problem—the detection of the the warm hot intergalactic medium (WHIM) that contains half of the baryons in the universe and is supposed to be correlated with dark matter filaments, and since galaxies trace dark matter, to galaxy filaments.

The data that we used are from the Sloan Digital Sky Survey (SDSS) and the first-year Wilkinson Microwave Anisotropy Probe (WMAP) results. Since the SZ effect does not depend on redshift, galaxy redshift information is not required. The SDSS photometric dataset perfectly suits our purpose: (i) it has a

very high-galaxy density (20,000 galaxies per square degree); (ii) it covers a large part of the sky (more than 5,000 square degrees); and (iii) it contains detailed information on small scales, which is important for finding the SZ effect. The WMAP dataset is the best all-sky CMB dataset so far. It contains independent CMB temperature maps on five different frequency bands, i.e., Ka (~ 22 GHz), K (~ 30 GHz), Q (~ 40 GHz), V (~ 60 GHz), and W (~ 90 GHz). The last three bands (Q, V, and W) have the least foreground contamination (i.e., contamination from the Milky Way and point sources).

In order to conveniently calculate the correlation functions, we pixelized the SDSS data in the exactly same way as the WMAP data, i.e., each pixel has a size of about 7 arcminutes, which is about two times larger than the angular size of a galaxy cluster at redshift z = 0.1. Scranton et al. (SDSS collaboration) have already shown that there is no evidence for the SZ effect using all the SDSS pixels overlapping with the WMAP data. However, this is not at all surprising. Because the SZ effect only occurs where a galaxy cluster is located, and galaxy clusters are located in only a small fraction of pixels, the tiny signal from the SZ effect averages to zero if all pixels are used to calculate the correlation functions. However, it is not a trivial task to select out all clusters photometrically or even spectroscopically. Here we apply a simple method to select out information related to clusters: generally, a pixel containing galaxy clusters has larger galaxy density than other pixels. Thus we carry out a cross-correlation between the CMB brightness temperature and the galaxy number density.

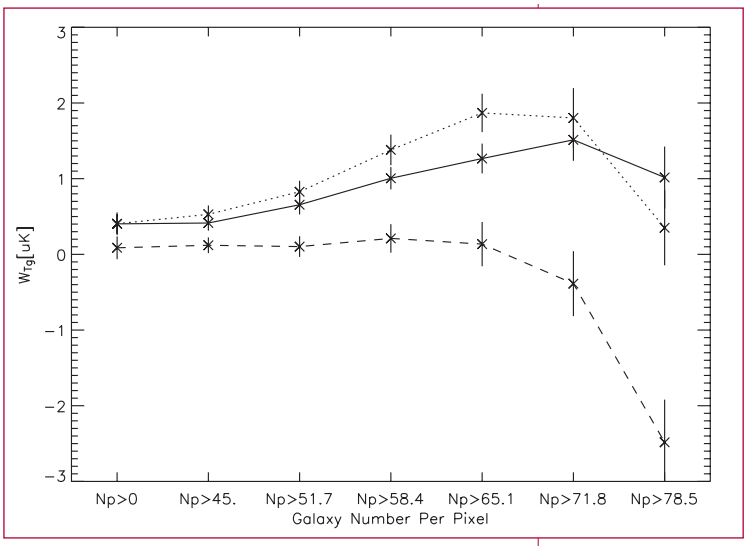

Figure 2—Cross-correlation between WMAP temperature and SDSS galaxy distribution on small scales. The solid line is the Q band, the dotted line is the V band, and the dashed line is the W band.

Figure 2 shows the cross-correlation between WMAP and SDSS on very small scales (< 7 arcmins) in three different frequency bands (Q, V, and W). As theoretically expected, the W band shows the largest effect with a clear decrement signal at large galaxy densities. The lowering trend is also seen in the Q and V bands at the highest galaxy density but further investigation is necessary as the statistics are poor. To sum up, we have found evidence for frequency dependence in the WMAP temperature-SDSS galaxy density cross-correlation. However, further work is needed to verify whether this frequency dependence is actually caused by the thermal SZ effect. Analyses of this kind will become much more definitive as higher resolution CMB temperature maps are released from next-generation observations such as the SPT and PLANCK.

[1] R. Scranton et al., astro-ph/0307335

T-11 Condensed Matter and Statistical Physics

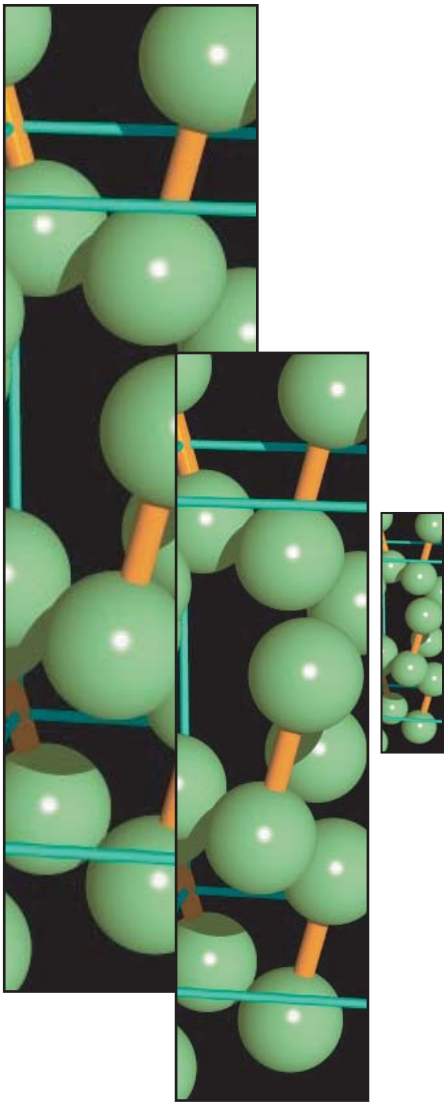

Atomistic Understanding of Ti Phase Transformations

Robert C. Albers, T-11; Sven P. Rudin, T-1; S. G. Srivilliputhur, MST-8; in collaboration with M. D. Jones, SUNY-Buffalo; R. G. Hennig, D. R. Trinkle, and J.W. Wilkins, Ohio State; D. M. Hatch and H. T. Stokes, BY Univ.; rca@lanl.gov

Titanium is an important surrogate material for understanding the effects of structural phase transformations in shocked materials. We have recently developed a detailed atomistic explanation of many of the details of the most important solid-solid transformation for this material (equilibrium α hcp and high-pressure ω). We have first studied the equilibrium phase diagram of Ti, using a tight-binding model that is fit to first-principles electronic-structure calculations for Ti to calculate quasi-harmonic phonons and the Gibbs free energy of the hexagonal close-packed (hcp) and omega (ω) crystal structures. The hcp phonon dispersion agrees with experiment; the ω phonon dispersion has yet to be measured. The model predicts that the true zero-temperature ground state is the ω structure and that it is the entropy from the thermal population of phonon states, which stabilizes the hcp structure at room temperature. We present the first completely theoretical prediction of the temperature-and pressure-dependence of the hcp-ω phase transformation and show that it is in good agreement with experiment. The quasi-harmonic approximation fails to adequately treat the bcc phase because the zero-temperature phonons of this structure are not all stable. Our predicted phase diagram [1] is shown in Figure 1.

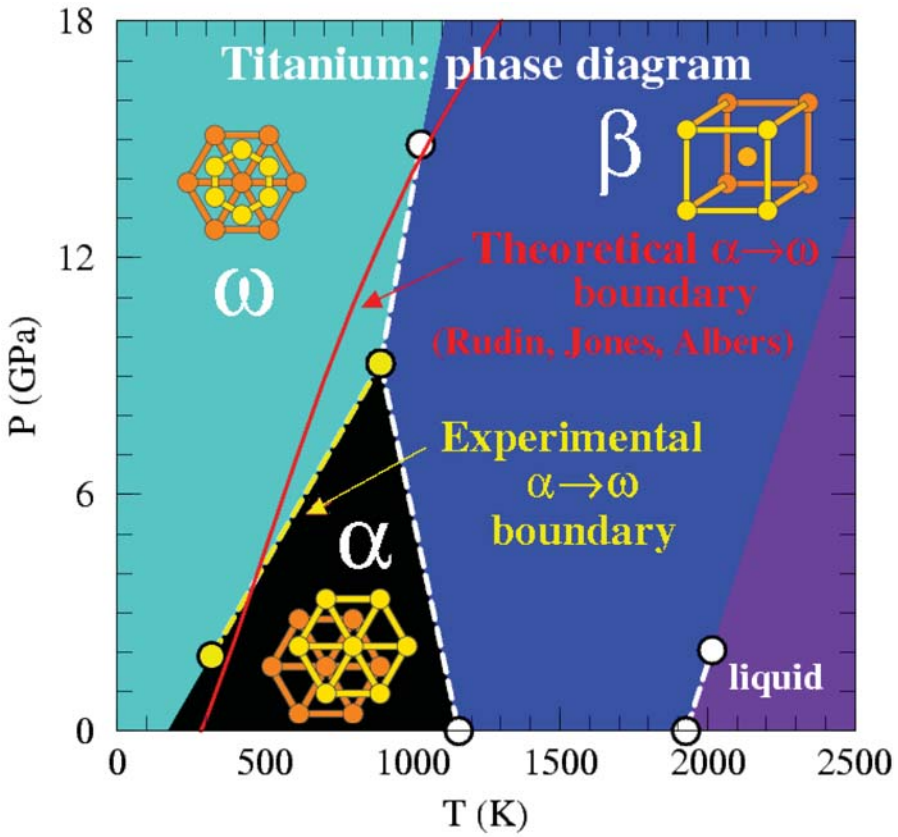

***Figure 1—** The phase diagram of titanium. The dashed lines connect the experimental data points; the solid line shows our calculated* α (hcp) *to* ω *transformation. Thermal stabilization explains why at room temperature the experimentally observed hcp structure is favored over the* ω *structure (the calculated zero-temperature ground state).*

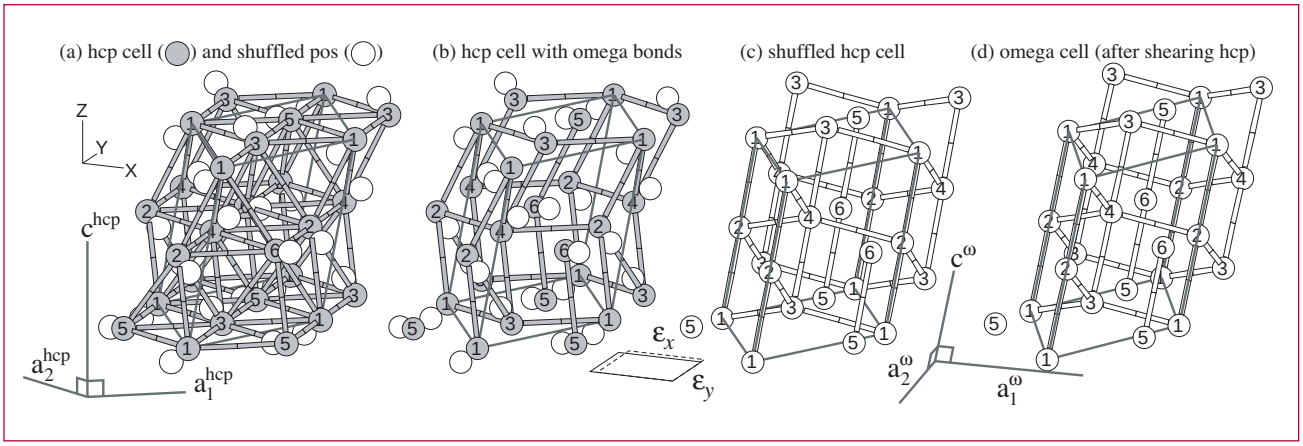

We have also studied the details of how the atoms continuously move between the two crystal structures. We have found a new mechanism [2] for this movement (shown in Figure 2), which has a lower energy barrier than the previously suggested mechanism. This new homogeneous transformation was found by systematically generating and sorting possible α to ω pathways by their energy barriers.

[1] Sven P. Rudin, Matthew D. Jones, and Robert C. Albers, "Thermal Stabilization of the HCP Phase in Titanium," *Phys. Rev. B.*

[2] D. R. Trinkle, R. G. Hennig, S. G. Srinivasan, D. M. Hatch, M. D. Jones, H. T. Stokes, R. C. Albers, and J. W. Wilkins, "A New Mechanism for the Alpha to Omega Martensitic Transformation in Pure Titanium," *Phys. Rev. Lett.* **91**, 025701 (2003).

Figure 2—
Our proposed α to ω transformation pathway. The direct 6-atom transformation is visualized (i) as a two-step process, (ii) with 21 additional atoms outside the heavy gray parallelepiped supercell. In α, atoms 1,3,5 and 2,4,6 are in the A and B stacking planes, respectively; whereas in ω, atoms 1–4 are in the Wyckoff d position of space group P6/mmm, and atoms 5–6 are in the Wyckoff a position. (a) The gray atoms in the α cell shuffle to new positions (white atoms), with atoms 1–4 shuffling 0.63 Å, and atoms 5–6 shuffling 0.42 Å. (b) The α cell is redrawn with the "bonds" of the ω structure. Step 1: Shuffling the gray atoms to the white positions, the α cell (b) produces a strained ω cell (c), contained in the same supercell. Step 2: Straining the supercell (c) e_{xx}=-0.09, e_{yy}=0.12, and e_{zz}=-0.02 produces the final ω supercell (d).

New Pseudostructure for α-Pu

M. Johan Bouchet and Robert C. Albers, T-11; rca@lanl.gov

Pure plutonium (which also includes Pu with small amounts of other solute atoms) is an exotic metal that is poorly understood. The *5f* electronic orbitals appear to be partially localizing in different ways in different crystal structures, leading to a large variation in the volumes of the different solid phases. The cause of this anomalous behavior is believed to be due to correlations between the *5f* electrons as they try to avoid each other in each Pu atom. Theoretical approaches for understanding such effects are extremely difficult and involve very complex theories. Up until now, almost all of these approaches have been applied only to the δ-phase of Pu, which has a simple fcc crystal structure. These correlation effects are believed to be weaker in the α-phase. However, the α-structure is so complicated (16 atoms per unit cell), that it has been impractical to apply the same approach to the α-phase.

We believe that we have now found a solution to this problem [1]. We have discovered a new pseudostructure for α-Pu that involves only two atoms per unit cell and is a relatively symmetrical orthorhombic crystal structure and can show that the real α crystal structure only involves small distortions of various atoms around this pseudostructure; the electronic-structure energy of both systems (at least at the band-structure level) is nearly identical. Sophisticated electronic-structure techniques should be just as easy for this pseudostructure as for δ Pu.

By a pseudostructure we mean a simpler crystal structure where the atoms are quite close to the positions of the more complex real structure. Pseudostructures are interesting for two reasons: (1) they provide insight into the geometrical structure of the atoms in the original structure and possible phase-transformation pathways, and (2) they provide an alternative less expensive crystal structure for complicated electronic and microstructural calculations. From a physics point of view, one can view the pseudostructure as an approximation to

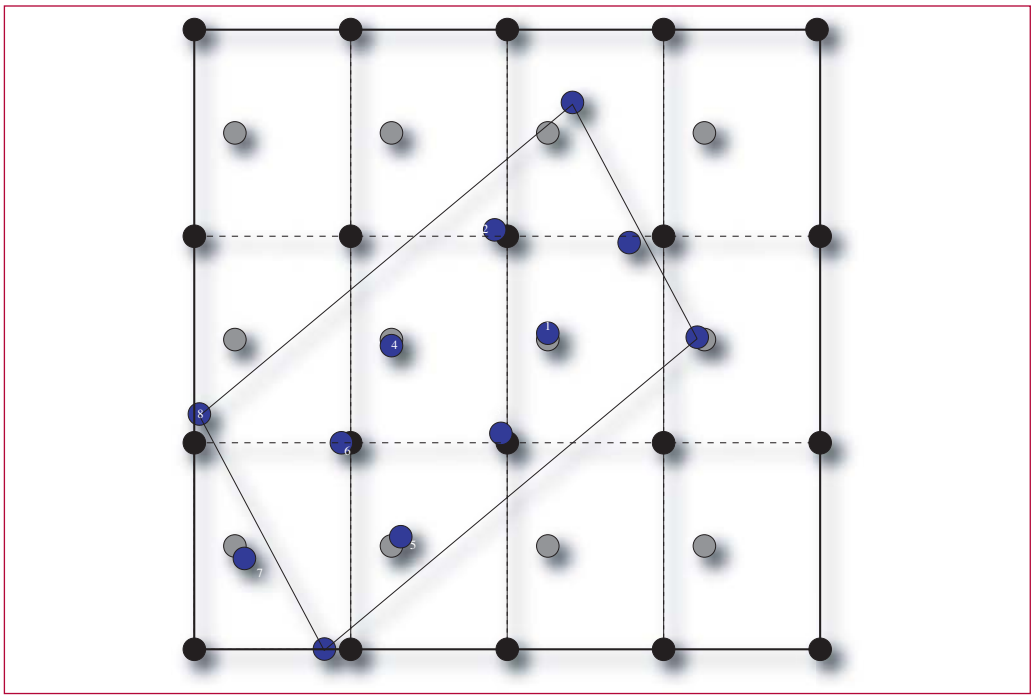

Figure 1—Pseudostructure in the (011) direction. The blue atoms are the eight positions in the α–Pu structure.

Near-Neighbor Distances in Å (number of nn)			
	Pseudostructure	α	
1st nn shell	2.47(4)	2.46–2.55(4)	short bonds
2nd nn shell	3.31(4)		
3rd nn shell	3.49(4)	3.21–3.59(10)	long bonds
4th nn shell	3.50(2)		

Table — Nearest-neighbour distances (in Å) for the pseudostructure and α-Pu (in parentheses are the number of atoms in each shell). These values are given for the theoretical equilibrium volume for each structure.

the real structure that captures the dominant total energy of the electronic-structure (heat of formation) and local bonding effects; the real structure can then be viewed as just a minor distortion of the pseudostructure, with only a small energy difference between the two structures.

In Figure 1 we show a comparison of the atomic positions of α-Pu with our pseudostructure, and in the table a comparison of near-neighbor distances between the two structures.

[1] J. Bouchet, R. C. Albers, M. D. Jones, and G. Jomard, "New Pseudo-Phase Structure for α-Pu," *Phys. Rev. Lett.*

Nondemolition Measurements of a Single Quantum Spin

Lev Bulaevskii and Marina M. Hruska, T-11; A. Shnirman, Institüt für Theoretische Festkörperphysik Universität Karlsruhe, Germany; Darryl L. G. Smith, T-11; and Yu Makhlin, Institüt für Theoretische Festkörperphysik Universität Karlsruhe, Germany and Landau Institute for Theoretical Physics, Russia; lnb@lanl.gov

Quantum measurements in mesoscopic systems by use of tunneling have recently attracted great interest, due to the challenges of single spin detection and quantum computing where the final state of a qubit after computation must be measured. A typical detector couples to a single observable of the qubit. If this observable commutes with the spin Hamiltonian, the quantum nondemolition (QND) regime is realized, i.e., the eigenvalues of the observable can be measured with proper probabilities even by a weakly coupled detector. If the observable does not commute with the spin Hamiltonian, the initial state is quickly destroyed and one can only observe the steady state properties of the qubit in a continuous measurement. In the spin detecting tunneling schemes, all components of the localized spin are coupled to the tunneling electrons via the exchange interaction. Thus QND tunneling measurements seem questionable.

We showed that, in fact, QND measurements of the spin projection on the direction of the applied magnetic field are possible with the use of spin dependent Josephson tunneling at low temperatures, when effects of quasiparticles are negligible. In this case, the amplitude of Josephson oscillations depends on the state of the spin just before the measurement. The amplitude can be measured, for example, in a circuit containing a single localized spin 1/2 between conventional singlet superconducting electrodes as in a superconducting STM setup, a dc-voltage source V, and a resistor R. The dissipative spin-dependent current in the circuit appears when the voltage exceeds a threshold and, effectively, it measures the squared amplitude of the Josephson-current oscillations. Due to spin conservation in a singlet-Cooper-pair tunneling in the absence of quasiparticles, the average spin projection onto the direction of the applied magnetic field is preserved to second order in the tunneling amplitude when voltage is smaller than twice the superconducting gap, though the spin projection operator does not commute with the Hamiltonian of the system. Thus a QND measurement of the spin state is performed by use of the singlet-pair tunneling as an intermediate nondissipative system that allows one to obtain information on the initial value of the spin projection without flipping the spin.

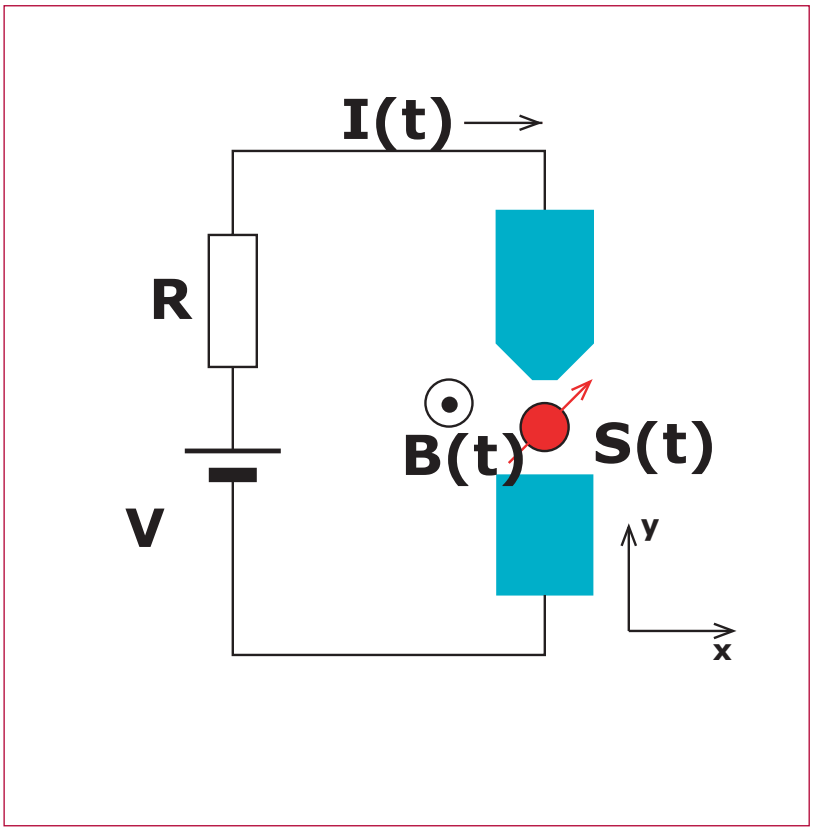
I(t)
R
V
B(t)
S(t)
y
x

Atomistic Description of Rayleigh-Taylor Instabilities

Kai Kadau, T-11; Timothy C. Germann, X-7; Peter S. Lomdahl, T-11; Brad Lee Holian, T-12; Guy Dimonte, X-4; Nicolas G. Hadjiconstantinou, Massachusetts Institute of Technology; and Berni Alder, Lawrence Livermore National Laboratory; kkadau@lanl.gov

We investigate the evolution of 3-dimensional (3D) Rayleigh-Taylor (RT) instabilities, which occur when a heavy fluid is laid on top of a light fluid under the influence of a gravitational field [1]. A series of quasi two-dimensional (2-D) atomistic computer simulations involving up to a million atoms, reveal that thermal atomistic disturbances build up long-wavelength instabilities, which eventually lead to a turbulent growth of bubbles into the heavier and spikes into the light fluid, see Figure 1. After the development of an unstable spectrum of waves at the interface, the most dominant wave leads to a growth of the mixing that is approximately quadratic in time, Figure 2, in accordance with experimental observations and theoretical approaches [2]. For small Mach numbers M ($M^2=\lambda g/c_h^2$ is the dimensionless compressibility, with λ = wavelength of pertubation, g = gravitational constant, c_h = sound velocity of the heavier fluid) the growth coefficients observed only depend on the magnitude of the gravitational constant and the Adwood number (density difference divided by the sum of densities). Larger Mach numbers lead to increased mixing due to compressibility effects.

So far, only 2-D atomistic simulations of the discussed fluid instability have been published, but these neglect compressibility effects and 3-D features

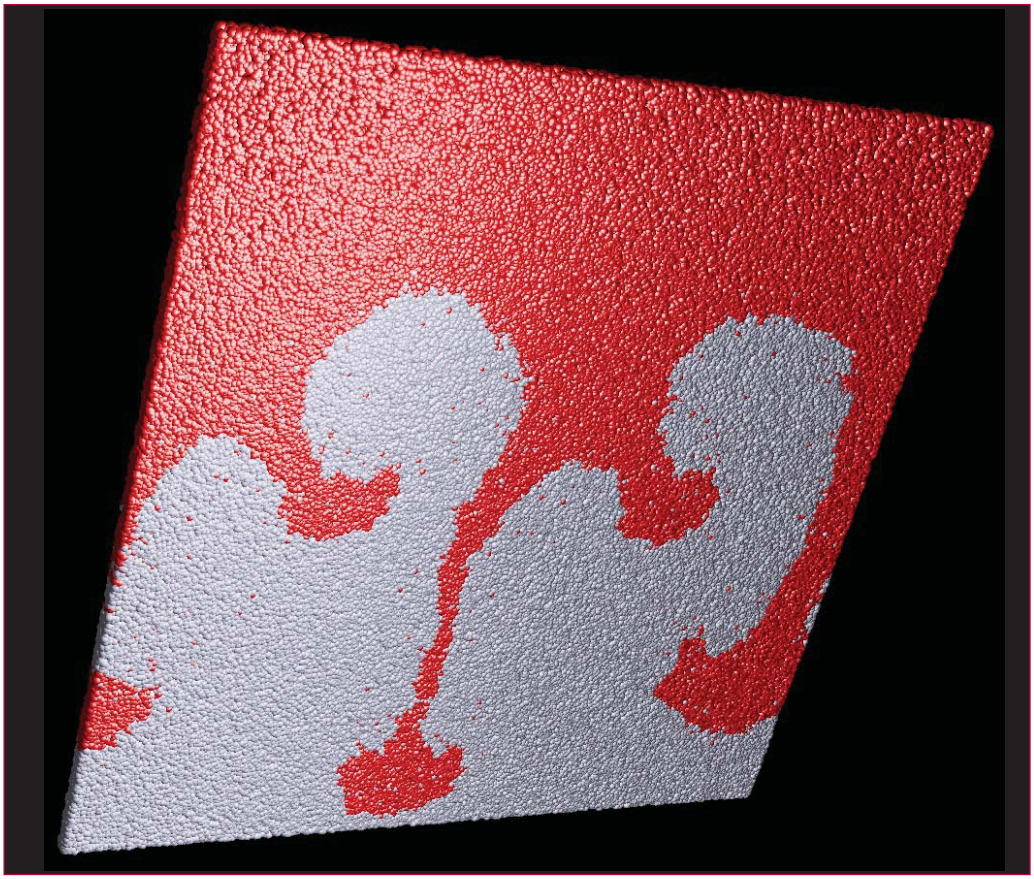

Figure — Turbulent Rayleigh-Taylor mixing on the atomic scale in a pseudo 3-dimensional system: A heavy fluid (red spheres) and a light fluid (gray spheres) penetrate each other under the influence of a downward gravitational field.

[3]. Experimental studies, as well as numerical hydrodynamic calculations, show contradictory results [4]. Therefore, the atomistic simulations performed here will help to illuminate these issues.

Acknowledgements:
This work has been supported by the U.S. Department of Energy.

[1] The SPASM ("Scalable Parallel Short-range Molecular dynamics") code is described in: Peter S. Lomdahl, P. Tamayo, N. Grønbech-Jensen, and D. M. Beazley, in *Proceedings of Supercomputing* **93**, G. S. Ansell, Ed. (IEEE Computer Society Press, Los Alamitos, CA, 1993), 520; D. M. Beazley and Peter S. Lomdahl, *Computers in Physics* **11**, 230 (1997); see also *http://bifrost.lanl.gov/MD/MD.html.*

[2] P. F. Linden, J. M. Redondo, and D. L. Youngs, *Journal of Fluid Mechanics* **265**, 97 (1994).

[3] W. Dzwinel, W. Alda, M. Pogoda, and D. A. Yuen, *Physica D* **137**, 157 (2000).

[4] J. Glimm, J. W. Grove, X. L. Li, W. Oh, and D. H. Sharp, *Journal of Computational Physics* **169**, 652 (2001).

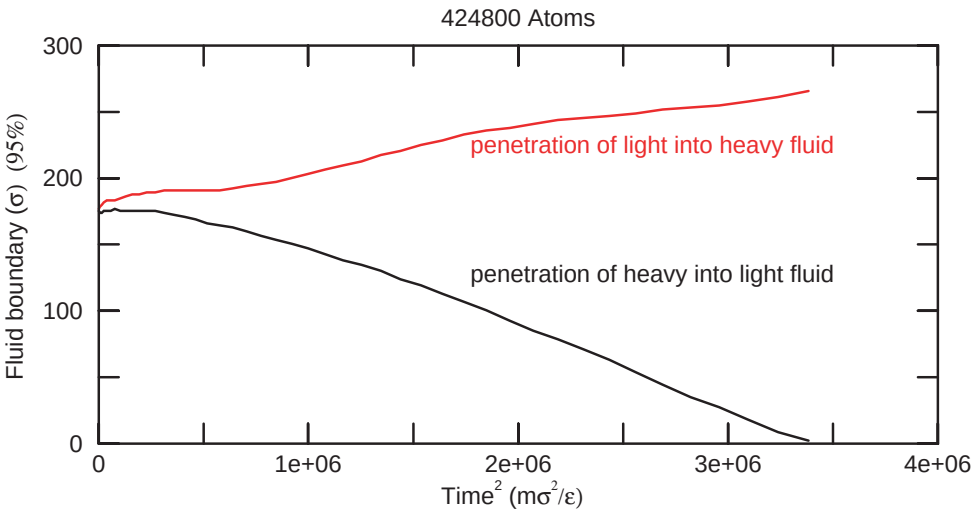

Figure 2—Penetration depth of bubbles/spikes into the heavy/light fluid for a quasi 2-dimensional Rayleigh-Taylor instability. After the initial development of a spectrum of unstable waves at the interface, the growth is approximately quadratic in time.

Molecular Dynamics Study of Mechanical Deformation in Nano-Crystalline Metals

Kai Kadau, T-11; Timothy C. Germann, X-7; Peter S. Lomdahl, T-11; and Brad Lee Holian, T-12; kkadau@lanl.gov

Nano-crystalline metals exhibit physical properties different from ordinary polycrystalline materials, which make these materials of technological interest [1]. One important example is the increasing hardness with decreasing grain size mostly blamed on dislocation immobilization at the grain boundaries, and this is known as the "Hall-Petch effect" [2,3]. However, when decreasing the grain size below a critical value, sliding processes between the grains decrease the hardness, and is called the inverse Hall-Petch effect [4,5].

Here we report on large-scale molecular-dynamics simulations [6] investigating the tensile testing of nano-phase Al and Cu, Figure 1. The atomic interactions were described by an embedded-atom method (EAM) potential especially designed to model Al [7] and Cu [8]. For grain-sizes below 12 nm we found the inverse Hall-Petch relation as shown in Figure 2. The deformation processes here are dominated by grain-rotation, grain-sliding, and grain-growth-mechanisms that result from the large fraction of grain-boundary atoms. In the case of nano-phase Al, we found that inter-grain fractures can occur, identified by a sudden drop in the stress-strain plot shown in Figure 3.

In the case of Cu we found a cross-over from the inverse Hall-Petch relation to the ordinary Hall-Petch relation for grain-sizes larger than 12 nm. In this regime dislocation activity becomes more and more active, whereas the inter-grain activities become less important. We have observed for the first time, using atomistic simulations, a cross-over between two regimes: one dominated by inter-grain activity and the other by an intra-grain mechanism.

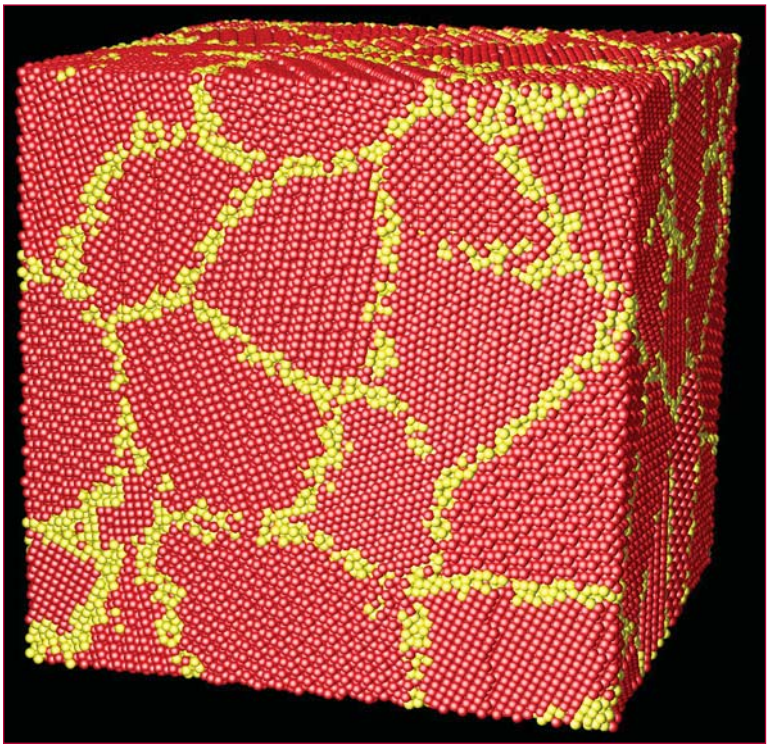

***Figure 1—** A nano-crystalline sample containing some 200,000 atoms, with an average grain-size of 4.73 nm. Grain-boundary atoms are yellow, and bulk atoms are marked red.*

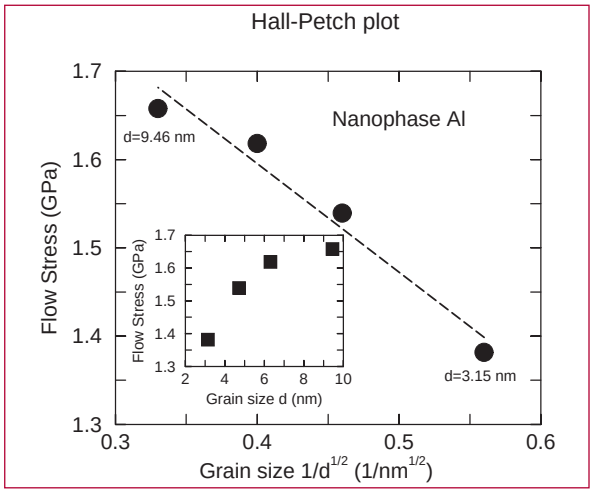

Figure 2— Hall-Petch plot for nano-phase Al showing the inverse Hall-Petch relation, i.e., softening with decreasing grain-size due to inter-grain processes. The inset shows the "raw-data" (squares) suggesting the cross-over between the inverse Hall-Petch and the Hall-Petch regime at larger grain-sizes.

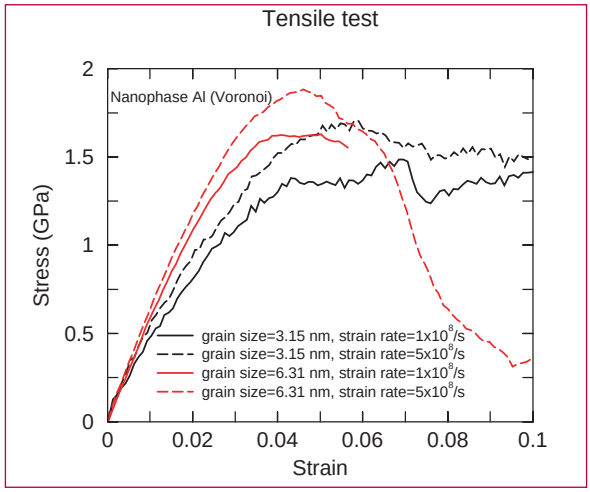

Figure 3— Stress-strain relation for tensile testing of nano-phase Al. Inter-grain fracture can occur, identified by the sudden drop in the stress-strain curves.

Acknowledgements:
This work has been supported by the U. S. Department of Energy.

[1] R. W. Siegel, in *Physics of New Materials,* F. E. Fujita, ed., 1994, Springer-Verlag, Heidelberg, p.64; C. L. Liu, J. B. Adams, and R. W. Siegel, *NanoStructured Materials* **4**, 265 (1994).
[2] E.O. Hall, *Proc. Phys. Soc. London* **64**, 747 (1951).
[3] N. J. Petch, *J Iron Steel Inst.* **174**, 25 (1953).
[4] T. G. Nieh and J. Wadsworth, *Scripta Metallurgica et Materialia* **25**, 955 (1991).
[5] J. Schiotz, F. D. Di Tolla, and K. W. Jacobsen, *Nature (London)* **391**, 561 (1998).
[6] The SPaSM ("Scalable Parallel Short-range Molecular dynamics") code is described in: P. S. Lomdahl, P. Tamayo, N. Grønbech-Jensen, and D. M. Beazley, in *Proceedings of Supercomputing* **93**, G. S. Ansell, Ed. (IEEE Computer Society Press, Los Alamitos, CA, 1993), 520; D. M. Beazley and P. S. Lomdahl, *Computers in Physics* **11**, 230 (1997); see also *http://bifrost.lanl.gov/MD/MD.html.*
[7] S. Grabowski, K. Kadau, and P. Entel, *Phase Transitions* (2002).
[8] A. F. Voter, *Phys. Rev. B* **57**, 13985 (1998).
[9] T. Campbell, R. K. Kalia, A. Nakano, F. Shimojo, K. Tsuruta, and P. Vashishta, "Structural Correlations and Mechanical Behavior in Nanophase Silica Glasses," *Phys. Rev. Lett.* **82**, 4018 (1999).

Structural Phase Transitions in Ga: Massive Parallel Implementation and Application of the Modified Embedded-Atom Method

Kai Kadau, T-11; Timothy C. Germann, X-7; Peter S. Lomdahl, T-11; and Brad Lee Holian, T-12; kkadau@lanl.gov

The Modified Embedded Atom-Method (MEAM) [1] applies to metals with greater covalent bonding than the conventional Embedded Atom Method (EAM) [2], which is restricted to nearly-free-electron (simple fcc) metals. MEAM can also describe different crystallographic structures of one element or compound correctly. As a result of the angular bonding terms, semiconductors like Ga [3] and Si [4] can be described reliably. An important aspect is the possible screening of the pair potential between two atoms, as well as the atomic electron densities. Screening takes place within an ellipse that is defined by the pair of atoms of interest, and limits the range of interactions in a natural and more physical manner than the usual radial cut-off of the involved functions. For instance, screening leads to different effective cut-off distances for different atomic arrangements, which might be important for the description of the dynamics of phase transformations. Since screening is continuous in space, it also has a contribution to the forces. Because of the more global description of the solid phase diagram, it is of great interest to study the dynamics of a solid-solid phase transformation using the MEAM framework. However, such a study requires the implementation of the MEAM formalism into a parallel molecular-dynamics (MD) code [5] like SPaSM [6], in order to describe the dynamics of millions of atoms. The principal challenge for the parallel implementation of MEAM is the treatment of the screening in the interatomic forces.

The pressure-induced solid-solid transformation of Ga will be investigated.

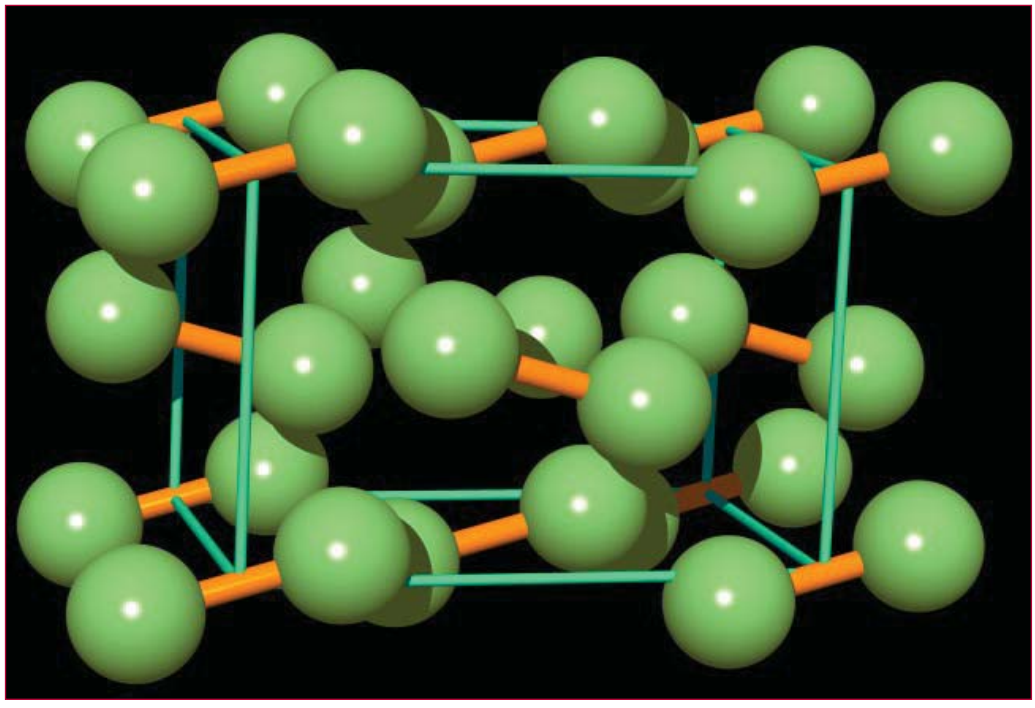

***Figure 1—** Unit cell of the Ga A11 ground-state structure. The structure is achieved by Ga dimers occupying an orthorhombic cell.*

Using the MEAM potential for Ga recently proposed by Baskes *et al.* [3], loading and unloading cycles of simulation cells of Ga will be performed. The pressure-induced A11, see Figure 1, to bcc transition will be discussed and compared to experimental diamond anvil cell data. A next step will be to describe the dynamics of the shock-induced structural phase transformations [7] for Ga and Pu-Ga alloys.

Acknowledgements:
This work has been supported by the U. S. Department of Energy LDRD-DR 20020053. It is also a pleasure to thank M. I. Baskes, S. G. Srinivasan, and R. Ravelo.

[1] M. I. Baskes, *Phys. Rev. B* **46**, 2727 (1992).

[2] M. S. Daw and M.I. Baskes, *Phys. Rev. Lett.* **50**, 1285 (1983); M. S. Daw and M. I. Baskes, *Phys. Rev. B* **29**, 6443 (1984); M. S. Daw, S. M. Foiles, and M. I. Baskes, *Mater. Sci. Rep*. **9**, 251 (1993).

[3] M. I. Baskes, S. P. Chen, and F. J. Cherne, *Phys. Rev. B* **66**, 1041007 (2002).

[4] J. G. Swadner, M. I. Baskes, and M. Nastasi, *Phys. Rev. Lett.* **89**, 085503 (2002).

[5] M. P. Allen and D. J. Tildesley, *Computer Simulation of Liquids* (Clarendon Press, Oxford, 1987); D. C. Rapaport, *The Art of Molecular Dynamics Simulation* (Cambridge University Press, Cambridge, 1995); W. G. Hoover, *Time Reversibility, Computer Simulation, and Chaos* (World Scientific, Singapore, 1999).

[6] The SPaSM ("Scalable Parallel Short-range Molecular dynamics") code is described in: P. S. Lomdahl, P. Tamayo, N. Grønbech-Jensen, and D. M. Beazley, in *Proceedings of Supercomputing* **93**, G. S. Ansell, Ed. (IEEE Computer Society Press, Los Alamitos, CA, 1993), 520; D. M. Beazley and P. S. Lomdahl, *Computers in Physics* **11**, 230 (1997); see also *http://bifrost.lanl.gov/MD/MD.html.*

[7] Kai Kadau, Timothy C. Germann, Peter S. Lomdahl, and Brad Lee Holian, *Science* **296**, 1681 (2002).

Understanding and Predicting the Initiation of DNA Transcription

Kim Ø. Rasmussen, T-11; Georgios Kalosakas, T-11/CNLS; Alan R. Bishop, T-DO; and C. H. Choi and A. Usheva, Division of Endocrinology, Harvard Medical School; kor@lanl.gov

All of the information necessary to establish and maintain the human body is stored in DNA. The human genome is a masterwork of engineering, storing billions of bits of data at the molecular level as sequences of only four distinct nucleotides: adenine (A), guanine (G), cytosine (C), and thymine (T). This sequence is strung together by a sugar-phosphate backbone, and stabilized by a complementary strand of DNA (T and A are complementary as are G and C) that protects each base in the sequence as a base pair, wrapped inside the well-known double helix. This structure is further coiled around proteins called histones and compacted into just a few microns of chromatin.

Genes are the stretches of DNA that contain the blueprints for specific proteins. They can range from just a few hundred to several thousands of base pairs in length. One may think of them as discrete, linear "files" stored within the genome. The sequential reading of these files by a protein complex (polymerase) is known as transcription. Each gene possesses a genetic "marker," called promoter DNA, which points to the exact base pair from which to begin transcription (see Figure 1). This spot, the transcription initiation site, is crucial to successful transcription. Accessing the information stored in DNA is not an easy task. First, enzymes restructure chromatin to unwrap it from storage structures known as nucleosomes. Then, the DNA double helix must be "unzipped" exactly at the proper place in order to read its base sequence. The machinery necessary for transcription to begin is known as the "transcription initiation complex." The DNA strands must separate, and this machinery must insert itself into the resulting open area—the transcription "bubble"—where it proceeds to transcribe a complementary copy of the DNA sequence as RNA, which informs the protein factories of cells (ribosomes), to produce proteins. The precise functioning of this transcription mechanism is critical to sustaining life, as the mutation of just one base pair can result in a crippling disease.

While sequence-specificity is known to be important for the binding of the preinitiation protein complex, the exact mode of binding has not been determined. Conventional theory would have the complex recognize the sequence of bases directly, or through subtly unique secondary structures in DNA. But it

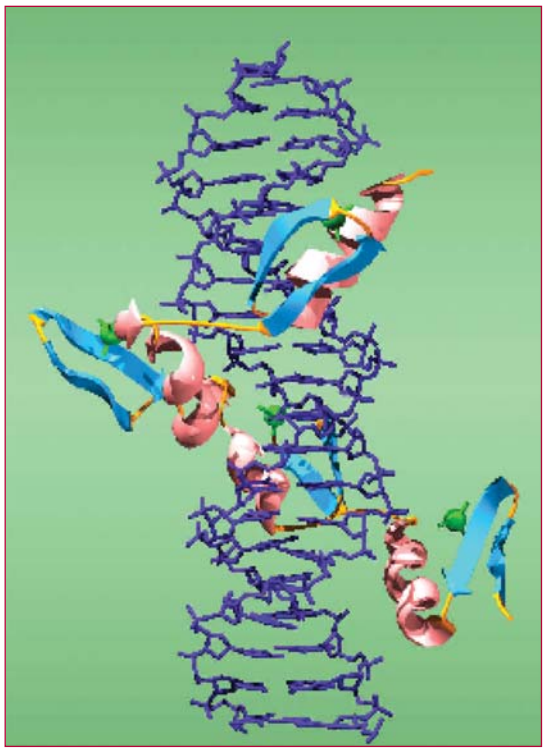

Figure 1—Promoter DNA with the polymerase bound to it.

must not be forgotten that DNA is a *dynamic*, flexible polymer. At room temperature, proteins and DNA are constantly fluctuating and vibrating. One may think of these motions as a type of "breathing" behavior of DNA. So the double helix is constantly being deformed and bent, and the base pairs are pressed together and pulled apart. Our working hypothesis is that perhaps this type of dynamics may open the way for proteins to bind DNA.

In order to test this idea we have used a microscopic model proposed by Dauxois, Peyrard, and Bishop [1] to describe the dynamics of the openings of double stranded DNA. This model focuses only on the most relevant degrees of freedom, namely the transverse stretching of the hydrogen bonds connecting complementary bases in the opposite strands of the double helix. Its reduced character, involving a small number of variables, makes it suitable for simulations over relatively long times and appropriate for gathering sufficient statistics. We have found that in the premelting regime, which correspond to biologically relevant temperatures, the model accurately reproduces the occurrence of local melting (bubbles). Figure 2 illustrates this result: The top panel shows in dark color the occurrence of bubbles in a T7 promoter sequence as it is observed in a sequencing gel experiment [2]. The bottom panel shows, for the same sequence, the calculated occurrence of large bubbles. It is seen that the model is able to quite accurately predict the regions in the promoter DNA sequence most likely to sustain large local openings. Further, it is interesting to note that the transition initiation site (+1) is the region where these large openings occur most frequently, and the other regions where bubble formation is observed are associated with the binding of protein complexes participating in the transcription initiations.

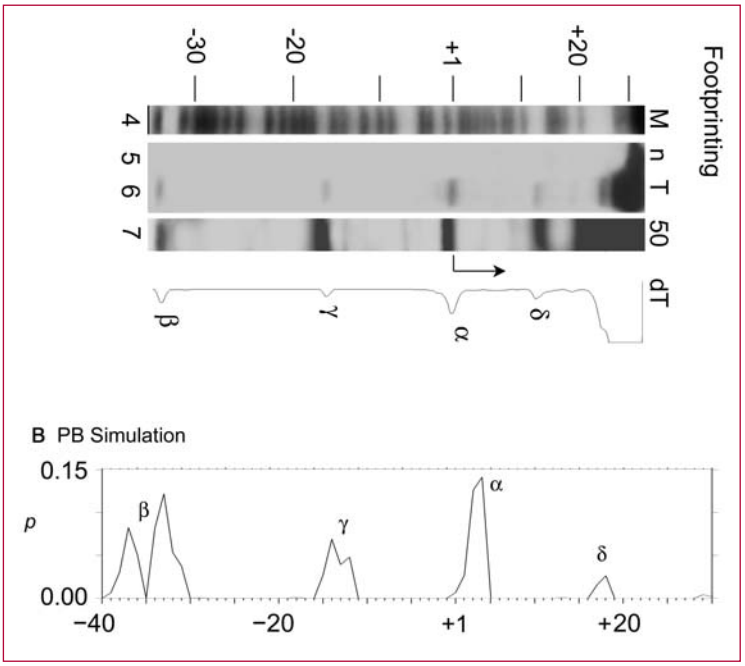

***Figure 2—** Top: Bubble formation versus sequence in T7 promoter at 21C (lane 6) and at 50C (lane 7) as observed in a sequencing gel experiment. Bottom: Bubble formation versus sequence in T7 promoter at 21C resulting from simulations. Note that the abscissas (sequence axes) are not quite aligned in the two panels, because the axis in the experimental plot is not quite linear.*

[1] T. Dauxois, M. Peyrard, and A. R. Bishop, "Dynamics and thermodynamics of a nonlinear model for DNA denaturation," *Phys. Rev. E.* **47**, 684 (1993).

[2] C. H. Choi, G. Kalosakas, K. Ø. Rasmussen, M. Hiromura, A. R. Bishop, and A. Usheva, "DNA Dynamically Directs Its Own Transcription Initiation," *Nucleic Acids Res.* **32**, 1584 (2004).

Elastic Moduli of Multiblock Copolymers

Russell B. Thompson, Kim Ø. Rasmussen, and Turab Lookman, T-11; and Edward M. Kober, T-14; rthompson@lanl.gov

We have developed a methodology based on self-consistent field theory by which we can calculate the linear elastic response of multiblock copolymer melts in terms of elastic moduli.

Multiblock or segmented block copolymers belong to a class of materials, which is used in a wide variety of industrial and strategic applications, consisting of covalently tethered blocks of homopolymer sequences (e.g., A_m and B_n). These sequences are thermodynamically incompatible under ambient conditions and undergo spontaneous phase separation. However, due to the covalent tether, they can only achieve microphase separation. The resulting micro (or nano) structures are of a length scale smaller than the total length of the polymer macromolecule. The details of how they are knitted together by the polymer chains, are what create the elastomeric properties of these materials.

Self-consistent field theory (SCF) is widely recognized as a powerful tool for determining the morphological behavior of block copolymer materials. We have developed a number of algorithmic improvements [1,2] allowing us to handle the increased complexity of multiblock copolymers efficiently. SCF is based on a free-energy functional, whose minimum is realized by balancing entropic stretching effects with molecular interaction and excluded volume effects. The foundation of the SCF free energy functional is first principles and thus retains information about the polymeric nature of the molecule and aspects of connectivity. We are particularly interested in modeling and understanding Estane® 5703, which is the polymeric binder component used in the high explosive PBX9501. because it has been strongly suggested that aging effects in this composite arise from chemical and physical changes in the binder. Estane® 5703 is a segmented block copolymer whose strength arises from the self-organization it undergoes. The chemical structure is shown in Figure 1. The "hard" segments are comprised of methylenediphenylisocyante (MDI) unites (with 1–3 repeats), and the "soft" segments are butyleneadipate (BA) oligomers of five segments. These components are repeated about 28 times as shown in Figure 1. Because of our algorithmic improvements we can apply SCF to determine the morphology of this highly segmented system where the overall volume fraction of hard segments is experimentally known to be 24%, see Figure 2.

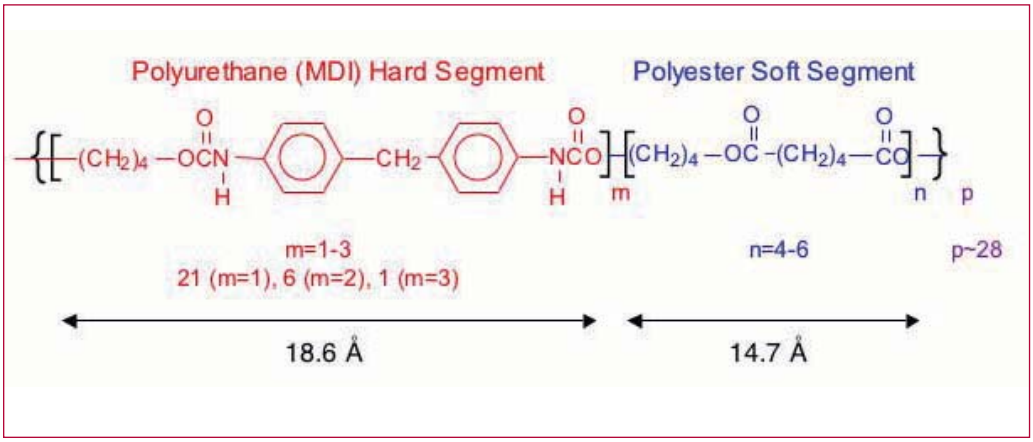

Figure 1—Estane chemical structure. The resulting morphology is shown in Figure 2.

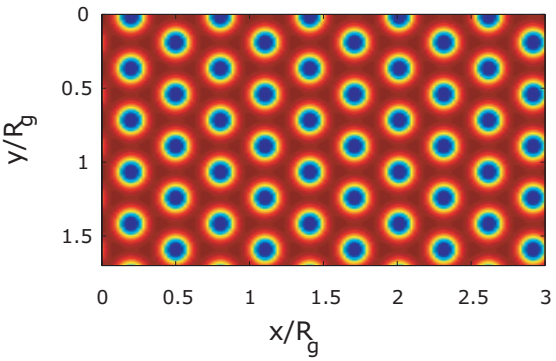

Having obtained the equilibrium structure of a given system from SCF we can further calculate the increase in the free energy as a function of small deformations and thereby extract the elastic moduli of the equilibrium structure.

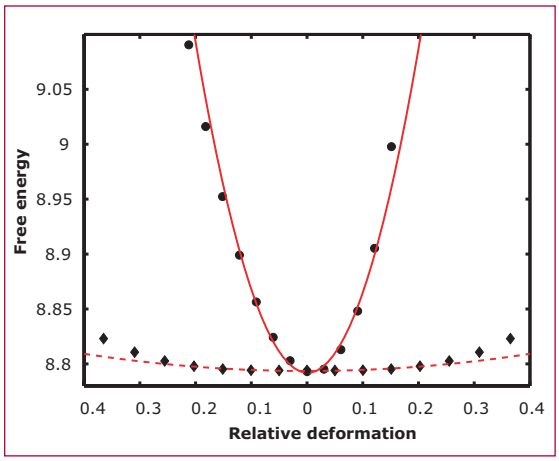

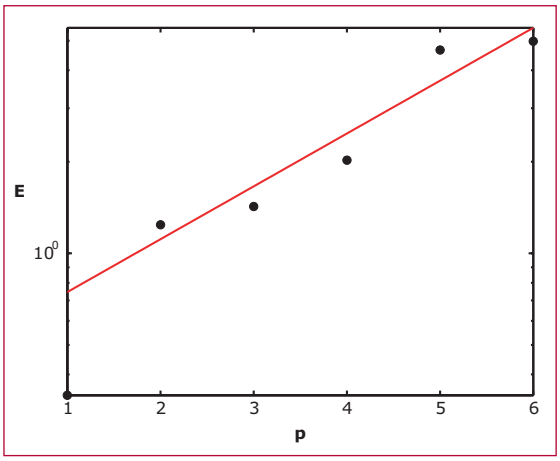

Depending on the symmetry of the equilibrium morphology, there is a finite number of deformations needed to extract all elastic moduli of the system. A simple example is the lamellar morphology (uniaxial) where only two elastic moduli (extensional and shear) are needed to describe the complete elastic response of the system. To extract these two moduli we need to calculate the change in free energy due to extensional (compressional) deformation and due to shear deformations. The results of such calculations are shown in Figure 3. The respective moduli are found from the curvature of these free energy curves. In this way we can determine the moduli's dependence on, for instance, the number of segments, which is thought to be a critical parameter in the aging process of Estane®. A result of such a calculation is shown in Figure 4.

In summary we have advanced SCF theory to enable calculations of structure for self-assembled materials. We have also developed the SCF methodology to extract elastic moduli of polymer materials with self-organized structure. These techniques will be applied towards formulating a "response" model.

[1] G. Tzeremens, K. Ø. Rasmussen, T. Lookman, and A. Saxena, *Phys. Rev. E* **65**, 041806 (2002).
[2] R. B. Thompson, K. Ø. Rasmussen, T. Lookman, "Improved convergence in block copolymer self-consistent field theory by Anderson mixing," in press *J. Chem. Phys.* **120**, 31 (2004).
[3] R. B. Thompson, K. Ø. Rasmussen, T. Lookman, "Elastic Moduli of Multiblock Copolymers in the Lamellar Phase," submitted to *J. Chem. Phys.***120**, 3990 (2004).

Figure 2—Equilibrium structure of 28 segment Estane® polymer system.

Figure 3—Plot of free energy versus relative distortion for a tetrablock copolymer in a lamellar morphology. The points are the values calculated from SCF with the black dots denoting an extension and the black diamonds indicating shear. The red lines are parabolic fits to the data with the solid line fitting the extension data and the dashed line the shear. All units are dimensionless. After [3].

Figure 4—Plot of the dimensionless tensile (Young's) modulus versus diblock number p. The black dots are the data points while the solid red line is an exponential regression. The data is plotted on a semi-log scale. After [3].

T-12 Theoretical Chemistry and Molecular Physics

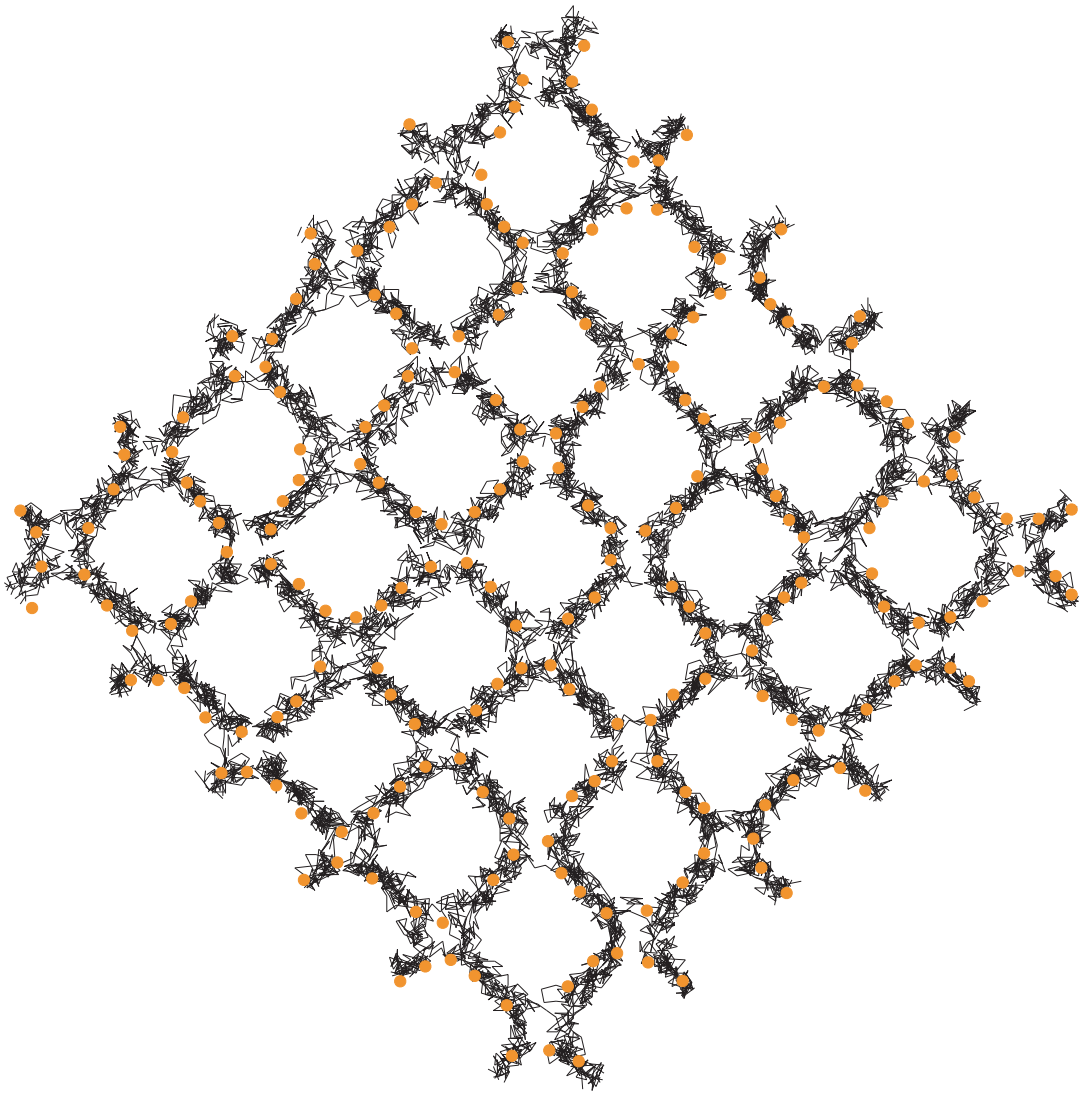

Los Alamos
NATIONAL LABORATORY

Quantum Chemical and Classical Studies of the High-Pressure Phase of Teflon

Holmann V. Brand, Jessica M. Ryan, and Kerri J. Kress; X-7, Dana M. Dattelbaum, MST-7; and Neil J. Henson, T-12; neil.henson@lanl.gov

Polytetrafluoroethylene (or Teflon) is a convenient, extensively studied system for many halogenocarbon polymers used as binders in high-explosive formulations. The Polymer DOE/DoD MOU project focuses on experimental and theoretical studies of Teflon under extreme conditions in order to be understand the relationship of bulk properties with polymer structure. Experimental measurements are made on teflon samples that contain both crystalline and amorphous domains. This computational study investigates the structure and properties of pure Teflon phase III crystals.

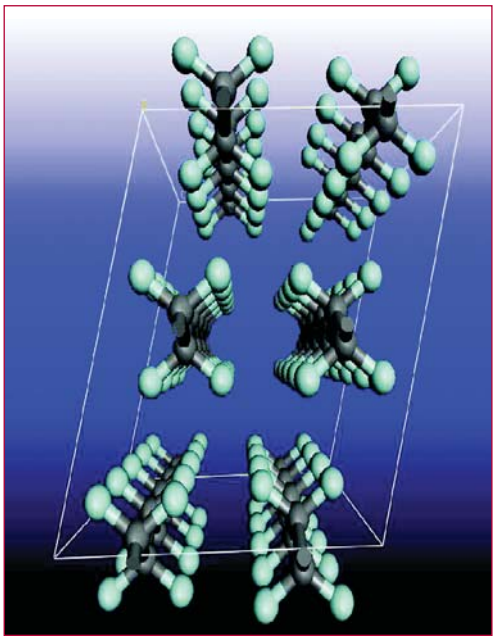

Figure 1—The crystal structure of phase III of Teflon.

Teflon exists in several crystalline phases as shown in Figure 1. Phases II and IV are based on helical chain structure, whereas phase III features a linear fluorocarbon chain and is the best characterized structurally (Figure 2).
The crystal structure for phase III has been proposed by Flack [1]. Models for phase III were constructed from this structure. Calculations were performed with two programs :
MOPAC – a general-purpose semiempirical quantum mechanics package for the study of chemical properties and reactions in gas, solution, or solidstate.
DISCOVER – a molecular simulation program for applications in computer-assisted molecular design Initially, lattice energy minimisation calculations were performed on supercells of the phase III unit cell to determine the minimum model size required to converged the lattice energy per CF_2 group. The 1 x 4 x 2 supercell with 32 CF_2 units was found to be optimal.

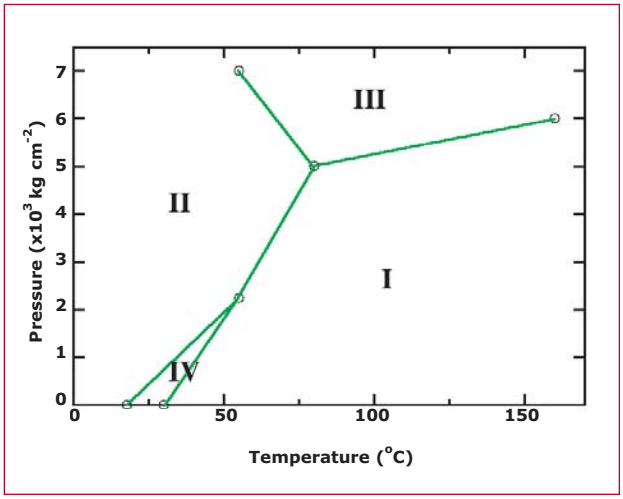

Figure 2—Phase diagram of Teflon.

An isotropic compression and expansion scan was performed to obtain the minimised lattice energies at different volumes. The normalized volumes ranged from 0. 97 to 1.03 times the initial volume. This allows the optimal cell vectors to be determined for each volume. The importance of conducting this scan can be seen in Figure 3.
The scan results in lower energy structures for points far from the equilibrium geometry.

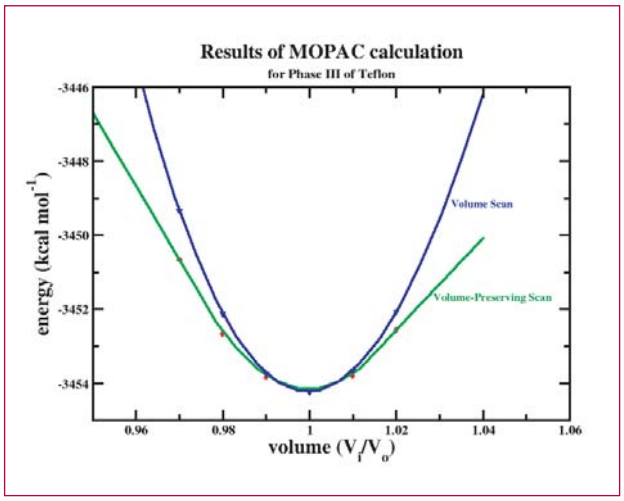

Figure 3— The effect of the volume preserving scan.

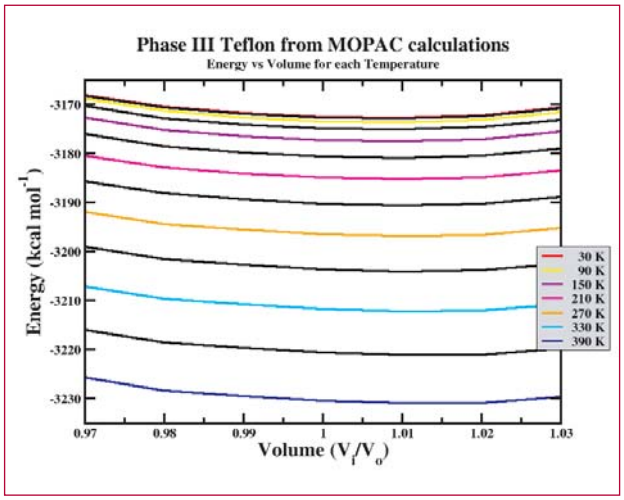

Figure 4— Variation in free energy as function of temperature.

Using the minimum energy geometries, vibrational spectra were calculated using MOPAC and DISCOVER. The vibrational frequencies can be used to calculate the free energy of the system using

$$F(V,T) = E(V) + F_{vib}(V,T) \equiv E(V) + k_B T \sum_j \ln\left\{2\sinh\left(\frac{h\nu_j}{2k_B T}\right)\right\}$$

the quasiharmonic approximation: where $F(V,T)$ is the free energy, $E(V)$ is the minimised lattice energy, and ν_j are the vibrational frequencies. The calculated free energy as a function of temperature is show in Figure 4.

Using this data, the free energy was fitted to a cubic equation from which the bulk modulus was determined by analytical differentiation. We are currently repeating this method for lower pressure phases II and IV which have a helical structure.

[1] H. D. Flack, *J. Poly. Sci. A2* **10**, 1799–1809 (1972)

All-Electron Density-Functional Studies of Hydrostatic Compression of Pentaerythritol Tetranitrate (PETN)

Chee Kwan Gan, T-12, Thomas D. Sewell, T-14, and Matt Challacombe, T-12; ckgan@lanl.gov

Pentaerythritol tetranitrate [PETN, $C(CH_2ONO_2)_4$] is an important secondary high explosive. PETN has received a lot of attention due to interesting anisotropic, nonmonotonic shock initiation sensitivity. The room temperature linear and volumetric hydrostatic compression of PETN has been measured by Olinger and co-workers [1] using x-ray diffraction for pressures up to 10.45 GPa.

In this work, we report condensed phase electronic-structure calculations of the hydrostatic compression of PETN at absolute zero and pressures up to 25 GPa. We employ an all-electron density-functional method using the PBE functional in conjunction with the 6-31G** Gaussian basis set.

Calculations were performed using a parallelized version of MondoSCF [2], a suite of programs for linear scaling electronic-structure theory and *ab initio* molecular dynamics. Periodic boundary conditions were used to study the PETN crystal. The MondoSCF code employs a number of advanced *O(N)* techniques. We used a cluster of 256 4-CPU HP/Compaq Alphaserver ES45 to perform the calculations in this work.

Calculated and measured lattice parameters are compared in Table I, where we also include the experimental results of Olinger *et al.*[1] and Conant *et al.* [3].

Percent errors in our calculations relative to the experimental results of Conant *et al.*[3] are 0.51%, 0.75%, and 1.8% for a_0, c_0, and V_0 respectively.

The volumetric hydrostatic compression is summarized in Figure 1. The variation of the energy with compression ratio V/V_0 is shown in Figure 1(a). The pressure is shown in Figure 1(b). The open circles in Figure 1(b) are the experimental data of Olinger *et al.*[1]. The calculated volumetric compression is in remarkably good agreement with experiment.

Table 1—Equilibrium lattice parameters and unit cell volumes for PETN.

a(Å)	c(Å)	V(Å^3)	Source
9.425	6.758	600.3	This work
9.383	6.711	590.8	Olinger *et al.* [1]
9.3776	6.7075	589.9	Conant *et al.*[3]

The linear compression along the *a* and *c* crystallographic directions is shown in Figure 2. Figure 2(a) reveals good agreement between our predictions and the experimental data for the relative compressions of a/a_0 and c/c_0. In Figure 2(b) we show the variation of the *c/a* ratio as a function of compression. The solid line is based on polynomial representations of $a = a(V)$ and $c = c(V)$ due to Olinger *et al.*[1]. We observe in both cases an initial decrease in the *c/a* ratio

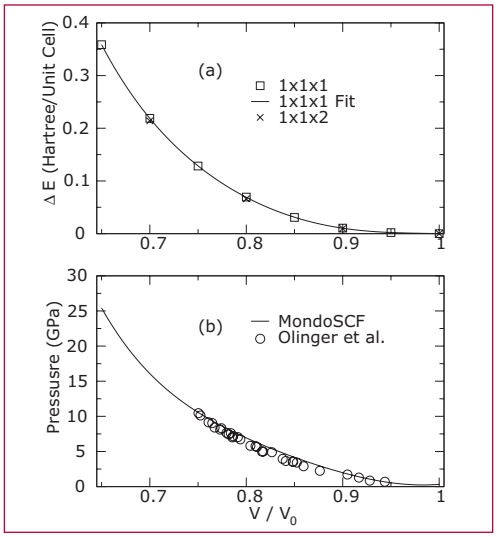

Figure 1—Volumetric hydrostatic compression for PETN. (a) Energy difference ΔE. Crosses are calculations for a 1x1x2 supercell. (b) Pressure-volume relationship.

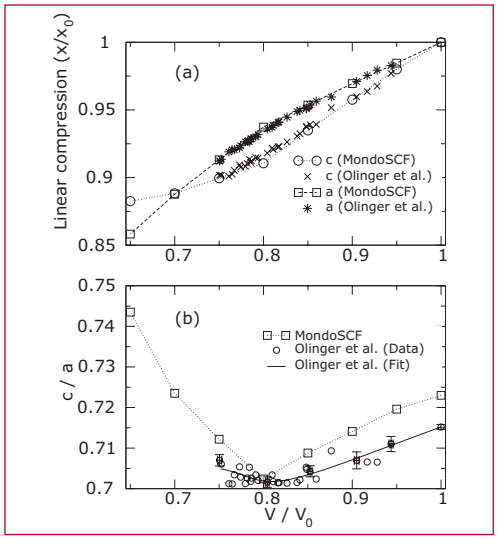

Figure 2—Linear compression of PETN. (a) Relative linear compression of the lattice parameters. (b) Ratio of c to a. Circles are experimental data [1].

with increasing compression, followed by an increase toward a more "cubic-like" lattice structure. The positions of the minima in the curves are in fairly good agreement, and correspond to a volume ratio of 0.8 and a pressure of about 7 GPa. Our calculations indicate essentially rigid-molecule compression for p< 7 GPa, with the onset of significant intramolecular distortions for higher pressures.

We can obtain the bulk modulus $B_0 = -V dP/dV$ and its initial pressure derivative $B'_0 = dB_0/dP$ using different equation of state fitting forms. The first form is the conventional Murnaghan equation. The second form is the third-order Birch-Murnaghan equation. The third form is derived from the shock Hugoniot conservation equations.

Calculated and measured values for the initial bulk modulus and its pressure derivative for PETN are summarized in Table II. The results among the fits of our isotherm to the three equations of state are fairly consistent, with B_0 = 14.5–16.0 GPa and B'_0 = 5.2–6.7.

Applying the same fitting forms to the experimental data of Olinger et al.[1], we obtain B_0 = 9.4–12.2 GPa and B'_0 = 6.4–11.3.

The average theoretical bulk modulus, which corresponds to zero Kelvin, is 32% larger than the corresponding average experimental value based on the room-temperature isotherm.

The success of these all-electron calculations for PETN demonstrates the precision of our *O(N)* algorithms, and suggests that it may be practical to undertake similar calculations on significantly larger, more complicated systems that are well outside the capabilities of conventional algorithms.

B_0(GPa)	B'_0	Source	Fitting form
15.8	5.3	This week	Murnaghan
14.5	6.7	This work	Birch-Murnaghan
16.0	5.2	This work	Hugoniot
11.7	6.8	Olinger *et al.*[1]	Murnaghan
9.4	11.3	Olinger *et al.*[1]	Birch-Murnaghan
12.2	6.4	Olinger *et al.*[1]	Hugoniot

Table II—Calculated and measured bulk moduli B_0 and pressure derivative B'_0 for PETN.

A full-length version of this report appears in *Physical Review B* **69,** 35116 (2004).

[1] B. Olinger, P. M. Halleck, and H. H. Cady, *J. Chem. Phys.* **62**, 4480 (1975).
[2] M. Challacombe, E. Schwegler, C. Tymczak, C. K. Gan, K. Nemeth, A. M. N. Niklasson, H. Nymeyer, and G. Henkleman, MONDOSCF *v1.0α7, A program suite for massively parallel, linear scaling SCF theory and ab initio molecular dynamics.* (2001).
[3] J. W. Conant, H. H. Cady, R. R. Ryan, J. L. Yarnell, and J. M. Newsam, Tech. Rep. LA-7756-MS, Los Alamos National Laboratory (1979).

EPnet, an Explicit Polymer and Node Network Model to Compute Micromechanical Properties of Crosslinked and Filled Polymer Systems

David E. Hanson, T-12; deh@lanl.gov

Two important aspects of filled polymer systems that can influence elasticity are the random position of filler particles and the nonuniformity of polymer chain lengths that form the chain/particle network. Historically, most network elasticity models have been based on idealized assumptions of uniform chain length constrained to highly symmetric orientations. As a part of an LDRD-ER project, we have developed a novel, three-dimensional explicit polymer and node network model (EPnet) [1] that includes both randomly distributed filler particles, or nodes, and random polymer chain lengths taken from a Gaussian distribution. Nodes may also be due to covalent cross links between adjacent chains. The molecular-level polymer forces that are exerted by the chains in response to a deformation produce the elasticity. These forces are assumed to operate directly between all pairs of connected network nodes. The numerical model is amenable to any molecular force that depends on the distance between two nodes, however, for the studies described here, we have assumed that the polymer chain segments that comprise the network obey a simple two-force model, i.e., a constant force required to stretch a single polymer chain and a force arising from the binding energy between a polymer chain and a filler particle surface or node. Free ends, i.e., polymer segments connected to only one node, do not contribute to the elasticity. With these assumptions, the model contains intrinsic mechanisms that appear to predict the phenomena of yield stress, tensile failure, permanent set, and stress hysteresis.

Two polymeric materials that are of interest to the laboratory weapons community are Estane 5703, a component of the binder material in the plastic explosive PBX 9501, and silica-filled polydimethylsiloxane that is used to produce foam cushions and supports. Estane is a diblock copolymer composed of "hard" methylene bis(phenylisocyanate) segments, and flexible poly(ester-urethane) "soft" segments. Phase separation occurs between the hard and soft segments producing nodes composed of hard segments from multiple chains. This produces a continuous network analogous to that of a filled polymer. With support from the Enhanced Surveillance Campaign, the model has been applied to mesoscale volume elements of these materials to study the micromechanical stress in response to various strains, e.g., tensile, compressive, shear, and swell. Model predictions of tensile stress/strain in both silica-filled PDMS (Figure 1) and Estane (Figure 2) are in quantitative agreement with experimental results, including tensile failure. Each plot shows the predicted stress/strain for five statistically independent network simulations. In the case of Estane, chain scission due to hydrolysis is thought to be the principal degradation that occurs as the weapon ages. We are using the EPnet code to relate the resulting change in average molecular weight of the chains to changes in the mechanical properties to predict the lifetime of the weapon. Estimates for the molecular forces used in the model have been obtained from atomistic simulations of isolated molecules using classical inter-atomic potentials. Typically, these estimates are within a factor of two of values required to

achieve agreement between model predictions and experiment. Ultimately, we would like to be able to compute these forces from simulations with high confidence, but, at present, computational limitations and uncertainties in the accuracy of the potential energy parameters pose a limitation. However, the current simulations do establish a plausible physical mechanism for the molecular forces. Because the model can quantitatively treat a multitude of strain types and associated phenomena, we expect that, by simulating several types of deformation experiments using the same material, a self-consistent set of molecular-level material parameter values can be inferred with high confidence. We anticipate that the numerical model will provide insight into how the molecular interactions affect elasticity in filled polymers and will be useful in developing simpler, more computationally efficient engineering models. The model will be made available to other investigators.

[1] D. E. Hanson, *Polymer 2004* **45**, 1058–1062.

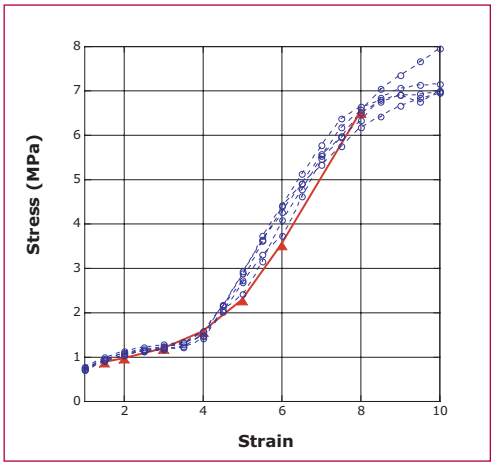

Figure 1—Predicted (blue-dashed) and experimental (red-solid) tensile stress/strain for silica-filled PDMS.

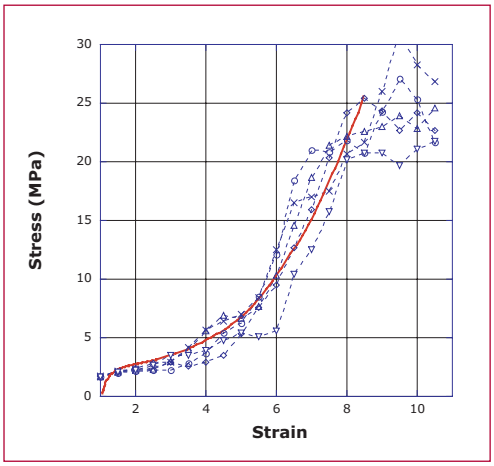

Figure 2—Predicted (blue-dashed) and experimental (red-solid) stress/strain for neat Estane.

Theoretical Studies of Surface Chemistry and Bulk Electronic Structure of Actinide Materials

P. Jeffrey Hay, Joel D. Kress, and Hank Ashbaugh; T-12, pjhay@lanl.gov

The surface chemistry of actinide materials plays an important role in corrosion and other processes involving adsorption of molecular species. When exposed to air, the actinide metals form oxide layers PuO_2 and Pu_2O_3 in the case of Pu and UO_2 in the case of U. The reactions of hydrogen with actinide metals represent another important area which involves a complex series of chemical reactions involving oxide and metal surfaces and their interfaces.

We have been exploring two aspects of this chemistry using density functional theory. One part of the current study has focused on H_2O adsorption on PuO_2 surfaces and comparison with previous calculations on UO_2 surfaces. The other part has examined the electronic structure and thermochemistry of bulk PuH_2. These studies represent a first step towards obtaining a detailed understanding of how species such as O_2, H_2O and H_2 react with actinide surfaces such as Pu and PuO_2. Comparisons can be made with surface probes such as thermal desorption studies and bulk measurement of structural, electronic and magnetic properties.

In the case of a surface, periodic models are used to represent a slab of material interacting with adsorbates. The calculations used the Vienna *ab initio* Simulation Package (VASP) with the following common characteristics: a plane-wave basis for the electronic wavefunction, the generalized gradient approximation (GGA) density functional, relativistic PAW (projector augmented wave) pseudopotentials without spin-orbit coupling.

H_2O adsorption on PuO_2. Bulk PuO_2 has the fluorite structure in which each actinide ion is surrounded by eight oxygen ions, and each oxygen has four nearest neighbor Pu ions. Two of the most widely observed surfaces on oxides with this structure are the (111) and (110) crystal faces that typically have the lowest surface energies. On the (111) surface the bulk oxide has been cleaved leaving the Pu ions with seven O neighbors and missing only an axial O ion lying perpendicular to the face. In the (110) surface the Pu has only six O neighbors. In the calculations we have examined the adsorption of H_2O on each surface both as molecularly adsorbed form, H_2O(ad), and in dissociated form in which one proton has been transferred to a neighboring O atom to form two hydroxy groups, OH(ad). With a five-layer slab model, the positions of the atoms in the top two layers and the adsorbed H_2O molecule are relaxed while the remaining atoms are fixed at their bulk positions.

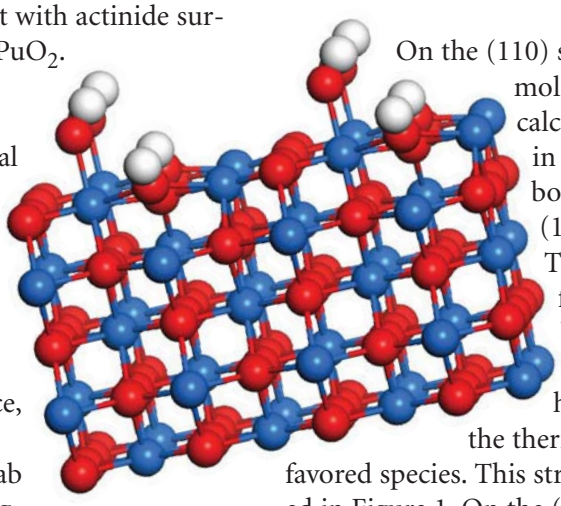

Figure 1—Calculated structure of dissociated H_2O molecules on PuO_2 (110) surface showing several unit cells of periodic five-layer slab.

On the (110) surface the molecular H_2O is calculated to adsorb in a form that is bound by 0.6 eV (14 kcal/mol). The dissociated form is bound by 0.85/eV (22 kcal/mol), and hence should be the thermodynamically favored species. This structure is depicted in Figure 1. On the (111) surface the

molecularly adsorbed H_2O is found to be the more stable species that is bound by ~ 0.75 eV (17 kcal/mol). These results are qualitatively similar to earlier calculations on the UO_2 surface where the (110) surface was also found to be the more reactive one.

Electronic structure of Pu and PuH_2. In bulk Pu metal, the ground state phase (α-Pu) is a monoclinic crystal structure that consists of a 16-atom unit cell with eight distinct atomic sites. At a temperature of about 600 K, bulk Pu metal exists in a fcc phase (δ-Pu) that consists of a one-atom unit cell. In calculations of the electronic structure of Pu, the magnetic behavior (electron spin) must also be considered. Three different spin-orderings were studied with VASP: (1) nonmagnetic (NM), with spin nonpolarized density functional theory; (2) ferromagnetic (FM), with all spins aligned in one direction, and; (3) antiferromagnetic (AF), with spin directions alternating up and down. The present results for the equilibrium volume, magnetic moment, and relative energy of δ-Pu are presented in the table along with the LCGTO (Linear Combinations of Gaussian Type Orbitals) results [1] of J. Boettger, X-7. Both VASP and LCGTO predict the AF state as the ground state. The predicted volume of the AF state is within 8% and 4% of the experimental volume for VASP and LCGTO, respectively. Although the AF state has a net zero magnetic moment for the bulk, the magnitude of the local magnetic moment on each atom can be calculated. VASP predicts a larger magnetic moment than LCGTO by about 1 μ_b (bohr magneton).

In bulk PuH_2, the ground state is the CaF_2 crystal structure (as in PuO_2 discussed above), where the Pu atoms form a fcc lattice and the H atoms are located in the tetrahedral interstices (see Figure 2). VASP calculations were performed on the NM, FM, and AF spin-orderings. The FM and AF were found to be nearly energetically degenerate, while experimentally the ground state is AF. The lattice constants for FM and AF were 5.32 and 5.33 Å, respectively, which compare favorably with the experimental value of 5.359 Å. The magnetic moment of the FM state = 5.4 μ_b per PuH_2 unit. Finally, the energy of formation of PuH_2 (solid) from Pu(solid) + H_2 (gas) was calculated to be $\Delta E = -30$ kcal/mol that compares favorably with the experimental enthalpy of formation, $\Delta H = -37$ kcal/mol.

[1] J. C. Boettger, *Int. J. Quantum Chem.* **95,** 380 (2003).

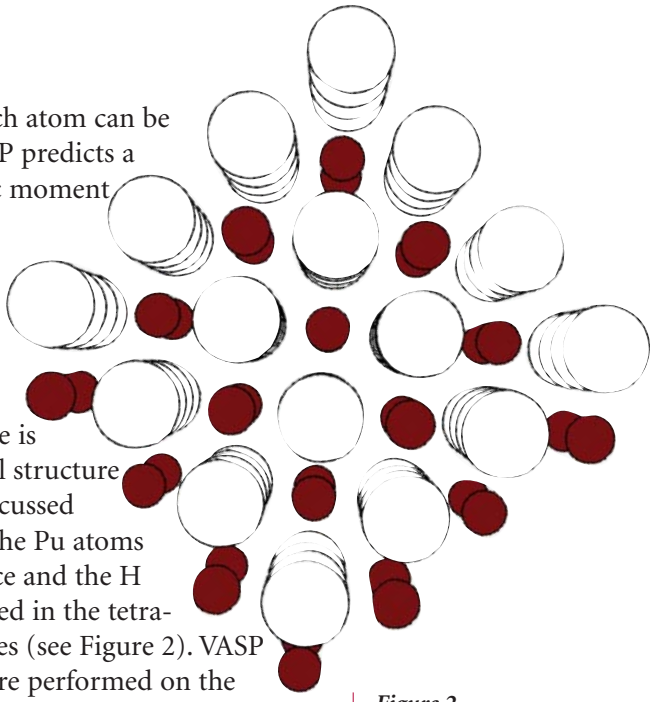

Figure 2— Crystal structure of PuH_2. White = Pu and Brown = H.

	Eq. Volume (Å^3)		Magnetic Moment (μ_B)		ΔE (eV/atom)	
	VASP	LCGTO	VASP	LCGTO	VASP	LCGTO
Nonmagnetic	18.0	18.1	0.0	0.0	0.0	0.0
Ferromagnetic	27.0	27.1	5.6	5.7	-0.54	-
Antiferromagnetic	23.2	24.2	4.4	3.2	-0.75	-0.54
Experiment	25.2					

Table— Electronic structure of fcc d-Pu calculated with VASP and LCGTO.

Conformational Dependence of a Protein Kinase Phosphate Transfer Reaction

Graeme Henkelman, Matt Challacombe, and Karoly Nemeth, T-12; Montiago LaBute, Chang-Shung Tung, Paul W. Fenimore, and Benjamin H. McMahon, T-10; graeme@lanl.gov

We have computed the reaction pathway for a protein kinase enzyme using (Ab Initio) density functional theory on the QSC supercomputer. Protein kinases catalyze the transfer of the terminal phosphate group of adenosine tri phosphate onto the hydroxyl group of serine, threonine, and tyrosine residues of target proteins in order to specifically modify their conformation and activity. Such reactions are central to most types of regulatory processes in living organisms. This type of calculation is an important step towards quantitative understanding of the regulation and specificity of this class of signaling enzyme.

Figure 1 shows the reactant, transition state, and product geometries of a phosphate transfer reaction in protein kinase A, together with the energy along the pathway for two different conformations of the protein. Structures were taken directly from the protein data bank and optimized with the VASP quantum chemistry package.

The calculations shown in Figure 1 contains three times as many atoms as previous calculations [1] and our work indicates the necessity of treating the larger systems. The work is part of a comprehensive modeling effort to understand protein kinase function from quantum mechanical, explicit solvent molecular dynamics, native-state bias simulations, and sequence analysis (see cellsignaling.lanl.gov/structure/kinase/kinase.html) funded as an LDRD/DR project.

[1] M. Valiev, R. Kawai, J. A. Adams, and J. H. Weare, *JACS*, **125**, 9926 (2003).

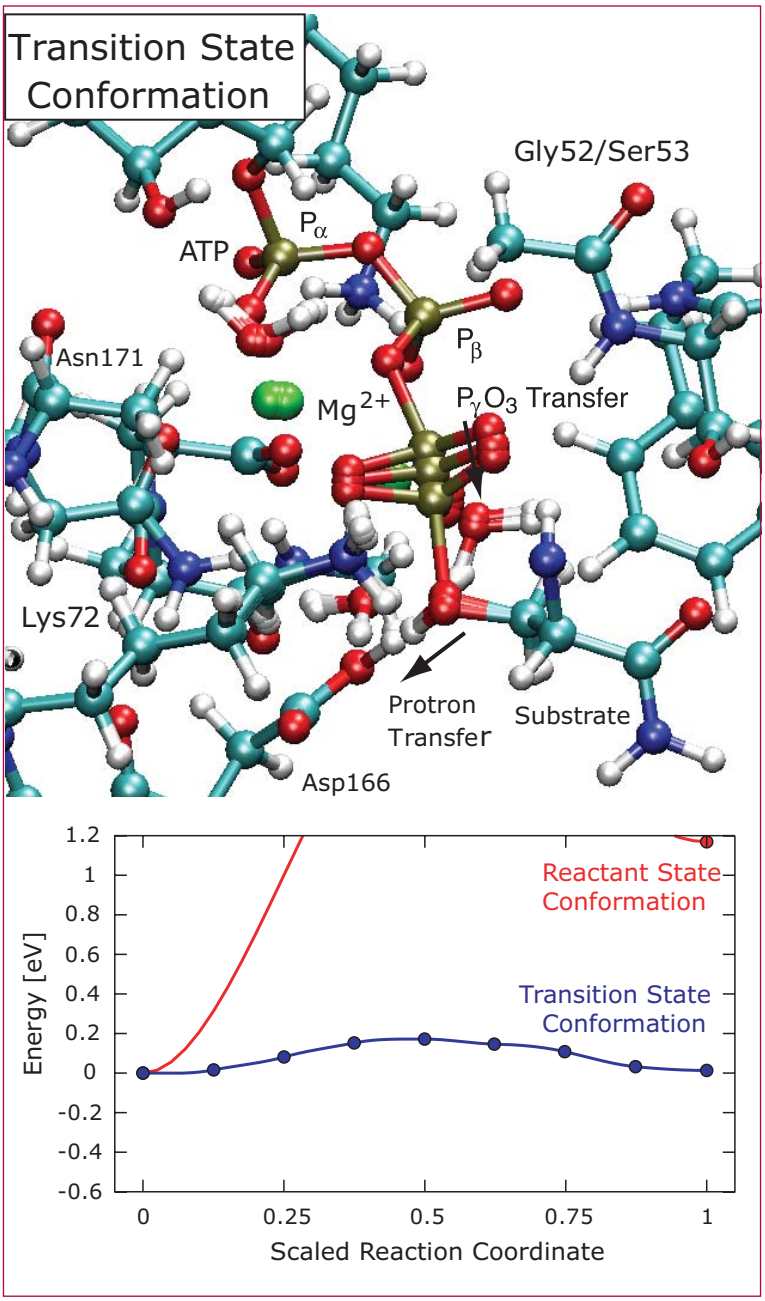

Figure 1—(top) Reaction pathway of phosphate transfer calculated on a 244 atom fragment taken from protein structure determined by x-ray diffraction on a crystal of protein kinase A (pdb accession code 1L3R). (bottom) Quantum mechanically calculated energy along pathway, comparing two different conformations of the protein. Clearly, the conformation of the protein strongly affects the energetics of phosphate transfer. Quantum chemistry calculations on under-constrained calculations elucidate the reasons for such sensitivities.

How Do Hotspots Happen? The View from the Atomic Scale

Brad Lee Holian, T-12 and Timothy C. Germann, X-7, blh@lanl.gov

Impacts upon perfect crystals of high explosives have to be pretty violent to get them to detonate; introduce defects into them, and the job is much, much easier. Porosity in the form of voids has been assumed to be the principal source of hot spots, or heterogeneous nuclei for chemical reaction, as a shock wave passes by. With our colleagues, Jean-Bernard Maillet of CEA (the French Atomic Energy Commission) and Carter White of the Naval Research Lab, we have investigated the interaction of shock waves with voids at the atomistic level, to see just how the hot spots are formed. B. L. Holian, T. C. Germann, J. B. Maillet, and C. T. White, "Atomistic Mechanism for Hot Spot Initiation," *Phys. Rev. Lett.* **89**, 285501 (2002).

We have used large-scale molecular-dynamics (MD) simulations to study the effect of impacts upon perfect crystals of high-explosive diatomic molecules whose interactions are modeled by a reactive empirical bond-order (REBO) potential. Reactions are simple, in that AB molecules can form AA and BB product molecules with release of energy. Perfect crystal shock simulations lead to detonation above a threshold impact velocity, with characteristics that satisfy the simplest theory of detonations (due to Zeldovich, von Neumann, and Doering). To see if the threshold for initiation of chemical reaction can be lowered, we also introduced a variety of defects into our samples.

The first thing that we found was that defects had to be a minimum size to have any effect whatsoever. A vacancy, or even a divacancy, can be passed over by a shock wave without so much as a hiccup. However, beyond a certain size, a void (or vacancy cluster) can produce not only a warp in the shock front, but serious heating upon its collapse. Such an overheat can subsequently lead to initiation of chemical reaction originating at the void, even for a shock wave that would not have been strong enough to produce initiation in a perfect crystal (see Figure 1). For materials that don't react chemically, such hotspots can still be nucleation sites for other shock-induced phenomena, such as plastic flow or polymorphic phase transformations.

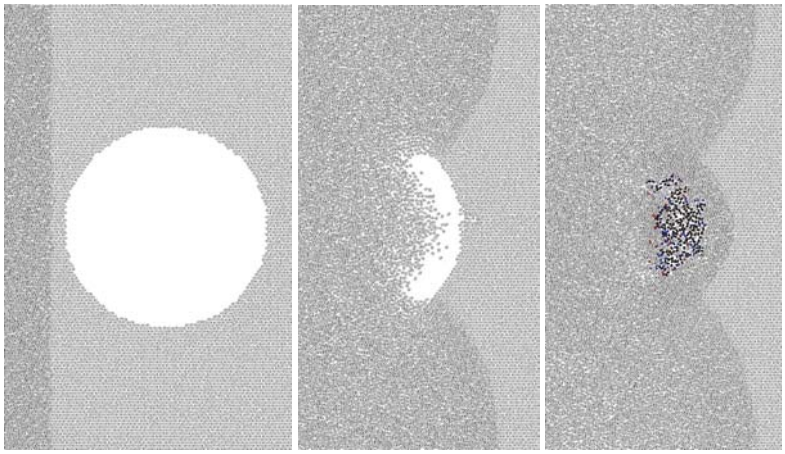

Figure 1— Initiation of chemical reactions due to void collapse in a 2-D diatomic (AB) solid.

Besides shock strength and void size, a third factor to be considered is the shape of the void. Consequently, that led White and co-workers at NRL to simplify the shape by considering planar gaps of varying width. They found that if the gap width was too small, no initiation occurred, unless the impact strength was above the perfect-crystal limit. No matter how wide the gap, there was a minimal velocity required to initiate chemical reactions.

We set about studying the thermal overheating that occurs in completely unreactive systems with planar gaps of varying widths, using the traditional Lennard-Jones pair potential in a monatomic solid. Again, we observed that significant overshoot in temperature occurred only when the initial impact was strong enough to eject material from the upstream side of the gap, corresponding to a shock temperature sufficient to nearly melt the material. Moreover, the gap had to be wide enough before overheating occurred at the downstream side of the gap.

In light of these observations from our MD simulations, we have proposed a simple model describing the role of shockwave interactions with microscopic voids that leads to significant heating, sufficient to thermally initiate chemical reactions in solid explosives, or phase transitions in metals. The key ingredients to this dramatic overshoot in temperature are shown in Figure 2.

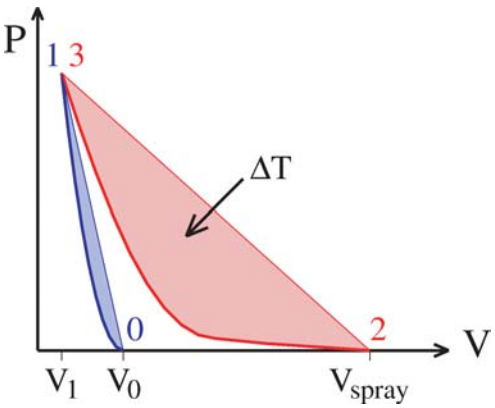

Figure 2—
Cartoon of planar gap collapse:

(1) initial shock from specific volume $V_0 = 1/\rho_0$ to V_1 with temperature rise T_1;

(2) adiabatic expansion (and cooling) of ejecta spray to a mean specific volume $V_{spray} \leq 2V_0$;

(3) recompression at the downstream side of the gap to V_1, with a temperature rise ΔT.

The dependencies on both shock strength and one-dimensional gap width that we observed in atomistic simulations of a two-dimensional unreactive Lennard-Jones solid for the thermal overshoot were well predicted by our straightforward model, showing how hot spots can be generated under shock wave conditions.

Theory and Simulation of Polymer Aging: Degradation via Free-Radical Oxidation

Joel D. Kress, T-12; Mike Salazar, Union Univ.; and Russell T Pack, T-12; jdk@lanl.gov

The plastic-bonded explosive PBX 9501, used in weapons, is 94.9% by weight HMX explosive, 2.5% nitroplasticizer (NP), 2.5% Estane“ 5703, and 0.1% Irganox 1010 stabilizer (anti-oxidant). Estane® 5703, made by B. F. Goodrich, is a poly(ester urethane) random copolymer which serves as a glue. The urethane units segregate into “hard” domains that act as physical crosslinks between the “soft” polyester domains. The NP softens the Estane, and together they markedly decrease the mechanical sensitivity of the PBX. However, the Estane slowly degrades in time, and the effect of that on the mechanical properties of the PBX raises safety and reliability concerns. Hence, the study of polymer aging is task LA-24, an integral part of the Enhanced Surveillance Campaign.

We are studying the chemical mechanisms and kinetics of degradation processes in PBX 9501. We are working very closely with a large number of experimentalists at LANL and Pantex (PX) to determine and connect the chemical and mechanical properties of the PBX. A great deal of work on many reactions and processes is being done. Up until now, task LA-24 has focused on the hydrolysis of the ester links in the soft domains. During this last year we have embarked on a new study of another degradation mechanism, the free-radical oxidation of the urethane segments. Which mechanism dominates in weapons storage? Free-radical oxidation may be as important as hydrolysis, especially as the PBX dries out, since the storage environment has both low moisture and oxygen content. In contrast, at “normal” relative humidity in the atmosphere, hydrolysis dominates over oxidation.

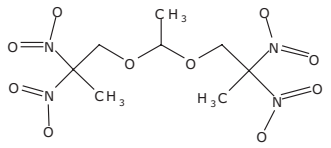

Bis-2,2-dinitropropyl acetal (BDNPA)

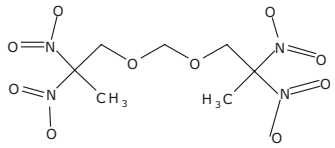

Bis-2,2-dinitropropyl formal (BDNPF)

Figure 1—Chemical structures of the two nitroplasticizer molecules.

The nitroplasticizer (NP) is composed of a mixture of two molecules (Figure 1). The mixture usually used is 45% BDNPA and 55% BDNPF by weight because this is a eutectic that is a liquid at room temperature that can plasticize (soften) polymers. Various research efforts are showing that upon heating NP loses nitro (NO_2) groups and produces oxidizing free radicals that can degrade Estane. The evidence includes (from experiments all carried out in MST Division): (1) identification of nitroxide radicals by Electron Spin Resonance (ESR) after exposing 50/50 mixtures of NP/Estane to X-rays and oxygen (W. Cooke et al.); (2) the observation of small changes in the NO_2 region of the ^{15}N NMR spectrum after reacting isotopically labeled NP with labeled Estane or an Estane analog (D. Wrobleski et al.); and, (3) loss of infrared (IR) transmission intensity in the NO_2 region after heating neat NP in a diamond anvil cell (D. Dattelbaum et al.).

Also, exciting results on the oxidative degradation of Estane are coming out of the Constituent Aging Study (CAS, conducted by M. Lightfoot, B. Russell, and

coworkers at Pantex). The goals of the CAS are to age PBX 9501 constituents (HMX, Estane, NP, stabilizer) in various combinations at accelerated rates, detect chemical reactions that take place, identify reaction products and possible degradation mechanisms, and provide data for lifetime prediction modeling. The samples are aged at different temperatures (ranging from 40^0 to 64^0 C) in a dry, oxygen-free enviroment for a period of three years with most samples extracted and analyzed at 1/2-year intervals. One of the most striking findings is that combinations containing NP (NP + Estane and NP + Estane + stabilizer) show a strong correlation between the total amount of gas products generated and significant changes in the molecular weight (MW) of the Estane. The NP is reacting with the Estane polymer and causing chain scission (decreased MW) and crosslinking (increased MW and gel formation), while small molecule remnants of the reactions are presumably being detected in the gas analysis. Such large changes in MW can have drastic (and undesirable) effects on the mechanical properties of the elastomer. Finally, the preliminary findings of the CAS suggests that the stabilizers currently in use may not be optimum as the anti-oxidant is intended to prevent (and not enhance!) crosslinking (one of the free-radical degradation reactions).

The overall goal in the modeling and simulation effort is to construct a detailed chemical kinetics mechanism that describes the oxidation of Estane in the presence of NP, which is consistent with the data provided by the CAS and other experiments. A first question to ask is: Where along the Estane hard segments is the chemistry taking place and what is the chemical identity of the reactants? Both the location of the chain scissioning and the location and chemical identity of structures of the crosslinks needs to be determined. Figure 2 displays a schematic of the chemical structure of two Estane hard segments. Does scissioning take place as depolymerization (forming isocyanate and alcohol) by breaking the bond between the O and C atoms on the backbone? Does crosslinking happen at the C atom on the methylene bridge between the two aromatic rings (as suggested by ^{13}C NMR studies and identification of the aldehyde oxidation product conducted in MST division)? At the N atom on the amide group (as suggested by IR spectroscopy studies of the products of oxidation of urethane by atmospheric molecular oxygen)? At a C atom on the aromatic ring? Do the crosslinks consist of fragments from the NP molecules (Figure 1)? Fragments from the stabilizer molecules? Perhaps NMR analysis of the gel (crosslinking) formed from isotopically labeled NP and/or stabilizer could provide some clues to the identity of the crosslinker.

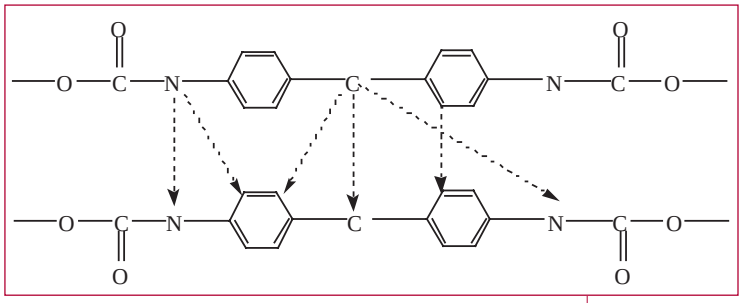

Figure 2—Schematic of the chemical structure of two Estane hard segments side-by-side. (H atoms suppressed for clarity.) Possible crosslinks indicated by the dashed arrows.

In future reports, we will describe our progress in identitifying key reactions in the chemical mechanism and in determining rate constants necessary to perform numerical simulations of the kinetics of the free-radical oxidation of Estane. We would like to thank our experimental collaborators at Los Alamos and Pantex for providing preliminary analyses of their data.

Fibrillar Templates and Soft Phases in Systems with Short-Range Dipolar and Long-Range Interactions

Cynthia J. Olson Reichhardt, T-12; Charles Reichhardt, T-13; and Alan R. Bishop, T-DO; cjrx@lanl.gov

Our understanding of the transport properties of most single crystal materials is based on the assumption that the underlying charge structure is homogeneous. This assumption has recently been challenged due to the unusual and poorly understood behavior of a wide class of complex electronic materials, including high-temperature superconductors. Recent theories for the mechanisms responsible for these phenomena suggest that the mobile charges are not homogeneously distributed throughout the media. Instead, charge-ordered states such as stripes or clumps may form.

We study the thermal properties of a quasiclassical model for charge ordering of holes in transition metal oxides. These materials, which include high-temperature superconducting materials, are composed of copper oxide planes separated by insulating layers. Each plane contains a two-dimensional system of strongly correlated electrons that are highly localized into an antiferromagnetic insulating phase. The electronic properties of the planes change dramatically from insulating to superconducting when the electron density in the plane is altered by doping with holes. The holes interact with competing long-range repulsion and short-range attraction, and organize into spatial patterns. At low densities, crosslike clumps form and organize into an ordered lattice structure (Figure 1a). At a higher density, the clumps begin to touch and are replaced by partially disordered filamentary patterns of the type illustrated in Figure 1b. These filamentary patterns persist within a glassy window that extends up to a higher density, when a more ordered anisotropic crystal pattern forms (Figure 1c).

As a function of hole density (doping), we observe an extended region that we term a "soft phase" comprised of partially ordered filaments. Ordered clumps form densities below this region, and ordered crystal-like phases occur above it. We find that the soft filamentary structures persist to high temperatures. Within the soft phase region there is a low-temperature onset of motion along the filaments coupled with fluctuations of the filamentary structures. The filaments act as a template for *correlated percolation* of particle motion. When the particle positions are averaged over long times, the filaments form an ordered checkerboard pattern. The presence of

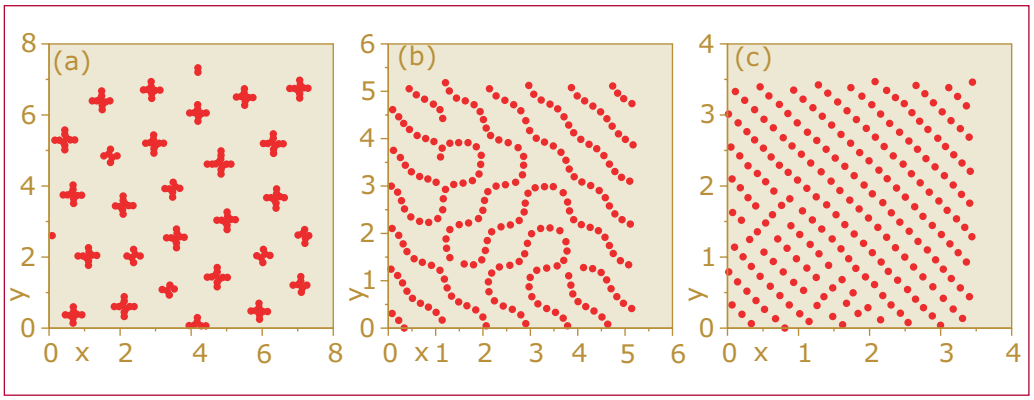

***Figure 1—** Static positions of holes for different densities: (a) Clump phase at low density, (b) Filamentary phase at intermediate density, (c) Anisotropic crystal phase at higher density.*

soft phases with low-temperature correlated percolation may be a generic feature of systems with competing long- and short-range interactions. The filamentary soft phase is amplified by the anisotropy in the transition metal oxide system, and the dynamics is typically softer on filaments than in clusters.

When the temperature is increased in the clump phase, the superlattice clump structure remains stable up to a very high temperature. The superlattice and clumps break up simultaneously at the melting temperature. Particles are confined within the clumps up to this temperature. In contrast, in the filamentary phase we observe a modulated liquid phase well below the melting temperature (Figure 2). The charges are constrained to remain within a filamentary square pattern, but are free to move along the filaments. The modulated liquid phase remains stable up to the melting temperature at which the pattern itself is destroyed. We define a second, lower temperature T_s at which the onset of the modulated liquid or checkerboard

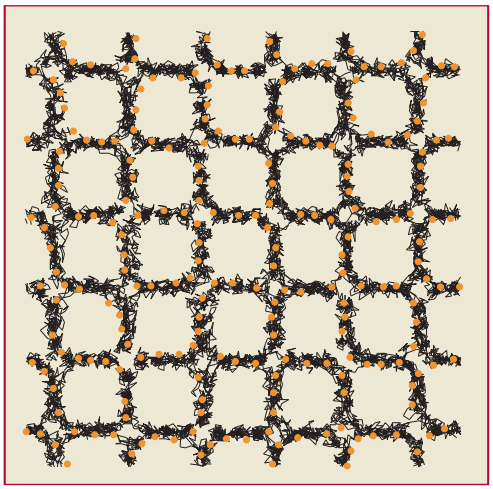

Figure 2— Image of system above the filamentary melting transition, with lines indicating the motion of the holes between consecutive simulation frames.

phase occurs. Although the hole density is not high enough to create this square structure in the static configuration, when the holes are moving their effective density increases, allowing them to form the square state. At any moment the square state is not fully formed; in a snapshot of the system, the square state contains imperfections and density modulations. On average over time, however, the square state is present, and the particles move in response to its structure.

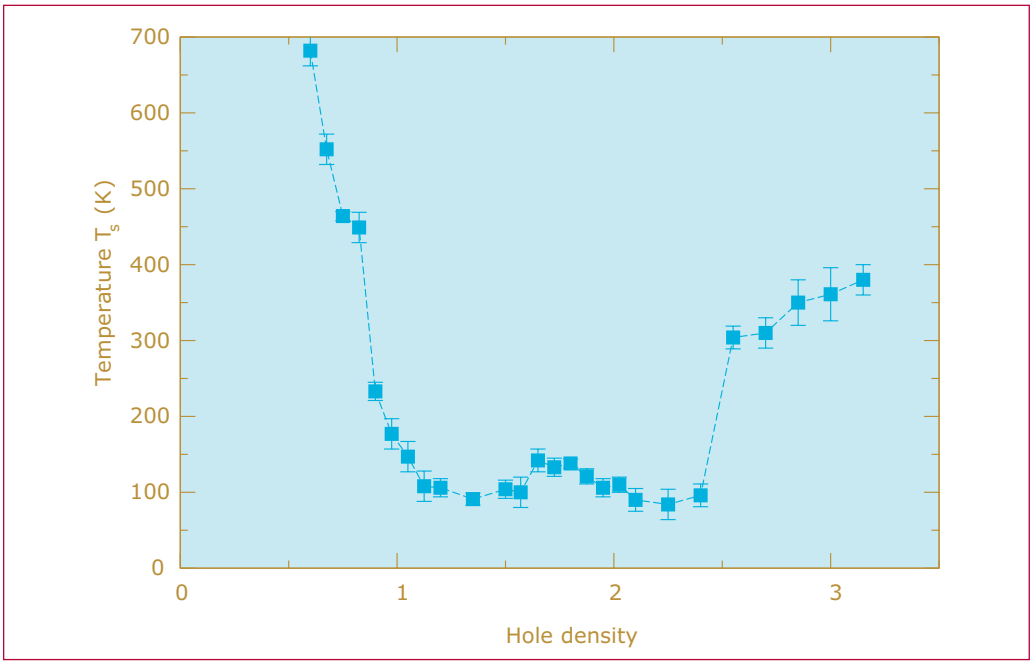

Figure 3— Onset temperature T_s of modulated liquid state as a function of hole density, showing a "soft window" corresponding to densities at which the filamentary state appears.

Mesoscale Modeling of Nanocrystalline Metals

Cynthia J. Reichhardt, Brad Lee Holian, Joel D. Kress, and Antonio Redondo, T-12; cjrx@lanl.gov

The goal of mesoscale model development is to provide a bridge between the atomistic level, where interactions are known ab initio, and the macroscopic level, where the physics is determined by a complex interplay of interactions at smaller length scales. Simulating the macroscopic scale at an atomistic resolution remains beyond the reach of even the largest computing resources. On the other hand, continuum simulations such as finite element mesh models suited for much larger scales are very limited in the degree to which discontinuities such as fractures can be included in the model. These discontinuities appear in a very natural way in atomistic simulations, due to the discreteness of the system arising from the fact that the individual elements being simulated are atoms. The time and length scales that are accessible through atomistic modeling are much shorter and smaller than those that appear in engineering applications, so a pressing problem is how to bring pertinent atomistic information up to the mesoscale level, while discarding unneeded details, and then to repeat this process from the mesoscale level to the macroscopic level. Such information propagation is the primary goal of this project.

It is natural to consider extending the discrete simulation technique to systems in which the individual elements are grains rather than atoms. Each grain is composed of a large number of atoms, but the individual atoms are not treated separately. Instead, the small-scale dynamics are averaged away, and we treat only the dynamics on a time scale relevant to the size scale of individual grains. We focus here on nanocrystalline metals, which are of significant practical interest due to their extremely high hardness and strength. Nanocrystallites can also form upon work hardening, such as when two metals wear against each other. This can change both the strength and the stress transmission properties of the materials.

Our model for mesoscopic grains is based on the Rydberg interaction potential between individual atoms, which has been shown to provide a good approximation to the actual atomic interactions in a wide range of materials. We replace groups of individual atoms with a single

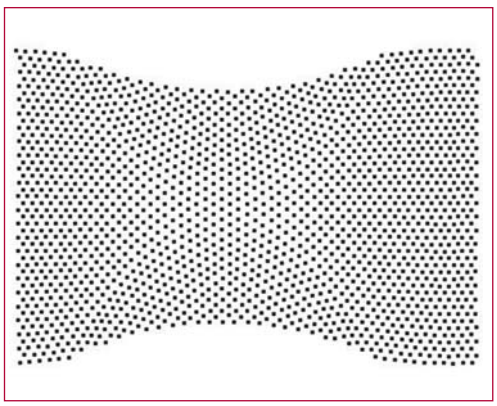

Figure 1—
(a) Mesograin sample deforming under tension at a low-strain rate.

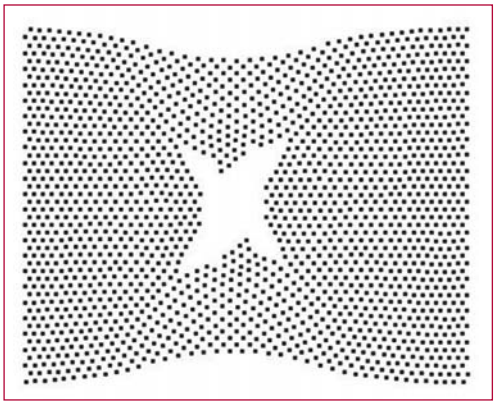

Figure 1—
(b) Mesograin sample failing under tension at a high- strain rate.

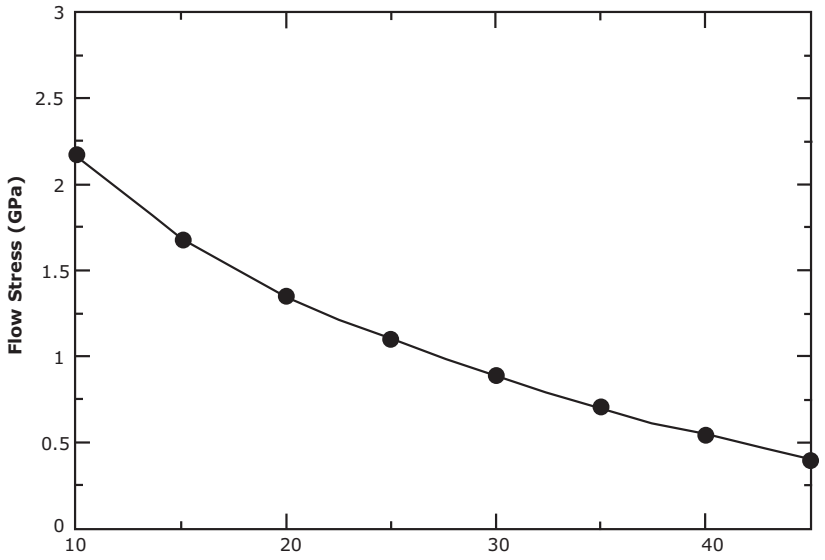

Figure 2—Yield strength from mesograin simulations of nanocrystalline copper.

grain, and implement a grain-grain interaction given by the form of a Rydberg interaction at larger length scales. The relevant energy scale is the binding energy along the interface between two grains, rather than the atom-atom binding energy. We match the speed of sound between our mesoscale model and the atomistic model. The resulting interaction produces a tensile strength that diminishes as the grain size becomes larger, due to the decreasing ratio of surface area to grain volume with increasing grain size.

Figure 1 illustrates the mesoscopic grain model subjected to tension, where each dot represents a single grain that is 25 nm in size. Plastic deformation is illustrated in Figure 1(a), while failure of the sample under tension is illustrated in Figure 1(b). The failure occurs along the interfaces between different grains, and not internally to the grains. This feature of our model is reasonable since the bond energy between adjacent grains is weaker than the bond energy within a given grain. A major advantage of the mesoscale modeling method is the ability to simulate samples of large spatial extent. In the sample shown in Figure 1, the 1600-grain sample is 1 micron across. Atomistic simulation of a sample of this size in 2-D would require 100 times as many particles.

The mesoscale model accurately reproduces the material strength of nanocrystalline materials. Shown in Figure 2 is a plot of the flow stress as a function of grain size. The strength decreases with increasing grain size according to the square root of the grain size, in good agreement with the Hall-Petch relationship that has been observed experimentally for a wide range of nanocrystalline materials. The magnitude of the material strength is in reasonable agreement with that observed in atomistic simulations.

Accelerated Dynamics Study of Vacancies in Pu

Blas P. Uberuaga and Arthur F. Voter, T-12; Steven M. Valone and Michael I. Baskes, MST-8; blas@lanl.gov

The importance of Pu as a material central to modern society can hardly be overstated. From its role in the nuclear weapons program to the dependence of fission reactors on Pu, it holds a prominent place in many important technologies. A complete understanding of the properties of this material is critical to being able to utilize it fully. Such an understanding begins at the atomic level, where point defects—vacancies and interstitials—dominate the behavior. Not only do these defects govern the self-diffusivity of Pu, but also the motion of impurities or dopants that might be present. The goal of this work is to study the properties of one of these defects (mono-vacancies) so that a deeper understanding of Pu can be gained.

Molecular dynamics (MD) simulation is an important tool for understanding materials at the atomic scale. Such simulations allow us to do what experiments cannot: focus on a small piece of material where we can follow the motion of individual atoms. In doing so, we can measure the properties of defects directly, providing input to higher levels of modeling. One limitation of MD, however, is that the time scales accessible—ns to μs—are relatively short. To overcome this time scale problem, we employ accelerated dynamics techniques, developed here at Los Alamos, in particular parallel-replica dynamics [1] and temperature accelerated dynamics (TAD) [2]. Both of these methods allow us to reach longer time scales than conventional MD.

Parallel-replica dynamics involves a straight forward parallelization of time. Each processor evolves an independent replica of the entire system until a transition to a new state is detected on any of the processors. If the rare events that govern motion from state to state in the material are first order processes, then parallel-replica dynamics is exact, even correctly describing correlated events. By parallelizing on M processors, one can reach a maximum speedup compared to a single processor run of M times. Reaching this maximum efficiency depends on how infrequent the events are, as there is some overhead involved each time an event is observed.

TAD is potentially much more powerful, but involves more assumptions about the nature of the system. In particular, if the system obeys harmonic transition state theory, TAD gives nearly exact state-to-state dynamics. The algorithm involves running MD at a high temperature, T_{high}, higher than that of interest, T_{low}. The behavior at T_{high} is then extrapolated to T_{low} and an event is accepted based on this extrapolation. Using this algorithm, experimental time scales are achievable for some systems [3].

In the following work, we use the modified embedded atom method (MEAM) [4] to describe the Pu-Pu interaction. To simplify the analysis somewhat, and to simulate the stabilizing effects of Ga-doped Pu, we have used both the parameters published in [5], as well as a modified parameter set in which $t_3 = 0$. This change in t_3 corresponds to removing a sensitivity to inversion symmetry in the crystal structure and results in the stabilization of the δ-phase of Pu, relative to the other phases, much as Ga does in real Pu. In what follows, these two parameterizations will be referred to as Pu^{sym} and $Pu^{no\text{-}sym}$, where $Pu^{no\text{-}sym}$ has $t_3 = 0$.
Parallel-replica dynamics has been used

to study the motion of a mono-vacancy in Pu^{sym} at 900 K. Running the simulation on 38 processors, we achieved a speedup of 36 times. This simulation, taking 1 week of wall-clock time, would have taken 36 weeks on a single processor.

The δ-phase of Pu^{sym} is characterized by tetragonal distortions of the lattice in which the Pu atoms become paired to one another. The distorted structure is more stable than the perfect δ-phase structure.

At 900 K, mono-vacancy hops are relatively rare; in simulations of Pu^{sym} for a total of 3 μs, we saw only 12 hops. Eight of these hops were simple moves, in which one Pu atom adjacent to the vacancy moves directly into the vacancy site, resulting in the mono-vacancy moving one nearest-neighbor distance. The energy profile of the minimum energy path for such an event has been calculated with the nudged elastic band (NEB) method [6], giving a barrier for the single hop of about 1.11 eV.

Surprisingly, we also saw four events in which the mono-vacancy executes a double hop. Two Pu atoms move in a concerted motion such that the mono-vacancy moves two lattice spacings during one event. Again using NEB, we find a barrier of 1.04 eV for this process.

We have performed TAD simulations for a mono-vacancy in $Pu^{no\text{-}sym}$. $Pu^{no\text{-}sym}$ is more amenable to TAD than Pu^{sym} since there are fewer local minima; the global tetragonal distortions in Pu^{sym} are not present in $Pu^{no\text{-}sym}$. In simulations of about 0.43 μs at T_{low} =1000 K (using T_{high} = 2000 K), we again saw both single and double hops. (The TAD simulations resulted in less total time than the parallel-replica simulations, but only required one processor.) The barriers for these are 1.55 and 2.18 eV, respectively.

We have estimated the rates for both of these processes for both parameterizations of Pu by finding the average rate for each at the simulation temperatures (for the parallel-replica simulations, 900 K, and for the TAD simulations, 2000 K). Assuming that the rate is Arrhenius up to these temperatures, we find

$$k_{\text{single hop, sym}} = 3.2\text{x}10^{11}\, e^{-1.11\ \text{eV}/k_B T}\ /\text{s}$$

$$k_{\text{double hop, sym}} = 8.5\text{x}10^{10}\, e^{-1.04\ \text{eV}/k_B T}\ /\text{s}$$

for Pu^{sym} and

$$k_{\text{single hop, no-sym}} = 3.4\text{x}10^{12}\, e^{-1.55\ \text{eV}/k_B T}\ /\text{s}$$

$$k_{\text{double hop, no-sym}}$$

$$= 3.1\text{x}10^{13}\, e^{-2.18\ \text{eV}/k_B T}/\text{s}$$ for $Pu^{no\text{-}sym}$.

These rates are summarized in the figure.

Both of the rates for Pu^{sym} are characterized by relatively low prefactors. The low prefactor is likely the consequence of the distorted ground state of the δ-Pu crystal. As mentioned above, in the distorted ground state structure, each atom is paired to one other atom and so, at any given time, the mono-vacancy only has one place to jump. Of course, the rearrangement of the distorted structure means that, over time, each of the twelve neighboring sites will become accessible to the mono-vacancy, but only one is available at any given time. This results in the lower prefactors.

The rates for both the single hop and the double hop in Pu^{sym} are very similar to one another. Because each double hop

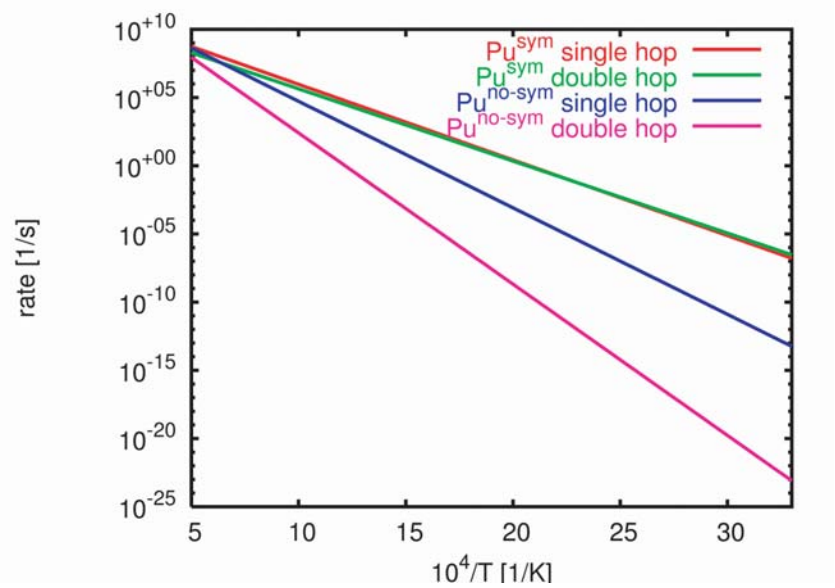

Figure—Arrhenius plot of the rates for the four mechanisms discussed in the text.

results in the mono-vacancy moving twice as far as for a single hop, the contribution to the diffusion constant is four times greater. That means that any model that includes a description of mono-vacancy migration must take into account both single and double hops, as both are important.

In $Pu^{no\text{-}sym}$, there is a greater separation of rates between the single and double hops. For all temperatures, the single hop dominates. In addition, the rates of both mechanisms are significantly lower for $Pu^{no\text{-}sym}$ than for Pu^{sym} for a very large temperature range. The stabilizing effect of removing inversion symmetry (setting $t_3 = 0$) results in a reduction of the mono-vacancy hop rate.

To summarize, we are applying accelerated dynamics methods to the δ-Pu system in an effort to understand the behavior of mono-vacancies. Using parallel-replica dynamics, we have identified two different mono-vacancy diffusing events —a single hop and a double hop mechanism—in the original MEAM parameterization for Pu. We find that the rates for both processes are nearly identical for a large temperature range with the double hop mechanism dominating the contribution to mass transport. Temperature accelerated dynamics was applied to a modified parameter set that stabilizes the δ-phase. Again, we see both types of hops, but single hops clearly dominate the behavior for this parameterization. Mono-vacancy diffusion occurs much more quickly in "pure" Pu (Pu^{sym}) than in the "Ga-stabilized" version ($Pu^{no\text{-}sym}$).

[1] A. F. Voter, *Phys. Rev. B* **57**, R13985 (1998).
[2] M. R. Sørensen and A. F. Voter, *J. Chem. Phys.* **112**, 9599 (2000).
[3] J. A. Sprague, F. Montalenti, B. P. Uberuaga, J. D. Kress, and A. F. Voter, *Phys. Rev. B* **66**, 205415 (2002).
[4] M. I. Baskes, J. S. Nelson, and A. F. Wright, *Phys. Rev. B* **40**, 6085 (1989); M. I. Baskes, *Phys. Rev. B* **46**, 2727 (1992).
[5] M. I. Baskes, *Phys. Rev. B* **62**, 15532 (2000).
[6] G. Henkelman, B. P. Uberuaga, and H. Jónsson, *J. Chem. Phys.* **113**, 9901 (2000); G. Henkelman and H. Jónsson, *J. Chem. Phys.* **113**, 9978 (2000).

Radiation-Damage Annealing in MgO

Blas Pedro Uberuaga, T-12; Roger Smith, MST-8; Antony R. Cleave, Imperial College, UK; Graeme Henkelman, T-12; F. Montalenti, Universitá degli Studi di Milano-Bicocca, Italy; R. W. Grimes, Imperial College, UK; Kurt E. Sickafus, MST-8; and Arthur F. Voter, T-12; blas@lanl.gov

Understanding the behavior of materials under radiation damage conditions is a critical issue in a variety of problems, from designing radiation-proof structural materials for nuclear reactors to implantation of dopants into semiconductors. Modeling such processes poses a classic multiscale problem, especially in the time domain. A molecular dynamics (MD) simulation follows the evolution of a collision cascade over ps timescales, sufficient time to observe the collisional phase of the cascade and identify features of the damage. However, the behavior of a material is determined not only by the number and nature of the residual defects associated with a cascade, but also by their longtime evolution. Over timescales much greater than ps, defects diffuse, annihilate, and aggregate. By merging MD with accelerated dynamics methods, we accurately evolve the system over the full range of time scales from fs to s and beyond.

As a model material for this study, we chose the oxide magnesia (MgO), which we describe using a standard ionic pair potential [1]. We generated collision cascades in MgO using MD by imparting energy to a primary knock-on atom (PKA). Representative defects from the cascades were then used as starting configurations for long-time simulations via temperature accelerated dynamics [2,3].

Collision cascades with PKAs at energies between 0.4 and 5 keV were run for 8 ps. Figure 1 shows a typical cascade with a PKA energy of 0.4 keV. Shortly after the initial knock-on, a large number of atoms are displaced from their original site, saturating at t = 80 fs (Figure 1a). Shortly afterwards (260 fs), most of the damage has annealed, leaving only two vacancies and two interstitials (Figure 1b). However, by t = 6.5 ps, the two interstitials combine to form a MgO di-interstitial (labeled A in Figure 1c). As expected, as the PKA energy increases, so does the total number of defects. Also, while point defects dominate the defect distribution at all energies, the size of defect clusters increases with PKA energy.

Typical defects found in the cascade simulations were analyzed via static energy minimization [4]. The binding energy of interstitial clusters is shown in Figure 2. The interstitial clusters are bound by many eV per atom, becoming increasingly stable with increasing size. Static

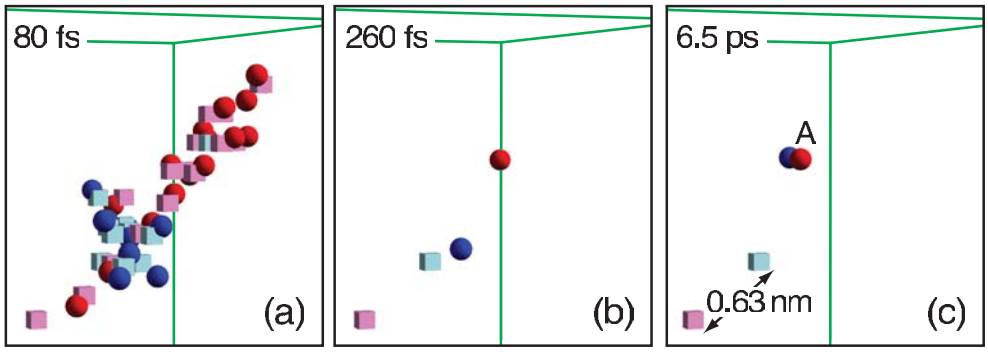

***Figure 1—** The defects in a cascade generated from a 400-eV impact. The scheme is dark blue spheres for Mg interstitials, dark red spheres for O interstitials, light blue cubes for Mg vacancies, and light red cubes for O vacancies.*

simulations were also used to identify the diffusion barrier of isolated interstitials: 0.40 eV for O and 0.32 eV for Mg.

Temperature accelerated dynamics (TAD) was used to follow the long-time behavior of the residual cascade damage. TAD involves running MD at a high temperature, T_{high}, while confining the trajectory to the current basin. The times of attempted escape events seen at T_{high} are extrapolated to the temperature of interest, T_{low}, and the event occurring first at T_{low} is accepted. Here, T_{low} was set to 300 K. To enhance the speed of the TAD simulations, we used a recent extension to TAD, the dimer-TAD method [5], which exploits the dimer method [6] to enhance the efficiency of the TAD algorithm.

The diffusion barriers found during the TAD simulations are shown in Figure 2. At 300 K, vacancies are immobile (barrier > 2 eV) while interstitials diffuse on ns timescales. For small clusters, the diffusion barrier increases with size: dimers and trimers diffuse on the second timescale with barriers between 0.75 eV and 0.80 eV, while tetramers, with a barrier of 1.68 eV, are immobile. The tetramer is also very stable: the barrier to split it is 2.5 eV, a process that essentially never occurs at 300 K.

This trend suggests that clusters of four or more interstitials act as immobile interstitial sinks. Surprisingly, however, the hexamer is mobile, with a diffusion barrier of 1.04 eV in its ground state (100-second timescale). Moreover, it can exist in a metastable state, which we actually observed to form in an encounter between a dimer and a tetramer during the TAD simulation, as shown in Figure 3. *This hexamer diffuses one-dimensionally on the ns timescale and lives for years in this metastable form.*

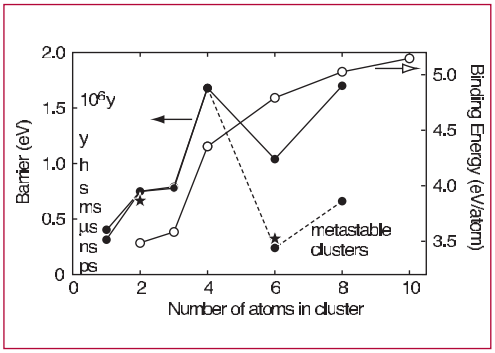

Figure 2—Binding energy, diffusion barriers, and diffusion timescale at 300 K for interstitial clusters versus cluster size. The ★s indicate DFT barriers.

Using density functional theory (DFT), we have checked some of the key properties observed during this study. For the dimer and hexamer, the DFT formation energies, 12.8 and 31.1 eV, respectively, compare well with the empirical potential values of 11.9 and 28.5 eV, considering the high energies involved in the collision cascades, and the diffusion barriers agree very well: 0.66 and 0.33 eV using DFT compared to the empirical potential values of 0.75 and 0.24 eV (see Figure 2). This makes us confident that the ionic model gives a good description of MgO for these processes.

From this multiscale study combining MD and TAD, augmented with molecular statics and DFT, an interesting picture emerges for the evolution of low-energy radiation damage in MgO. Point defects and small interstitial clusters

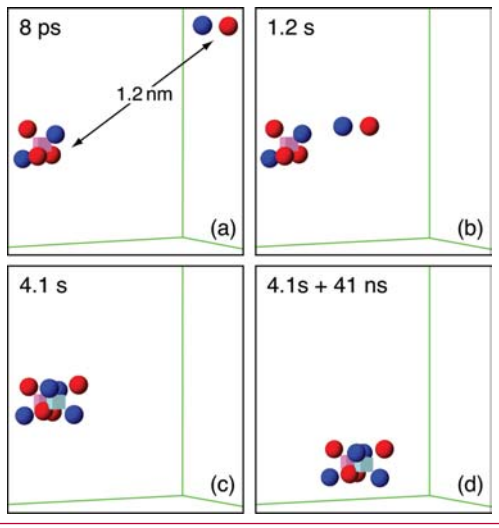

Figure 3—TAD simulation of the formation of a 6-atom interstitial cluster from an interstitial dimer and interstitial tetramer, 300 K.

form during the cascades. Vacancies are immobile at room temperature, but interstitials diffuse quickly, either recombining with vacancies or clustering with other interstitials. These clusters become more stable with size, but certain sizes and forms can be unexpectedly mobile. They can thus aggregate with clusters from other cascades, increasing the overall damage accumulation rate. Because of their importance, such clusters must be included in any higher level description of radiation damage in MgO.

[1] G. V. Lewis and C. R. A. Catlow, *J. Phys. C: Solid State Phys.* **18**, 1149 (1985).

[2] A. F. Voter, F. Montalenti , and T. C. Germann, *Ann. Rev. Mater. Res.* **32**, 321 (2002).

[3] M. R. Sørensen and A. F. Voter, *J. Chem. Phys.* **112**, 9599 (2000).

[4] G. Busker et al., *Nucl. Instrum. and Meth. B* **171**, 528 (2000).

[5] F. Montalenti, B. P. Uberuaga, G. Henkelman, and A. F. Voter, in preparation.

[6] G. Henkelman and H. Jónsson, *J. Chem. Phys.* **111**, 7010 (1999).

T-14 Explosives and Organic Materials

Numerical Simulation of Full Densification of Foams

Scott G. Bardenhagen, T-14; bard@lanl.gov

Foamed materials are increasingly finding application in engineering systems because of their unique properties. They are extremely light weight and can provide gentle packaging or energy absorption during crush-up. The basic mechanics that gives rise to these properties is well established and is due to the foam microstructure, a network of struts and, possibly, membranes. Foams compress at nearly constant load (the "stress plateau") over a large range of deformation while the load is supported primarily by strut bending. As the network begins to collapse upon itself ("densification") the material stiffens dramatically as the primary load-carrying mechanism transitions to contact between struts. Microstructural models and simulations have provided substantial insight regarding foam mechanics, but primarily at small deformations. Numerical simulation of foam deformation physics in the stress plateau and densification regimes, where accounting for large material deformations and contact mechanics is essential, remains a significant computational challenge.

A particle-in-cell (PIC) numerical simulation technique (a "meshless method") has been shown to perform well-modeling precisely the physics relevant to foam mechanics, i.e., large material deformations and contact. PIC algorithms were developed at Los Alamos to model fluid flow. More recent developments have allowed the application of these methods to solid mechanics. Model foam unit cell microstructures, with relative density ~ 90%, have been generated. Compression of these unit cells was simulated to full densification (90% engineering strain). These simulations are preliminary, but represent a computational "first" in this field.

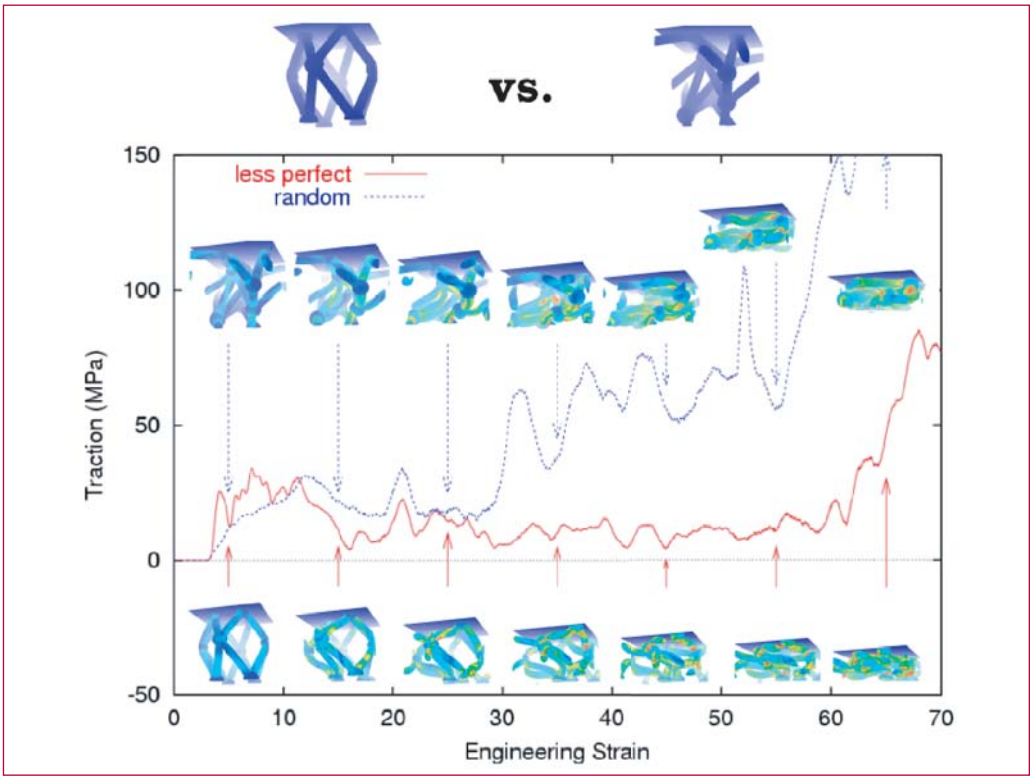

***Figure—** The force required, as a function of deformation level, to crush up two idealized foam microstructures. Insets indicate deformed configurations.*

Simulation results were found to be in qualitative agreement with expectations and experimental work. The stress plateau and densification deformation regimes may be easily distinguished in the macroscopic stress strain response depicted in the figure. Effects due to regularity of the foam microstructures have also been identified. More regular unit cells appear to exhibit a much flatter stress plateau. Future work includes linux cluster simulations of much larger microstructures, representative of bulk foam material.

Numerical Simulation of Stress Wave Propagation in PBXs

Scott G. Bardenhagen, T-14; bard@lanl.gov

Stewardship of the nuclear weapons stockpile places stringent demands on the understanding of materials and their behavior under extreme conditions. Homogeneous continuum models have been developed to describe the response of a material to dynamic loading, including equation of state, strength, and reactive burn models. However many strategic materials, in particular plastic bonded explosives (PBXs), are heterogeneous at the microscale (<1 mm). PBXs are composites containing energetic grains, ranging in size from less than one to a few hundred micrometers, embedded in a matrix of high-polymer binder. Low levels of applied stress can cause substantial material damage and even lead to violent reactions because of the heterogeneous nature of its distribution.

Homogeneous continuum models provide good estimates of bulk material response. However, as there is little connection to the underlying physics, these models cannot be extrapolated with confidence. The orientation dependent properties of the individual crystals and the presence of material interfaces result in strongly heterogeneous stress and energy distribution. To develop accurate, quantitative, and predictive models it is imperative to develop a sound physical understanding of the grain-scale material response.

One approach to capturing this behavior is to perform microscale simulations where the crystals and the binder of the PBX are explicitly represented. While easy in principle, a very crucial feature is how the interfaces between materials are handled. Such contacts can be fixed with strong adhesion, free with very weak adhesion, or exhibit frictional sliding. Exactly what type of behavior is exhibited is highly dependent on the material properties and strain-rates. This behavior can not be accurately captured with conventional Lagrangean or Eulerian simulation codes for a realistic polycrystalline sample with a large number of irregular shapes and contact surfaces.

A better approach for this class of simulations is to use a particle method. One particular method, the Material Point Method (MPM), provides a convienent framework for modeling material interfaces. It has been used here to perform numerical simulations indicating the importance of accurately modeling composite material constituent interfacial conditions. The computational technique has been developed primarily by researchers at LANL and UNM, with the particular code implementation coming from the University of Utah's

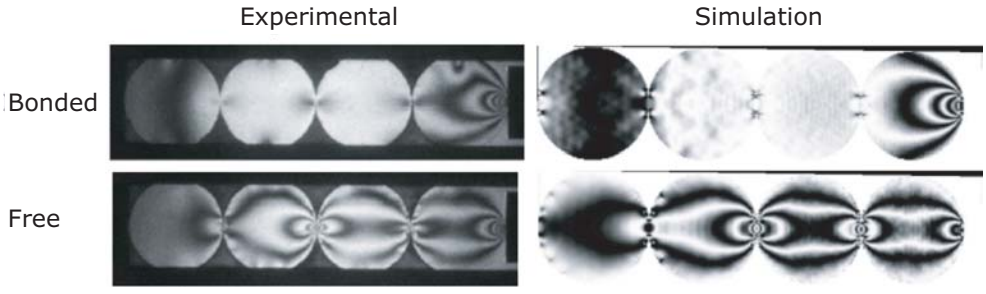

Figure—Comparison of experimental data and simulation of stress wave propagation through photoelastic cylinders embedded in an opaque binder. In one case the binder is allowed to adhere (bonded) to the cylinders during casting, in the other case adhesion is prevented (free).

ASCI/ASAP program. The particular algorithm for handling interfaces was developed at LANL as part of this project.

As an example of validation, we compare our computations to a set of experiments performed by Joe Foster and coworkers at Elgin AFB. There, stress wave propagation experiments were performed on simple composite microstructures–polymeric cylindrical "grains" embedded in a polymeric binder. A comparison of results is shown in the figure. Two cases, perfect adhesion (bonded) and complete decohesion (free) of the grain binder interfaces, were examined. With perfect adhesion (bonded), a substantial amount of the stress is transferred to the binder, and there is very little localization in the crystal. With complete decohesion (free), the stress is carried almost completely in the crystals, and there is substantial stress amplification at grain contacts. Validation simulations successfully capture differences in stress distributions in near quantitative agreement. As the constitutive properties and strain-rates in these experiments and simulations are in the range of interest, the importance of properly describing the interface conditions is clearly demonstrated.

Simulations containing hundreds of crystals have also been performed in both two- and three-dimensional geometries. These have utilized particle size distributions appropriate for the PBXs. Previous work has been done without a binder, and substantial stress fluctuations were observed. It was found that these could be characterized by a power law distribution. We are in the process of redoing these simulations with binder included, to determine the factors that control the stress distribution. The results will be used to assess and parameterize a homogenized model for the PBXs that can be used in macro-scale simulations.

The Nexus between Reactive MD Simulations of RDX and the Reactive Euler Equations

Shirish M. Chitanvis, T-14; chitanvis@lanl.gov

Our past calculations have focused on pre-ignition phenomena that cause a local temperature rise when a single void in HMX collapses under the action of a shock wave. Working in the melting regime, a time-line can be associated with the collapse of a single void through a consideration of the time scales on which these mechanisms are activated.

Among the phenomena we studied, the *hydrodynamic mechanism* is generally considered to be an important pre-ignition step. In this mechanism, the shock driven incident side of the void impinges on the shadow side of the void, and is brought to rest, causing a considerable temperature rise in the HMX. This mechanism comes into consideration as the void closes up under the action of the shock wave. The resulting increase in pressure and temperature causes a shock wave to emanate from the collapse. This shock wave very quickly attains cylindrical symmetry in our two-dimensional calculation. If the energy contained in this outgoing shock wave is sufficiently high, it could produce a local microdetonation.

In order to study the energy release provided by the hydrodynamic collapse of the void, one needs to understand the chemical reaction pathway through which this homogeneous explosive decomposes. Very recently, A. Strachan (T-14) found that the complicated reaction pathway in RDX can be simply represented as a single-step energy release step governed by Arrhenius kinetics. The activation energy is about 1 eV and is weakly pressure-dependent. This result was obtained by using the ReaxFF potential developed at Caltech in cook-off-like simulations of RDX at high temperature and pressure. These simulations were performed at various temperatures and pressures, and it is of interest to investigate the applicability of the resulting parameterization of the kinetics at a macroscopic scale.

The incorporation of the single-step Arrhenius rate into continuum dynamics can be accomplished by solving the

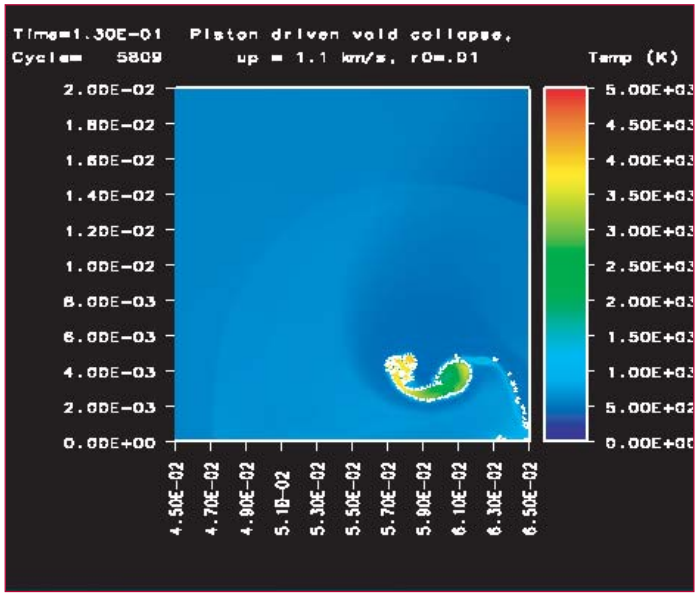

Figure 1—Temperature contours obtained from high-resolution calculations of a collapsing void using Comadreja are displayed in this figure.

reactive Euler equations. The width of the reaction zone, which develops as the rarefaction Taylor wave behind the von Neumann pressure spike, may be estimated in an order of magnitude sense by the product of the sound speed (typically a kilometer per second or less) and the characteristic chemical time scale, viz., picoseconds. This yields a scale of the order of 1/100th of a micron. Since voids in explosives are expected to be of the order of microns, it follows that a numerical solution of the reactive Euler equations would be at best a difficult job in two dimensions.

An alternative method of solution is to develop a sub-grid model, such as Bdzil's Detonation Shock Dynamics (DSD). This technique consists of performing an asymptotic (perturbative) expansion of the reactive Euler equations in a shock-based frame of reference and coordinate system. The formalism eventually reduces to the solution of a transcendental equation for the relation between the detonation velocity normal to the shock front (D_n) and the local curvature (κ). It is possible to obtain from this analysis an estimate of the minimum size and energy of the hotspot that would be required to sustain a microdetonation during void collapse in a melted homogeneous RDX sample.

Strachan's reaction rate was successfully incorporated into DSD theory. The profiles shown in the following figures display the Zeldovich-Neumann-Raizer (one-dimensional results for the structure of the reaction zone).

Using available data, we have adjusted the material parameters in the model to obtain reasonable values for the CJ detonation velocity viz., 8.7 km/s and the CJ pressure 0.3482 Mbars. Unfortunately,

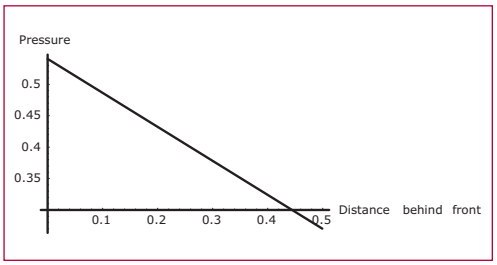

Figure 2—Pressure profile for a one-dimensional detonation.

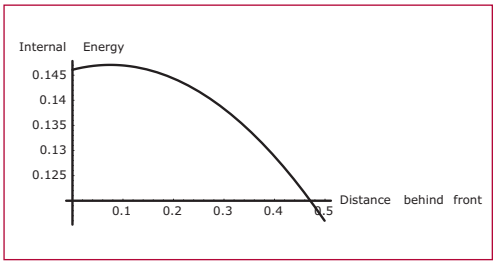

Figure 3—Internal energy profile for a one-dimensional detonation.

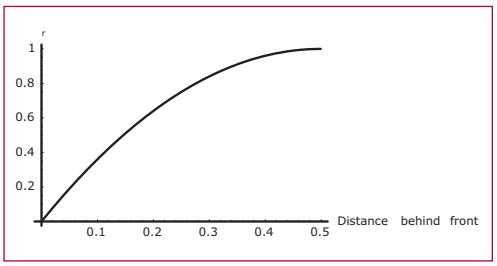

Figure 4—Profile of the progress variable for a one-dimensional detonation.

the specific heat of RDX is as yet unknown as a function of temperature, so we adjusted it until reasonable values for the detonation temperature were obtained viz., 1000–1400 K. The values of the specific heat were ~ 1.5 cal/g. With these material properties in hand, a self-consistent equation was solved for Δn as the curvature κ was varied. $\kappa \sim 2/w$ (w being the radius of the rate stick) was increased until the self-consistent equation does not yield a real solution. This provides a minimum value of $w = w_{min} = 1$ mm for $C_v = 1.5$ cal/g , which yields a detonation temperature of ~ 1000 K. The calculation was repeated for a lower specific heat that yielded a detonation temperature of ~ 1500 K, and failure radius about ~ 0.1 mm. We expect the failure radius to be in the range of microns for a detonation temperature of 3000 K.

On Validating SCRAM

John K. Dienes, T-14; John Middleditch, CCS-3; and Q. Ken Zuo, T-3; jkd@lanl.gov

The SCRAM algorithm for modeling brittle behavior was designed to complement various algorithms that characterize ductile behavior of materials and to account for the sensitivity of explosives and propellants to very low speed impacts. In its current form it accounts for the opening, shear, growth and coalescence of an ensemble of cracks, the heating in shear (closed) cracks, and reactions in high explosives that result from crack heating; hence the acronym SCRAM, for Statistical CRACK Mechanics. The SCRAM algorithm operates over a range of scales, accounting for reactions in a zone near the crack surface that is only microns in width, while allowing for the formation of cracks that may be many centimeters in length. The algorithm has been embedded in a variety of finite-element codes so that it can compute damage in large structures. The new coalescence formulation accounts for percolation behavior representing the formation of very large cracks (visible to the naked eye).

The various concepts that contribute to SCRAM are generally wellknown, qualitatively, but they have been extended to account for complex damage processes, which require tensor constitutive laws and must be valid at large deformations. The current emphasis has been on verifying and validating the programming and physical concepts. They are considered crucial at this point because the introduction of new physics such as the set-size theory for percolation processes makes the damage behavior very complex and, consequently, it is challenging to confirm the calculations. This is especially the case where three-dimensional behavior is involved, and three-dimensions are required to represent impacts that involve extensive damage.

One kind of test problem we have developed concerns the response of a thick uniform ring to sudden internal pressure. We have confirmed that the finite-element solution is uniform and consistent with the analytic solution. This constitutes one kind of verification because the computing is actually done in the SCRAM algorithm, though the nonlinearity is small. The primary purpose of this test, however, is to confirm that the damage is homogeneous around the ring when SCRAM is activated. This is far from trivial for a number of reasons. First, the finite-element programs are noisy. Second, there could be bugs and/or noise in the SCRAM algorithm or its implementation. Third, materials that allow only a few crack orientations are anisotropic and anisotropy would lead to inhomogeneous behavior in a symmetric geometry. By examining calculations with various numbers of orientations we can test for bugs and determine how many orientations are needed to get accurate damage response. We have found that 9 orientations is hardly enough, 30 is adequate, and 480 gives good uniformity, as shown in the figure.

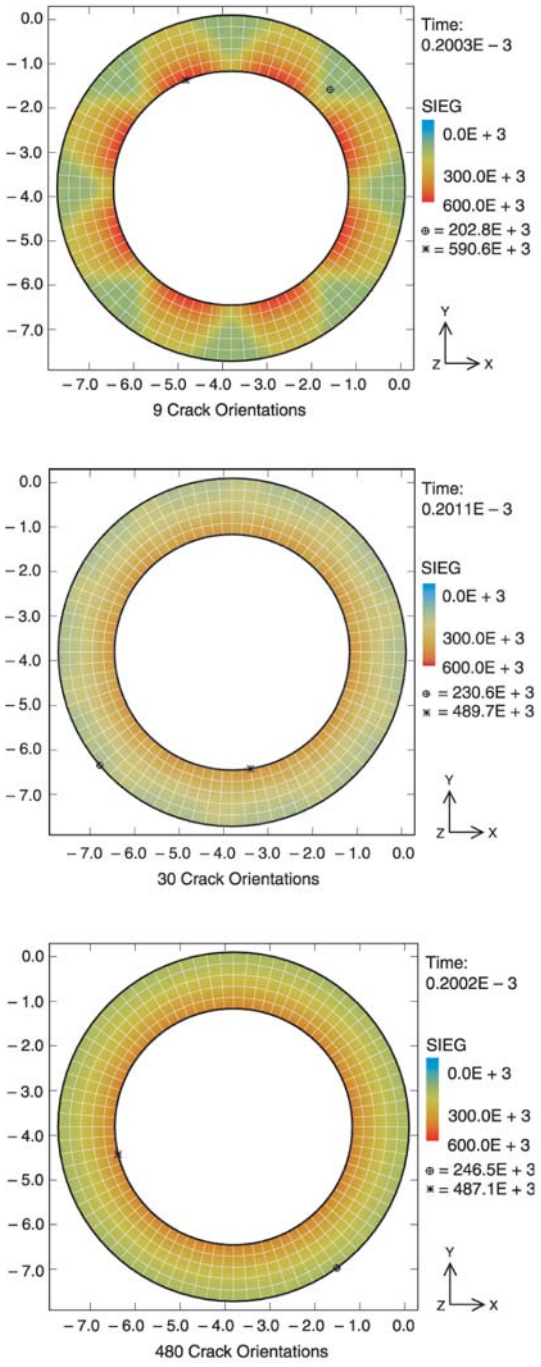

Figure—
The response of a thick ring to internal pressure for three levels of resolution of crack orientation. With 9 orientations the anisotropy is quite large, while with 480 the uniformity is good. The internal pressure ramps to 25 bars in 30 μs.

Fundamental Detonation Behavior from Molecular Dynamics Simulations

Andrew J. Heim, T-14/UC-Davis; Timothy C. Germann, X-7; Brad Lee Holian and Edward M. Kober, T-14; and Niels G. Jensen, UC-Davis; aheim@lanl.gov

While most aspects of detonation behavior of plastic-bonded explosives (PBXs) are well-understood and modeled at an empirical level, there are essentially no aspects of their behavior that can be predicted quantitatively from basic physical models. Examples include changes due to large temperature variations, curvature effects, changes in manufacturing processes, and aging phenomena. Improving our predictive capabilities in this regard is one of the primary goals of the ASC Materials and Physics Program.

To establish this predictive capability, we are using classical molecular dynamics (MD) simulations to investigate the relationship between molecular properties and the detonation response. Advances in computational resources and algorithms now make it possible to perform atomistic simulations on quite large systems. In particular, using the SPaSM parallel MD code and computer clusters available at LANL, simulations containing billions of atoms can be performed that corresponds to absolute physical dimensions on the order of microns. While there are important phenomena that can not be captured at this length scale, it has been shown that many basic detonation features can be. These include homogeneous and heterogeneous initiation, steady-state detonation propagation, failure diameter and curvature effects, and, void collapse physics. Because all of the physical properties of the system are defined by the atomistic potentials, one can then determine the fundamental relationships that control the detonation properties.

As one example of this, we are studying the detonation properties of a simple model diatomic molecule (AB) utilizing the REBO (reactive empirical bond-order) model. This system reacts exothermically by the reaction 2AB -> $A_2 + B_2 + 2Q$, where Q is the amount of energy released in the reaction. A snapshot of a steady-state propagating detonation is shown in Figure 1. The complete simulation is much larger (~100,000 atoms) to ensure that the propagation is indeed steady-state and to capture the expansion and equilibration of the gaseous products. An important point here is that the propagation properties are controlled by the equations of state (EOS) of the reactants and "products", where the definition of "products" is the state of the reaction at the end of the very narrow compressed reaction zone associated with the shock wave. In this system, this is ~2 lattice spacings long. It can be seen that the reaction does not proceed completely to products (even at the far left end of the figure), and the extent of the reaction is certainly not complete at the end of reaction zone.

To deconvolute this further, the relationship between microscopic properties that can be explicitly defined and the macroscopic response are determined. For this system, the dominant parameters are the initial A-B bond strength, the exothermicity (Q) of the reaction (determined by the differences in bond strengths), and the intermolecular interaction energy (e). By either increasing the A-B bond strength or decreasing the exothermicity of the reaction, the detonation velocity is decreased in a smooth monotonic fashion until a critical point

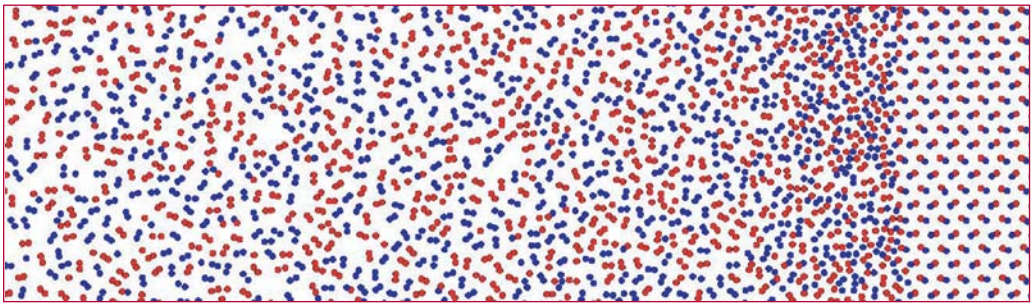

Figure 1—shows a snapshot from a propagating detonation in a model AB diatomic system. The A atoms are red, and B atoms are blue. The crystalline undisturbed reactants are at the far right, with the etonation/shock wave progressing to the right. The highly compressed region is supporting reaction zone, followed by an expanding gaseous region where the reaction continues towards an equilibrium composition. Note that some unreacted AB as well as isolated A and B atoms are present in the product mixture.

is reached where the detonation is no longer self-propagating. These results can be explained in terms of the amount of reaction (and related heat release) that occurs in the reaction zone. A rather interesting dependence of the detonation velocity (D) on the intermolecular interaction energy (ε) is shown in Figure 2. Here, two distinct linear regimes are observed. While not yet completely understood, this is attributed to contributions to the differences in the EOS of the reactants and products, and to changes in the reaction pathway/progress. Further analysis in underway.

Despite the apparent simplicity of this system, it exhibits a complexity in behavior expected and observed for real systems. Complete analysis of this system will result in a more complete formulation of our current detonation models. This work will subsequently be extended to triatomic systems (ABC) reaction, which should make a stronger connection to real systems by extending the reaction zone. The results of this analysis will be applied to other studies on curvature effects and void collapse to attain a complete description of the physics for those phenomena.

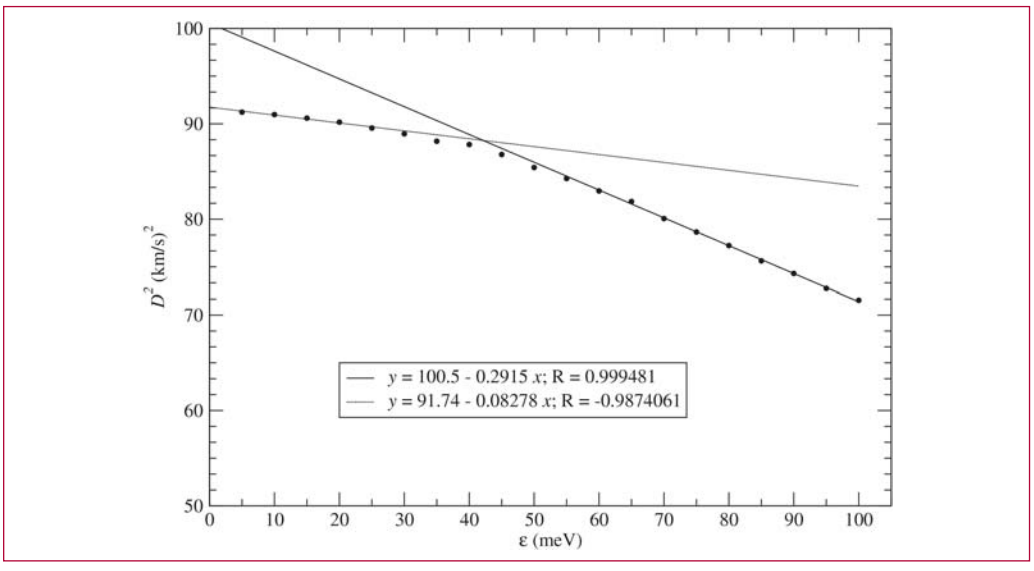

Figure 2—Dependence of the square of the detonation velocity (D) on the intermolecular interaction parameter (ε). Two distinct regions with a linear dependence are observed.

β-HMX Isotherms at Multiple Temperatures and Liquid HMX Equation of State

Eugenio Jaramillo and Thomas D. Sewell, T-14; sewell@lanl.gov

In previous editions of this annual compilation we reported calculations of numerous thermophysical and elastic mechanical properties and liquid state transport coefficients of the high explosive HMX. The motivation for the work [1], which is based on classical molecular dynamics and Monte Carlo methods using an analytic force field, is to provide information needed as input to equation-of-state models for use in mesoscale simulations. (These simulations, in which the grains and binder in a plastic-bonded explosive or propellant formulation are resolved within a continuum hydrodynamic framework, are used to improve our understanding of the initiation mechanisms for such materials under various dynamic loading scenarios.) Ultimately, we hope to provide an internally consistent "model mechanics and thermodynamics" for HMX.

In last year's report, we described calculations of the elastic tensors and isotherms for β-, α-, and δ-HMX at room temperature; that work now appears in final form in the *Journal of Chemical Physics* [2]. We also reported the development of a quantum chemistry-based force field for Estane, which is the poly(ester urethane) copolymer used in the binder formulations for the HMX-based explosives PBX-9501 and LX-14; that work has been published in the *Journal of Physical Chemistry, Part A* [3], and should enable future simulations of the HMX/binder interface. (In connection with ongoing work on force field development for the nitroplasticizer in PBX-9501 binder, we anticipate detailed studies of all essentially all major chemical interactions in PBX-9501.)

In the past year we computed six additional isotherms for β-HMX crystal, in direct response to requests from the mesoscale modeling community. In particular, we calculated isotherms at 223, 273, 323, 373, 423, and 473 K, for pressures between 0 and 10 GPa. These are shown in Figure 1. (Note that 473 K is above the nominal β-δ phase transi-

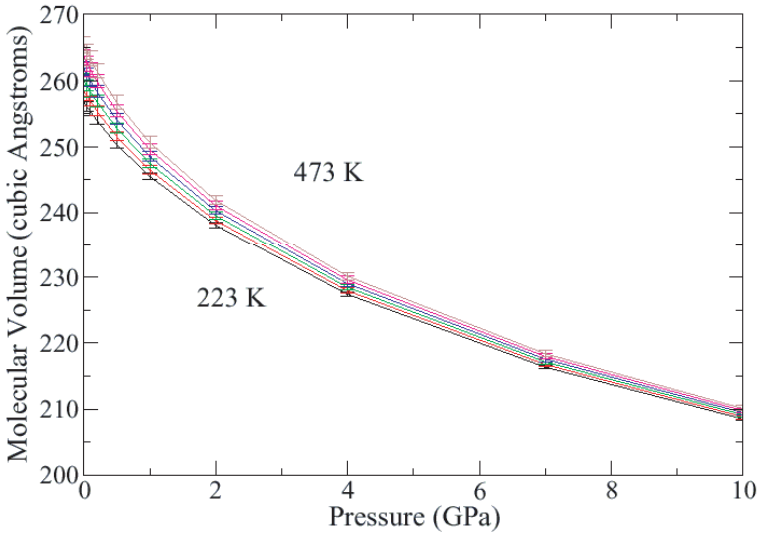

***Figure 1—** β-HMX crystal isotherms.*

tion temperature at zero pressure, but that the β-HMX crystals are metastable at this temperature on the several nanosecond time scale of our simulations.) Our expectation is that these isotherms will be published in tandem with experimental isotherms measured by personnel from the Naval Surface Warfare Center (Indian Head) [4].

We have also undertaken simulations to predict the P-V-T equation of state of liquid HMX and calculations of the bulk modulus along multiple isotherms. Preliminary predictions of the bulk modulus at selected pressures and temperatures are shown in Figure 2.

The question arises naturally in simulations of liquid properties at elevated pressures as to the length of physical time required to adequately sample the liquid. We show one aspect of this in Figure 3, namely the autocorrelation time for molecular rotation in HMX as a function of pressure at T = 800 K. This temperature is close to the atmospheric pressure boiling point of HMX. For pressures of 1 GPa and below, molecular tumbling occurs on a sub-nanosecond time scale. For higher pressures, the time scale become much longer and indeed, for pressures above 4 GPa, it appears that rotational relaxation times will quickly increase to hundreds of nanoseconds or even longer.

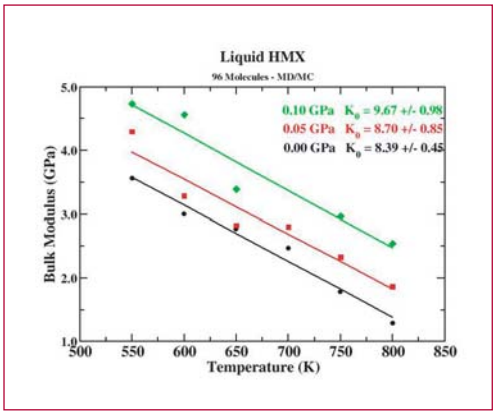

Figure 2— Preliminary predictions of temperature dependent bulk modulus of HMX liquid at three pressures.

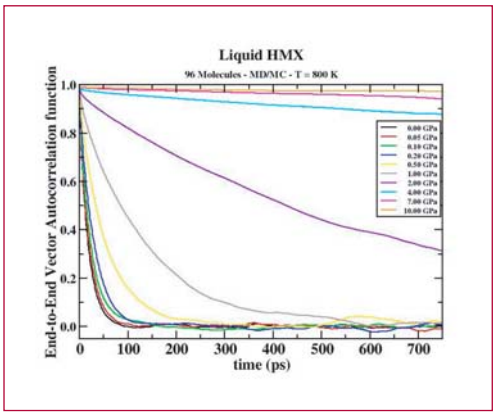

Figure 3— Time scales for molecular rotation in HMX liquid at 800 K, for ten pressures between 0 and 10 GPa. See text for details.

[1] R. Menikoff and T. D. Sewell, "Constituent properties of HMX needed for mesoscale simulations," *Combustion Theory and Modelling* **6**, 103 (2002).

[2] T. D. Sewell, R. Menikoff, D. Bedrov, and G. D. Smith, "A molecular dynamics simulation study of elastic properties of HMX," *Journal of Chemical Physics* **119**, 7417 (2003).

[3] G. D. Smith, D. Bedrov, O. Byutner, O. Borodin, C. Ayyagari, and T. D. Sewell, "A quantum-chemistry-based potential for a poly(ester urethane)," *Journal of Physical Chemistry A* **107**, 7552 (2003).

[4] S. M. Pereis and T. D. Sewell, in preparation.

Constitutive Model Development for Filled Polymer Systems

Edward M. Kober, T-14; James S. Smith and Grant D. Smith, Univ. Utah; emk@lanl.gov

Filled polymeric systems are used for several applications within nuclear weapons systems, typically as adhesives and cushions. Many of these materials are silica-filled polydimethylsiloxane (PDMS) systems such as the foam S5370. While there is extensive literature describing various constitutive models for filled polymeric systems, these models tend to be highly empirical in nature and lack any significant predictive capability. One facet of this is that the fillers are irregularly shaped, are unevenly dispersed, tend to agglomerate in clusters, and there is limited data available characterizing those distributions in the manufactured materials. Another aspect is the large surface area of the fillers (typically 100–300 m2/g with particle dimensions of 10–100 nm), where this indicates that adhesion of the polymer to the surface will be an important parameter. This also suggests that a large fraction of the bulk polymer may be influenced by these surface interactions and may have properties modified with respect to the bulk material.

The purpose of this effort is to develop physicallybased constitutive models for the polymeric systems of this type, primarily the silica-filled PDMS systems. Our approach to this is to determine the fundamental properties and response characteristics of the polymer system and the polymer surface interface from a combination of atomistic molecular dynamics (MD) simulations. These results are extended to time and length scales beyond the domain of the MD simulations by the use of well-established analytic formulations and utilizing coarse-grained simulations. The resulting properties will then be input into existing constitutive formulations or those modified to accept these properties. In particular, current formulations tend to treat the polymer bulk as an ideal elastic material whose response is entirely entropic, whereas PDMS is known to have a viscoelastic response and 10–20% of the elastic response is enthalpic in nature. Also, most formulations tend to ignore the surface boundary layer.

The first area of work was to establish an MD force-field from high-level quantum chemistry calculations. The current commonly used force-field is about 10 years old and was based on lower-level calculations. Our work found that the PDMS system was more polar than previously estimated, and that some of the bond-bending motions were not well-described. Corrections in these terms results in an improved level of agreement with the bulk polymer properties

We then characterized the silica-PDMS interaction as the second area of work. A large body of experimental work clearly demonstrates that the strength of this interaction is highly dependent on the number of surface hydroxyl groups on the silica, and that strong hydrogen-bonds occur between those hydroxyl groups and the oxygen atoms in the PDMS chains. However, a recent theoretical study concluded that this interaction did not take place, but suggested no alternative mechanism for why the hydroxyl groups affected the interaction. From a thorough quantum chemical study, we found that strong hydrogen-bonding interactions should occur and our calculated spectroscopic shifts were consistent with experiment.

This data was also then included in our MD force-field parameterization, and the effects of the surface hydroxyl groups

were studied. First, simulations were performed with a "clean" silica particle (that had no surface hydroxyl groups) immersed in a bath of PDMS oligomers. The surface would wet, but no strong interactions or ordering were found, as shown in Figure 1. This shows the concentration profiles of the silicon, oxygen, carbon, and hydrogen atoms as a function of distance from the silica surface. These profiles are all broad and diffuse and show no particular ordering, other than a preference for the methyls groups to interact with the surface rather than the oxygen atoms. The relaxation times of the PDMS chains were not significantly altered compared to what they were for a bulk solution without filler. In contrast, a hydroxyl covered silica particle showed a strong ordering effect as shown in Figure 2. The sharp oxygen peak at ~ 3 Å is due to species involved in hydrogen-bonds with the surface. It is also interesting to note the subsequent bumps in the oxygen profile at 6 and 8 Å (along with the associated shadows in the silicon distributions). This shows that the second and third layers of polymer chains also have a level of induced ordering arising from polar interactions. The relaxation times of the PDMS in this sample are increased by a factor of ~10 compared to the nonhydroxylated surface. This shows that there is an induced stiffening of the polymer near the surface, a result in agreement with NMR and neutron scattering experiments.

Therefore, it is important that a constitutive model should represent this interaction depending on the type of silica present (e.g., fumed silica with a large number of surface hydroxyl groups or quartz with a farily "clean" surface). For fumed silica in particular, where the basic entity particles are ~10 nm in size, the presence of a 1-nm stiffened surface layer could alter how one represents the system. Future work will refine the evaluation of the thermodynamic properties of these systems and their relaxation times. These will then be incorporated into existing constitutive formulations (or modified versions) and the results evaluated. Assessment of the significance of the filler distribution will then become the area of focus.

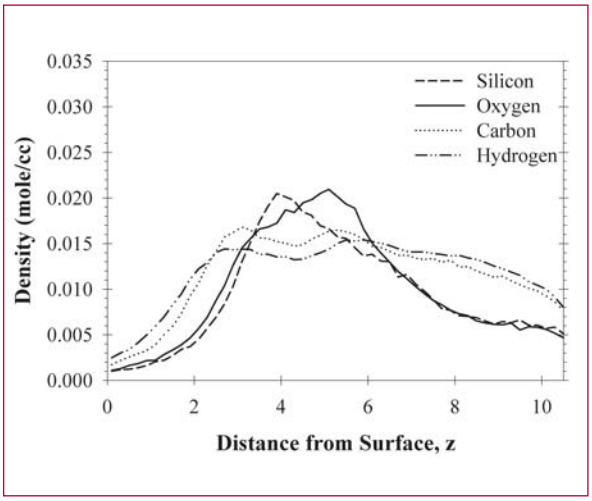

Figure 1—The PDMS atomic profiles next to a bare (111) SiO_2 surface.

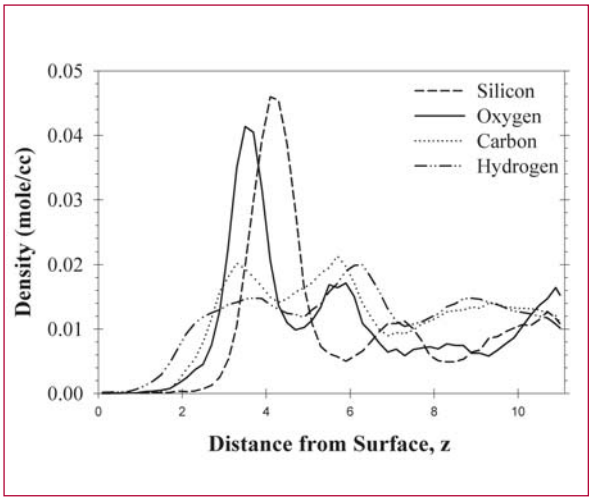

Figure 2—The PDMS atomic density profiles next to a hydroxyl covered (111) SiO_2 surface.

Models for the Aging of Fogbank

Edward M. Kober, T-14; emk@lanl.gov

We continue our assessment of the physical and chemical aspects of the aging of this material and how it could interact with other materials in the Canned Sub-Assembly (CSA). An impurity, which we had previously predicted the existance of, has now been observed, and we are involved in analyzing its role in the aging properties.

Pore Collapse and Hot Spots

Ralph Menikoff, T-14; rtm@lanl.gov

It has been known since the 1950s that initiation of a detonation wave in a plastic-bonded explosive (PBX) is due to thermal reactions but requires hot spots. Hot spots reconcile the large discrepancy between the time to detonation from Pop-plot data and the induction time based on the bulk shock temperature and the chemical reaction rate. Shock desensitization experiments and the increased sensitivity of a PBX with increasing porosity imply that hot spots generated by pore collapse dominate a shock-to-detonation transition.

Early hydrodynamic simulations of initiation utilized artificial viscosity for shock waves as the only dissipative mechanism. They showed that, when a strong shock impinges on a pore, a micro-jet is formed and subsequently produces a hot spot on impact with the downstream side of the pore. Furthermore, simulations with arrays of pores in an explosive showed a shock-to-detonation transition. When the simulations were performed (2-D flow in the 1960s and 3-D in the 1980s), the available computer power limited the resolution. Consequently, the simulations displayed the qualitative features of initiation but were not quantitatively accurate.

High-resolution simulations can now be run on a PC. This has led to a renewed interest in studying hot-spot ignition. As a first step, simulations of a shock wave passing over and collapsing a pore have been performed to better understand the properties of a hot spot, such as peak temperature and hot-spot mass. With shock dissipation as the dominant heating mechanism, the temperature field after a strong shock has passed over a pore is shown in Figure 1A. The collapse of the pore gives rise to an outgoing rarefaction wave in the material compressed by the lead shock, followed by an outgoing shock wave. These secondary waves give rise to the main features seen in the temperature field. For example, the secondary shock has caught up to the lead shock resulting in a Mach wave pattern. The temperature discontinuity corresponds to the contact emanating from the Mach triple point.

The temperature distribution is shown in Figure 1B. The first peak at 300 K corresponds to the ambient state ahead of the lead shock front. The second peak centered at 575 K corresponds to the material heated by the lead shock and then cooled by the rarefaction from the pore implosion. The third peak centered about 675 K corresponds to the material

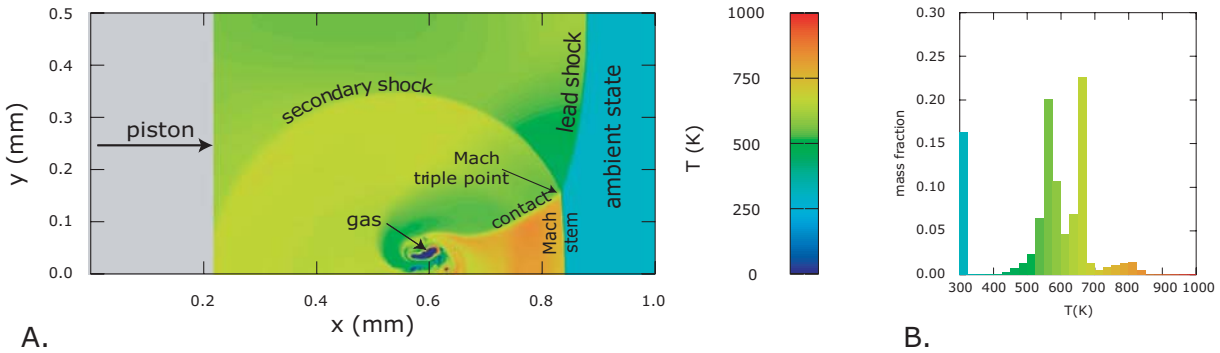

Figure 1—Temperature after pore collapse. Simulation with piston velocity of 1.3 km/s, shock dissipation only and resolution of 100 cells in the initial pore radius (0.1 mm and centered at x=0.4 mm, y=0). A. 2-D temperature field. Bottom boundary is symmetry plane. B. Temperature distribution.

heated by the lead shock and backward expanding portion of the secondary shock from the explosion of the pore. The low broad peak between 700 and 850 K corresponds to the region between the Mach stem and the material directly impacted by the micro-jet. The peak temperature is consistent with the estimates based on Riemann problems [1].

With additional dissipative mechanisms, plastic work, or viscous heating, the tail of the temperature distribution can be greatly enhanced. This is important since hot-spot reaction is due to the extreme tail of the temperature distribution. The tail of the temperature distribution is best described by the integrated temperature distribution, mass *(T1)* at $T1 > T$. It is convenient to normalize the mass relative to the equivalent mass in the pore volume at the initial explosive density.

Simulations with additional dissipative mechanisms are summarized by the integrated temperature distribution shown in Figure 2. A striking feature of the integrated distributions is that the tail of the distributions, above 600 K, is approximately linear on a log-log scale. This implies that the tail of the distribution has a power-law behavior. Moreover, the exponent of the powerlaw is related to the viscous parameter such that the effective hot-spot mass increases as the viscous parameter increases.

The viscous parameter has not been directly measured. Instead it is usually fit to reproduce integral data for a limited class of experiments. The fact that both the viscous heating and plastic work have similar distributions implies that either dissipative mechanism can be used in a fit. To discriminate between these mechanism requires a range of experiments that are sensitive to differences in the scaling behavior of each dissipative mechanism [2].

[1]
http://t14web.lanl.gov/Staff/rsm/preprints.html#beta-HMX
[2]
http://t14web.lanl.gov/Staff/rsm/preprints.html#PoreCollapse

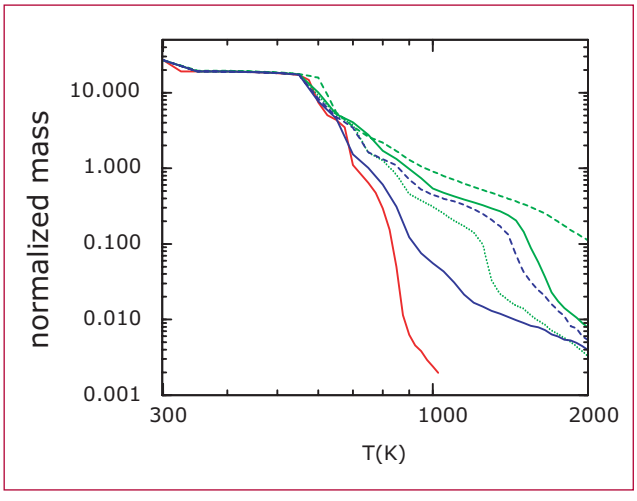

***Figure 2—** Variation of temperature distribution with dissipative mechanism. Dissipative mechanisms: red, shock heating; blue, shear viscosity, solid and dashed η =10 and 100Poise, respectively; green, rate dependent plasticity, solid, dashed and dotted η = 800, 8000, and 80 poise, respectively.*

Multiscale Mapping Techniques for Polymers

Thomas D. Sewell, T-14; Kim Ø. Rasmussen, T-11; Russell B. Thompson, T-11; and Dmitry Bedrov and Grant D. Smith, Univ. of Utah; sewell@lanl.gov

Based on most generally accepted characteristics of a complex system, polymers or polymer-containing materials are both complex and multiscale in nature. Indeed, most of the hallmarks of complexity apply to individual polymer chains of any significant length and/or interesting topological structure; let alone polymer blends; di-, tri-, or multi-block copolymers; or composite materials containing such constituents. In our view, any useful description of the constitutive response of a given polymeric material requires a sequence of upscaling and/or homogenization steps, each of which entails capturing the essential information that must be included in the successively larger-scale abstraction(s) of the material, and that culminates in a macroscopic constitutive model suitable for use in engineering-scale calculations. The goal of our work is the development of bi-directional scale-bridging methods for polymeric systems, extending from chemically detailed, atomistic treatments (nanometers) up through mesoscopic descriptions (microns).

In the present summary, we focus on the connection between coarse-grained molecular dynamics (MD) simulations and self-consistent field theory (SCFT), in which the only adjustable parameters are the "Flory-Huggins" interaction parameter, χN, and a "statistical segment length" a used in the reverse-mapping step. Our objectives are (1) to develop and demonstrate a *practical* means for extracting information from MD simulations to define an *effective* χN value for use in SCFT that reproduces the salient features obtained from the MD simulations (forward mapping, Figure 1), (2) to use this MD-based effective χN-parameter to generate ensembles of representative freely-jointed chain configurations based on Monte Carlo sampling from the SCFT monomer densities (reverse mapping, Figure 2), and (3) to validate the system configurations thus generated by direct comparison to the results of well-equilibrated MD simulations (Figure 3). Our initial focus is on immiscible homopolymer blends and, for purposes of method

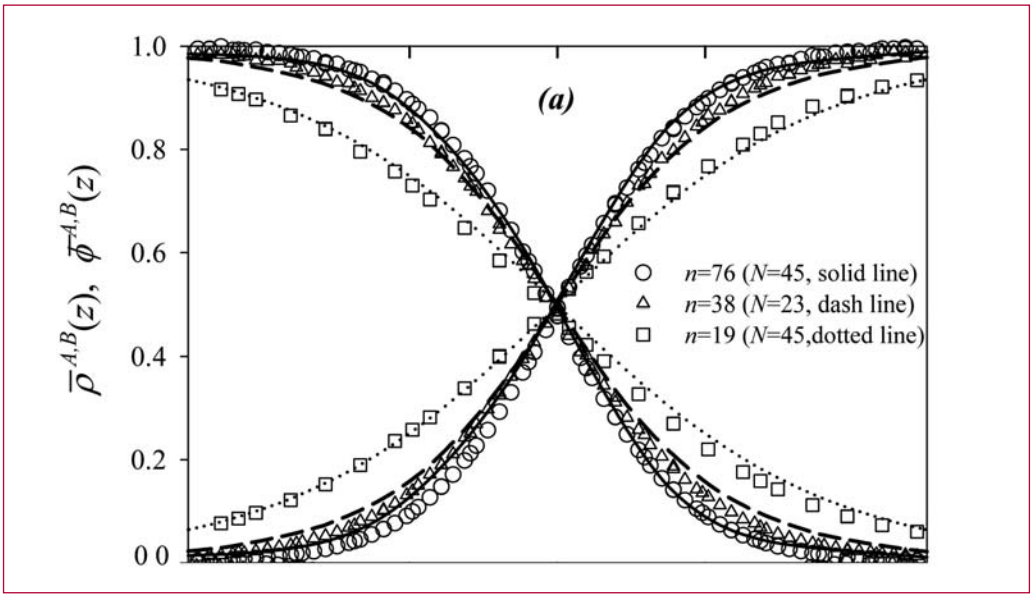

***Figure 1—** Interfacial density profiles calculated from MD simulations (symbols) and predicted by SCFT (curves) using a best-fit effective value for χN. Results are shown for three different molecular weights.*

validation, chain lengths below the entanglement threshold, for which MD simulations can reliably yield well-equilibrated melt configurations.

The criterion for the forward mapping is concurrence between MD- and SCFT-based interfacial widths and local concentration gradients as functions of polymer chain length and interaction potential parameters (Figure 1). In the case of reverse mapping (Figure 2), we compare relevant properties for individual and system ensemble averages of SCFT- and reverse-mapped chains (Figure 3). In future work we shall proceed to the arguably more challenging (and interesting) case of diblock and multiblock copolymer systems, which undergo microphase segregation.

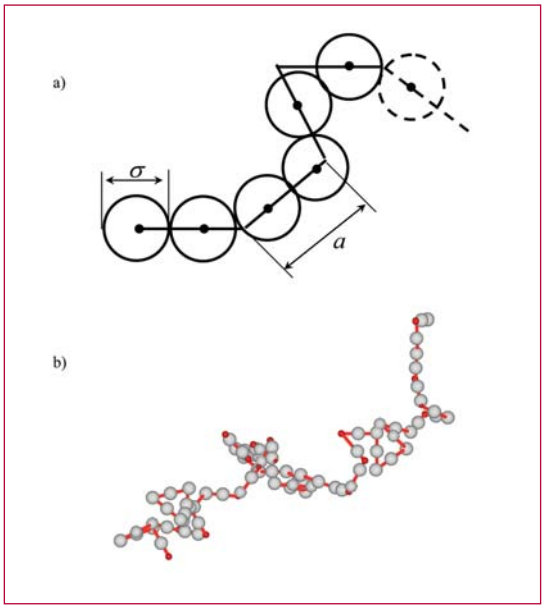

Figure 2—Panel a: Schematic illustration of the reverse mapping-technique used to transform chain configurations predicted using SCFT (line segments, of length a) onto initial conditions for use in MD simulations (spheres, of diameter σ). Panel b: specific example of reverse mapping for a representative chain with σ/a = 45/76.

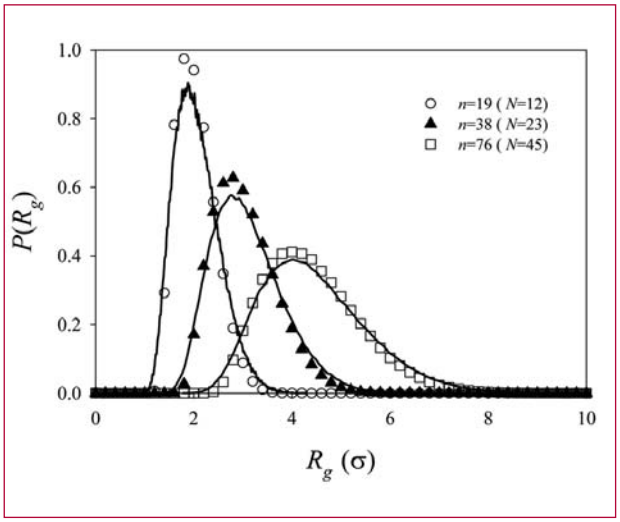

Figure 3—Probability distribution function for polymer chain radius of gyration calculated from MD simulations (symbols) and obtained by reverse mapping from SCFT (lines). Results are shown for three different molecular weights.

Detonation Products Equation of State

M. Sam Shaw, T-14; mss@lanl.gov

The final major step has been completed in the development of a Monte Carlo simulation method capable of including all aspects needed to characterize detonation products EOS for real explosives of interest. That step is the inclusion of carbon clusters with surface groups, where the amount of carbon in clusters and the composition of the surface are allowed to reach equilibrium. These features are in addition to the other features of my new Composite Monte Carlo Method [1,2], which combines chemical equilibrium composition, fluid-fluid phase separation, and incorporation of solid forms of carbon. The extended method [3] was presented at the 2003 APS Topical conference on Shock Compression of Condensed Matter.

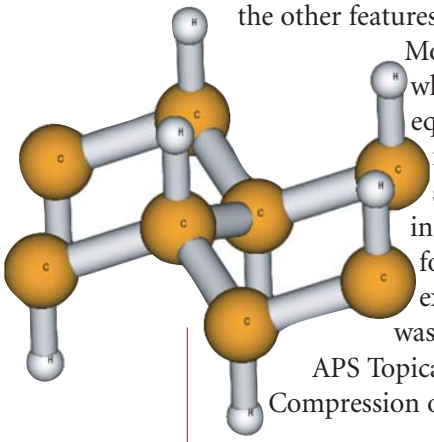

Figure 1— A model of the cluster surface and an approaching N_2 molecule. Periodic boundary conditions are applied in the two directions perpendicular to the surface.

As with bulk carbon, the cluster is treated using a model Gibbs free-energy in the exponent of the probability distribution while the positions and interactions in the molecular fluid mixture are explicitly included in the simulation. The cluster treatment differs from the bulk in that several distinct atom groups are present; surface groups such as H and OH, surface carbon atoms, and interior carbon atoms. Instead of a single reaction adding or subtracting from the total, multiple reactions are included with changes to various combinations of atom group types. For initial simulations, the effective size of the cluster model is kept near that found in recovery experiments, around 2-nm diameter with around 1000 atoms. Instead of a very large simulation with full size clusters, the ratios of types of groups are constrained to remain near that of the full cluster. Small variations from these ratios are allowed so that individual reaction steps can take place. The various groups are characterized by additive contributions.

One particular complication is the effective volume occupied by a cluster. A series of simulations were made with model clusters included as a single very large particle. By varying the cluster interaction with the fluid and comparing to simulations where the cluster is removed, an effective volume was established relative to the interactions. The actual interactions between the fluid and surface are not known. Electronic structure calculations have begun in collaboration with C. J. Tymczak (T-14) using the MondoSCF code[4] to evaluate the interaction of molecules from the fluid with a small scale model of the surface. In Figure 1, we see a N_2 molecule approaching a 111 surface of diamond with H-caps on the dangling bonds. Periodic boundary conditions are applied in the two directions perpendicular to the surface and a finite thickness of the surface layer is chosen. Application to larger model surfaces with various surface groups and molecules from the fluid are under development. From the first model, however, it is clear that the H-caps do not extend the effective surface by their bond distance with the carbon surface and that geometry alone doesn't determine the location of the surface.

The previous large set of simulations of HMX (high explosives) has been extended to include diamond clusters with surface chemistry. By interpolation of the tabulated points, the Hugoniot and the CJ state are calculated for HMX as a function of initial density. The calculated results for several cases of detonation velocity versus initial density are compared with experimental data in Figure 2. RDX data is included with the HMX data since the two are essentially identical for detonation velocity. The types of calculations are specified in the caption.

Work continues in collaboration with C. J. Tymczak (T-14) on the combining of Monte Carlo methods with very efficient (linear scaling) many particle ab initio electronic structure calculations using MondoSCF [4]. Having demonstrated an effective scheme to evaluate thermodynamics with a small set of configurations from a reference Monte Carlo simulation, the focus has shifted to the accurate evaluation of the many-body energy in those configurations. An extensive study of basis set dependence for individual molecules, pairs of molecules, and full many-body configurations, is in progress. In addition, the effect of relaxing the usual rigid-rotor harmonic oscillator approximation is being studied.

The equation of state (EOS) for products of polymers and foams is being studied with the chemical equilibrium thermodynamic perturbation theory code HEOS, which was originally developed for detonation products. A study of a large set of polymer and foam Hugoniot data has been used to refine the parameters for H_2 and CH_4 that are minor species for explosives, but major constituents of polymer products due to typically low oxygen content. Predictions have been made for VCE and related materials where data is limited. Because of similarities in composition of VCE to other polymers, the predictions are expected to be accurate because the materials with data are accurately represented.

In collaboration with Maria Rightley (X-4), a PBX-9501 EOS based on high- and medium-pressure data (Hugoniot, sound speed, and interface velocimetry) has been extended to match cylinder test data in the low-pressure regime. Variations in the low-pressure part are transmitted through the SESAME EOS form. Iteration through hydrodynamics calculations of the difference between the results for a given EOS and cylinder test data, determine the best fit of the lower pressure part of the EOS. Results indicate that the details of the low-pressure EOS depend on the higher pressure EOS assumed. That is, there is a family of curves that fit the cylinder data when other constraints are not included.

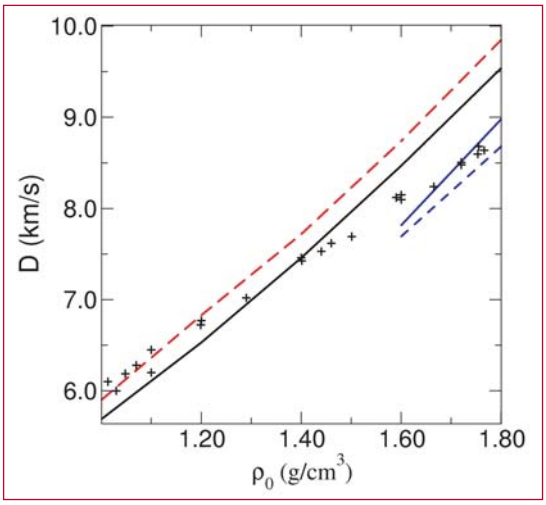

Figure 2—Detonation velocity versus initial density. HMX and RDX data (+), calculations with graphite and two different sets of cross potentials (red dash and black line), calculations with diamond clusters of two sizes (blue line, blue dash).

[1] M. Sam Shaw, "Direct Simulation of Detonation Products Equation of State by a Composite Monte Carlo Method," proceedings of the 12th Detonation Symposium, to be published.

[2] M. Sam Shaw, "A Hybrid Monte Carlo Method for Equilibrium Equation of State of Detonation Products," in Shock Compression of Condensed Matter – 2001, edited by M. D. Furnish, N. N. Thandhani, and Y. Horie, *AIP*, pp. 157–160 (2002).

[3] M. Sam Shaw, "Direct Simulation of Detonation Products Equation of State," to be published in proceedings of the 2003 APS Topical Conference on Shock Compression of Condensed Matter.

[4] Matt Challacombe, Eric Schwegler, C. J. Tymczak, Chee Kwan Gan, Karoly Nemeth, Anders M. N. Niklasson, Hugh Nymeyer, and Graeme Henkleman, "MondoSCF, A Program suite for massively parallel, linear scaling SCF theory and ab initio molecular dynamics." Los Alamos National Laboratory (LA-CC01-2).

Polymer and Foam Products Equation of State

M. Sam Shaw, T-14; mss@lanl.gov

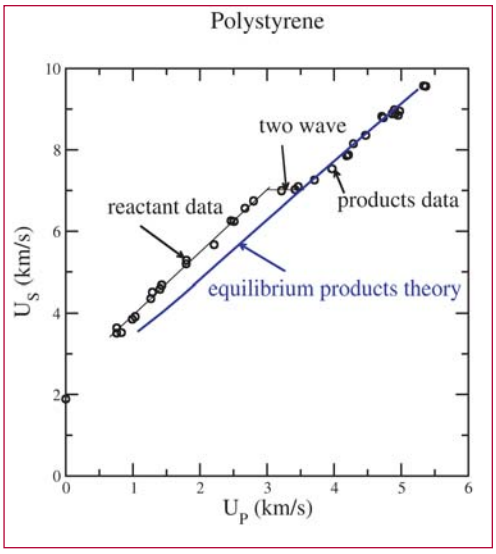

Figure 1—Shock velocity versus particle velocity for full density polystyrene. Hugoniot data (O) and equilibrium products theory (blue line).

The equation of state (EOS) of polymers are very similar to that of high explosives (HE) in that under shock conditions of sufficient strength the initial material decomposes to a mixture of molecular fluids (N_2, H_2O, CO, CO_2, H_2, CH_4, etc.) and sometimes solids (C, SiO_2, etc.). Although the energy released in decomposition of polymers is small compared to HE, the final state can still be at high temperature due to shock heating. In the case of foams, the shock heating is quite substantial and the resulting temperature is often in the same range as for HEs. The difference between polymer products and HE products is primarily in the concentration of product species and not in the type. Consequently, the same theoretical methods can be applied to both. Having already developed a theoretical EOS for HEs, minor modifications are required to apply the same method to polymer products. Also, a limited amount of experimental calibration is needed to make the jump from HEs to polymers.

Polymer materials that have not decomposed are readily treated in the same fashion as other inert materials. Hugoniot data at full density supplies simple parameters such as a U_sU_p fit for a reference curve. A set of Hugoniot data for different initial densities (e.g., foams) is sensitive to the choice of Gruneisen gamma and allows calibration of the EOS off the reference curve.

The treatment of polymers is incomplete without at least an estimate of the conditions required for decomposition. If the rate of decomposition is sufficiently sensitive to the state, then there is only a very narrow region that requires the rate and the rest is accurately approximated as either reactant or product. This appears to be the case for some common polymers such as polystyrene. Hugoniot data in Figure 1, show two linear U_sU_p segments connected by a constant region, similar to a large phase transition in an inert material. Recovery experiments by Morris et al. [1] show that the lower line results in the recovery of the initial polymer. Higher shocks, corresponding to the two-wave structure and the high-pressure phase, result in the recovery of products such as CH_4, H_2, and carbon. For many polymers, the transition to products seems to occur at about the same particle velocity (around 3 km/s) and consequently the same specific internal energy added by the shock.

The primary focus of the modeling has been on the EOS of decomposition products. The molecular fluid products are treated using thermodynamic perturbation theories in two steps. Nonspherical potentials are replaced by effective spherical potentials through a thermodynamic perturbation method shown to give very accurate thermodynamics [2]. Then the thermodynamic perturbation method developed by Ross [3] for spherical potentials is used to determine the EOS (including free

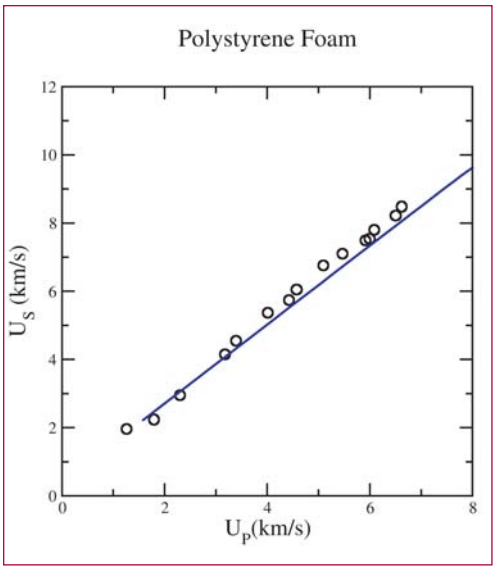

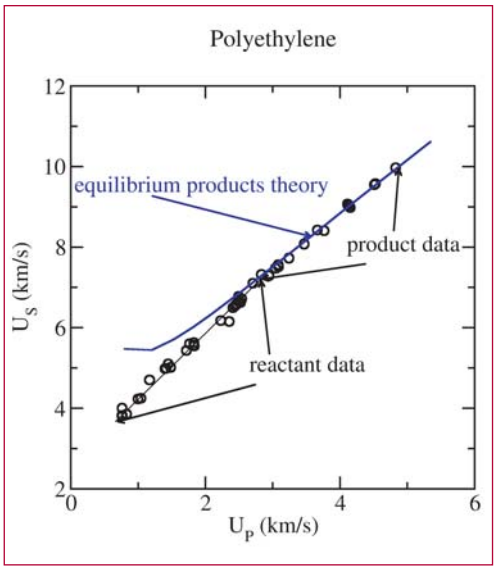

Figure 2— Shock velocity versus particle velocity for polystyrene foam at density around 0.3 g/cm³. Hugoniot data (O) and equilibrium products theory (blue line).

Figure 3— Shock velocity versus particle velocity for full density polyethylene. Hugoniot data (O) and equilibrium products theory (blue line).

energies) for the molecular fluid. The solid components are treated using a Murnaghan cold curve plus a Debye model. In addition, there is an option for solid carbon in the form of clusters of a size found in recovery experiments. This treatment includes variations in chemical composition of the surface groups on dangling bonds in the diamond phase. The Gibbs free energy of the mixture of all components is then minimized with respect to composition in order to generate the equilibrium EOS. This method is incorporated in a computer code, HEOS, with molecular fluid potentials and solid model parameters adjusted to match data of individual species as well as a variety of data on HE products [4].

Similar results are shown in Figure 2 for polystyrene foam. Because of the low-initial density, the polymer decomposes at a much lower pressure. The equilibrium products theory is the same as used for full density, but a different line is sampled by the Hugoniot in the two-dimensional P,T space.

The results for polyethylene are shown in Figure 3. Here the reactant and product EOSs are much closer than for polystyrene and the two wave structure is not seen. However, recovery experiments [1] confirm that the change in slope occurs with the transition from reactants to products.

These results illustrate a small part of a much larger study to improve the EOS of CHNO polymers by comparison with a wide variety of shock data [5, 6]. An equilibrium EOS with specific choices for the H_2 and CH_4 potentials was found to be in good agreement with the data. These values do not affect the EOS for HE products because the equilibrium composition only has very small amounts of H_2 and CH_4, mostly due to the relative abundance of oxygen compared with polymers.

Work on Si containing polymers continues. The S5370 EOS has been converted to a SESAME tabular form for use in codes. This EOS has been passed to Maria Rightley (X-4) and Randy Bos (X-7). Specific Hugoniot state conditions were also passed along and used to verify the implementation of the EOS in SESAME form. The EOS treatment is being refined by comparison with similar materials while waiting for new S5370 data.

VCE (Ethylene-vinyl acetate-vinyl alcohol terpolymer) is a polymer where very limited data is available. The composition is approximately 84 ethylene (C_2H_4), 17 vinyl acetate ($C_4H_6O_2$), and 4 vinyl alcohol (C_2H_4O), plus an added cross-linking. In 100 g, effective formula is roughly $C_{6.11}H_{11.37}O_{0.95}$, without cross-linking. With cross-linking, this changes to $C_{6.06}H_{10.48}N_{0.09}O_{1.00}$. This composition is similar to several polymers in the large study, so the predicted EOS is expected to be accurate.

[1] C. E. Morris, E. D. Loughran, G. F. Mortensen, G. T. Gray, and M. S. Shaw, "Shock Compression of Condensed Matter," 687 (1989).
[2] M. S. Shaw, J. D. Johnson, and J. D. Ramshaw, *J. Chem. Phys.* **84**, 3479 (1986).
[3] M. Ross, *J. Chem. Phys.* **71**, 1567 (1979).
[4] M. S. Shaw, "Shock Compression of Condensed Matter— 1999," 235 (2000). M. S. Shaw, "11th International Detonation Symposium," 933 (1998).
[5] Stanley P. Marsh, "LASL Shock Hugoniot Data," University of California Press, Berkeley, 1980.
[6] W. J. Carter and S. P. Marsh, LA-13006-MS (1995), edited from a 1977 report.

Energy Exchange between Mesoparticles and Their Internal Degrees of Freedom

Alejandro Strachan, T-14; and Brad Lee Holian, T-12; strachan@lanl.gov

Large-scale atomistic simulations enable a detailed understanding of complex, many-body problems in materials science, chemistry, physics and biology. Unfortunately, despite the advances in methodologies and computer power, a wide range of phenomena is beyond present capabilities. In many of these cases full atomistic descriptions are neither necessary nor desirable and coarse-grained descriptions of matter, where groups of atoms are described by a single mesoparticle, provide the desired detailed while significantly reducing the computational cost. These mesoparticles can represent molecular groups in polymers, molecules in molecular crystals [1] or grains in polycrystalline metals [2]. While these approaches can be formulated to give accurate treatment of mechanical properties, there has been, up to now, no realistic thermo-mechanical treatment of the energy exchange between the mesoparticle and its internal degrees of freedom. This is due to the fact that the thermal role of many degrees of freedom has been, heretofore, either completely disregarded or treated only crudely.

In order to incorporate the thermal role of the internal degrees of freedom in the equations of motion of the mesoparticles we assign a finite, internal thermostat to each particle and couple the local external energy to its internal energy, the sum of which is conserved. The internal degrees of freedom are characterized by their specific heat that relates internal energy to internal temperature. We couple the mesoparticle's internal temperature to its local neighborhood temperature via the meso-coordinate update, rather than through the momentum update, as is customary for all other thermostatting techniques. As a result, the new mesodynamics equations of motion satisfy the following desirable properties:

- The total energy and momentum of the system (mesoparticles plus internal degrees of freedom) are conserved;
- The exchange of energy is done on a spatially local basis;
- The implicit variables are described by their specific heat that can be calculated from first principles;
- The ballistic regime is handled correctly—an isolated particle moves at a constant velocity with no force on it and no exchange of energy with its internal degrees of freedom;
- The equations of motion are Galilean invariant;
- As the coupling between internal and external modes is reduced to zero, Newton's equations of motion are recovered.

We test the new mesodynamics by studying shock propagation in the crystalline polymer poly-(vinylidene diflouoride) [PVDF, $(CH_2CF_2)_n$] and compare the results with all-atom MD. The interactions between mesoparticles (the so-called mesopotential) are described by pair-wise Rydberg functions parameterized to reproduce the uniaxial compression of PVDF along the x-direction. We study shock propagation using high-velocity impact nonequilibrium MD simulations. In all-atom simulations of molecular crystals we can define two types of temperatures: (1) the *intermolecular* temperature, defined as the fluctuations of the center-of-mass (c.m.) velocities of each polymer chain around the c.m. translational velocity of the whole slab; and (2) the *internal* temperature, defined as atomic velocity

fluctuations around the c.m. velocity of each molecule. The two all-atom temperatures have well defined counterparts in the mesoscopic description; the internal temperature is that of the implicit degrees of freedom and the inter-molecular temperature is calculated from the velocity of the mesoparticles. Figure 1 shows the time evolution of the local inter-molecular and intra-molecular temperatures of a thin slab of PVDF as the shock passes through it. The all-atom results are shown as red lines (solid represents inter-molecular temperature and dashed lines intra-molecular). The black line shows the results obtained with the mesopotential but with no coupling to the internal degrees of freedom; as expected the reduced number of degrees of freedom leads to a large overestimation of the temperature of the shocked material. The blue lines show the results of the new mesodynamics method with internal thermostatting, using a common-sense choice of parameters. Figure 2 shows the time evolution of the local intra-molecular temperature obtained from all-atom MD (full lines) and mesodynamics (dashed lines). **Our method yields essentially identical results as the all-atom simulations, both in final temperature achieved and in the profile of temperature with distance throughout the shock front.**

This new thermo-mechanical formulation of mesodynamics is general and should be useful in a wide variety of problems in chemistry, biology, materials science, and physics enabling more accurate and computationally efficient particle-based mesoscopic simulations.

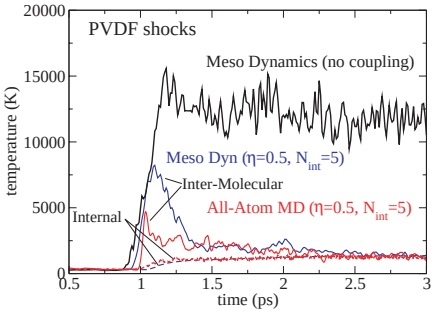

Figure 1— Shock loading of PVDF. Intra- (dashed lines) and inter-molecular (full lines) local temperatures from an all-atom simulation (red), mesodynamics with no coupling with internal degrees of freedom (black) and using the new mesodynamics (blue).

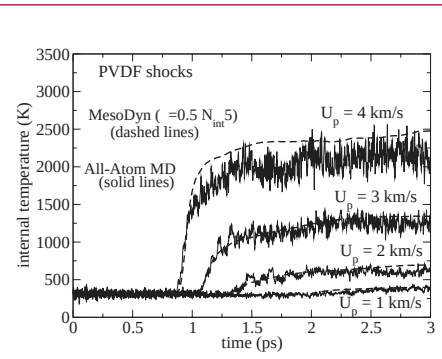

Figure 2— Shock loading of PVDF. Intra-molecular temperature during shock loading of PVDF at various particle velocities; full lines show all-atom MD results and dashed lines denote mesodynamics results.

[1] Florian Muller-Plathe, *ChemPhysChem* **3**, 754 (2002).

[2] B. L. Holian, *Europhys. Lett.* **64**, 330 (2003).

Molecular Dynamics Studies of Reactive Processes in RDX I: Thermal Loading

Alejandro H. Strachan, T-14; strachan@lanl.gov

A molecular level understanding of condensed-matter chemistry is among the central issues facing the energetic materials community. Recent breakthroughs in atomistic modeling (such as reactive interatomic potentials) enable the use of molecular dynamics (MD) to study chemistry in solid energetic materials providing unprecedented spatiotemporal resolution [1,2]. We report here the use of the reactive force field ReaxFF [2,3] to study thermal decomposition of the cyclic nitramine RDX.

Molecular Dynamics with ReaxFF

We study the decomposition of RDX at various temperatures between T = 1200 K and T = 3000 K at three densities: at normal density (volume V = V_0), under compression (V = 0.8 V_0), and at low density (V = 8 V_0) using the reactive potential ReaxFF with MD. We start with RDX perfect crystals using simulation cells containing eight RDX molecules (one unit cell) and 3-D periodic conditions. After relaxing the atomic positions at each density, we study the time evolution of the system at the desired temperature with isothermal isochoric (NVT ensemble) MD simulations (using a Berendsen thermostat). We then follow the decomposition of the RDX molecules using a molecule recognition method that uses not only atomic positions but also velocities to determine whether two atoms are bonded or not [2]. The lower temperatures reported here required very long times (for MD standards) of several nano-seconds (one nano-second requires 10 million steps of reactive MD).

Thermal Decomposition of RDX from MD Simulations

Figure 1 shows the time evolution of the potential energy of the RDX unit cell for temperatures T = 1200, 1500, 2000, 2500, and 3000 K for normal density (V_0). Our simulations at V = 0.8 V_0 show faster time-scales and those at 8 V_0 a slower rate of reactions. The time evolution of the potential energy can be described reasonably well with an exponential function:

$$U(t;T,\rho) = U_0(T,\rho) - \Delta U(T,\rho)\exp[-t/\tau(T,\rho)],$$

where U_0 is the energy of the products, ΔU is the exothermicity and τ is the characteristic time; all three parameters are temperature and density dependent.

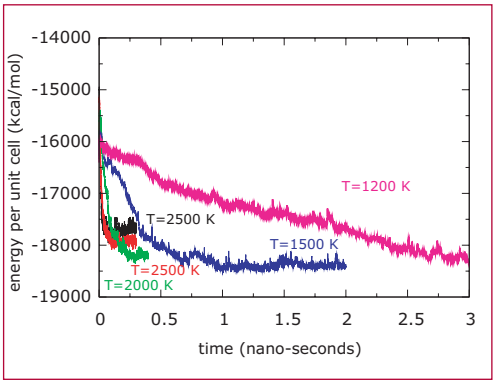

Figure 1—Time evolution of potential energy for various temperature and V = V_0 (ambient pressure volume).

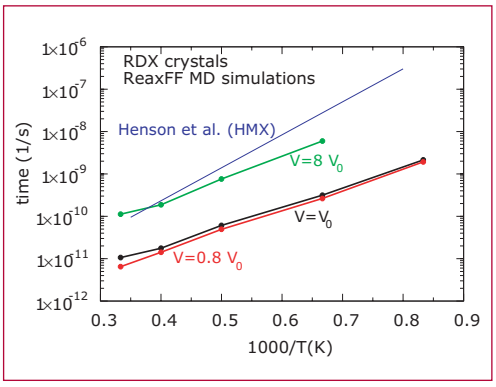

Figure 2—Characteristic time vs. inverse temperature from ReaxFF MD simulations for different volumes: V = 0.8 V_0 (red line), V = V_0 (black line), and V = 8V_0 green line. We also include the Arrhenius behavior obtained from a wide range of experimental ignition times in HMX (blue line) [4].

In Figure 2, we plot the characteristic times (in logarithmic scale) as a function of inverse temperature (Arrhenius plot). The red line corresponds to MD results under compression (V = 0.8 V_0), the black line corresponds to V = V_0 and the

green one represents the theoretical results at 8 V_0. The blue line represents the behavior of HMX obtained from a wide variety of experimental ignition times [4]. Figure 2 shows that our first principles calculations are in reasonable *quantitative* agreement with experiments. The linear behavior of the MD and experimental data in the Arrhenius plot can be attributed to a single rate limiting step in the sequence of reactions that lead to decomposition. From the MD simulations we obtain an activation energy (E_a) for this limiting step that increases as the density decreases: for $V = 0.8V_0$ and $V = V_0$ we obtain $E_a \sim 23$ kcal/mol and for $V = 8V_0$ $E_a = 35.6$ kcal/mol.

Figure 3 shows the final populations of the key products (N_2, H_2O, CO, and CO_2). We can see that at low densities, CO is preferred over CO_2, while at high densities this relationship changes and we find almost no CO and considerable amounts of CO_2.

In Figure 4, we show the time evolution of the population of N_2, H_2O, CO, and CO_2; the time is scaled with the corresponding characteristic time obtained from the energy evolution. For each condition of temperature and density time-scales of H_2O and N_2, formations are similar to one another and to the overall characteristic time (τ); formations of H_2O and N_2 occur at the early stages of the process. The formation of CO and CO_2 shows a marked dependence on compression: while at normal or high density we find there is an induction before CO and CO_2 form (see top panel of Figure 4); at low density, CO forms promptly and with time scales similar to those of H_2O and N_2 (see bottom panel of Figure 4).

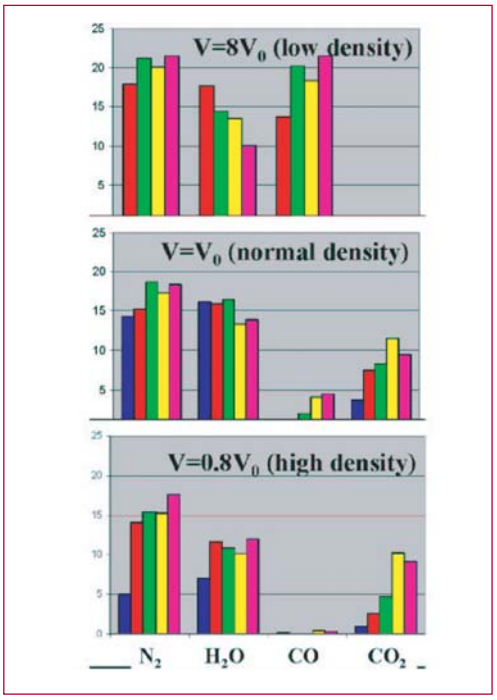

Figure 3— Final population of key molecules for various temperatures and densities. T = 3000 K (magenta), T = 2500 K (yellow), T = 2000 K (green), T = 1500 (red), T = 1200 K (blue). (The simulation corresponding to 0.8 V_0 and T = 1200 K has not fully converged; data are preliminary.)

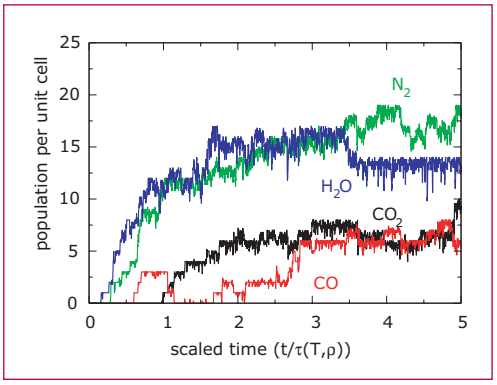

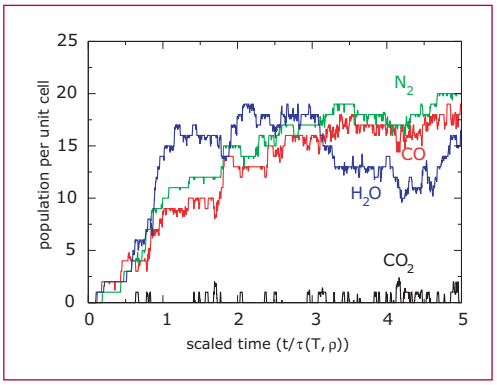

Figure 4— Time evolution of main products for T = 2500 K and V = V_0 (top panel) and V = $8V_0$ (bottom panel). For each temperature and density, time is scaled with the corresponding characteristic time obtained from the energy evolution. The first-principles time-scales obtained from MD for the decomposition of RDX under thermal load are in reasonable quantitative agreement with experimental data.

Conclusions

Atomistic modeling with new-generation reactive potentials is becoming a very important tool to investigate condensed-phase chemistry under dynamical or static loading. Such simulations provide very detailed information regarding the decomposition and subsequent reactions in energetic materials that should allow sense to made out of the very complex mechanical and chemical processes.

[1] M. R. Manaa, L. E. Fried, C. F. Melius, M. Elstner, and Th. Frauenheim, *J. Phys. Chem. A* **106**, 9024, (2002).
[2] A. Strachan, A. C. T. van Duin, D. Chakraborty, S. Dasgupta, and W. A. Goddard, III, *Phys. Rev. Lett.* **91**, 098301, (2003).
[3] A. C. T. van Duin, S. Dasgupta, F. Lorant and W. A. Goddard III, *J. Phys. Chem. A* **105**, 9396 (2001).
[4] B. F. Henson, L. Smilowitz, B. W. Asay, P. M. Dickson, and P. M. Howe Proceedings of the 12th Symposium (International) on Detonation (2002), `http://www.sainc.com/det-symp/technicalProgram.htm`

Molecular Dynamics Studies of Reactive Processes in RDX II: Shock Loading

Alejandro H. Strachan, T-14; strachan@lanl.gov

Understanding the initial chemical events in condensed-phase high-energy materials under shock loading is among the central problems in detonation theory. The coupling between the fast loading, induced mechanical response and complex chemistry makes the study of such process very challenging and there has been little progress in establishing a molecular level understanding. Recent advances in atomistic modeling techniques and the enormous increase in computer power enabled, over the last years, the atomistic simulation of thermal- and shock-induced chemistry in condensed-phase high-energy materials such as RDX and HMX. Both Quantum Mechanics-based Molecular Dynamics (MD) simulations of HMX at conditions of pressure and temperature close to the CJ point [1] as well as our nonequilibrium MD simulations of shocks on RDX using the reactive force field ReaxFF [2] show that the initial chemical events occur at very short time-scales (pico-seconds). Both these two types of simulations focused on perfect crystals while most real energetic materials are heterogeneous and defective (polycrystalline, porous, plastic bonded, etc.). Such defects are believed to facilitate detonation initiation under shock loading. We report here on the simulation of shock propagation on defective RDX crystals and the influence of such defects on the initial chemical events using the reactive force field ReaxFF [3] with nonequilibrium molecular dynamics.

MD Shock Simulations

We simulate the impact between two two-dimensionally periodic slabs, one of which contains a gap, Figure 1 (a), of length l_{gap}. We impose free boundary conditions in the direction of the shock and periodic boundary conditions in the other two directions. The gap simulates the center of an ellipsoidal void with two long axes perpendicular to the shock direction [4]. After thermalization, we assigned the desired relative velocity (v_{imp}) to each slab on top of thermal velocities and followed the dynamics with constant energy MD. This arrangement leads to a particle velocity $u_{p=1/2}v_{imp}$. Figure 1 shows snapshots of the process at different times for $u_p = 3$ *km/s* and $l_{gap} = 20$Å: we can see the initial shock propagation in perfect crystals (t = 0.5 ps), the molecules ejected from the upstream surface of the gap expanding into the void (t = 0.95 ps), and the ejected material colliding against the remainder of the slab and recompressing (t ≥ 1.5 ps). We will focus on $u_p = 3$ *km/s* since for perfect

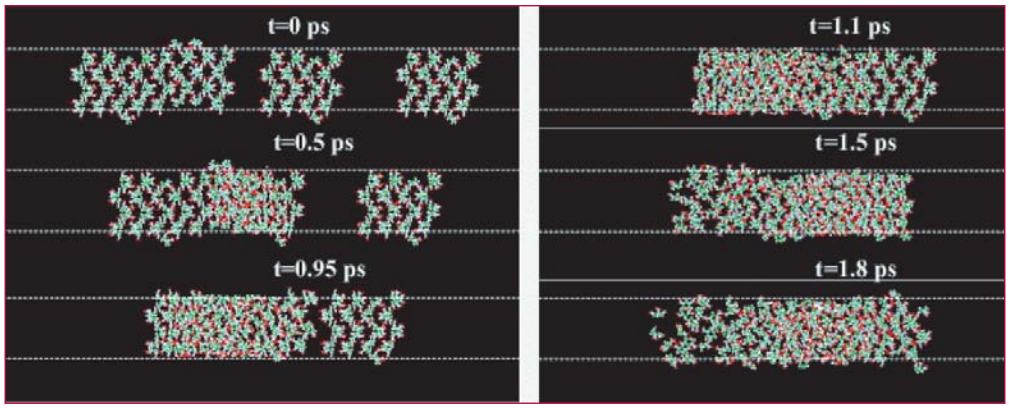

Figure 1—Snapshots from ReaxFF MD shock simulation at different times for $u_p = 3$ *km/s* ***and gap width 20 Å.***

crystals it separates two different regimes: for shocks with $\upsilon_p > 3$ *km /s* a variety of small molecules are formed while for lower velocities only small fractions of NO_2 are observed [2].

When a strong shock reaches the upstream surface of the gap, molecules are ejected into the void; the ejecta expands and re-compresses when it collides with the remainder of the slab. This recompression can lead to significant local heating [4]. In order to quantify this effect and its dependence on gap width we plot, in Figure 2, the time evolution of the local temperature of the last two molecular monolayers on the upstream half of the defective slab for l_{gap} = 5 Å (red), l_{gap} = 10 Å (blue), and l_{gap} = 20 Å (green). We also show time evolution of the local temperature of the corresponding region in the perfect (left) slab; the temperatures of the regions in the perfect slab are independent of the gap width and are displayed as black lines. We can see that the initial heating of the regions by the gap is similar to that of the ones in the perfect slab but they reach a lower temperature (independent of gap width) because some of the shock energy is used to accelerate them into the void. When the ejected (expanding) molecules collapse with the downstream part of the right slab (at a time that depends on void width) they re-compress and heat up to a temperature much higher than that attained in the perfect slab. Holian and collaborators proposed a model to explain this overheating based on the recompression of the evaporated ejecta and validated it with large-scale two dimensional MD simulations [4]. In agreement with their model we find that the over-heating increases with gap width and it can reach 1000 K even for a small gap (2 nm) for υ_p=*3 km /s*.

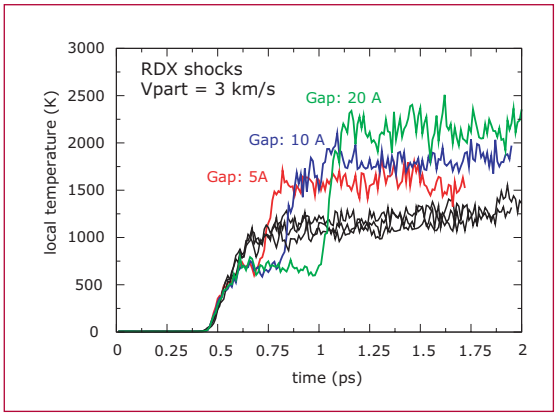

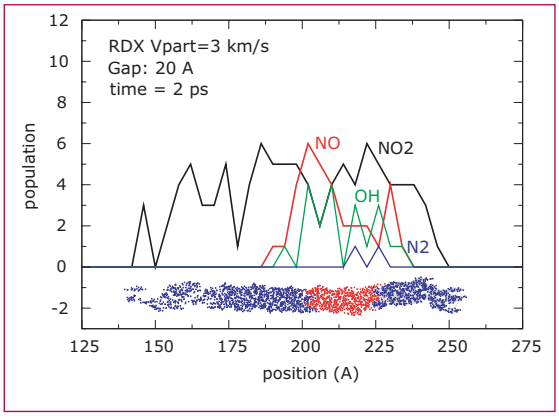

***Figure 2—** Time evolution of local temperature of the last two molecular monolayers of the upstream half of the right slab for lgap = 5 Å (red), lgap = 10 Å (blue), and lgap = 20 Å(green). We also show that time evolution of the local temperature of the corresponding (mirror) region in the perfect slab (black).*

***Figure 3—** Profile of the population of several species for t = 2 ps. RDX shock υ_p = 3 km /s, gap width 20 Å.*

Once we have quantified the local heating due to void-shock interaction the main question is: is the over-heating achieved with these void widths enough to significantly facilitate the chemistry? Figure 3 shows the profiles (along the shock propagation direction) of the population of four small molecules [NO_2 (black), NO (red), OH (green) and N_2 (blue)] at time t = 2 ps. Blue and red circles below the profiles show the atomic positions at t = 2 ps differentiating the atoms belonging to the perfect slab and to both portions of the defective slab. It is clear from Figure 3 that the profiles are very asymmetric with a larger quantity of products formed in the defective crystal. The quantities of NO and OH produced on the defective half are comparable to those obtained in perfect crystals for stronger shocks.

Conclusions

First Principles-based atomistic modeling of shock loading of high-energy nitramines have become feasible due to the development of the reactive force field ReaxFF. ReaxFF with MD allows full-physics, full-chemistry simulations of shock waves propagating in perfect and defective HE crystals and the chemical reactions they induced. It is important to stress that no approximation is made as to what type of chemical reactions are allowed or what type of molecules can be formed.

We found that even small gaps (few nanometers) can lead to a local increase in temperature of over 1000 K on top of the shock heating. This heating enhances and facilitates the initial chemical reactions. Much larger simulations will be necessary to establish if this enhancement is enough to generate a self-sustained detonation and consequently increase the sensitivity of the material or if instead it will die out. Future work will focus on quantifying the decrease in detonation threshold as a function of void size.

[1] M. R. Manaa, L. E. Fried, C. F. Melius, M. Elstner, and T. Frauenheim, *J. Phys. Chem. A,* 9024 (2002).

[2] A. C. Stachan, T. van Duin, D. Chakraborty, S. Dasgupta, and W. A. Goddard III, *Phys. Rev. Lett.* **91**, 098301 (2003).

[3] C. T. van Duin, S. Dasgupta, F. Lorant, and W. A. Goddard III, *J. Phys. Chem. A* **105**, 9396 (2001).

[4] L. Holian, T. C. Germann, J. B. Maillet, and C. T. White, *Phys. Rev. Lett.* **89**, 285501 (2002).

The Physics of SemiFlexible Polymers

Paul M. Welch, T-14; and Shirish Chitanvis, T-14; pwelch@lanl.gov

How does one predict the dynamics and size of double stranded DNA (dsDNA)? This is more than merely an academic question since answering it will provide insight into a myriad of biological processes. Within a living organism dsDNA is constantly compressed, stretched, transported across membranes, complexed with proteins, and even pulled apart. Though we typically think of the information that dsDNA encodes when we first consider modeling this polymer, it is the semiflexibility that is of importance when studying the chain's response to the mechanical rigors listed above. The dynamics of other polymers, both biological and synthetic, are similarly dominated by stiffness. Thus motivated, we are developing an analytical theory for semiflexible chains and comparing our predictions with computer simulations and scaling arguments.

The simplest theoretical picture for polymers, the "Gaussian Model," considers the chain to be a random walker characterized by a fixed-step length. Thus, the radius of the chain is predicted to vary as the square root of its molecular weight. But real polymers have dimensions dictated by more than just their bond length. Real systems are subject to energetic penalties when two chain segments overlap, for example. This "excluded volume interaction," in addition to local constraints such as bond angles and torsion angles, perturbs the dimensions away from that of a simple random walk. Therefore a chain in an environment where the overlap penalty is strong, such as in a good solvent, exhibits a radius that varies with molecular weight to the 3/5 power. When long-range repulsions or additional topological constraints are introduced, the polymer can behave more like a semirigid rod with its radius varying nearly linearly with molecular weight. The dsDNA, with its charges and helical topology, falls into this latter category. Naturally, these molecular details that determine a polymer's size also strongly affect its dynamics [1].

While the well-known Kratky-Porod "worm-like chain" model [2] captures many of the salient features of semiflexible polymers, it can be an analytically cumbersome framework to work within. This model begins with a microscopic description of the chain in which there is local stiffness arising from what is in essence a local bond angle constraint. The distribution of chain radii can be obtained from this model with relative ease when there are no intersegment interactions. However, the model quickly becomes unwieldy when excluded volume, charges, or external forces are introduced [3]. Our approach is both conceptually more simple and mathematically more tractable. Instead of beginning with a microscopic model, we picture the semiflexible chain at a coarse-grained level. The signature feature of semiflexibility is a segment-to-segment distribution function that deviates significantly from that of a random walker toward that of a semirigid rod-like structure. Rather than derive this, we begin our theoretical investigations by proposing a functional form that reflects this behavior and incorporates the thermal fluctuations of the local conformations. The proposed analytical form permits application of a number of field-theoretical tools, such as Renormalization Group and variational treatments, to investigate semiflexible chains decorated with a variety of interactions and subjected to external perturbations.

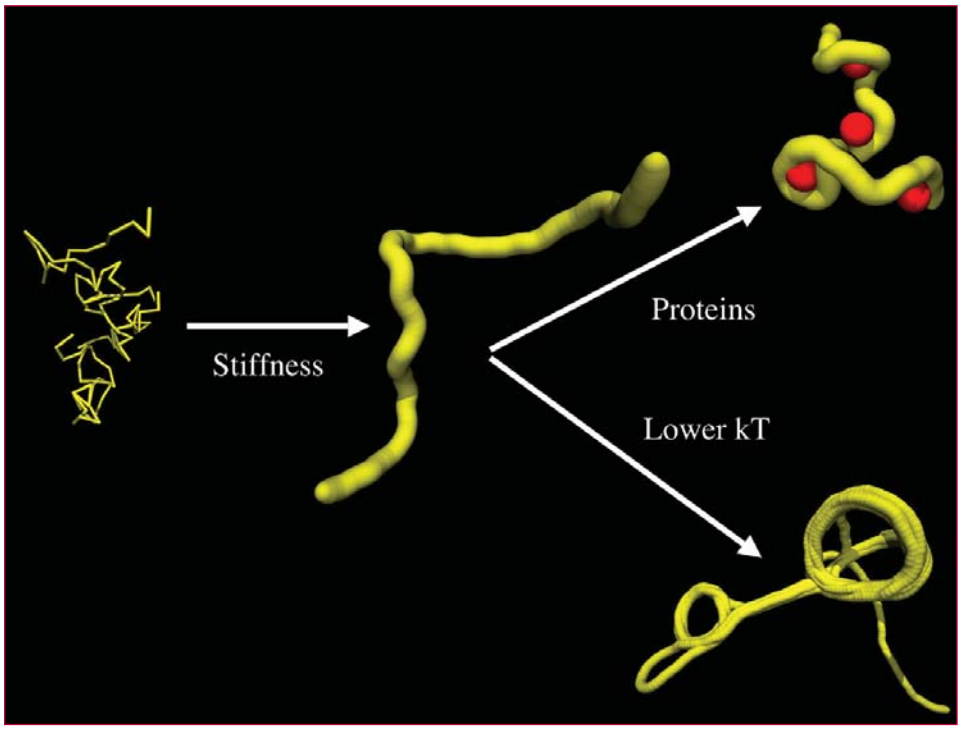

The figure caricatures some of the phenomena we are pursuing. The left-most portion contains a snapshot from a Monte Carlo simulation of a Gaussian chain. The central image typifies the snapshots from Monte Carlo simulations of the same chain after local stiffness has been introduced, demonstrating that increasing the stiffness along the backbone results in a swelling of the volume occupied by the polymer. The image in the bottom right corner derives from Brownian dynamics simulations of a longer semiflexible chain at lower temperatures. Dropping the temperature, equivalent to placing the chain in a poor solvent, forces the polymer into toroidal and "tennis racket" conformations [4]. Adding binding agents, such as proteins, causes the semiflexible chain to deform and wrap around the smaller inclusions [5]. The cartoon in the upper right corner illustrates the conformations we anticipate observing upon adding simple model proteins (the red balls) to the simulation. We are in the process of developing a theory for how these transitions depend upon the molecular and environmental details based upon our *ansatz* and computer simulations.

[1] P. G. de Gennes, *Scaling Concepts in Polymer Physics* (Cornell University Press, Ithaca, 1979).

[2] H. Yamakawa, *Modern Theory of Polymer Solutions* (Harper and Row, New York, 1971); O. Kratky and G. Porod, *Recl. Trav. Chim.* **68**, 1106 (1949).

[3] See for example: J. F. Marko and J. D. Siggia, *Macromolecules* **28**, 8759 (1995).

[4] See for example: B. Schnurr, F. C. MacKintosh, and D. R. M. Williams, *Europhysics Letters* **51**, 279 (2000); S. M. Chitanvis, *Physical Review E* **68**, 061802 (2003).

[5] See for example: P. Welch and M. Muthukumar, *Macromolecules* **33**, 6159 (2000).

T-16 Nuclear Physics

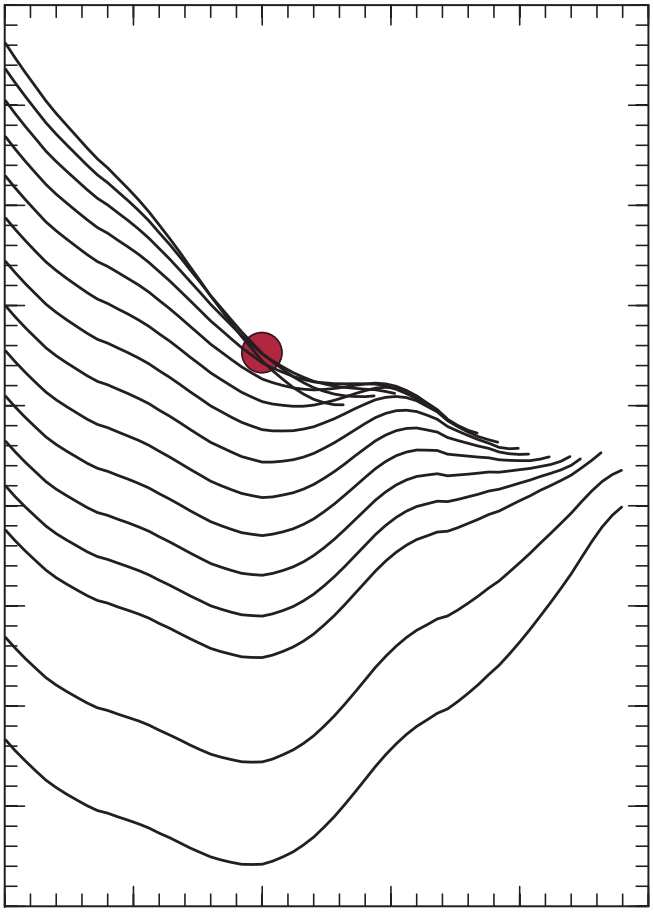

The Energy Surface at a Critical Point

Joseph N. Ginocchio, T-16; gino@lanl.gov

Dynamical systems such as nuclei can undergo phase transitions associated with a change of shape of their equilibrium configuration from spherical to deformed. For nuclei at the critical point of the phase transition between a spherical shape and a deformed shape, the energy surface is flat with respect to the quadrupole deformation β. The energy surface E (β) of Barium-134 is shown in Figure 1a as an example. Near $\beta = 0$ the energy surface increases like β^4 and does not have a stable minimum. Hence the dynamics of such nuclei cannot be treated accurately by assuming the nucleus has a rigid deformed shape.

The radius of the nucleus in the x, y, and z directions determines the shape of a deformed nucleus. However, the energy surface of these nuclei depends only on the average deviation from the spherical shape, which is proportional to β, but not on each individual radius. Therefore we computed the average energy surface E (β) by averaging over the relative lengths of the radii in the three directions. This average energy surface is shown in Figure 1b. This average energy surface has a stable minimum at an effective deformation $\beta_{eff} = 0.03$. This effective deformation provides good estimates for the excitation energies and quadrupole transition rates of critical point nuclei [1].

[1] A. Leviatan and J. N. Ginocchio, *Physical Review Letters* **90**, 212501 (2003).

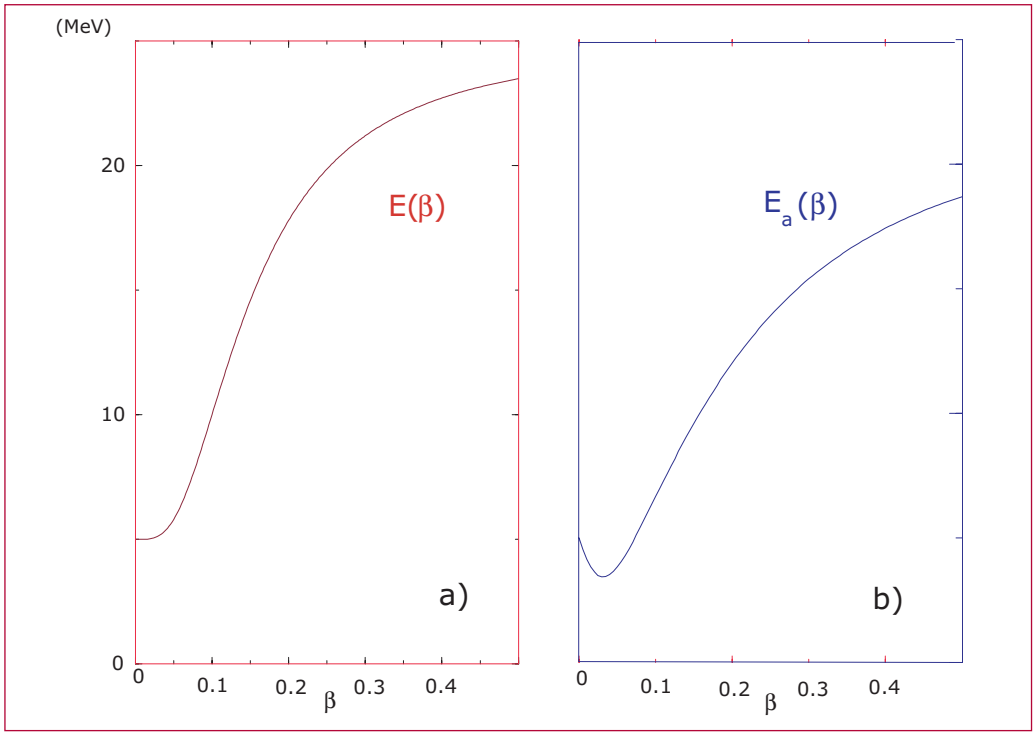

Figure 1—

Data for Charged-Particle Capture Reactions

Gerald M. Hale, T-16; ghale@lanl.gov

During the last fiscal year we have studied the capture processes associated with the thermonuclear burn (TNB) reactions for light systems in the mass range A=4–9. In some cases, these reactions are of interest as diagnostics of TNB in hot plasmas, and in all cases they are desired to give a more complete set of charged-particle reactions for the light nuclei. The study resulted in a new approach [1] to including photon channels in R-matrix theory, which is the primary theory we have used to describe nuclear reactions in the light systems. It also involved a generalization of the thermally-averaged quantities normally given for TNB to the limiting case of zero-mass particles (photons).

An example of the types of data analyzed is given in the figure, showing the calculated branching ratio for the d+t reactions compared to some of the data. Note that disagreements among the measurements are larger than a factor of three in some cases. The red curve shows the result finally used for this reaction. New measurements are planned later this year at the Omega facility at the University of Rochester to test this choice in a laser-imploded (ICF) *d-t* capsule.

[1] G. M. Hale and A. S. Johnson, "Results for n+p capture from an R-matrix analysis of N-N scattering," 17th Intl. IUPAP Conf. on Few Body Problems in Physics, Durham NC (June 2003).

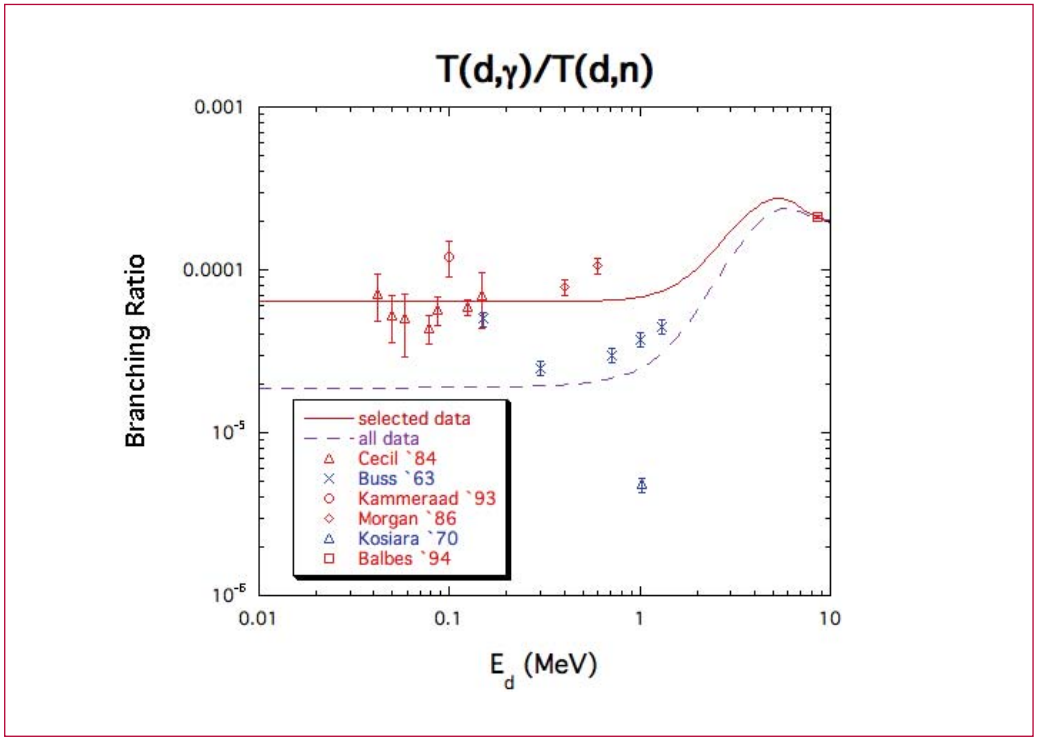

Figure—Branching ratio for the d+t reactions. The red curve, resulting from considering only the most recent measurements (red points), was used to produce the evaluated capture cross section.

Leptoquark Contributions to Atomic Electric Dipole Moments

Peter Herczeg, T-16; herczeg@lanl.gov

CP-violation (CPV) [1] has been seen in the mixing of the neutral kaons and recently also in the $K^0 \to 2\pi$ amplitudes and in the decays of the neutral B mesons. Although the observed effects can be accounted for by the Kobayashi-Maskawa phase δ_{KM} present in the quark mixing matrix in the Standard Model (SM), contributions from new CP-violating interactions are not ruled out. New sources of CP-violation are expected in many extensions of the SM. It is relevant to mention in this connection that δ_{KM} is not sufficient to generate the baryon asymmetry of the universe. The most suitable observables to probe the existence of new CP-violating interactions are those for which the contribution from δ_{KM} is small. Prominent examples of such observables are the electric dipole moments (EDMs) of the neutron and atoms, and the spin-flip parameter ν in molecules. The EDMs violate both parity (P) and time-reversal (T) invariance. Contributions to EDMs from CPT invariant interactions are therefore CP-violating.

We investigated the information on CPV couplings of leptoquarks (LQs) to the first fermion family provided by experimental bounds on atomic EDMS and ν [2]. LQs are bosons that couple to lepton-quark pairs. They occur in many extensions of the SM, for example in grand unified theories and in composite models. LQs can have zero spin or spin one. LQs that do not induce proton decay can potentially be light enough to cause observable effects in low-energy processes.

We investigated both contributions from single LQs, assumed to be in mass eigenstates, and contributions arising as a result of mixing of LQs of given SM quantum numbers. Let us consider as an example the coupling of the spin-one Q (= electric charge) = 2/3 leptoquark U_1 [3]. The coupling of the U_1 to the first fermion family has the form

$$L = \left[h'_{1L}\left(\bar{u}_L \gamma_\mu \nu_{el} + \bar{d}_L \gamma_\mu e_L\right) + h'_{1R}\bar{d}_R \gamma_\mu e_R \right] U_1^\mu + \text{H. c.} \qquad (1)$$

In (1) the effective coupling constants h'_{1L} and h'_{1R} contain the elements of the fermion mixing matrices.

Atomic EDMs and ν are induced by P,T-violating electron-nucleon and nucleon-nucleon interactions, and by the EDMs of the electrons, protons and neutrons [4]. Stringent experimental limits have been set on the EDMs of Tl, Cs, Hg, Xe, and on ν(TlF). The contributions to these from all the relevant LQs turn out to be dominated by the contribution from the electron-nucleon (e-N) interaction. The e-N interaction is induced by the electron-quark interactions resulting from the exchange of the LQs. For the U_1 the electron-quark interaction is of the form (see Figure)

$$H = \frac{\text{Im}\left(h'_{1L}h'^{*}_{1R}\right)}{M_1^2}\left(\bar{e}\, i\gamma_5 e\, \bar{d}d - \bar{e}e\, \bar{d}\, i\gamma_5 d\right), \qquad (2)$$

where M_1 is the mass of the U_1. We find that the best limit on (2) comes from d(Tl). The experimental limit $|d(Tl)| < 9.4 \times 10^{-25}$ ecm (90% c.l.) yields

$$\left|\text{Im}\left(h'_{1L}h'^{*}_{1R}\right)\right| < 2 \times 10^{-8}\left[\frac{M_1}{250\ \text{GeV}}\right]^2. \qquad (3)$$

This implies that the strength of the interaction (2) cannot be stronger than about $10^{-7}\ G_F$, where G_F is the Fermi constant, characterizing the strength of

the weak interaction! A limit on $\mathrm{Im}(h'_{1L}h'^{*}_{1R})$ comes also from the direct experimental limit $|d_n| < 6.3 \times 10^{-26}$ ecm (90% c.l.) on the EDM of the neutron. This limit is weaker than (3) by five orders of magnitude.

The limits on the strength of the LQ-exchange interactions for the other cases are in the range of few times 10^{-8} G_F to 10^{-6} G_F. We note yet that the experimental limits on atomic EDMs and molecular P, T-violating observables are expected to improve in the future considerably[5].

[1] For reviews, see L. Wolfenstein, hep-ph/0210025; Y. Nir, *Nucl. Phys. B* (Proc. Suppl.) **117**, 111 (2003).

[2] P. Herczeg, *Phys. Rev. D* 6**8**, 116004 (2003).

[3] For references regarding various aspects of the subject see Ref. [2].

[4] For a review, see I. B. Khriplovich and S. K. Lamoreaux, *CP-Violation Without Strangeness* (Springer-Verlag, Berlin, 1997).

[5] For a review, see M. V. Romalis, in *The Expanding Frontier of Atomic Physics*, Proceedings of the XVIII International Conference on Atomic Physics, Cambridge, MA, edited by H. R. Sadeghpour, E. J. Heller, and D. E. Pritchard (World Scientific, Singapore, 2003), p. 317.

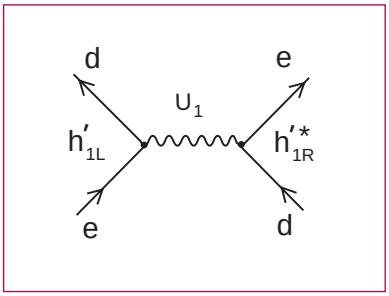

Figure—
The contribution of U_1-exchange to P, T-violating electron-quark interactions.

Correlated Neutron Emission in Fission: Initial Results

Sebastien Lemaire, Patrick Talou, Toshihiko Kawano, David G. Madland, and Mark B. Chadwick, T-16; lemaire@lanl.gov

Discovered about 65 years ago, the phenomenon of fission of heavy nuclei, either spontaneous or induced, still remains a challenge for theoretical interpretation. From the fundamental point of view, when a slow moving neutron strikes a heavy nucleus like uranium it breaks up into two fragments. The puzzling feature of this reaction is how a nucleus consisting of well over 200 protons and neutrons could split into two pieces with so little provocation.

Since then there have been numerous theoretical attempts to better understand the fission process.

The research we have been doing relates to correlated prompt neutron emission in fission. It is motivated by needs in detecting correlated neutrons from a fission chain, for active and passive detection of special nuclear materials for nonproliferation applications.

So far, to calculate the neutron energy spectrum and the average number of prompt emitted neutrons per fission ($\bar{\nu}$) the Los Alamos model (or Madland-Nix model) [1] is used, but it doesn't incorporate any information on neutron correlations, such as the probability $\boldsymbol{P}(\nu)$ of observing ν neutrons from fission and other various neutron energy correlations. This model implements the Weisskopf compound nucleus evaporation process and addresses both induced and spontaneous fission. It accounts for the fission fragment excitation energies, the energy dependence of the inverse process of compound nucleus formation (provided by an optical model potential with an explicit isospin dependence to describe as well as possible neutron rich fission fragments), the motion of the fission fragments emitting neutrons, and multiple-chance fission at higher incident neutron energies.

To go further, we have begun implementation of a Monte-Carlo simulation of the statistical decay of the fission fragments by sequential neutron emission. Initial work on the correlations within the emitted neutron energy spectrum for the n(0.53 MeV) + ^{235}U reaction has been completed and we report on that here.

We first investigate the center of mass neutron energy spectrum given by this approach. It has been compared with the result obtained with the original calculation of Madland-Nix. Reasonable agreement is achieved giving us confidence in our other calculated quantities.

In particular, we can now calculate the neutron multiplicity distribution $\boldsymbol{P}(\nu)$, in addition to the average multiplicity $\bar{\nu}$. Figure 1 illustrates the neutron multiplicity distribution. A Gaussian fit to this distribution gives an average number of emitted neutrons of $\bar{\nu} = 2.08$ (to be compared with the experimental value $\bar{\nu}_{exp} = 2.47$). In comparison to the experimental neutron multiplicity from Terrell [2] our distribution falls too sharply.

A partial explanation may be that the same average neutron binding energy $\langle B_n \rangle = 6.7$ MeV has been used in our

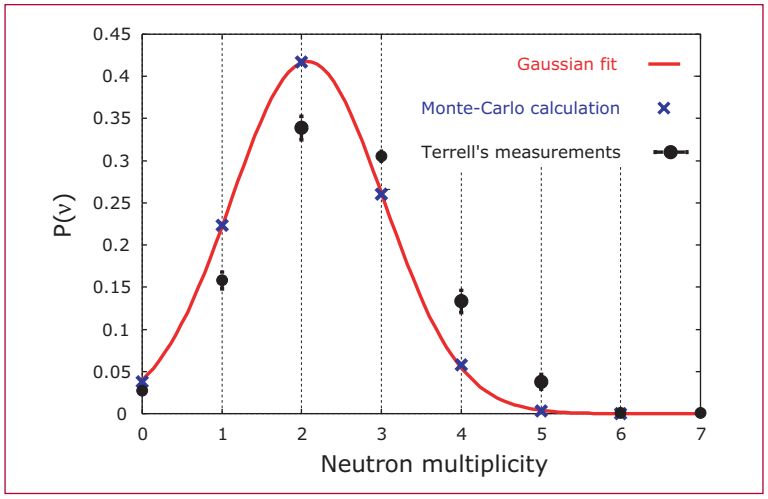

Figure 1— Neutron multiplicty distribution.

calculations to evaporate neutrons from successive residual fission fragment although B_n varies strongly with mass number A for nuclei away from the beta-valley of stability, hence affecting the total number of neutrons emitted through the sequence.

A more likely explanation may be the constraint that we have imposed: the initial excitation energies of the two fission fragments are uncorrelated. We will relax this constraint in our future work.

We are also interested in the correlations between the energies of the first and second emitted neutrons from the fission fragments (Figure 2). In particular, our first results show that the first-neutron energy spectrum is harder than that of the second neutron.

In the near future we shall extend this approach to sample over the entire fission fragment mass distribution, with an explicit dependence of the neutron binding energy B_n on the mass number, and with and without correlations in the initial fragments excitation energies.

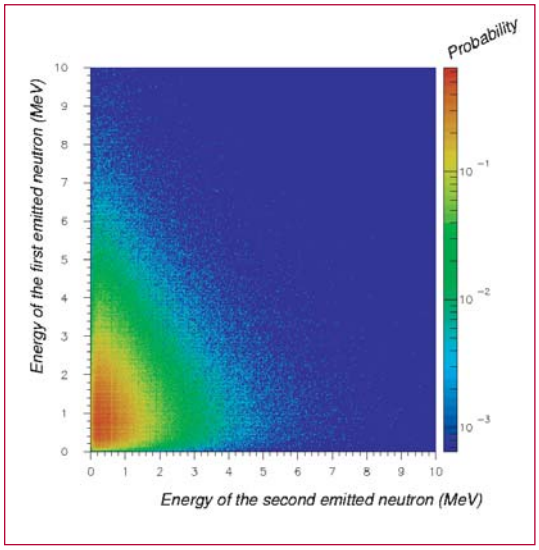

Figure 2— Neutron energy correlations.

[1] D. G. Madland and J. R. Nix, *Nucl. Sci. Eng.* **81**, 213 (1982).

[2] J. Terrell, *Phys. Rev.* **108**, 783 (1958).

Fission Barriers at the End of the r-Process

Peter Möller and Arnold J. Sierk, T-16; Ragnar Bengtsson (Lund, Sweden), and Peter Olivius (Lund, Sweden); moller@lanl.gov

A large part of the elements on earth heavier than iron have been formed in stars in the rapid-neutron-capture process, abbreviated r-process. In an intense neutron environment, nuclei capture neutrons and reach isotopes close to the neutron drip line, β-decay to more proton-rich elements that again capture neutrons. The process continues until the very heaviest elements near uranium are reached within a time-span of a few seconds. Here the process terminates, probably because nuclei become unstable to fission. An isotope may fission immediately following neutron capture, or after β-decay, so-called β-delayed fission. To model the r-process in the heavy-element region it is necessary to know the fission-barrier heights of nuclei in this region.

We are calculating fission barriers of several thousand nuclei with nucleon number $A \geq 190$. In the region near the ground state to slightly beyond the second minimum corresponding to fission isomers, we calculate the barrier in terms of three shape parameters ε_2, ε_4, and axial asymmetry γ, see [1] for a definition of this shape parameterization. For the region from slightly before the second minimum to beyond, towards fission-fragment separation, we use our three-quadratic-surface parameterization and explore five-dimensional multi-million grid-point deformation spaces as described in [2,3].

The inner-barrier region of many actinide nuclei can be described in terms of a deformed ground state at about $\varepsilon_2 \sim 0.20$) followed by a first barrier peak at about $\varepsilon_2 \approx 0.40$ and a second minimum at around $\varepsilon_2 \approx 0.55$. However, for many neutron-rich nuclei in our current calculation, the inner barrier region is much more complex, which makes it difficult to characterize the inner barrier in these terms. An example is shown in Figure 1.

Our calculations are still very much "in progress." At this point we have obtained outer barrier heights calculated in our full 5-D deformation space for a long sequence of uranium isotopes cf. Figure 2. A striking feature is the region of quite low barriers near $A = 260$. In one case the calculated neutron separation energy is about equal to the barrier height. Thus, the r-process might not progress beyond this point. Other nuclear-structure quantities that are needed to model the r-process are, for example, various reaction Q-values, β-decay half-lives, and the magnitude of branchings to β-delayed fission and β-delayed neutron emission. We are also calculating these quantities within our global nuclear-structure model framework [1,3,4].

[1] P. Möller, J. R. Nix, W. D. Myers, and W. J. Swiatecki, *Atomic Data Nucl. Data Tables* **59**, 185 (1995).

[2] P. Möller, D. G. Madland, A. J. Sierk, and A. Iwamoto, *Nature* **409**, 785 (2001).

[3] P. Möller, A. J. Sierk, and A. Iwamoto, *Phys. Rev. Lett.* **67**, 072501 (2004).

[4] P. Möller, B. Pfeiffer, and K.-L. Kratz, *Phys. Rev. C,* **67**, 055802 (2003).

Figure 1—
Calculated potential-energy surface for ^{264}U. The energy has been calculated versus three shape parameters, ε2, ε4, and γ. The displayed energy has been minimized with respect to ε4 at each point in ε2 and γ. In the general case this procedure does not give a correct representation of the important structures in the full, higher-dimensional space, but in this case they appear in the 2-D surface. Our tabulated saddle-point heights are determined from an analysis of the full 3-D space by a water-immersion technique [2]. Minima are indicated by colored dots and saddle points by crossed lines. The nuclear shapes corresponding to some of the minima have been plotted in the colors corresponding to the dots. It is clear that the structure of this nucleus is much more complicated than a deformed ground state separated from a fission-isomeric minimum by a single peak. We count five minima and four saddle points in the figure.

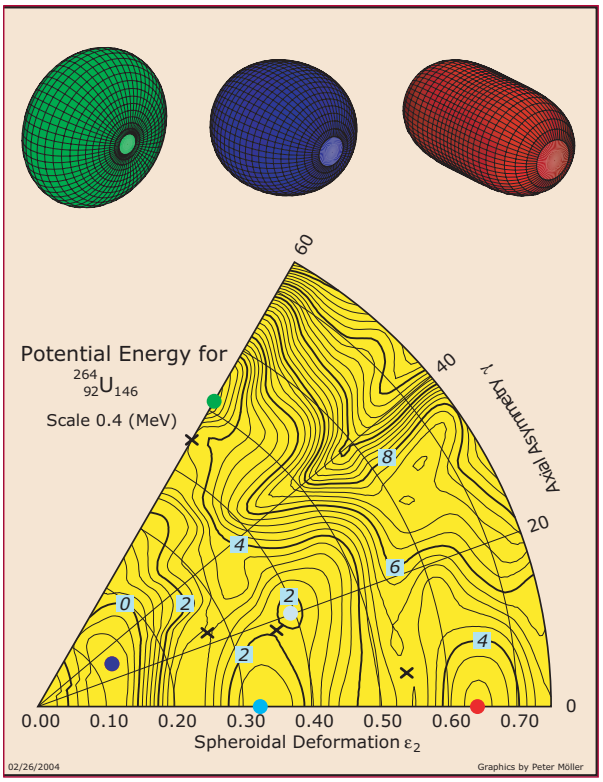

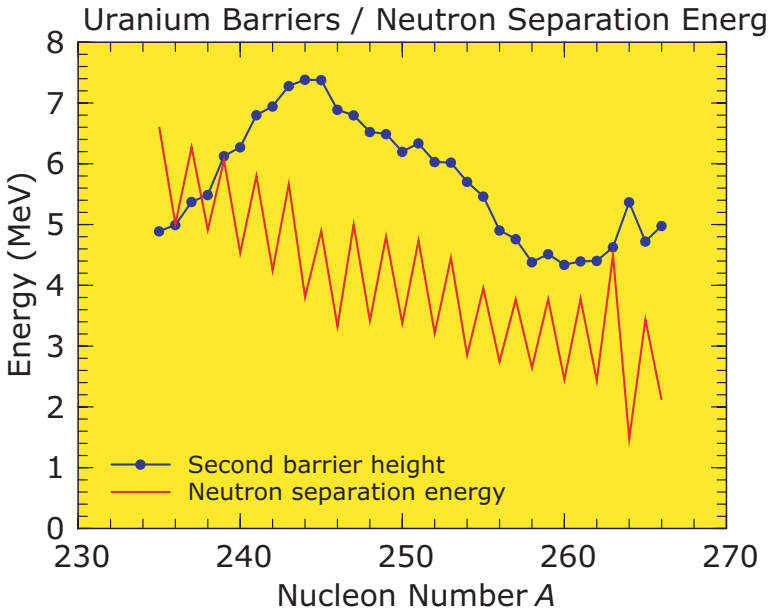

Figure 2—
Outer fission-barrier saddle-point heights obtained in a five-dimensional calculation and calculated 1n separation energies. There is a region of low-barrier heights near A = 260. The inner barrier height is about the same height or lower, as can be seen for ^{264}U in Figure 1. Thus the r-process may terminate near A = 260.

Potential-Energy Sufaces for Heavy-Ion Collisions

Peter Möller and Arnold J. Sierk, T-16; Akira Iwamoto (Tokai, JAERI); and Takatoshi Ichikawa (Tokai, JAERI); moller@lanl.gov

The six heaviest man-made elments with proton number Z ranging from 107 to 112 have all been made in heavy-ion reactions in which an appropriate light projectile nucleus is accelerated to a specific energy and is then brought to collide with a ^{208}Pb or ^{209}Bi target. It is well known that the target and projectile completely fuse and form a surviving nucleus only if the collsion energy is in a very narrow range, about 5 MeV. The favorable energy is thought to correspond to an energy interval just above the energy barrier (fusion barrier) between target and projectile. This barrier arises because the positive charges of the target and projectile nuclei repel each other until they have approached sufficiently close so that the stronger, but short-range, attractive nuclear force dominates. Even when the energy is in the favorable range only one collision in about 10^{18} leads to formation of a new element. To see one event of this type requires days to weeks of "beam time" at a major accelerator. It is therefore desirable to develop an accurate model of the fusion-barrier height so that the collision energy can be optimally chosen.

It is well known that the "Coulomb barrier"calculated in simple macroscopic models assuming spherical targets and projectiles is much higher than the optimal energy for forming heavy evaporation residues in heavy-ion collisions. We therefore use a more realistic approach and calculate below the energy of a colliding heavy-ion system as

$$\begin{aligned} E_{\mathrm{P+T}}(\varepsilon_{2\mathrm{P}}, \varepsilon_{2\mathrm{T}}, X_{\mathrm{P}}, y_{\mathrm{P}}, z_{\mathrm{P}}, \alpha, \beta, \gamma) &= E_{\mathrm{P}}^{\mathrm{self}}(\varepsilon_{2\mathrm{P}}) - E_{\mathrm{P}}^{\mathrm{self}}(\varepsilon_{2\mathrm{P}} = \mathrm{gs}) \\ &+ E_{\mathrm{T}}^{\mathrm{self}}(\varepsilon_{2\mathrm{T}}) - E_{\mathrm{T}}^{\mathrm{self}}(\varepsilon_{2\mathrm{P}} = \mathrm{gs}) \\ &+ E_{\mathrm{PT}}^{\mathrm{int}}(\varepsilon_{2\mathrm{P}}, \varepsilon_{2\mathrm{T}}, \chi_{\mathrm{P}}, y_{\mathrm{P}}, z_{\mathrm{P}}, \alpha, \beta, \gamma) \end{aligned} \quad (1)$$

Here $E_{\mathrm{P+T}}$ is the total energy of the colliding system relative to infinitely separated targets and projectiles in their ground states (gs). The quantity E^{self} is the macroscopic-microscopic potential energy as a function of shape as given by our FRLDM model [1,2]. Since we give the system energy *relative* to the separated fragments we obviously need to subtract the ground-state self-energies of the target and projectile; thus the second and fourth terms in the right member of (1) above. The interaction-energy-term calculation is extensively discussed in [3]. We assume that the *interaction* shell-correction energy can be neglected for separated target and projectile. However, it is taken into account, and is important for the self-energy terms. The Cartesian triplet (X_{P}, y_{P}, z_{P}) gives the location of the center of the projectile relative to the center of the target. The Euler angles α, β, and γ specify the orientation of the projectile symmetry axis relative to the target symmetry axis. The energetically most favorable configuration, at least for prolate deformations, for a specific distance between target and projectile, is when the axes of the target and projectile are collinear. To limit the problem to a moderately low-dimensional parameter space we therefore only consider these relative positions of target and projectile and only spheroidal deformations $\varepsilon_{2\mathrm{T}}$ and $\varepsilon_{2\mathrm{P}}$ of the target and projectile, respectively. Thus, we have $X_{\mathrm{P}} = 0$, $y_{\mathrm{P}} = 0$, $\alpha = 0$, $\beta = 0$, and $\gamma = 0$, so that the space we investigate is 3-dimensional and is characterized by target and projectile spheroidal deformations and their relative distance z_{P}. We have found that the doubly-magic ^{208}Pb is strongly stabilized by the microscopic-energy (shell-correction) contribution to

the self-energy and therefore remains spherical.

We now argue that if the system loses stability with respect to target and/or projectile deformation as the ions approach each other then the energy at which this occurs defines a more realistic fusion-barrier height. In Figures 1 and 2 we show the energy of the colliding system for a spherical target versus projectile deformation for a succession of distances as the projectile approaches the target for two heavy-ion reactions. We indicate by a big blob the energy corresponding to the "conventional" Coulomb barrier calculated as the maximum in the macroscopic energy between spherical target and projectile. For the light compound system, our more realistic model gives a barrier that is only marginally lower than given by the conventional Coulomb-barrier model but for the heavy system we obtain a difference of more than 10 MeV. Thus, there is a large effect from shell-correction and deformation effects which were previously usually ignored in the context of heavy-ion collisions.

It is also of interest to study the energy after the target and projectile have come into contact. We have performed such calculations in the current version of our macroscopic-microscopic model in which we calculate the nuclear potential energy for several million different shapes for five different shape degrees of freedom and determine the structure of potential by imaginary water flow [2,4]. The result for the system ^{272}Ds is shown in Figure 3. The similarity of the fusion-valley shape with the touching configuration in the collision and the ridge "shielding" the fusion valley from the fission valley both facilitate the formation of a compound system.

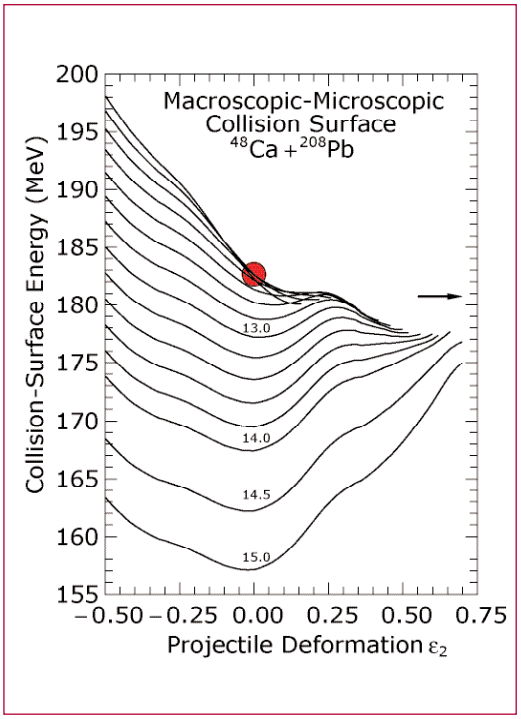

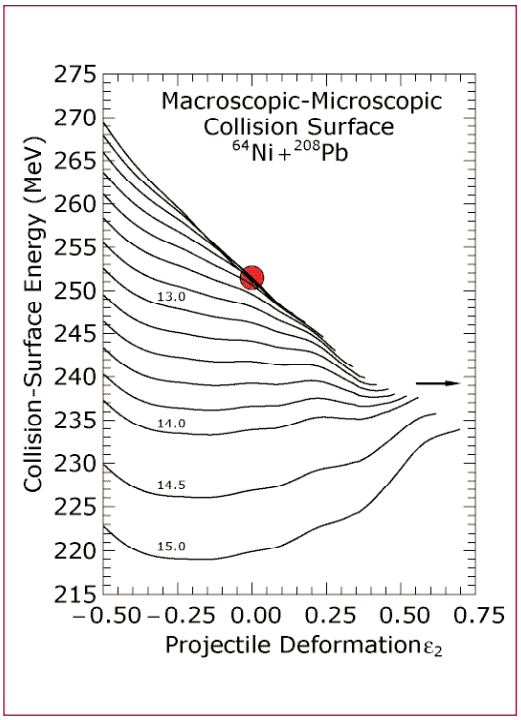

Figure 1—Calculated macroscopic-microscopic potential energies for the collision of $^{48}Ca + ^{208}Pb$. Each of the plotted curves shows the center-of-mass energy of the system versus projectile deformation, for spherical ^{208}Pb and a specific distance between the centers-of-mass of the target and projectile. The distance in fermi is written above the potential-energy curve. For distances less than 14.0 fm the separation between projectile and target decreases by 0.2 fm for each successive curve. The dot corresponds to the calculated value of the one-dimensional "Coulomb barrier" in a macroscopic model. The arrow indicates the potential-energy at the point when the projectile becomes unstable with respect to deformation, due to the field of the target nucleus.

Figure 2—Same as Figure 2, but for the collision $^{64}Ni + ^{208}Pb$. Here the difference between the conventional Coulomb barrier and the collision-surface saddle-point height is substantial.

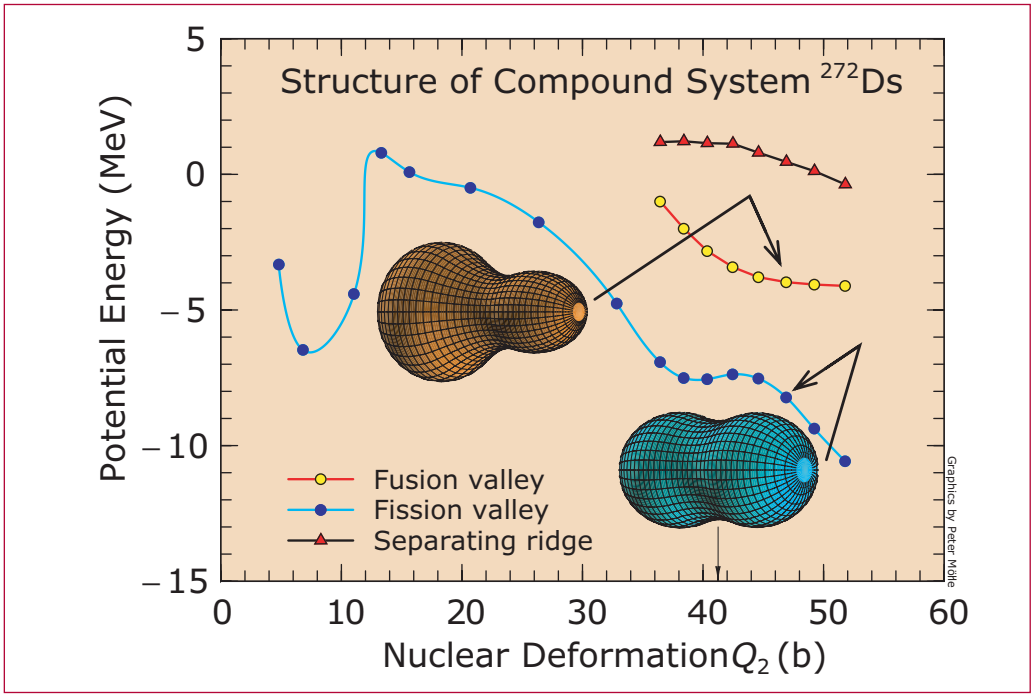

Figure 3—Structures in the calculated 5-D potential-energy surface of ^{272}Ds. The lower curve corresponds to the fission barrier. For large values of Q_2 there is an additional well-defined valley in the 5-D energy surface, which is stabilized with respect to the fission valley by the ridge shown in the top curve. One shape in the fission valley and one shape in the additional valley are shown. The shape in the fission valley is mass symmetric. The shape in the other valley is asymmetric. The two partially formed nuclei correspond closely to the target and projectile masses; the ratio between the heavy and light nuclear masses is $M_H / M_L = 201/71$.

[1] P. Möller J. R. Nix, W. D. Myers, and W. J. Swiatecki, *Atomic Data Nucl. Data Tables* **59**, 185 (1995).

[2] P. Möller, D. G. Madland, A. J. Sierk, and A. Iwamoto, *Nature* **409**, 785 (2001).

[3] P. Möller and A. Iwamoto, *Nucl. Phys.* **A575**, 381 (1994).

[4] P. Möller, A. J. Sierk, A. Iwamoto, *Phys. Rev. Lett.* **67**, 072501 (2004).

Studies of Fission-Product Yields with Improved Data Bases for β-Decay Half-Lives and β-Delayed Neutron-Emission Probabilities (II)

Peter Möller and William B. Wilson, T-16; moller@lanl.gov

Delayed neutrons (DN) are important for the nuclear weapons ASCI program. Specifically, we perform actinide integral data testing against unclassified critical-assembly measurements since one must account for DN in the simulations of these experiments. DN also play a role in nonproliferation projects at the Laboratory, including detecting clandestine HEU using active interrogation.

We have previously discussed how we have extended our original, microscopic QRPA-FY model to account also for first-forbidden decays in a statistical model [1]. This and other models of ours are able to provide not only calculated values for β-decay half-lives, $T_{1/2}$, and β-delayed neutron-emission probabilities P_n, for decays from the nuclear ground state, but also provide these for decays from spin-isomeric states. In addition, they provide single-particle levels and complete β-strength functions for nuclei throughout the nuclear chart.

We have now applied the model to the calculation of $T_{1/2}$ and P_n for nuclei throughout the periodic system. This calculated data set [1] has been incorporated into the CINDER data libraries and it also serves as a data base in various astrophysical nucleosynthesis calculations. In our CINDER data libraries we use experimental data for $T_{1/2}$ and P_n where available. The experimental data are from the NuBase data file [2]. We base calculations of temporal delayed-neutron production in ^{235}U, ^{238}U, and ^{239}Pu, and other fission systems on the CINDER'90 library corresponding to this set supplemented by calculated values.

A brief summary of our results are as follows. Calculated temporal DN production rates for ^{235}U fission systems are shown in Figures 1–3, but we have also carried out studies for ^{238}U fast and high-energy fission and for ^{239}Pu thermal, fast, and high-energy fission. The calcualtions based on the NuBase experimental data and our calculations of $T_{1/2}$ and P_n otherwise agree better with data than do calculations based on a previously used data set denoted England 1994 in seven out of eight studied reactions and about equally well in the remaining reaction.

We have earlier carried out calculations with another experimental evaluations. During those calcualtions we became aware that this evaluation was incompletely documented. In one of our calculations with the earlier evaluation, incorrect data were present for two nuclei. We use studies with this earlier data base as an interesting "parameter study" and find that the difference between calculations with the incorrect data present and a calculation with these two known errors corrected is as large as the difference between our current results and those based on the England 1994 set.

While we are extremely pleased with the current convergence of the calculated and recommended experimental DN temporal production data, we make the following further observations. It is somewhat disconcerting that different data values for just two (high-yield) fission isotopes affect the calculations enormously. This indeed shows that the evaluated experimental data set needs to

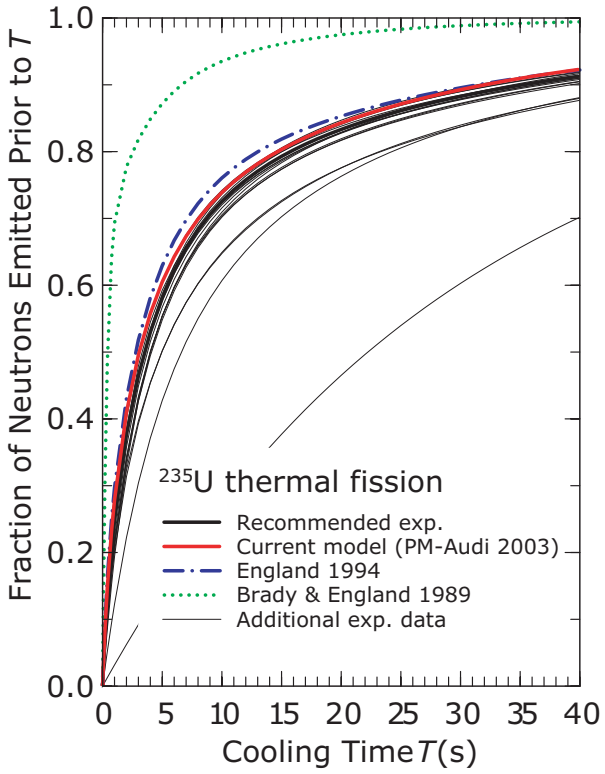

Figure 1—Comparisons of measured temporal DN production following ^{235}U thermal fission and calculations based on CINDER'90 with $T_{1/2}$ and P_n from set NuBase where available, otherwise from our theoretical model. The current model exhibits a striking improvement relative to the calculations based on the at-the-time existing $T_{1/2}$ and P_n values and the England 94 yields.

be maintained in a form that is easily subjected to analysis and review. Moreover it is clear that accurate (preferably experimental) data for high-yield isotopes are necessary. We are currently establishing collaborations to set up such a data base for $T_{1/2}$ and P_n. It is also highly desirable to understand details of the fission yield with high accuracy.

More details about our work can be found in the publications listed below, and other publications available at *http://t16web.lanl.gov/Moller/abstracts.html.*

[1] U. C. Bergmann, C. A. Diget, K. Riisager, L. Weissman, G. Aubock, J. Cederkall, L. M. Fraile, H. O. U. Fynbo, H. Gausemel, H. Jeppesen, U. Koster, K.-L. Kratz, P. Möller, T. Nilsson, B. Pfeiffer, H. Simon, K. Van de Vel, and J. Aysto, "Beta-Decay Properties of the Neutron-Rich $^{94-99}$Kr and $^{142-147}$Xe Isotopes," *Nucl. Phys. A* **714,** 21–43 (2003). LA-UR-02-6963.

[2] Peter Möller, William B. Wilson, Bernd Pfeiffer, and Karl-Ludwig Kratz, "β-Delayed Neutron Emission," in LA-UR-03-2682.

[3] Peter Möller, Arnold J. Sierk, Takatoshi Ichikawa, and Akira Iwamoto, "Global Calculations of Fission Barriers and Beta-Decay Properties of Neutron-Rich Nuclei," Proc. Conf. on Origin of Matter and Evolution of the Galaxies, November 17–19, 2003 RIKEN, Wako, Saitama, Japan (World Scientific, Singapore, 2004). LA-UR-04-0448.

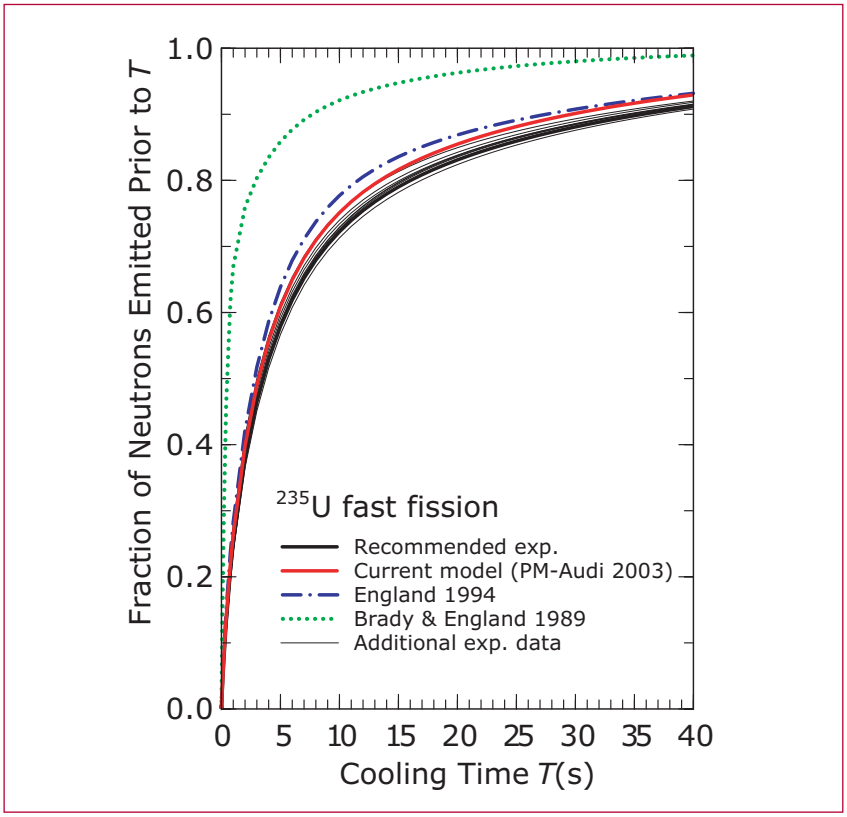

Figure 2—Same as Figure 1, but for ^{235}U fast fission.

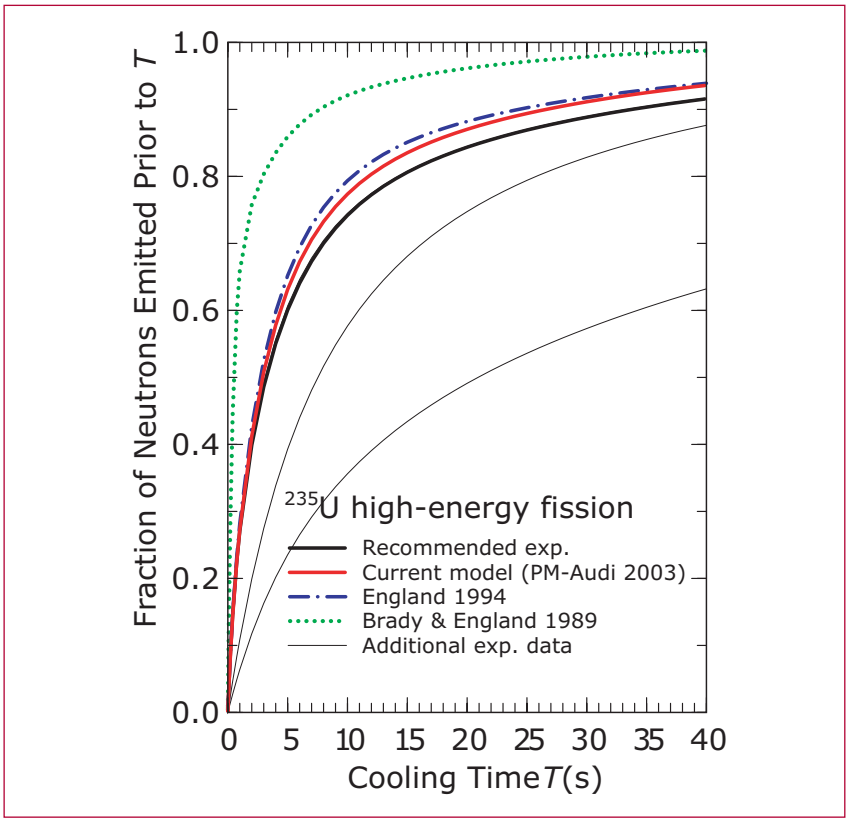

Figure 3—Same as Figure 1, but for ^{235}U high-energy fission.

The ^{8}Be Nuclear Data Evaluation

Philip R. Page and Gerald M. Hale, T-16, prp@lanl.gov

A R–matrix analysis of experimental nuclear data on the reactions ^{4}He(α,α), ^{4}He(α,p), ^{7}Li(p,α), ^{7}Li(p,p), ^{7}Li(p,n), ^{7}Be(n,p), ^{6}Li(d,α), ^{6}Li(d,p) and ^{6}Li(d,n) leading to the ^{8}Be intermediate state is being performed. The excitation energy above the ^{8}Be ground state has been brought up to 22–24 MeV for all reactions except ^{4}He(α,α) and ^{7}Be(n,p). The data for the reactions ^{4}He(α,α) and ^{4}He(α,p) do not fit well, but the other six reactions fit with a reasonable χ^2/(point). The possibility of two units of orbital angular momentum between ^{7}Li and p, and between ^{7}Be and n, was added. Most of the resonances found in the R-matrix analysis correspond to resonances formerly known from experiment. There are 17 resonances in the 2003 analysis, while there were only 10 resonances in the 2002 analysis. The figure indicates the 2003 R-matrix analysis cross section in barns for the ^{7}Li(p,n) reaction up to a proton laboratory energy $E_{lab\ p}$ of 3 MeV. Two sets of experimental data are also showed.

Details of the 2003 analysis are available in [1].

[1] P. R. Page, "Status of ^{8}Be Nuclear Data Evaluation," LANL Memo T-16: NW-125/9-03 (2003).

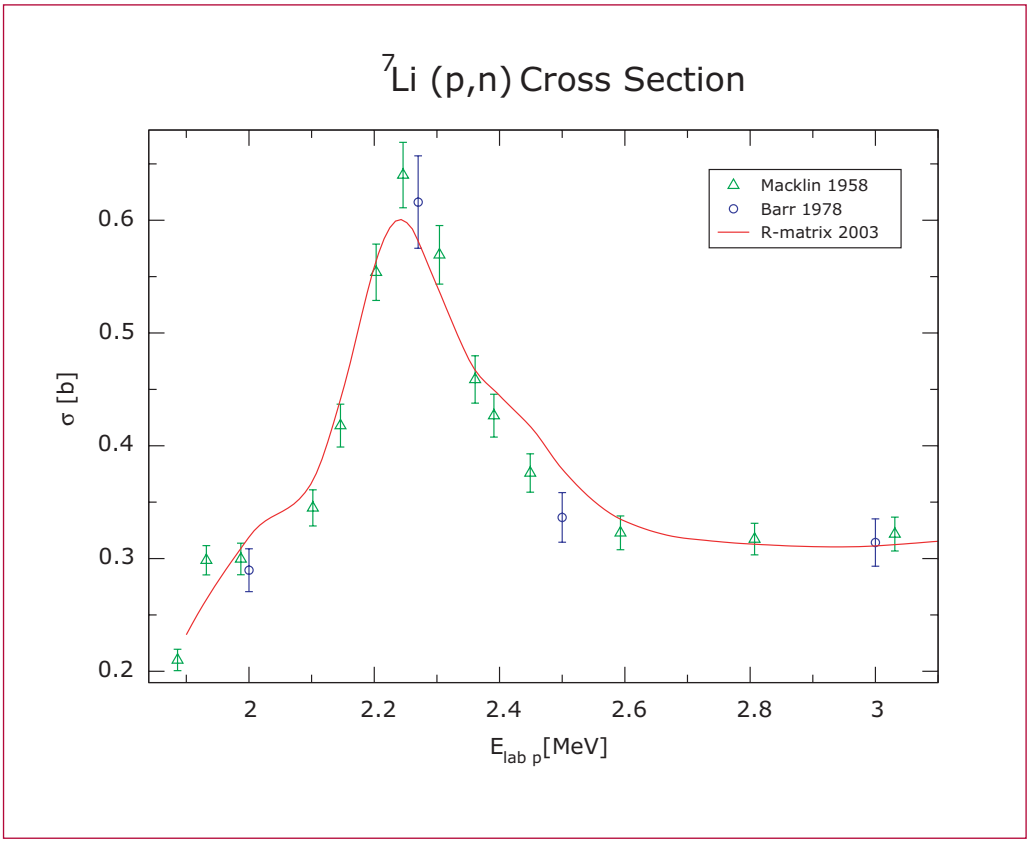

Figure— indicates the 2003 R-matrix analysis cross section.

Iridium Nuclear Cross Sections for Radchem

Patrick Talou, Mark B. Chadwick, and Robert E. MacFarlane, T-16; Ronald O. Nelson and Nikolaos Fotiadis, LANSCE-3; Holly R. Trellue, D-5; Morgan C. White and Stephanie C. Frankle, X-5; talou@lanl.gov

Iridium plays a unique role in radiochemical diagnostics of nuclear weapons performance. Many detectors were developed to study high-energy (~14 MeV) fusion reactions using threshold (n,2n) reactions, and to study low-energy processes via the (n,γ) capture process. However, iridium is uniquely used to study fast neutrons in the few-MeV region, particularly prompt fission neutrons.

The ^{193}Ir(n,n') reaction to the isomer is used for these diagnostics. Measuring the production of the isomer is also a uniquely difficult problem, and was solved by some of the great figures from LANL's radchem past, such as Jim Gilmore, Don Barr, and Moses Attrep. The experimental problem was so difficult that other labs, such as Livermore and AWE, relied upon Los Alamos radiochemistry for this task!

However, to interpret the Nevada Test Site (NTS) post-detonation data, one needs an accurate cross section for the isomer production. Some earlier measurements were made above 7.5 MeV at Los Alamos, by Bayhurst *et al.*, but no data existed below this energy, and the historic cross section data set was based purely on nuclear theory predictions from T-Division.

Our new results represent a LANSCE – T-Division collaboration, where the GEANIE gamma-ray detector was used to measure important contributions to the cross section, and the GNASH code was used to predict important (but unmeasured) additional contributions. The GEANIE/GNASH results cover the whole energy range region of interest, from threshold at 80 keV to above 20 MeV. Figure 1 validates our GNASH theory code through comparisons with the gamma-ray measurements. Figure 2 shows our new evaluated cross section for the isomer production, that is needed in the X-Division applications.

In the few-MeV region we have additional measurements from a critical assembly experiment at LANL's LACEF facility at TA-18, and these comparisons provide an important validation of the energy-dependence of our cross section. Our new results are being provided to X-Division in different nuclear data table formats by X-5.

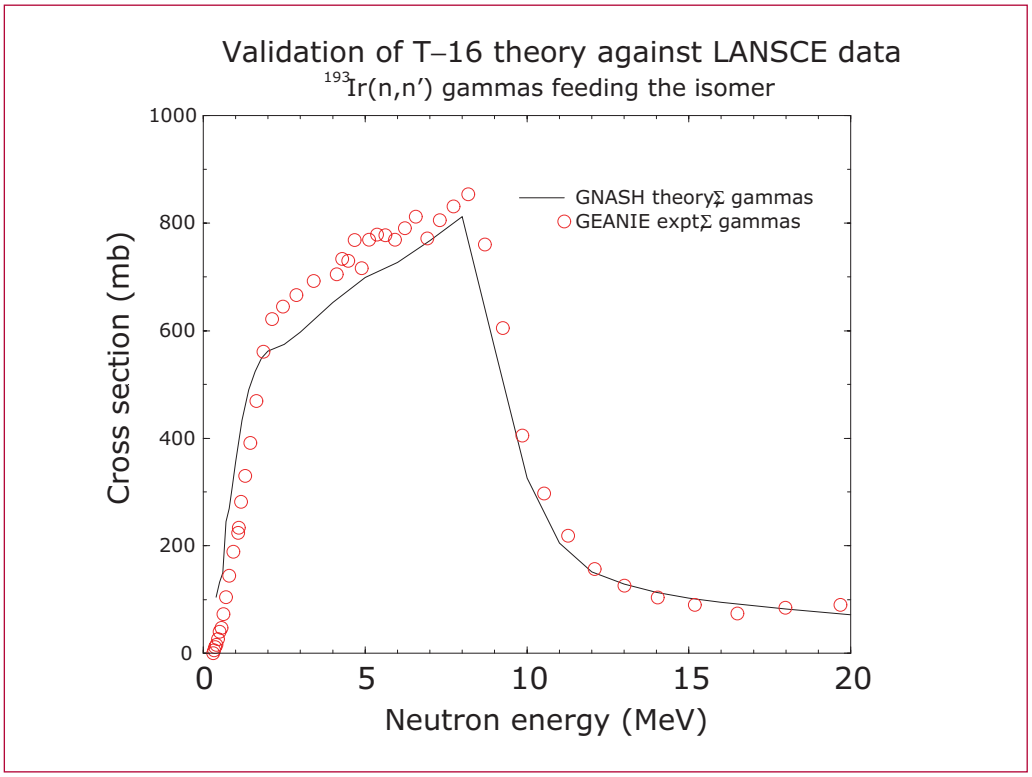

Figure 1— Validation of our theoretical (GNASH) calculations against LANSCE data for the sum of the four strongest gamma-lines feeding the isomer.

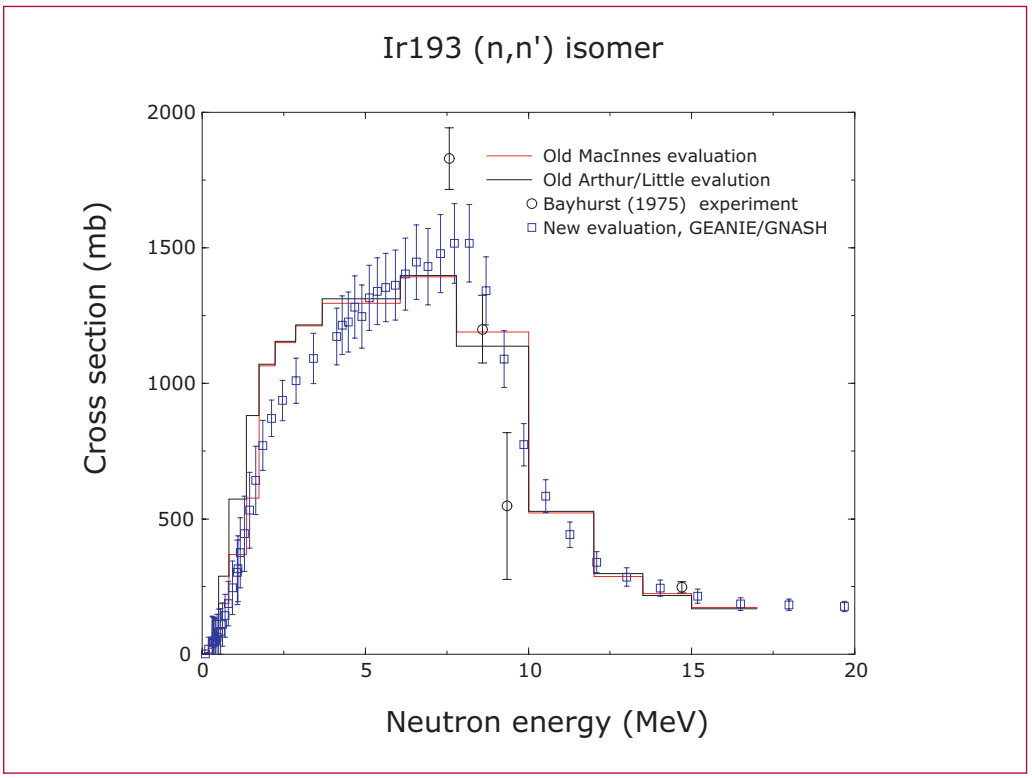

Figure 2— New evaluated cross section for the Ir-193 (n,n') Ir-193m isomer production vs. older existing evaluations and activation measurement data.

New Suite of Evaluated Nuclear Reaction Cross Sections on Uranium Isotopes

Phillip G. Young Jr., Patrick Talou, Robert E. MacFarlane, Mark B. Chadwick, Toshihiko Kawano, David G. Madland, Peter Möller, and William B. Wilson, T-16; pgy@lanl.gov

Group T-16 has completed a new suite of evaluated neutron reaction cross section files for uranium isotopes ranging from A = 232 to 241. The new cross section evaluations are important for weapons simulations of yield and inventory diagnostics. The nuclear data have been processed by X-5 into a number of different formats (including NDI), for use in a variety of ASCI and legacy X-Division burn codes. We have received useful and positive feedback on their performance, and further feedback from X-Division users will lead to future improvements to these cross section sets.

These files were released in the standard ENDF format and provide a complete representation of all important reaction cross sections, such as capture, fission, inelastic, (n,2n), (n,3n), etc., as well as energy spectra of the emitted neutrons (prompt and delayed). These studies encompass the neutron incident energy range from sub-keV to 30 MeV, and the files were combined with existing ENDF/B-VI data files at lower energies to form a complete evaluation from 10^{-5} eV up to 30 MeV. These evaluations represent a major improvement over the previous available US database for these elements.

Because some of these isotopes are unstable, very few measurements exist, in particular for capture and fission reactions, to guide the evaluations, and the role of nuclear modeling therefore plays a very important role. The theoretical analyses involved complex coupled-channels optical model calculations with the ECIS code and statistical Hauser-Feshbach plus preequilibrium computations with the GNASH code. Both codes have been developed and tested over the years and constitute the backbone of most modern T-16 evaluation studies.

A very important ingredient entering in such calculations is a reliable optical model potential, which is used not only to get accurate neutron total, elastic and inelastic cross sections (and angular distributions), but also to provide reliable particle transmission coefficients for the GNASH calculations. Therefore, a large part of the analysis consisted in obtaining such a reliable optical model potential, and involved assessing various existing potentials.

The relative strength of the fission channel is notoriously very difficult to obtain accurately with theoretical input only. In our reaction calculations, the fission channel importance depends on so-called fission barrier parameters that are quite difficult to estimate accurately, and even small variations of their values can often lead to quite different fission cross sections. In this study, an effort was made to obtain/refine these parameters from a combined analysis of all uranium target isotopes studied in the present work. Some parameters were finally optimized to better fit experimental data available for some isotopes.

As an integral part of this evaluation process, the new released files have been tested in Monte-Carlo MCNP simulations of critical assemblies at the LACEF experimental facility. The new files performed very well in these new

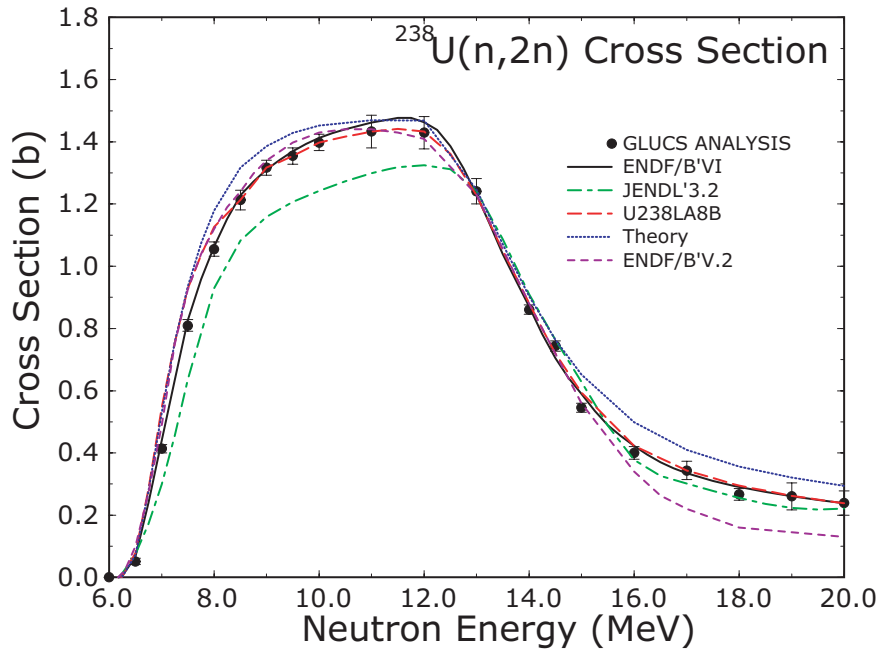

Figure 1— The $^{238}U(n,2n)$ cross section from threshold to 20 MeV. The solid circles (GLUCS ANALYSIS) are a composite of the available experimental data obtained in a covariance analysis. The smooth curves compare our current analysis ($U_{238}LA8B$) with existing ENDF/B-VI, JENDL-3.2, and ENDF/B-V.2 data evaluations and with a theoretical calculation using the GNASH nuclear theory code.

Critical Assembly Data Testing of LANL ENDF6++

	Old ENDF/B-VI	New ENDF6++
Godiva (^{235}U)	0.9961	0.9993
Flattop- ^{235}U	1.0018 (bias)	1.0024
Jezebel (^{239}Pu)	0.9978	1.0004
Flattop- Pu	1.0033 (bias)	1.0019
Jezebel-23 (^{233}U)	0.9925 (v. bad!)	0.9987
Flattop- ^{233}U	1.0024 (bias)	0.9999
BigTen (lots of 238)	1.0127 (v. bad!)	0.9985

k-eff C/E shown

Notes:

ENDF6++ more reactive with better k-eff

^{233}U greatly improved

^{238}U reflection problem largely improved (flattop versus unreflected k-eff)

BigTen now much better (due to 238 inelas)

BUT: Godiva spectral index 238f/238f C/E=0.961 (calc = too soft)

calculations, with some major improvements, compared to previous evaluations. Note that in order to be used in such MCNP simulations, the files were first successfully processed through the NJOY nuclear data processing code.

Author Index

A

Abazajian, Kev 200
Abdallah, Jr., Joseph 174, 176
Addessio, Francis L. 4, 30
Akahane, Y. 176
Albers, Robert C. 234, 236
Alder, Berni 240
Aoyama, M. 176
Ashbaugh, Henry S. 258
Austin, Travis M. 52

B

Bardenhagen, Scott G. 280, 282
Baskes, Michael 270
Baumgardner, John R. 6
Bedrov, Dmitry 298
Berman, Gennady P. 88, 90, 92
Bengtsson, Ragnar 328
Bergen, Benjamin K. 52
Berndt, Markus 34, 52
Bhattacharya, Tanmoy 202
Bishop, Alan R. 88, 246, 266
Blottiau, P. 182
Boozer, A. H. 120
Borgonovi, F. 88
Bouchet, Johan M. 236
Bower, Kevin 122
Brackbill, Jeremiah U. 118
Brand, Holmann V. 142, 252
Bronkhorst, Curt A. 8
Brown, Eric 142
Bulaevskii, Lev 238
Burakovsky, Leonid 128

C

Carlson, Neil N. 54, 56
Cerreta, Ellen K. 8
Chacón, Luís 98
Chadwick, Mark B. 326, 340, 342
Challacombe, Matt 154, 254, 260
Chisolm, Eric D. 130, 132, 134, 136, 138, 144, 178
Chitanvis, Shirish M. 284, 316

Choi, C. H. 246
Cleave, Antony R. 274
Clements, Brad E. 140, 142, 152
Colgate, Sterling A. 190
Collins, Lee A. 178, 182
Cooke, W. 102
Crockett, Scott D. 130, 132, 134, 138, 144, 178
Csanak, George 110, 112, 176

D

Dalvit, Diego A. 88
Dattelbaum, Dana M. 142, 252
Daughton, William S. 112, 118
De Lorenzi-Venneri, Giulia 130, 146
Delzanno, Gian L. 100
Dendy, Joel E. 52
Desjourlais, M. 178
Dienes, John K. 286
Dimonte, Guy 240
Dodelson, Scott 200
Donley, Derek 214
Dukowicz, John K. 6

.

F

Faeder, James R. 76
Faenov, A. Ya. 176
Feldman, Hume 210
Fenimore, Paul W. 68, 260
Finn, John M. 102
Fontes, Christopher J. 174
Fotiadis, Nikolaos 340
Frankle, Stephanie C. 340
Fraser, Andy 36
Frauenfelder, Hans 68
Fryer, Christopher L. 194
Fukuda, Y. 176

G

Gan, Chee Kwan 254
García, Angel E. 70, 72
Garimella, Rao V. 38
George, Denise C. 130, 148, 152
Germann, Timothy C. 240, 242, 244, 262, 288
Ginocchio, Joseph N. 320
Glasser, Alan H. 104, 106

Gnanakaren, S. 72
Goldstein, Bryon 76
Gray III, George T. 8, 142
Greenbaum, Ben 224
Grimes, R. W. 274
Gruber, Jason 148
Guadagnini, A. 62

H

Habib, Salman 200, 202, 204, 206, 208, 210, 212, 214, 216, 218, 220, 222, 224, 228, 230
Hadjiconstantinou, Nicolas G. 240
Hakel, Peter 174
Hale, Gerald M. 322, 338
Hanson, David E. 256
Harlow, Francis H. 24, 26
Harstad, Eric N. 142
Hatch, D. M. 234
Hay, P. Jeffrey 258
Hayes, Anna C. 192
Hayes, Dennis B. 4
Heim, Andrew J. 288
Heitmann, Katrin 200, 204, 206, 208, 214, 216, 218, 220
Hengartner, Nick W. 36
Henkelman, Graeme 260, 274
Hennig, R. G. 234
Henson, Neil J. 142, 252
Herczeg, Peter 324
Higdon, David 218
Hlavacek, William S. 76, 80
Hochstrasser, Robin M. 72
Holian, Brad Lee 240, 242, 244, 262, 268, 288, 306
Holmström, Erik 156
Hruska, Marina M. 238
Hsu, S. C. 120
Hui, Lam 206, 216
Hungerford, Aimee L. 194
Hunke, Elizabeth C. 6, 10
Hyman, J. Mac 44, 54

I

Ichikawa, Takatoshi 330
Inoue, N. 176
Iwamoto, Akira 330

J

Jacobs, Kurt 202, 222
Jain, Bhuvesh 214
Jiang, Yi 40
Jaramillo, Eugenio 290
Jensen, Niels G. 288
Johnson, J. D. 130
Johnson, Paul 218
Jones, M. D. 234
Jones, Phillip W. 6
Jungman, Gerard 192

K

Kadau, Kai 240, 242, 244
Kalosakas, Georgios 246
Kamenev, Dmitry I. 90, 92
Kashiwa, Bryan A. 12
Kawano, Toshihiko 326, 342
Kilcrease, David P. 174
Knoll, Dana A. 98
Kober, Edward M. 248, 288, 292, 294
Kress, Joel D. 178, 182, 258, 264, 268
Kress, Kerri Jean 142, 252
Kronberg, Phillip 212
Kuprat, Andrew P. 148, 150

L

LaBute, Montiago 260
Lapenta, Giovanni M. 100, 108, 118
Leitner, Thomas K. 82
Lemaire, Sebastian 326
Lewis, Matthew W. 142
Li, Hui 120, 122
Li, Weiye 44
Lidz, Adam 204, 206, 216
Lipnikov, Konstantin 48
Lipscomb, William H. 6, 10
Lomdahl, Peter S. 240, 242, 244
Lookman, Turab 248
Loubère, Raphaël 50
Lushnikov, Pavel 94

M

Ma, Xia 14
Mabuchi, Hideo 202
MacFarlane, Robert 340, 342
Maciucescu, Luca A. 142
McMahon, Benjamin H. 68, 260
Madland, David G. 326, 342
Magee, Norman H. 174, 178
Magunov, A. I. 176
Makhlin, Yu 238
Maltrud, Mathew E. 6, 16, 18
Mas, Eric M. 140, 142, 152
Maudlin, Paul J. 8, 30, 140
Mazevet, Stephane F. 174, 178, 182
Menikoff, Ralph 296
Middleditch, John 286
Milne, Peter A. 194
Möller, Peter 328, 330, 334, 342
Montalenti, F. 274
Morel, Jim E. 48
Moulton, John D. 52
Murillo, Michael S. 110, 112

N

Nebel, Richard A. 116
Nelson, Ronald O. 340
Nemeth, Karoly 260
Niklasson, Anders M. N. 154, 156, 158, 170

O

O'Rourke, Peter J. 20
Onuchic, Jose N. 70
Olivius, Peter 328
Orler, Edward B. 142

P

Pack, Russell T 264
Padial-Collins, Nely 22, 28
Page, Philip R. 338
Park, J. Y. 116
Pasqualini, Donatella 218
Pikuz, T. A. 176
Preston, Dean L. 128

R

Rae, Philip 142
Raman, R. 120
Rasmussen, Kim Ø. 246, 248, 298
Rauch, Michael 206
Rauenzahn, Rick M. 12
Redondo, Antonio 268
Reichhardt, Charles 266
Reichhardt, Cynthia J. 266, 268
Ricci, Paolo 118
Richardson, S. 102
Ricker, Paul 208
Robbins, David L. 142
Rohrer, Gregory S.148
Rollett, Anthony D. 148
Rose, Harvey A. 94
Rudin, Sven P. 158, 160, 162, 164, 170, 234
Ryan, Jessica M. 142, 252
Ryne, Robert 204

S

Salazar, Michael 264
Sargent, Wallace 206
Schlei, Bernd R. 166, 168
Schraad, Mark W. 24
Sewell, Thomas D. 254, 290, 298
Shashkov, Mikhail J. 34, 48, 50, 54, 56, 58
Shaw, M. Sam 300, 302
Sheffield, Stephen 142
Sherrill, Manolo E. 174, 186
Shizume, Kosuke 222, 224
Shnirman, A. 238
Sickafus, Kurt E. 274
Sierk, Arnold J. 328, 330
Skobelev, I. Yu. 176
Smith, Darryl L. G. 238
Smith, Grant D. 292, 298
Smith, James S. 292
Smith, Justin R. 18, 30
Smith, Richard D. 6
Smith, Roger 274
Srivilliputhur, S. G. 234
Staley, Martin F. 58
Steck, Daniel 202
Steinkamp, Michael J. 26
Stokes, H. T. 234

Strachan, Alejandro H. 306, 308, 312
Strange, S. 116
Sundaram, Bala 224
Swart, Blair K. 38
Switzer, Eric 200
Szalay, Alex 220
Szsapudi, István 226

T

Taccetti, J. M. 116
Talou, Patrick 326, 340, 342
Tang, Xianzhu 120, 122
Tartakovsky, Daniel M. 62
Teodoro, Luís F. 196, 204, 210, 226
TenCate, James A. 218
Thompson, Russell B. 248, 298
Torres, David J. 20
Tracy, E. R. 102
Trellue, Holly R. 340
Trinkle, D. R. 234
Tsifrinovich, V. I. 90, 92
Tung, Chang-Shung 84, 260

U

Uberuaga, Blas P. 270, 274
Ueda, H. 176
Usheva, A. 246

V

Valone, Steven M. 270
VanderHeyden, W. Brian 22, 28
Vixie, Kevin R. 36
Voter, Arthur F. 270, 274

W

Wall, Michael E. 80
Wang, Zhehui 124
Wallace, Duane C. 130, 132, 134, 136, 138, 144, 146
Warren Michael S. 196, 208, 226
Weber, Valery 154
Welch, Paul M. 316
White, Morgan C. 340
Wilde, Bernhard, H. 26

Wilkins, J. W. 234
Wills, John M. 130, 132, 156, 158, 160, 162, 170
Wilson, William B. 334, 342
Wohlberg, Brendt E. 36, 64

X

Xu, Yongzhong 212, 228, 230

Y

Yamakawa, K. 176
Young, Phillip G. 342
Young, Robert D. 68

Z

Zhang, Duan Z. 14, 28
Zhang, Honglin 174
Zou, Qisu 28
Zuo, Q. Ken 30, 286